

DTIC FILE COPY

12

ARCCB-SP-87023

PROCEEDINGS OF THE
FIFTH U.S. ARMY SYMPOSIUM ON GUN DYNAMICS

AD-A186 238

THE INSTITUTE ON MAN AND SCIENCE
RENSSELAERVILLE, NY

23-25 SEPTEMBER 1987

DTIC
ELECTE
OCT 22 1987
C&D

SPONSORED BY
U.S. ARMY ARMAMENT RESEARCH, DEVELOPMENT
AND ENGINEERING CENTER
CLOSE COMBAT ARMAMENTS CENTER
BENET LABORATORIES
WATERVLIET, NY 12189-4050

APPROVED FOR PUBLIC RELEASE: DISTRIBUTION UNLIMITED

FOREWORD

The theme of the 1987 Symposium was Gun System Dynamics. The Symposium was divided into five sessions: (I) Analytical Dynamics, (II) Data Analysis - Correlation, (III) Computer Codes and Models, (IV) Experiments and Metrology, and (V) Electromagnetic Propulsion/Stochastic Modeling. The Proceedings follow the same format..

During recent years, one has witnessed great strides in various branches of continuum mechanics, kinematic designs, and numerical and computer techniques for solving problems of great complexity as well as in the areas of experimental mechanics and instrumentation. Now more than ever it appears feasible to gain understanding and to improve the design of gun systems for greater accuracy by exploiting new technological advances. The Fifth Symposium represents the continuing interest of the United States Army in this direction.

The Proceedings of the Fifth U.S. Army Symposium on Gun Dynamics contains the technical papers presented at the Symposium held at the Institute on Man and Science, Rensselaerville, New York, 23-25 September 1987. The papers represent the current research efforts on gun dynamics and the effect on precision and design by industrial, university, and Department of the Army, Department of the Navy, and Department of Energy laboratories throughout the United States, and two allied nations - the United Kingdom and the Federal Republic of West Germany.

I am grateful to everyone who submitted a paper for inclusion in the Proceedings. Unfortunately, however, not all of the papers arrived in time to be included. Every effort will be made to publish these papers in a supplement at a later date.

As in previous years, I am delighted by the number of scientific and technical people who have gathered to share their knowledge and experience.

Thomas F. Simkins, Chairman
Fifth U. S. Army Symposium on Gun Dynamics



Allocation For	
NTIS GRA&I	<input checked="" type="checkbox"/>
DTIC TAB	<input type="checkbox"/>
Unannounced	<input type="checkbox"/>
Justification	
By	
Date	
Availability Codes	
1. 2. 3. 4. 5. 6. 7. 8. 9. 10.	
A-1	

CONTENTS

SESSION I. ANALYTICAL DYNAMICS

DYNAMICS OF MOVING MASSES AND RECOIL INSTABILITY IN GUNS 1

I.G. Tadjbakhsh

THE GASDYNAMICS OF PERFORATED MUZZLE BRAKES.....10

G.C. Carofano

GAS FLOWS THROUGH SMALL HOLES IN GUN TUBE WALLS.....30

H.J. Sneek

IMPACT RESPONSE OF HIGH CYCLIC RATE FLEXIBLE MECHANISMS.....44

P. Benzkofer, C.W. Chang, and A.A. Shabana

RESONANCE OF FLEXURAL WAVES IN GUN TUBES.....64

T.E. Simkins

SESSION II. DATA ANALYSIS - CORRELATION

THE EFFECTS OF INTERIOR HEATING ON THE ACCURACY OF TANK GUNS.....79

J.N. Walbert

ANALYSIS OF THERMALLY INDUCED BARREL DISTORTION FROM FIRING.....80

M. L. Bundy

TECHNIQUES FOR THE ANALYSIS OF MICROBALLISTIC DATA FROM PROJECTILES IN FREE FLIGHT.....	95
--	----

S.A. Coates

THREE-GUN TURRET SALVO FIRING ACCURACY IN USS IOWA CLASS BATTLESHIPS.....	106
--	-----

J.J. Yagla

SESSION III. COMPUTER CODES AND MODELS

DYNACODE-G/P AND ITS APPLICATION TO THE 120 MM TANK GUN.....	129
--	-----

M.T. Soifer and R.S. Becker

MODELING GUN DYNAMICS WITH DOMINANT LOADS.....	150
--	-----

T.F. Erline and M.D. Kregel

THE THEORETICAL MODELLING OF THE DYNAMICS OF INITIALLY NON-STRAIGHT BARRELS USING FINITE DIFFERENCE TECHNIQUES.....	151
--	-----

S.E. Powell and P.H.G. Penny

A COMPARISON OF THEORETICAL JUMP FOR RIFLED AND NON-RIFLED BARRELS.....	153
---	-----

D.N. Bulman

NORMAL MODES ANALYSIS OF GUN VIBRATIONS BY THE UNIFORM SEGMENT METHOD.....	175
---	-----

R.G. Gast

USER EXPERIENCE WITH ABAQUS AT BENET LABORATORIES.....	202
--	-----

G.P. O'Hara

ADAPTING COSMIC NASTRAN TO GUN DYNAMICS PROBLEMS.....	203
---	-----

P.A. Cox and M.A. Polcyn

A SIMPLE THEORETICAL MODEL FOR PROJECTILE IN-BORE MOTION OF ELECTROMAGNETIC RAILGUNS.....	204
--	-----

S.H. Chu

SESSION IV. EXPERIMENTS AND METROLOGY

GUN DYNAMICS MEASUREMENTS FOR TANK GUN SYSTEMS.....	224
---	-----

B.T. Haug and J.A. Bornstein

AN ACCOUNT OF SOME EXPERIMENTS UNDERTAKEN TO CORRELATE MEASURED GUN BARREL FEATURES WITH THE MOVEMENT OF SERIAL MEAN POINTS OF IMPACT.....	241
--	-----

P.H.G. Penny and J.A. Perry

INVERTED DYNAMIC CHARACTER OF SMOOTH-BORE CANNON.....	242
---	-----

D.W. Petty and J.N. Walbert

EXPERIMENTAL MEASUREMENTS OF GUN TUBE MOTION DUE TO CURVATURE AND SUPPORT INDUCED LOADS.....	243
---	-----

G.A. Pflegl

STATE-OF-THE-ART TECHNIQUES FOR THE MEASUREMENT OF THE INITIAL PROJECTILE MOVEMENT IN GUNS AT THE ERNST-MACH-INSTITUTE, FRG.....	245
--	-----

G. Zimmermann and H. Grumann

AN EXPERIMENTAL INVESTIGATION INTO IN-BORE YAW IN A RIFLED BARREL USING THE RMCS AIR POWERED GUN.....	259
--	-----

G. Barker

SESSION V. ELECTROMAGNETIC PROPULSION/STOCHASTIC MODELING

STOCHASTIC MODELING FOR IMPROVED WEAPON PERFORMANCE.....	284
--	-----

A. Baran, J. Groff, H. Cohen,
J. Cantor, S. Carchedi, and B. Gibbs

NUMERICAL PREDICTIONS OF EML SYSTEM PERFORMANCE.....	300
--	-----

N.M. Schnurr, J.F. Kerrisk, and R.F. Davidson

RAIL DAMAGE IN A SOLID ARMATURE RAIL GUN.....	317
---	-----

T.V. Brassard and C.G. Homan

STRUCTURAL INTEGRITY OF METALLIC ARMATURE RAIL GUNS.....	328
--	-----

G.P. O'Hara and M. Cascio

TRANSVERSE VIBRATIONS OF ELECTROMAGNETIC RAILGUNS.....	344
--	-----

S.H. Chu

SESSION 1

ANALYTICAL DYNAMICS

Dynamics of Moving Masses and Recoil Instability in Guns

Iradj Tadjbakhsh

Department of Mechanical Engineering, Aeronautical Engineering and Mechanics
Rensselaer Polytechnic Institute

Troy, New York 12180-3590

The problem of mechanical interaction of a fast accelerating projectile and a flexible gun tube is considered. Models that show the effect of shear deformation and finite speed of axial wave propagation is presented. It is shown that projectile acceleration may cause loss of stiffness of the system and hence a strong indication of occurrence in dynamic instability.

Present Assignment: Professor of Civil Engineering and Mechanical Engineering

Past Experience: Teaching and research in industrial and academic institutions.

Degrees Held: Ph.D.

Dynamics of Moving Masses and Recoil Instability in Guns

Iradj Tadjbakhsh*

Department of Mechanical Engineering, Aeronautical
Engineering and Mechanics
Rensselaer Polytechnic Institute
Troy, New York

INTRODUCTION

Gun dynamics generally falls in a larger class of problems involving interaction of fast moving rigid masses or projectiles with flexible structures. The problem is even more complex if in addition to mechanical interaction thermal effects are also considered.

A great deal of prior work has taken place in the general area of dynamics of moving masses on a beam or string. These problems have important structural applications in diverse fields such as bridge design and space applications [1-3]. Additionally these problems generally lead to dynamical systems with temporal and spatial variation of mass, damping and flexibility matrices.

BASIC EQUATIONS

We shall begin our study of the dynamics of moving projectile and a gun tube by considering the idealized situation of a moving mass M on an inextensible elastica as shown in Fig. 1. Confining our attention to the vertical plane of the gun and the gravitation we denote the position vector of a material point by

$$\underline{r} = x(s,t)\underline{i} + y(s,t)\underline{j} \quad (1)$$

where s and t denote respectively the arc length and time. If the position of the projectile on the medium is denoted by $\bar{s}(t)$ then the velocity and acceleration of the projectile is given by

$$\underline{v}_M = \frac{d}{dt} (\underline{r}|_{s=\bar{s}}) = (\underline{v} + \bar{s}_t \underline{t})_{s=\bar{s}} \quad (2)$$

$$\underline{a}_M = \{ \underline{a} + \bar{s}_{tt} \underline{t} + [2\bar{s}_t \theta_t + (\bar{s}_t)^2 \theta_s] \underline{n} \}_{s=\bar{s}} \quad (3)$$

where subscripts s and t denote differentiation with respect to these quantities and \dot{y} and \ddot{a} are the velocity and acceleration of the material point of the elastica. The vectors $\underline{\tau}$ and \underline{n} denote the unit tangent and normal vectors

$$\underline{\tau} = \underline{\tau}_s = \cos\theta \cdot \underline{i} + \sin\theta \cdot \underline{j} \quad (4)$$

$$\underline{n} = -\sin\theta \underline{i} + \cos\theta \cdot \underline{j} \quad (5)$$

and θ is the inclination of $\underline{\tau}$ with the x -axis.

The equations governing the balance of linear and angular momentum are

$$\underline{F}_s + \underline{f} = m\ddot{a} + M\ddot{\theta}_M \cdot \delta(s-\bar{s}) \quad (6)$$

$$M_s + N = J \theta_{tt} \quad (7)$$

where \underline{F} is stress resultant vector in the elastica

$$\underline{F} = T \underline{\tau} + N \underline{n} \quad (8)$$

and T and N are the axial and transverse shear components. Mass per unit length and mass moment of inertia per unit length are denoted by $m = \rho A$ and $J = \rho I$ where ρ is density per unit length and A and I are area and moment of inertia respectively. The external load is denoted by \underline{f} and the bending moment M is given by the constitutive relation.

$$M = EI \theta_s \quad (9)$$

Point action is represented by dimensionless Dirac-Delta function $\delta(s-\bar{s})$.

In this work we shall suppose that the load \underline{f} on the system consists only of the weight of the gun and the projectile and frictional resistance imposed on the gun by the projectile. Hence

$$\underline{f} = -mg \underline{j} - (\mu Mg \underline{\tau} + Mg \underline{j}) \delta(s-\bar{s}) \quad (10)$$

where g is the acceleration of gravity.

The preceding equations can be linearized to describe small motion about the undeformed state of the gun which is characterized by $y = 0$ and $x = s$. Then the governing equations become

$$-EI y_{ssss} + \rho I y_{sstt} + (T v_s)_s - mg = m y_{tt} + M[y_{tt} + \bar{s}_{tt} y_s + 2\bar{s}_t y_{st} + (\bar{s}_t)^2 y_{ss} - g] \delta(s-\bar{s}) \quad (11)$$

$$T_s - \mu Mg\delta(s-\bar{s}) = M \bar{s}_{tt} \cdot \delta(s-\bar{s}) \quad (12)$$

The inextensibility of the mathematical model implies instantaneous transmission of disturbances in the axial direction of the gun. In order to account for finite speed wave action (11)-(12) can be modified by introducing axial displacement $u(s,t)$ and

$$T = EA u_s \quad (13)$$

Also (12) may be modified to include axial inertia

$$EAu_{ss} - \mu Mg\delta(s-\bar{s}) = mu_{tt} + M \bar{s}_{tt} \cdot \delta(s-\bar{s}) \quad (14)$$

Additional refinement of the linearized model is possible to include the effect of shear deformation of the gun tube. Thus the Timoshenko-Rayleigh model will consist of

$$EI\psi_{ss} + G^*A (y_s - \psi) = \rho I \psi_{tt} \quad (15)$$

$$G^*A(y_{ss} - \psi_s) + EA(u_s y_s)_s - mg = m y_{tt} + M[y_{tt} + \bar{s}_{tt} y_s + (\bar{s}_t)^2 y_{ss} + 2\bar{s}_t y_{st} - g] \delta(s-\bar{s}) \quad (16)$$

$$EAu_{ss} - \mu Mg\delta(s-\bar{s}) = mu_{tt} + M \bar{s}_{tt} \cdot \delta(s-\bar{s}) \quad (17)$$

Equations (15)-(17) successively describe the balance of angular momentum and dynamic equilibrium in the transverse and axial directions and G^* stands for the effective shear modulus of the cross section.

The preceding models can adequately deal with a variety of situations such as slender or thick gun tubes and projectiles with variable acceleration. The effect of gas pressure behind the projectile and the expansion wave that it will set up in the gun tube cannot be included in these equations. For such effects a flexible cylindrical shell theory may be employed.

LOSS OF STIFFNESS AND RECOIL INSTABILITY

We now consider the problem of dynamic behavior of a constantly accelerating projectile along a gun tube. We represent the instantaneous dimensionless position of the projectile by r as given by

$$r = \frac{a}{2L} t^2 \quad (18)$$

where a is the constant acceleration and L is the length of the gun. Also we introduce

$$\zeta = \frac{s}{L}, \quad \tau = \frac{a}{L} t, \quad \eta = \frac{y}{L} \quad (19)$$

Thus in dimensionless terms $r = \tau^2/2$ and the time interval during which projectile is in the gun tube is $0 \leq \tau \leq \sqrt{2}$. For our dynamical model we adopt the inextensible Euler-Bernoulli equations (11)-(12). In dimensionless terms they become

$$\begin{aligned} & -\hat{f} \eta_{\zeta\zeta\zeta\zeta} + k^2 \eta_{\zeta\zeta\tau\tau} + \varepsilon \left(\nu \frac{g}{a} + i \right) [H(r-\zeta) \eta_{\zeta}]_{\zeta} - \frac{g}{a} \\ & = \eta_{\tau\tau} + \varepsilon (\eta_{\tau\tau} + \eta_{\zeta} + 2\tau \eta_{\zeta\tau} + \tau^2 \eta_{\zeta\zeta} - \frac{g}{a}) \delta(\zeta-r) \end{aligned} \quad (20)$$

where

$$H(r-\zeta) = \begin{cases} 1 & \text{for } 0 < \zeta < r \\ 0 & \text{for } r < \zeta < 1 \end{cases} \quad (21)$$

and

$$\varepsilon = \frac{M}{Lm}, \quad k^2 = \frac{I}{L^2 A}, \quad \hat{f} = \frac{EI}{L^3 m a} \quad (22)$$

We now employ Galerkin's procedure and use the coordinate function expansion

$$\eta(\zeta, \tau) = \sum_{i=1}^N \eta_i(\zeta) x_i(\tau) \quad (23)$$

where $\eta_i(\zeta)$ are prescribed functions that satisfy the boundary conditions and $x_i(\tau)$ are variable modal amplitudes. Substitution of (23) into (20) and minimization of the error of the approximation in the space of function η_i leads to

$$(\underline{M}_0 + \varepsilon \underline{M}_1) \dot{x} + \varepsilon \underline{C}_1 \dot{x} + (\underline{K}_0 + \varepsilon \underline{K}_1) x = \underline{d}_0 + \varepsilon \underline{d}_1, \quad (\dot{} = \frac{d}{d\tau}) \quad (24)$$

where \underline{M}_0 and \underline{K}_0 are constant $N \times N$ matrices and \underline{d}_0 is a constant N -vector.

The remaining matrices and vectors are functions of τ . These are given by

$$\underline{M}_0 = \underline{D} + k^2 \underline{B}, \quad \underline{C}_1 = 2\tau \underline{V}, \quad \underline{K}_1 = \underline{V} + \tau^2 \underline{Y} - \left(\mu \frac{g}{a} + 1\right) \underline{Z} \quad (25)$$

The elements of the matrices are given by

$$\begin{aligned} K_{0ji} &= \frac{1}{f} \int_0^1 \eta_i^{IV} \eta_j d\zeta, \quad B_{ji} = - \int_0^1 \eta_i'' \eta_j d\zeta, \quad D_{ji} = \int_0^1 \eta_i \eta_j d\zeta \\ z_{ji} &= \int_0^r \eta_i''(\zeta) \eta_j(\zeta) d\zeta, \quad M_{1ji} = \eta_i(r) \eta_j(r), \quad V_{ji} = \eta_i'(r) \eta_j(r), \\ y_{ji} &= \eta_i'(r) \eta_j(r) d_{0j} = - \frac{g}{a} \int_0^1 \eta_j(\zeta) d\zeta, \quad d_{ij} = \frac{g}{a} \eta_j(r) \end{aligned} \quad (26)$$

and it should be noted that $r = \tau^2/2$.

The system (24) is a nonstationary dynamical system. Its mass, stiffness and damping are functions of time. In the limit $\epsilon \rightarrow 0$ the system reduces to the problem of vibrations of the gun tube under its own weight. Methods of solution range from exact numerical integration to various approximate methods including the method of averaging.

The question of occurrence of dynamic instability is of primary importance. An indication of the occurrence of such instabilities is the loss of stiffness of the dynamical system. In fact loss of stiffness will be a sufficient condition for the occurrence of dynamic instability in most dynamical systems. For this purpose we will investigate vanishing of $(K_0 + \epsilon K_1)$ in the time interval $0 < \tau < 1$ which corresponds to $0 < r < 1/2$.

Let a one-mode approximation for a clamped-free beam representing the gun tube be

$$\eta = 2\zeta^4 - 5\zeta^3 + 3\zeta^2$$

Consequently we find

$$\frac{1}{f} (k_0 + \epsilon k_1) \equiv \bar{g}(r; \alpha, \beta) = \frac{36}{5} + \alpha \{ \eta(r) (56r^3 - 75r^2 + 18r) - \beta \int_0^r \eta(\zeta) \eta'(\zeta) d\zeta \}$$

where

$$\alpha = \frac{E}{f} \quad \beta = \left(\mu \frac{g}{a} + 1 \right)$$

For a fast accelerating projectile β could be fixed at its lowest value $\beta=1$. Fig. 2 shows variation of \bar{g} with r in the interval $0 < r < 1$ for various values of α . It is clear that \bar{g} vanishes momentarily for α sufficiently large. This can be taken as a strong indication of the occurrence of instability. Additional work on the behavior of system (24) is in progress and will be reported elsewhere.

REFERENCES

1. E.C. Ting and J. Genin, "Dynamics of Bridge Structures" SM Archives, Vol. 5, Issue 3 (1980) 217-252.
2. C.R. Steele, "The Timoshenko Beam with a Moving Load" Journal of Applied Mechanics, Transactions of ASME (1968) 481-488.
3. J.D. Achenbach and C.T. Sun, "Moving Load on a Flexibly Supported Timoshenko Beam" Int. J. Solids Structures (1965) 53-370.

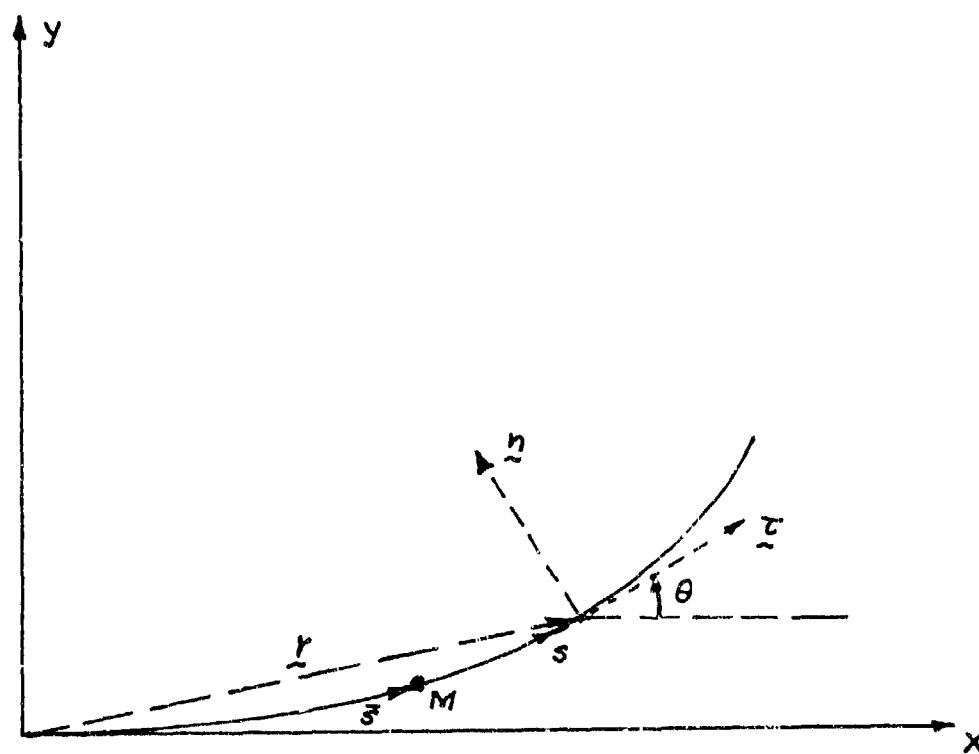


Fig. 1 Schematic of the Gun and Projectile

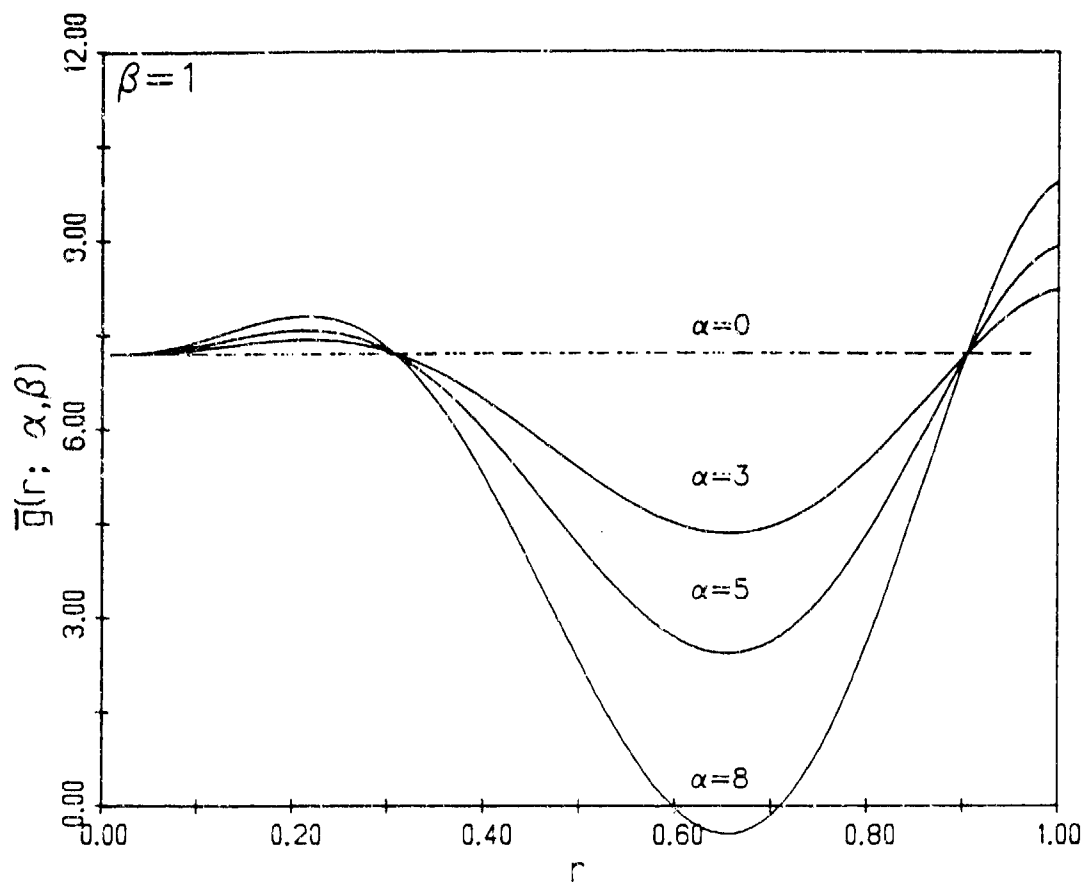


Fig. 2 Loss of Stiffness

CAROFANO

TITLE: THE GASDYNAMICS OF PERFORATED MUZZLE BRAKES

G. C. CAROFANO

US ARMY ARMAMENT RESEARCH, DEVELOPMENT, AND ENGINEERING CENTER

CLOSE COMBAT ARMAMENTS CENTER

BENET LABORATORIES

WATERVLIET, NY 12189-4050

ABSTRACT

In a study of perforated muzzle brakes, Nagamatsu, Choi, Duffy, and Carofano calculated the three-dimensional steady flow of a perfect gas through one vent hole and used the results to predict overall brake performance. The importance of the gas covolume is considered here by using the Abel equation state.

The brake performance calculations in the above study were limited to sets of holes of a single diameter. The merit of using sets of varying diameter is explored with particular emphasis on enhancing the structural integrity of the brake.

In studies of conventional muzzle brakes, the gasdynamic efficiency, β , has been found useful for comparing various brake designs and for scaling. A simple formula is presented which represents the efficiency of a wide variety of axisymmetric perforated brakes.

BIOGRAPHY:

PRESENT ASSIGNMENT: Dr. Garry C. Carofano is a mechanical engineer in the Applied Mathematics and Mechanics Section at Benet Laboratories.

PAST EXPERIENCE: He is currently working in the field of computational fluid dynamics. Previously, he has done numerical and experimental research in areas such as blast produced by recoilless weapons and heat transfer from and stress analysis of finned mortar tubes.

DEGREES HELD: B.M.E., Clarkson University, 1961; M.S., Cornell University, 1964; Ph.D. Cornell University, 1968.

THE GASDYNAMICS OF PERFORATED MUZZLE BRAKES

G. C. Carofano
 US Army Armament Research, Development, and Engineering Center
 Close Combat Armaments Center
 Benet Laboratories
 Watervliet, NY 12189-4050

INTRODUCTION

A perforated muzzle brake consists simply of a set of vent holes drilled through the wall of a cannon near the muzzle (see Figure 1). Compared with conventional baffle brakes, they are lighter and simpler to manufacture and, as shown in a series of reports by Dillon and Nagamatsu [1-5], they can be designed to provide significant levels of recoil reduction. Also, because the vented area can be located symmetrically around the tube, a more favorable flow environment is provided for finned projectiles. This is an important consideration for weapon accuracy and the structural integrity of the projectile. In a field study of 105-mm brake designs, it was found that asymmetrical venting can lead to bending and even breakage of the fins.

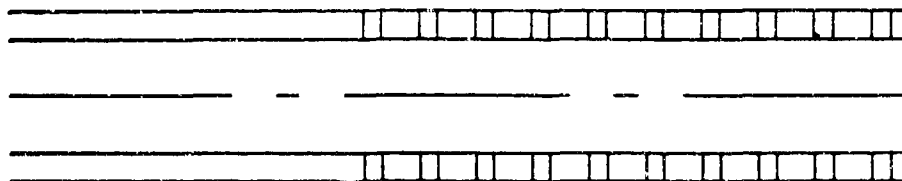


Figure 1. Schematic drawing of a perforated muzzle brake.

Nagamatsu, Duffy, Choi, and Carofano [6] made a numerical calculation of the steady three-dimensional flow through a vent hole in the wall of a shock tube. The predicted pressure distribution on the vent wall compared favorably with the experimental measurements of Nagamatsu, Duffy, and Choi [7]. It was also shown that these results could be combined with a one-dimensional model of the transient flow in a cannon to predict the impulse reduction produced by a perforated muzzle brake. The predictions agreed well with the experimental measurements of Dillon [1] for a 20-mm cannon.

These calculations were made for a perfect gas, but at the pressure levels found in larger caliber weapons, the necessity of including the gas covolume correction in internal ballistics solutions is well known [8]. The importance of this factor on perforated muzzle brake performance will be considered here.

It is also of interest to know if and how experimental results obtained with a small caliber weapon can be scaled up in an effort to avoid the high costs associated with testing larger weapons. In studies of conventional muzzle brakes [9-11], the gas dynamic efficiency, β , has been found useful for this purpose. Its application to perforated muzzle brakes will be discussed here.

THE THREE-DIMENSIONAL MODEL

When the propellant gas expands through the brake, an asymmetric pressure distribution develops in each hole with the highest pressures acting on the downstream surface. The vector and pressure contour plots of Figures 2 and 3 show typical flow patterns in the symmetry plane of one hole and the portion of the tube associated with it. The flow variables in the tube are uniform across the entrance plane. The solid lines in the vector plot indicate where the local Mach number is unity.

In Figure 2, the flow enters at Mach one and accelerates to supersonic velocities as a portion of the gas expands and turns into the hole. The shock at the downstream lip of the hole turns the expanded flow parallel to the solid surfaces and reduces the velocities to subsonic levels. The pressure on the lip is nearly twice the static pressure of the incoming stream. The flow accelerates away from this region and leaves the tube and hole at supersonic velocities. There is a large subsonic region on the upstream portion of the hole where the pressure is nearly uniform. A more complete description of the three-dimensional flow pattern and a comparison with experimental data is given in Reference 6.

To calculate the resulting braking force, a detailed knowledge of the pressure distribution acting on all surfaces of the brake is required at each instant of time during tube blowdown. Because the flow is three-dimensional, it is not practical to obtain the complete solution with one numerical calculation. Fortunately, the flow contains many features which permit a vigorous simplification of the problem.

First, because of the large volume of the gun tube, the blowdown process takes on the order of tens of milliseconds while the three-dimensional calculations indicate that the flow in a hole is established in a fraction of a millisecond. Therefore, the latter can be treated as quasi-steady and only the flow within the tube must be considered as a time-dependent process.

Secondly, in the applications of interest, the flow is either sonic or supersonic as it enters the brake and, due to the venting, expands to higher Mach numbers as it travels downstream. Also, because of the high tube pressures, the gas exits each hole near sonic or supersonic velocity over most of the exit plane area (see Figures 2 and 3). Experience has shown that the flow is rather insensitive to the outflow boundary condition over the remaining subsonic portion. Thus, the flow at a particular hole location is not

influenced by events occurring further downstream or outside of the tube. It depends solely on the conditions in the tube upstream of the hole. This observation permits a dramatic reduction in the amount of three-dimensional computation required to predict brake performance.

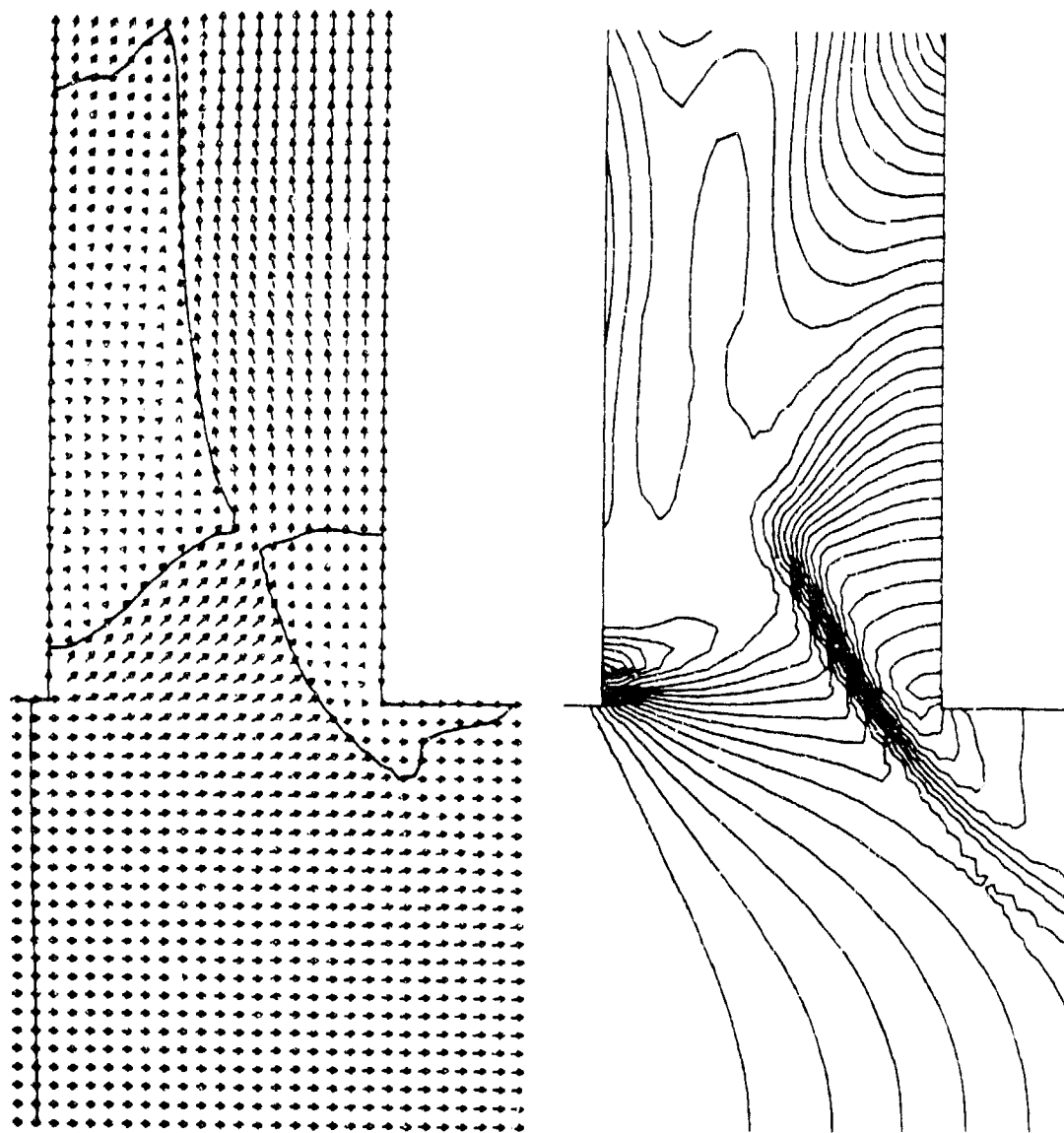


Figure 2. Velocity vector and pressure contour plots for a flow with a Mach number of unity at the entrance plane.

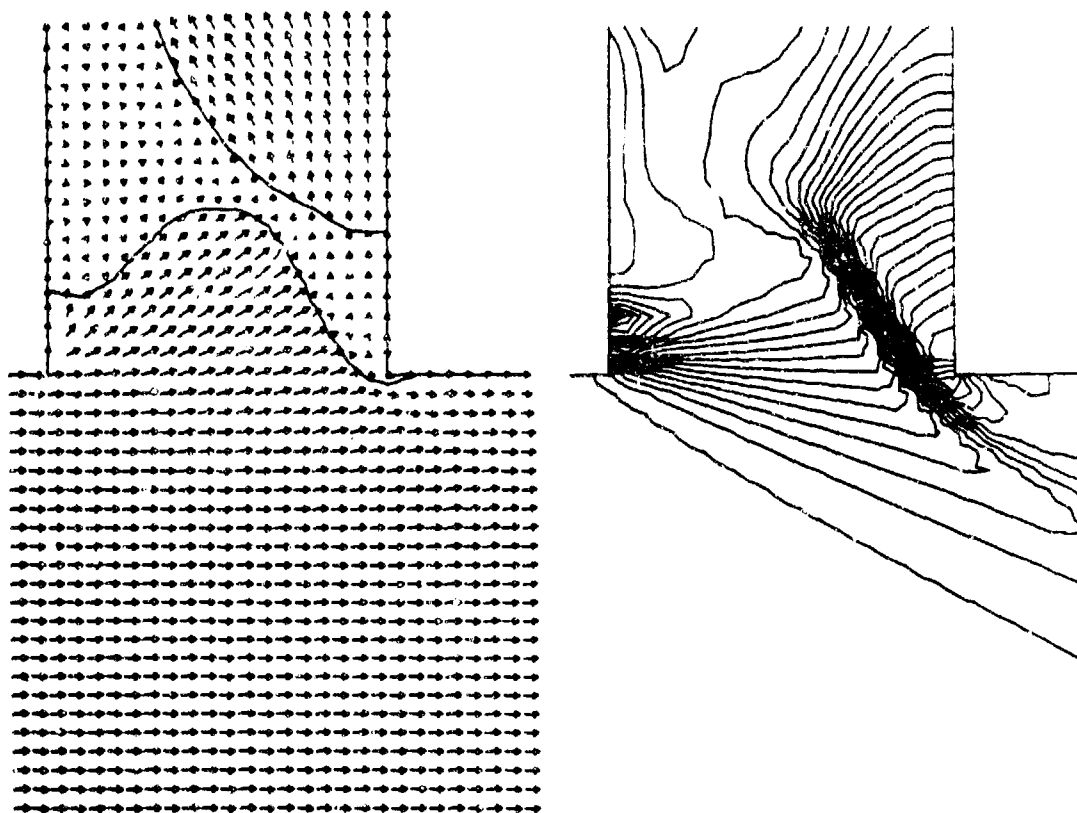


Figure 3. Velocity vector and pressure contour plots for a flow with a Mach number of two at the entrance plane.

The Euler equations may be written in conservative form as

$$\frac{\partial Q}{\partial t} + \frac{\partial F}{\partial x} + \frac{\partial G}{\partial y} + \frac{\partial H}{\partial z} = 0 \quad (1)$$

where

$$Q = \begin{bmatrix} \rho \\ m \\ n \\ l \\ E \end{bmatrix}, \quad F = \begin{bmatrix} m \\ m^2/\rho + P \\ mn/\rho \\ ml/\rho \\ (E+P)m/\rho \end{bmatrix}, \quad G = \begin{bmatrix} n \\ nm/\rho \\ n^2/\rho + P \\ nl/\rho \\ (E+P)n/\rho \end{bmatrix}, \quad H = \begin{bmatrix} l \\ lm/\rho \\ ln/\rho \\ l^2/\rho + P \\ (E+P)l/\rho \end{bmatrix}$$

ρ is the density; $m = \rho u$, $n = \rho v$, and $l = \rho w$ are the momentum components in the x , y and z directions, respectively; u , v , and w are the corresponding velocity components. P is the pressure and E is the total energy per unit volume defined

as

$$E = pe + (m^2 + n^2 + l^2)/2\rho \quad (2)$$

where e is the specific internal energy.

To include the influence of the gas covolume, η , the Abel equation of state is used. For this model, the pressure and soundspeed, c , are related to the state variables p and e by the expressions

$$P = (\gamma - 1)pe / (1 - \eta p) \quad (3)$$

$$c^2 = \gamma(\gamma - 1)e / (1 - \eta p)^2 \quad (4)$$

where γ is the specific heat ratio.

Consider the result of nondimensionalizing the Euler equations in the following way:

$$\rho' = \rho/\rho_2, \quad m' = m/\sqrt{P_2\rho_2}, \quad n' = n/\sqrt{P_2\rho_2}, \quad l' = l/\sqrt{P_2\rho_2}$$

$$P' = P/P_2, \quad E' = E/P_2, \quad e' = e\rho_2/P_2, \quad c' = c\sqrt{\rho_2/P_2}$$

$$x' = x/D, \quad y' = y/D, \quad z' = z/D, \quad t' = t\sqrt{P_2/\rho_2}/D$$

where ρ_2 and P_2 are the density and pressure of the uniform flow at the upstream plane of the tube and D is the vent diameter. The form of the Euler equations remains unchanged while the inflow boundary conditions become

$$\rho' = 1 \quad (5)$$

$$m' = M_2\sqrt{\gamma/(1 - \eta\rho_2)} \quad (6)$$

$$n' = l' = 0 \quad (7)$$

$$E' = (1 - \eta\rho_2)/(1 - \gamma) + \gamma M_2^2/2(1 - \eta\rho_2) \quad (8)$$

The pressure and soundspeed relations become

$$P' = (\gamma - 1)\rho'e'/(1 - \eta\rho_2\rho') \quad (9)$$

$$c'^2 = \gamma(\gamma - 1)e'/(1 - \eta\rho_2\rho')^2 \quad (10)$$

Since the flow depends only on the inflow boundary conditions, which are seen to be completely described by the upstream Mach number, M_2 , the specific heat ratio, γ , and the dimensionless product $\eta\rho_2$, one solution with these parameters specified is valid for all upstream pressures and densities. Although a wide range of physical states are encountered during blowdown, it is found that only a few three-dimensional solutions are required to describe them.

Harten's Total Variation Diminishing scheme [12] was used in conjunction with a time-splitting algorithm to solve the Euler equations after they were transformed to a generalized grid. Separate grids were used for the vent and the tube. A cylindrical grid was used for the vent with a Cartesian grid at its center to avoid the geometrical singularity there. The circular tube was replaced with a rectangular channel to simplify interpolation between the two grids. As can be seen in the vector plot of Figure 2, nineteen grid points were used across the vent diameter and for the azimuthal coordinate. The length of the rectangular channel (the primary flow direction) was represented with 28 grid points, its height by 24 points, and its depth (into the paper) by 13 points.

Of course, the size of the channel could affect the flow through the vent. To check this possibility, the example shown in Figure 2 was repeated with the number of grid points used to represent the height and depth of the channel approximately doubled. The effect on the solution in the vent was minimal, indicating that the channel was essentially an infinite reservoir. The inflow Mach number in this example was unity. At Mach two, the effect would be expected to be even less because the disturbance produced by the vent occupies much less of the channel (see Figure 3).

THE ONE-DIMENSIONAL MODEL

The one-dimensional equations of motion with venting at the tube wall are

$$\frac{\partial \rho}{\partial t} + \frac{\partial m}{\partial x} = \frac{1}{A} \frac{dm}{dx} \quad (11)$$

$$\frac{\partial m}{\partial t} + \frac{\partial (m^2/\rho + P)}{\partial x} = \frac{m}{\rho A} \frac{dm}{dx} \quad (12)$$

$$\frac{\partial E}{\partial t} + \frac{\partial (m(E+P)/\rho)}{\partial x} = \frac{(E+P)}{\rho A} \frac{dm}{dx} \quad (13)$$

The vent term $(1/A)dm/dx$ represents the mass of fluid per unit time per unit volume leaving the tube at x . A is the bore area. The fluid is assumed to leave at the local velocity u in the momentum equation and with the local enthalpy per unit mass $(E+P)/\rho$ in the energy equation (see Reference 13 for the derivation of these equations).

Data from the three-dimensional solution are used to obtain an average value for the dimensionless mass flux leaving the vent using the expression

$$\overline{\rho'w'} = (1/A_H) \int_{A_H} \rho'w'dA \quad (14)$$

where w' is the dimensionless velocity in the z -direction, i.e., parallel to the vent axis. The integration is carried out over the vent exit area, A_H . The

flux is applied instantaneously at each axial location in the one-dimensional model. It is a function of the three parameters that appear in the three-dimensional solution.

The mass flux also depends on the aspect ratio of the hole, which is defined as the ratio of its height, L , to its diameter, D . In Reference 6, the brake configurations were limited to sets of uniform diameter holes. However, from the structural point of view, it may be advantageous to use progressively smaller holes away from the muzzle, since the web of material between each successive row of holes must support the full load generated by all of the holes further downstream. To allow for this possibility, the hole diameter will be taken as the following function of distance, y , along the brake:

$$D = D_{\min} + (D_{\max} - D_{\min})(y/L_V)^a, \quad 0 < a < 1, \quad 0 < y < L_V \quad (15)$$

where L_V is the length of the vented region, D_{\min} is the diameter of the first row of holes at the brake entrance, and D_{\max} is the diameter of the last row of holes near the muzzle. Let N_R be the number of rows of holes (rows run around the circumference of the tube) and N_C be the number of columns of holes (columns run parallel to the tube axis). For a uniform spacing of the holes along the brake, the vent area per unit length is $N_C N_R \pi D^2 / 4 L_V$ and the total vent area, A_V , is found by integration to be

$$A_V = (\pi N_C N_R D_{\min}^2 / 4) (1 + 2r/(a+1) + r^2/(2a+1)) \quad (16)$$

where r is the ratio

$$r = (D_{\max} - D_{\min}) / D_{\min} \quad (17)$$

The vent term can be written in dimensional form as

$$(1/A) dm/dx = \frac{-\rho' w' \sqrt{P \rho}}{\rho' w' \sqrt{P \rho}} (N_C N_R / L_V) (D/D_b)^2 \quad (18)$$

where D_b is the tube diameter. P and ρ are the local values of pressure and density in the one-dimensional solution; they appear since these quantities were used to nondimensionalize the product $\rho' w'$ in the three-dimensional solution.

Using a control volume drawn around the outer boundaries of the tube, including the muzzle exit plane, the following equation for the impulse, I , is obtained:

$$I = W V_{pe} + A \int_0^\infty (P_e - P_0 + p_e u_e^2) dt + A \int_0^\infty [N_C N_R / L_V] \int_0^{L_V} \rho' w' u' P (D/D_b)^2 dy dt \quad (19)$$

The first term is the projectile momentum as it passes the brake exit plane with velocity V_{pe} . The second term is the thrust produced by the gas discharged through this plane. The subscript "e" refers to time-dependent properties obtained from the one-dimensional solution. P_0 is atmospheric pressure.

The quantity in brackets in the third term represents the axial thrust produced by the gas venting through the holes. As can be seen from the vector plots in Figures 2 and 3, the gas velocity is not, in general, parallel to the hole axis everywhere across the exit plane, so this integral may be negative, zero, or even positive. The average value of the momentum flux is calculated from the three-dimensional solution using the expression

$$\overline{\rho'w'u'} = (1/A_H) \int_{A_H} \rho'w'u' dA \quad (20)$$

where u' is the dimensionless axial velocity component of the vented gas. This quantity is a function of the local Mach number and geometry, just as with the mass flux. The local values of pressure and hole diameter appear in the spatial integral in Eq. (19) because they are position-dependent. The integral is evaluated at each time-step in the one-dimensional solution.

The calculation is started with the projectile base just upstream of the vented region. Initial conditions are taken from an internal ballistics code which uses the Pidduck-Kent limiting solution [8] to compute the gradients of pressure, density, and velocity. These are given by

$$\Omega = \frac{(\gamma-1)}{2\gamma} \frac{C}{W} \left(\frac{(\gamma-1)}{2\gamma} \frac{C}{W} + \int_0^1 \left(\frac{1-\Omega\mu^2}{1-\Omega} \right)^{1/(\gamma-1)} d\mu \right)^{-1} \quad (21)$$

$$X = x/x_S \quad (22)$$

$$X = Z - \eta \frac{C}{U} \left(Z - \int_0^Z \left(\frac{1-\Omega\mu^2}{1-\Omega} \right)^{1/(\gamma-1)} d\mu / \int_0^1 \left(\frac{1-\Omega\mu^2}{1-\Omega} \right)^{1/(\gamma-1)} d\mu \right) \quad (23)$$

$$P = P_V \left(\frac{1-\Omega}{1-\Omega Z^2} \right)^{-\gamma/(\gamma-1)} \quad (24)$$

$$\frac{1}{\rho} - \eta = \left(\frac{U}{C} - \eta \right) \frac{(\gamma-1)}{2\gamma} \frac{(1-\Omega)}{\Omega} \frac{C}{W} \left(\frac{1-\Omega}{1-\Omega Z^2} \right)^{1/(\gamma-1)} \quad (25)$$

$$u = ZV_{P_V} \quad (26)$$

where P_V is the projectile base pressure at the starting time, t_S , and V_{P_V} is the projectile velocity. C and W are the charge and projectile masses, respectively. Ω is a parameter which depends on the ratio C/W and γ . It is evaluated once at the start of the solution by solving Eq. (21) by iteration. x_S is the projectile position at time t_S ; it includes a uniform extension of the tube of length U/A where U is the chamber volume and A is the bore area.

At each grid point in the one-dimensional solution, X is computed, then Z is found by iteration from Eq. (23). The values of pressure, density, and velocity are then calculated and the conservative variables in the Euler equations are formed from these.

The equation of motion for the projectile is solved together with the conservation equations until the projectile exits the barrel. The effect of brake venting on the final projectile velocity is thus determined. The remainder of the calculation deals with the motion of the gas in the barrel until complete blowdown is achieved.

THE DIMENSIONLESS FLUX FUNCTIONS

Four factors affect the values of the dimensionless flux functions: the specific heat ratio, γ ; the covolume parameter, ηp_2 ; the upstream Mach number, M_2 ; and the vent geometry. γ does not vary much for different propellants and its effect on the three-dimensional solution has been found through experience to be small. A single value of $\gamma = 1.22$ was used here to reduce the amount of calculation.

A study of internal ballistics solutions for various caliber weapons showed that the covolume parameter is not likely to exceed 0.2, therefore, this study used only this value and the perfect gas limit, $\eta p_2 = 0.0$.

In an earlier study [6], the flux functions were found to vary nearly linearly with M_2 , therefore, the calculations were limited to the two cases $M_2 = 1$ and $M_2 = 2$.

The hole geometry is characterized by the ratio of its height, L , to its diameter, D . The height is equal to the tube wall thickness which, in most designs, would be uniform throughout the brake. Manufacturing considerations suggest a range of L/D from 1 to 2 so these two values were used here.

These parameter choices required a total of eight three-dimensional solutions. The averaged flux functions are shown in Figure 4.

The dashed lines represent the effect of including the covolume term in the equation of state. Since the covolume parameter was chosen to represent an upper limit of conditions expected in a brake, it would not appear to be very important. This was confirmed with several test cases using the one-dimensional code. It can be concluded that in any future three-dimensional studies, the effect of covolume on the flux functions and brake performance is too small to warrant doubling the amount of computation. The covolume term should be included in the equation of state used in the one-dimensional code, however, to be consistent with the internal ballistics code used to generate the starting solution.

Note that the momentum flux is negative for both vent heights, especially the shorter one. This is consistent with the velocity vector plots of Figures 2 and 3 -- the flow leaving the shorter vent is, on balance, directed more upstream.

The linear functions shown in Figure 4 were incorporated into the one-dimensional code as simple analytical expressions. Interpolation was used wherever necessary. The covolume correction was included since the information had already been obtained.

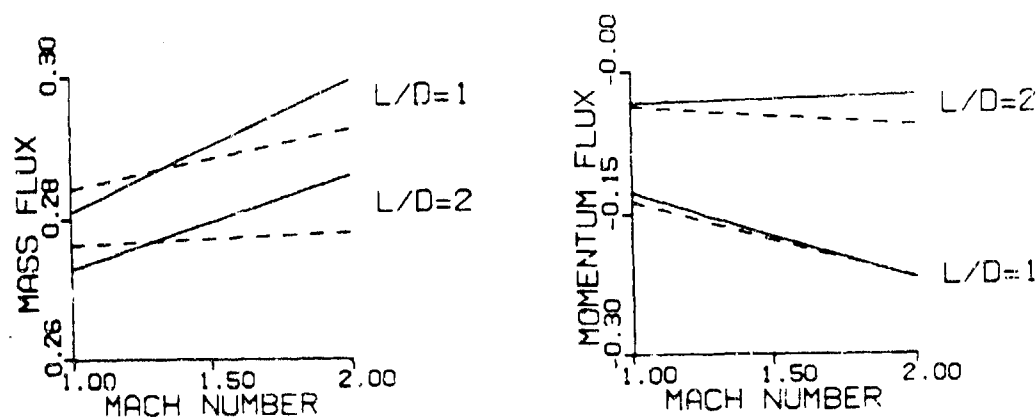


Figure 4. Averaged mass and momentum flux functions computed from the three-dimensional solutions.

BRAKE PERFORMANCE VERSUS VENT AREA DISTRIBUTION

Previous work [1-6] has shown that when a brake is made with a set of uniform diameter holes, the hole diameter, D , should be set equal to the tube wall thickness, L , to achieve the greatest reduction in weapon impulse for a given vented area. This is a result of the asymmetrical pressure distribution in the hole. With reference to Figure 2, as the gas expands to supersonic velocities along the downstream wall, the gas pressure falls below the level acting on the adjacent upstream surface. The crossover occurs at a distance into the hole of about one diameter. Beyond this point the net braking load decreases. Thus, the most efficient brake is a set of uniform holes with $L/D = 1$. However, a less efficient brake might be preferred or even required based on structural considerations. This will be demonstrated using a 120-mm cannon as an example. The values in Table 1 were used to start the solution.

TABLE 1. STARTING SOLUTION DATA

Parameter	120-mm Cannon	20-mm Cannon
P_V (lb _f /in. ²)	12604.0	4219.0
C (lb _m)	19.59	0.0878
W (lb _m)	15.60	0.2161
U (in. ³)	595.0	2.545
V_{pV} (ft/sec)	5073.6	3429.0
γ	1.22	1.25
η (in. ³ /lb _m)	27.2	30.0
D_b (in.)	4.724	0.7874
x_s (in.)	170.9	56.3
L_b (in.)	198.0	63.7
L (in.)	0.945	0.1575

L_b is the barrel length, i.e., the total distance traveled by the projectile base. The other symbols were defined earlier.

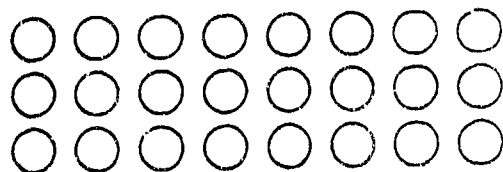
Finned projectiles generally have six fins. To reduce asymmetrical loading of the fins as the projectile passes through the vented region and to limit circumferential pressure gradients, brakes are usually designed with twelve columns of holes so $N_C = 12$ will be used in all of the calculations below. The number of rows of holes, N_R , will be varied to obtain the vent area desired.

Consider the two hole patterns in Figure 5 where three of the twelve columns of each brake are shown; the flow is from left to right. The uniform pattern has $D_{min} = D_{max} = L = 0.945$ " for maximum efficiency; to maintain the same vent area, the stepped pattern used $D_{min} = 0.563$ ", $D_{max} = 1.0$ ", and $a = 0.6$ in the power law expression, Eq. (15). As indicated by the data above the patterns, redistributing the area in this manner increases the recoil impulse by less than two percent. However, because the total brake load is supported by a larger web area in the stepped design, the maximum axial load per unit web area is reduced by 40 per cent (the maximum occurs at the instant the projectile base is at the muzzle). The variation of axial load per unit web area with distance along the brake is shown in Figure 6. The reduced stress levels near the brake entrance should have a favorable effect on fatigue life.

Because of the more gradual increase in vent area with distance in the stepped design, the drop in propellant gas pressure is more moderate, as shown in Figure 7. This implies that the pressure gradient in the azimuthal direction will also be smaller so a finned projectile will be exposed to a less severe loading as it passes through the brake.

This example demonstrates that redistributing a given vent area along the tube can result in a structurally more acceptable design with only a modest loss in gasdynamic performance. In practice, of course, the stepped pattern would consist of a few different hole sizes rather than continuously varying diameters.

UNIFORM AREA DISTRIBUTION
 RECOIL IMPULSE = 3.995 LB-SEC
 MAXIMUM AXIAL LOAD / WEB AREA = 76.000 PSI



STEPPED AREA DISTRIBUTION
 RECOIL IMPULSE = 4.058 LB-SEC
 MAXIMUM AXIAL LOAD / WEB AREA = 45.600 PSI

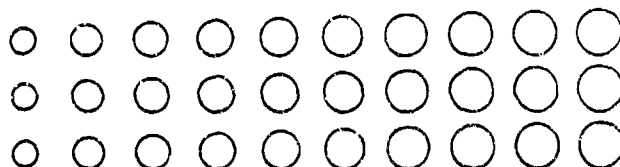


Figure 5. A comparison of a uniform hole pattern with a stepped pattern.

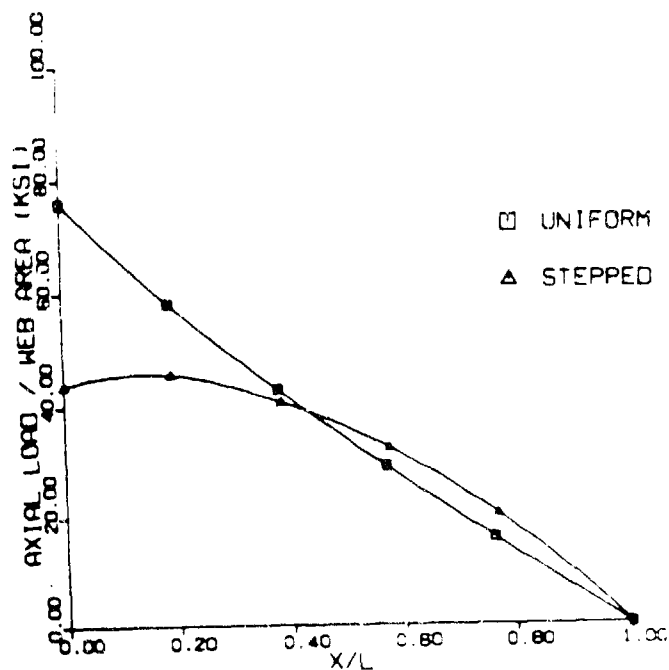


Figure 5. Axial load per unit web area along the brakes for the two patterns shown in Figure 5.

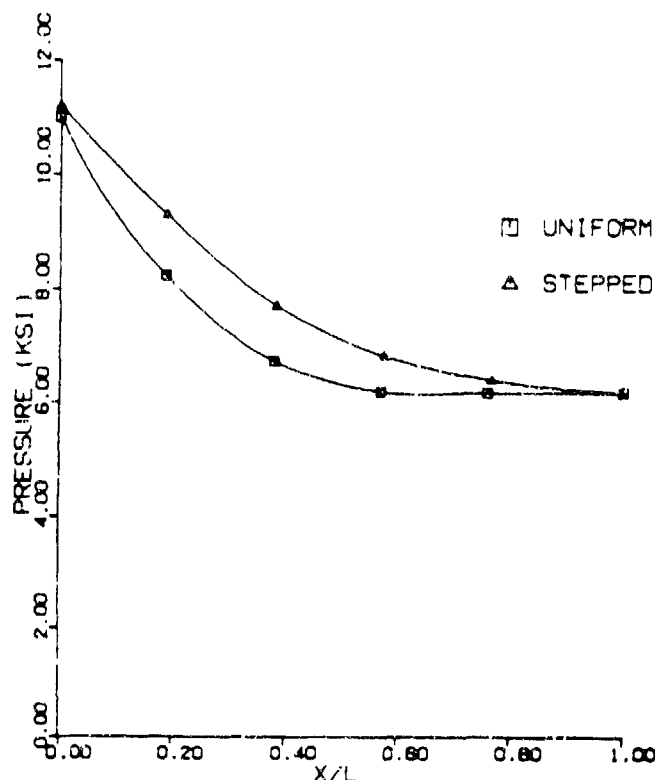


Figure 7. Pressure distribution along the brakes for the two patterns shown in Figure 5.

BRAKE EFFICIENCY AND SCALING

A parameter that is useful for comparing the performance of conventional muzzle brakes is the gasdynamic brake efficiency, β , defined as

$$\beta = (I_{wo} - I_w) / (I_{wo} - W V_p) \quad (27)$$

where I_w is the recoil impulse, W is the projectile mass and V_p is its muzzle velocity. The subscript "wo" refers to the bare muzzle case.

β is often found to be remarkably insensitive to the weapon caliber and internal ballistics and dependent only upon brake geometry. It is a practical tool for comparing various brake designs on a given weapon or for estimating performance based upon data obtained with a different caliber weapon. It will be demonstrated that this utility carries over to perforated muzzle brakes by comparing the performance of geometrically similar brakes on a 120-mm cannon and a 20-mm cannon. The data in Table 1 for the 20-mm cannon were taken from Reference 1.

The brakes have 4, 8, and 12 rows, respectively, of uniform diameter holes with $D = L$. The eight row pattern is shown in Figure 5. The 20-mm brake dimensions were one-sixth those of the 120-mm designs.

In Figure 8, brake efficiency is plotted as a function of the vent area ratio, AR, which is defined as the ratio of the vented area to the bore area. The solid curve labeled $L/D = 1$ represents the calculated 20-mm data; the three triangular symbols are the 120-mm results. Even though the internal ballistics differ considerably for the two cannons, geometric similarity appears to be sufficient to guarantee nearly the same gasdynamic performance.

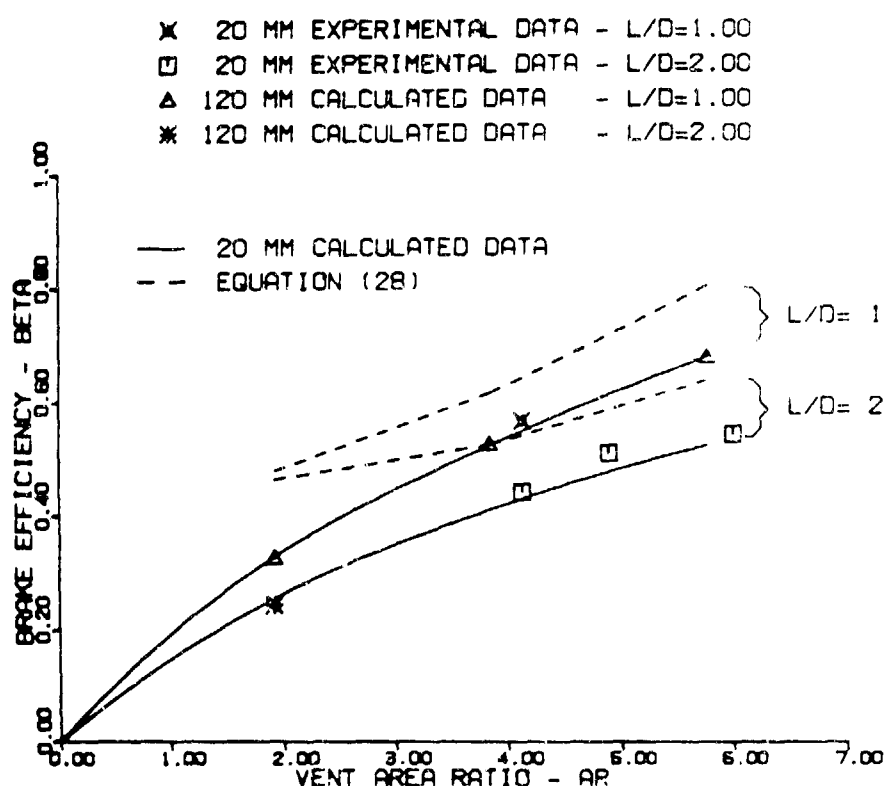


Figure 8. Brake efficiency as a function of vent area ratio, AR.

The solid curve labeled $L/D = 2$ represents 20-mm calculations where the wall thickness, L , was doubled but the number of holes was kept the same. This conforms to the experimental configurations of Reference 1 and facilitates comparison with those data. The asterisk symbol is a 120-mm calculation with L fixed, but D halved to obtain $L/D = 2$; the number of holes was quadrupled to maintain the area ratio. This is most likely how a high aspect ratio (L/D) would occur in practice. The close agreement between the two sets of calculations suggests that even geometrical similarity is not a strict requirement,

rather, the aspect and area ratios may be the controlling parameters. This notion is reinforced by the remaining four symbols on the plot. These represent a portion of the 20-mm experimental data of Reference 1 and correspond to brakes which had only 9 columns of holes and 16, 19, and 23 rows, respectively, rather than 12 row designs studied here.

Dillon [2] recognized the relevance of these two parameters and presented the following formula for brake efficiency:

$$\beta = 0.208 + 0.312(AR) - 0.145(L/D) - 0.062(AR)^2 + 0.087(L/D)^2 - 0.039(AR)(L/D) + 0.006(AR)^3 - 0.008(L/D)^3 \quad (28)$$

The dashed lines in Figure 8 were obtained using this expression. It overestimates the experimental data and the present calculations, particularly at small area ratios. This happens because the formula was based upon a larger sample of brake configurations, some of which were quite different geometrically from the rest.

For example, one brake consisted simply of two holes drilled perpendicular to the bore axis with diameters equal to the bore diameter. While this baffle-like configuration represented an interesting comparison for the more "conventional" perforated brakes, its inclusion in the formula accounts for the two dashed lines converging to a high β at $AR = 2$ in the plot.

Another configuration had vents only on the sides of the tube. The lateral venting arrangement was an attempt to reduce possible obscuration effects associated with axisymmetric venting. As noted in the Introduction, full-scale testing of the idea resulted in damage to finned projectiles. It did produce somewhat higher efficiencies in the 20-mm tests, however, and this contributes to the high estimates of the formula.

Nevertheless, Dillon's idea of possibly representing a wide range of perforated configurations with a single formula has obvious appeal and can be more successfully realized if it is limited to axisymmetric configurations. The curve in Figure 9 represents the formula

$$\beta/(1-0.18 L/D) = 0.273(AR)[1 - 0.14(AR) + 0.01(AR)^2] \quad (29)$$

This was obtained using the 20-mm calculations of Figure 8. All of the data in Reference 1 for axisymmetric configurations with aspect ratios between 1 and 2 are shown as well as the uniform and stepped 120-mm data calculated here. This information is summarized in Tables 2 and 3.

TABLE 2. SUMMARY OF EXPERIMENTAL DATA FROM REFERENCE 1

Model	Pattern	AR	L/D	β (%)
1	staggered	6.32	1.26	70.4
2	staggered	5.00	1.89	51.3
3	uniform	4.13	1.00	56.8
4	uniform	4.13	2.00	44.3
6	uniform	4.89	2.00	51.1
7	uniform	5.99	2.00	54.4
8	staggered & stepped	3.38	0.95	50.4

TABLE 3. SUMMARY OF 120-mm CALCULATIONS

Model	Pattern	AR	L/D	β (%)
A	uniform	1.92	1.00	32.8
B	uniform	3.84	1.00	52.6
C	uniform	5.76	1.00	67.9
D	stepped	3.82	1.09	50.5
E	stepped	5.74	1.09	65.0
F	uniform	1.92	2.00	24.6

The model numbers in Table 2 correspond to those in Reference 1. However, the values of β are slightly lower than reported there. In computing the brake efficiency from the impulse measurements, Dillon used the muzzle velocity obtained with the brake in place rather than the bare muzzle velocity. To be consistent when comparing the various brake configurations, the latter was used here.

The staggered patterns in Table 2 had every other row of 12 holes rotated 15 degrees with respect to the adjacent rows. The uniform pattern refers to the column arrangement shown in Figure 5. Staggering is expected to reduce azimuthal pressure gradients near projectile fins. It does not appear to affect gasdynamic performance, but calculations show that the column pattern produces somewhat lower stresses for a given load [14].

The stepped pattern in Table 2 had three rows of holes with 1/16" diameters, three rows with 1/8" diameters and four rows with 3/16" diameters. The center-to-center spacing in the axial direction was constant, as in the stepped pattern of Figure 5, although the rows were staggered. Each row had 12 holes.

To calculate an average hole diameter for the stepped patterns, the following formula was used:

$$\bar{D} = \sum_{n=1}^N N_n D_n A_n / \sum_{n=1}^N N_n A_n \quad (30)$$

where N is the number of different hole sizes and N_n is the number of rows with diameter D_n and area A_n . Each diameter is weighted by its area in the belief that a large hole contributes more to brake performance a small hole. The weighting factor shifts the data closer to the curve in Figure 9.

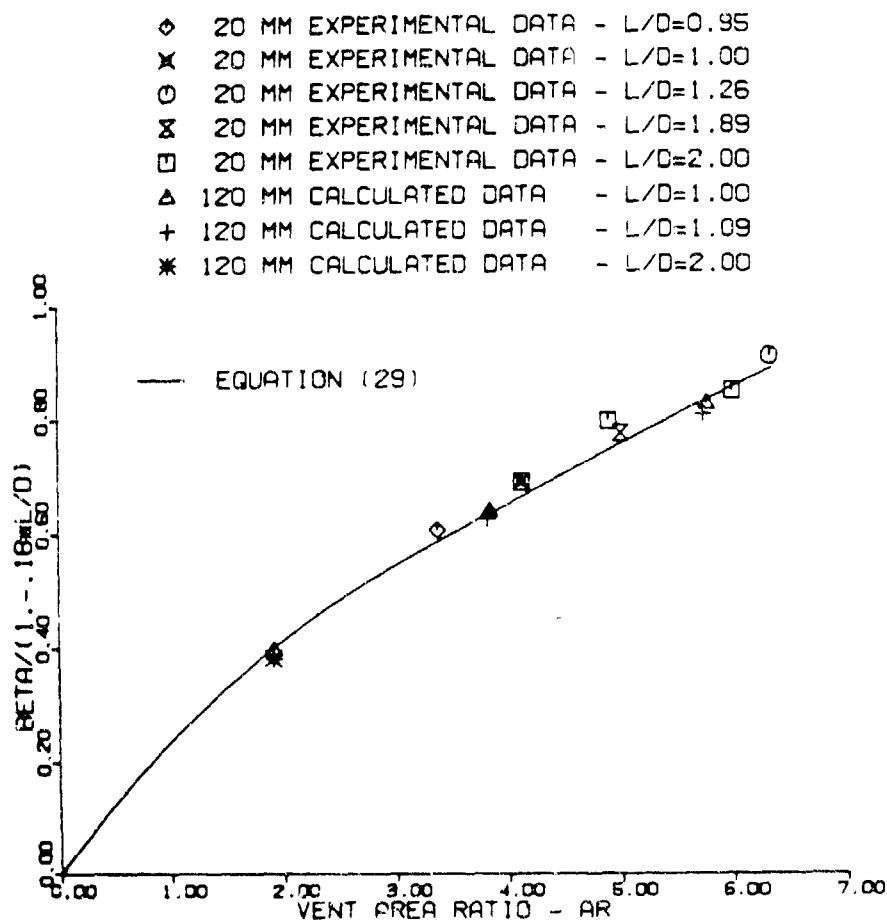


Figure 9. Correlation of computed and experimental brake efficiencies.

The close correlation of the tabulated data by the predicted curve supports Dillon's observation that brake performance is primarily dependent on vent area ratio and aspect ratio. Stepped patterns are included by using a suitably weighted average diameter to compute the aspect ratio.

CONCLUSIONS

The influence on brake performance of including covolume in the three-dimensional calculations was found to be too small to warrant the added computation. The covolume term should be included in the one-dimensional code, however, to be consistent with the internal ballistics code used to generate the starting solution.

Redistributing a given vent area along the tube using a set of holes with varying diameters can result in a structurally more acceptable design with only a modest loss in gasdynamic performance. It may also present a more favorable environment for finned projectiles by reducing axial and azimuthal pressure gradients in the vented portion of the tube.

Brake performance is primarily dependent on vent area ratio and aspect ratio. The dependence can be expressed by a simple formula for axisymmetric designs. Stepped patterns are included by using a suitably weighted average diameter to compute the aspect ratio.

REFERENCES

1. Dillon, R. E. Jr., "A Parametric Study of Perforated Muzzle Brakes," ARDC Technical Report ARLCB-TR-84015, Benet Weapons Laboratory, Watervliet, NY, May 1984.
2. Dillon, R. E. Jr. and Nagamatsu, H. T., "An Experimental Study of Perforated Muzzle Brakes," ARDC Technical Report ARLCB-TR-84004, Benet Weapons Laboratory, Watervliet, NY, February 1984.
3. Dillon, R. E. Jr. and Nagamatsu, H. T., "A Method of Analyzing Perforated Muzzle Brake Performance," ARDC Technical Report ARLCB-TR-84002, Benet Weapons Laboratory, Watervliet, NY, February 1984.
4. Dillon, R. E. Jr., "Wall Thickness and Vent Area Effects on Perforated Muzzle Brake Performance," ARDC Technical Report ARLCB-TR-84020, Benet Weapons Laboratory, Watervliet, NY, May 1984.
5. Dillon, R. E. Jr. and Nagamatsu, H. T., "An Experimental Study of Perforated Muzzle Brakes," AIAA Paper 84-1642, presented at the AIAA 17th Fluid Dynamics, Plasma Dynamics, and Lasers Conference, June 25-27, 1984, Snowmass, Colorado.
6. Nagamatsu, H. T., Choi, K. Y., Duffy, R. E., and Carofano, G. C., "An Experimental and Numerical Study of the Flow Through a Vent Hole in a Perforated Muzzle Brake," ARDEC Technical Report ARCCB-TR-87016, Benet Weapons Laboratory, Watervliet, NY, June 1987.

CAROFANO

7. Nagamatsu, H. T., Choi, K. Y., and Duffy, R. E., "Wall Thickness and Flow Mach Number Effects on Pressure Distribution in the Vent Hole for Perforated Muzzle Brakes," ARDEC Contractor Report ARCCB-CR-86038, Rensselaer Polytechnic Institute, Troy, NY, November 1986.
8. Corner, J., Theory of the Interior Ballistics of Guns, John Wiley and Sons, New York, 1950.
9. Fansler, K. S., "A Simple Method for Predicting Muzzle Brake Effectiveness and Baffle-Surface Pressure," Technical Report ARBRL-TR-02335, Ballistic Research Laboratory, Aberdeen Proving Ground, Maryland, June 1981.
10. Pater, L. L., "Scaling of Muzzle Brake Performance and Blast Field," Technical Report TR-3049, Naval Surface Weapons Center, Dahlgren Laboratory, Dahlgren, Virginia, October 1974.
11. Pater, L. L., "Muzzle Brake Parameter Study," Technical Report TR-3531, Naval Surface Weapons Center, Dahlgren Laboratory, Dahlgren, Virginia, October 1976.
12. Harten, A., "High Resolution Schemes for Hyperbolic Conservation Laws," J. Computational Physics, Vol. 49, No. 3, March 1983, pp. 357-393.
13. Zucrow, M. J. and Hoffman, J. D., Gas Dynamics - Volume 2: Multidimensional Flow, John Wiley and Sons, New York, 1977, Chapter 19.
14. Glennon, M., Private Communication, US Army ARDEC, Benet Weapons Laboratory, Watervliet, NY, February 1987.

SNECK

TITLE: Gas Flows Through Small Holes in Gun Tube Walls
H.J. Sneck
Benet Weapons Laboratory
Watervliet Arsenal
Watervliet, New York
also
Professor of Mechanical Engineering
Rensselaer Polytechnic Institute
Troy, New York

ABSTRACT:

The flow of gun-tube gases through the holes leading to a bore evacuator cannister are examined analytically. Simple methods are proposed for estimating the flow from supersonic tube flows based on classical two-dimensional gas dynamic concepts. The results are compared with the results of more elaborate computer solutions, experiments and water table simulations. Many of the basic features of those flows are revealed and explained by the technique. A simple expression for the quasi-steady flow rate suggested by Carofano for supersonic tube flows is extended to cover the subsonic regime as well.

BIOGRAPHY:

PRESENT ASSIGNMENT: Mechanical Engineer - Benet Weapons Laboratory (WAE), Watervliet Arsenal, Watervliet, New York 12189

PAST EXPERIENCE: Professor of Mechanical Engineering - 1953 to present, consultant.

DEGREES HELD: B.M.E., Rensselaer Polytechnic Institute, Troy, NY, 1951; M. Eng., Yale University, New Haven, CT, 1952; Ph.D., Rensselaer Polytechnic Institute, Troy, NY, 1961.

SNECK

GAS FLOWS THROUGH SMALL HOLES IN GUN TUBE WALLS

H.J. Sneck
Benet Weapons Laboratory
Watervliet Arsenal, Watervliet, NY 12189

PREVIOUS WORK

The flow through holes at 90° to a gun bore have been investigated by Dillon [1] using a two-dimensional Godonov hydrocode and Carofano et al. [2] using a three-dimensional compressible flow code. In each case the flow in the tube is assumed to be sonic or supersonic. They showed that the tube gas initially turns toward the hole via a fan which resembles a Prandtl-Meyer flow. A majority of this accelerated flow then passes through a slightly curved oblique detached shock in the hole, entering a subsonic region next to the muzzle-side wall where it completes its turn to parallel the hole axis. This high pressure fluid then accelerates again exiting the hole supersonically. The remainder of the fan-flow passes through a small portion of the shock at its tube-end, whence it enters a subsonic region near the corner of the hole. This portion of the fan is then returned to parallel the tube axis as it accelerates to the tube flow velocity. The shock front thickness is shown to be small relative to the hole diameter. The presence of this shock was anticipated by Smith in an earlier investigation [3].

The Mach number contours plotted by Dillon and Carofano for the hole center plane show that the sonic line at the exit from the subsonic region in the hole is roughly normal to the hole wall. At the subsonic exit on the tube side only a portion of the sonic line is normal to the wall. The streamlines and constant entropy contours are shown by Dillon to be nearly parallel. The presence of a stagnation point on the hole wall is indicated by nearly circular Mach contours centered on the wall in the subsonic region [2]. Both investigators found a large comma-shaped low pressure separation bubble attached to the breach-side wall of the hole. This recirculating region extends several diameters into the hole and at its widest point occupies about one-half the hole diameter.

SIMPLIFIED MODEL - TUBE MACH NUMBER > 1.0

A simplified two-dimensional flow field based on the above observations is shown in Figure 1. This model incorporates all the salient features of the computer-generated solutions. Dillon's results indicate that the flow field adapts rapidly to changing bore conditions which suggests that the flow can be treated as quasi-static. The rapid formation of the shock and separation

bubble have also been observed by the author in numerous water-table simulations performed at BWL.

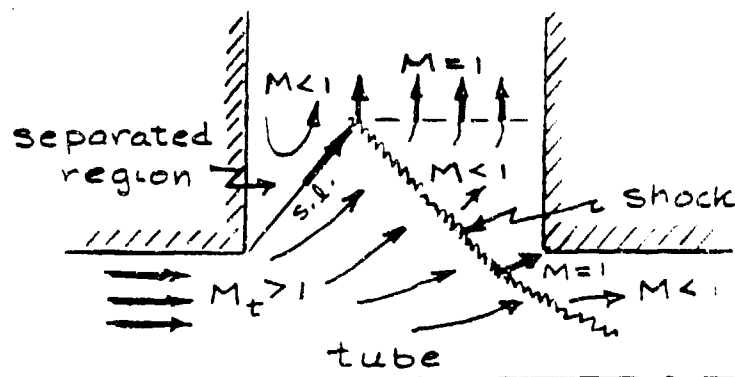


Figure 1 Simplified Flow Model at Hole Entrance

To facilitate the simplified analysis the following assumptions are made:

1. The flow is homentropic in the Prandtl-Meyer fan before the shock, and isentropic thereafter.
2. The shock front has zero thickness.
3. The hole end of the shock is terminated by a streamline bounding the separation bubble. An oblique shock reduces this streamline Mach number to unity and turns it to parallel the hole wall.
4. A sonic line normal to the hole wall joins this shock terminus to the wall at the exit from the subsonic region.
5. In the vicinity of the downstream corner of the hole the shock turns a streamline toward the corner and reduces its Mach number to unity, the maximum possible in this region following the shock. This establishes the location of the streamline dividing the down-hole flow from that which spills back out into the tube. Further discussion of this assumption will accompany the examples to follow.
6. The shock front between the streamlines bounding the down-hole flow can be approximated by intersecting straight line continuations of the shocks crossing the bounding streamlines.

SNECK

where

M_{ya}, M_{yb} = normal Mach number leaving shock.

The geometry of the flow yields the following geometric relations:

$$\begin{aligned} \alpha + \varphi &= \omega + \epsilon & \frac{a}{b} &= \frac{\sin \theta_2}{\sin \theta_1} \frac{\sin \alpha}{\sin \varphi} \\ \alpha + \Delta + \theta_1 &= 180 & \frac{A}{b} &= \frac{\sin \theta_2}{\sin \varphi} \\ \Delta + \theta_3 &= 180 + \theta_3 \end{aligned} \quad (4)$$

Assumptions 1 - 6 yield θ_1 , θ_2 , θ_3 , ω , and ϵ . Assuming α yields a/b and A/b . Closure is obtained by requiring that the unity post-shock Mach number on the dividing streamline (s.l.) be directed toward the hole corner as illustrated in Figure 2.

ANALYSIS OF A 90° HOLE, TUBE MACH NUMBER > 1.0

To illustrate the step-by-step application of the method the flow previously investigated by Dillon will be analyzed first. In this case $M_t = 1.2$, $P = 4.3 (10^3)$ psia, $P^0 = 287$ atm, $\gamma = 1.25$.

Using the Prandtl-Meyer and the oblique shock equations of two-dimensional flow we find that the down hole bounding streamline parallels the hole walls with unity Mach number following an oblique shock when $M_a = 2.88$, $\omega = 52.5^\circ$, $\theta_1 = 65.5^\circ$, $\delta = 37.7^\circ$, $M_x = 2.62$, $M_y = 0.47$

The Mach numbers M_A , M_{xa} , M_{xb} , M_{ya} and M_{yb} can only be determined by trial. For the initial trial assume $M_{xa} = M_x = 2.62$ so that $M_{ya} = M_y = 0.47$. The number of trials can be reduced if M_A is initially chosen so that Mach line A lies very near the hole mouth with the shock front angled to yield a unity post-shock Mach number which nearly parallels the tube centerline. This establishes trial values of θ_2 , θ_3 , M_{xb} and M_{yb} . The angle α is then chosen so that a/b and A/b of Eq.(4) satisfy the supersonic region continuity equation, (1).

In this case trial $M_A = 2.0$ yields A near the hole mouth. With this assumption Eq.(1) cannot be satisfied for $\alpha < \omega + \varphi$ from which we conclude that the shock is probably all "a", and "b" exists only on the short portion of the shock which returns the fan flow back into the tube. Using $\alpha = \omega$, $D(M_{xa})$ can be adjusted (averaged) to satisfy continuity. The "average" $D(M_{ya})$

can be found from $D(M_{xa})$ and the ratio a/b determined from the subsonic region continuity equation (3). In this case $a/h = 1.4$.

The graphical solution begins with the construction to scale of the locus of points satisfying the ratio $a/h = 1.4$ as shown in Figure 3a. We now return to the assumed M_A and test it to see if by chance the crossing of its Mach line with the locus yields a unity post-shock Mach number directed at the

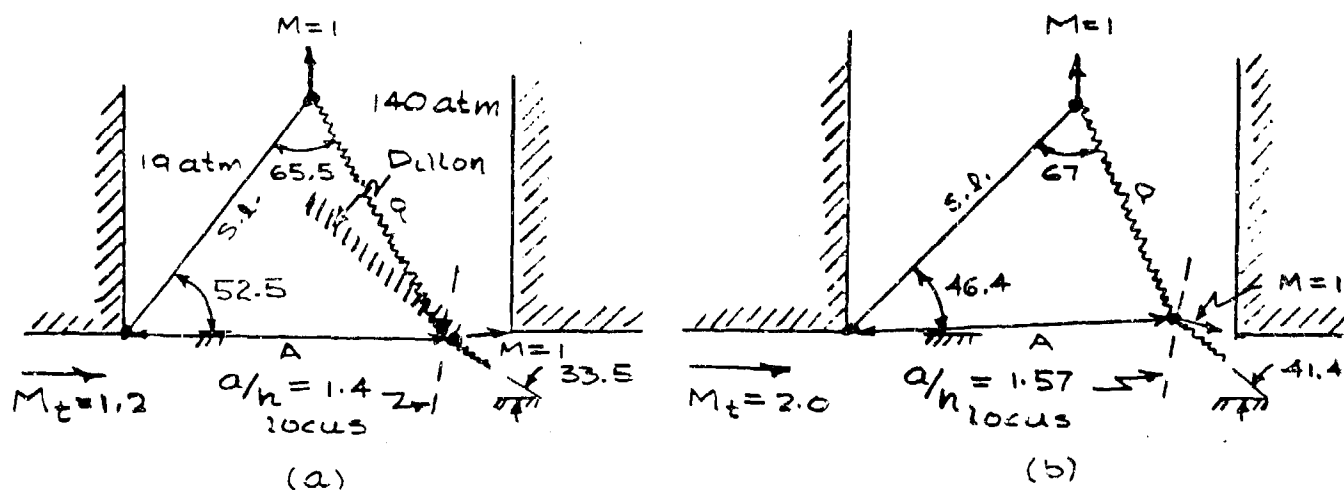


Figure 3 Flow Fields, $M_t = 1.2$ and $M_t = 2.0$

hole corner. A fortuitous initial guess for M_A would require only a modest adjustment of M_A to accomplish this closure with no further adjustment a/h or a/b . After several trials the following consistent results were obtained: $M_A = 2.07$, $\omega = 27.8^\circ$, $A = 1.6''$, $a/h = 1.4$.

Carofano correlates his results for the mass flow rate down a 90° hole with the formula

$$\frac{\dot{m}}{A_h \sqrt{P \rho}} = K(M_t) \quad (5)$$

where P , ρ and M are tube values, and A_h is the hole area. Using the classical two-dimensional compressible flow equations

$$K(M_t) = \sqrt{\gamma} \frac{A}{A_h} \frac{D(M_A)}{D(M_t)} \left(\frac{M_t}{M_A} \right) \quad (6)$$

This coefficient is very sensitive to M_A , more so than area A . A reasonably correct criterion for M_A , such as assumption 5, is therefore essential. In this case, with $A_h = 2.0''$, $K(1.2) = 0.273$ compared to Carofano's 0.308 and Smith's $K(1) = 0.31$. To illustrate the sensitivity to M_A , if $M_A = 2.0$, then $K(1.2) = 0.3$.

Dillon's shock is shown superposed in Figure 3a for purposes of comparison. The Prandtl-Meyer turning angle of 52.5° compares well with Dillon's velocity plot. The 19 atm pressure along the separation bubble is comparable to his predictions in this region, but the calculated 140 atm at the sonic exit, h , is somewhat lower than his predicted muzzle-side wall pressure. These comparisons may be somewhat fortuitous since $M_a = 2.88$ is larger than his highest predicted Mach number and the shocks are only coincident near the hole mouth.

Figure 3b shows the shock construction for $M_t = 2.0$ using the procedures described above. Once again the shock is all "a". The dividing streamline intersects the shock slightly inside the hole with $M_A = 2.78$ and $A = 1.68''$ yielding $K(2.0) = 0.276$. Intuitively one would expect this coefficient to be lower than $K(1.2)$ due to three-dimensional effects as indicated by Carofano.

FLOW THROUGH A 90° HOLE-TUBE MACH NUMBER < 1.0

Subsonic flows, unlike supersonic, do not lend themselves to simplified analytical procedures. As a consequence most of these flows are described globally by empirical correlations such as Eq. (7) for the velocity (U_h) through a small hole in the side of a pipe [4].

$$U_h = C_D \left[\frac{2}{\rho} \left(P - P_a + \frac{1}{2} \rho U_t^2 \right) \right] \quad (7)$$

In this formula P_a = hole discharge pressure, P = tube pressure, and U_t = tube velocity. The empirical discharge coefficient, C_D , is for incompressible fluids issuing from holes whose diameters are larger than the pipe wall thickness. The coefficient, C_D , is tabulated in Table 1 [4].

TABLE 1 DISCHARGE COEFFICIENTS, C_D

$R^2 = \frac{\rho U_t^2 / 2}{P - P_a + \rho U_t^2 / 2}$	0.0	0.1	0.2	0.3	0.4	0.5	0.6	0.7	0.8	0.9	1.0
C_D	0.68	0.64	0.61	0.58	0.55	0.51	0.46	0.39	0.29	0.16	0.0

Equation (7) is a generalization of the equation for the flow from a large quiescent reservoir through a long hole, i.e.,

$$\frac{P - P_a}{\frac{1}{2} \rho U_h^2} = 1 + k + f \frac{\ell}{d} \quad (8)$$

On the right side of this equation the first coefficient, 1, allows for the Bernoulli effect, k for the entrance dissipation, and $f \frac{\ell}{d}$ for the hole dissipation. For short holes $f \frac{\ell}{d}$ is negligible, $k = 0.5$, and the Bernoulli coefficient given by the vena-contracta ratio which is approximately $1/0.6$. Thus, for $R^2 = 0$, $C_D = 1/\sqrt{2.17} = 0.68$ as indicated in the table. Variations in C_D for $R^2 > 0$ reflect the effects of the tube flow on the entrance dissipation and vena-contracta. For longer holes, such as bore evacuator holes where $(\frac{\ell}{d} \sim 6)$, the vena-contracta pressure would probably be recovered. For these holes $f \frac{\ell}{d} \sim 0.1$ yielding $C_D \approx 1/\sqrt{1.6} = 0.8$, which is 18% higher than the $R^2 = 0$ value of Table 1. Thus, it is anticipated that the coefficients in Table 1 would probably increase for longer holes.

To adapt (7) to compressible flow let $P^0 = P + \frac{1}{2} \rho U_t^2$ so that

$$\frac{M_h}{M_t} \approx \frac{U_h}{U_t} = C_D \sqrt{\frac{\frac{P^0}{P} \left(1 - \frac{P_a}{P^0}\right)}{\frac{P^0}{P} - 1}} = \frac{C_D}{R} \quad (9)$$

When $P_a/P^0 \ll 1.0$, $P^0/P \rightarrow 1/(1 - R^2)$ so that

$$M_t = \sqrt{\frac{2}{\gamma - 1} \left[\left(\frac{1}{1 - R^2} \right)^{\frac{\gamma - 1}{\gamma}} - 1 \right]} \quad (10)$$

Table 2 shows the computed relationship between the tube Mach number (M_t) and the hole Mach number (M_h), assuming that the incompressible C_D 's of Table 1 are applicable. It should be noted that higher values of C_D would cause the hole Mach numbers M_h to be very nearly unity.

TABLE 2 HOLE MACH NUMBERS AND $K(M_t)$

R^2	M_t	C_D	M_h	$K(M_t)$
0	0	0.68	0.86	0.36
0.10	0.41	0.64	0.83	0.34
0.20	0.60	0.61	0.82	0.32
0.30	0.77	0.58	0.82	0.31
0.40	0.93	0.55	0.81	0.29
0.45	1.00	0.51	0.78	0.27

The mass flow-rate through the hole is given by

$$\dot{m} = C_D \sqrt{\frac{\gamma}{\pi T_h^0}} P_h^0 A_h D(M_h) \quad (11)$$

Figure 4 shows a control volume adjacent to the hole.

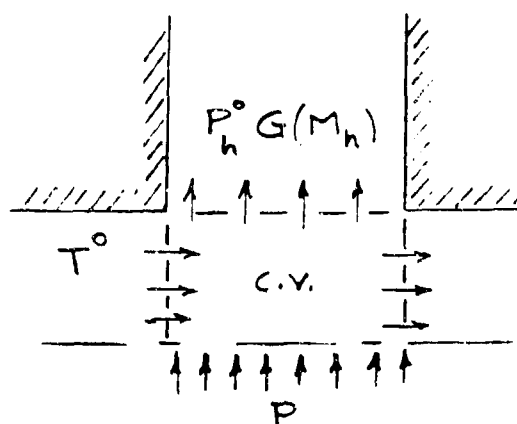


Figure 4 Momentum Balance-Control Volume

A momentum balance at the hole shows that $P = P_h^0 G(M_h)$. If it is assumed that $T_t^0 \approx T_h^0$, then (11) becomes

$$\frac{\dot{m}}{A_h \sqrt{P \rho}} = C_D \sqrt{\gamma} N(M_h) \quad (12)$$

The quantity $N(M_h)$ is relatively insensitive to Mach numbers in the range $0.8 < M_1 < 1.4$ so that in this range $\sqrt{\gamma} N(M_h) \cong \sqrt{\gamma/2(\gamma+1)}$. As a result for $\gamma = 1.25$

$$K(M_t) = 0.527 C_D \quad (13)$$

The values of $K(M_t)$ shown in the last column of Table 2 were calculated from this formula.

Figure 5 shows a plot of the results obtained here for a 90° hole, as well as the results obtained by Carofano [2]. If allowance is made for the possibility that the values of C_D used in Eq.(12) may be too low, the subsonic curve could approach a continuous extension of the Carofano curve into the subsonic region.

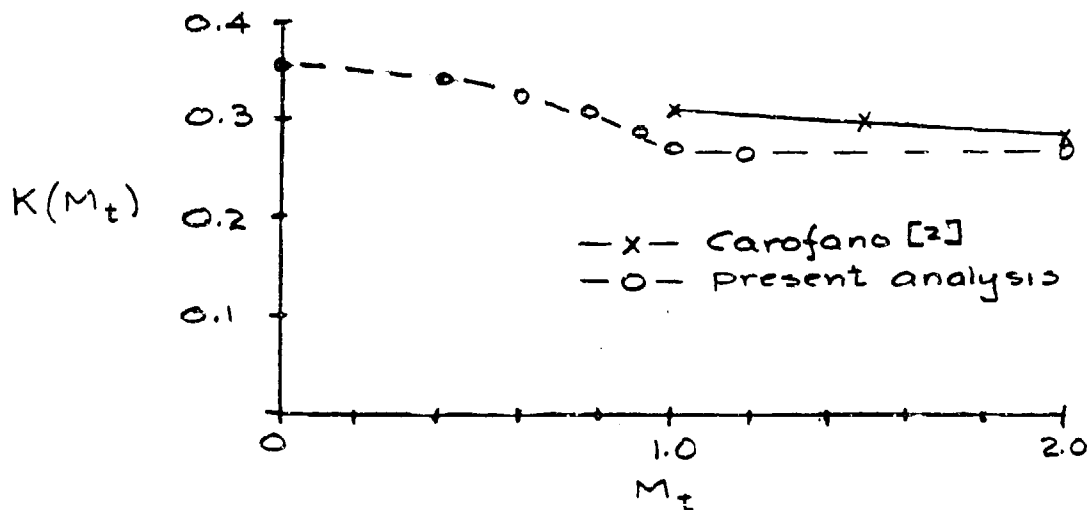


Figure 5 $K(M_t)$ for 90° Hole

FLOW THROUGH A 135° HOLE - TUBE MACH NUMBER > 1.0

The purpose of developing an approximate method is to provide a means for estimating $K(M_t)$ for a variety of hole orientations. Encouraged by the results of the 90° hole analysis the above techniques were extended to an orientation more typical of bore evacuator applications.

Bore evacuators which are filled and discharged through the same holes require that these holes be slanted down-tube, typically at 135° to the down-tube direction. For the case $\theta = 135^\circ$ and $M_t = 1.2$, in the hole $M_a = 4.65$, $\omega = 88.2^\circ$, $\theta_1 = 69^\circ$, $\delta = 46.6^\circ$.

With an initial assumption of $M_A = 2.0$ the continuity equations yield $a/b = 1.7$ and $a/h = 0.92$ indicating the presence of both "a" and "b" portions of the shock. When adjusted for "average" values of D along "a" and "b" these ratios become $a/b = 1.8$ and $a/h = 0.93$. Figure 6a shows the final construction for which $M_A = 2.06$, $\omega = 28.1^\circ$, $A = 1.25$, $a/h = 0.93$, $a/b = 1.8$.

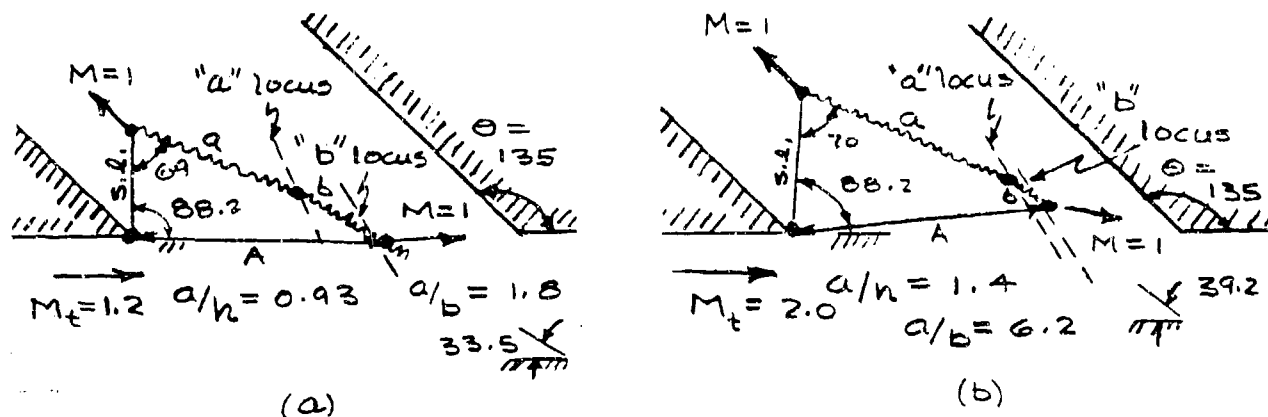


Figure 6 Flow Fields, $M_t = 1.2$ and $M_t = 2.0$

Equation (6) yields $K(1.2) = 0.217$ or 79% of the flow for the 90° hole. Smith's experimental results indicate that for $M_t = 1.0$ the flow rate for the 135° hole is 75% of the flow for a 90° hole.

Figure 6b shows the construction for $M_t = 2.0$. The shock also consists of both "a" and "b" portions in the ratio $a/b = 6.2$, with $a/h = 1.4$, $A = 1.2$ " and $\pi_A = 2.9$. Equation (6) yields $K(2.0) = 0.171$ or 62% of the 90° value.

FLOW THROUGH A 135° HOLE - TUBE MACH NUMBER < 1.0

The coefficient C_D does not appear to be available for the 135° hole. For the case $R^2 = 0$, Ref.[4] suggests the empirical coefficient

$$k = 0.5 + 0.3 \cos(180 - \theta) + 0.1 \cos^2(180 - \theta) \quad (14)$$

Assuming that $\theta = 135^\circ$ and $f \frac{l}{d} = 0.1$ yields $C_D = 0.72$ and $K(0) = 0.38$. Using the Smith result at $M = 1.0$ and Carofano's $K(1.0)$ for 90° yields a value of $K(1) = 0.75 (0.308) = 0.23$. A curve faired through these points and through the results of the supersonic analysis is sketched in Figure 7.

PROPOSED CORRELATION

Scaling $K(0) = 0.36$ of Table 1 by the ratio $0.80/0.68$ to account for "longer hole effects" in the 90° hole yields $K(0) = 0.42$. Fairing this to the Carofano value of $K(1.0) = 0.308$ yields the 90° hole interpolation curve shown as a dashed line in Figure 7. Carofano's 90° hole results are shown as a solid line in the range $1.0 \leq M \leq 2.0$. The results obtained here for the 135° hole are also shown with a solid line.

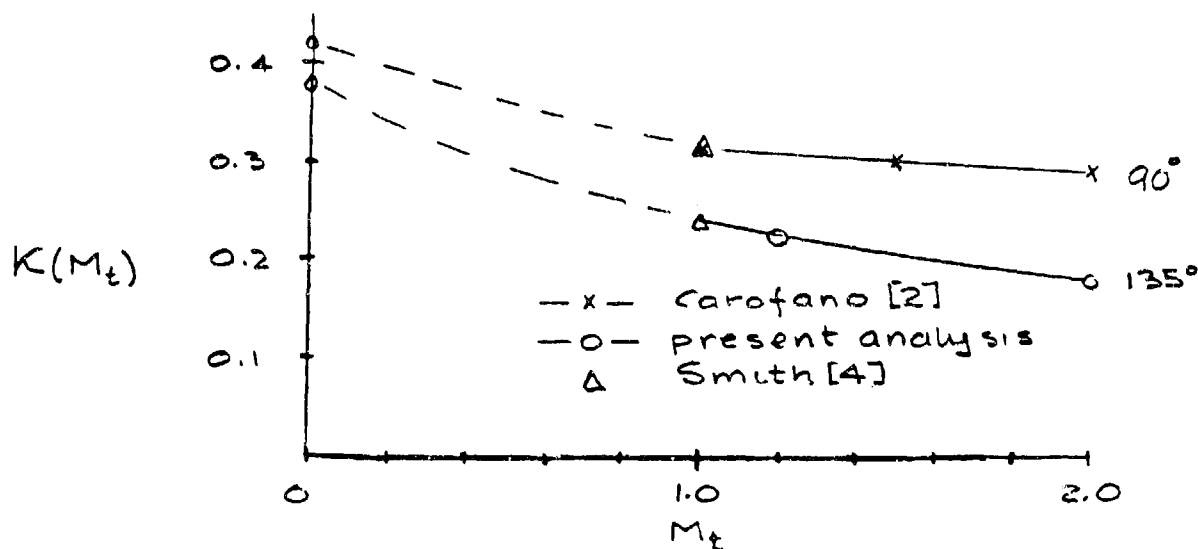


Figure 7 Interpolated $K(M_t)$ for 90° and 135° Holes

Figure 7 combines the results of this analysis and those of Refs. [1-4] into continuous curves of $K(M_t)$ for 90° and 135° holes.

RESULTS

1. The proposed approximate method for analyzing the flow through the hole when the tube flow is supersonic somewhat underestimates the hole flow rate. The error appears to decrease with hole angle.
2. The proposed empirical method for predicting the flow through the 90° hole when the tube flow is subsonic appears to be, with reasonable adjustments, a continuous extension of the sonic and supersonic results of Smith and Carofano.
3. A subsonic correlation is proposed for the 135° hole based on an interpolation of available empirical correlations for incompressible flow. It appears to be continuation of the supersonic results obtained by the approximate method proposed here.
4. The criterion for locating the dividing streamline (assumption 5), yields reasonably accurate results when compared to previous work.
5. Equation (5), proposed by Carofano, provides a convenient method for joining the interior ballistics to the hole flow over the full range of tube operation.
6. A proposed correlation of $K(M_t)$ has been obtained for two commonly used hole angles.

SNECK

NOMENCLATURE

a	hole side shock length
A	Mach line length
A _h	hole area
b	tube side shock length
C _D	subsonic incompressible discharge coefficient
d	hole diameter
D(M)	$= \frac{M}{\left[1 + \left(\frac{\gamma - 1}{2}\right) M^2\right]^{\frac{\gamma + 1}{2(\gamma - 1)}}}$
f	pipe friction factor
G(M)	$= \frac{1 + \gamma M^2}{\left[1 + \left(\frac{\gamma - 1}{2}\right) M^2\right]^{\frac{\gamma}{\gamma - 1}}}$
h	sonic exit length
k	pipe entrance dissipation factor
K(M _t)	hole flow coefficient
ℓ	hole length
\dot{m}	mass flow rate
M _a	Mach number at hole end of shock
M _A	Mach number on Mach line A
M _h	hole Mach number
M _t	tube Mach number
M _x	normal Mach number entering shock
M _y	normal Mach number leaving shock
N(M)	$= D(M)/G(M) = \frac{M}{1 + \gamma M^2} \sqrt{1 + \left(\frac{\gamma - 1}{2}\right) M^2}$
P	tube pressure
P ^o	tube stagnation pressure
P _a	evacuator pressure
P _h ^o	hole stagnation pressure

SNECK

R	gas constant
$R^2 = \frac{\rho U_t^2 / 2}{P - P_a + \rho U_t^2 / 2}$	
T^o	tube stagnation temperature
T_h^o	hole stagnation temperature
U_t	tube gas velocity
U_h	hole gas velocity
γ	specific heat ratio - 1.25
δ	deflection angle through shock
θ	hole angle
θ_1	hole side shock angle
ρ	tube gas density
ω	Prandtl-Meyer turn angle
s.l.	streamline
m.l.	Mach line

REFERENCES

1. Dillon, R.E., "Wall Thickness and Vent Area Effects on Perforated Muzzle Brake Performance," ARLCB-TR-84020, June 1984.
2. Nagamatsu, H.T., Choi, K.Y., Duffy, R.E., Carofano, G.C., "An Experimental and Numerical Study of the Flow Through a Vent Hole in a Perforated Muzzle Brake," ARCCB-TR-87-016.
3. Smith, F., "Investigation of Flume Extractor Design by Model Techniques," RARDE Memo. 13/67, Fort Halstead, U.K. 1967.
4. Blevins, R.P., "Applied Fluid Dynamics Handbook," Van Nostrand Reinhold Co., 1984, pp.71, 72, 94-95.

***TITLE: IMPACT RESPONSE OF HIGH CYCLIC RATE FLEXIBLE MECHANISMS**

Philip Benzkofer*
U.S. Army Armament Research, Development
and Engineering Center
Dover, New Jersey 07801

C. W. Chang and A. A. Shabana
Department of Mechanical Engineering
University of Illinois at Chicago
P.O. Box 4348
Chicago, Illinois 60680

***ABSTRACT:**

In this investigation a mechanism that provides a model for mechanical systems with variable kinematic structure is studied. The mechanism components experience only infinitesimal rotations owing to the elasticity of the support system. Because of the change in the system kinematic structure, the time domain is divided into subintervals. Over each subinterval, the motion of the mechanism is governed by a new set and a different number of kinematic constraint equations, and accordingly the rank and dimension of the system Jacobian matrix become time dependent. An impulsive continuous force with high magnitude and high frequency contents acts on the system components during a very short duration. The effect of this force is introduced to the dynamic formulation by developing continuous generalized impulsive forces associated with the system generalized coordinates using the virtual work expression. Effect of impacts between system components is predicted using generalized impulse-momentum balance approach that employs the coefficients of restitution.

IMPACT RESPONSE OF HIGH CYCLIC RATE FLEXIBLE MECHANISMS

Philip Benzkofer*

U.S. Army Armament Research, Development
and Engineering Center
Dover, New Jersey 07801

C. W. Chang and A. A. Shabana

Department of Mechanical Engineering
University of Illinois at Chicago
P.O. Box 4348
Chicago, Illinois 60680

1. INTRODUCTION

Many mechanical systems such as robotics, mechanisms, rockets, weapon systems, launch vehicles, and missiles are designed as light weight structures in order to achieve optimum performance. In many situations, these structure components are prone to dynamic excitation arising from impulsive forces, impacts or/and change in the system kinematic structure. The dynamic excitation, if significant, may not only induce significant dynamic stress levels but may also significantly affect the system performance. Therefore it becomes necessary to quantify the dynamic response of flexible mechanical systems at the design stage in order to achieve optimum performance. The present study examines the dynamic behavior of a multibody mechanism supported elastically, with a view to investigate the dynamic coupling between the mechanism and the elastic support system.

One of the main sources of undesirable intermittent motion behavior[2] is due to impacts or a change in the system kinematic structure due to mass captures and mass releases. This change in the kinematic structure may occur smoothly or accompanied by redistribution of the system momentum due to impacts between the system components. Even though the impact may occur locally(i.e. between two bodies in the system), the resulting impulsive forces affect the dynamic behavior of the entire system. Hunt and Crossley[1] presented a method for analyzing impacts between two rigid bodies. The coefficient of restitution is assumed to depend on the relative velocity between the impacting bodies. Lee and Wang[2] formulated a predictive model for the study of the dynamics of intermittent motion mechanisms. Their mathematical model includes clearance, damping, material compliance and mechanism elasticity. A new damping function was introduced, which characterizes the speed and load dependent nature of damping. Ehle and Haug[3] developed a logical function technique for smoothing the discontinuous behavior of the system in the short-lived interval of impact. Wehage and Haug[4] developed an automated method for the dynamic analysis of large scale rigid body systems using the generalized coordinate partitioning. In this technique

the dynamic equations of motion are formulated in terms of a minimum set of generalized coordinates. This technique has been extended to incorporate pieced interval intermittent motion analysis based on a generalized impulse-momentum balance[5] that accounts for the effect of the kinematic constraints.

A method for the dynamic analysis of large-scale constrained system of mixed rigid and flexible bodies with intermittent motion was presented in Ref.6. In the automated formulation of Ref.6, equations of motion are computer generated and integrated forward in time using an explicit-implicit direct numerical integration algorithm. Generalized impulse-momentum equations are solved at those points in time at which impacts occur. Solutions of these impulse-momentum relations define the jump discontinuity in the system velocity vector as well as the jump discontinuity in the system reaction forces. The technique developed in Ref.6 has been extended[7] to study the dynamics of multibody systems with variable kinematic structure.

In this investigation a method for the dynamic analysis of high cyclic rate mechanisms that are subjected to the combined effect of impacts, change in the kinematic structure and impulsive force is presented. Because of the change in the mechanism kinematic structure, a pieced interval analysis method is employed, wherein the time domain is divided into subintervals. Over each subinterval the motion of the multibody mechanism is governed by a new set and a new number of kinematic constraint equations and accordingly the system nonlinear Jacobian matrix has a dimension and a rank that depend on time. During each subinterval, a new set of system degrees of freedom is identified by the generalized coordinate partitioning of the constraint Jacobian matrix. The generalized impulsive force vector acting on the system is developed using the virtual work expression. While impacts between system components are described using a set of algebraic impulse-momentum equations, the generalized impulsive forces are introduced to the dynamic differential equations as continuous functions of time that act during a very short time duration. The mechanism support system that forms a structure with zero degree of freedom is discretized using the finite element method. Coupling between the rigid body degrees of freedom of the main system and the small elastic deformation of the support system is considered in this investigation.

2. DESCRIPTION OF THE SYSTEM

The two dimensional multibody system shown in Fig.1 is used to study the dynamic response of high cyclic rate mechanisms mounted on an elastic support. The mechanical system shown in Fig.1 consists mainly of two subsystems; the main system and the elastic support system. Each subsystem consists of several bodies. Relative translation between these two subsystems is allowed, it is however limited by the restoring force created by a spring with a nonlinear stiffness coefficient. The change in the kinematic structure, intermittent contacts and impacts, and impulsive forces occur in the main subsystem. The motion of the two subsystems,

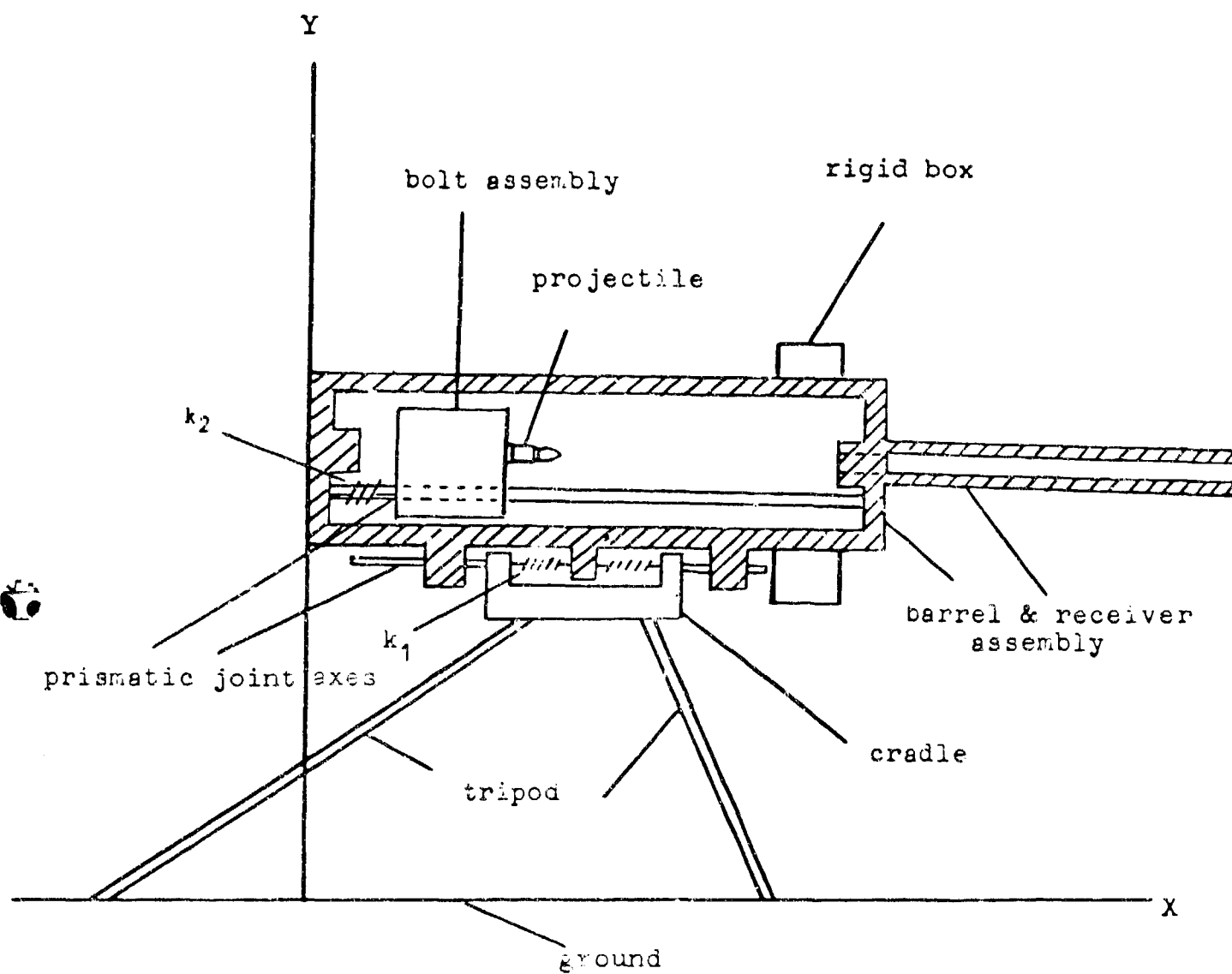


Fig. 1 High Cyclic Rate Mechanism

however, are coupled because of the relative motion between them is limited to be a translation along an axis shown in the figure and also because of the restoring spring force. In the following the two subsystems are described in more details.

2.1 Elastic Support Subsystem

The elastic support subsystem shown in Fig.1 forms a closed loop kinematic chain which consists of four bodies. Body one is the ground or the fixed link, bodies two and six are the flexible legs, and body five is the cradle assembly on which the main subsystem is mounted. The flexible tripod(bodies 2 and 6) is rigidly connected to the rigid cradle. Assuming that the tripod is fixed on the ground, it is obvious that the elastic support system has only deformation degrees of freedom and represents a closed loop structure. The flexible tripod(bodies 2 and 6) is discretized using two dimensional beam elements, each element has six nodal coordinates that describe the axial and transverse displacements and slopes at the selected nodal points. The rear and front legs are divided, respectively, into four and two beam elements. The natural frequencies and the type of mode shapes resulting from the finite element discretization are shown in table 1 and compared with the exact values obtained by solving the partial differential equations of the flexible legs[14]. It can be observed from this table that the natural frequencies which associated with the higher modes are not estimated as precisely as the lower frequencies when only a finite number of elements are used to model an elastic beam.

2.2 Main Subsystem

The main subsystem is shown in Fig.1 and consists of four rigid components. The first component in this subsystem is the receiver and barrel assembly which is denoted as body three. The 40mm-diameter barrel is rigidly connected to the receiver which is a steel housing that supports all other components. The receiver and the barrel assembly(body 3) is allowed to translate with respect to the cradle which is rigidly attached to the elastic support. The relative translation between the receiver and the cradle is constrained by the nonlinear stiffness spring k_1 which has a stiffness coefficient of 76870.(N/m). This spring, however, is active only when the compressive deformation of the spring is larger than 0.03(m). In addition to this rigid body translation, the receiver assembly may experience small rotations because of the deformation of the elastic tripod. The second body in the main subsystem(body 7) is a heavy box that is rigidly attached to the receiver. This heavy box physically represents the ammunition box. The third and fourth components in the main subsystems(bodies 4 and 8) are, respectively, the bolt assembly and the projectile. As shown in Fig.1, the projectile is initially connected to the bolt assembly by a rigid joint. The bolt assembly is allowed only to translate relative to the receiver along the axis shown in the figure. A trigger and sear mechanism are used to release the spring k_2 which provides the driving forces necessary to move forward the bolt assembly and the projectile. The driving spring k_2 has a stiffness coefficient of 1123.2(N/m). This

Table 1A Natural Frequencies of the Front Leg Using
Simply-Supported Reference Conditions

Frequency (1/s)	Mode Type	True Value	Calculated	Error %
1st	Bending	3783.11	3790.79	0.20
2nd	Bending	15132.45	16763.8	10.8
3rd	Axial	34048.00	20544.7	39.7
4th	Bending	60529.78	42137.1	30.4

Table 1B Natural Frequencies of the Rear Leg Using
the Simply-Supported Reference Conditions

Frequency (1/sec.)	Mode Type	True Value	Calculated	Error %
1st	Bending	835.36	836.13	0.12
2nd	Bending	3341.4	3357.7	0.49
3rd	Bending	7518.2	7662.4	1.9
4th	Axial	13366.	9234.0	30.9
5th	Bending	20903.	14847.	29.0
6th	Bending	30101.	23601.	21.6

spring, however, is under compression all the time and accordingly provides only a driving force that moves the bolt assembly and the projectile forward into the firing position. After the bolt travels a specified distance $x_0 = 0.30226(m)$, the projectile and the bolt assembly are separated due to the detonation of the propellant behind the projectile, and the mechanism encounters the first variation in its kinematic structure. At this instant of time the projectile starts traveling inside the barrel and a time-dependent firing force acts on the bolt assembly and the projectile. This firing force which is of impulsive nature tends to decelerate the bolt assembly while accelerating the projectile. While the projectile leaves the barrel after traveling a specified distance d and becomes under the influence of gravity only, the bolt encounters an impact with the front buffer of the receiver. Under the combined effect of the impulsive force and the impact force, the bolt assembly starts moving rearward until it encounters a second impact with the back buffer of the receiver and takes its original position ready to start another cycle. In this investigation the impulsive firing force was obtained by experimental measurements, and two different cases of firing forces are considered. In the first case, a low level impulsive force is considered, while in the second case, an impulsive force with higher magnitude is considered. Frictional resistance to projectile motion is not considered in this model.

The sequence of events can then be summarized as follows:

- (1) After the release of a trigger and sear mechanism, the driving spring exerts a force which drives the bolt assembly and the projectile in the forward direction.
- (2) After the bolt assembly and the projectile travel a specified distance, the firing pin strikes the percussion primer to ignite the propelling charge, thus producing a very high impulsive force.
- (3) Very shortly after firing, the system encounters the first variation in the kinematic structure when the projectile is separated from the bolt assembly and travels in the barrel under the action of the impulsive force. This impulsive force, however, tends to decelerate the forward motion of the bolt assembly.
- (4) With a reduced acceleration because of the firing impulsive force, the bolt continuously moves forward until it encounters an impact with the front buffer of the receiver.
- (5) Under the action of the impulsive force and the firing force, the bolt starts moving backward until it encounters a second impact with the back buffer of the receiver to occupy its original position and complete one cycle.
- (6) During the time of the rearward motion of the bolt, the projectile travels in the barrel under the pressure created by the impulsive firing force. The system encounters a second variation in its kinematic structure when the projectile leaves the barrel.

3. CONSTRAINT JACOBIAN AND COORDINATE PARTITIONING

Because of the change in the type of constraints imposed on the projectile motion, the variation in the system kinematic structure of the

high cyclic rate mechanism is expected. This variation in the kinematic structure determines the configuration space accessible to the components trajectories. The dynamic analysis of multibody systems with variable kinematic structure and with a number of kinematic constraint equations that is not time dependent has been studied in Ref. 7. This is however not the case in the problem under investigation, because the change in the kinematic structure is accompanied by a change in the number and type of constraint equations and the number of system degrees of freedom, and accordingly the dimension of the configuration space becomes time dependent. This can easily be understood if we consider the motion of the projectile. Before separation, the projectile is rigidly connected to the bolt assembly and the entire mechanism, if it were rigid, has only two degrees of freedom that describe the translation of the receiver with respect to the cradle and the translation of the bolt assembly and the projectile with respect to the receiver. After separation, the projectile translates in the barrel and the system gains an additional degree of freedom. The dimension of the configuration space which is defined as the number of the system coordinates minus the number of holonomic constraint equations is then two before separation and three after separation, again if the mechanism were rigid. If we write the vector function of the system holonomic constraint equations in a compact form as

$$C(q,t) = 0$$

where $C(q,t) = [C_1, C_2, \dots, C_m]^T$ is the vector of linearly independent constraint functions, t is time, m is the number of constraint functions that depends on time, and q is the vector of system coordinates that contains the vector of system rigid body coordinates q_r and the vector of system flexible coordinates q_f [9]. Let t_s be the time at which separation between the projectile and the bolt assembly occurs, and let $m=m_1$ before separation and $m=m_2$ after separation. In the problem under investigation, one can easily verify that

$$\Delta m_1 = m_1 - m_2 = 1$$

Therefore Δm_1 indicates the increase in the number of system degrees of freedom and the decrease in the number of constraint equations for the first kinematic structure change. Let t_1 be the time at which the projectile leaves the barrel. At this instant of time, the mechanism encounters the second change in its kinematic structure, and the projectile has unconstrained motion because it is influenced only by the gravity. At this point in time, the number of constraint equations becomes m_3 where $m_3 < m_2$. One can easily verify that

$$\Delta m_2 = m_2 - m_3 = 2$$

which implies that the system gains two more degrees of freedom. Therefore, one may write Eq.1 in a more explicit form as follows

$$C(q, t) = \begin{cases} C^s(q, t) = 0 & \text{for } t \leq t_s \\ \bar{C}^s(q, t) = 0 & \text{for } t_s < t \leq t_f \\ C^f(q, t) = 0 & \text{for } t > t_f \end{cases} \quad (2)$$

where

$$\begin{aligned} C^s(q, t) &= [C_1^s \quad C_2^s \quad \dots \quad C_{m_1}^s]^T \text{ for } t \leq t_s \\ \bar{C}^s(q, t) &= [\bar{C}_1^s \quad \bar{C}_2^s \quad \dots \quad \bar{C}_{m_2}^s]^T \text{ for } t_s < t \leq t_f \\ C^f(q, t) &= [C_1^f \quad C_2^f \quad \dots \quad C_{m_3}^f]^T \text{ for } t > t_f \end{aligned}$$

When a mixed set of Cartesian and elastic coordinates is used to describe the dynamics of multibody systems consisting of interconnected rigid and flexible bodies, it is more convenient to determine the set of independent coordinates (degrees of freedom) based on the numerical properties of the Jacobian matrix. For a virtual change in the system coordinates, Eq.2 leads to

$$C_q \delta q = \begin{cases} C_q^s \delta q = 0 & \text{for } t \leq t_s \\ \bar{C}_q^s \delta q = 0 & \text{for } t_s < t \leq t_f \\ C_q^f \delta q = 0 & \text{for } t > t_f \end{cases} \quad (3)$$

It is obvious, therefore, that the Jacobian matrix is not a continuous function of time. In fact the row rank of the Jacobian matrix is not constant either. Let $RR(A)$ denotes the row rank of the matrix A , one can easily then verify that

$$RR(C_q^s) - RR(\bar{C}_q^s) = 1 \quad (4)$$

$$RR(\bar{C}_q^s) - RR(C_q^f) = 2$$

The row rank of the Jacobian matrix C_q can be then described as a function of time by the step function. This leads accordingly, in addition to a change in the dimension of the configuration space, to a change in the basis and coordinates of this space. In order to further illustrate this fact, one may partition the vector of system coordinates to dependent and independent coordinates. According to this partitioning, Eq.3 can be

written as

$$C_{q_i} \delta q_i + C_{q_d} \delta q_d = \begin{cases} C_{q_i}^s \delta q_i^s + C_{q_d}^s \delta q_d^s = 0 & \text{for } t \leq t_s \\ \bar{C}_{q_i}^s \delta q_i^s + \bar{C}_{q_d}^s \delta q_d^s = 0 & \text{for } t_s < t \leq t_f \\ C_{q_i}' \delta q_i' + C_{q_d}' \delta q_d' = 0 & \text{for } t > t_f \end{cases} \quad (5)$$

where subscripts i and d refer, respectively, to independent and dependent coordinates, and the subJacobians associated with the dependent coordinates are nonsingular square matrices which have full row rank, thus nonsingular.

4. GENERALIZED FORCES

In this section the generalized forces associated with the system generalized coordinates are developed. Among the forces acting on the system components are the firing force, the spring forces and other external forces such as the weight of the system components. Constraint forces which arise because of mechanical joints such as prismatic and rigid joints are introduced in the following section using the vector of Lagrange multipliers. The impulsive force considered in this section is the firing force which acts on the projectile and the bolt assembly during a very short duration. Impacts that the bolt encounters with the receiver during the forward and backward motion, and the resulting impulsive forces are not considered in this section. The effect of the impact will be predicted using the algebraic generalized-momentum-balance equations.

4.1 Generalized Impulsive Forces

As it was pointed out in preceding sections, after the bolt assembly moves forward a specified distance, a firing pin strikes the percussion primer to ignite the propelling charge in a combustion chamber. The pressure resulting from the expanding gases exerts an impulsive force which drives the projectile forward in the barrel and resists the forward motion of the bolt assembly. This firing forces apply in a very short duration $\Delta t = t_2 - t_1 = 0.0021$ sec. For this high cyclic rate mechanism, the firing instant is determined by a logical function that depends on the system coordinates. The impulsive force is assumed to act only on the bolt and the projectile. Therefore, one can write the virtual work of this force as

$$\delta W_i = Q_i^b \delta q^b + Q_i^p \delta q^p \quad t_1 \leq t \leq t_2 \quad (6)$$

where δW_i is the virtual work of the impulsive force, q^b and q^p are, respectively, the vectors of generalized coordinates of the bolt and the projectile, and Q_i^b and Q_i^p are, respectively, the generalized impulsive forces associated with the generalized coordinates of the bolt and projectile. Equation 6 can be written in terms of the system generalized coordinates as

$$\delta W_i = Q_i^T \delta q \quad t_1 \leq t \leq t_2 \quad (7)$$

where q is the total vector of system generalized coordinates and Q_i is the generalized impulsive force vector, keeping in mind that the vector Q_i has nonzero entries only associated with the generalized coordinates of the bolt and the projectile. Perhaps it is important to mention at this point that even though the impulsive force resists the forward motion of the bolt, this force is not enough to reduce the bolt velocity to zero before it encounters the first impact with the front-buffer of the receiver. The backward motion of the bolt is then due to the combined effect of the impulsive firing force and the impact force.

4.2 Generalized Spring Forces

Two springs are used in the high cyclic rate mechanism. The first spring is the driving spring which is connected between the bolt and the receiver, while the second spring is connected between the receiver and the cradle assembly. These two springs are compressed all the time. In general, one can write the virtual work of the spring force between two bodies i and j as

$$\delta W_s^{ij} = F_s \delta l = -k(l - l_0) \delta l \quad (8)$$

where F_s is the spring force, k is the spring stiffness, l is the current spring length, l_0 is the undeformed spring length, and δl is the virtual change in the spring length. As shown in Ref.11, the virtual change δl can be written as a function of the generalized coordinates of bodies i and j , that is

$$\delta l = \delta l(q^i, q^j) \quad (9)$$

where q^i and q^j are, respectively, the vectors of generalized coordinates of body i and body j . In fact δl can be written as

$$\delta l = B^i \delta q^i + B^j \delta q^j \quad (10)$$

where B^i and B^j are matrices defined in Ref.11 and depend on the generalized coordinates of body i and body j . Substituting Eq.10 into Eq.8 yields

$$\delta W_s^{ij} = Q_s^{iT} \delta q^i + Q_s^{jT} \delta q^j = Q_s^T \delta q \quad (11)$$

where Q_s is the vector of generalized spring forces associated with the system generalized coordinates q .

4.3 Elastic and Gravity Forces

The virtual work of the weight of the mechanism components can be written in the compact form

$$\delta W_g^{ij} = Q_g^i \delta q^i + Q_g^j \delta q^j \quad (12)$$

where Q_g is the generalized force vector due to the weight which acts in the vertical direction.

The elastic forces resulting from the flexibility of the tripod can be obtained using the following definition of the strain energy for each flexible leg.

$$U = \frac{1}{2} \int_V \epsilon^T \sigma \, dV \quad (13)$$

where ϵ is the vector of strain components, σ is the vector of stress components and V is the volume of the flexible leg. Using Euler-Bernoulli theory, the strain energy which includes the effect of the transverse and axial deformation can be written as

$$U = \frac{1}{2} \int_0^l [EI(v'')^2 + EA(u')^2] \, dx \quad (14)$$

where E , I , l and A are, respectively, the modulus of elasticity, second moment of area, length and cross-sectional area of the flexible leg, u and v are, respectively, the axial and transverse displacements of the flexible leg and $(')$ denotes differentiation with respect to the spatial coordinates. Using the finite element method and following the procedure described in Ref.9, the strain energy of the flexible tripod U^t can be written in terms of the vector of system elastic coordinates as

$$U^t = \frac{1}{2} q_f^T K_{ff} q_f \quad (15)$$

where q_f is the vector of system elastic coordinates and K_{ff} is the stiffness matrix. If $q = [q_r^T, q_f^T]^T$ is the total vector of system coordinates and q_r is the vector of reference coordinates, the strain energy U^t of the flexible tripod can be written as [9]

$$U^t = \frac{1}{2} \begin{bmatrix} q_r^T & q_f^T \end{bmatrix} \begin{bmatrix} 0 & 0 \\ 0 & K_{ff} \end{bmatrix} \begin{bmatrix} q_r \\ q_f \end{bmatrix} = \frac{1}{2} q^T K q \quad (16)$$

where K is the system stiffness matrix.

5. DYNAMIC EQUATIONS AND IMPACT ANALYSIS

It has been shown in Ref.8, that the dynamic equations of multibody mechanisms consisting of a set of interconnected rigid and flexible bodies can be written as

$$\ddot{M}q + Kq + C_q^T \lambda = Q + F \quad (17)$$

where M and K are respectively the system symmetric mass and stiffness matrices, λ is the vector of Lagrange multipliers, Q is the vector of externally applied forces which includes the gravity effect, spring forces and the impulsive firing force that acts over a short-lived time interval, F is a quadratic velocity vector that contains the gyroscopic and coriolis effect [10], and C_q is the Jacobian matrix of the constraint functions of Eq.2.

5.1 Dynamic Equations

Because of the change in the kinematic structure of the mechanism, a pieced-interval analysis is employed where the time-domain is divided into subintervals. Over each subinterval, the motion of the high cyclic rate mechanism is governed by a different set of differential and algebraic constraint equations. In this investigation, the time domain is divided into three subintervals, i.e. $t \in (0, t_s]$, $t \in (t_s, t_f]$, and $t > t_f$, where t_s is the time at which separation between the projectile and the bolt assembly occurs and t_f is the point in time at which the projectile leaves the barrel. The impact between the front buffer of the receiver and the bolt assembly occurs during the third interval. The method of the impact analysis used in this investigation is discussed in the following section. The motion of the mechanism is then governed by the following set of differential and algebraic equations.

$$\begin{cases} \ddot{M}q + Kq + C_q^{sT} \lambda = Q + F \\ C^s(q, t) = 0 \end{cases} \quad 0 < t \leq t_s \quad (18)$$

$$\begin{cases} \ddot{M}q + Kq + \bar{C}_q^{sT} \lambda = Q + F \\ \bar{C}^s(q, t) = 0 \end{cases} \quad t_s < t \leq t_f \quad (19)$$

$$\begin{cases} \ddot{M}q + Kq + C_q^{fT} \lambda = Q + F \\ C^f(q, t) = 0 \end{cases} \quad t > t_f \quad (20)$$

The use of component modes synthesis techniques to reduce the number of elastic coordinates and accordingly the number of differential equations is described in Ref.9, while the numerical solution of the mixed set of differential and algebraic equations that describe the dynamics of

multibody systems consisting of interconnected rigid and flexible bodies is discussed in more details in Ref.12.

5.2 Impact Analysis

During one cycle of the motion, the bolt assembly encounters two impacts; one impact with the front buffer of the receiver during the forward motion and the other impact with the back buffer of the receiver during the backward motion. In this investigation, the effect of the impact on the dynamic response of the high cyclic rate, multibody mechanism is predicted using a pieced interval, generalized momentum balance approach. The method of impact analysis used in this investigation is similar to the one presented in Ref.7, wherein the time domain is divided into subintervals comprising points in time at which impacts occur. These impact points are determined using logical functions that depend on the system generalized coordinates, velocities and possibly on time. At those points in time the generalized impulse-momentum equations[7] are formulated and solved to obtain the jump discontinuity in the system velocity vector as well as the jump discontinuities in the generalized reaction forces[7].

6. NUMERICAL RESULTS

In the present investigation, two bending modes of vibration are used to describe the deformation of the front leg, and four modes of vibration are used to describe the deformation of the rear leg. A firing cycle, which starts from the initial position and ends with the second impact, takes 0.16133(sec.) and 0.15351(sec.), respectively, for the cases I and II of the impulsive firing forces.

The trajectory of the bolt assembly is shown in Fig.2. The relative velocity of the bolt with respect to the receiver is shown in Fig.3. While the first jump in the velocity is due to the impulsive force as well as the impact between the bolt and the front buffer of the receiver, the second jump in the velocity is the result of the back buffer impact. The deflections of the tripod assembly(bodies 2 and 6), which is composed of linear Hookean beam-like legs, are shown in Figs.4 and 5. It can be observed from these figures that both legs experience larger deflections after the impulsive firing force and the impacts.

7. SUMMARY

A method for the kinematic and dynamic analysis of a high cyclic rate mechanism is presented. The mechanism which is supported elastically, is subject to impact, impulsive forces and changes in the kinematic structure. The flexible support subsystem which has zero rigid body degree of freedom is discretized using the finite element method. The displacements and slopes of the selected nodal points represent the support system elastic coordinates which are coupled with the rigid body coordinates of the main system because of the mechanical constraints.

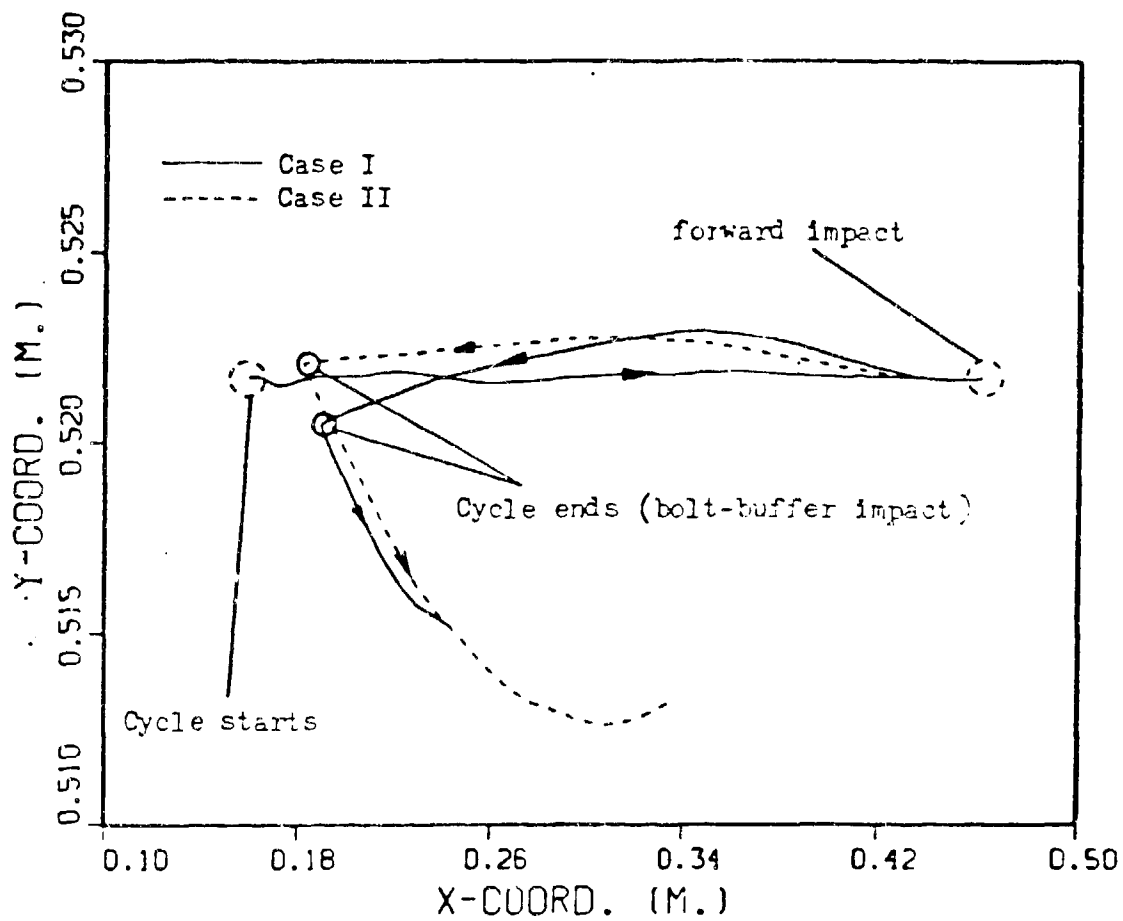


Fig. 2 Trajectory of the Bolt

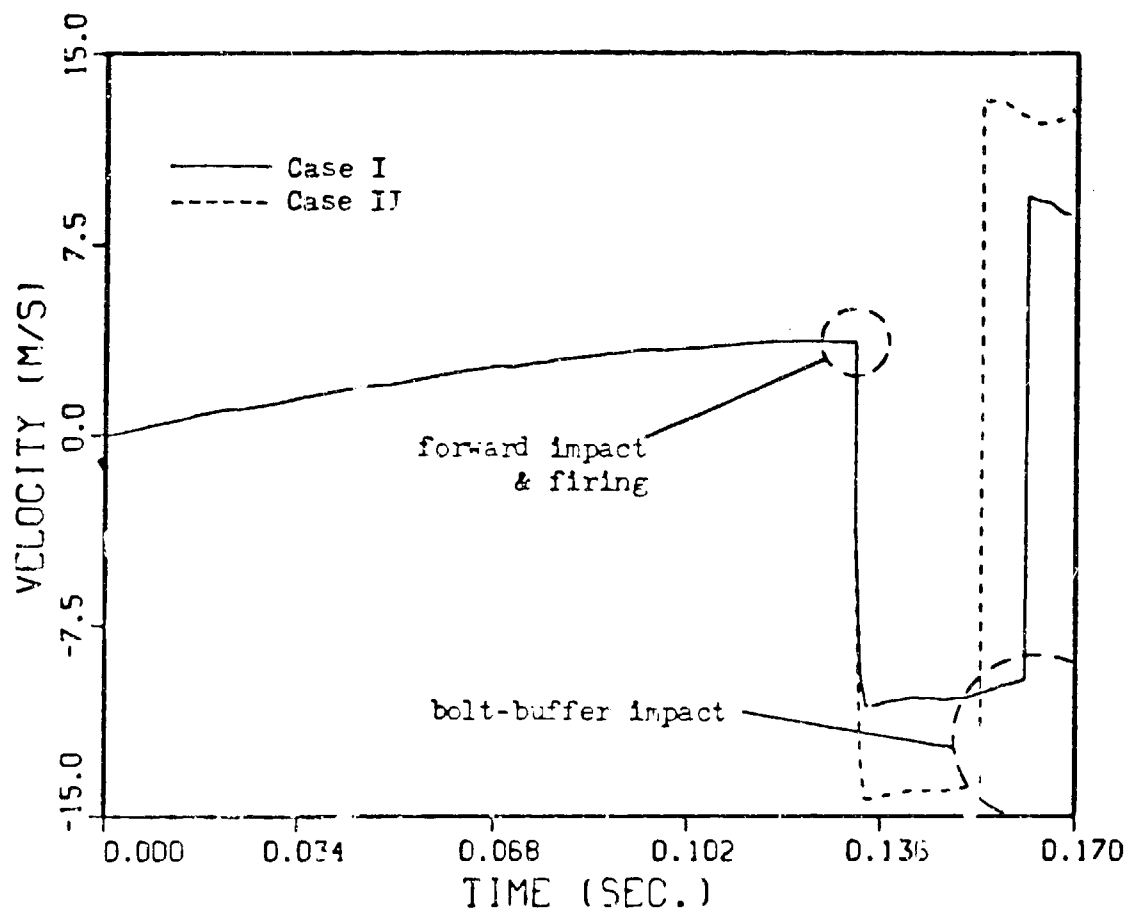


Fig. 5 Relative Velocity of the Bolt W.R.T. the Receiver

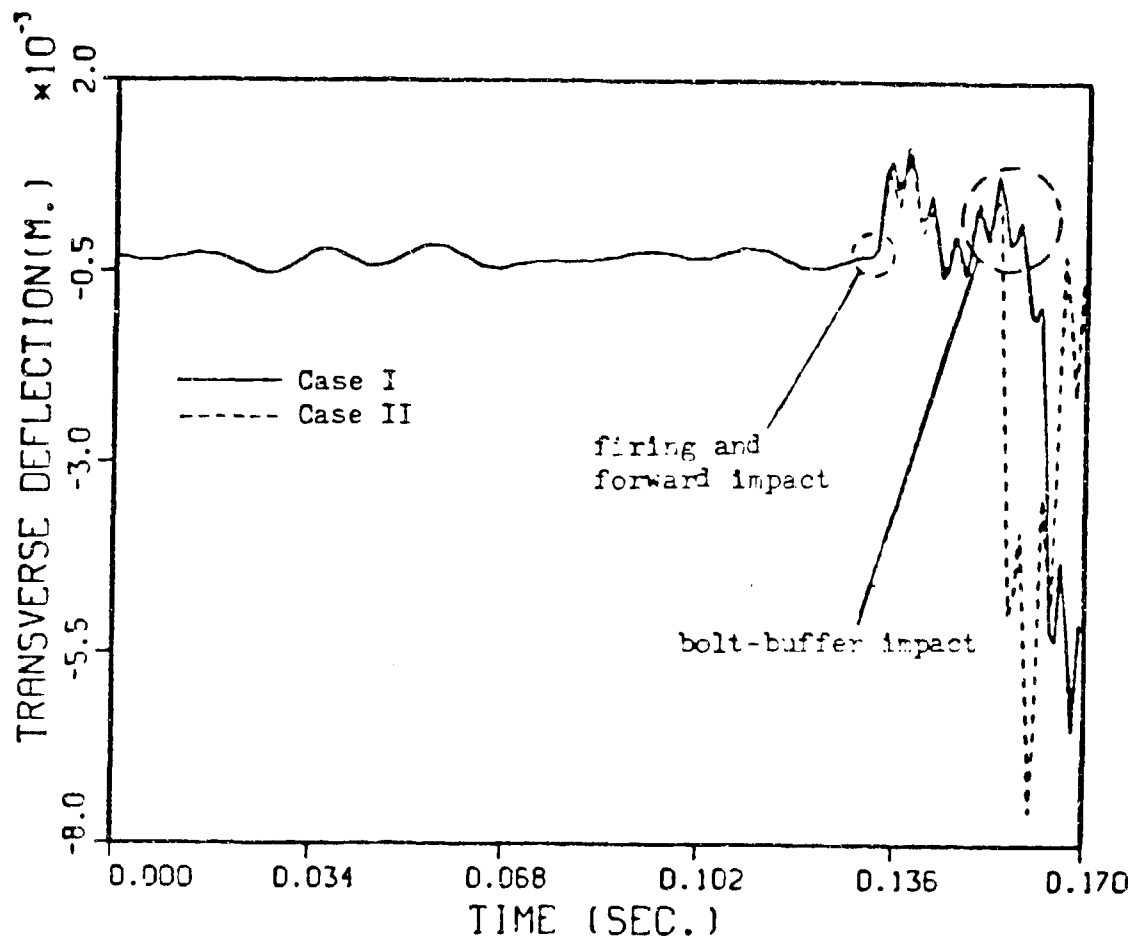


Fig. 4 Mid-point Deflection of the Rear Leg

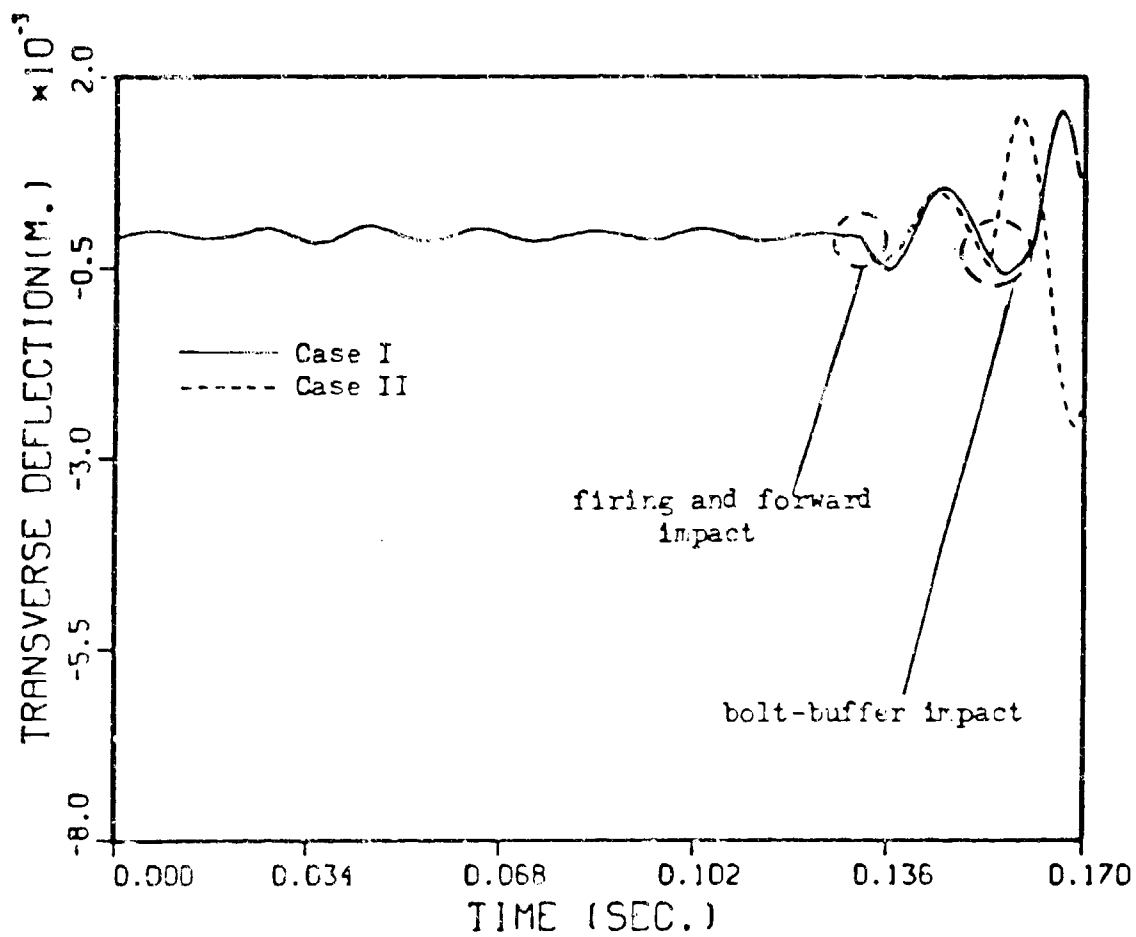


Fig. 5 Mid-point Deflection of the Front Leg

Smooth continuous functions of time are used to represent the impulsive forces while the effect of impact between the system components is predicted using the generalized impulse-momentum equations. Because of the change in the system kinematic structure, the time domain is divided into subintervals. Over each subinterval, the motion of the mechanism is governed by a new set of differential and algebraic equations. The system differential and algebraic equations are written in terms of a coupled set of reference and modal coordinates. Using the generalized coordinate partitioning of the constraint Jacobian matrix, a set of independent coordinates is identified over each subinterval. These coordinates are integrated forward in time using a direct numerical integration method. Dependent coordinates are then determined using the kinematic relations.

REFERENCES

1. Hunt, K. H., and Crossley, F. R. E., "Coefficient of Restitution Interpreted as Damping in Vibroimpact," ASME Journal of Applied Mechanics, June 1975, pp.440-445.
2. Lee, T. W., and Wang, A. C., "On the Dynamics of the Intermittent Motion Mechanisms, Part I and II," ASME Journal of Mechanisms, Transmissions, and Automation in Design, Vol.105, No.4, Sep. 1983, pp.534-551.
3. Ehle, P. E., and Haug, E. J., "A Logical Function Method for Dynamic Intermittent Motion," ASME Journal of Mechanical Design, 1981.
4. Wehage, R. A., and Haug, E. J., "Generalized Coordinate Partitioning for Dimension Reduction in Analysis of Constrained Dynamic Systems," ASME Journal of Mechanical Design, Vol.104, 1982, pp.247-255.
5. Kane, T. R., "Impulsive Motion," ASME Journal of Applied Mechanics, Dec. 1962, pp.715-718.
6. Khulief, Y. A., and Shabana, A., "Dynamic Analysis of Constrained System of Rigid and Flexible Bodies with intermittent Motion," ASME Journal of Mechanisms, Transmissions, and Automation in Design, Vol.108, No.1, March 1986, pp.38-45.
7. Khulief, Y., and Shabana, A., "Dynamics of Multibody Systems with Variable Kinematic Structure," ASME Journal of Mechanisms, Transmissions, and Automation in Design, Vol.108, No.2, June 1986, pp.167-175.
8. Shabana, A., and Wehage, R. A., "Variable Degree of Freedom Component Mode Analysis of Inertia-Variant Flexible Mechanical Systems," ASME Journal of Mechanisms, Transmissions, and Automation in Design, Vol.105, No.3, Sep. 1983, pp.371-378.
9. Shabana, A., and Wehage, R. A., "A Coordinate Reduction Technique for Transient Analysis of Spatial Substructures with Large Angular Rotations," Journal of Structure Mechanics, 11(3), 1983, pp.401-431.
10. Shabana, A., "Transient Analysis of Flexible Multibody Systems," Computer Methods in Applied Mechanics and Engineering, Vol.54, 1986, pp.75-91.
11. Agrawal, O. P., and Shabana, A., "Automated Viscoelastic Analysis of Large Scale, Inertia-Variant Spatial Vehicles," Int. Journal of Computers and Structures, Vol.22, No.2, 1986, pp.165-178.
12. Shabana, A. A., "Effect of Using Composites on the Dynamic Response of

- Multibody Systems." Journal of Sound and Vibration, Vol.108, No.2, July 1986.
13. Shabana, A., "Dynamics of Inertia-Variant Flexible Systems Using Experimentally Identified Parameters," ASME Journal of Mechanisms, Transmissions and Automation in Design, Vol.108, No.3, Sep. 1986, pp.358-366.
 14. Timoshenko, S. P., Young, D. H., and Weaver, W., "Vibration Problems in Engineering", John Wiley & Sons, Inc., 1974.

SIMKINS

TITLE: RESONANCE OF FLEXURAL WAVES IN GUN TUBES
T. E. SIMKINS
US ARMY ARMAMENT RESEARCH, DEVELOPMENT, AND ENGINEERING CENTER
CLOSE COMBAT ARMAMENTS CENTER
BENET LABORATORIES
WATERVLIET, NY 12189-4050

ABSTRACT:

Experimental and analytical studies have verified the existence of high amplitude dynamic strains in large caliber gun tubes. These strains have been observed to travel with the projectile as axially symmetric waves and are large enough to exceed the yield stress of the gun tube material and become even larger as the wave reflects from the muzzle. The possibility for such waves in cylinders has been known since 1964 and physical evidence for their existence in gun tubes was first reported in 1978 and in 1986 by the author. These waves not only create strains higher than those for which the gun tube is designed, but are capable through coupling of producing beam-like motions affecting projectile launch conditions. Muzzle motions affecting round accuracy have long been suspect and their spurious character has evaded the most arduous attempts to predict them.

The existence of large amplitude dynamic strains in gun tubes implies a projectile environment more hostile than previously supposed. Designers of projectile casings, warheads, fuzes, etc., should be interested in these ramifications as should those concerned with projectile/tube friction and wear.

BIOGRAPHY:

PRESENT ASSIGNMENT: Research Mechanical Engineer, US Army ARDEC, Benet Laboratories, Applied Mathematics and Mechanics Section, Watervliet, NY.

DEGREES HELD: Ph.D. - Mechanics, Rensselaer Polytechnic Institute, Troy, NY; B.S. - Mechanical Engineering, Northeastern University.

RESONANCE OF FLEXURAL WAVES IN GUN TUBES

T. E. Simkins

US Army Armament Research, Development, and Engineering Center
Close Combat Armaments Center
Benet Laboratories
Watervliet, NY 12189-4050

INTRODUCTION

The work presented herein was motivated by a series of unusual strain data collected during a series of test firings of a 120-mm gun tube at Aberdeen Proving Ground (APG) during the latter part of 1985. During these tests, circumferential strains exceeding three times those predicted by the customary Lamé design formula [1] were recorded from the outer surface of this tube a few feet from the muzzle. The strain data was unusual in that a very sudden strain 'spike' was recorded as the projectile passed the gage location (see Figure 1). Initially it was thought that this spike might be due to faulty gage bonds, electrical interference, etc. Subsequent verification of the data, however, resulted from additional measurements in which displacement eddy probes located close to the strain gages showed surface displacements in very good agreement with those predicted by the strain gages. The 'spike' was real.

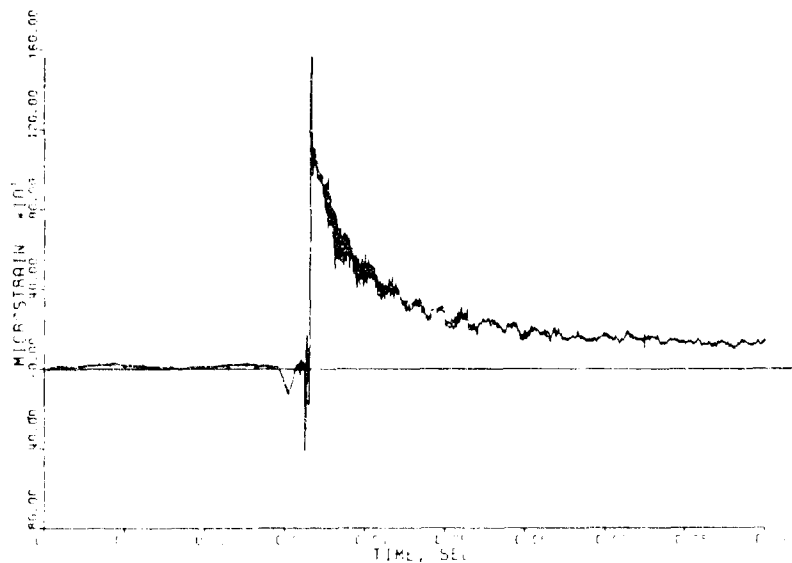


Figure 1. Typical Strain Record.

SIMKINS

As more data was accumulated, analysis showed a strong dependency of the strain magnitudes on projectile velocity (see Figure 2), and it was this feature more than any other which guided the research reported herein.

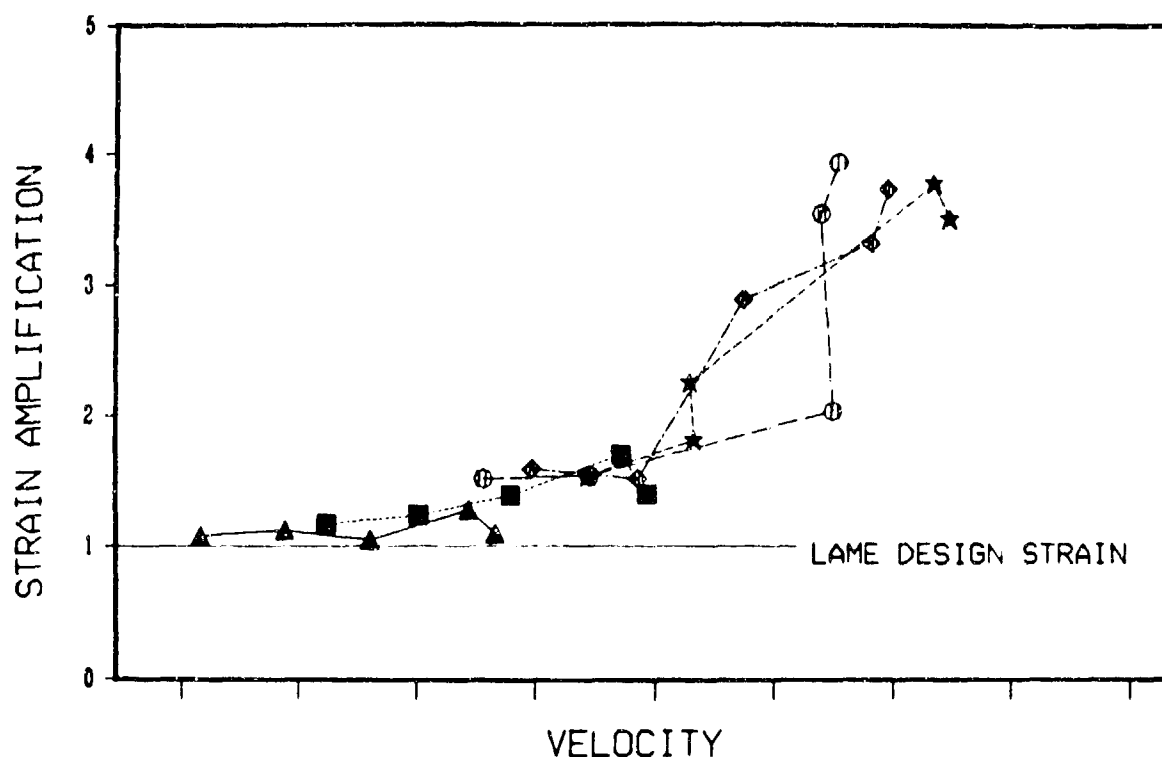
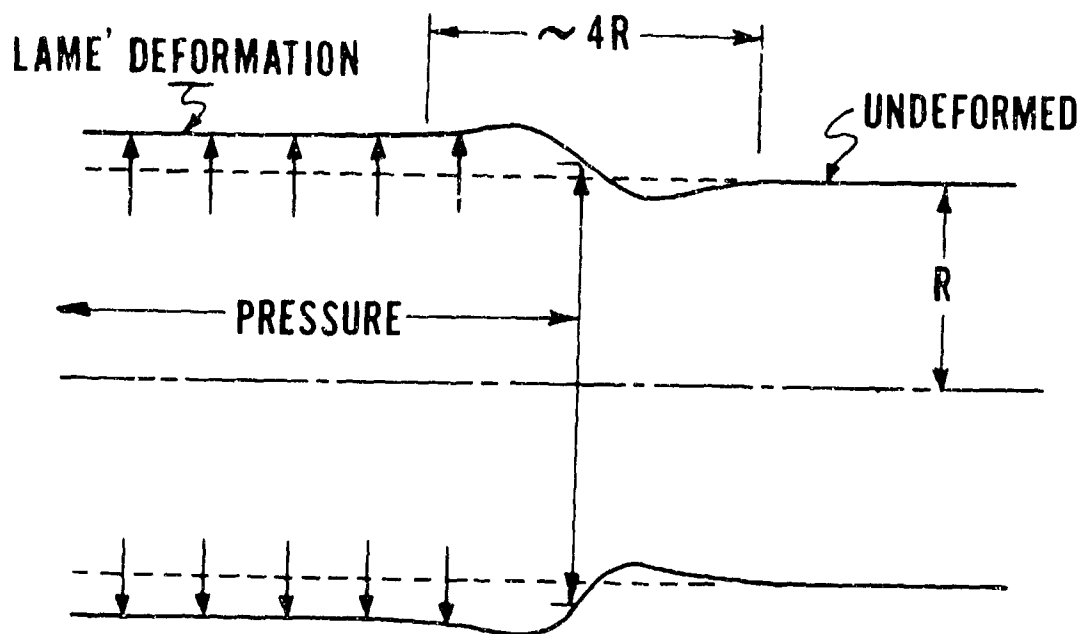


Figure 2. Strain Dependence on Projectile Velocity.

HYPOTHESIS

The key idea to be explored was that there may be a limit as to how fast the tube deformation - in the immediate vicinity of the projectile - could be made to travel before some sort of a wave would develop. An exaggerated view of this deformation when the projectile velocity is low is shown in Figure 3. Under these 'quasi-static conditions', the deviation from the Lame' predicted deformation is less than three percent. A search of the literature showed that this idea had received attention at least thirty years ago, although not with application to gun tubes. According to the literature [2-5], there is indeed a critical projectile speed at which one can anticipate a resonance phenomenon accompanied by very high strain levels within the tube wall.



DEFORMATION OF BORE SURFACE (STATIC)

Figure 3

VERIFICATION

Calculations based on much simplified thin-walled shell equations showed that the strain data of Figure 1 was much too compressed in the time scale to ascertain even a qualitative resemblance to the strain versus time predicted by the 'critical velocity' theory. In April 1986, new test firings were therefore conducted for the purpose of gaining more detail to the tube response at the instant of projectile passage. The results showed the 'spike' not to be a spike at all - but a high amplitude, high frequency (approximately 15 khz) strain very close to that predicted by the 'critical velocity' theory, which by this time had been considerably refined and quantified for the 120-mm gun tube application. Two strain gages and eddy probes mounted on diametrically opposite sides of the tube gave the same measured values, attesting to the perfect axial symmetry of the phenomenon. A comparison of the predicted strains with these measured values appears in Figure 4.

The work herein attempts to give an overview of the mathematical physics involved in the 'critical velocity' theory of axial symmetric tube deformation and explores the implications this theory holds for nonaxisymmetric motions of the tube. A special case of these are the beam-like motions which influence the launch angle of the projectile at shot exit, a subject which has occupied the forefront of gun dynamics during the past decade [6-9].

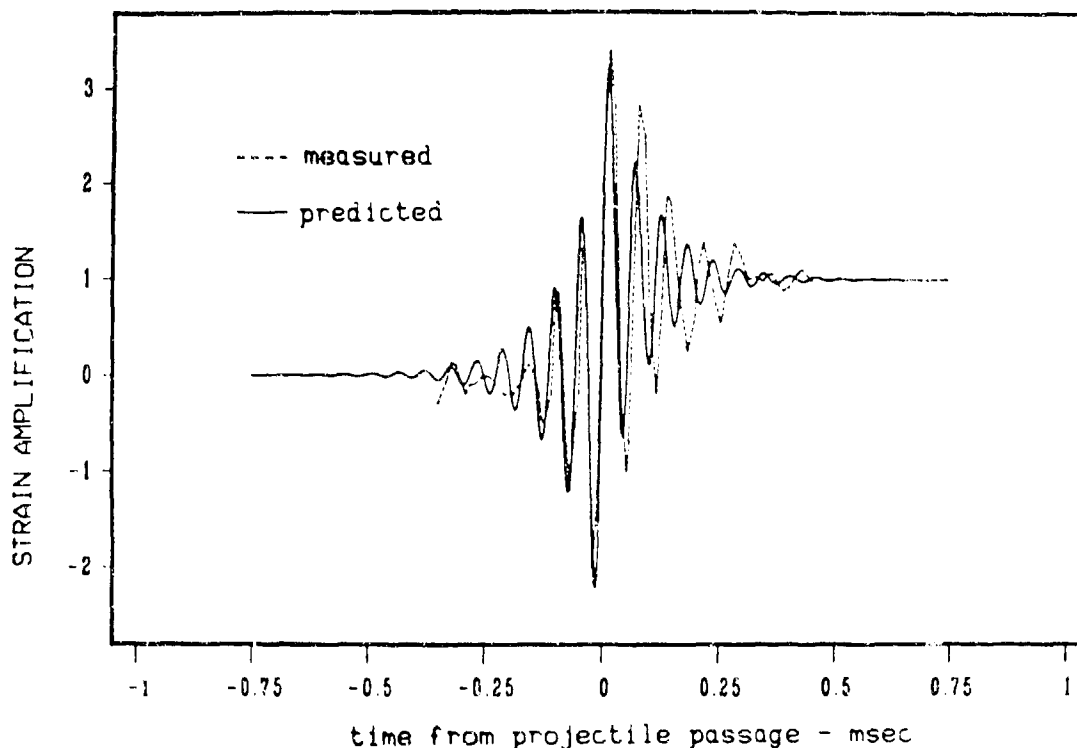


Figure 4. Verification of the Critical Velocity Theory.

THE ESSENTIALS OF THE CRITICAL VELOCITY THEORY

In Figure 3 the tube is imagined to be infinitely long, of uniform cross section, and subjected to an axisymmetric pressure step moving at constant velocity. The simplest equation containing the essential physics of the situation is [2]

$$\frac{D\partial^4 w}{\partial x^4} + \frac{Ehw}{R^2} + \frac{m\partial^2 w}{\partial t^2} = Q(1-H(x-vt)) \quad (1)$$

where Q is a constant and represents the magnitude of the moving pressure and H is the Heaviside step function:

$$H(x-vt) = 0 \quad x < vt$$

$$= 1 \quad x > vt$$

In this equation, w is the radial displacement of the median surface of the cylindrical shell located at a distance x along, and R from, the central axis; h is the shell thickness and is assumed to be small compared to R ; $m = \rho h$ where ρ is the mass density of the shell material; $D = Eh^3/12(1-\nu^2)$; E is Young's modulus of elasticity; ν is Poisson's ratio; and v is the velocity of the moving pressure, assumed to be finite and constant. Equation (1) is equivalent to the equation governing the motion of a Bernoulli-Euler beam on an elastic foundation, and accordingly, the effects of shear deformation and rotatory inertia are neglected.

Conventionally, steady state solutions are sought to this equation under the conditions that the displacement remain bounded as $x \rightarrow \pm \infty$ and that the stresses and displacements be continuous at the location of the pressure front, $x = vt$. In particular, these solutions have the form $w = Ae^{ik(x-vt)}$ and are steady when seen by an observer moving with the pressure front at $x = vt$. k is the wave number and, in general, is complex. Only when k is real does the assumed form of the solution represent a wave. To find what waves can exist naturally in the cylinder, one sets $Q = 0$, and by substituting the assumed solution into Eq. (1), it is seen that real waves are possible for those values of k which are the real roots of the equation

$$k^4 \gamma^2 + 2\lambda k \gamma + 1 = 0 \quad (2)$$

where

$$\gamma^2 = Eh/R^2 D$$

$$\lambda = mv^2 \sqrt{\frac{R^2}{EhD}}$$

and v is the phase velocity. (real). A plot of these wave numbers versus phase velocity is called a dispersion curve and is shown in Figure 5 ($C_0 = \sqrt{E/\rho}$). This plot shows that waves with low wave number (long waves) travel with phase velocities which decrease with wave number, while waves with high wave numbers (short waves) have phase velocities which increase with wave number. This happens because of two competing restoring forces contained within the model. The tube can deform as a cylindrical membrane in which case the second term of Eq. (1) dominates the behavior, or it can deform as a beam in which case the first term dominates. The fact that these two mechanisms compete to produce a minimum in the dispersion curve in Figure 5, is the important part of the critical velocity theory.

Phase and Group Velocities vs. Wave Number

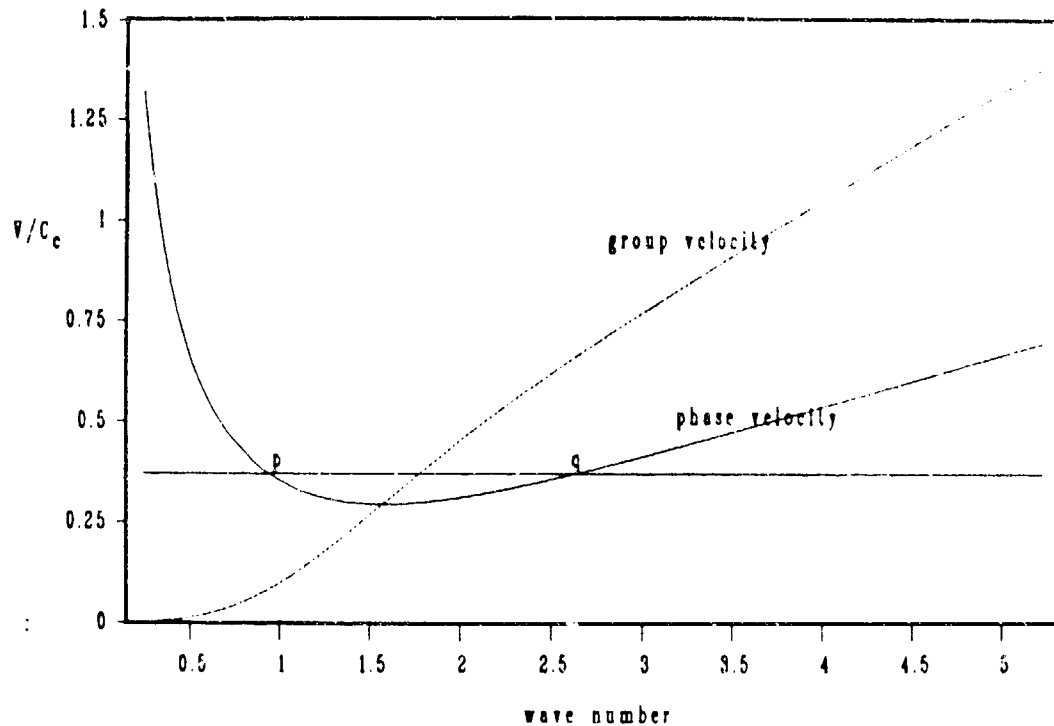


Figure 5

For the purpose of discussion, it can be considered axiomatic that if waves are to be generated by a moving axisymmetric pressure Q , the phase velocity of these waves will be the velocity of the moving load. That is, the load must be in phase with the wave(s) it creates. With this in mind, Figure 5 shows that such waves are possible provided the load velocity equals or exceeds the minimum possible value. Let us assume for the moment that the load velocity (the projectile velocity) somewhat exceeds this minimum. Figure 5 shows that under these circumstances two waves can exist with this phase velocity. In this case, the solution for the midwall displacement w is

$$w/C = \frac{-b^2}{b^2 - a^2} \cos a(x-vt) + 1 \quad ; \quad x \leq vt$$

and

$$w/C = \frac{-a^2}{b^2 - a^2} \cos b(x-vt) \quad ; \quad x \geq vt \quad (3)$$

SIMKINS

where

$$a = \sqrt{\frac{1+\lambda}{2}} - \sqrt{\frac{\lambda-1}{2}}, \quad b = \sqrt{\frac{1+\lambda}{2}} + \sqrt{\frac{\lambda-1}{2}}$$

and $C = QR^2/Eh$ approximates the Lamé displacement. Note that for $\lambda \gg 1$, the solution for $x \leq vt$ approaches $2C$, twice the Lamé displacement.

Now, physically we know that the energy contained in these two waves must radiate away, not toward, the source of the disturbance, namely the pressure front. Further, it is known that energy travels not at the phase velocity, but at another velocity called the 'group velocity'. The group velocity is related to the phase velocity as follows:

$$V_g = kdv(k)/dk + v(k)$$

where $v(k)$ is the phase velocity curve of Figure 5.

It can easily be seen that should dv/dk ever vanish, the group velocity and phase velocity would be equal and that energy could then not radiate away from the pressure front, but would continually build the deformation in the neighborhood of the front as time progressed, i.e., resonance would result. Thus, the minimum phase velocity of Figure 5 is indeed a 'critical velocity' and it is the near attainment of this velocity which caused the high strains in the 120-mm gun tube.

If the velocity of the moving pressure is less than the minimum possible for wave formation, the wave number k is complex and the solution to Eq. (1) has the form of a damped harmonic:

$$w/C = \frac{e}{2} \begin{matrix} d(x-vt) \\ (-\cos c(x-vt) + \frac{d^2-c^2}{2cd} \sin c(x-vt)) + 1 \end{matrix} \quad x \leq vt$$

and

$$w = \frac{e}{2} \begin{matrix} -d(x-vt) \\ (\cos c(x-vt) + \frac{d^2-c^2}{2cd} \sin c(x-vt)) \end{matrix} \quad x \geq vt \quad (4)$$

where

$$c = \sqrt{\frac{\lambda+1}{2}}, \quad \text{and} \quad d = \sqrt{\frac{1-\lambda}{2}}$$

From the standpoint of gun tube design, it is important to be able to predict critical velocities as accurately as possible and to be able to predict results for different wall thicknesses. It is also of interest to accurately predict the steady state deformation at any velocity of the pressure front. Thus, it is necessary to use a model which is not restricted to cylinders of thin wall thickness. Equations of motion representing such a model have been derived by Mirsky and Herrmann [10] and are considerably more complicated than Eq. (1). They are used to obtain the results which follow in much the same way as discussed previously. (Tang [3] has solved this moving pressure problem using the three shell equations of Lin and Morgan. The set of four equations derived by Mirsky and Herrmann are reportedly better for thick-walled cylinders, however.)

Although transient effects, boundary reflections, nonuniformity of wall thickness, and variable pressure (projectile) velocity are ignored, steady state calculations for thick-walled cylinders nevertheless produce results in remarkable agreement with measured values when the projectile velocity is close to critical (see Figure 4). (The assumption of constant projectile velocity is justified in the forward regions of many gun tubes where the projectile velocity/travel curve is relatively flat.)

The best prediction of critical velocity can be obtained using the exact equations of three-dimensional elasticity as opposed to the approximate shell equation (Eq. (1)) used thus far. The relevant equations are [11]

$$\begin{aligned}
 f(K) = & [K_{10}(\beta)K_{01}(\gamma) + K_{01}(\beta)K_{10}(\gamma) + (8/\pi^2\beta\gamma ab) + FK_{11}(\gamma)K_{00}(\beta) \\
 & + (1/F)K_{11}(\beta)K_{00}(\gamma)] + [(1+\bar{B})^2/F\gamma^2 ab]K_{11}(\beta)K_{11}(\gamma) \\
 & - [(1+\bar{B})/\gamma ab][aK_{11}(\gamma)K_{10}(\beta) + bK_{11}(\gamma)K_{01}(\beta)] \\
 & - [(1+\bar{B})/F\gamma ab][aK_{11}(\beta)K_{10}(\gamma) + bK_{11}(\beta)K_{01}(\gamma)] = 0
 \end{aligned} \tag{5}$$

where

$$K_{mn}(z) = J_m(zb)Y_n(za) - J_n(za)Y_m(zb)$$

$$\beta^2 = \alpha^2 \left(\frac{V^2}{C_C^2} - 1 \right)$$

$$\gamma^2 = \alpha^2 \left(\frac{V^2}{C_S^2} - 1 \right)$$

$$\bar{B} = \frac{V^2}{2C_S^2} - 1$$

$$F = \frac{\alpha^2 \bar{B}^2}{\beta \gamma}$$

$$C_C^2 = (\bar{\lambda} + 2\mu)/\rho$$

$$C_S^2 = \mu/\rho$$

SIMKINS

- α = wave number
- a = the inner radii of the cylinder
- b = the outer radii of the cylinder
- $J_m(z)$ = Bessel functions of the first kind
- $Y_m(z)$ = Bessel functions of the second kind
- $\bar{\lambda}$ = Lamé elastic constants

Equation (5) is now the dispersion relation in place of Eq. (2) and the corresponding dispersion curve for the 120-mm gun tube is shown in Figure 6. It is interesting to note that the critical velocity, α , determined from Eq. (5), is only about eight percent lower than that predicted by the much simplified dispersion relation (Eq. (2)).

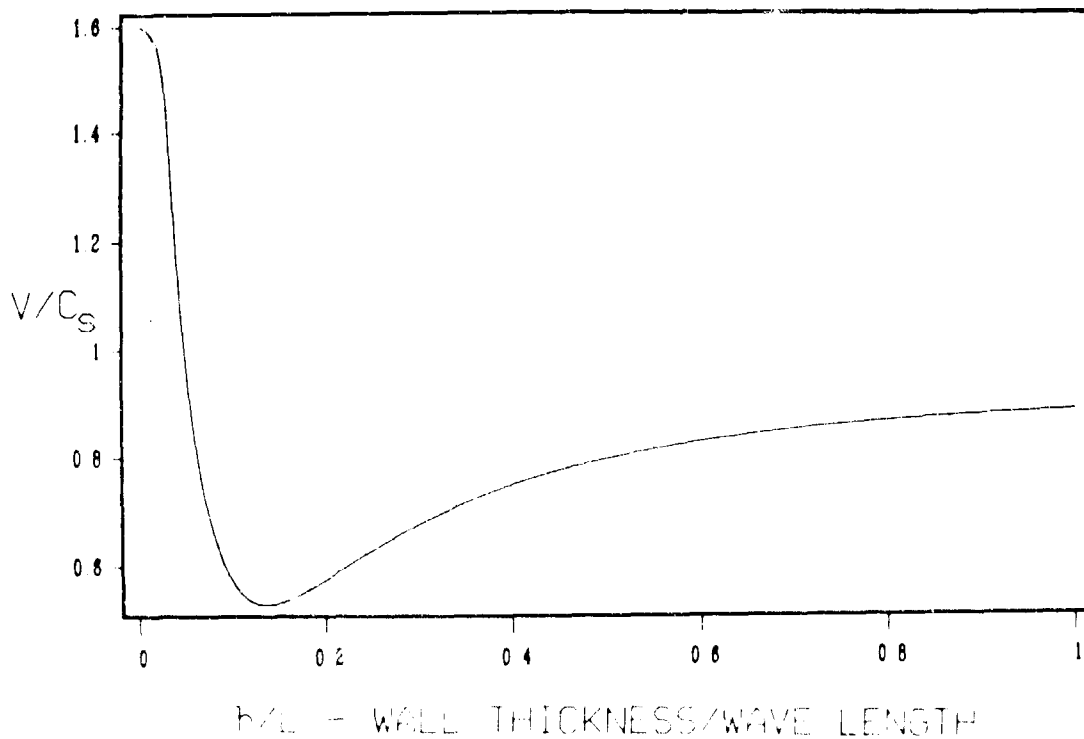


Figure 6. Dispersion Curve - 3-D Elasticity.

A complete account of the steady state calculations can be found in a technical report [12] by the author. Pertinent results are shown in Figure 7 - an amplification curve comparing the dynamic strains with those computed by the 'static' Lamé formulation, and in Figure 8 - a curve showing the variation of critical velocity with tube wall thickness.

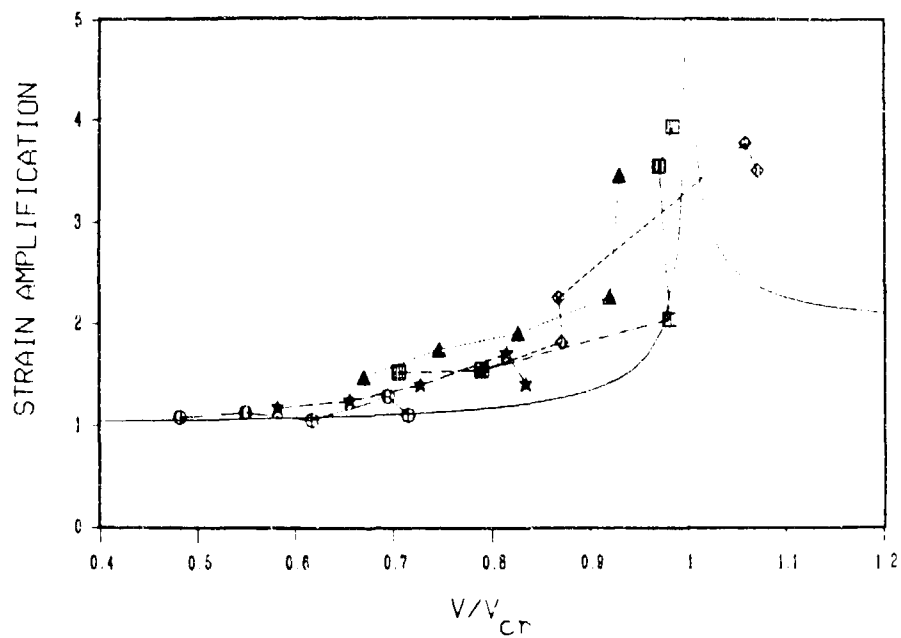


Figure 7. Predicted and Measured Strains.

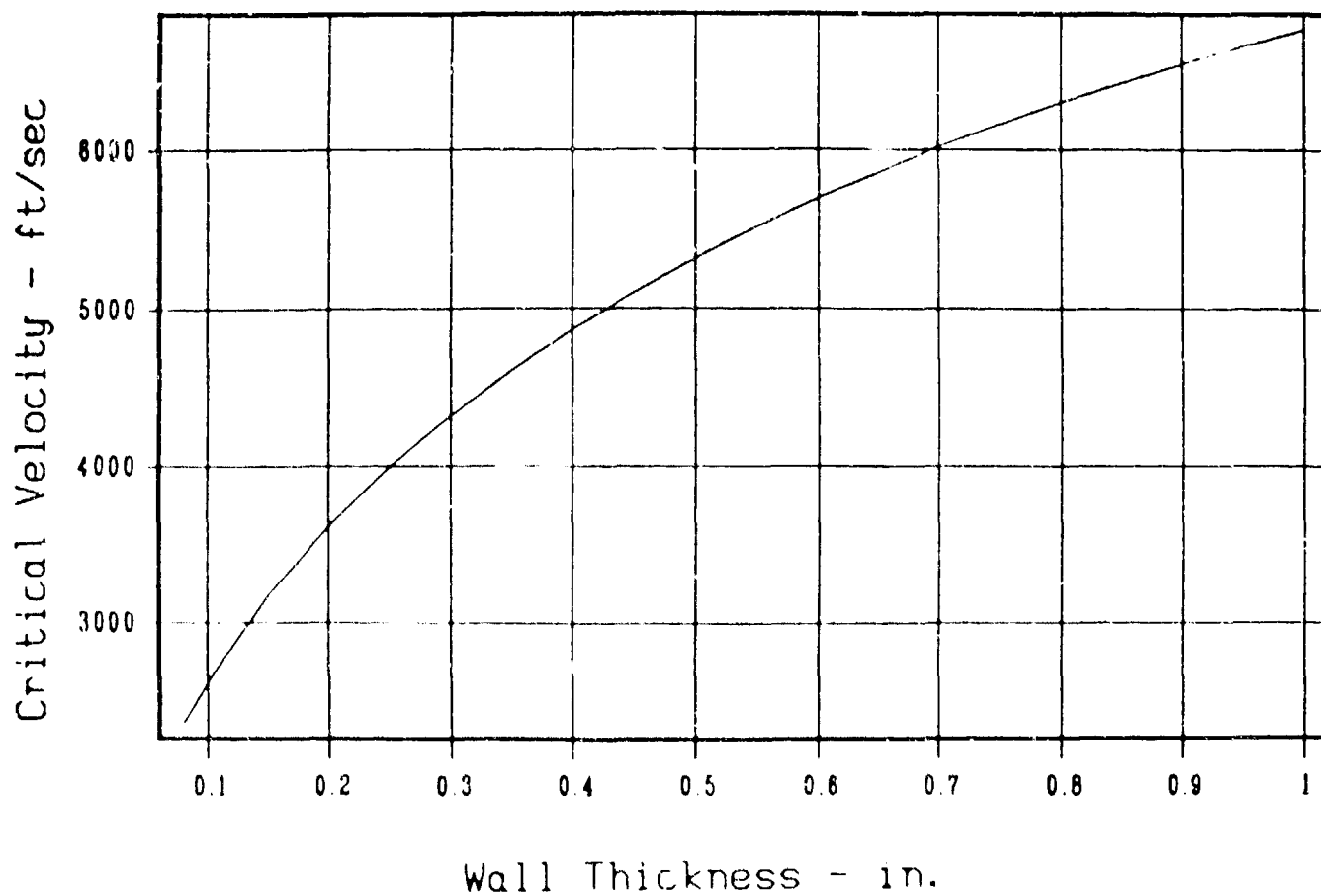


Figure 8. Critical Velocity Versus Wall Thickness.

NON-AXISYMMETRIC MOTIONS - IMPLICATIONS OF THE CRITICAL VELOCITY THEORY

Mirsky and Herrmann [13] have also derived a set of five equations which govern both axisymmetric and nonaxisymmetric motions of a uniform hollow cylinder. Gazis [14] has gone a step further, accomplishing the same end using the more accurate three-dimensional equations. Briefly, solutions for the radial displacements at midwall are sought of the form

$$Ae^{ik(x-vt)} \cos n\theta \text{ or } Ae^{ik(x-vt)} \sin n\theta \quad (6)$$

where $n = 0, 1, 2, \dots$ and x and θ are the coordinates of any midwall material point. The cases of interest to gun dynamics are

$n = 0$, axisymmetric motions

$n = 1$, the deformation is beam-like (the top and bottom of the tube move equal amounts in the same direction so that the bore axis is displaced). The dispersion curve is shown in Figure 9.

$n = 2$, the bore axis is not displaced and the tube assumes a shape somewhat of an ellipse. The dispersion curve for this case is shown in Figure 10.

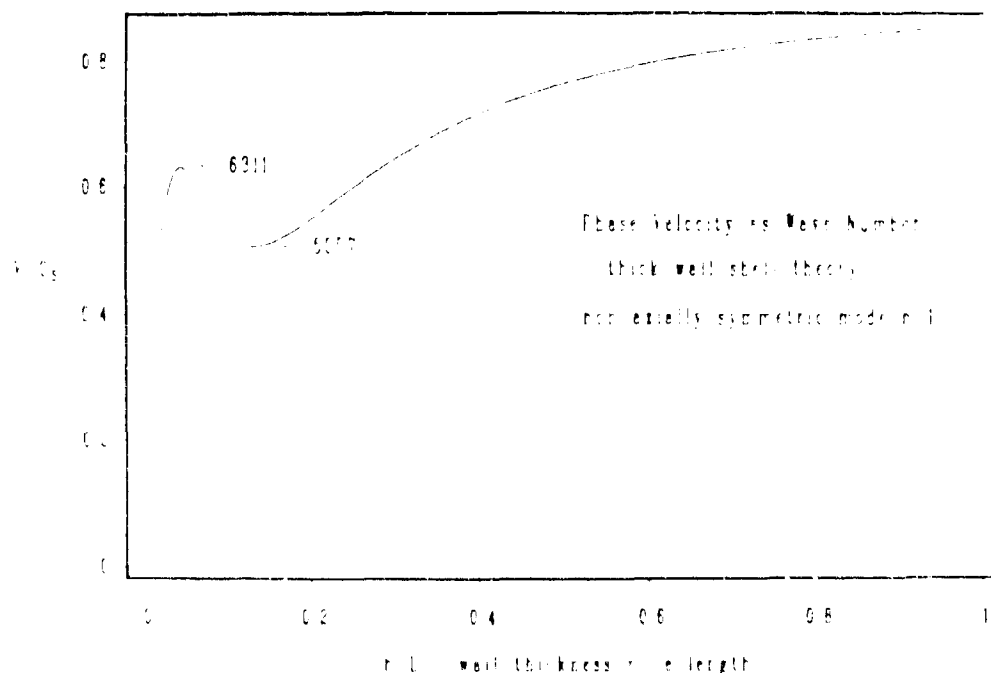


Figure 9

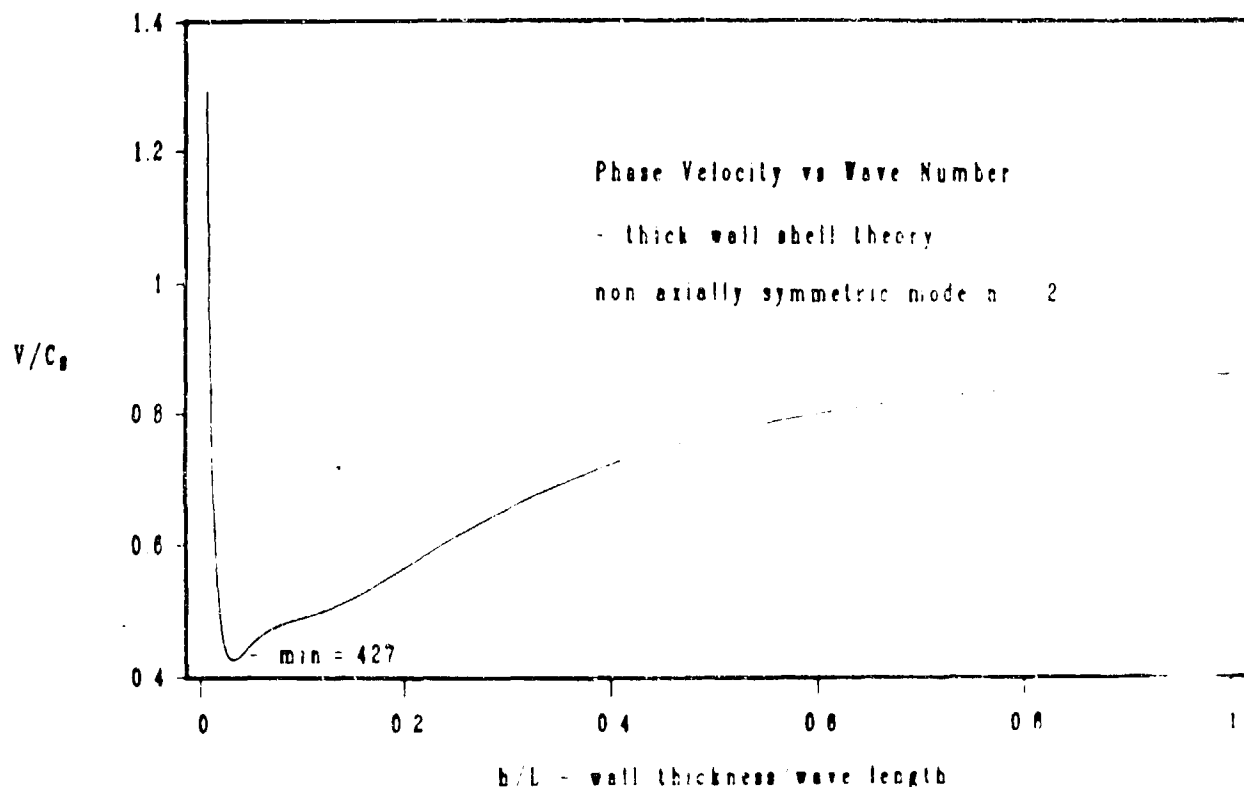


Figure 10

Recalling the importance of extreme values of the dispersion relation, i.e., $dv(k)/dk = 0$, the dispersion curves for the cases $n = 1$ and $n = 2$ are of some interest. The curve for $n = 1$ shows two possible critical velocities, one which is probably above the range of current ammunition for conventional cannon, but certainly of interest in more exotic weaponry such as electromagnetic cannon. The lower critical velocity is probably attainable in some conventional weapons. However, work in progress seems to indicate that the resonant band associated with this minimum is extremely narrow, most of the energy flowing into the longer wave having the same phase velocity. (The term 'resonant band' is defined here as the range of projectile velocity near a critical value which will cause appreciable strain and displacement amplification.) The width of the resonant band at the higher critical velocity seems to be much greater - more closely resembling the $n = 0$ case - leading to the speculation that energy tends to flow in the longer wave lengths. When $n = 2$, a critical value even lower than that for $n = 0$ is predicted.

In order to excite one or more of the many natural waves possible in a uniform cylinder, it is not only necessary that the load travel at the phase velocity of some possible wave, but the load must be distributed in such a way as to encourage the deformed shape (i.e., the load distribution must contain some

modal content). Thus, an axisymmetric wave requires an axisymmetric component of pressure for its excitation. Similarly, the beam-like wave requires that some of the pressure be distributed asymmetrically about the bore axis, etc. In gun tubes, however, the ballistic pressure load is strictly axisymmetric and it may seem at first that nonaxisymmetric motions will not be excited. However, only uniform cylinders have been considered thus far, and if the real nonuniformities of gun tubes are considered, energy may flow to these modes by coupling. This prospect seems particularly feasible for the beam-like modes ($n = 1$) because beam displacements of significant magnitudes do not require a great deal of energy at the longer wave lengths. Thus, if even a little energy is transferred from axially symmetric motion to $n = 1$ motion, significant motion of the tube access may occur. Analysis is presently underway to quantify these effects in gun tubes.

REFERENCES

1. S. P. Timoshenko and J. N. Goodier, Theory of Elasticity, Third Edition, McGraw-Hill, 1970, pp. 68-71.
2. H. Reismann, "Response of a Prestressed Cylindrical Shell to Moving Pressure Load, Developments in Mechanics," Solid Mechanics - Proceedings of the Eighth Midwestern Mechanics Conference, Pergamon Press, Part II, Vol. 2, 1965, pp. 349-363.
3. S. Tang, "Dynamic Response of a Tube Under Moving Pressure," Journal of the Engineering Mechanics Division Proceedings of the ASCE, October 1965, pp. 97-122.
4. J. T. Kenney, Jr., "Steady-State Vibrations of Beams on Elastic Foundations for Moving Loads," Journal of Applied Mechanics, Vol. 21, Trans. ASME, Vol. 76, December 1954, pp. 359-364.
5. J. P. Jones and P. G. Bhutta, "Response of Cylindrical Shells to Moving Loads," Journal of Applied Mechanics, Vol. 31, Trans. ASME, Vol. 86, Series E, March 1964, pp. 105-111.
6. E. J. Haug, editor, "Proceedings of the First Conference on Dynamics of Precision Gun Weapons," Report No. R-Tk-77-008, US ARRADCOM Rock Island, 26-27 January 1977.
7. T. E. Simkins, editor, "Proceedings of the Second US Army Symposium on Gun Dynamics," ARLCB-SP-78013, Benet Weapons Laboratory, Watervliet, NY, 19-22 September 1978.
8. T. E. Simkins and J. J. Wu, editors, "Proceedings of the Third US Army Symposium on Gun Dynamics," ARLCB-SP-82005, Benet Weapons Laboratory, Watervliet, NY, 11-14 May 1982.
9. T. E. Simkins and J. Vasilakis, editors, "Proceedings of the Fourth US Army Symposium on Gun Dynamics," ARLCB-SP-85009, Benet Weapons Laboratory, Watervliet, NY, 7-9 May 1985.

SIMKINS

10. I. Mirsky and G. Herrmann, "Axially Symmetric Motions of Thick Cylindrical Shells," Journal of Applied Mechanics, March 1958, pp. 97-102.
11. G. Herrmann and I. Mirsky, "Three-Dimensional and Shell Theory Analysis of Axially Symmetric Motions of Cylinders," Journal of Applied Mechanics, December 1956, pp. 563-568.
12. T. E. Simkins, "Resonance of Flexural Waves in Gun Tubes," ARDEC Technical Report ARCCB-TR-87008, Benet Weapons Laboratory, Watervliet, NY, July 1987.
13. I. Mirsky and G. Herrmann, "Nonaxially Symmetric Motions of Cylindrical Shells," Journal of the Acoustical Society of America, Vol. 29, No. 10, October 1957, pp. 1116-1123.
14. D. C. Gazis, "Three-Dimensional Investigation of the Propagation of Waves in Hollow Cylinders, I. Analytical Foundation," and II. "Numerical Results," Journal of the Acoustical Society of America, Vol. 31, No. 5, May 1959, pp. 569-578.

SESSION II

DATA ANALYSIS - CORRELATION

WALBERT

TITLE: THE EFFECTS OF INTERIOR HEATING ON THE ACCURACY OF TANK GUNS
DR. JAMES N. WALBERT
US ARMY BALLISTIC RESEARCH LABORATORY
ABERDEEN PROVING GROUND, MD 21005-5066

ABSTRACT

The advent of longer and thinner gun tubes for tanks and other armored vehicles has introduced a family of thermally-related phenomena in the dynamic behavior of these tubes. Recent experimental evidence has demonstrated that these phenomena have a direct relationship to the accuracy of the weapon system. This paper presents experimental evidence of these phenomena, provides some theoretical analysis of them, including computer simulation, and finally, some suggested design changes which, for future tank gun systems, could avoid a recurrence of such accuracy problems.

The most fundamental of these phenomena is the tube motion, especially at the muzzle, caused by rapid-fire sequences. Such muzzle motion precludes accurate aiming of subsequent rounds; since this motion has been observed to begin after only three to five rounds fired rapidly, there is cause for concern in certain engagement scenarios. It should be noted that while certain types of thermal jackets reduce this motion, it is by a relatively small amount, since these jackets are designed primarily to alleviate the effects of external heating and cooling. Such motion can also have an effect on the apparent dispersion of ammunition as measured during standard proving ground tests.

This paper was not available for printing in this publication. Every effort will be made to include this paper in a supplement at a later date.

BUNDY

ANALYSIS OF THERMALLY INDUCED BARREL DISTORTION FROM FIRING
MARK L. BUNDY
U.S. ARMY BALLISTIC RESEARCH LABORATORY
ABERDEEN PROVING GROUND, MD 21005-5066

ABSTRACT

The effects of external, non-axisymmetric heat flux from sun, rain, and air convection on unshrouded and shrouded gun barrels have been studied for many years and are well understood. The effects of internal non-axisymmetric heating are less well known and are discussed here. Using Finite Element Modeling, it is shown that cross-barrel temperature gradients on the order of those measured in thermal shroud tests, can significantly change the bore centerline curvature and muzzle pointing angle. Firing induced cross-tube temperature perturbations of less than 5% in the overall temperature increase are shown to distort the muzzle pointing angle by several tenths of a mil, and change the bore centerline by as much as 100%. Recent test evidence indicates that both changes, muzzle pointing angle and centerline curvature, will affect tank gun accuracy.

BIOGRAPHY:

PRESENT ASSIGNMENT: Acting Branch Chief, Fluid Physics Branch, Launch and Flight Division, Ballistics Research Laboratory, Aberdeen Proving Ground, MD., 21005-5066.

PAST EXPERIENCE: Six years experience as a Research Physicist in the Launch and Flight Division, BRL, two years of which have involved thermal shroud testing, analysis, and development.

DEGREES HELD: B.A./M.S./Ph.D. in Math, Physics/Physics/Physics from Augsburg College, Mpls., MN. (1972)/Drake Univ., Des Moines, IA. (1975)/Univ. of Maine, Orono, ME. (1980)

ANALYSIS OF THERMALLY INDUCED BARREL DISTORTION FROM FIRING

MARK L. BUNDY
U.S. ARMY BALLISTIC RESEARCH LABORATORY
ABERDEEN PROVING GROUND, MD 21005-5066

INTRODUCTION:

Cross-barrel temperature gradients produce uneven thermal expansion which distorts the bore centerline and degrades tank gun accuracy. Tank cannon thermal shrouds are designed to minimize cross-barrel temperature differences caused by external thermal gradients such as sun, rain, and air convection. Shroud tests have shown, however, that external heat flux asymmetries are not the only source of non-uniform barrel heating. Internal heating from projectile-barrel friction and propellant heat transfer can also be circumferentially asymmetric. Furthermore, non-axisymmetric barrel heating from the influx of hot gases into the bore evacuator during firing, and asymmetric barrel cooling in the bore evacuator between firing, produce measureable cross-barrel temperature differences. Additionally, the last 5% of the barrel, left uncovered by conventional shroud designs, can produce significant barrel curvature during firing, especially in the event of rain.

Gun barrel thermal distortion caused by external (environmental) heating and cooling is well understood. However, internal heating effects are not well known. As discussed here, they will be separated into: centerline related, bore evacuator induced, and bare muzzle effects. Thermocouples attached to the test gun barrel at 1.0, 1.6, 2.0, 2.3, and 2.7 meters, from the muzzle recorded cross-barrel temperature differences under the shroud and bore evacuator. The effects of external temperature gradients on these thermocouples were considered negligible in comparison to that produced by internal (gun-fire) generated heat.

Using Finite Element Modeling (FEM), the change in the bore centerline due to several representative barrel temperature profiles will be calculated. These calculations show that cross-tube temperature perturbations of less than 5% in the overall elevated barrel temperature can distort the muzzle pointing angle by several tenths of a mil, and change the bore centerline as much as 100%. Both of these effects appear to influence tank gun accuracy [1].

INTERNAL HEATING EFFECTS

Centerline Correlation:

Heat transfer to the gun barrel from projectile-barrel friction and high temperature propellant gas is not uniform over the in-bore surface.

Axial temperature gradients are expected to occur as the propellant gas expands; however, temperature measurements at fixed axial positions indicate that heat transfer is also circumferentially asymmetric. It is only the latter type of temperature asymmetry which affects gun barrel straightness.

Circumferential asymmetries appear to correlate with the centerline curvature. Figure 1 shows the horizontal (azimuth) and vertical (elevation) static centerline profile for the test gun barrel. Also shown is an estimate of the dynamic gun barrel curvature in the projectile reference frame. This is obtained from recent test evidence [1] that the gun barrel motion during firing is, to a large extent, predictable, for a given type of gun barrel, mount and round type. Superposition of the two curves would give an estimate of the dynamic trajectory of an in-bore projectile. Figure 2 gives the cross-barrel temperature difference at various axial locations. Horizontal temperature differences at 1.6 m and 2.3 m from the muzzle were not measured. The reference time $t=0$ corresponds to the time when internal firing heat has, through conduction, reached the outer barrel surface thermocouples.

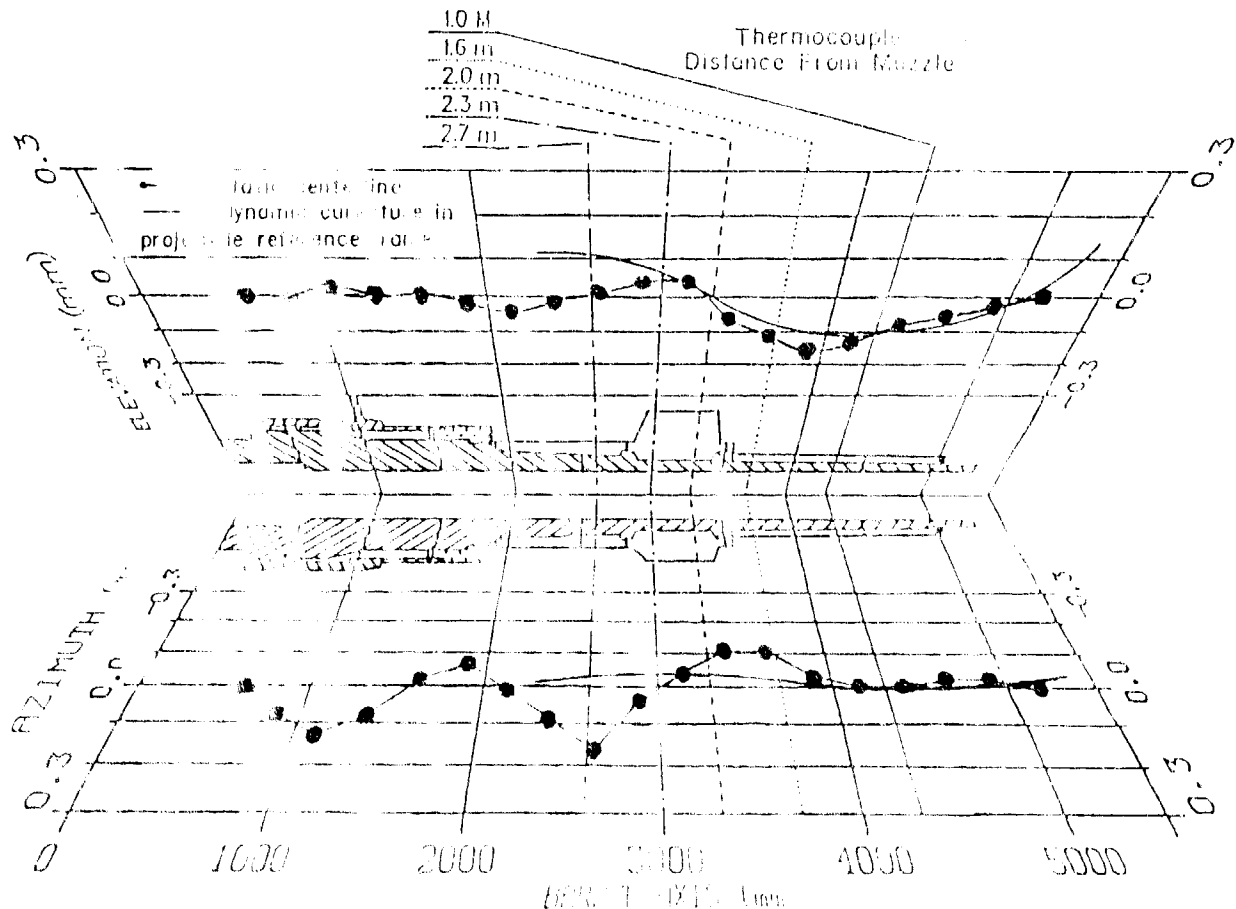


Figure 1. Horizontal (azimuth) and vertical (elevation) static centerline curvature, and dynamic curvature (assuming no static curvature) in the projectile reference frame.

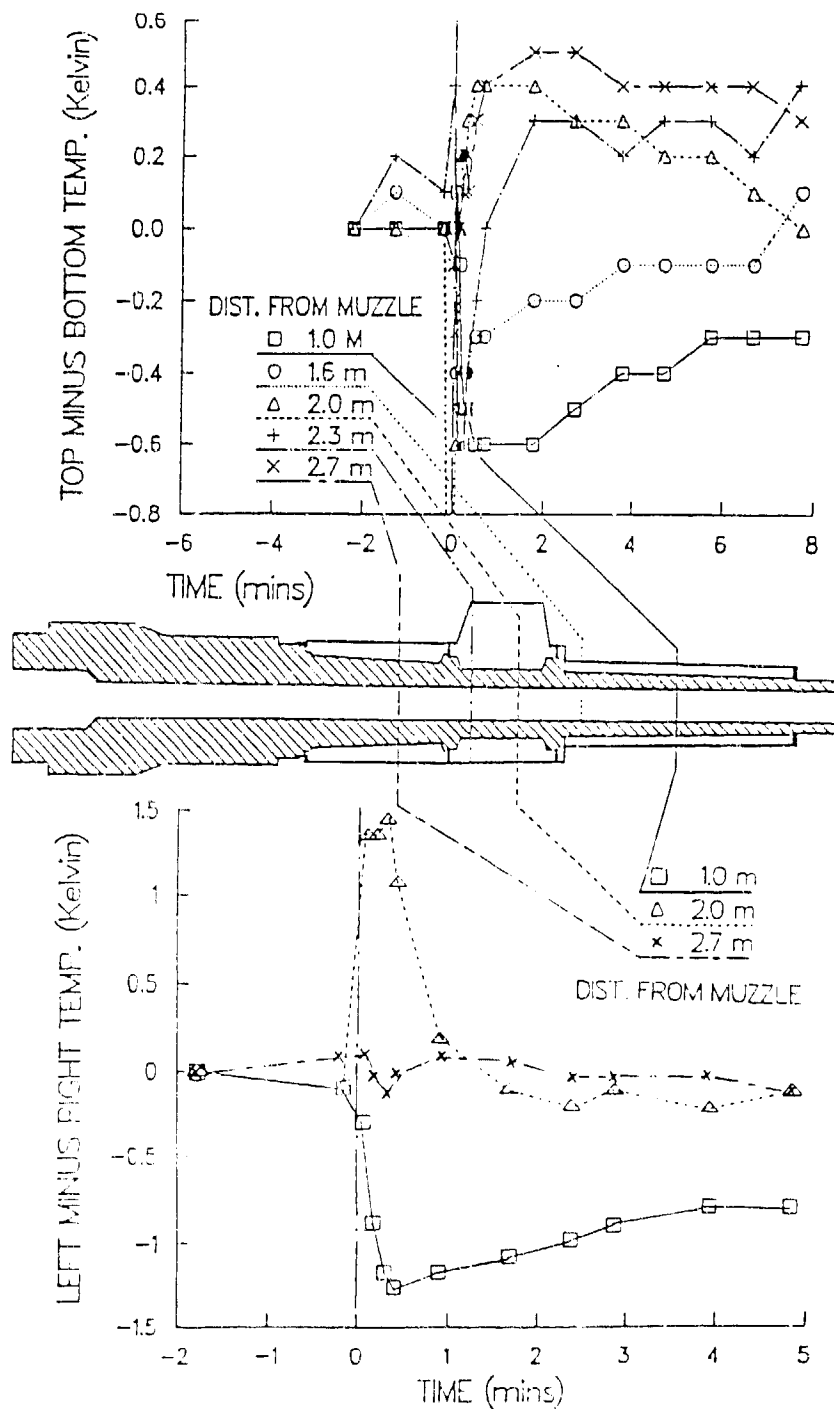


Figure 2. Cross-barrel temperature differences along barrel. Time $t=0$ is when firing heat reaches the surface thermocouples at 1.0 m from muzzle.

Comparing Figures 1 and 2, it appears that excess heat is transferred to the barrel on the outside surface of local curves in the in-bore projectile trajectory. For example, the concave upward curve in the elevation plane between 3.5 m and 4.5 m from the breech is consistent with more heat input to

the bottom of the barrel, and thus, the appearance of a negative temperature difference measured at 3.7 m and 4.3 m from the breech (or 1.6 m and 1.0 m from the muzzle). Likewise, the three positive temperature differences in the elevation plane correlate with the concave downward centerline curvature over that region of the barrel. Similar comparisons can be made in the azimuthal plane. In general, the correlation was found to weaken with distance from the muzzle.

The dependence of cross-barrel temperature gradients on the static and dynamic centerline curvature is consistent with the intuitive notion that higher friction would occur between the barrel and the projectile on the outside surface of such curves. Furthermore, it is plausible that the propellant residue layer would be wiped thinner, allowing more propellant heat transfer, where the friction force is higher. This type of frictional dependence would increase with in-bore velocity, or conversely, decrease with distance from the muzzle, as observed. In addition to, but separate from, this apparent bore centerline effect, there is evidence that the physical characteristics of the bore evacuator influence the cross-barrel temperature difference in that region.

Bore Evacuator Region:

Close inspection of the temperature difference curves in Figure 2 reveals that the cross-barrel temperature difference changes before time $t=0$ only for those thermocouple positions in the bore evacuator region. This is thought to be caused by the asymmetric influx of hot propellant gas into this chamber. Certainly, the fact that the temperature difference changes before the propellant heat has time to reach the outer surface by conduction, indicates that the process is convective heating. However, to understand the sign of this convection effect -- consider Figure 3 -- which is a schematic of the cross section through the bore evacuator holes for this barrel. It can be seen that there are two holes in the lower left quadrant (viewed from the breech) and only one hole in each of the other three quadrants. This arrangement, combined with the closeness of the inner bore evacuator surface to the barrel in this quadrant, would suggest that the propellant gas will have a stronger reflection off the bore evacuator and back onto the barrel in this quadrant than in any other quadrant. This would explain the fact that the lower left side has a higher temperature than the upper right side in this region, before time $t=0$.

The convective heat transfer asymmetries in the bore evacuator region are temporary, beginning about 10 seconds before $t=0$ and lasting 20-30 seconds. They are replaced by the conductive heat transfer asymmetries from within, which appear to reach their maximum roughly 30 seconds after $t=0$. However, when the gun is rapid-fired the convection effects are prolonged. For example, it can be seen in Figure 4 that the relatively small negative temperature spike (nominally -0.5 K) after each shot in the elevation plane at 2.0 m from the muzzle accumulates during rapid-fire (rounds 5 - 14), reaching a maximum of -1.6 K, 1.5 min. after $t=0$. The internal heat flux asymmetry eventually swings the gradient to a proportionately larger positive temperature difference.

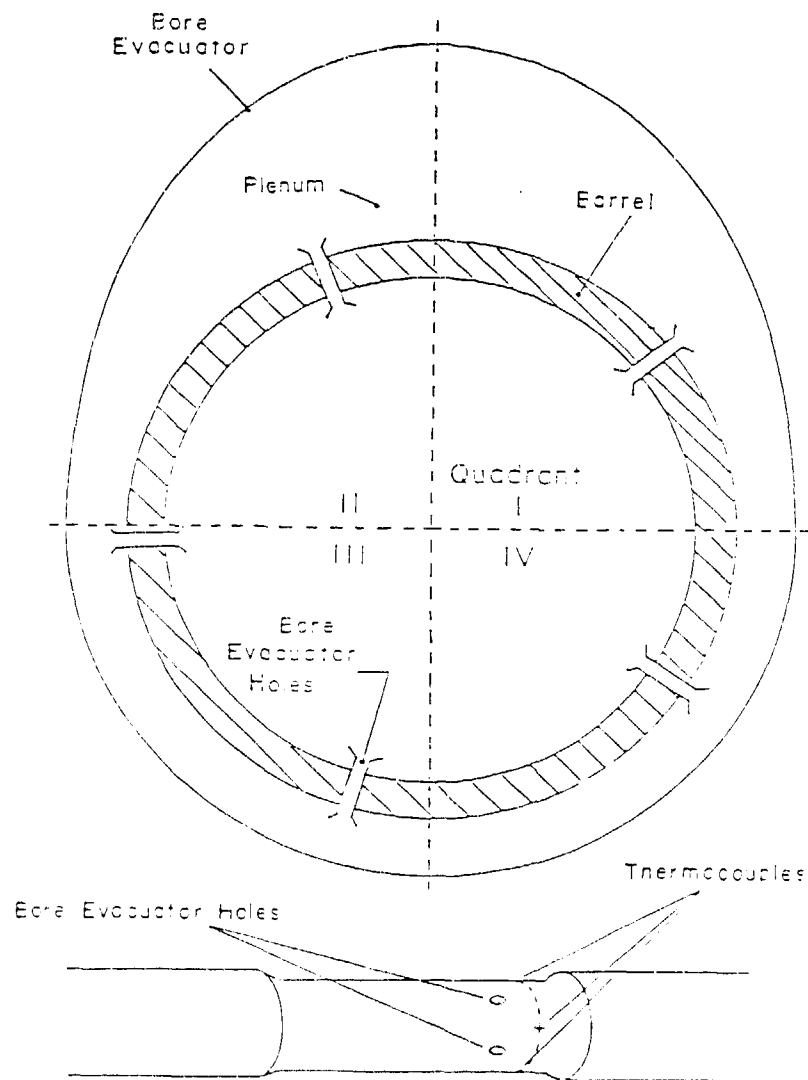


Figure 3. Orientation of bore evacuator holes on the test gun barrel relative to the bore evacuator canister, viewed from the breech.

The third factor influencing cross-barrel temperature gradients in the bore evacuator region occurs between firing: it is due to vertically stratified hot air recirculation. After firing, rising air currents around the barrel will transport heat to the evacuator surface, cool, fall, and begin to rise around the barrel again. Such a recirculation process favors a faster cooling rate for the bottom of the barrel than the top. This could explain why the vertical temperature difference continues to increase, even after firing has ceased (round 32, Figure 4). If the firing rate is slow, but steady, this circulation effect could be sustained indefinitely, which appears to happen between rounds 25 through 29. However, if the rate of fire is too fast, the time for the differential cooling rate to act is reduced, and the vertical temperature gradient will diminish. This could explain the drop in the temperature difference between rounds 29-32.

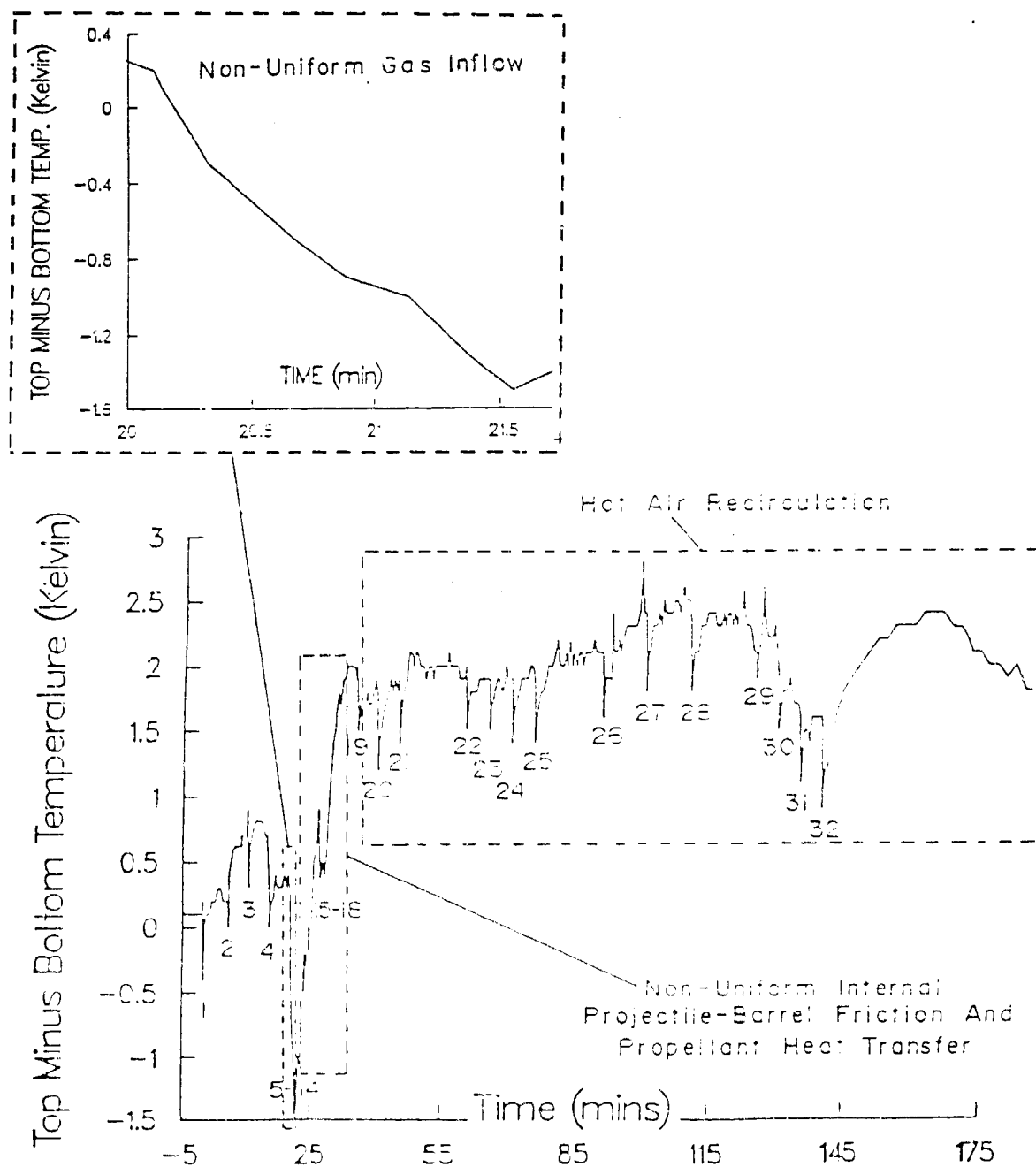


Figure 4. Vertical cross-barrel temperature difference in the bore evacuator region (2.3 m from muzzle) during firing, with presumed sources of heating asymmetry.

Thus, three sources of non-uniform barrel heating in the bore evacuator region are possible: propellant gas convection, internal heat conduction, and hot air circulation. These effects can help explain the measured barrel temperature differences in this section of the gun tube.

BUNDY

Bare Muzzle Effects:

Conventional gun barrel shrouds leave the last 5% of the barrel, near the muzzle, uncovered. When the barrel is heated by firing, natural air convection rising around the barrel establishes a vertical temperature gradient there. Measurements across a hot bare tube at 1 m from the muzzle (Figure 5) indicate that the top of the barrel can be 5-6 K hotter than the bottom after firing 10-15 rounds. Moreover, were it to rain on a hot bare muzzle, the temperature gradient would reverse, and the top could become as much as 25 K cooler than the bottom. These gradients are expected to be even larger near the muzzle, where the barrel is thinner, its temperature higher, and convection effects are larger.

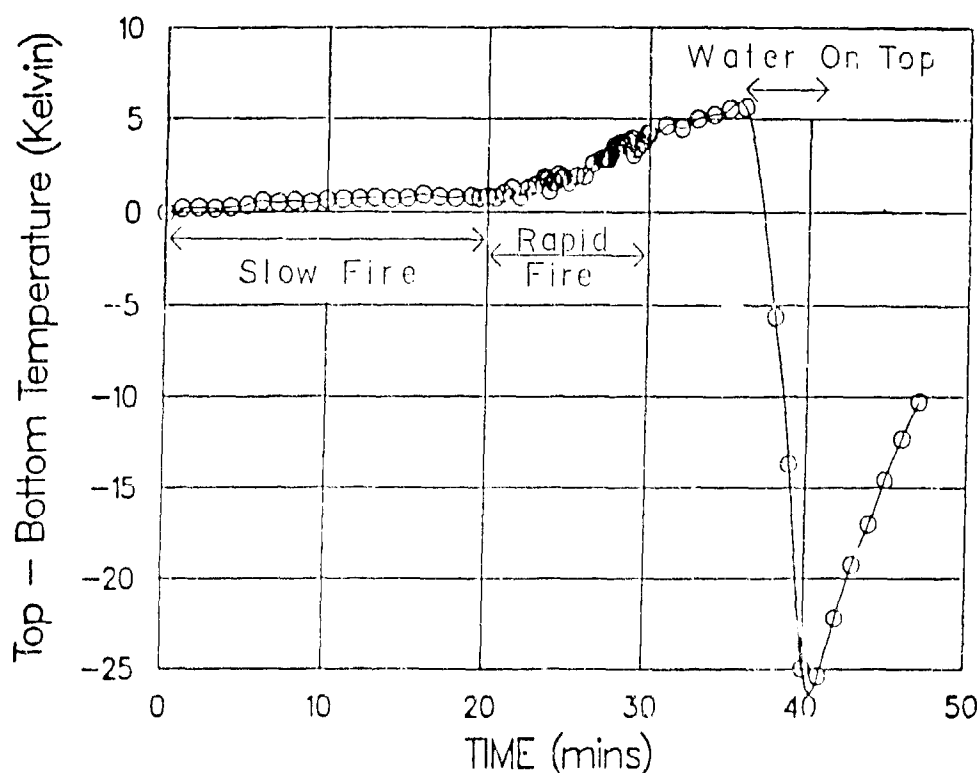


Figure 5. Vertical temperature difference across the unshrouded barrel, at 1m from the muzzle, during firing.

Large temperature differentials such as these can significantly change the muzzle pointing angle. Figure 6 shows the thermal distortion predicted by FEM [2] for a 25 K temperature difference across the end of a straight tube, similar in size, and having the same thermal and mechanical properties as that of the test gun barrel outside the turret. The "muzzle" pointing angle change of this tube is approximately 0.33 mils. In addition to the sharp centerline bend, the water cooled muzzle undergoes a change in bore diameter as well. After rapid-fire, the average tube temperature is approximately 100 K above ambient. At this temperature the bore diameter expands by 0.002 calibers. (As a reference, the projectile's bore riding surface is typically 0.001 calibers smaller than the ambient temperature bore diameter.) Cooling by the ambient

temperature rain reduces the average barrel temperature at the muzzle to 50 K above ambient. The bore diameter expansion at this temperature is correspondingly smaller, roughly 0.001 calibers. Such abrupt changes in the bore curvature and diameter are expected to degrade accuracy and increase tube wear. Using this same FEM, other representative temperature gradients and thermal displacements will be calculated and discussed next.

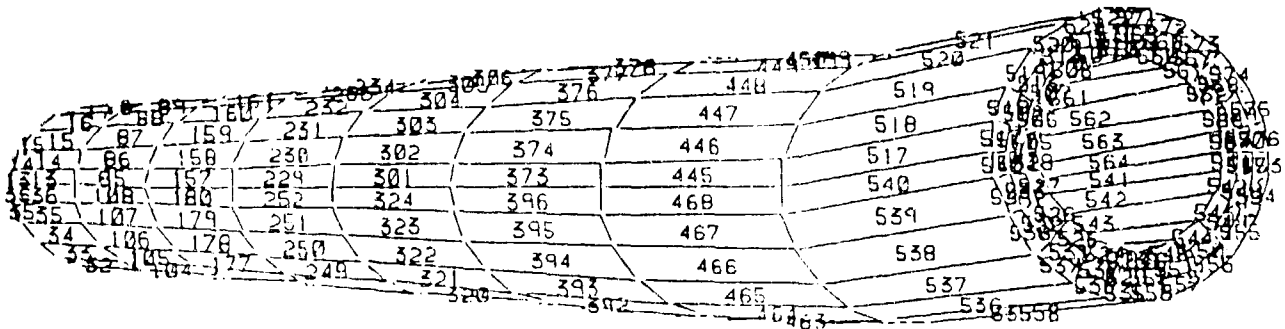


Figure 6. Predicted thermal distortion using Finite Element Modeling for a -25 K temperature difference across the end of a simulated gun tube, muzzle angle is 0.33 mils (scale factor is 200).

FIRING INDUCED CENTERLINE DISTORTION:

As previously described, cross-barrel temperature gradients produce uneven thermal expansion and thereby change the gun barrel straightness. With only a limited number of temperature measurements, it is not possible to accurately predict the entire barrel straightness profile at any given time during firing. However, an order-of-magnitude estimate can be made based on the partial temperature data available.

Figure 7 is a composite graph of measured temperature differences in the vertical plane at four axial locations. Based on the previous discussion on the causes of non-uniform heating, a nominal temperature difference profile can be constructed which is consistent with these values. For example, the temperature difference profile of Case A in Figure 8 is an estimate of the vertical temperature difference over the last three meters of the barrel. The temperature difference values at 2.7 m, 2.3 m, 2.0 m, and 1.0 m from the muzzle are in close agreement with Figure 7, and the temperature difference at the bare muzzle is estimated from Figure 5.

Case B corresponds to the gun barrel during slow but sustained firing, such as during rounds 26 - 27 in Figure 4. The temperature difference in the bore evacuator region is close to that measured, as is the temperature

difference at 1 m from the muzzle (data not shown). The temperature difference at the muzzle is assumed to be higher than after rapid-fire (Case A) since the barrel will be hotter, and convection effects larger, in this case.

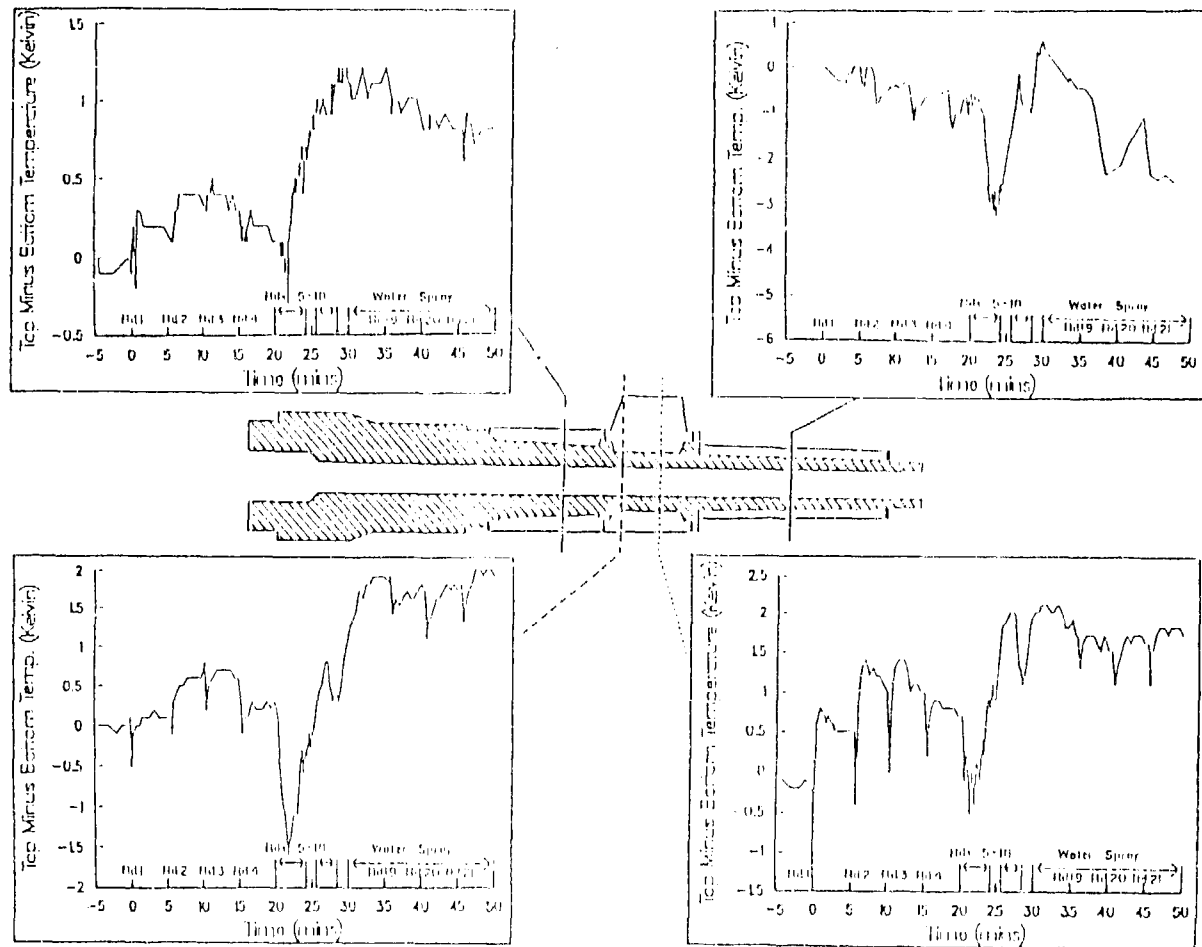


Figure 7. Vertical cross-barrel temperature difference along the barrel versus time, for the first 21 rounds fired.

Case C in Figure 8, corresponds to a conservative estimate of the change in barrel temperature difference during rapid-fire due to a change in thermal shrouds; for example, changing from a thermally conductive material (corresponding to Case A) to a non-conductive material. In this case the temperature difference would be magnified in the region covered by the thermal shroud, roughly 0.2 m - 1.7 m from the muzzle for this gun barrel.

Having described the various temperature difference profiles, FEM can be used to predict the corresponding change in bore straightness associated with these temperature gradients. A qualitative view of the thermal distortion caused by Case A is shown in Figure 9. It can be seen that the thermally induced curvature correlates with the curve fit of the associated cross-barrel temperature difference.

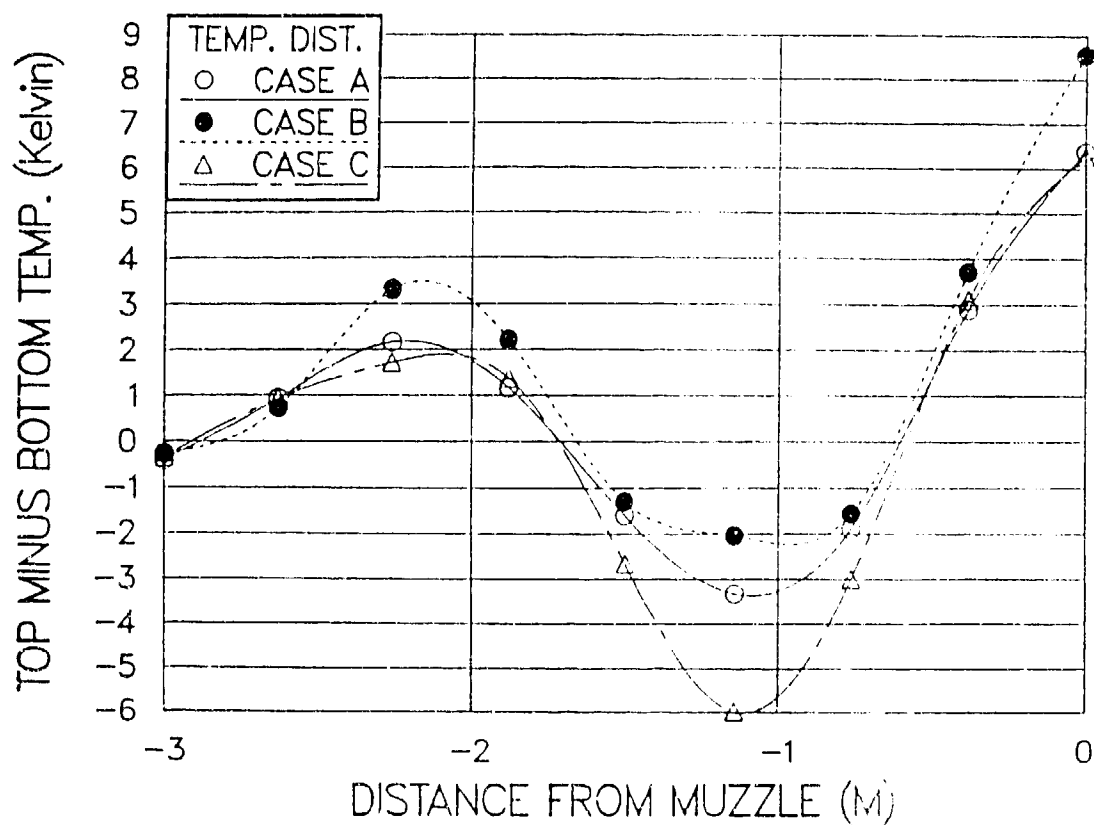


Figure 8. Estimates of the vertical cross-barrel temperature difference over the last 3 m of the gun barrel for: Case A, after rapid-fire; Case B, after slow but sustained fire; Case C, after rapid-fire with a thermally insulating shroud in place of a thermally conducting shroud (Case A).

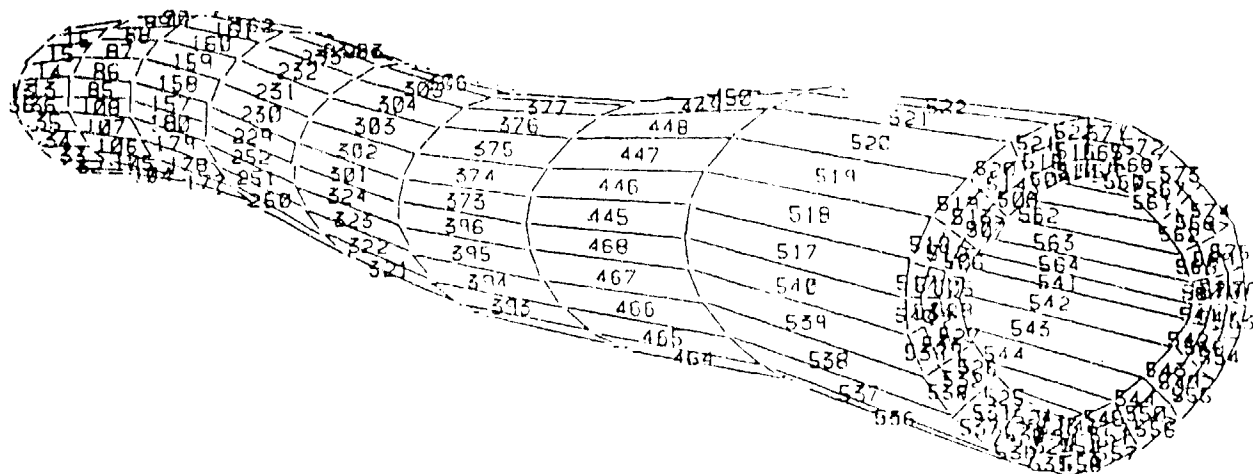


Figure 9. Estimate gun barrel thermal distortion from case A, Figure 8 (scale factor 100,000).

Figure 10 compares the thermally distorted bore centerline for all three cases in Figure 8. The muzzle pointing angle is also denoted on the three plots. The FEM calculations show that a mere 2-3 degree Kelvin change in the cross-barrel temperature difference over a relatively short section of the barrel can alter the pointing angle of the muzzle by several tenths of a mil. Since the absolute barrel temperature increase after rapid-fire is on the order of 100 degrees Kelvin, a 2-3 degree Kelvin difference from side to side is a heating asymmetry of only a few percent.

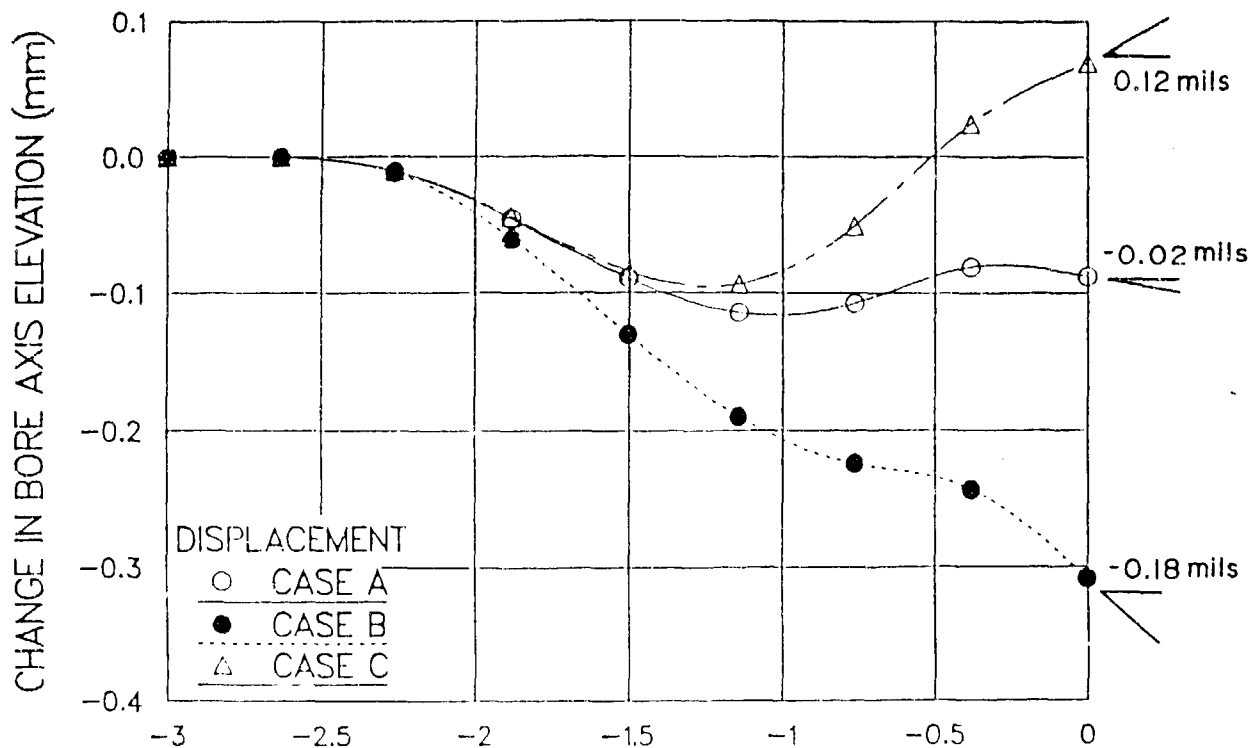


Figure 10. Thermally distorted bore centerline and muzzle pointing angle for the three temperature cases in Figure 8.

It can also be seen in Figure 10 (Case A, for example) that the muzzle pointing angle change is not necessarily a good indicator of the bore centerline change. Figure 11 gives a better perspective on this by depicting the curves in Figure 10 as displacements relative to the chord joining the muzzle end with the end 3.0 m from the muzzle. It can now be seen that changes in the bore centerline due to thermal distortion from firing are in some cases (Case C, for example) as great as those naturally present in the static, ambient temperature gun barrel, Figure 1.

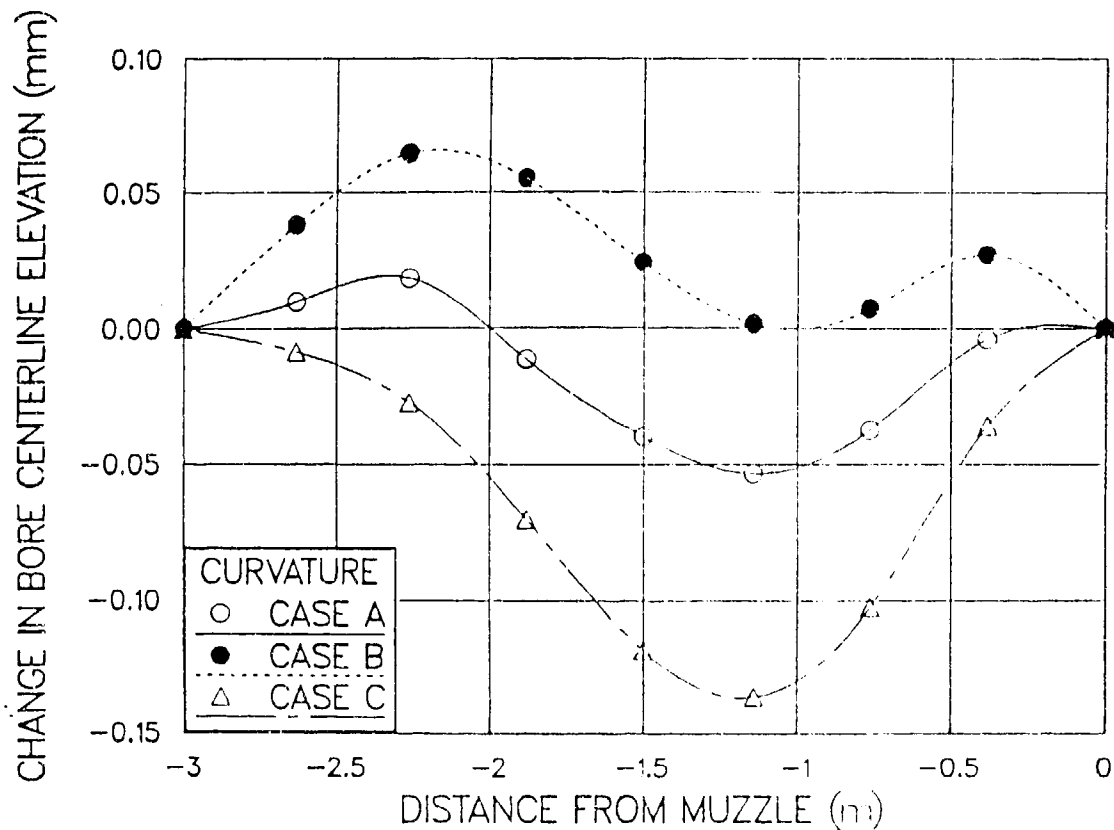


Figure 11. Displacements of the bore centerline curvature in Figure 10 relative to the chord joining the end points.

CONCLUDING REMARKS:

Experiments have shown that gun barrel heating, and hence thermal expansion, is both axially and circumferentially asymmetric. Circumferential, or cross-barrel, expansion differences influence gun barrel straightness. Three potential sources of uneven heat input into the barrel have been discussed: 1) uneven projectile-barrel friction and propellant heat transfer, which appear to correlate with the in-bore projectile trajectory and axial velocity; 2) uneven convection in the bore evacuator caused by the propellant gas entry during firing and residual hot air circulation between firing; 3) uneven cooling around the hot unshrouded barrel near the muzzle from both ambient air convection and rainfall.

FEM calculations have shown that thermal centerline distortion can represent a significant fraction of the overall bore centerline curvature when the gun barrel is heated by firing. In one case, non-uniform barrel heating produced a significant change in the centerline curvature but a negligible change in the muzzle pointing angle. In another case, which modeled the effect of rain on a hot bare muzzle, it was shown that not only did the muzzle pointing

BUNDY

angle change by 0.33 mils but the barrel diameter underwent a rather abrupt shrinkage over the last 5% of its length, due to the equally abrupt axial temperature change. Overall, the calculations showed that a change of only a few percent in the absolute barrel temperature from side to side could cause several tenths of a mil change in the muzzle angle.

BUNDY

References:

- (1) Haug, B.T. and Bornstein, J., "Gun Dynamics Measurements for Tank Gun Systems," Proceedings of the Fifth U.S. Army Symposium on Gun Dynamics, The Institute on Man and Science, Rensselaerville, NY, September 1987.
- (2) Algor Finite Element System, Release Date November 1986, Algor Interactive Systems, Inc., Essex House, Essex Square, Pittsburgh, PA, 15206.

COATES

**TITLE: TECHNIQUES FOR THE ANALYSIS OF MICROBALLISTIC DATA FROM PROJECTILES
IN FREE FLIGHT**

Susan A. Coates

U.S. Army Ballistic Research Laboratory

Aberdeen Proving Ground, Maryland 21005-5066

ABSTRACT:

Analysis of flight characteristics of a projectile requires knowledge of its spin and yaw rate. In the analysis of a kinetic energy projectile existing facilities to do high resolution Fast Fourier Transforms (FFT) were expanded upon. It was desirable to be able to extract spin and yaw rates from the waterfall plots of high resolution FFT's. Tracking the peaks of the waterfall plots yields a velocity or frequency versus time plot. Superimposed on this curve is the frequency information that describes the spin and yaw rate. Techniques to extract the higher frequencies were developed by subtracting a parabolic fit of this curve leaving the data of interest centered about zero. For this particular projectile yaw rates (or harmonics of the yaw rates) were found which were consistent round to round. The spin return was too low in amplitude to be detected.

BIOGRAPHY:

PRESENT ASSIGNMENT: Mathematician, U.S. Army Ballistic Research Laboratory, Aberdeen Proving Ground, Maryland

DEGREES HELD: B.A., Susquehanna University, 1983.

Techniques for the Analysis of Microballistic Data from Projectiles in Free Flight

Susan A. Coates
U.S. Army Ballistic Research Laboratory
Aberdeen Proving Ground, Maryland

When analyzing the flight characteristics of a projectile a knowledge of its spin and yaw rate are required. This paper describes the methodology for extracting the spin and yaw rate of a kinetic energy projectile from microwave radar data. This methodology is based on both new and old Fourier analysis techniques.

The methodology was developed to provide as much flexibility in applications as possible. An example of this is in time scaling the data. Time scaling is done because the A/D system has an upper sample rate of 40kHz and this sample rate is often too low for the analysis of microwave radar data. The tape recorder used has tape speeds ranging from .9375 to 120 inches per second (ips). Normally data is recorded at 60 ips or 120 ips. Then the tape can be slowed down to a speed as slow as .9375 ips for a direct record card or 1.875 ips for an FM record card. The slow down factor is based on how high the sample rate needs to be. When digitizing, a pulse may be used to trigger the digitizer if a common time is needed. This also allows for a time delay to be added. At other times the data may be triggered manually. When sampling data the highest sample rate possible is 40kHz. If data was recorded at 120 ips and slowed down to .9375 ips this makes a real time sample rate of 5120kHz possible ($120\text{ips} / 0.9375\text{ips} \times 40\text{kHz} = 5120\text{kHz}$).

The analysis of this particular microballistic data starts with microwave radar data that has been recorded on tape at 60ips. The tape was played back at 3.75 ips and sampled at a rate of 25kHz. This gave a real time sample rate of 400kHz. An arbitrary time zero reference pulse was also recorded at the same time but on a different channel. This pulse was used for the trigger when digitizing and was assumed to be zero time. A typical time delay for the rounds looked at was three seconds which means the actual start of data typically occurred at .188 seconds. A common length of time for digitizing was thirty seconds which means the length of the record was approximately 1.88 seconds. A raw data record is shown in Figure 1.

The spectrum analyzer was used to obtain an initial time dependent spectral analysis (waterfall plot). This allowed an approximate frequency range to be found and any abnormal behavior of the projectile to be seen. Figure 2 is a portion of a waterfall plot from the spectrum analyzer. In this particular round the sabot can be seen as well as a piece of the projectile that broke off. These are indicated by the two parabolic shaped curves to the left of the plot.

Once the data has been digitized a Fast Fourier Transform (FFT) is performed to provide a waterfall plot of the data. This technique was discussed at the Fourth U.S. Army Symposium on Gun Dynamics and will not be discussed here (Reference 1). The FFT's allows for flexibility by adjusting the resolution, overlap, and frequency range of interest. Figure 3 is a portion of a waterfall plot with a delta frequency of 49 Hz, no overlap, and a frequency range of 89990.2 to 114941 Hz.

A velocity or frequency versus time plot was obtained by tracking the peaks of the waterfall plot (Figure 4). In Figure 4 the y-axis is proportional to velocity and frequency. All of the above techniques have been used before.

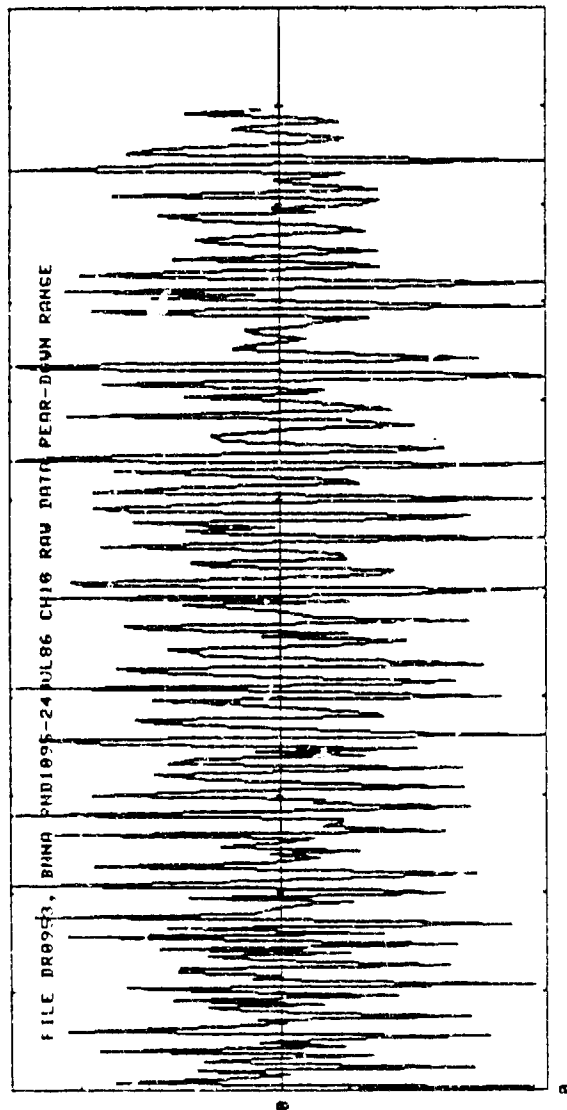


Figure 1. Raw Data from Radar Doppler
Signal

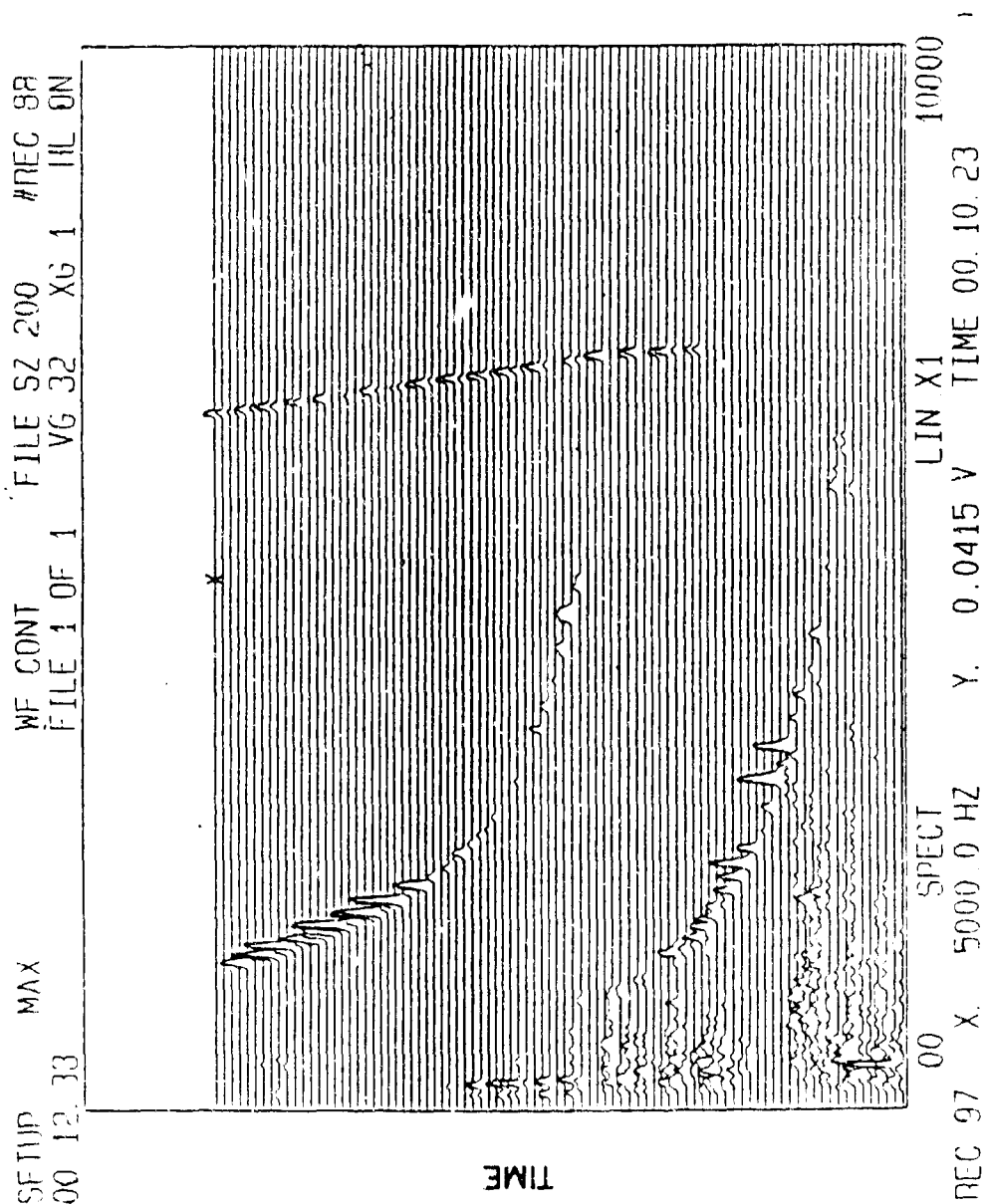


Figure 2. Plot from Spectrum Analyzer

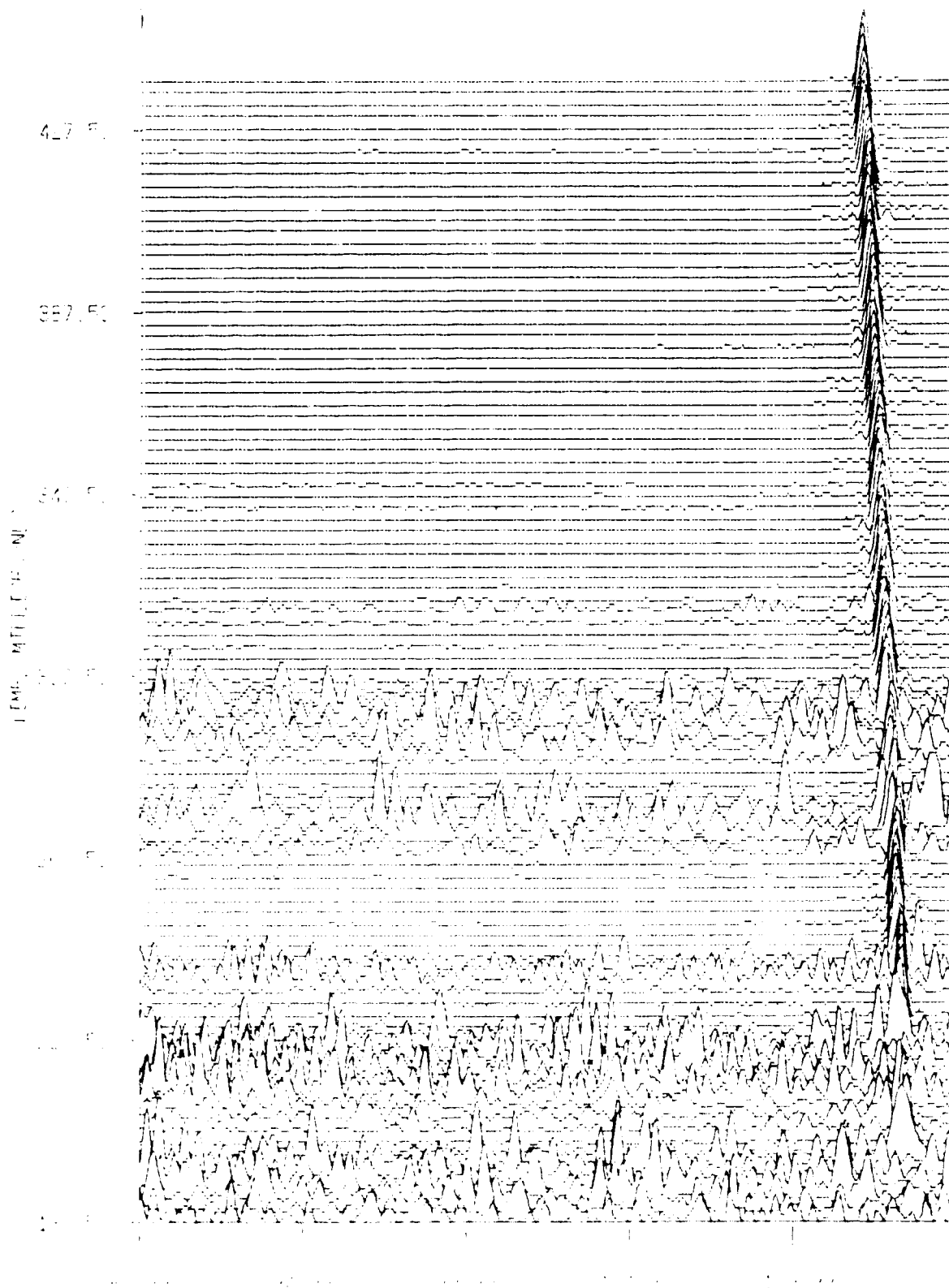


Figure 3. Waterfall Plot from High Resolution FFT Program with
Delta Frequency of 49 Hz and No Overlay

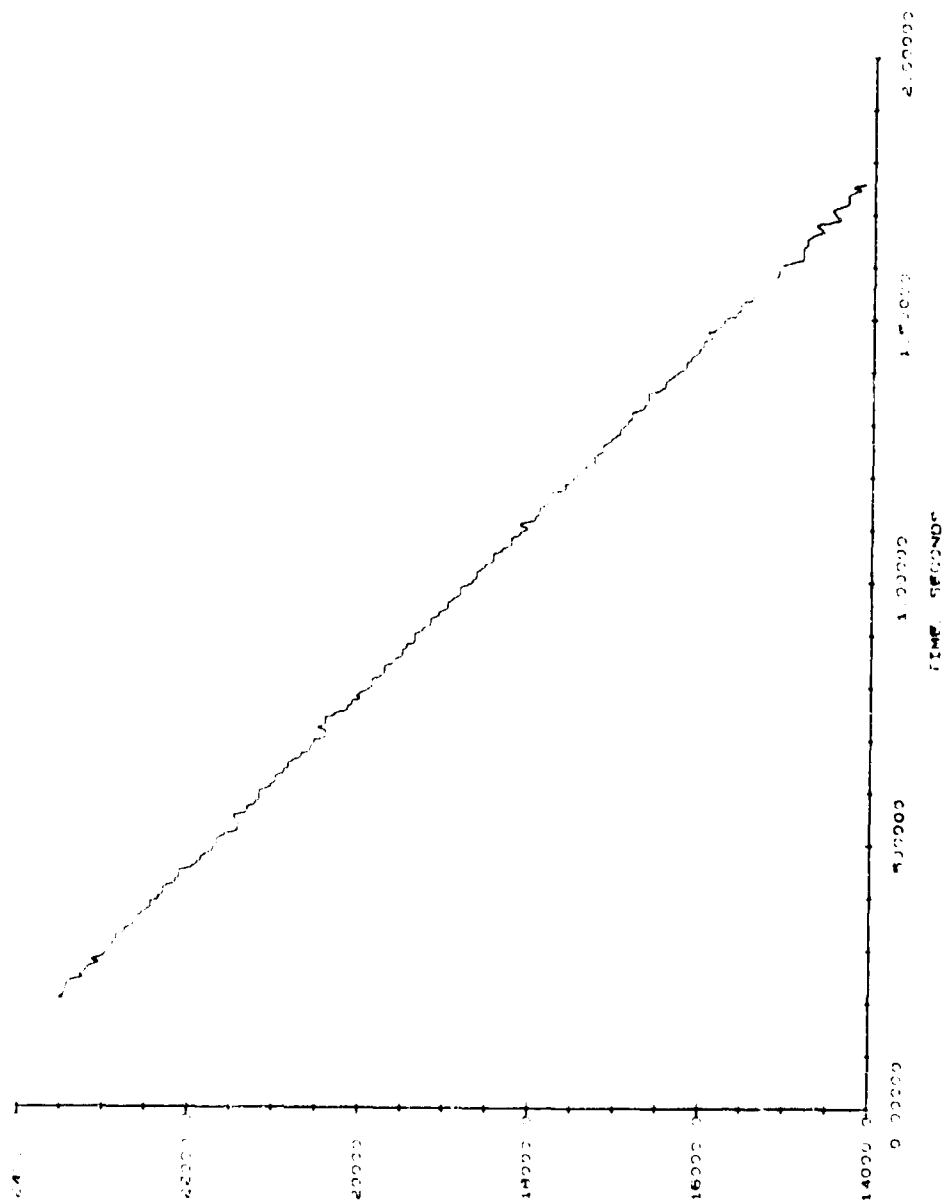


Figure 4. Velocity vs Time Plot

COATES

Superimposed on the data versus time plot is the frequency information that describes the spin and yaw rate. The assumption was made that the main velocity component was the velocity of the center of mass and that this component could be subtracted out. The shape of the data versus time plot is a parabola with frequencies superimposed on it. A parabola was chosen to approximate this curve. The parabola was generated by selecting three points on the curve and finding the parabola that goes through each of these three points. Both the original data and the parabola may be plotted in order to decide if the correct three points were used for the fit. If the correct three points were not used a different set of three points may be chosen. Once a parabolic fit of the data has been chosen the data is "zeroed" by subtracting the parabolic fit from the original data. This data may be filtered if desired. The filtering of the data may filter out some low frequency components that are important in the analysis. A spectral analysis of the "zeroed" data was done to see what frequencies were superimposed on the velocity versus time curve.

The following example will demonstrate this new technique. Usually the first, last, and middle points were used to fit the parabola (Figure 5). The velocity curve was "zeroed" by subtracting the parabolic fit from the original data (Figure 6). Then a spectral analysis was performed on this new curve to determine the frequency content (Figure 7).

The frequencies that were found for this particular projectile were consistent round to round and were the yaw rates (or harmonics of the yaw rates). The spin return was too low in amplitude to be detected.

In order to check the data to see if it was valid, the velocity-time data was integrated to obtain range information. The velocities at three different ranges were compared to the velocities obtained from skyscreens, which is another method of finding velocity. The following table shows what was found.

	Distance from Muzzle(m)	Velocity from Skyscreen Data (m/sec)	Velocity from Velocity-Range Plots (m/sec)
Round A	0	1722	1707
	1000	1665	1654
	2000	1608	1597
Round B	0	1710	1691
	1000	1653	1643
	2000	1597	1587

Table 1

The velocities were consistently lower for the data from the velocity-range plots but within reason for the error associated with the analysis process. The muzzle velocities for approximately thirty rounds were found using the spectrum analyzer. This data was compared to the muzzle velocity found using the skyscreens. Again the muzzle velocity of the skyscreens was consistently higher by 15.1 m/sec to 36.3 m/sec or an error of approximately .9% to 2%. Part of the reason for this consistently higher velocity was that the round was not immediately visible on the spectrum analyzer, usually there was a .188 second delay between time zero and actually seeing the round.

It would have been nice to compare the data obtained from this analysis to what was supposed to happen according to the Six Degree of Freedom Model for the Aerodynamics. Unfortunately this model has not been

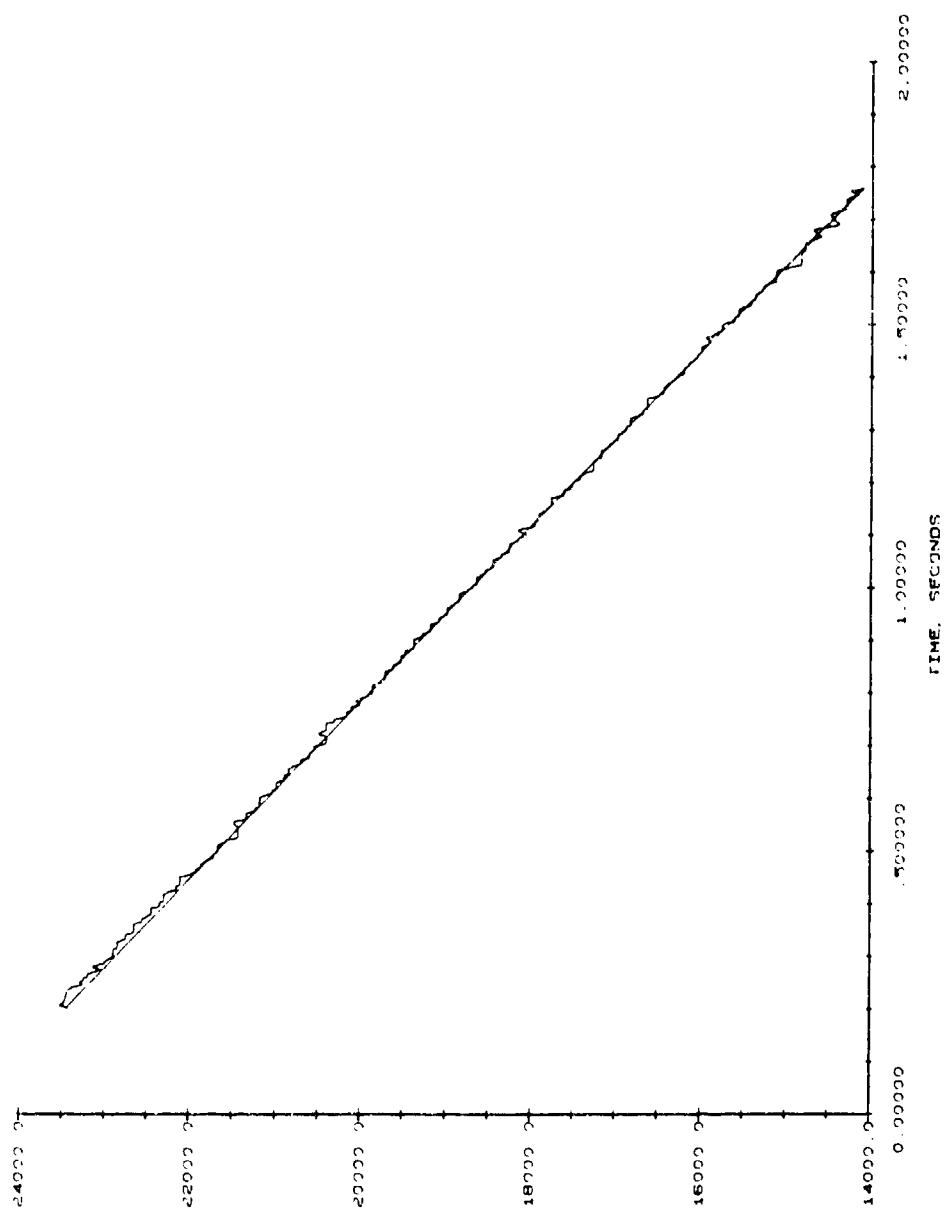


Figure 5. Parabolic Fit

COATES

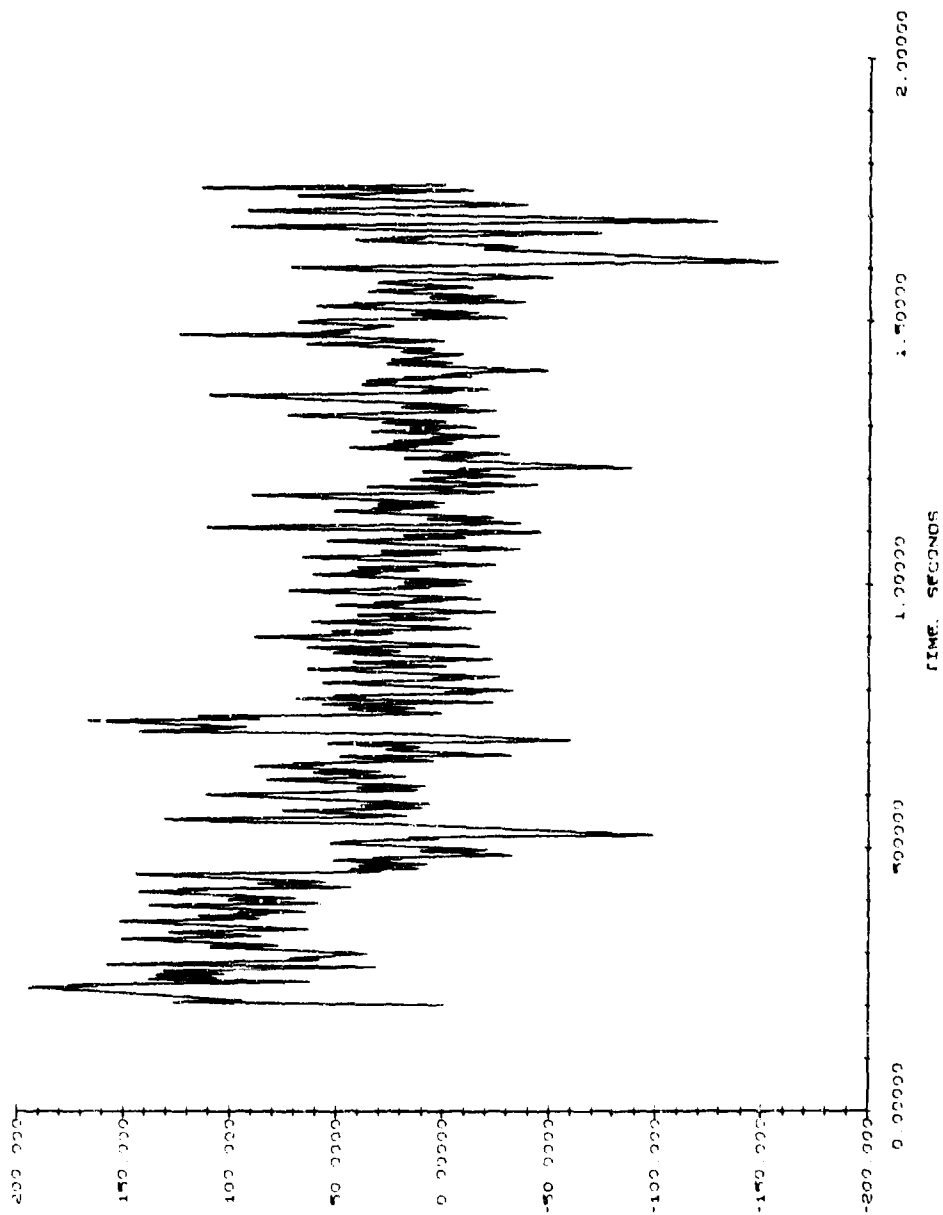


Figure 6. "Zeroed" Data

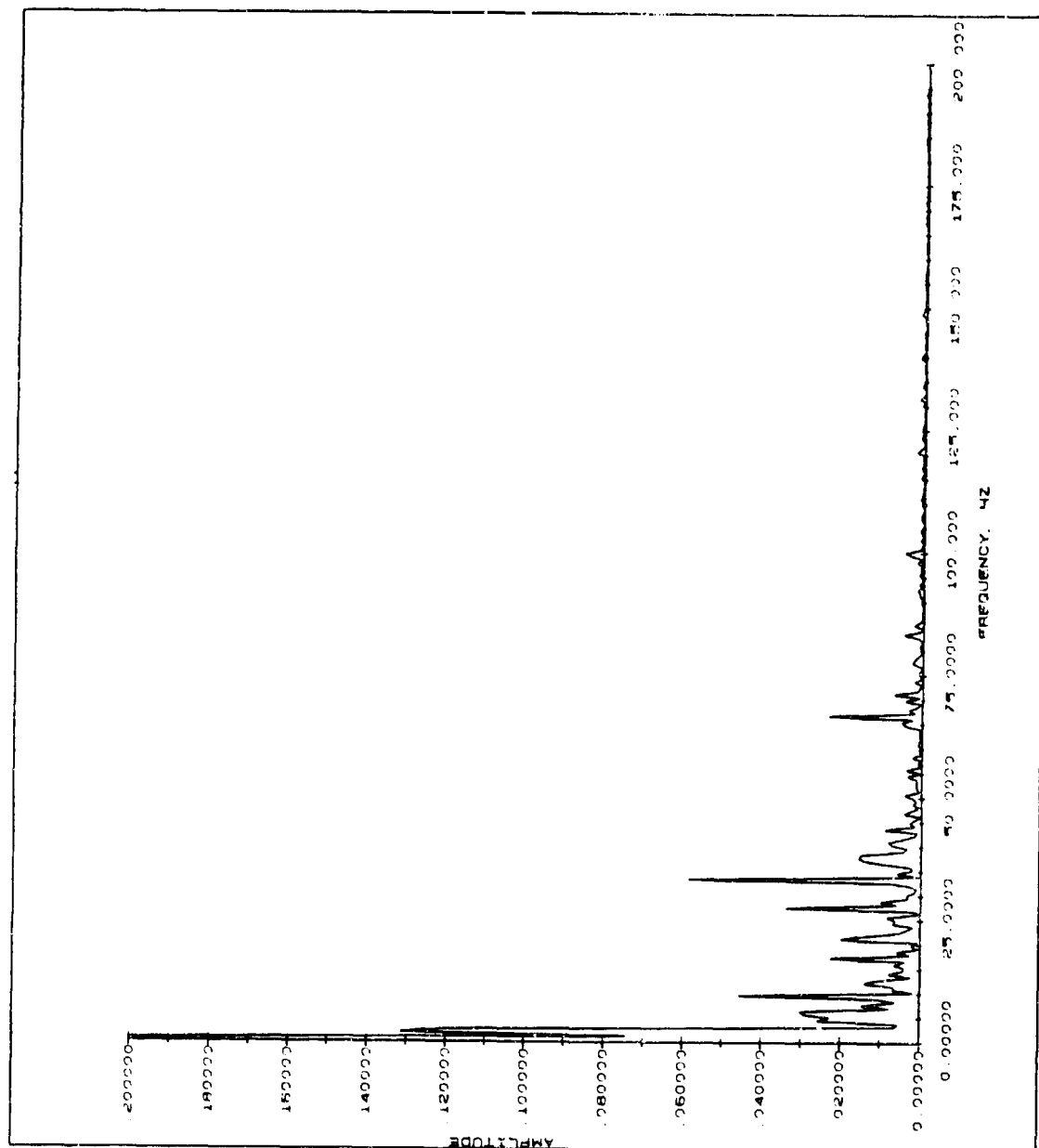


Figure 7. Spectral Analysis of "Zeroed" Data

COATES

run for this particular projectile because all the data needed for the model is not available at the present time.

In conclusion, for this particular projectile yaw rates (or harmonics of the yaw rates) were found that were consistent round to round. The spin return was too low in amplitude to be detected.

REFERENCES:

1. S.A. Coates, J.N. Walbert, "In-Bore Projectile Motion in a 37-mm Weapon System," Proceedings of the Fourth U.S. Army Symposium on Gun Dynamics, May 1985.

YAGLA

THEEE-GUN TURRET SALVO FIRING ACCURACY IN USS IOWA CLASS BATTLESHIPS

Jon Yagla
Naval Surface Weapons Center
Dahlgren, Virginia 22448-5000

ABSTRACT

A study of the recoil dynamics of the 16-in. gun turrets in USS IOWA class battleships has led to significant improvements in salvo accuracy. A rigid body dynamical model of the turret response to recoil and experimental acceleration data from one of IOWA's turrets was used to determine an optimum firing sequence.

The possibility of gun blast damage to new equipment items on the modernized battleships mandated the sequential firing (rather than simultaneous) of the guns in a salvo. Wave mechanics and statistical analyses of ignition delays led to a minimum separation of 0.20 sec for the firing of guns in each turret. The analysis of the dynamical response of the turret showed that accuracy could be maximized by firing in the sequence center, left, right, with delays of 0.20 and 1.0 sec, respectively.

The dynamics model was combined with a statistical analysis of propellant ignition delay times to compare the salvo fire accuracy attainable with the old firing circuits, which fired the outer guns simultaneously. The analysis showed the new firing circuits would provide improved accuracy.

Experimental firings with 65 rounds of various types of ammunition, with the new firing sequence, have shown consistently tight groups, often observed as a single splash. The final evaluation was conducted using an RPV to observe and measure the individual impacts from salvos fired at a target ship in the open ocean. These measurements showed an average deflection spread of 1.4 mils. The RPV data were used to construct hits against various Soviet naval targets. A video tape report of the results is available.

BIOGRAPHICAL INFORMATION

Dr. Yagla received his B.A. degree in science (physics) from the State College of Iowa in 1965. He received his M.S. degree in engineering mechanics in 1968 and his Ph.D in aerospace engineering and engineering science in 1981 from Arizona State University. He has done analytical and experimental research in the field of weapons blast since 1965 at the Naval Surface Weapons Center in Dahlgren, Virginia. As a supervisory research mechanical engineer, he was previously head of the Physical Response Analysis Branch, Blast Effects Branch, and Ship Engineering Branch. Dr. Yagla is the test development agent and was test conductor for the gun and missile structural test firings in USS IOWA class battleships. He is a consultant to the Naval Sea Systems Command battleship combat system engineer and the Naval Air Systems Command Cruise Missile Project for blast and structural response. He is presently analyzing shock and vibration problems for the Standard Missile Program Office.

YAGLA

THEEE-GUN TURRET SALVO FIRING ACCURACY IN USS IOWA CLASS BATTLESHIPS

JON YAGLA
NAVAL SURFACE WEAPONS CENTER
DAHLGREN, VIRGINIA 22448-5000

INTRODUCTION

USS IOWA class battleships employ three 16-in. three-gun turrets as the main battery. Any combination of the turrets can be fired singly, or together. The turrets can fire any combination of their guns. The maximum rate of fire is attained when the three turrets are salvoed together, with all nine guns firing.

The reactivation program for the battleships has included many new equipment items, none of which were designed to withstand blast from the 16-in. guns. The new equipment included four Close-In Weapon Systems (CIWSs), four Harpoon canister missile launching systems with four missiles each, eight armored box launchers with four Tomahawk missiles each, and SLQ-32 electronic countermeasures (ECM) equipment, Figure 1. Placement of the new equipment items on the ships was driven by the need to impose the smallest possible restrictions on the arcs of fire of the guns. [1]

The blast field is so large and intense that it could not be avoided in the new equipment installation (Figure 2). It became apparent very early that restrictions on the arcs of fire would be required. Experimental data measured by the author at Dahlgren showed that the firing arc restrictions for salvo firing would significantly impair the ships' capability. It was decided to sequentially fire the guns in the turrets so that blast waves from two or more guns could not coalesce and travel together as a single wave of higher intensity. The requirements for firing arc restrictions were thereby minimized, but there was not time to analyze the effects of the new sequential firing circuits on salvo fire accuracy. The salvo firing circuits were set to fire the three guns of a turret in the sequence of center, left, then right. The delays were set at the minimum possible value to preclude blast reinforcement at equipment items but still provide the maximum rate of fire. Statistical and wave mechanics analyses provided a value of 0.20 sec as the minimum possible delay. [2]

During exercises, USS IOWA recognized a systematic error in the fall of shot that only seemed to occur in three-gun salvos from any given turret. The author confirmed this observation during exercises in August, 1985. The right barrel plainly shot about 7 mils to the left whenever a three-gun salvo was fired.

The significance of a 7-mil miss is shown in Figures 3 and 4. Besides missing the target and wasting a valuable round of ammunition, the stray projectiles could cause unacceptable collateral damage or pose a hazard to friendly forces.

Approximate calculations of the recoil dynamics of a turret were performed at sea while the ship was underway. The calculations showed that the recoil force from the left gun was applying a moment to the turret of sufficient magnitude to drive the turret off the gun-target line. The theoretical analysis, which is explained in the following section, predicted a 7-mil miss. Spare accelerometers from another experiment in progress were installed on USS IOWA's Turret 3 to measure the dynamical response of the turret during gun firing. The acceleration measurement confirmed the calculations and provided valuable insight for correcting the problem. It appeared from the calculations and the accelerometer data that the 7-mil miss could be remedied by increasing the delay time between the second and third barrel firings to approximately 1.0 sec.

YAGLA

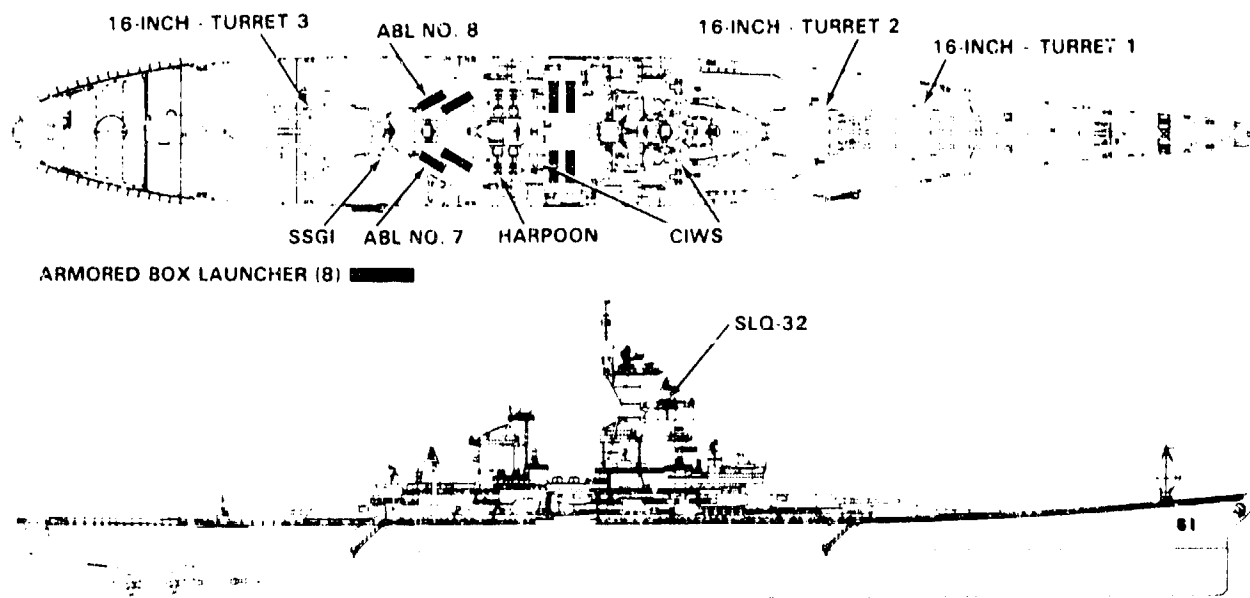


FIGURE 1. WEAPONS AND EQUIPMENT IN IOWA CLASS BATTLESHIP

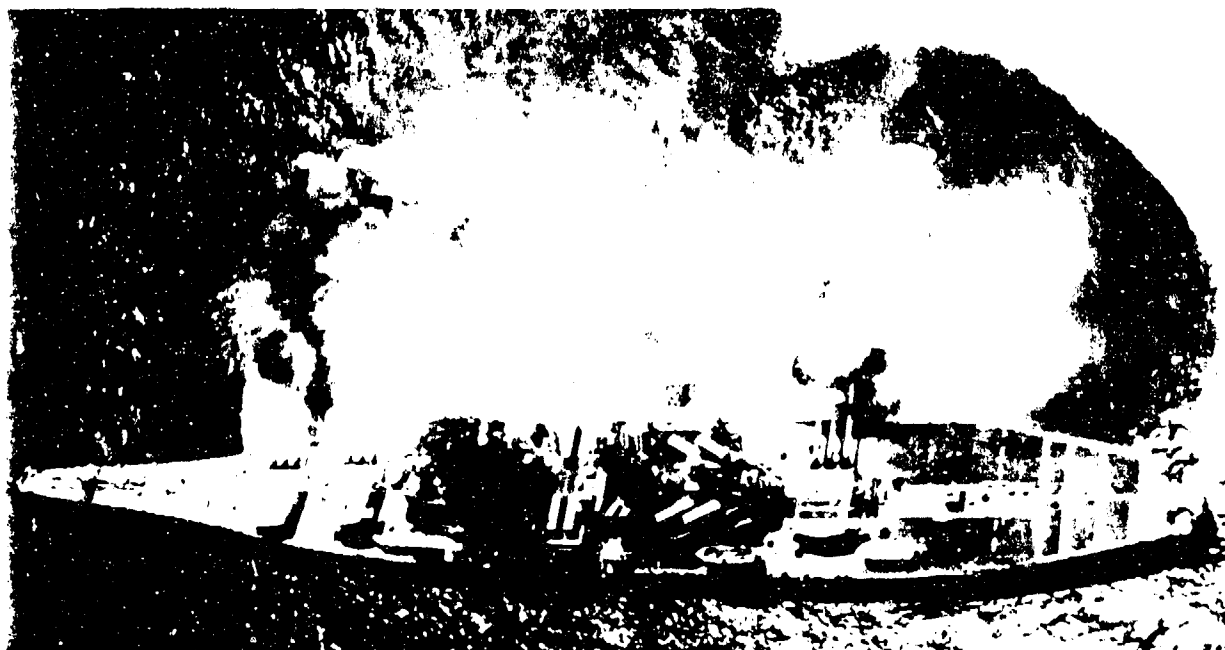


FIGURE 2. USS IOWA FIRING BROADSIDE. CAREFUL OBSERVATION OF THE THREE MAIN TURRETS SHOWS THE BARRELS IN VARIOUS STATES OF RECOIL

YAGLA

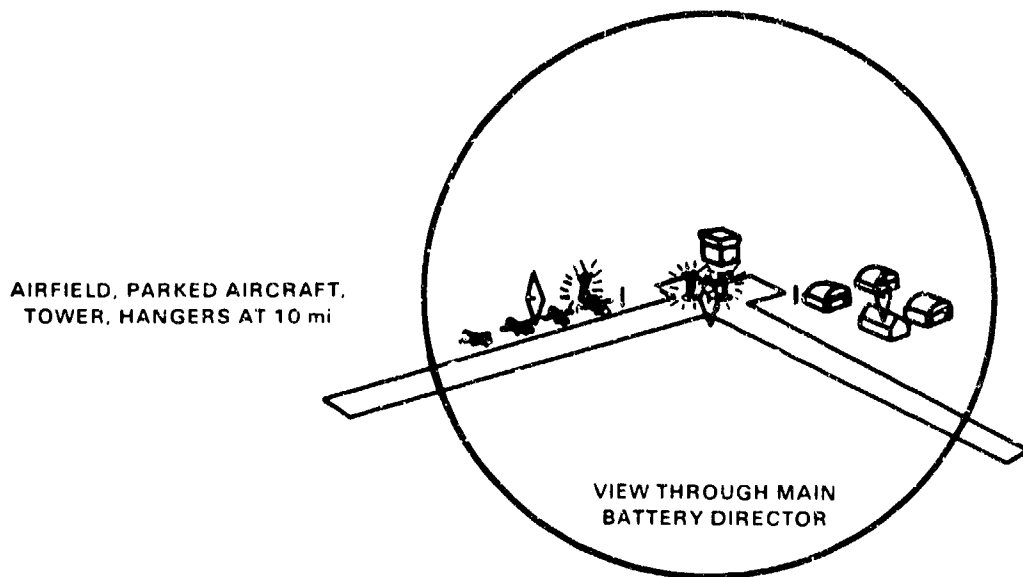


FIGURE 3. VIEW FROM MAIN BATTERY DIRECTOR OF AIRFIELD AT A RANGE OF 10 MILES AND A PARTIAL SALVO WITH A RIGHT BARREL MISS 7 MILS TO THE LEFT

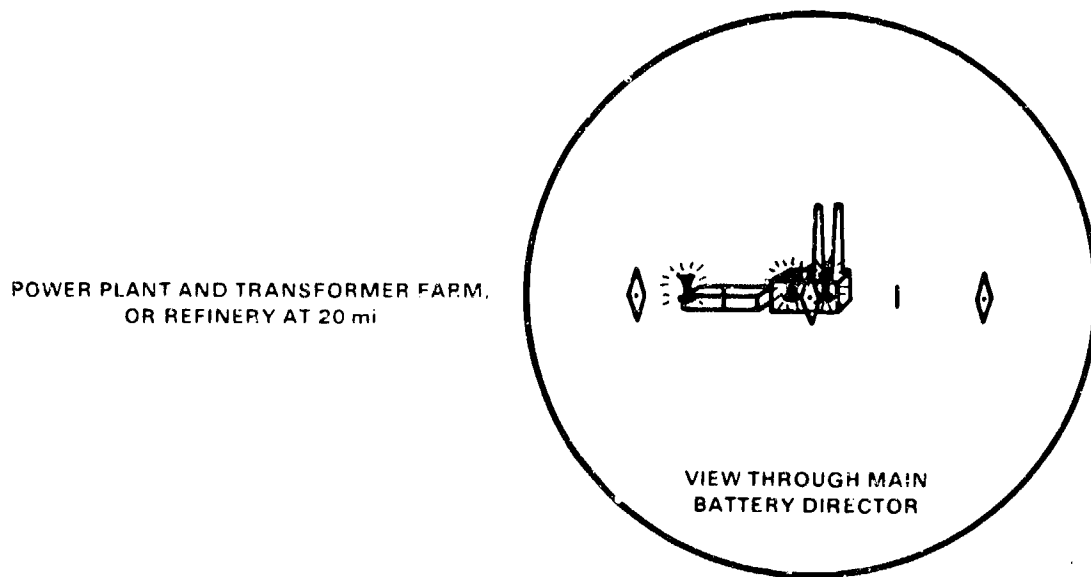


FIGURE 4. VIEW FROM MAIN BATTERY DIRECTOR OF INDUSTRIAL TARGET AT A RANGE OF 20 MILES AND A PARTIAL SALVO WITH A RIGHT BARREL MISS 7 MILS TO THE LEFT

YAGLA

Meanwhile, an engineering change proposal (ECP) was proffered to revert back to the old salvo firing circuits. Presumably this would correct the 7-mil miss, but improved accuracy would be obtained at the price of greatly reduced firing arcs to protect equipment from combined blast waves. The reduced firing arcs would have serious consequences for mission planning and execution and would have been unacceptable to the operating community. A further analysis of the problem was carried out to quantify the accuracy under the proposed 1.0-sec delay for the third barrel and the old firing circuits that fired the two outer barrels of a turret simultaneously, then the center barrel 0.070 sec later.

Ignition delays were an important part of the calculations leading to the 0.200-sec firing delays. The ignition delays were measured at Dahlgren and aboard USS NEW JERSEY during structural test firings. The average ejection time was 0.113 sec with a standard deviation of 0.021 sec. The random component is attributed to a variable "ignition delay time" that seems to be much worse in a statistical sense than for cased propellants. Subsequent measurements have shown that the delay times may be much larger than in the early data.

The dynamical response model was used with a statistical analysis of the ignition delays to show the expected accuracy in reverting back to the old firing circuits. The analysis showed that the old circuits would lead to accuracy problems and pointed out the requirement for carefully designed delays.

Final recommendations were made to USS IOWA to conduct salvo firing experiments at various ranges with the left barrel firing 0.20 sec after the center barrel, and the right hand firing 1.0 sec after the left. The data from a number of firings in the range of 14,000 to 34,300 yd has shown the new firing circuits provide vastly improved salvo firing accuracy. Deflection patterns as narrow as 1.0 mil wide have been observed at ranges as far as 29,000 yd.

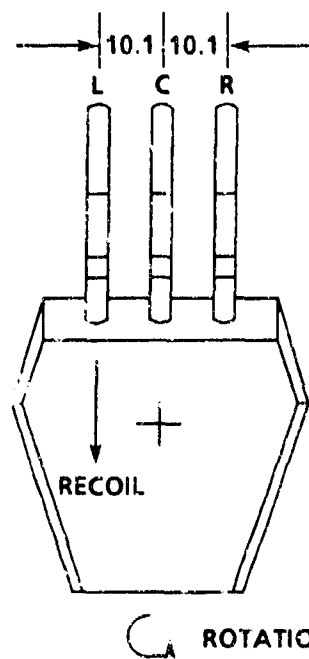
The next section explains the dynamical model and the basis for recommending the new firing delays. The third section shows the significance of the statistical variation in ejection time to the accuracy attainable with the old firing circuits. The final section presents experimental data on the deflection pattern obtained with the new firing circuits.

DYNAMICS MODEL OF TURRET

Figure 5 is a sketch of a three gun turret. The firing sequence is center, left, then right. The center barrel is aligned with the train axis of the turret, and therefore produces no net moment on the turret during recoil. The barrel axes are 10.1 ft apart. The maximum force in the recoil is 1,380,000 lb. [3] (The value of the recoil force was measured subsequent to the present calculations and found to be more nearly 1,000,000 lb. The recoil force data are presented in the APPENDIX A section).

The first step of the analysis used rigid body dynamics to compute the angular acceleration, angular velocity, and rotation of the turret during the recoil period. The calculations showed that the brake load from the left gun causes the turret to rotate 0.606 degrees during the 0.20-sec interval between firing the left and right gun.[4] The rotation of the turret creates a moment on the trunnion of the right barrel, which mainly causes it to rotate within the turret. An impulsive moment at the trunnion should also cause flexural vibrations of the barrels. Because no better data could be found, the moments of inertia of the barrel and turret armor were estimated from data on plate thicknesses and various component weights in Reference [3]. The data and calculated moments of inertia are shown in Table 1.

The estimated 0.606-degree deflection amounts to 7.16 mrad, which agrees with the deflections of 5 to 10 mil initially reported by the ship.



$$F_{\text{recoil}} = 1,380,000 \text{ lb}$$

ROTATION DUE TO MOMENT OF RECOIL OF LEFT GUN

FIGURE 5. SKETCH OF TURRET SHOWING RECOIL FORCE AND MOMENT

TABLE 1. FORCES, INERTIAL PROPERTIES, RESPONSE

Rotating weight: $1701.1 \text{ tons} \times 2240 \text{ lb/1. ton} = 3,810,000 \text{ lb}$

Recoiling weight: 292,000 lb per gun

Oscillating weight: 387,900 lb

Brake load: 1,381,000 lb per gun

Trunnion "pressure" at 45-degree elevation fire: 1,687,000 lb per gun

Recoil stroke: 4.0 ft

Maximum elevation gear rate: 12degree per sec (60 hp)

Maximum train gear rate: 4degree per sec (300 hp)

Projectile initial velocities:	2700 lb AP at 2,425 ft/sec	$203.6 \times 10^5 \text{ lb sec}$
	1900 lb HC at 2,690 ft/sec	$158.9 \times 10^5 \text{ lb sec}$

Counter recoil force: 372,857 lb

Recoil period: 0.43 sec

Counter recoil period: 0.90 sec

Moment of inertia of barrel about trunnion axis: $5.67 \times 10^6 \text{ sl-ft}^2$

Moment of inertia of turret plus three guns about train axis: $39,100,000 \text{ sl-ft}^2$

YAGLA

The rigid body dynamics calculations were continued through the recoil period to determine how long it would take the fire control system and train drive motors to correct the train error. The calculations showed that the 300 hp train drive motor in the turret could have the right gun back on the gun-target line in about 0.811 sec.

The turret train is also disturbed by recoil from the right gun as the projectile travels through the bore. The actual motion of the turret is therefore the rotational motion due to the left gun recoil load, minus the negative motions due to the brake load of the right gun, and the 300-hp train drive motor. The motions and the net result are shown in Figure 6. The pointing error at the time the right gun is fired is shown. The total error has to be evaluated after the "in-bore" period for the right projectile. The "correct" time to fire the right gun is also shown. The turret should be back to the gun-target line at 0.811 sec.

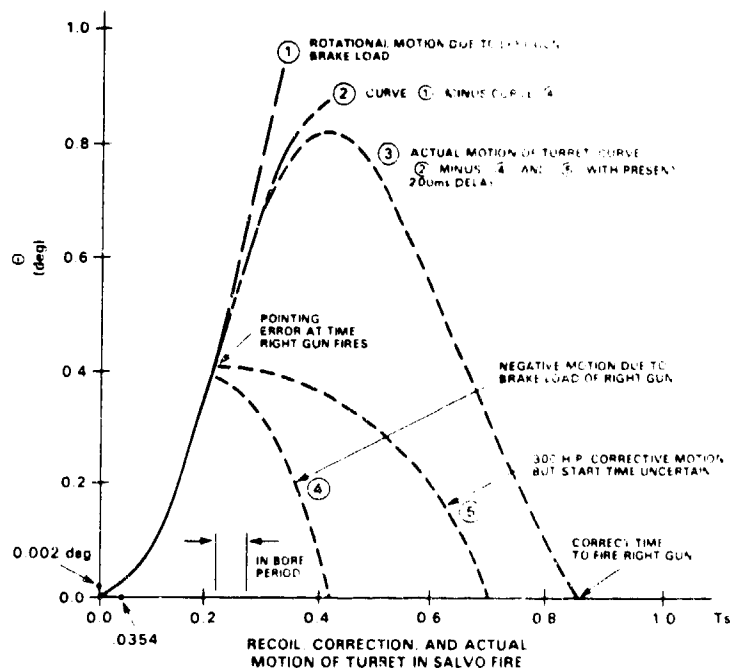


FIGURE 6. APPROXIMATE MOTION OF TURRET

The acceleration of the turret was measured during firings of Turret 3. The instrument was located 36 ft from the train axis as shown in Figure 7. Unfortunately, the turret train drive was not operating correctly, so the data only show the motion due to recoil of the left gun. The data show higher frequency vibrations superimposed on a half sinusoid about 0.760 sec long. The vibrations are believed to be caused by impulsive moments at the trunnions of the barrels and damp out well before the half sinusoid motion is complete. Data from seven rounds were averaged to obtain a value of 0.957 sec for the settling time of the turret. Unfortunately, magnetic tape recordings could not be made, so further processing of the data was not possible.

The available data and approximate calculations considered together seemed to indicate a delay time of approximately 1 sec would be sufficient to get the turret back on the gun-target line. The firing

YAGLA

circuits were reset to fire the barrels in the sequence center, left, and right after delays of 0.200 and 1.00 sec, respectively. A number of deflection patterns were observed in the period 10 December 1986 to 14 July 1987. The results are presented in a later section and show that the entire deflection pattern for all nine guns firing can now be taken as 1 to 3 mils. Many of the patterns were seen as a broad, single splash. Photographic measurements made from an aircraft showed a deflection pattern only 1.03 mils wide at a range of 29,000 yd.

DEFLECTION DISPERSION DUE TO RANDOM IGNITION DELAYS

Background

An ECP to revert back to original firing circuits was briefly entertained by the Naval Sea Systems Command (NAVSEA) in 1986. The old firing circuits fire the left and right guns simultaneously and then fire the center gun 0.070 sec later. The assumption is that the simultaneous firing of the two outer barrels provides a balanced brake load on the turret, and therefore, the turret would stay on the gun-target line during the salvo. The assumption is defective, however, due to a random component of ignition delay and shot ejection. Experimental ejection time data have been analyzed and used in mathematical models of the turret response. The results of the analysis show that there is an unbalanced torque on the turret for a significant period of time, and the unbalanced torque can cause unacceptable dispersion in deflection. Reference [4] responded to the ECP, which was subsequently withdrawn.

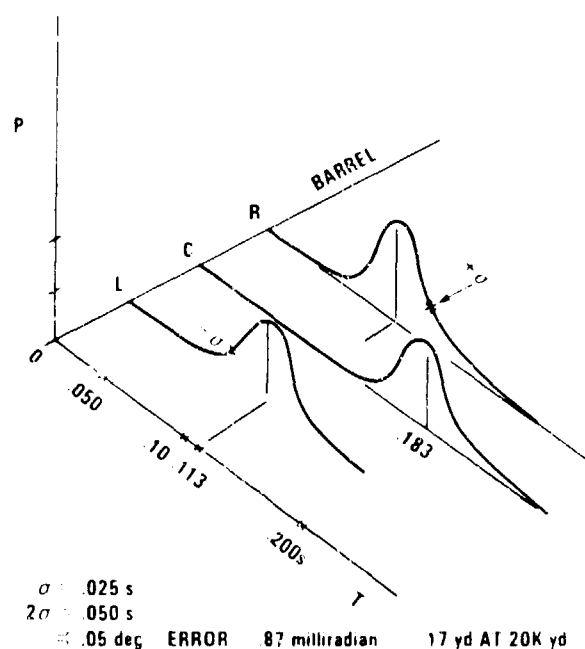
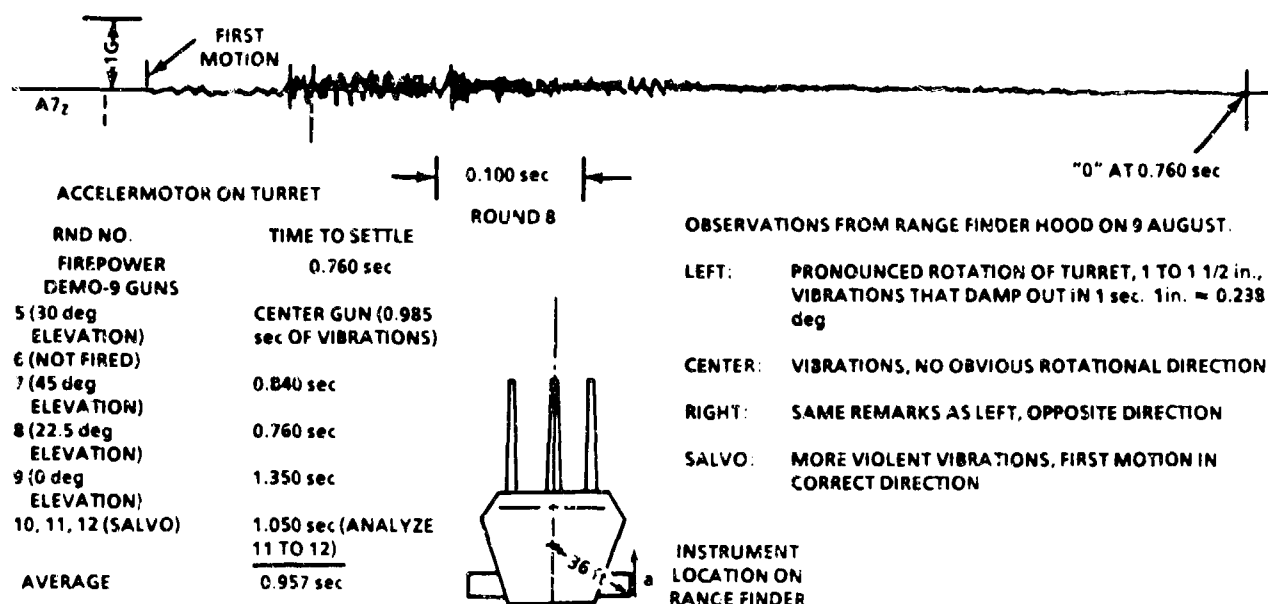
When one closes the firing key of a 16-in. gun firing circuit, it usually takes about 0.1 sec for the projectile to leave the barrel. The projectiles consistently exit at the same speed, so it is very unlikely that the in-bore, space-time trajectory varies significantly. Therefore, any observed variation in the ejection time is presumed to be due to a variable "ignition delay" time. The shortest ejection time the writer is aware of was one measured as 0.071 sec. Any delays beyond this value are thus attributed to random delays from the time the primer is electrically initiated (assumed zero delay) to the time enough combustion of the black powder priming charge and propellant grains has occurred to begin the so-called ballistic cycle. The ballistic cycle is precisely repeatable. It will be shown that the variability of the ejection time (as measured by its variance or standard deviation) has a profound importance on accuracy of salvo fire from 16-in. three-gun turrets.

There are a number of bodies of data on ejection time available for use in the analysis below. Unfortunately, they are inconsistent and a subjective decision is required to carry out an analysis. The data are listed in Table 2.

There was a period of time after NEW JERSEY's reactivation in which a number of 16-in./50-caliber misfires occurred. It is not known how the old primers or other factors contribute to the database. It would be prudent to use the larger of the above standard deviations to estimate the possible deflection dispersion due to statistical variation of ejection time. Therefore a standard deviation of ejection time of 0.025 sec is used for most of the analysis, although the data in Table 2 are convenient for discussion and grasping the problem. The value of 0.025 sec may be optimistic, as the composite standard deviation from all 1986 Dahlgren data has a variance of 0.0679 sec.

Calculations are done in this section only for the case where the left and right barrel are fired simultaneously.

Figure 8 shows probability curves based on a mean ejection time of 0.113 sec and a standard deviation of .025 sec. Separate curves are shown for the left (L), center (C), and right (R) barrels. The center barrel is shown firing with an intentional delay of 0.070 sec after the left and right barrels. The actual ejection from the left or right barrel occurs at any time, but the average is at the time 0.113 and varies in accordance with the normal distribution with standard deviation $\sigma = 0.025$ sec. The fractional area accumulated under the curve out to a given time, say T , is the probability that ejection would have



YAGLA

occurred by this time.* Ejection from any barrel can occur at any time, but 68 percent of the time ejection will occur within $\pm\sigma$ of the intended time. If the probability curves are so broad as the composite data set, the 0.070 delay would only be significant in the statistical sense. Ejection would occur in any order, and frequently the center barrel would be first!

TABLE 2. MEASURED EJECTION TIMES FOR 16-IN./CALIBER AMMUNITION

Data Set	Number of Rounds	Mean Ejection Time (sec)	Variance (Standard Deviation) (sec)	Data Source
1	36	0.113	0.021	16-in. blast test, Dahlgren, 1981, IR Infrared Detector
2	10	0.126	0.025	USS NEW JERSEY Phase I Structural Test Firing, 1982, Infrared Detector
3	23	0.0906	0.010	USS NEW JERSEY Phase II Structural Test Firing, 1983, Infrared Detector
4	8	0.126	0.00881	Dahlgren, 5/8/86, Doppler Radar
5	4	0.132	0.0189	Dahlgren, 5/15/86, Doppler Radar
6	10	0.1146	0.0107	Dahlgren, 6/10/86, Doppler Radar
7	4	0.107	0.0118	Dahlgren, 6/12/86, Doppler Radar
8	6	0.1248	0.0057	Dahlgren, 6/25/86, Doppler Radar
9	17	0.2075	0.0947	Dahlgren, 7/31/86, Doppler Radar
A	19	0.149	0.0679	Composite of all 1986 Doppler Radar Data from Dahlgren

Computation of Deflection Error for Second Outer Barrel that Fires

It is apparent from the normal distribution that: e.g., the left barrel will fire prior to $0.113 - \sigma$ 16 percent of the time, and the right barrel will fire after $0.113 + \sigma$ 16 percent of the time. When these

*Capital "T" is used for time. In keeping with standard statistical nomenclature, small "t" is reserved for the "t" statistic

events occur together, the firing times are spaced more than 2 σ apart; e.g., more than 0.050 sec. During the time between left and right projectile ejection, the turret is torqued by the moment of the brake load of the barrel that has fired. There is no compensating "equal but opposite" counter torque from the unfired barrel. The turret responds as a dynamical system during this time which results in a rotational motion off the intended gun-target line and a possible miss at the target.

The probable miss angle in deflection can be calculated by statistical methods. This requires computation of the distribution of the difference in ejection times. The "t" distribution applies.[5] The mathematical problem is to estimate the time difference between ejection from the left and right barrels and the standard deviation of the time difference. The probability distribution for the difference between two normal distributions is governed by the so called "t" parameter. Equation (1) for the "t" parameter for the difference distribution is

$$t = \frac{(T_1 - T_2) - (\mu_1 - \mu_2)}{\sqrt{2\sigma^2}} \quad (1)$$

Here T_1 and T_2 are normally distributed variables with means T_1 and T_2 and the same variance v and standard deviation σ . For a sample calculation for the distribution of time differences, $\mu_1 = \mu_2$, $\sigma = 0.010$, and the data from Data Set No. 3 of Table 2 are used. Equation (1) then becomes

$$t = \frac{T_1 - T_2}{0.01414} \quad (2)$$

To compute the probability that the difference in the firing times is greater than $T_1 - T_2 = 0.02$, one calculates

$$t = 0.02/0.01414 = 1.414. \quad (3)$$

For $t = 1.414$, and 22 degrees of freedom (the number of data points in the sample minus one), Table 3 provides (by interpolation) a probability $p(0.02) = 0.18$. The data in Table 3 for 22 degrees of freedom are plotted in Figure 9. To compute the probability that the difference in firing time is greater than 0.04,

$$t = 0.04/0.01414 = 2.828 \quad (4)$$

and $p(0.04) = 0.01$.

The probability versus time difference curve is shown as Figure 10. The curve shows that there is a 0.33 chance that the time difference will exceed 0.1414 sec. The table and curves were generated using the firing data from Data Set No. 3 of Table 2. The standard deviation of the sample was $\sigma = 0.010$ sec. As previously stated, it would be prudent to use a standard deviation of $\sigma = 0.025$ sec because of the uncertainty in the small available database, and even this may be optimistic. It can be reasonably assumed that the effect of a larger value of σ would be to proportionally broaden the curve of Figure 10. The result would be a 0.33 chance that the time difference will exceed 0.0354 sec. The following paragraph shows how this time difference can be used to estimate dispersion in deflection.

Figure 6 showed the angular response of the turret due to the left gun brake load. The figure did not show the random component of ejection time, but starts with $T = 0$ at the time ignition occurs and the true in-bore period of projectile motion begins. For the present purpose, the curve could be for either the left or right barrel. The amount of rotation corresponding to a time difference of 0.0354 sec can be read off the curve as 0.022 degrees (0.386 mrad). As indicated in Reference [7], the 2700-lb AP

YAGLA

round is capable of a deflection dispersion of 16 yd at a range of 30,000 yd, or 0.533 mrad. The 1900 lb HC projectile is capable of 10 yd at 40,000 yd. This corresponds to a deflection of 0.25 mrad.

TABLE 3. DISTRIBUTION OF t

Degrees of Freedom	Probability												
	0.9	0.8	0.7	0.6	0.5	0.4	0.3	0.2	0.1	0.05	0.02	0.01	0.001
1	0.158	0.325	0.510	0.727	1.000	1.376	1.963	3.078	6.314	12.706	31.821	63.657	636.619
2	0.142	0.280	0.445	0.617	0.816	1.061	1.386	1.896	2.920	4.303	6.965	9.925	31.598
3	0.137	0.277	0.424	0.584	0.765	0.978	1.250	1.638	2.353	3.182	4.541	5.841	12.924
4	0.134	0.271	0.414	0.569	0.741	0.941	1.190	1.533	2.132	2.776	3.747	4.604	8.600
5	0.132	0.267	0.408	0.559	0.727	0.920	1.156	1.476	2.015	2.571	3.365	4.032	6.869
6	0.131	0.265	0.404	0.553	0.718	0.906	1.134	1.440	1.943	2.447	3.143	3.707	5.959
7	0.130	0.263	0.402	0.549	0.711	0.896	1.119	1.415	1.895	2.365	2.998	3.499	5.408
8	0.130	0.262	0.399	0.546	0.706	0.889	1.108	1.397	1.860	2.306	2.806	3.355	5.041
9	0.129	0.261	0.398	0.543	0.703	0.883	1.100	1.383	1.833	2.262	2.821	3.250	4.781
10	0.129	0.260	0.397	0.542	0.700	0.879	1.093	1.372	1.812	2.228	2.764	3.169	4.387
11	0.129	0.260	0.396	0.540	0.697	0.876	1.088	1.363	1.796	2.201	2.718	3.105	4.437
12	0.128	0.259	0.395	0.539	0.695	0.873	1.083	1.356	1.782	2.179	2.681	3.055	4.318
13	0.128	0.259	0.394	0.538	0.694	0.870	1.079	1.350	1.771	2.160	2.650	3.012	4.221
14	0.128	0.258	0.393	0.537	0.692	0.868	1.076	1.345	1.761	2.145	2.624	2.977	4.140
15	0.128	0.258	0.393	0.536	0.691	0.866	1.074	1.341	1.753	2.131	2.602	2.947	4.073
16	0.128	0.258	0.392	0.535	0.690	0.865	1.0	1.337	1.746	2.120	2.583	2.921	4.015
17	0.128	0.257	0.392	0.534	0.689	0.863	1.069	1.333	1.740	2.110	2.567	2.898	3.965
18	0.127	0.257	0.392	0.534	0.688	0.862	1.067	1.330	1.734	2.101	2.552	2.878	3.922
19	0.127	0.257	0.391	0.533	0.688	0.861	1.066	1.328	1.729	2.093	2.539	2.861	3.883
20	0.127	0.257	0.391	0.533	0.687	0.860	1.064	1.325	1.725	2.086	2.528	2.845	3.850
21	0.127	0.257	0.391	0.532	0.680	0.859	1.063	1.323	1.721	2.080	2.518	2.831	3.819
22	0.127	0.256	0.390	0.532	0.686	0.858	1.061	1.321	1.717	2.074	2.508	2.811	3.792
23	0.127	0.256	0.390	0.532	0.685	0.858	1.060	1.319	1.714	2.070	2.500	2.807	3.767
24	0.127	0.256	0.390	0.531	0.685	0.857	1.059	1.318	1.711	2.066	2.492	2.797	3.745
25	0.127	0.256	0.390	0.531	0.684	0.856	1.058	1.316	1.708	2.060	2.485	2.787	3.725
26	0.127	0.256	0.390	0.531	0.684	0.856	1.058	1.315	1.706	2.056	2.479	2.779	3.707
27	0.127	0.256	0.389	0.531	0.684	0.855	1.057	1.314	1.703	2.052	2.473	2.771	3.690
28	0.127	0.256	0.380	0.530	0.683	0.855	1.056	1.313	1.701	2.048	2.467	2.763	3.674
29	0.127	0.256	0.389	0.530	0.683	0.854	1.055	1.311	1.699	2.045	2.462	2.756	3.659
30	0.127	0.256	0.389	0.530	0.683	0.854	1.055	1.310	1.697	2.042	2.457	2.750	3.646
40	0.126	0.255	0.388	0.520	0.681	0.851	1.050	1.303	1.684	2.021	2.423	2.704	3.551
60	0.126	0.254	0.387	0.527	0.679	0.848	1.046	1.296	1.071	2.000	2.390	2.660	3.460
120	0.126	0.254	0.386	0.526	0.677	0.845	1.041	1.289	1.658	1.980	2.358	2.617	3.373
∞	0.126	0.253	0.385	0.524	0.674	0.842	1.036	1.282	1.045	1.960	2.326	2.576	3.291

Source: Table II is reprinted from Table III of Ronald A. Fisher and Frank Yates, *Statistical Tables for Biological, Agricultural, and Medical Research*, 4 ed., 1953, published by Oliver & Boyd, Ltd., Edinburgh, by permission of the authors and publishers.

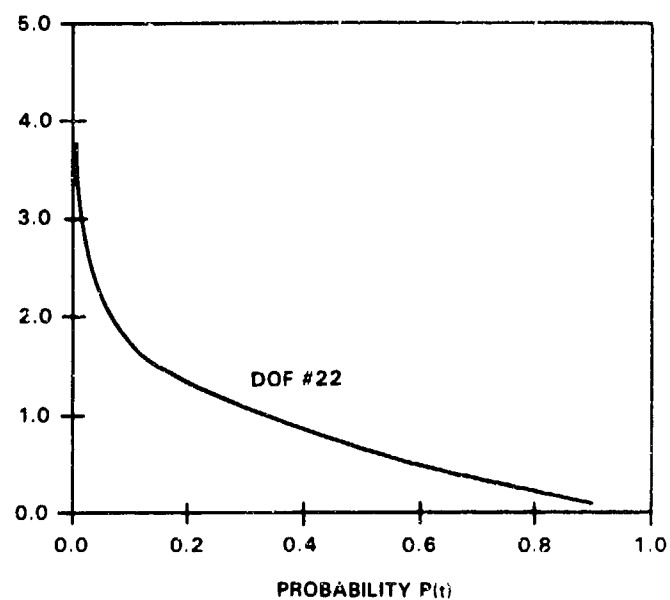


FIGURE 9. DISTRIBUTION OF t FOR 22 DEGREES OF FREEDOM

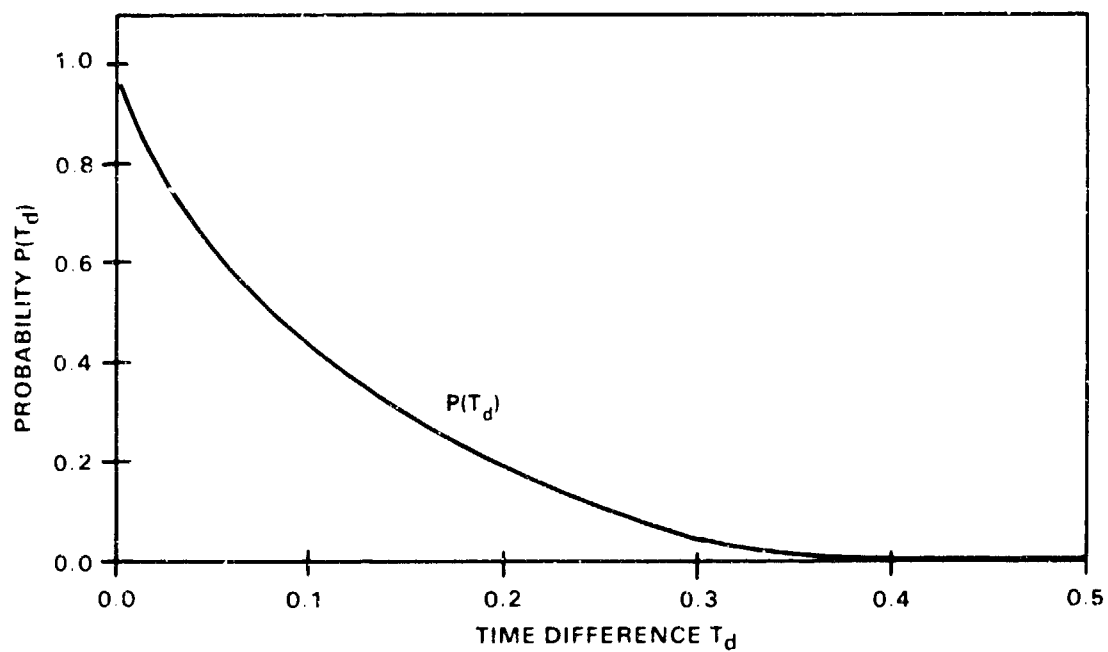


FIGURE 10. PROBABILITY VERSUS TIME DIFFERENCE FOR OUTER BARRELS

YAGLA

The error due to ejection time difference is 16 yd in 30,000 yd when θ on Figure 4 is 0.0305 degrees, which corresponds to $T_d = 0.048$ sec. The probability for the ejection time exceeding $T_d = 0.048$ sec, from Figure 10, is about 0.008, which is very small.

The turret is rotating when the second barrel fires, and the second barrel to fire has the same angular velocity as the turret. The brake load due to recoil causes an angular acceleration of 0.358 rad/sec².

In a time interval of 0.0354 sec, the barrel attains an angular rate of 12.7 mrad per sec. The tangential velocity at the muzzle for a barrel firing horizontally would be 0.775 ft/sec. For an elevation of 45 degrees, the effective radius is reduced and the tangential velocity is 0.589 ft/sec. For a flight time of 52.2 sec to a range of 30,000 yd, the throw-off would be 10.2 yd or 0.34 mrad. For a flight time of 95.6 sec to a range of 42,000 yd, the throw-off would be 19 yd, or 0.45 mrad. The deflection due to throw-off for the second barrel to fire is comparable to the deflection due to the pointing error. The combined errors are significant.

Computation of Deflection Error of Center Barrel

For firings as shown in Figure 8 where the center barrel is fired after a 0.070-sec delay, the turret will not be on the gun-target line when the center barrel is fired unless both outer barrels fire precisely at the same time. The previous calculations were carried out for $\sigma = 0.025$ sec and show a probability of 0.67 for $T_d \leq 0.0354$ sec. When the second barrel fires, the turret is not only in a displaced position but has angular velocity as well. The time variation of the brake load was not known at the time of the original analysis. It was taken as essentially constant in the early portion of the stroke; then when the second barrel fires, the two brake loads provide equal and opposite torques on the turret. The turret would coast at a constant angular rate until the train drive begins to correct the pointing error. A rigid body model was used to compute the velocity of the turret after $T_d = 0.0354$. The angular acceleration of the turret was 0.358 rad/sec² during the unbalanced period. The angular velocity at 0.0354 sec would be 12.7 mrad/sec. Then the second barrel fires and the turret coasts at constant angular rate until, on the average after 0.070-sec delay, the center barrel fires. Then the turret has coasted through an additional arc of 12.7 mrad/sec times 0.07 sec = 0.887 mrad. This pointing error must be added to the error already present when the second barrel fired, which was 0.386 mrad, or a total angular deflection of 1.27 mrad.

Because of the coast angular rate and the 0.070-sec delay, the center barrel deflection is much larger than the second barrel deflection.

The "t" distribution can be used to compute the distribution of the firing time between the second and third barrels. Then the statistics of the error as a result of coasting at constant angular rate can be computed. The distribution consists of the programmed 0.070 sec plus a random component with t given by Equation (5)

$$t = \frac{T_1 - T_2}{\sqrt{\sigma_1^2 + \sigma_2^2}} \quad (5)$$

Here the time difference $T_1 - T_2$ has the same meaning as before. The standard deviation of the time delay between the firings of the outer barrels is σ_1 , which was $\sqrt{2}\sigma$, and $\sigma_2 = \sigma$. Using $\sigma = 0.025$, the random component (Equation (6)) provides

$$t = \frac{T_1 - T_2}{\sqrt{0.00125 + 0.00062}} = \frac{T_1 - T_2}{0.0433} \quad (6)$$

YAGLA

Calculations similar to those leading to Figure 10 provide a standard deviation of 0.0433 for the distribution of the mean ejection time of 0.0070 sec for the center barrel relative to outer barrels. The probability curve for the random component of time delay of the difference for the center barrel relative to the outer barrel is plotted on Figure 11. The curve shows the 67 percent of the time the random component of the interval between the two firings is 0.0433 sec or less. The coast time is therefore 0.070 ± 0.0216 67 percent of the time. The additional angular pointing error is within $0.614 \leq \theta \leq 0.916$ mrad 67 percent of the time. The error has to be added to the mean outer barrels pointing error of 0.386 mrad. The 67 percent probable pointing error is $1.0 \leq \theta \leq 1.302$ mrad. Because the order of fire of the outer barrels is not controlled, this error can be either to the right or to the left.

For firings to 30,000 yd, the miss of the center barrel due to pointing error would be 30 to 39 yd, which is twice the demonstrated capability of the gun-projectile system. When one considers the additional 10-yd miss due to throw-off in the same direction, the total error for the center barrel becomes 40 to 50 yd at least 67 percent of time.

Summary of Analysis of Old Firing Circuits

Probability theory, measured shot ejection times, and mathematical models for the rotational dynamics of the 16-in./50-caliber three-gun turret have shown that the random delays in ignition of the propelling charge lead to significant dispersion at the target. The error is due to unbalanced moments acting on the turret when the outer barrels are fired. The pointing error in the second projectile to be fired is relatively small, exceeding the published accuracy of 0.533 mrad of the 16-in./50-caliber gun only one in 125 rounds. If throw-off due to rotation of the turret is also considered, dispersion of an additional 0.5 mrad occurs. The error in the third projectile fired is significantly worse because of the assumed 0.070-sec delay and the angular rate of the turret acquired as a result of the random interval between ejection from the outer barrels. The center barrel pointing dispersion is 1 to 1.3 mrad 67 percent of the time. When throw off is included, the dispersion increases to from 1.5 to 1.8 mrad. This constitutes a "built-in" error of 40 to 50 yd at a range of 30,000 yd, which is four times the capability of the 16-in./50-caliber gun.

The calculations are based on limited data on ejection time and on the exact time variation of brake load and train drive response. The ejection time random variable bears critically on the problem. If the standard deviation of ejection time could be reduced to $\sigma = 0.005$ sec, the errors calculated here would simply disappear. Therefore an improved ignition system would greatly improve accuracy. Good primers, good bags, and good powder would be vital for salvo accuracy when using the old firing circuits.

EXPERIMENTAL DATA

The experimentation to analyze and improve the salvo accuracy problem was carried out in four distinct efforts. The first was described in the DYNAMICS MODEL OF TURRET section and involved installing an accelerometer in Turret 3 of USS IOWA. The second experimental effort was to measure the recoil force at the recoil cylinder in a 16-in. gun. The recoil data are presented in Appendix A. The third phase of the experiment was observation of the fall of shot from salvo firings with new settings for the firing time of the right barrel. The final phase of the experiment was further firings against a target in the open ocean. A remote-piloted vehicle (RPV) was used to measure the fall of shot.

It was envisioned that several delay settings would have to be tried to find the optimum delay time. The first attempt employed a delay of 1 sec. On 10 December 1986, the ship fired the first test rounds to a range of 18,000 yd. Turret 1 fired left and right barrels with 1900-lb-high-capacity projectiles and reduced propelling charges. Two distinct splashes about 2 mils apart were observed. Then Turret 2 fired left and right barrels with the same ammunition to the same range and two distinct splashes were observed 1 mil apart. With these good results at the first attempt with a delay of 1 sec, it was decided to continue the observations at other ranges and with other projectiles and propelling charges, and to keep the delay set at 1 sec. The next five salvos, including a battleship broadside with all three turrets

YAGLA

firing, produced patterns so tight that individual splashes could not be discerned. The ranges were between 16,000 and 20,000 yd.

In January and March of 1987, there were three more opportunities to observe broadside firings. They again produced tight deflection patterns that appeared as one big splash, approximately 3 or 4 miles across. The data are summarized in Table 4.

The final phase of the experiment employed an RPV to observe the fall of shot. Reference [7] is a videotape report of this phase of the experiment. The target was an old Army dredging barge approximately 50 yd long. The firings were conducted in three phases. The first phase was conducted at 34,350 yd. The fall of shot was observed by the RPV with a television picture of the RPV's field of view being continuously recorded in the ship. The fall of shot data from the video tape was replotted onto a rectangular grid, Figure 12. There are two distinct groups with small deflection error, but it was not possible to conclusively determine which turret fired which projectile. The order of impacts was used to determine the left, right, and center projectiles. Analysis of the data showed that the deflection spread, D , was in the range $2.8 \leq D \leq 5.8$ miles for the firing turrets. Also, the right barrels did not enlarge the pattern by more than 28 yd (or 0.8 mil).

For the second phase of the firing, the range was closed to 29,000 yd. Full propellant charges and 1900-lb-high capacity projectiles were fired. The fall of shot from this phase of the exercise was plotted on a rectangular coordinate system, Figure 13. The fall of shot from the only partial salvo (more than one firing gun in a turret) fired in this phase is shown on the plot. The deflection pattern was only 1.03 miles wide and was from all three barrels of Turret 2 and the center barrel of Turret 1.

The ship then closed to 21,500 yd for the third phase of the exercise. The RPV had been called back to the ship, so optical observation from the main battery director and radar range data were used to plot the fall of shot, Figure 14. The data were plotted on a rectangular grid as before. The partial salvos provided deflection patterns of widths 1.3, 1.5, 2.2, 1.5, and 1.2 miles. Seven of the projectiles exploded on impact with the target vessel. The target began to list, then sank.

To further explain the data and to better assess the accuracy of the USS IOWA's main battery, the fall of shot data were used to reconstruct hits against several larger targets typical of Soviet naval forces. A TARANTUL missile boat, a KASHIN guided missile destroyer (DDG), and a KIROV battle cruiser (CGSN) were used for targets. The ships were drawn to the same scale as the impact plots. Transparent overlays of the targets were placed over the impact plots and the hits were determined. The results from the three phases of the exercise are shown in Figures 15 through 17.

The results show that the performance of the main battery was excellent in all three phases. The targets were straddled, bracketed, and/or hit on the first salvo. In all cases hits were obtained in the early salvos of the exercise. The Phase III performance was most dramatic--all three ships would have broke and sank immediately.

The data conclusively show the deflection dispersion problem has been solved, and USS IOWA is now capable of putting very tight groups of projectiles exactly on target.

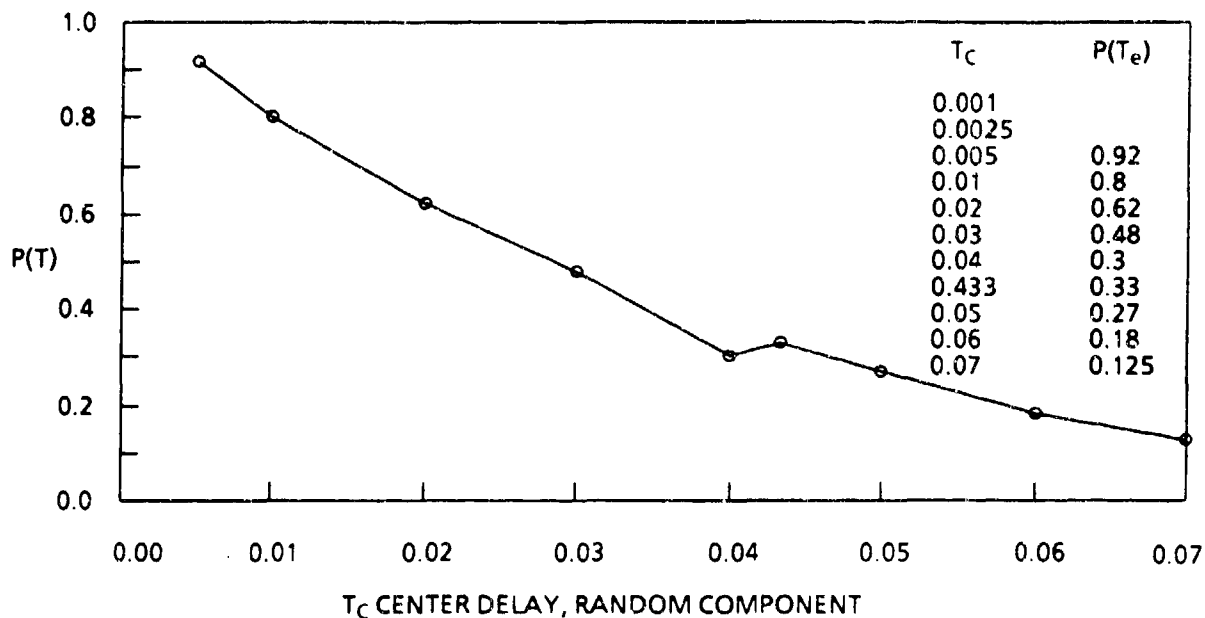


FIGURE 11. PROBABILITY VERSUS TIME DIFFERENCE FOR CENTER BARREL RELATIVE TO OUTER BARRELS

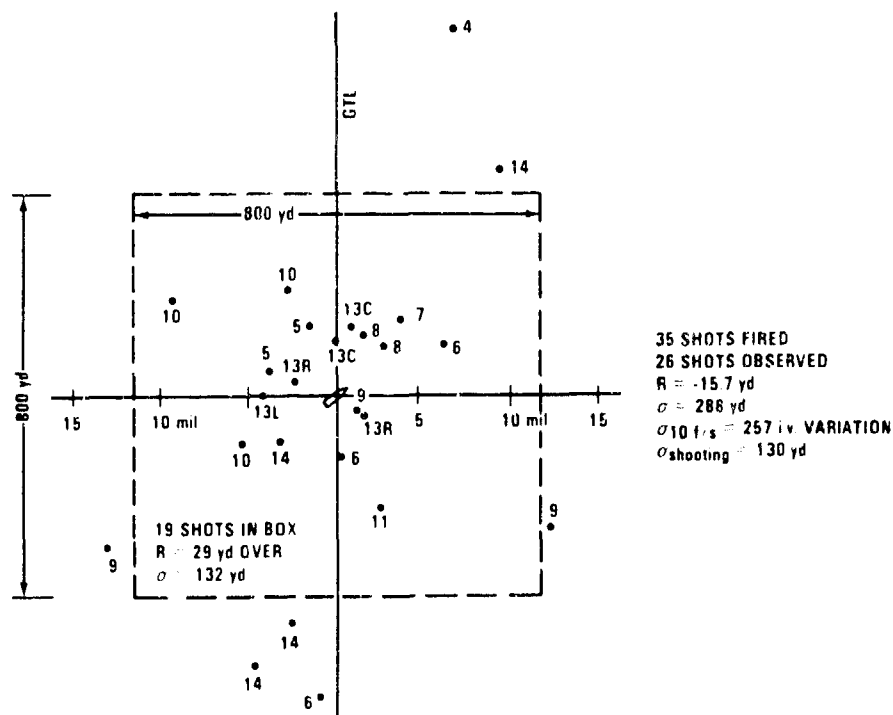


FIGURE 12. SINKEX, 14 JULY 1987, PHASE I, FALL OF SHOT 34,350 YD

TABLE 4. DEFLECTION DATA FROM USS IOWA

Date	Range (yd)	Charge F = Full R = Reduced AP = 2700 lb HC = 1900 lb	Salvo	Spread mils or Splash width	Splash D = distinct S = appeared as one splash	Deflection Group (yd)
12/10/86	18,000	R/HC	I L,R	2	D	36
			II L,R	1	D	18
12/14/86	16,000	R/HC	I C,R	3	S	46
			II L,C,R	3	S	48
			II L,C		S	
1/12/87	17,000	F/AP	III L,R	3	S	60
1/24/87	18,000		I C,R II L,C,R III L,C,R	< 4	S	72
1/27/87	17,000	R/HC	II L,C,R III L,C,R	4	D (right guns distinct)	68
1/31/87	14,000	R/HC	I L,C,R II L,C,R III L,C	4	S	56
2/17/87	17,000	R/HC	I L,C II L,C,R III L,C,R	3	S	51
7/14/87	21,580	R/HC R/HC	I C,R II L,C,R	1.3 1.5	D D	28 32
7/14/87	21,500	R/HC	I C,R II L,C,R	2.2 1.5	D D	47 32
7/14/87	21,500	R/HC	I C,R	1.2	D	47
7/14/87	29,000	F/HC	I C II C,L,R	1.0	D	30
7/14/87	34,350	F/HC	3 Turrets Fire 6 rnds T1:2, T2:3, T1:1 in to two straight lines with 0 deflection dispersion (salvo 13 of Phase 1)			

Note: Wear on all barrels at the conclusion of firing was in the range of 35 to 54 equivalent service rounds

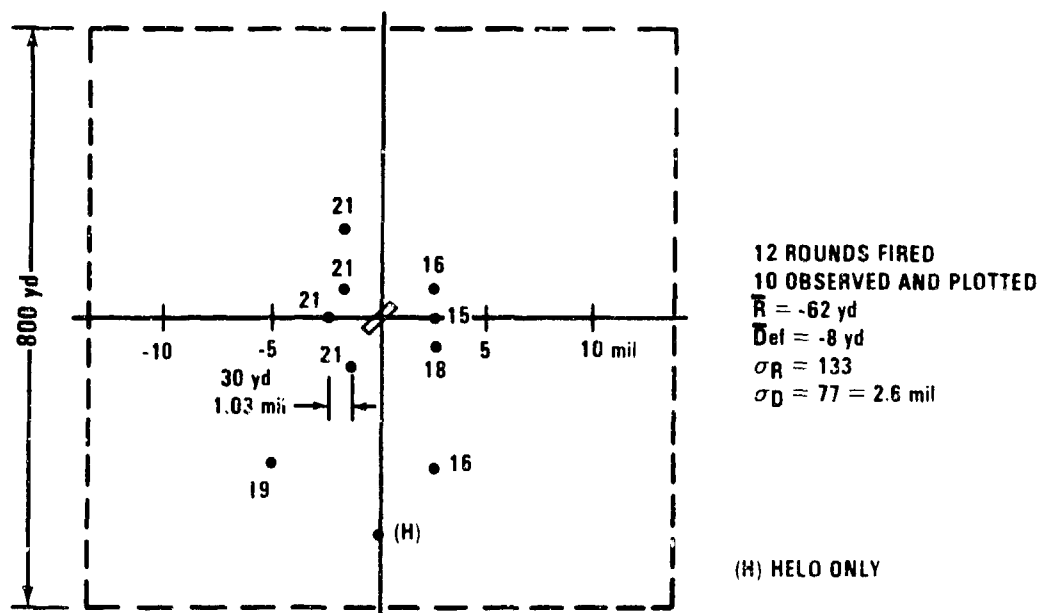


FIGURE 13. SINKEK, 14 JULY 1987, PHASE 2, FALL OF SHOT, 29,000 YD

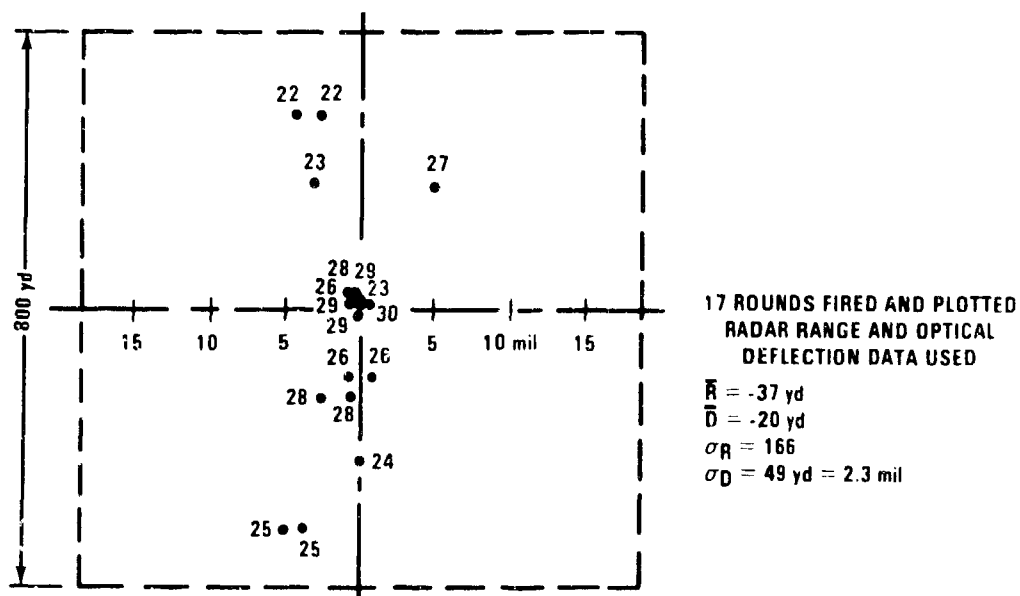


FIGURE 14. SINKEK, 14 JULY 1987, PHASE 3, FALL OF SHOT, 21,500 YD

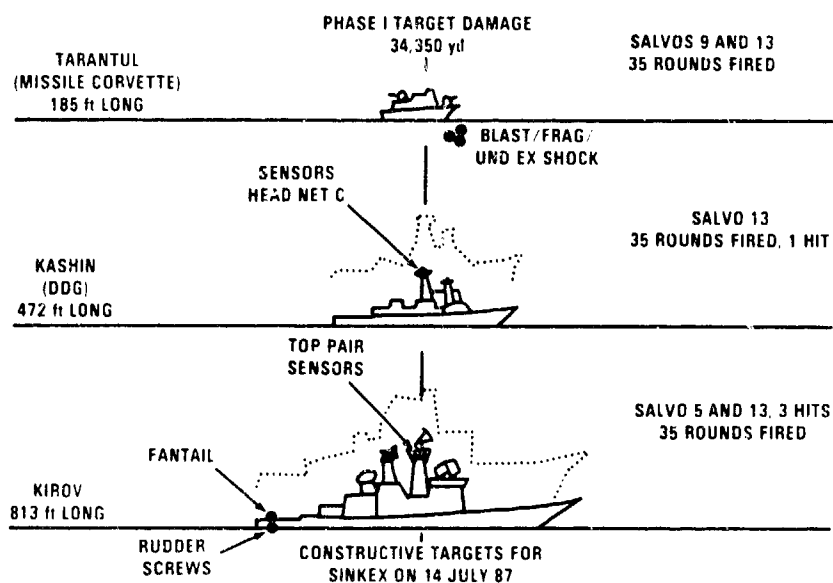


FIGURE 15. PHASE I TARGET DAMAGE, 34,350 YD

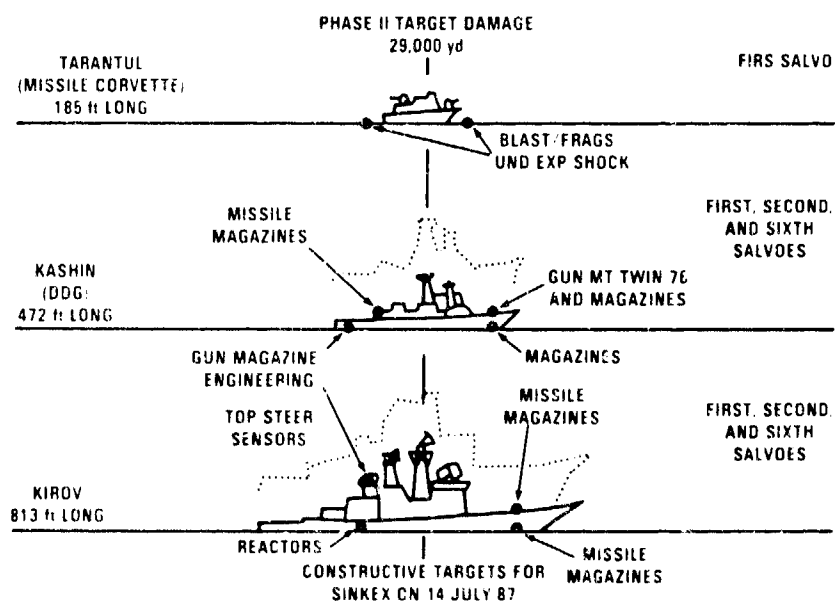


FIGURE 16. PHASE II TARGET DAMAGE, 29,000 YD

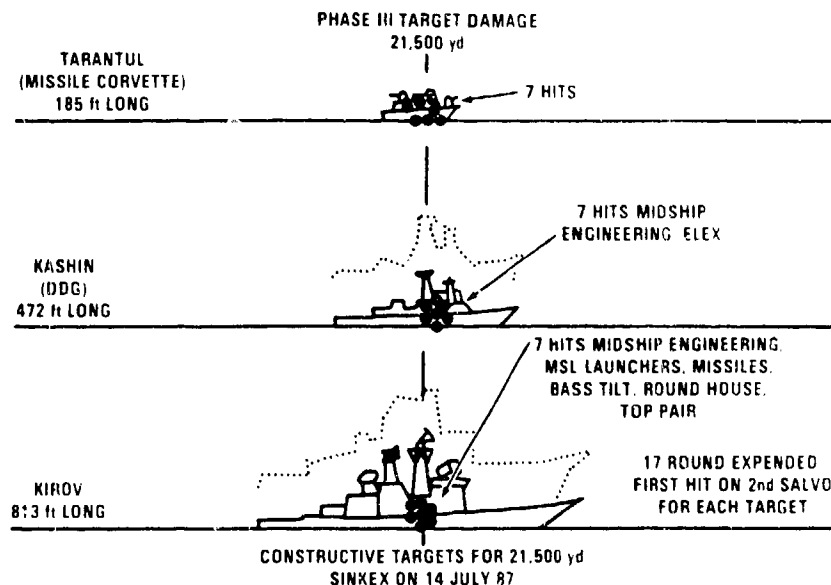


FIGURE 17. PHASE III TARGET DAMAGE, 21,500 YD

REFERENCES

1. Sims, P. J., J. R. Edwards, Sr., R. L. Dickey, and H. S. Shull, "Design for NEW JERSEY, IOWA, and DES MOINES Modernization," *Naval Engineers Journal*, May 1984.
2. Yagla, J. J., "16-In. Gun Blast and The Battleship Reactivation Program," *Naval Engineers Journal*, May 1987.
3. OP 1112 (3rd Rev.), Gun Mounts and Turret, 16-In./50-Caliber Three-Gun Turret, BB 61 Class.
4. Yagla, J. J., "Deflection Dispersion in 16-In. Three-Gun Turret Salvo Firings," NSWC H13-JJY 8300.54, 13 November 1985.
5. Bryant, E. C., *Statistical Analysis*, McGraw-Hill Book Company, Second Edition, 1966.
6. NAVORD OP758 (First Revision), OP 770 (First Revision), and OP 1100 (First Revision), *Dispersion for 16-In. 50-Caliber Ammunition*.
7. Yagla, J. J., NSWC Film Technical Report, N60921-87-TR-64, *USS IOWA Sinkex 1987 with RPV Spotting*, Naval Surface Weapons Center, Dahlgren, Virginia.

APPENDIX A--RECOIL FORCE FROM 16-IN./50 CALIBER GUN

The recoil piston in the 16-in./50-caliber gun is 9.5 in. in diameter and is solid steel. The piston transmits the force of recoil to the gun mount. The recoil force was measured by installing strain gauges, as shown Figure A-1. The strain gauges were installed 90 degrees apart, in symmetrical locations, top and bottom, and either side. Typical strain records are shown in Figure A-2. The records were offset in playback so the traces could be kept distinct.

In each case the maximum strain was measured at 0 degrees, and minimum at 180 deg. This indicates there was some bending in the piston. The bending could result from a bending moment at either end or the center of force or reaction not being applied on the axis of the piston. The data are shown in Table 1.

The formula $\sigma = \bar{\epsilon}E$ was used to compute the stress in the cylinder. The average peak strain, $\bar{\epsilon}$, and values of $E = 30 \times 10^6$ psi were used. The force was then computed by multiplying the stress by the cross-sectional area of the piston. The force was 930,100 lb. This differs from the published force of 1,381,000 lb.[3] The difference could be due to higher pressures (proof compared to service) or a nonuniform stress across the cross section.

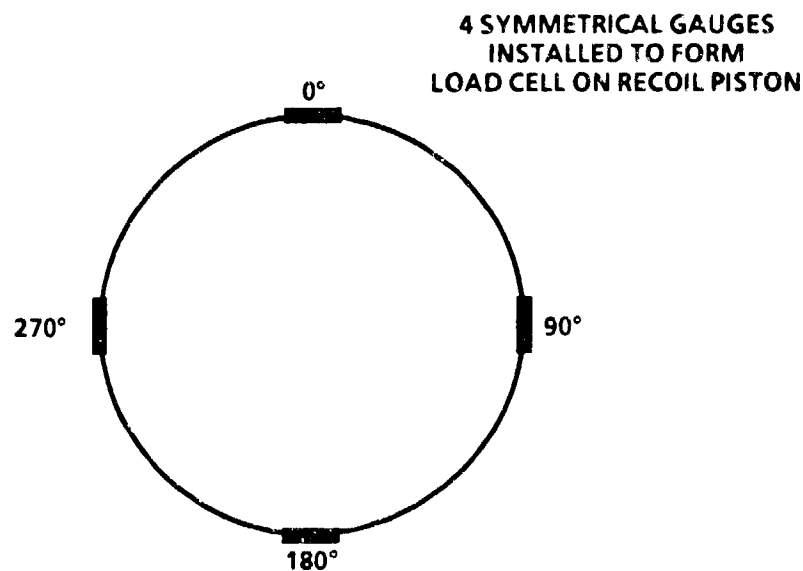


FIGURE A-1. STRAIN GAUGE INSTALLATION ON
16-IN./50-CALIBER GUN RECOIL PISTON

TABLE A-1. STRAIN DATA AND RECOIL FORCE CALCULATIONS

Round	ϵ_1	ϵ_2	ϵ_3	ϵ_4
6	558.5	441.2	314.3	430.6
7	565.3	450.9	305.2	467.1
8	562.7	447.3	306.2	440.0
9	566.4	425.9	292.0	445.2
10	555.3	431.5	313.8	447.3
11	555.3	438.1	324.0	458.7
12	556.9	436.1	325.5	471.3
13	556.3	443.2	313.3	453.0
average	559.6 ± 4.5	439.3 ± 8.2	311.7 ± 10.7	451.6 ± 13.7

$$(\bar{\epsilon}_1 + \epsilon_3)/2 = 435.7$$

$$(\epsilon_2 + \epsilon_4)/2 = 445.4$$

$$\bar{\epsilon} = 440.57$$

Note: all strains in 10^{-6} in./in.
16-in./50-caliber 2700-lb projectiles
full charges

$$\text{Recoil force} = \bar{\epsilon} E \pi d^2/4 = 930,100 \text{ lb}$$

where

$$\bar{\epsilon} = 440.57 \times 10^{-6}$$

$$E = 30 \times 10^6 \text{ psi}$$

$$d = 9.5 \text{ in.}$$

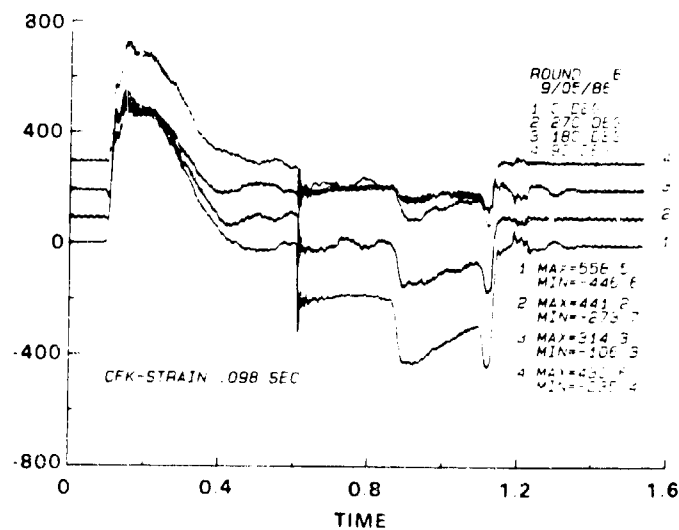


FIGURE A-2. 16-IN. RECOIL STRAIN

SESSION III

COMPUTER CODES AND MODELS

SOIFER & BECKER

TITLE: DYNACODE-G/P AND ITS APPLICATION TO THE 120MM TANK-GUN
MARTIN T. SOIFER AND ROBERT S. BECKER
S&D DYNAMICS, INC.
755 NEW YORK AVENUE
HUNTINGTON, N.Y. 11743

ABSTRACT:

DYNACODE-G/P is a 3-D, generic, gun dynamics computer simulation code for the firing of a flexible projectile in a flexible gun system. It is fully user interactive with respect to both projectile and gun design, and offers a broad spectrum of output options including projectile bending and balloting, gun-tube motion, interface loads, launch conditions, etc.

DYNACODE-G/P has been successfully applied in a number of 120mm programs for the purpose of evaluating the in-bore behavior, structural integrity and launch conditions of a variety of ammunition designs. For illustrative purposes, DYNACODE-G/P is applied here to the firing of the standard M865 round in the 120mm M1A1 tank-gun with M256 gun tube No. 84. DYNACODE-G/P is available for licensing.

BIOGRAPHY:

PRESENT ASSIGNMENT: President of S&D Dynamics, Inc., Principal Investigator for R&D programs, and Independent Consultant, 1972-Present.

PAST EXPERIENCE: Senior Project Engineer, Colt Firearms, Hartford, CT, 1970-72; Senior Project Engineer, Technik, Inc., Jericho, NY, 1968-70; Program Manager, Dynamic Science, Monrovia, CA, 1967-68; Research Scientist, New York University, Bronx, NY, 1964-67; Engineer, Technik, Inc., Jericho, NY, 1963-64.

DEGREES HELD: B.S. (Aeronautics & Astronautics), New York University, Bronx, NY, 1962; M.S. (Aeronautics & Astronautics), New York University, Bronx, NY, 1963; Ph.D. (Aeronautics & Astronautics), New York University, Bronx, NY, 1967.

DYNACODE-G/P AND ITS APPLICATION TO THE 120MM TANK-GUN

MARTIN T. SOIFER, PH.D.
ROBERT S. BECKER, M.S.
S&D DYNAMICS, INC.
755 NEW YORK AVENUE
HUNTINGTON, NEW YORK 11743

INTRODUCTION

DYNACODE-G/P is a dynamic analysis computer code which simulates the firing of a flexible projectile in a flexible gun. DYNACODE-G/P is fully user interactive with respect to both projectile and gun design characteristics. Structured in modular form, DYNACODE-G/P offers the user the ability to perform parametric design studies on one segment of the gun system without affecting data files for other segments. Output from DYNACODE-G/P provides a complete 3-D description of the instantaneous orientation, motion and loading of the projectile (including bending and balloting) and gun from shot-start through shot-exit.

The gun dynamics and in-bore balloting concepts leading to DYNACODE-G/P have been in development since the late 1970's. References [1] through [8] track various stages of development to its present level of analysis capability. The U.S. Army Ballistic Research Laboratory has been a primary supporter of the development (for application to the 75mm ADMAG, Ref. [2], and 120mm, Ref. [8], tank-gun systems). Additional support has been provided by the U.S. Army Research Office (for in-bore balloting of 37mm ammunition, Ref. [5]), ARES, Inc. (for 75mm gun dynamics studies, Ref. [3]) and Honeywell, Inc. (for in-bore balloting of 120mm ammunition, Ref. [6]). Gun dynamics output from DYNACODE-G/P has been correlated with both 75mm, Ref. [4], and 120mm, Ref. [8], experimental gun-tube motion data; balloting output has been correlated with 37mm experimental in-bore radar doppler data, Ref. [5]. DYNACODE-G/P has been adopted as the "... code of choice for future simulations of gun systems..." by the Mechanics & Structures Branch, Interior Ballistics Division, U.S. Army Ballistic Research Laboratory, Ref. [9].

S&D Dynamics, Inc. has recently applied DYNACODE-G/P, under purchase order No. 121262 to General Defense Corporation, Tactical Systems Division, for the purpose of evaluating the effects of a variety of proprietary M865 design modifications on in-bore motions and launch conditions and, under purchase order No. OP-02798 to Olin Corporation, Winchester Group, for the purpose of evaluating the in-bore motions and loadings of proprietary 120mm ammunition designs. In addition, Olin Corporation has entered into a Software License Agreement with S&D Dynamics, Inc. for its in-house use of DYNACODE-G/P.

UNDERLYING THEORY

The underlying theory of DYNACODE-G/P rests in a finite element (lumped parameter) analysis technique employing modal analysis concepts, Refs. [2] and [4]. Based on a set of gun system drawings, the physical structure of the gun system is separated into "free-free" recoiling, non-recoiling, projectile, and support sub-systems or "modules", as depicted in Figure 1; isolating purely structural deformations within each module from relative rigid-body motions accommodated at the interface between modules during firing. Interface load descriptions based on the physical constraints and admissible relative motions at each interface "tie" the modules to each other and to ground; reconstructing the integrity of the system.

The physical structure within each module is simulated by a lumped parameter representation consisting of "n" elastically connected mass points. Allowing six degrees-of-freedom per mass point, each module is mathematically characterized by " $6n \times 6n$ " stiffness and inertia matrices, Ref. [2]. "n" of course varies from one module to the next depending on the nature of the structure modeled and the level of analysis capability desired. DYNACODE-G/P automatically computes the elements of these matrices for uniform "beam-type" structural segments (with correction for shear deformation) based on geometry and mass data. Pre-processing programs, Ref. [10], handle tapered and off-set beam sections, while local stiffness and inertia data are required input for non-beam structural elements.

For simplicity of presentation, DYNACODE-G/P will be considered here to be comprised of the two interactive programs "ASSEM" and "FORCE". The functions of each program are described in the discussion which follows.

For each "free-free" module of the system, program "ASSEM" computes and stores " $6n$ " frequencies and " $6n$ " associated mode shapes, as depicted in Figure 2. Six frequencies are identically zero, corresponding to six rigid-body modes. The remaining " $6(n-1)$ " frequencies and " $6(n-1)$ " mode shapes correspond to the (conventional) natural frequencies and normal mode shapes of the system. In addition, DYNACODE-G/P also computes and stores the " 6×6 " generalized mass matrix associated with the six rigid-body modes and the (conventional) " $6(n-1) \times 6(n-1)$ " (diagonal) generalized mass matrix associated with the " $6(n-1)$ " normal modes.

Application of conventional normal mode theory precludes admittance of relative rigid-body motions, requires that the system be "tied" to ground and is predicated on the orthogonality of the normal modes, Refs. [11] and [12]. Hence, in order to treat a "free-free" gun system module, the basic equations of modal analysis were reformulated to accommodate rigid-body modes which, although orthogonal to conventional normal modes, are not, in general, orthogonal to each other.

In accordance with conventional modal analysis, the time-dependent response of an elastic system to applied loads and moments is obtained by superposition of the normal mode solution with time-dependent "weighting" amplitudes. The time-dependent amplitude associated with each normal mode is obtained as the

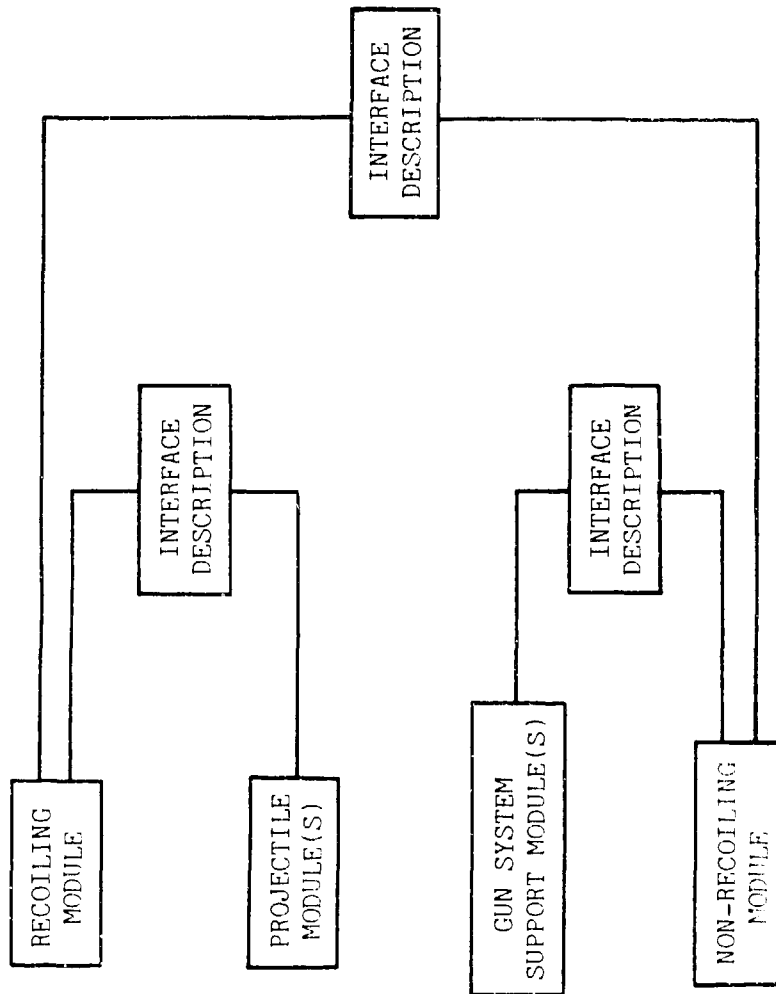


Fig. 1 - Schematic of DYNACODE-G/P Modular Approach to Gun System Dynamic Analysis

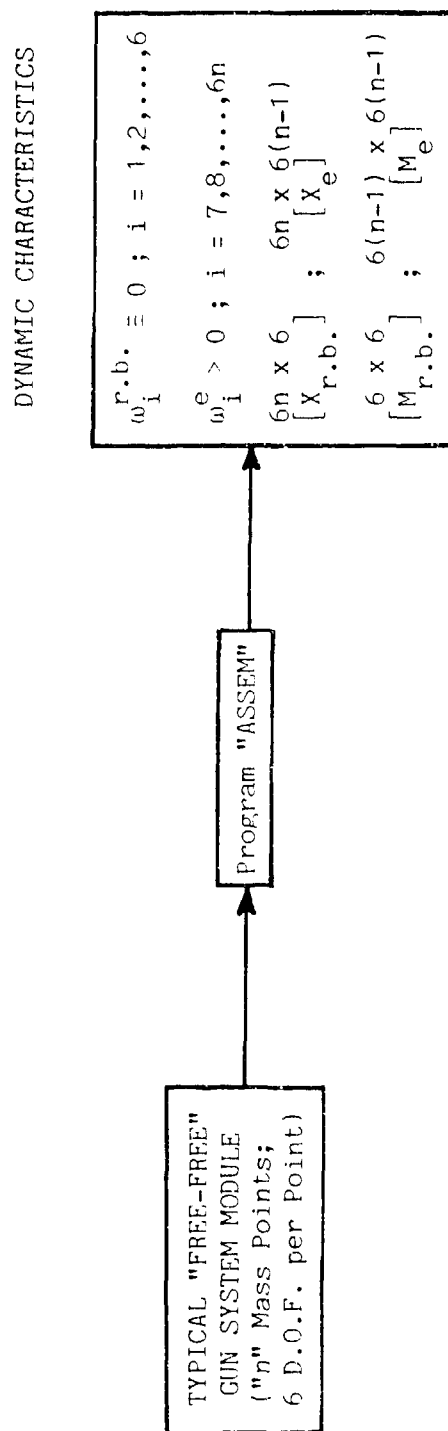


Fig. 2 - Application of Program "ASSEM" to Typical "Free-Free" Gun System Module

solution to the single equation of a simple harmonic oscillator with mass equal to the generalized mass for the mode under consideration and applied load equal to the corresponding generalized load, Refs. [11] and [12]. However, since the loads and moments acting on the mass points of each gun system module are motion as well as time-dependent, the single, simple, harmonic oscillator equation obtained in conventional modal analysis is replaced here by a simultaneous set of (coupled) oscillator equations.

The time and motion-dependent loads and moments acting on the mass points of the projectile module include projectile weight, interior ballistics and ram-air pressures, projectile/bore interface loads and moments transmitted through the bore-riding (rotating-band) surface, and intermittent (impact) loading transmitted through the bourrelet. The time and motion-dependent loads and moments acting on the mass points of the recoiling module include interior ballistics pressure, the so-called "Bourdon" load (arising as a consequence of pressurization of a curved gun tube), interface loads and moments between recoiling and non-recoiling modules, and the negative of the projectile/bore interface loads acting on the projectile module. Finally, the time and motion-dependent loads and moments acting on the mass points of the non-recoiling module include recoil pressure, the negative of the interface loads and moments applied to the recoiling module, and gun-mount support loads and moments. The reader is referred to Refs. [2] and [5] for detailed derivations of typical projectile/gun system loadings during firing.

Program "FORCE" assembles the simultaneous set of coupled oscillator equations, computes and stores the instantaneous loads and moments acting on each mass point of each module, and solves for the time-dependent amplitude (and velocity) associated with each mode shape, as depicted in Figure 3. DYNACODE-G/P then offers the user a variety of output options with regard to studying the response characteristics of the projectile/gun system. As depicted in Figure 4, the user may elect to output gun tube muzzle motion as a function of time, projectile and gun tube centerline motion as a function of time, projectile bending and balloting behavior, instantaneous loads and moments transmitted across an interface, etc.

APPLICATION TO 120MM TANK-GUN

DYNACODE-G/P has been applied to the firing of the 120mm M1A1 tank-gun with a variety of different M256 gun tubes of varying geometry and initial curvatures, and for a variety of ammunition types (e.g., DM13, M829, M865, etc.). For the purposes of this presentation, we shall consider application of DYNACODE-G/P to the firing of the standard M865 round in a typical, standard M256 gun tube (No. 84).

The recoiling module developed for this application is as depicted in Figure 5. The 12 mass-point simulation depicted offers 72 degrees-of-freedom for the description of the instantaneous motion of its components. The non-recoiling module developed is as depicted in Figure 6. The 2 mass-point simulation depicted offers 12 degrees-of-freedom for the description of its instantaneous motion. The projectile module developed is as depicted in Figure 7.

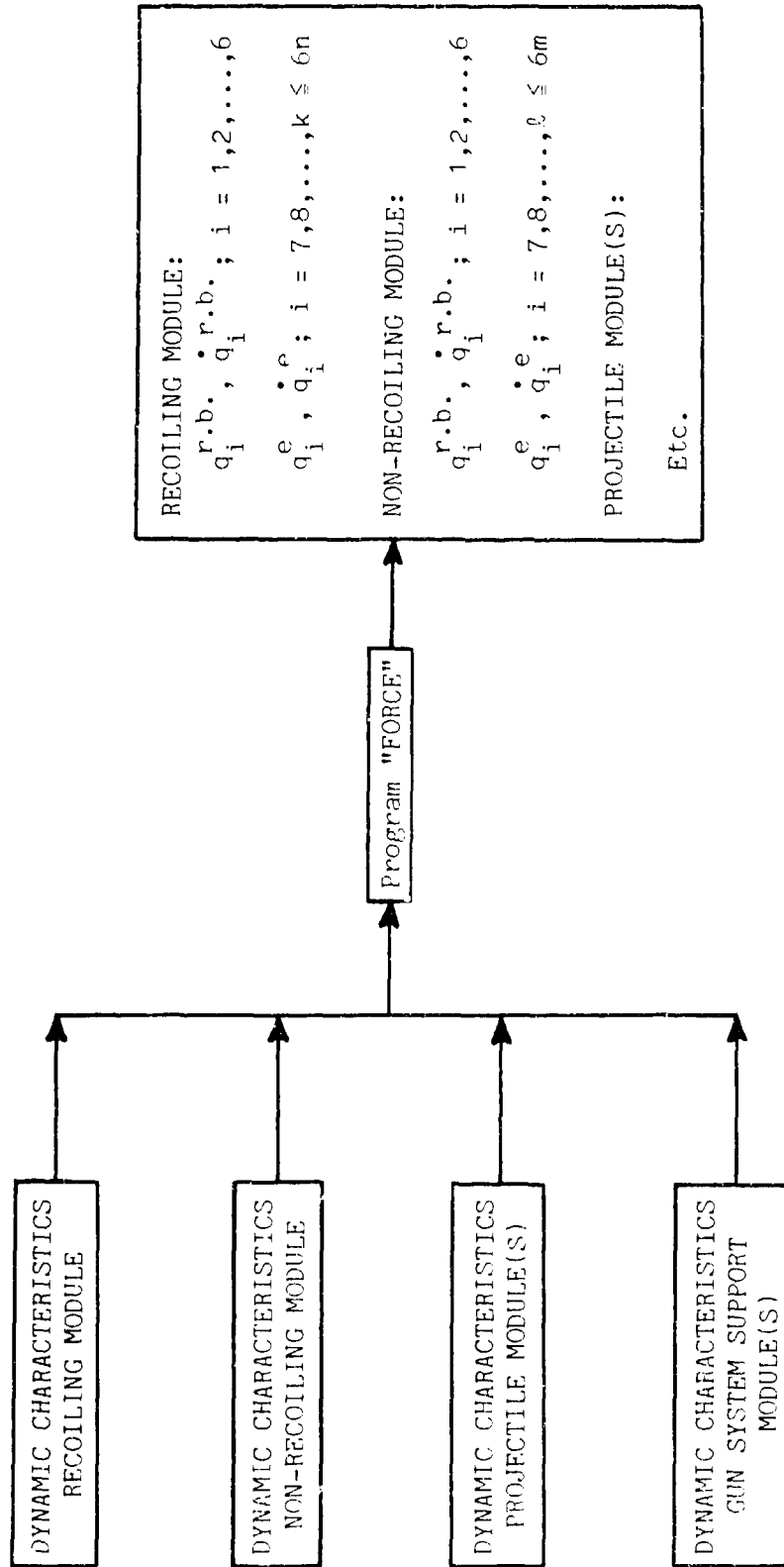


Fig. 3 - Application of Program "FORCE"

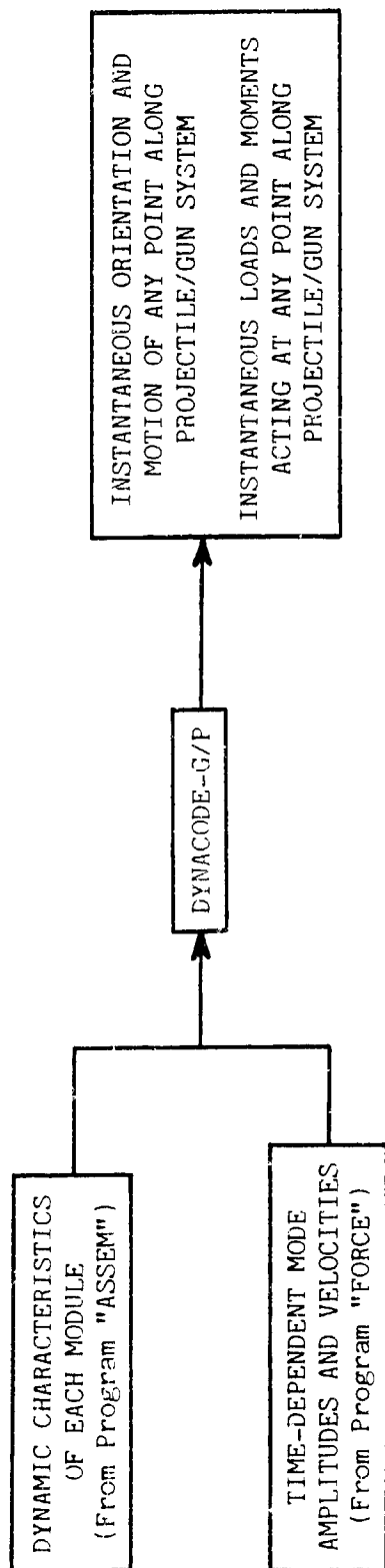


Fig. 4 - Typical User Output Options

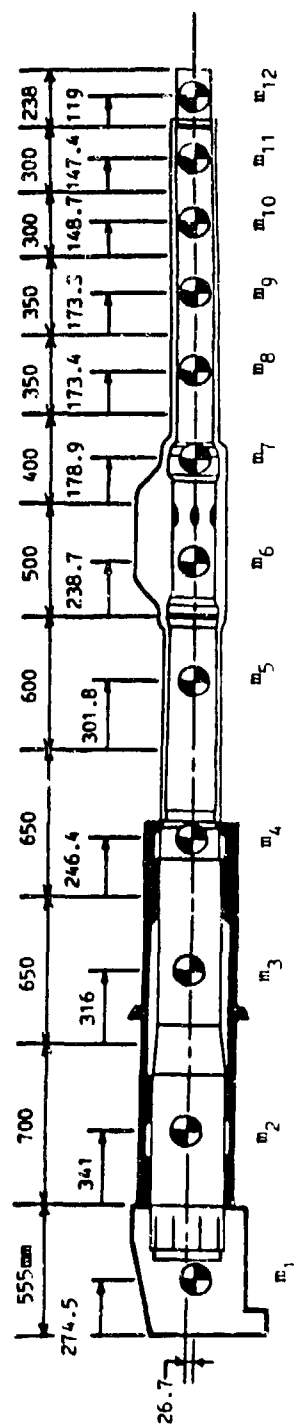


Fig. 5 - 120mm Recoiling Module with M256 Gun-Tube

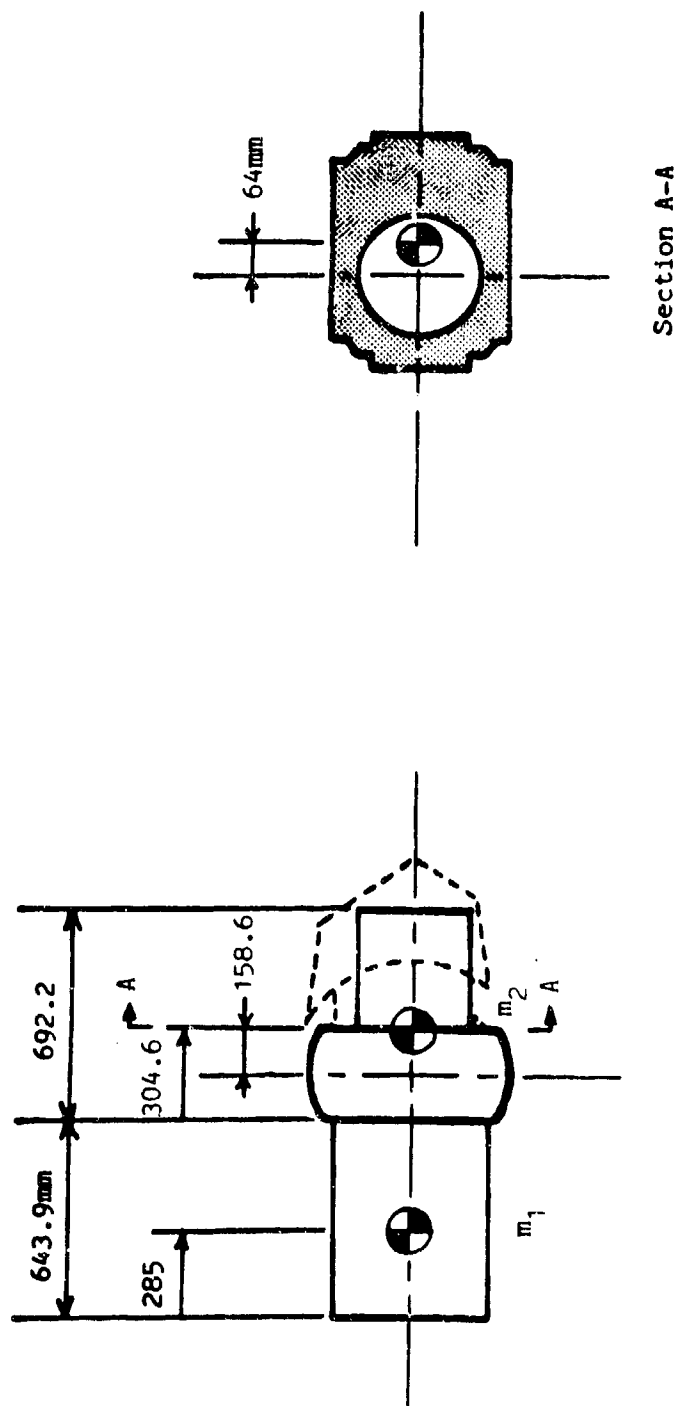


Fig. 6 - 120mm Non-Recoiling Module

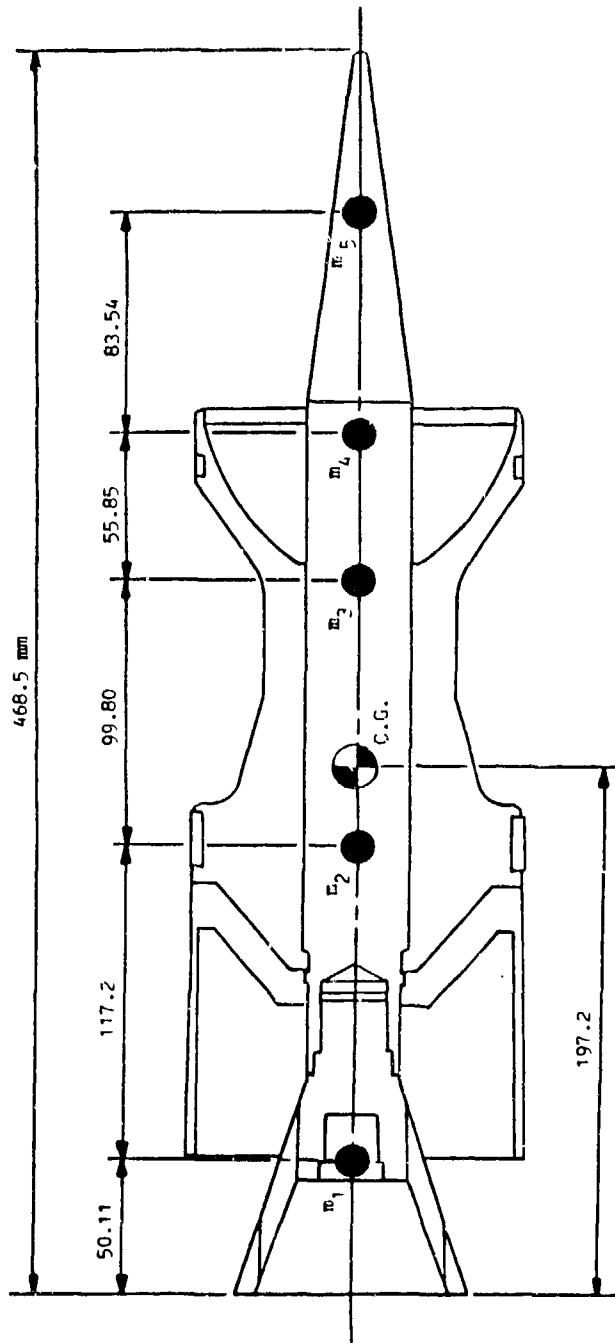


Fig. 7 - M865 Projectile Module

The 5 mass-point simulation depicted offers 60 degrees-of-freedom for the description of the instantaneous in-bore motion of the projectile during firing. Finally, and for the purposes of this presentation, the gun system support module has been replaced by a set of "ground" springs representative of the M1A1 tank suspension system.

Additional input required to exercise DYNACODE-G/P consists of interior ballistics chamber and projectile-base pressure-time data and initial gun tube curvature data. General Defense Corporation, Tactical Systems Division, provided the required interior ballistics data. Vertical and horizontal-plane projections of the initial (pre-firing) shape of M256 gun tube No. 84 are presented in Figure A-7 of Ref. [13].

As has been previously noted, DYNACODE-G/P offers the user a variety of output options (e.g., gun-tube muzzle motion, interface loads and moments, projectile c.g. motion, projectile bending and balloting motions, transverse projectile shear and bending moments, etc.). For illustrative purposes, and through the courtesy of General Defense Corporation, Tactical Systems Division, for whom this output was originally generated in support of ammunition design studies, we have elected to present, in Figs. 8 through 15, vertical and horizontal-plane projections of the instantaneous shape of the M865 projectile centerline superimposed on the instantaneous gun-tube centerline at selected time intervals during in-bore motion. Each of Figs. 8 through 15 present a "frozen" view of instantaneous projectile motion superimposed on gun-tube motion; a complete sequence of figures, which could not be presented here due to the page limitation constraint, presents a "motion" picture of projectile/gun-tube behavior during firing.

CONCLUSIONS

DYNACODE-G/P is a validated, user interactive, generic, gun dynamics computer simulation code for the firing of a flexible projectile in a flexible gun; offering a comprehensive and broad-based level of analysis capability in support of ammunition and gun system design.

DYNACODE-G/P has been successfully implemented in support of a number of 120mm programs for Honeywell, Inc., General Defense Corporation and Olin Corporation. DYNACODE-G/P is available for licensing.

REFERENCES

1. "Natural Frequencies and Normal Mode Shapes of the ADMAG Gun System Mounted on the M240 Artillery Mount", S&D Dynamics, Inc., Interim Report, November 1979.
2. "Dynamic Analysis of the 75mm ADMAG Gun System", S&D Dynamics, Inc., BRL Contract Report ARBEL-CR-00495, AD# ADA123867, December 1982.

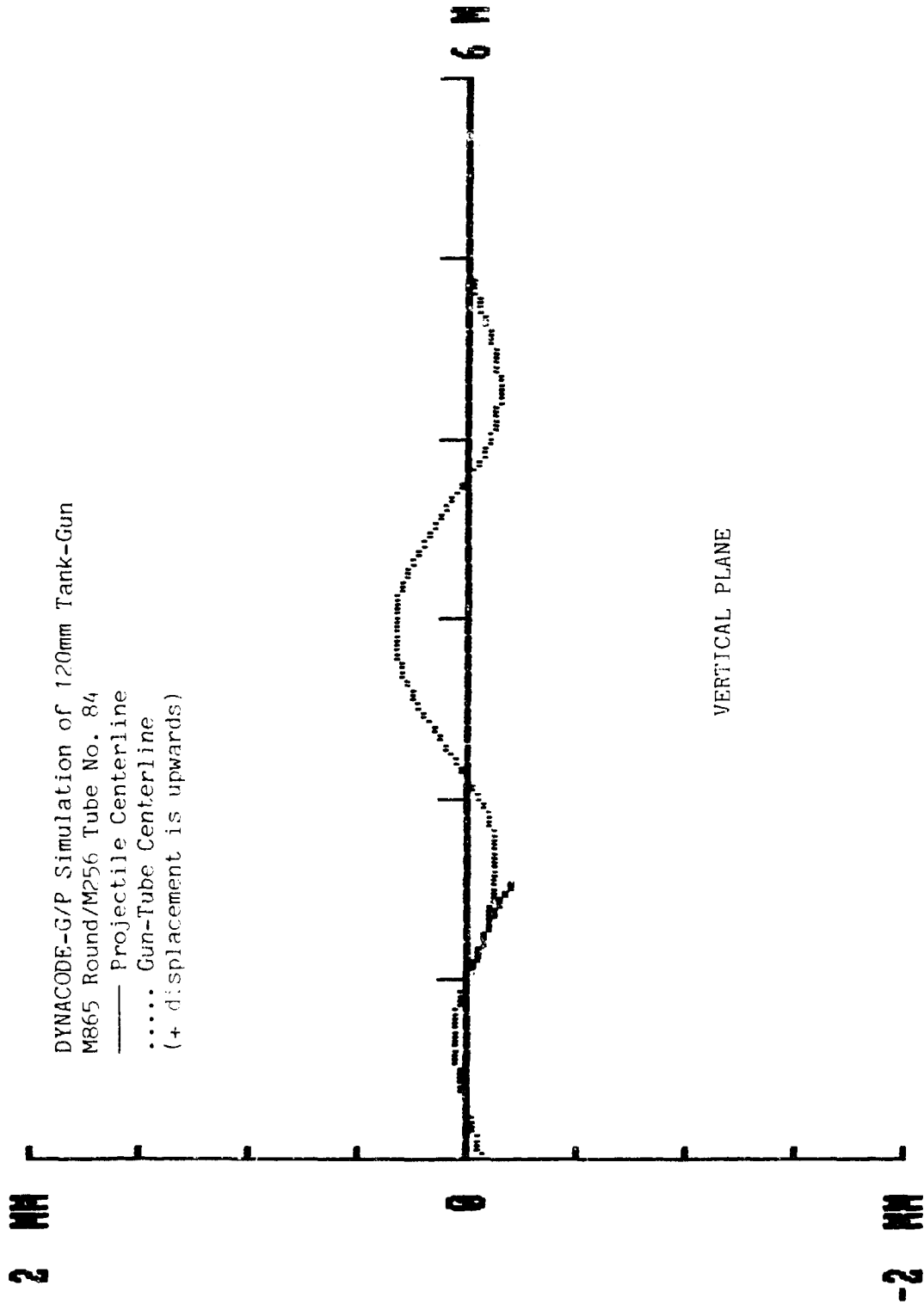


Fig. 8 - Projectile/Gun-Tube Centerline Overlay at 3ms

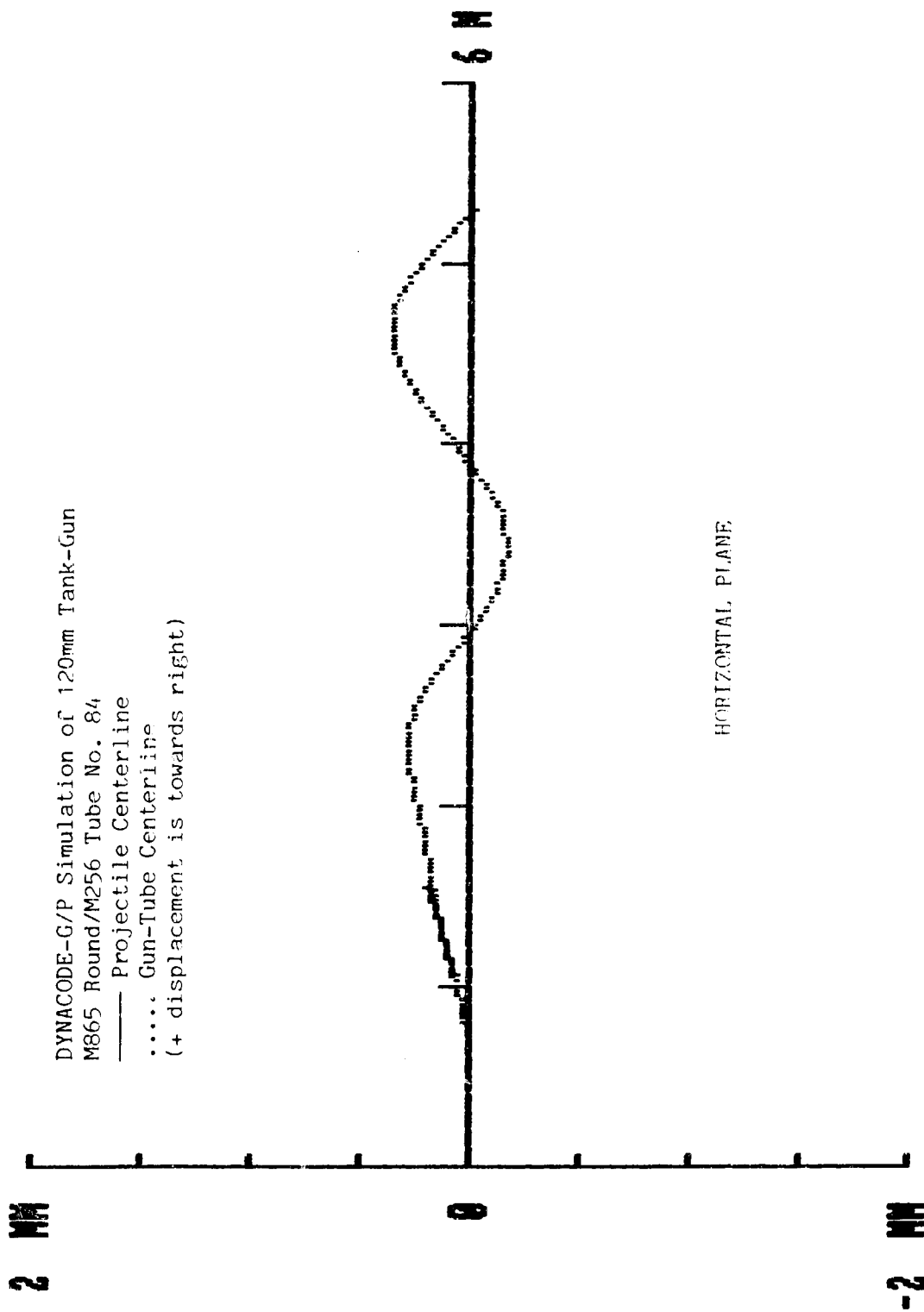


Fig. 9 - Projectile/Gun-Tube Centerline Overlay at 3ms

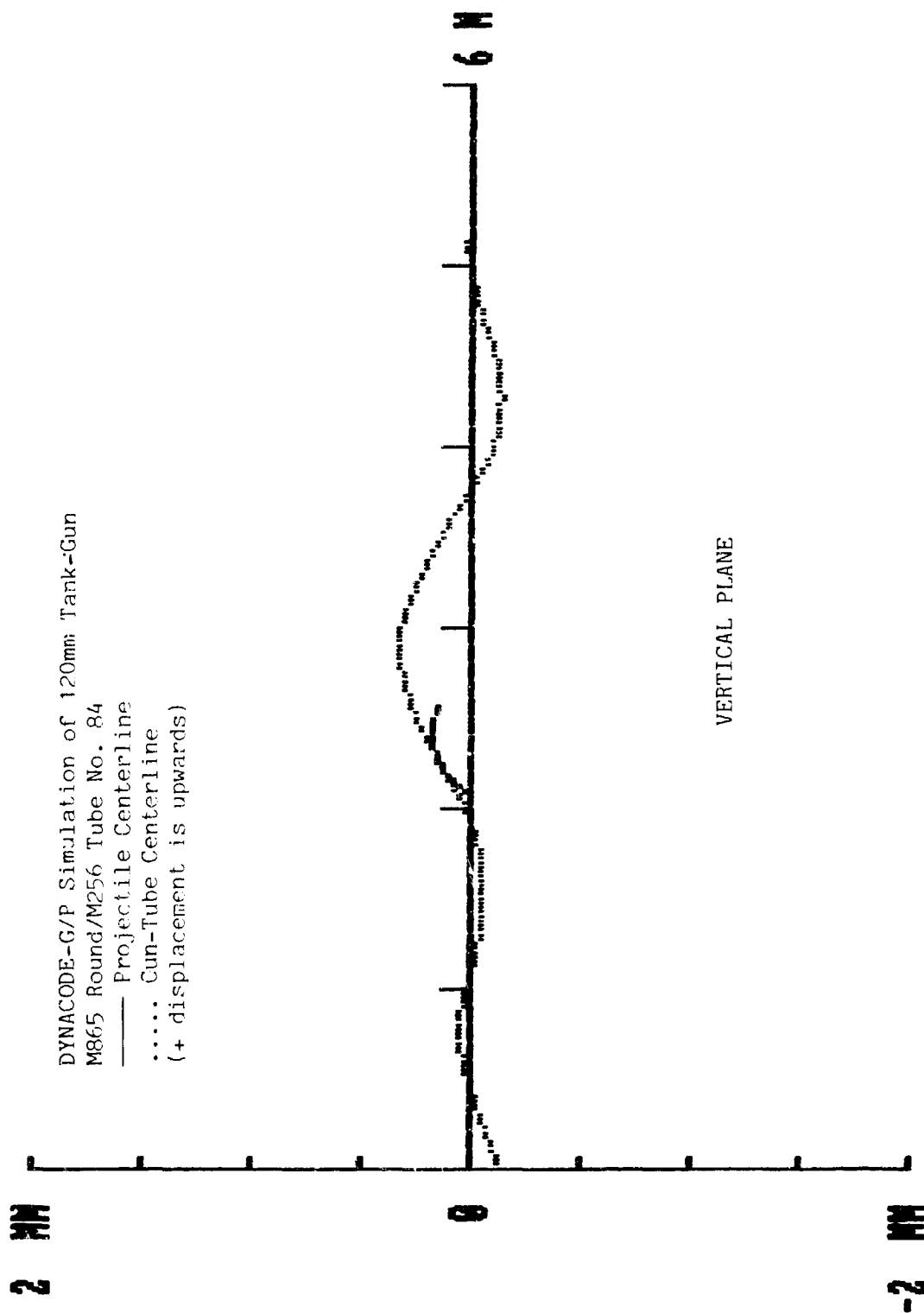


Fig. 10 - Projectile/Gun-Tube Centerline Overlay at 4ms

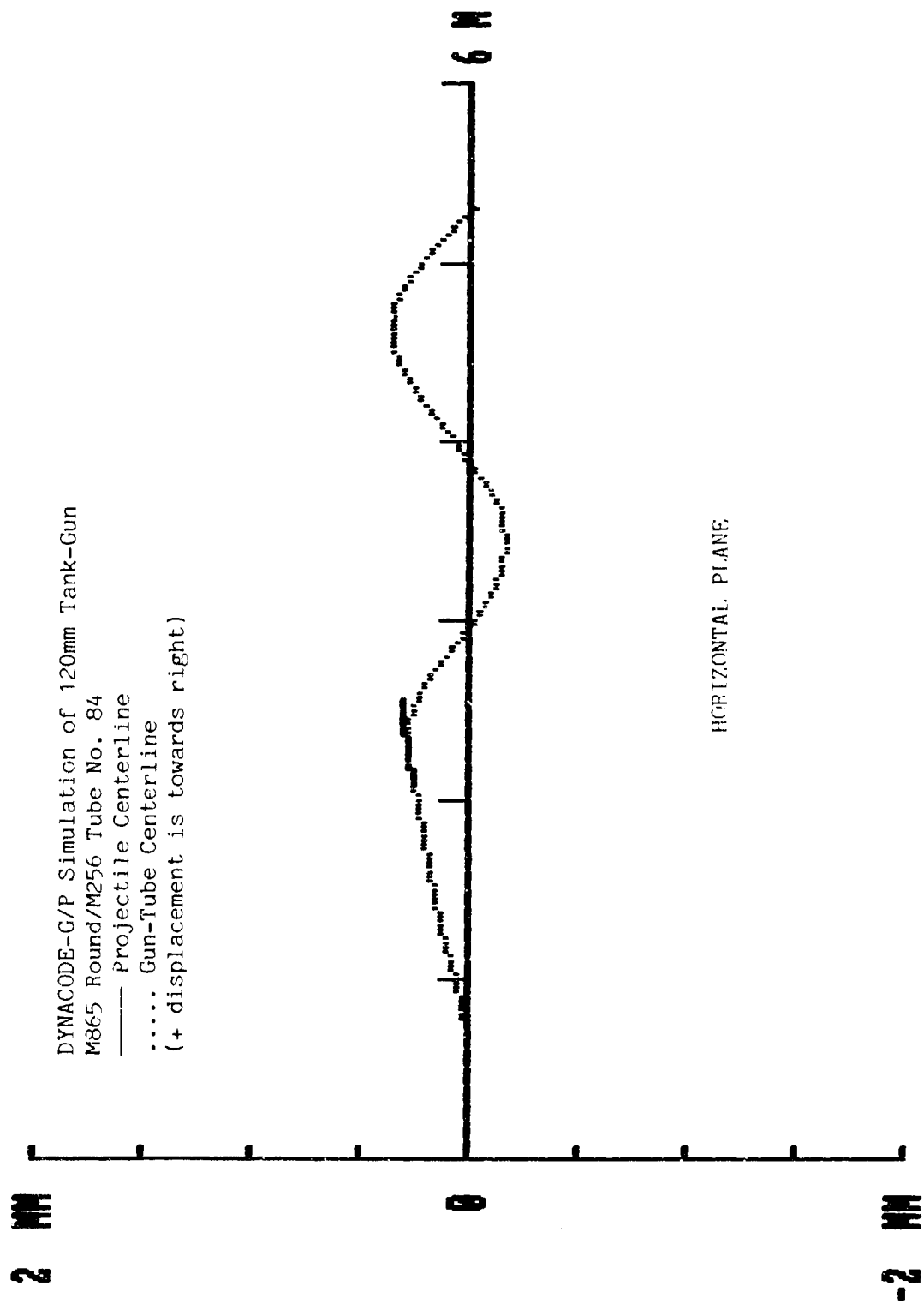


Fig. 11 - Projectile/Gun-Tube Centerline Overlay at 4ms

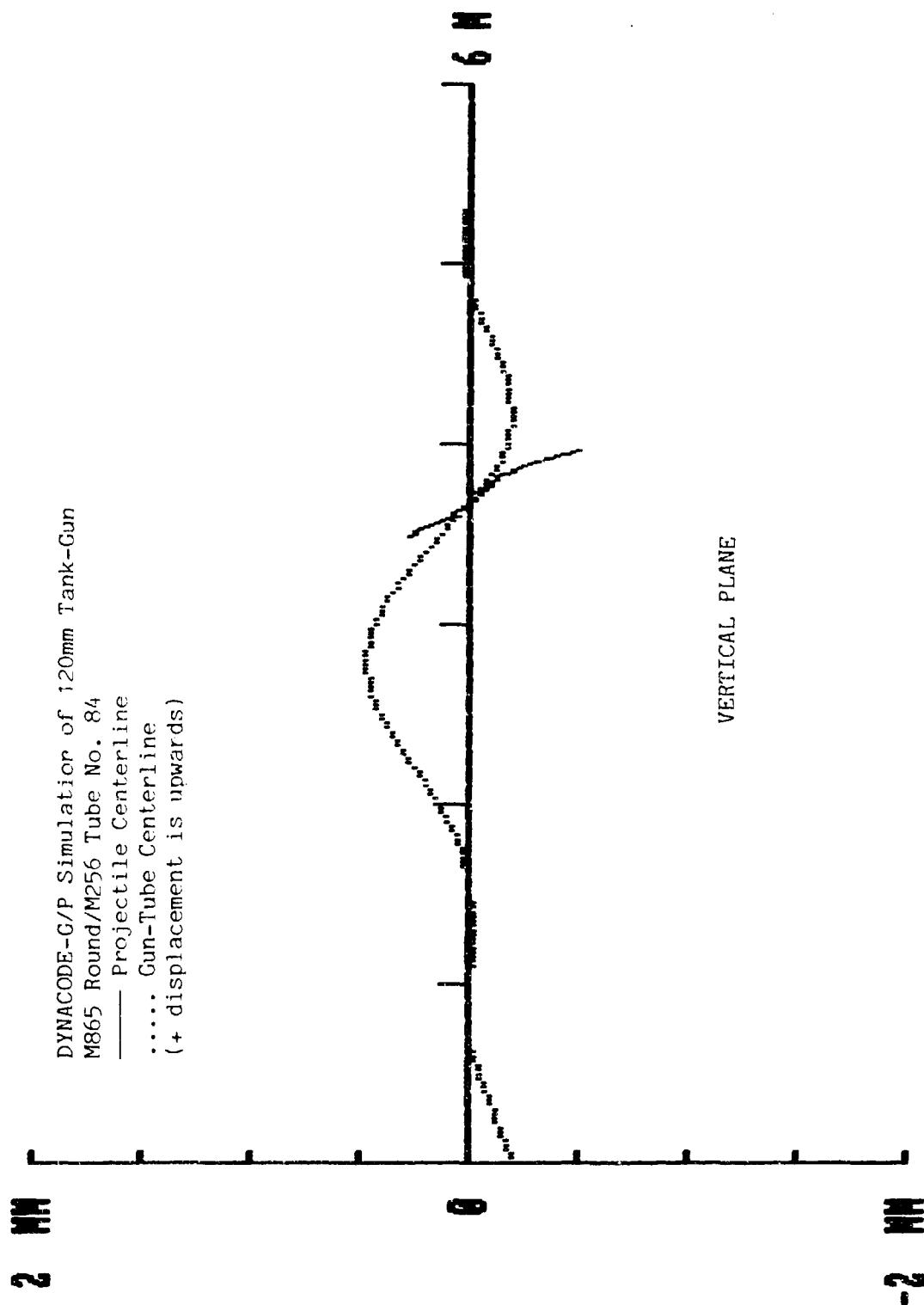


Fig. 12 - Projectile/Gun-Tube Centerline Overlay at 5ms

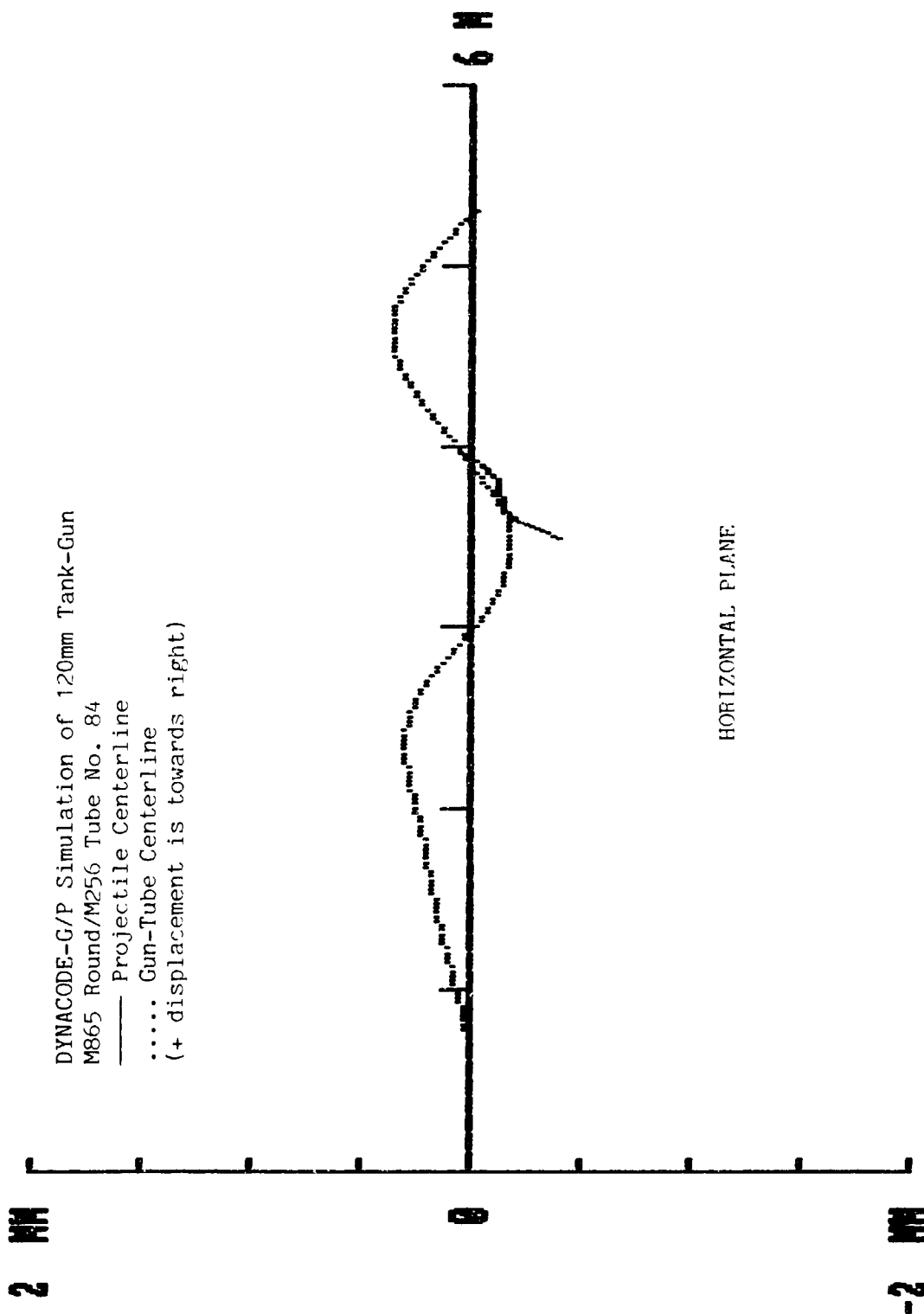


Fig. 13 - Projectile/Gun-Tube Centerline Overlay at 5ms

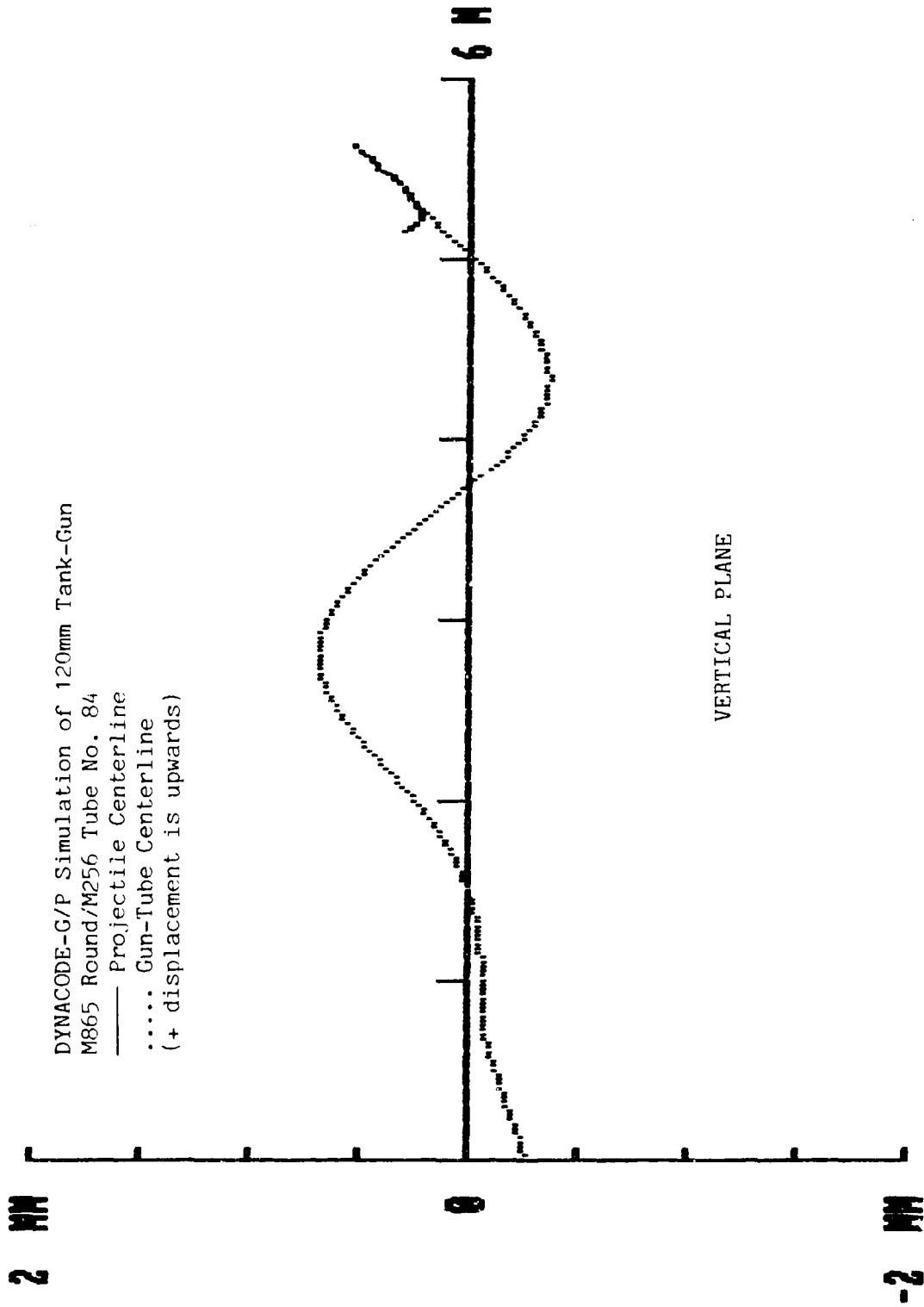


Fig. 14 - Projectile/Gun-Tube Centerline Overlay at Shot-Exit

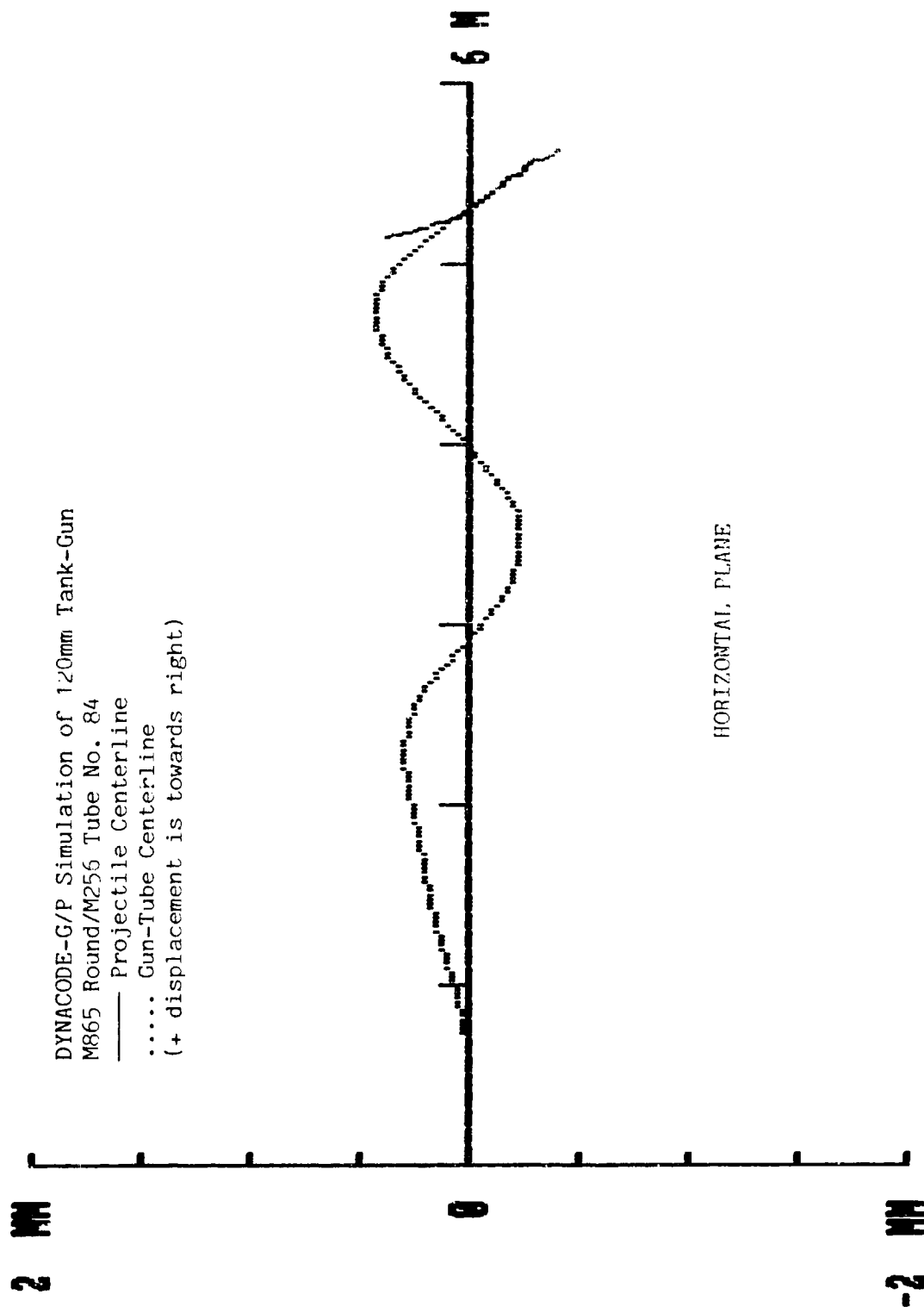


Fig. 15 - Projectile/Gun-Tube Centerline Overlay at Shot-Exit

SOIFER & BECKER

3. "Validation of the 75mm Gun Dynamics Simulation Model", S&D Dynamics, Inc., Final Report TR#81-04, Submitted to ARES, Inc. under Purchase Order No. 11100, September 1981.
4. Soifer, M.T. and Becker, R.S., "Gun Dynamics Simulation Model of the 75mm ADMAG Gun System", Proceedings of the Third U.S. Army Symposium on Gun Dynamics, Volume I, pp. I-48 through I-71, 11-14 May 1982.
5. "Projectile Motion in a Flexible Gun Tube", S&D Dynamics, Inc., BRL Contract Report BRL-CR-536, October 1984.
6. "Comparison of the In-Bore Motion and Launch Characteristics of the XM829 and DM13 Rounds at Ambient and Cold Temperatures", S&D Dynamics, Inc., Final Report submitted to Honeywell, Inc. under Purchase Order No. 934808-VJ, February 1985.
7. Soifer, M.T. and Becker, R.S., "In-Bore Projectile Motions", Proceedings of the Fourth U.S. Army Symposium on Gun Dynamics", Volume I, pp. II-70 through II-88, 7-9 May 1985.
8. "Dynamic Analysis of the 120mm Tank-Gun", S&D Dynamics, Inc., Interim Report TR#86-05, August 1986.
9. Disposition Form, DA Form 2496, from J.O. Pilcher, MSB, BRL, to DRDAR-LCS-D (Attn: Kenneth D. Rubin), dated 28 April 1982.
10. Program "AXISYM", ©Copyright 1986 S&D Dynamics, Inc.
11. O'Hara, G.J. and Cunniff, P.F., "Elements of Normal Mode Theory", U.S. Naval Research Laboratory, Washington, D.C., AD# 428774, 15 November 1963.
12. Hurty, W.C. and Rubinstein, M.F., Dynamics of Structures, Prentice-Hall, Inc., Englewoods Cliffs, New Jersey, 1964.
13. Schmidt, E.M., Plostins, P., et al., "Jump from M1A1 Tank (U), Interim Memorandum Report BRL-IMR-868, U.S. Army Ballistic Research Laboratory, Aberdeen Proving Ground, MD June 1986. (CONFIDENTIAL)

TITLE: Modeling Gun Dynamics with Dominant Loads
Thomas F. Erline and Mark D. Kregel, Ph.D.
US Army Ballistics Research Laboratory
Aberdeen Proving Grounds, Md. 21005-5066

ABSTRACT:

Insight on the dominant causes of gun barrel response due to firing the weapon can be obtained through "Rascal" a finite element program for analyzing dynamic events. This program implements a direct transient analysis approach, in contrast to doing a modal analysis then applying the loads. The program performs integration by a stiff differential equation solver method which provides gun dynamics response in two dimensions.

In one case a well documented small bore weapon experiment served as basis for a gun dynamics model. Rifled and smooth bore 7.62 mm rifle barrels were carefully set up in a laboratory environment and were mounted on a hard mount for no recoil. In this experiment the major cause of dynamic response is the barrel projectile interaction. This insight was obtained by closely duplicating the experimental results where the barrels were modeled by a cantilevered beam and where the barrel projectile interaction is the sole loading condition.

In another case, field tests involving a large bore weapon mounted on an M1 tank served as a more complex example for dynamic modeling. In this case the high energy in recoil coupled with imbalances in the recoil system turns out to be the most dominant cause of gun system motion. Major modeling changes and additional assumptions were required. The additional physical modeling was developed and included in the Rascal program. The results of the dynamic analysis were within a small neighborhood of the test results.

BIOGRAPHY:

PRESENT ASSIGNMENT: Mathematician, Mechanics and Structures Branch,
Interior Ballistics Division, Ballistics Research Laboratory.

PAST EXPERIENCE: Mathematician, Vulnerability Lethality Division,
Ballistics Research Laboratory, 1973-1982. Scientist, Physics Division
Chemical Research and Development Center - PAD, 1982-1985.

DEGREES HELD: Bachelor of Science, Towson State University, 1973.

This paper was classified Distribution Limited, therefore, only the abstract appears in the Proceedings. For further information, contact the authors.

TITLE: THE THEORETICAL MODELLING OF THE DYNAMICS OF INITIALLY NON-STRAIGHT BARRELS USING FINITE DIFFERENCE TECHNIQUES

S.E. POWELL

ROYAL MILITARY COLLEGE OF SCIENCE

SCHOOL OF MECHANICS, MATERIALS, AND CIVIL ENGINEERING

SHRIVENHAM

SWINDON WILTS SN6 8LA

ENGLAND

and

P.H.G. PENNY

ROYAL ARMAMENT RESEARCH AND DEVELOPMENT ESTABLISHMENT

CHOBHAM LANE

CHERTSEY

SURREY KT16 0EE

ENGLAND

ABSTRACT

Computer based mathematical models are playing an increasingly important role in the search for greater tank gun accuracy. One such model is the gun dynamics program suite RAMA which has been written at RMCS under contract to the Royal Armament Research and Development Establishment (Chertsey). The theoretical basis for the model has been described in a paper by King, Pagan and Thomas (Ref 1).

The simulation is based on equations derived from the Euler-Bernoulli beam theory, to describe the transverse vibrations in the vertical plane, and from the wave equation to describe the longitudinal vibrations caused by recoil. These equations are solved using an implicit finite difference method.

To begin the dynamic simulation with a non-straight barrel it is necessary that, when the barrel is in the required initial position, the shear and bending forces at each node sum to zero. To achieve this the initial values of displacement, slope, curvature and change in curvature have to be carefully calculated so that the stresses in the model are in equilibrium before the firing sequence begins. To this end the analysis is arranged so that the static configuration of the barrel is calculated separately from the dynamic simulation. In the computer model the information is stored in a 'Static Configuration File', which can be used by the dynamic model for any number of runs requiring that particular ordnance configuration.

Three methods are available when creating a 'Static Configuration File.' Firstly, to allow the calculation of the barrel profile from a given beam configuration as a beam supported at the cradle bearings under gravity. Secondly, to specify a deflection and slope of the barrel at the muzzle, and hence allow the program to calculate the barrel profile. Thirdly, to input the initial barrel profile as a series of ordered pairs; two further routines can then be used to calculate the profile.

In addition to a comparison between experimental results and theoretical predictions for a simple recoiling beam with an offset mass, selected gun barrels were measured and simulated by the computer program. Predicted changes to the transient response of the gun barrel are presented and discussed in this paper, whilst further trials results are presented in a companion paper by Penny and Perry entitled, "An Account of Some Experiments Undertaken to Correlate Gun Barrel Features With the Movement of Serial Mean Points of Impact."

REFERENCES

1. King, W.P.C., Pagan, G., and Thomas, M.D., "A Model for Tank Gun Movements During Firing Using an Implicit Difference Numerical Algorithm," Third US Army Symposium on Gun Dynamics, Rensselaerville, NY, May 1982.

This paper was not available for printing in this publication. Every effort will be made to include this paper in a supplement at a later date.

BULMAN

TITLE: A COMPARISON OF THEORETICAL JUMP FOR RIFLED AND NON-RIFLED BARRELS
DR D N BULMAN
LAND SYSTEMS
THE ROYAL MILITARY COLLEGE OF SCIENCE
SCHOOL OF MECHANICAL, MATERIALS AND CIVIL ENGINEERING
SHRIVENHAM
SWINDON WILTSHIRE SN6 8LA ENGLAND

For presentation at the Fifth United States Army Symposium on Gun Dynamics,
Institute of Man and Science, Rensselaerville, New York. September 23-25 1987

ABSTRACT:

New generation tank guns are generally smooth bore and rely for shot stabilization on finned projectiles. There are many reasons for this change from established rifled barrels, but some countries and manufacturers still contend that these advantages are not enough to warrant this change.

One overriding factor is accuracy of the weapon. As ranges increase the effect of rifling or otherwise on the hit probability will no doubt sway future decisions. This paper examines the shot to barrel dynamics of rifled and non-rifled barrels. It then attempts to predict the shot jump sensitivity to various parameters.

A description of the barrel and shot models is given. These models are totally interactive with each other, the solution being achieved by a direct integration technique. Each model has degrees of freedom in all directions about a fixed set of cartesian coordinates. The barrel sits in a cradle with elevation gear stiffness and backlash. The bearings are elastic, with or without clearance, and barrel expansion within the bearings is accounted for. The barrel recoils with buffer and recuperator forces included, and any non-straightness of the barrel is automatically accounted for.

The shot reacts with the barrel through elastic driving and centering bands in which damping can be included, and a shot rear band foundation moment is also present. The equations of motion of the shot are relative to a set of axes fixed to the shot. This allows for non-symmetrical shots and centre of gravity offsets. The final motion of the shot is referred back to the stationary axes for easy interpretation of the results.

D N Bulman BSc PhD (Eng MIMechE
Head of Land Systems
Royal Military College of Science

BULMAN

A COMPARISON OF THEORETICAL JUMP FOR RIFLED AND NON-RIFLED BARRELS

D N BULMAN

LAND SYSTEMS
THE ROYAL MILITARY COLLEGE OF SCIENCE
SCHOOL OF MECHANICAL, MATERIALS AND CIVIL ENGINEERING
SHRIVENHAM
SWINDON WILTSHIRE SN6 8LA
ENGLAND

Introduction

A lot of discussion has taken place concerning the various merits of using smooth bore or rifled barrels for tank weapons. Decisions have generally been made based on reasoned assessment rather than evidence from simulation of the two possible systems.

Basically, it is generally believed that the spin stabilization previously given to a round, can now be achieved aerodynamically by fin stabilization. The need for rifling is removed, but the shot may now be more susceptible to in flight disturbances. It is believed however that the in bore disturbances due to rifling, and hence the round to round variations, will be much greater than those in flight disturbances. The weight of opinion therefore tends to fall towards the non rifled barrel because of accuracy. A further point is that the requirement for long rod projectiles (with large length to diameter ratios) to assist in penetration, requires much higher rates of spin if spin stabilization were to be used. This is a physical fact, and therefore rifling rates would need to rise if these projectiles were fired from rifled barrels. This could pose even more problems.

It would, therefore, appear from the above brief discussion that the choice of smooth bore is inevitable. However the actual disturbance which rifling may produce on the shot and the barrel has generally not been analysed, or quantified. This paper therefore sets out to predict the differences in jump which may be found between rifled and non rifled barrels. The predictions are based purely on launch characteristics and take no account of aerodynamic disturbances following launch.

Theoretical Approach

The analysis is based on a fully interactive barrel and shot model. Each model has total freedom to move within fixed global coordinates. The shot then interfaces with the barrel through elastic driving bands, which may or may not have clearance.

The Barrel

The equations for the barrel are based on Euler Bernoulli beam theory together with a finite element approach. The barrel is divided up into elements joined at nodes which each have a full six degrees of freedom. This means that the stretching of the barrel during recoil, and the twisting of the barrel due to the shot reaction against the rifling, is accounted for. The first of these can produce a significant effect on the jump figure when an offset muzzle reference sight is used.

A stiffness matrix for each element is formed relative to the fixed global set of axes, and each matrix is combined to produce the overall barrel stiffness matrix, $[K]$. In this way barrel bend in either the vertical or horizontal direction is accounted for.

The equation

$$[F] = [K] [\delta] \quad (1)$$

now relates the forces at the nodes to the displacements $[\delta]$. In this case $[F]$ can be a function of time and the equation will then hold true at any instant in time provided that any inertia or damping terms are included.

We let

$$[F] = [F_t] - [M] [\ddot{\delta}] - [C] [\dot{\delta}] \quad (2)$$

where $[F_t]$ represents applied external forces which may be time dependent
 $[M]$ represents the equivalent masses and inertias of the barrel at the nodes
 and $[C]$ represents viscous damping coefficients at the nodes.

We can now write

$$[M][\ddot{\delta}] + [C][\dot{\delta}] + [K][\delta] = [F_t] \quad (3)$$

Equation (3) represents a set of simultaneous second order differential equations. The formation of the relevant matrixes $[M]$, $[C]$ and $[K]$ is already well documented, and it is now a relatively simple matter to solve the equations for any particular combination of applied forces $[F_t]$. In our case, the damping term $[C]$ is assumed to be zero, but it has been found to be important with repeat fire simulations.

The force vector $[F_t]$ consists of all external forces applied to the barrel. These include the main pressure forces, the reaction between the barrel and cradle bearings, and of particular interest, the reaction between the shot and the barrel.

The Shot

The solution of the barrel equations produces displacements, velocities and accelerations of the nodes in the global directions. It is therefore important that the shot model should relate to these same directions. Unfortunately, although the translation of the shot centre of gravity can be analysed directly in the global directions, the angular motion needs initially to be defined relative to axes attached to the shot. This then enables Eulers Dynamical equations to be applied directly. A transformation from the shot's own axes to the global axes will then need to be carried out.

We make the assumption that the shot band forces are a function of the relative displacements and velocities between the shot and the barrel. These forces can be reduced to the global directions and applied as necessary to the shot or the barrel. It is therefore necessary to carefully define what these relative displacements are.

The Shot Relative Displacements and Velocities

If we consider Diagram 1 which is a view of the OXY plane. The figure shows a representation of the shot with a pitch angle, Θ , which is defined more fully later. The front band sits between nodes $n+1$ and $n+2$ and the rear band between $n-1$ and n . This is a general case and allows interpretation for any point on the barrel, or any number of nodes.

The deflection of the shot at the rear band is a combination of the pitch angle, the distance from the shot centre of gravity to the rear band, and the displacement of the centre of gravity in the y direction. The displacement of the barrel at the rear band can also be found by linear interpolation between the deflections of nodes $n-1$ and n . For small angles the perpendicular deflection of the rear of the shot relative to the barrel tangent is now given by

$$\delta_{ry} = (Y_{rs} - Y_{rb})$$

Similarly for the relative velocity it can be shown that

$$\dot{\delta}_{ry} = \dot{Y}_{rs} - \dot{Y}_{rb} - \dot{X}_{rs} \alpha_r$$

The term $\dot{X}_{rs} \alpha_r$ is actually the vertical component of velocity required for the shot to follow the tangent to barrel at that point.

The relative deflection and velocity can now be used to give the rear band force in a direction perpendicular to the tangent to the barrel. This force need not necessarily be linearly dependant upon the displacement, but may be any function of the displacement or velocity. The resulting force can then easily be related to the global directions.

A similar force could also be found for the OXZ plane to give two perpendicular forces as required. However, if the force displacement

relationship of the band was non linear, the resultant reaction would not necessarily be correct. For instance, for a circular shot and barrel bore, with say 1 unit of clearance around the circumference, a movement of 1 unit in both the y and z directions would give a result (using the above method) of zero force. This is because the band would theoretically have just made contact with the bore. In reality the band would have moved 2 units at a direction 45° to the y and z axes, and a force would have been generated. The above theory therefore needs modification to deal with non linearities of this type.

The band force is therefore a function of

$$\sqrt{(Y_{rs} - Y_{rb})^2 + (Z_{rs} - Z_{rb})^2} \text{ for displacement}$$

$$\text{and } \sqrt{(\dot{Y}_{rs} - \dot{Y}_{rb} - \dot{X}_{rs}\alpha_r)^2 + (\dot{Z}_{rs} - \dot{Z}_{rb} - \dot{X}_{rs}\beta)^2} \text{ for velocity}$$

This gives a single force in each case along one single direction which needs to be resolved into the global OXYZ directions.

Basically if the band forces can be modelled in this way, they can be applied to the barrel and shot as required. In practice, three band forces should be considered. The first is the perpendicular rear band force. Second is a similar force for the front band. Third is the rear band foundation moment which is dependent upon the relative angular displacements. The longitudinal forces are assumed to be symmetrically disposed around the band, and to be accounted for in the internal ballistics model.

The Shot Motion

As stated earlier, the equations of motion for the translation of the shot can be carried out directly in the global directions. Hence

$$\ddot{M}_y = \text{Sum of all the forces the shot in the global Y direction}$$

$$\text{and } \ddot{M}_z = \text{Sum of all the forces the shot in the global Z direction}$$

In this case the forces not only include the band forces but also include any pressure forces acting on the base of the shot.

In the case of general shot rotation the forces (moments) must be in directions about axes Oxyz which are attached to the shot, and preferably aligned with the principal axes. We therefore need to set up a set of direction cosines relating the shot axes to the fixed axes.

$$\text{Let } [\delta] = [T][\delta_s]$$

where $[\delta_s]$ is a vector attached to the shot axes,
 $[\delta]$ is the resulting vector relative to the fixed axes

and $[T]$ is the transformation matrix containing the direction cosines

The transformation matrix $[T]$ in this case is a 3×3 square matrix and has to be updated at each time step during the integration of the dynamic equations. It can be shown that if $[T']$ represents the direction cosines for the change in angles over the small increment of the time step, the new value for the transformation matrix becomes

$$[T]_{\text{NEW}} = [T][T']$$

Hence we now have a method of relating forces (or any vector) between the global axes and the shot axes. Using these translated forces, the moments on the shot about its own axes can be applied to Eulers dynamical equations. The solution of these gives the increment in angles to produce $[T']$ and hence the new position of the shot.

The Rifling

The driving torque on the shot provided by the rifling is derived by assuming a torsional stiffness of the rear driving band, plus a viscous damping term. The stiffness need not necessarily be linear, as long as it is assumed that the torque is some function of the relative displacements between the shot and the barrel. In this case the torque will be a function of

$$R + \beta - \phi$$

where R is the angle through which the shot would have turned if it followed the rifling exactly and the barrel did not twist, eg the rifling rate multiplied by the distance travelled,

β is the angle of twist of the barrel at the shot driving band,

and ϕ is the actual spin angle of the shot.

A similar reasoning can be made for a damping term.

The derived torque, Q , is then assumed to act about an axis which is a tangent to the barrel at the point concerned. The direction cosines linking this axis with the global axes are given by 3×1 column matrix, $[L]$. The torque, $[Q_0]$ applied to the three axes of the shot is now given by

$$[Q_0] = Q[T]^T[L]$$

Shot C of G offset

If the shot centre of gravity is offset from its geometric centre, this will produce two main effects. First the gas pressure on the rear of the shot will produce a moment about the centre of gravity. Second, as the shot is spun by the rifling it will exert a centrifugal force on the side of the barrel.

In the first case the solution is simple in that an extra moment can be added directly to Eulers equations.

In the second case, it can be dealt with by the correct definition of the shot band forces. With all the dynamic equations, the forces are applied through or about the centre of gravity. Hence in reality the shot tries to spin about its centre of gravity and is actually restrained from doing so by the band forces. In the calculation of the band displacements we should therefore consider the movement of the geometric centre of the shot and calculate Y_{rs} , Z_{rs} etc using this. If e is the centre of gravity offset which is aligned along the shot Oy axis, the position of the geometric centre is given by

$$Y_s = e \cos \phi \text{ in the global OY direction}$$

$$\text{and } Z_s = e \sin \phi \text{ in the global OZ direction}$$

The values of the band displacements ie Y_{rs} , Z_{rs} etc, can now be modified accordingly.

Definition of Shot Pitch and Yaw

In a two dimensional simulation, purely in the OXY plane, the definition of shot pitch is fairly obvious and is shown in Diagram 1. In a three dimensional analysis the definition needs to be more explicit. This is because the shot Oy and Oz axes no longer remain aligned in the global directions. A definition of angular displacement about axes attached to the shot would therefore be difficult to understand. However it is necessary to define some angular displacements which can be used to define the displacements of the shot relative to the barrel as discussed earlier.

If small angles are considered, it is possible to define pitch as the angle between the shot Ox (longitudinal) axis and the global OX axis when projected on to the global OXY plane. Similarly shot yaw is defined in the same way, but for the global OXZ plane. Therefore using the transformation matrix and assuming small angles:

$$\text{pitch} = T_{21}$$

$$\text{yaw} = -T_{31}$$

In a similar way it can also be shown that the pitch and yaw velocities are given by

$$\text{pitch velocity} = T_{22}\omega_2 + T_{23}\omega_3$$

$$\text{and yaw velocity} = T_{32}\omega_2 + T_{33}\omega_3$$

respectively, where ω_2 and ω_3 are the angular velocities of the shot about its own Oy and Oz axes.

Method of Solution

The equations which can be produced by using the definitions already given can be solved in a number of ways. In the case of this particular study, a modified second order Runge Kutta method was used. At each time step, the displacements and velocities of the barrel and shot were used to find the related forces as described earlier. These forces were then applied and the equations solved for the next time step. In the case of the barrel, the solution was done on a single block matrix. For the shot, the three translation equations, and three rotation (Euler) equations were solved individually.

Simulation

In order to investigate the difference in jump and dispersion between smooth bore and rifled barrels, simulations were made on a representative 120 mm tank weapon.

The simulations included the following parameters:

1. Straight and non straight barrels
2. Offset breech in y and z directions
3. A cradle with elevation gear stiffness and backlash
4. Cradle bearings with clearance and non linear stiffnesses
5. Barrel expansion on the cradle bearings
6. A balanced and non balanced shot
7. A non linearly elastic shot rear band with foundation moment
8. A non linearly elastic shot centering band with clearance

Although many simulations were made, resulting in over 1000 results, only a few will be presented here for clarity.

Basically a study was made of those parameters which might obviously vary from round to round, and which would be different between the rifled and non rifled cases. In this study the main parameter concerned was the shot centre of gravity offset and its orientation when loaded prior to firing. Further work involved the effect of barrel bend and a study to optimise certain parameters in order to reduce dispersion. These particular results are not presented here, but the basic conclusions are mentioned in the discussion.

BULMAN

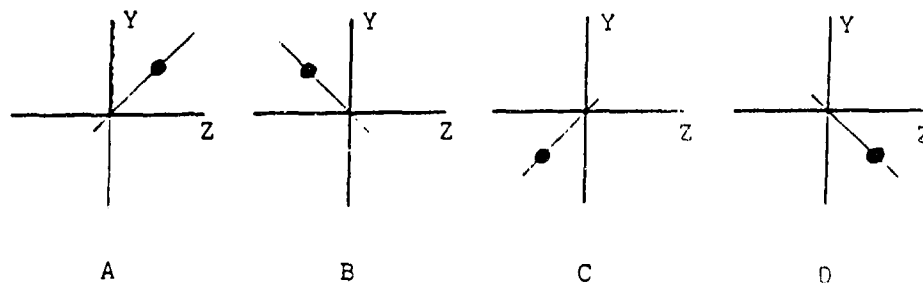
The results shown in table 1 are from simulations with the shot configured as shown below.

Barrel	Shot number	C of G offset (mm)	C of G position	Centering Band Clearance (mm)
S T A N D A R D	1	0.1	A	0
	2	0.1	B	0
	3	0.1	C	0
	4	0.1	D	0
	5	0.25	A	0
	6	0.25	B	0
	7	0.25	C	0
	8	0.25	D	0
	9	0.1	A	.1
	10	0.1	B	.1
	11	0.1	C	.1
	12	0.1	D	.1
	13	0.25	A	.1
	14	0.25	B	.1
	15	0.25	C	.1
	16	0.25	D	.1
B A L A N C E D	17	0.1	A	0
	18	0.1	B	0
	19	0.1	C	0
	20	0.1	D	0
	21	0.25	A	0
	22	0.25	B	0
	23	0.25	C	0
	24	0.25	D	0

An initial run was made with a balanced shot, and all the simulations were made with a rifled and a smooth bore barrel.

BULMAN

The shot centre of gravity positions are shown in the figure below, and are as viewed from the breach.



The standard barrel included all the normal offsets and also bearing clearances. The balanced barrel had zero bearing clearance, and no input from the expansion of the barrel.

The results shown in Table 1 give the calculated shot jump in the vertical Y and horizontal Z directions. The jump is considered to be the difference between the final trajectory of the shot and the initial direction in which the muzzle was pointing. The dispersion is found by calculating the greatest difference in both the vertical and horizontal jump figures for each set of four centre of gravity positions, and then finding the resultant. This is simply a convenient way for quickly assessing the difference between the rifled and smooth bore cases.

Shot Number or Type	Barrel Type				Dispersion		
	Rifled		Smooth				
	Jump Y	Jump Z	Jump Y	Jump Z	Rifled	Smooth	
Balanced	.838	.359	.837	.36	-	-	
STANDARD BARRELS	1	1.106	.397	.84	.362	.757	.007
	2	.875	.092	.84	.357		
	3	.571	.322	.835	.357		
	4	.802	.627	.835	.357		
	5	1.508	.453	.843	.366	1.893	.017
	6	.929	-.31	.843	.353		
	7	.169	.266	.831	.353		
	8	.748	1.028	.831	.366		
	9	.931	.349	.913	.489	.264	.073
	10	.813	.379	.934	.448		
	11	.725	.48	.91	.42		
	12	.904	.415	.913	.482		
	13	1.296	.241	.904	.417	.314	.1
	14	.693	-.093	.922	.477		
	15	.359	.524	.836	.383		
	16	.979	.828	.909	.443		
BALANCED	17	.269	.035	.002	.002	76	.006
	18	.035	-.269	.002	-.022		
	19	-.269	.035	-.002	-.002		
	20	-.035	.269	-.002	.002		
	21	.672	.089	.006	.006	1.901	.016
	22	.089	-.672	.006	-.006		
	23	-.672	-.089	-.006	-.006		
	24	-.089	.672	-.006	.006		

Table 1 Jump figures for the various shots and barrels

Discussion of Results

The results shown in Table 1 give a clear indication that in general the accuracy and dispersion of the rifled barrel is much worse than the smooth bore. This assumes that the shot will have some imbalance, and it is clear from the results that even a small imbalance does effect the jump figures considerably with the rifled barrel.

In the case of the standard barrel which had an offset breech, in Y and Z, the jump caused by the barrel motion was a significant part of the result. This is shown in the balanced shot case and also by the fact that with the balanced barrel the overall level of shot jump was much smaller. However, the balanced barrel does not improve dispersion for either the rifled or smooth bore cases.

A simple calculation shows why the rifled case is so poor. If a shot velocity of 1000 m/s is assumed with a rifling rate of 180 degrees per metre, the centrifugal force generated by a centre of gravity offset of 0.1 mm would be 9.8 KN for a 10kg shot. This force either has to be absorbed by a deflection of the driving bands and the barrel, or else results in a transverse velocity component of the shot of approximately 0.31 m/s. Obviously the final result is somewhat more complex, but the overall trend must be the same. We can demonstrate this by examining figures 1 to 24.

Figures 1 to 4 show muzzle motion in Y and Z directions for a number of cases. Figures 1 and 2 show how a balanced shot produces the same effect on the barrel for either the rifled or smooth bore cases (note that the dashed line is directly over the solid line). However, the unbalanced shot in the rifled barrel obviously affects the muzzle motion considerably. Figures 3 and 4 show the same shot configuration for the standard rifled barrel, the balanced rifled barrel, and the balanced smooth barrel. When the shot is not spinning the effect on the barrel is small (dotted line), but for the rifled case (dashed line) the shot obviously affects the barrel near shot exit. The difference between the dashed and solid lines is the effect of the out of balance breech and barrel expansion on the bearings.

It is now interesting to examine the actual motion of the shot. These are shown in groups of four graphs, displaying shot bounce or shot pitch and yaw when viewed from the muzzle for the rifled and smooth bore cases.

Figures 5 to 8 are the baseline of a balanced shot in the standard barrel. The small arrows on the drawings for the rifled cases show the direction of the shot OY axis, and hence indicate the rotation of the shot. It will be noted that there is little difference between the two cases, demonstrating the fact that when the shot is balanced there is little difference between the rifled and smooth bore barrels.

The small deviation in the pitch/yaw trace near shot exit is due to the tip off as the front band leaves the barrel, and the rear band is still in contact. This is shown more clearly in figures 9 and 10 which show the pure pitch and pure yaw as the shot travels along the barrel. It further demonstrates that although the traces in figures 5 to 8 may appear to show abrupt changes, the real motion is quite smooth. The traces do give a good appreciation as to what the overall motion of the shot is.

Figures 11 to 14 show the unbalanced shot motion in the standard rifled and smooth bore barrels. It will be noted that for the bounce motion, the shot starts in the top left quadrant. This is the location of the shot centre of gravity at shot start. It should be noted that the bounce motion is the absolute motion and not the motion relative to the barrel. Apart from being displaced, the bounce motion for the smooth bore barrel is similar to that for the balanced shot case (figure 7). In the case of pitch, the shot is initially pitched towards the top left quadrant at shot start. This is caused by the unbalance tending to pitch the shot during its initial acceleration. After this point the motion in the smooth bore barrel is similar to that for the balanced shot (figure 8). Both the bounce motion and pitch motion for the rifled barrels is much more complex and it can now be appreciated why the initial location of the shot centre of gravity can have such a large effect on the final jump figure.

Figures 15 to 18 show similar results to those of figures 11 to 14, but in this case the shot has clearance around its centering band. It is obvious in all the traces how the shot front band must initially move until the clearance is taken up and impacts with the side of the barrel. This subsequently modifies the overall motion considerably.

Figures 19 to 23 show the unbalanced shot in the smooth bore barrel. As might be anticipated the overall motion is generally smoother. In the case of the smooth bore barrel, figures 21 and 22, because there is no coupling of the vertical and transverse motions, there is simply a displayed motion along the direction of the centre of gravity offset. This may result in a large pitch or yaw angle at shot exit, but the bounce velocity is liable to be small and hence the jump as defined for this paper is also small.

Figures 23 and 24 are two additional cases which have been included to demonstrate more clearly the effect of centering band clearances. They should be compared with figures 19 and 20. From the pitch trace it is obvious how the shot is pitched until the front band impacts with the barrel when the band clearance is taken up.

Conclusions

It would appear from all the results that, based on the assumption that it is not possible to produce a perfectly balance shot, a rifled barrel will generally produce jump figures which will give much larger dispersion than a smooth bore barrel. This is based purely on the trajectory at launch and does not take into account disturbances which occur after launch.

The results shown were based on a representative shot, but it must be emphasized that the actual figures produced are highly dependent upon such parameters as the shot band stiffnesses, the mass and inertia of the shot, and also the position of the shot centre of gravity between the two bands.

As briefly mentioned earlier, this particular investigation did include different barrels with varying degrees of straightness, plus different bearing clearances. Results have shown that although certain barrels did produce particularly high jump figures, there is no clear trend. The results were also dependent upon shot characteristics, showing that barrel/shot combinations are important. However, because of the volume of data, the results were not presented at this time.

REFERENCES

1. King, W.P., Pegan, G., Thomas, M.D. 'A model for tank gun movements during firing using an implicit difference numerical algorithm'. 3rd US Army Symposium of Gun Dynamics, Rensselaerville, N.Y., May 1982.
2. Soifer, M.T. and Becker, R.S. 'Development, validation and implementation of a finite element (lumped parameter) model of the 75 mm ADMAG gun system'. TTCP WTP-2 (KTA6), BRL Aberdeen, Maryland, October 1983.
3. Taylor, B.A. and Thomasson, P.G. 'A consistent R&D technique for the modelling of gun system dynamics'. 3rd US Army Symposium on Gun Dynamics, 1982.
4. Soifer, M.T. and Becker, R.S. 'In bore projectile motion'. 4th US Army Symposium on Gun Dynamics 1985.
5. Chu, S.H. 'New approach for analysis of transverse projectile-tube interactions'. 3rd US Army Symposium on Gun Dynamics 1982.
6. Bulman, D.N. 'The effects of barrel droop on gun barrel response'. 9th International Symposium on Ballistics, RMCS Shrivenham, UK. Aug 1986.
7. Bulman, D.N. 'Theoretical and experimental observations on the effect of bearing spacing, pressure time curve, bearing and barrel damping on barrel motion'. TTCP-WPT-2 (KTA-6) RARDE Fort Halstead, UK, Sept 1984.
8. Megson, T.H.G. 'Aircraft Structures for Engineering Students', Pub. Edward Arnold, Chapter 11.
9. Patton, M.E. 'Projectile Foundation Moment Generation', 4th US Army Symposium on Gun Dynamics, 1985.
10. Powell, S.E. 'A simple theoretical model of shot/barrel interaction within a smooth bore gun', 4th US Army Symposium on Gun Dynamics 1985.
11. Bulman, D.N. 'The Effect of Bearing Clearance and Barrel Expansion on Barrel Response', 4th US Army Symposium on Gun Dynamics, 1985.

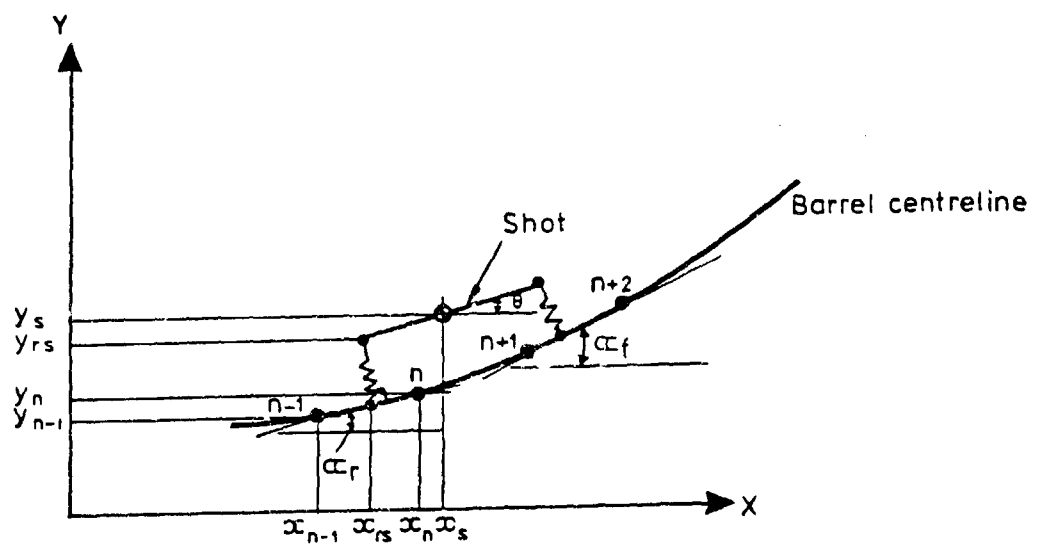
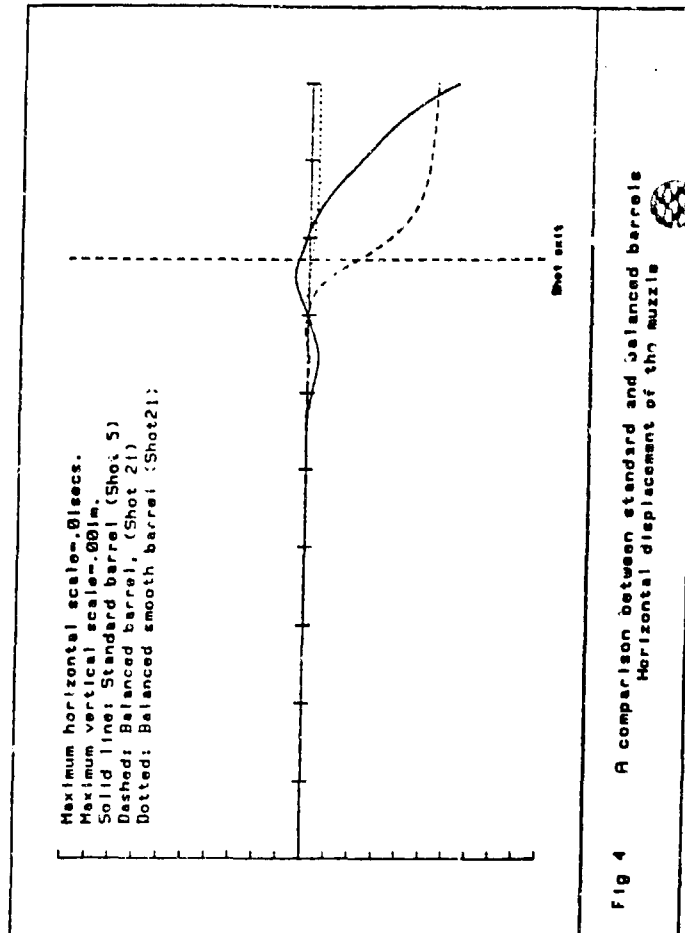
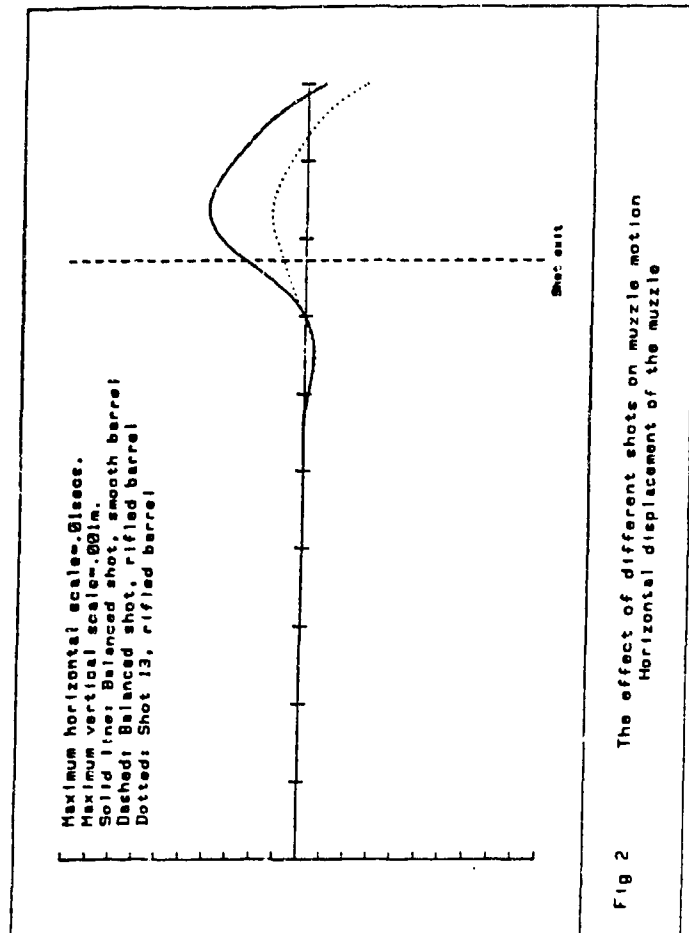
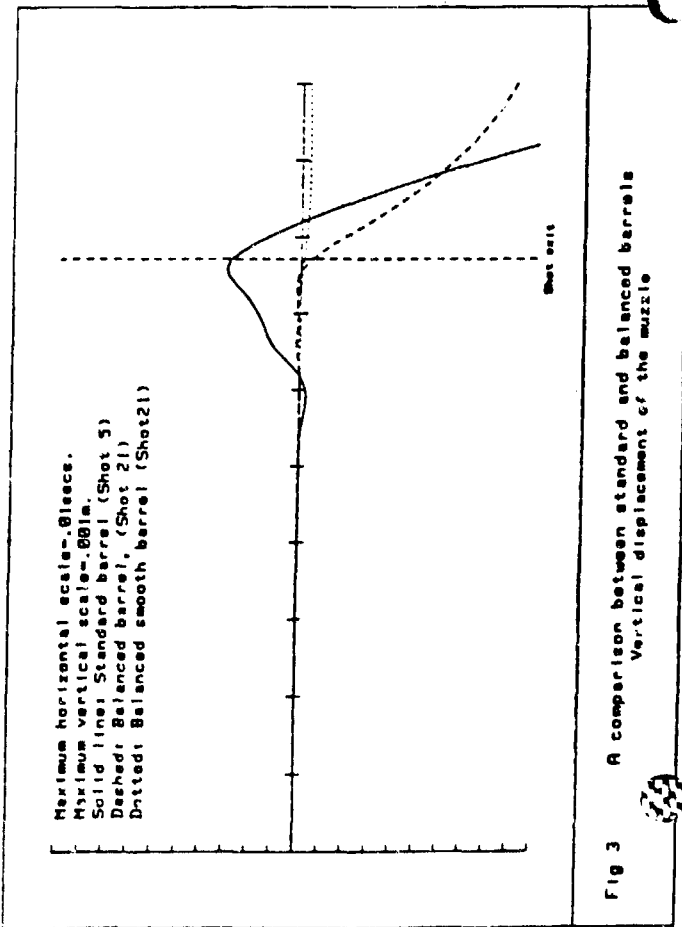
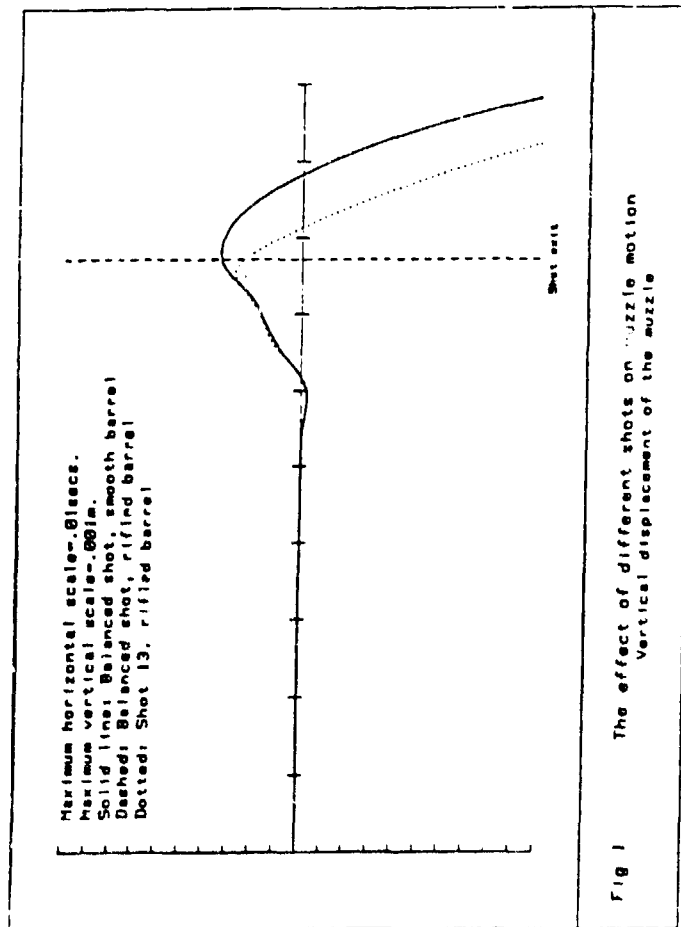


Diagram 1



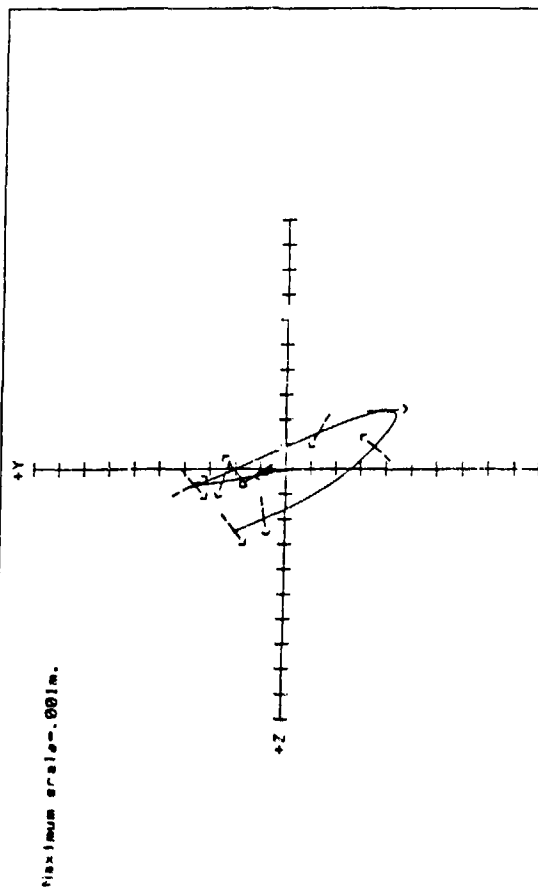


Fig 5
Balanced shot with standard rifled barrel
Shot bounce motion viewed from the muzzle

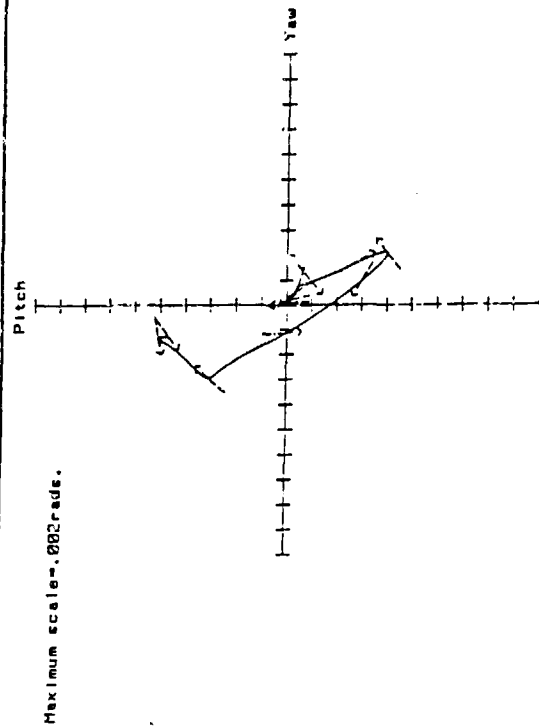


Fig 6
Balanced shot with standard rifled barrel
Shot pitch and yaw viewed from the muzzle

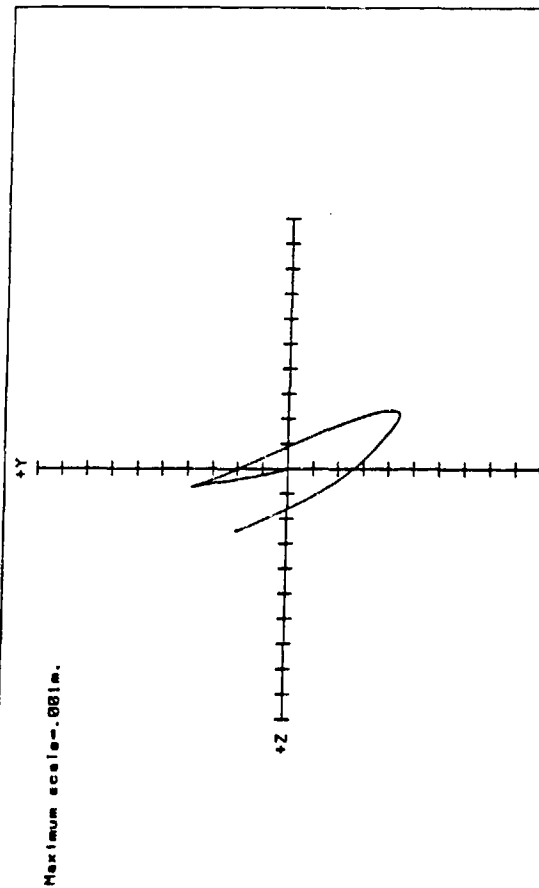


Fig 7
Balanced shot with standard smooth barrel
Shot bounce motion viewed from the muzzle

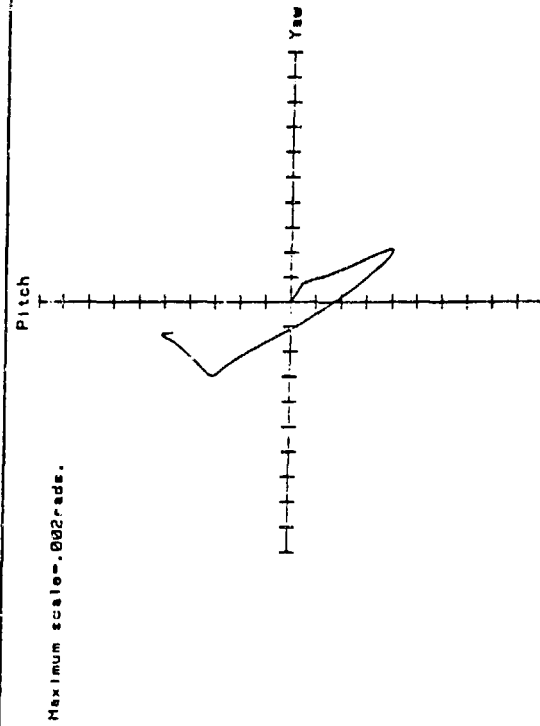


Fig 8
Balanced shot with standard smooth barrel
Shot pitch and yaw viewed from the muzzle

Horizontal scale indicates barrel length
Maximum vertical scale=.002rads.

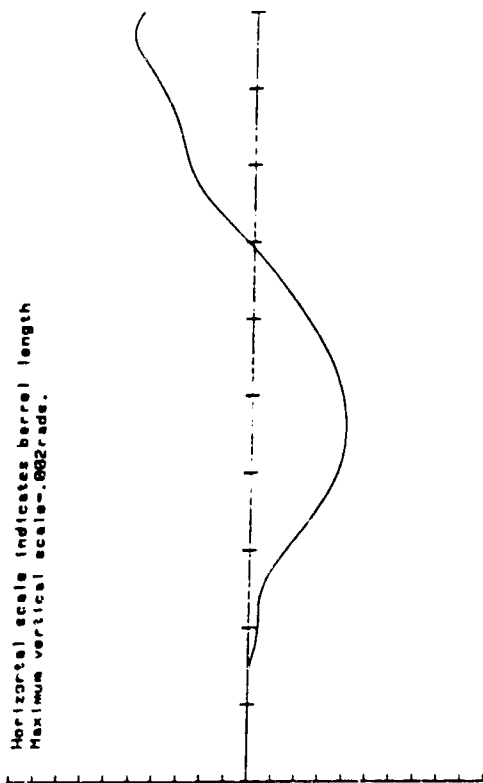


Fig 9 Balanced shot with standard rifled barrel
Shot pitch angle

Horizontal scale indicates barrel length
Maximum vertical scale=.002rads.

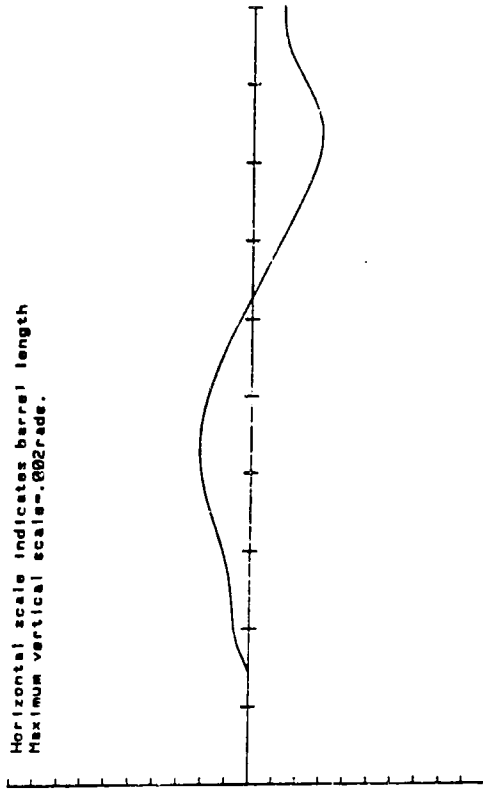


Fig 10 Balanced shot with standard rifled barrel
Shot yaw angle

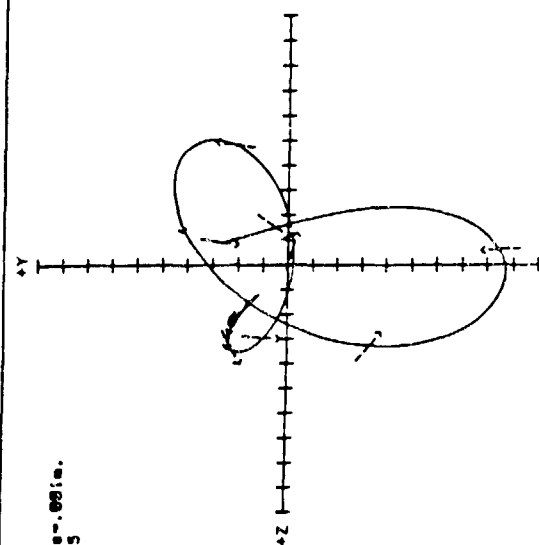


Fig 11 Unbalanced shot with standard rifled barrel
Shot bounce motion viewed from the muzzle

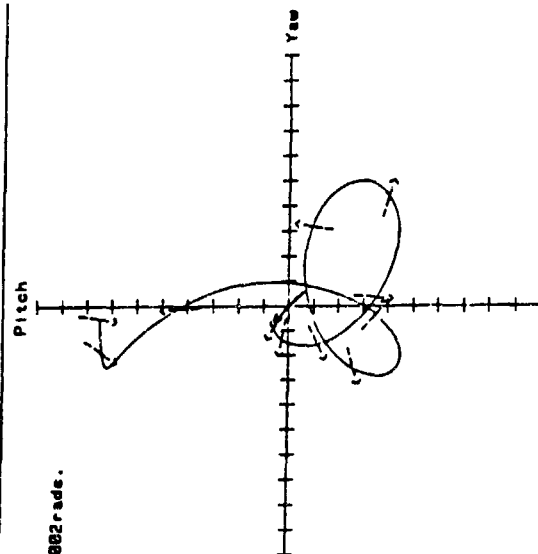


Fig 12 Unbalanced shot with standard rifled barrel
Shot pitch and yaw viewed from the muzzle

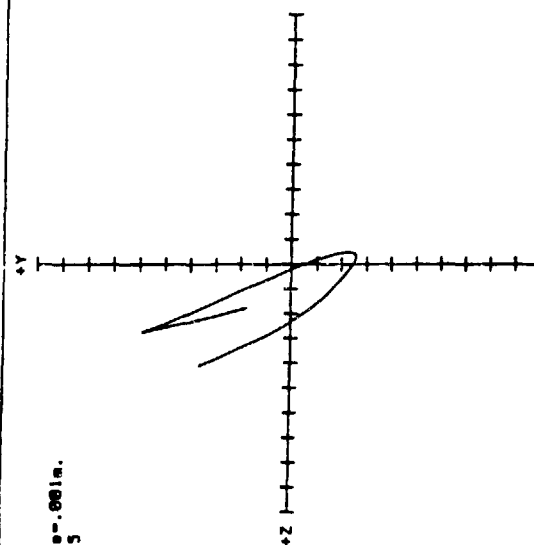


Fig 13 Unbalanced shot with standard smooth barrel
Shot bounce motion viewed from the muzzle

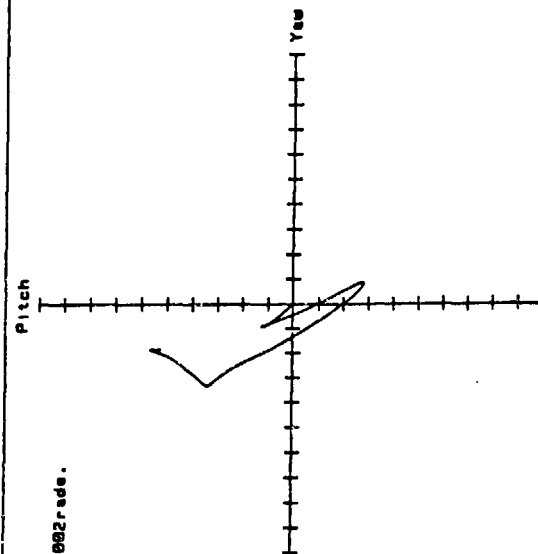
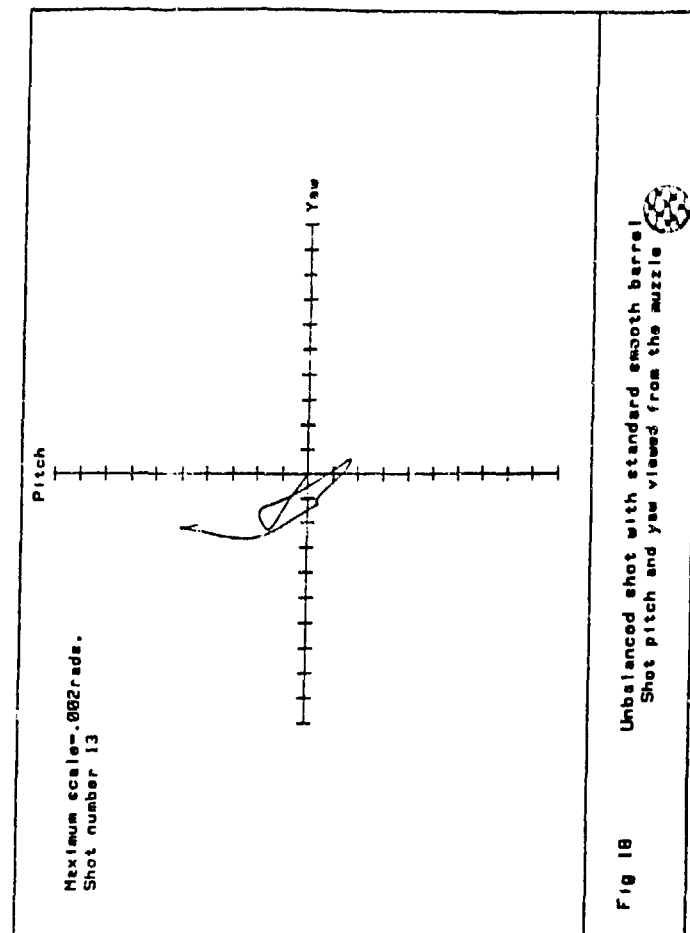
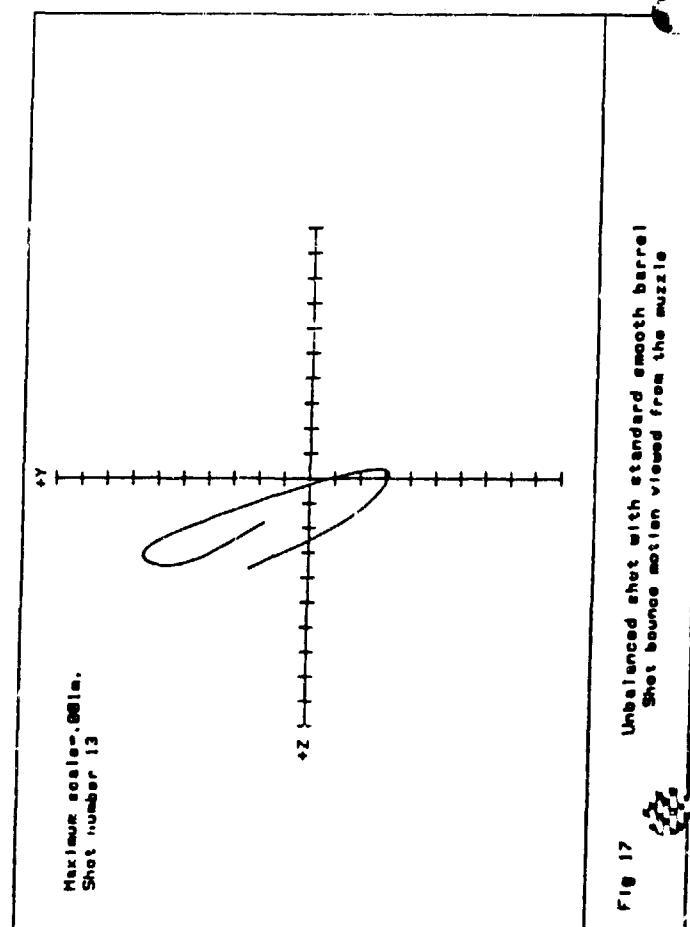
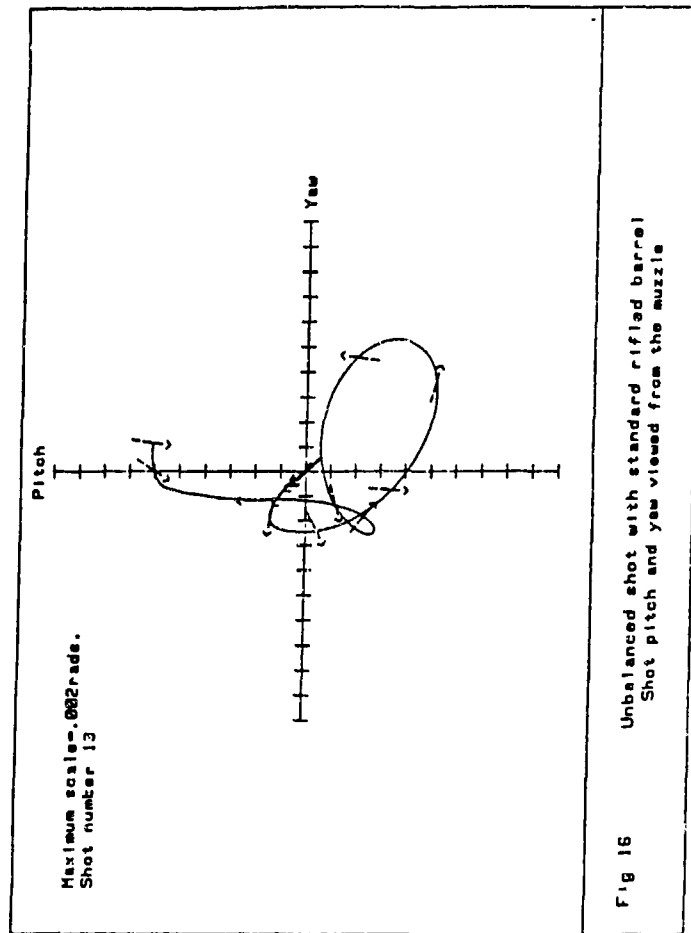
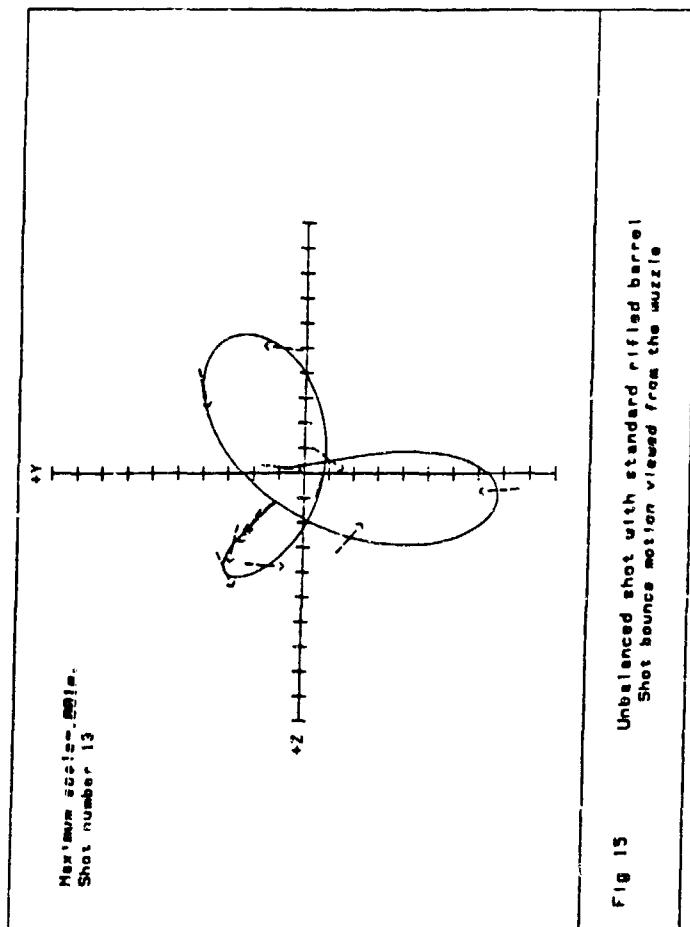
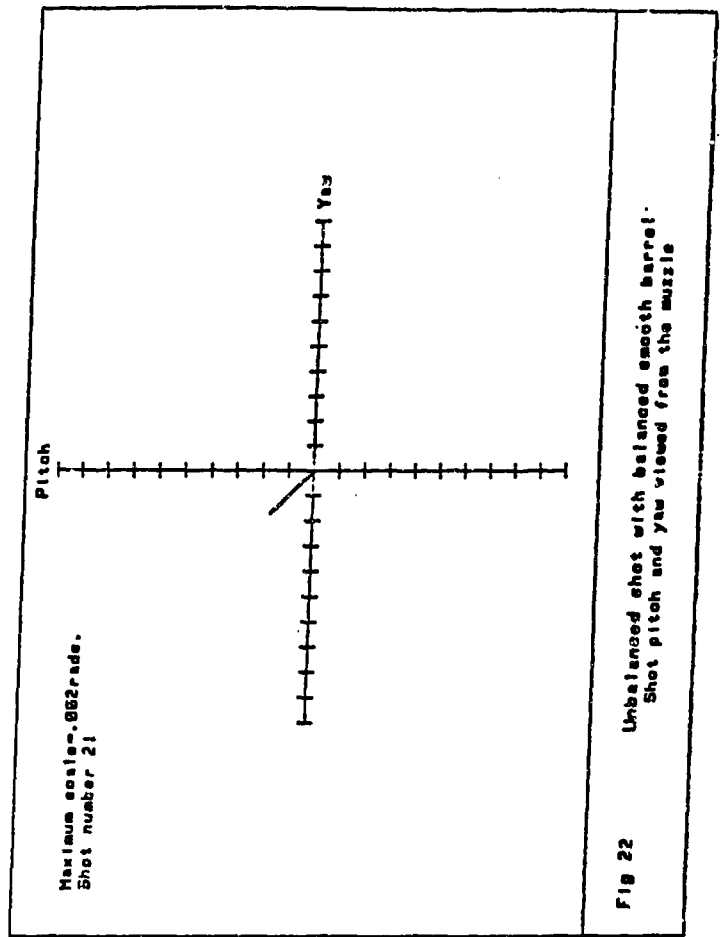
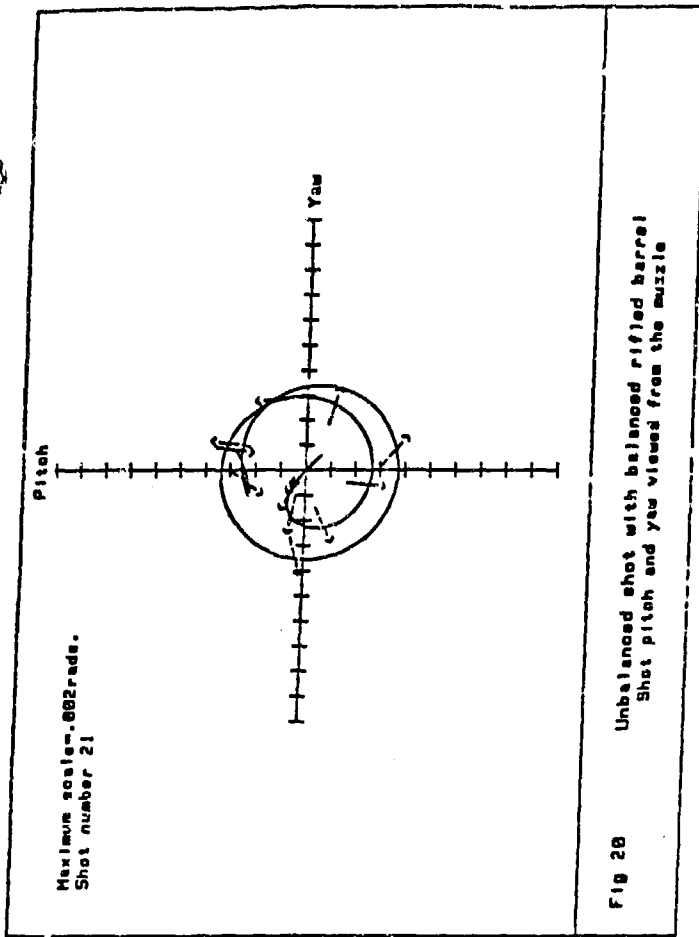
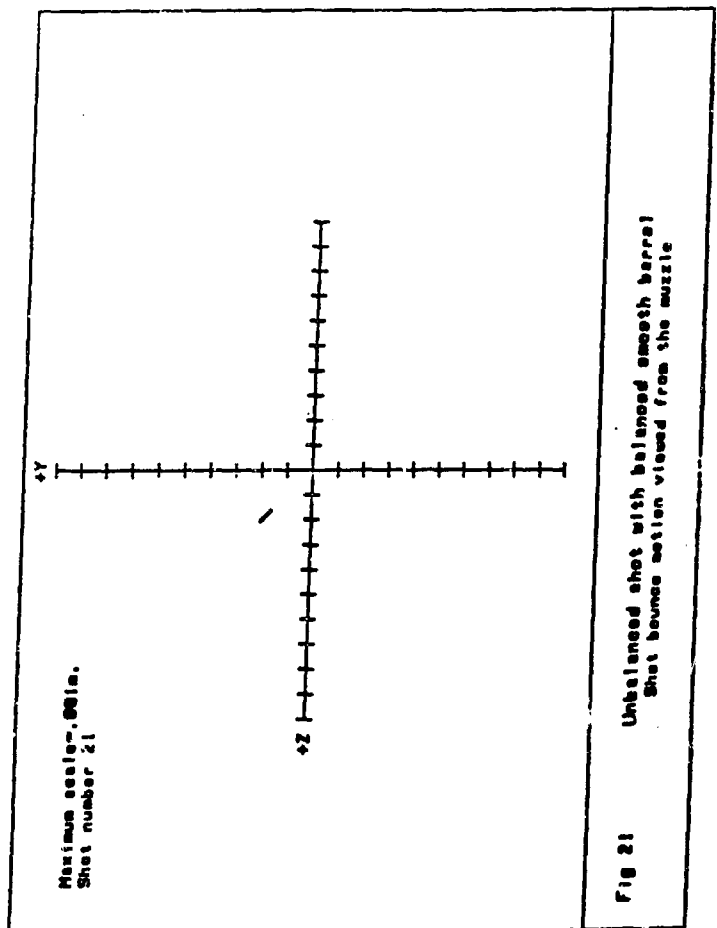
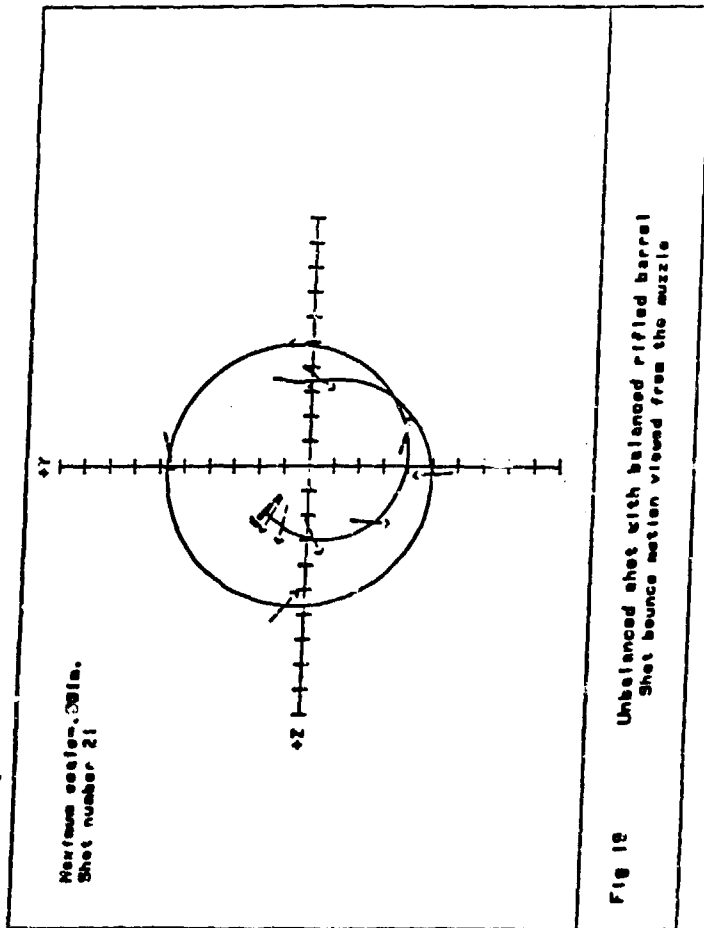


Fig 14 Unbalanced shot with standard smooth barrel
Shot pitch and yaw viewed from the muzzle





Maximum scale = .001 in.
 Shot number 21
 plus front band clearance

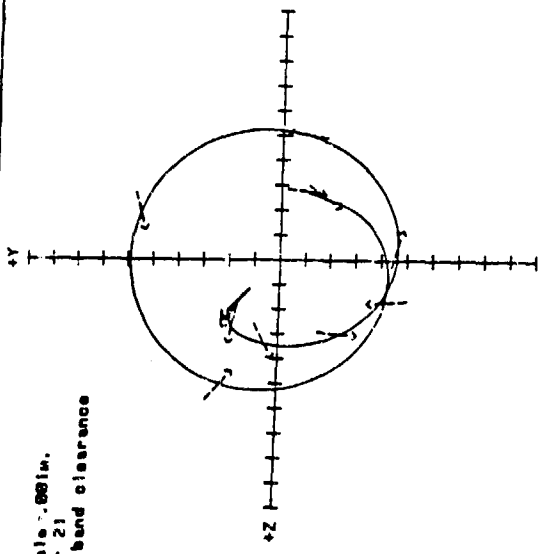


Fig 23

Unbalanced shot with balanced rifled barrel
 Shot bounce motion viewed from the muzzle

Maximum scale = .002 rads.
 Shot number 21
 Plus front band clearance

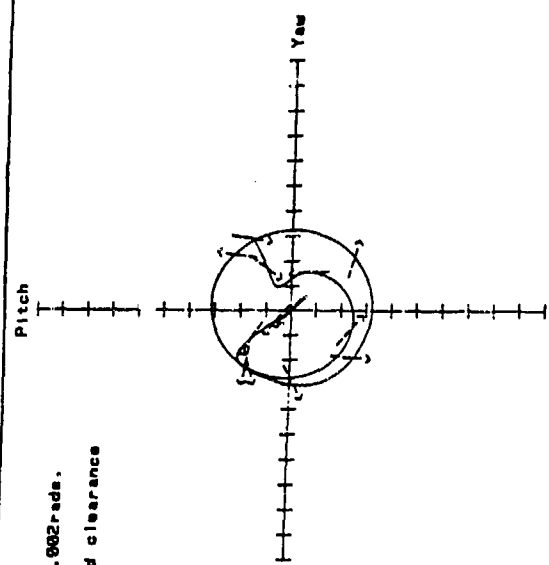


Fig 24

Unbalanced shot with balanced rifled barrel
 Shot pitch and yaw viewed from the muzzle

GAST

TITLE: NORMAL MODES ANALYSIS OF GUN VIBRATIONS BY THE UNIFORM SEGMENT METHOD

RONALD G. GAST

US ARMY ARMAMENT RESEARCH, DEVELOPMENT, AND ENGINEERING CENTER

CLOSE COMBAT ARMAMENTS CENTER

BENET LABORATORIES

WATERVLIET, NY 12189-4050

ABSTRACT

In a related paper published in the Proceedings of the Fourth U.S. Army Symposium on Gun Dynamics (Sneck and Gast, "Normal Modes Analysis of Gun Dynamics"), the Euler-Bernoulli equation for a prismatic gun/beam elastically supported (transverse and rotation) at the breech was solved for its normal vibration modes and response to various transient loadings. This paper is an extension of the reference in that the axially varying tube properties are now considered, whereas the boundary conditions are removed and applied as external displacement dependent loads.

In the Uniform Segment Method the spatial domain is divided into a finite number of prismatic sections within which the Euler equation is applied. Solutions to this equation yield functional relationships for mode shapes in the form of trigonometric and hyperbolic functions. The overall structure is modelled as a free-free beam with intersegment continuity assured by the matching of displacement, slope, moment, and shear transfer at segment boundaries. By applying the free-free boundary and continuity conditions results in a system of equations in the unknown frequencies and coefficients. The solution of this system yields the natural frequencies and mode shape coefficients within an arbitrary constant.

The main advantage of using this method over finite elements lies in the reduced number of degrees of freedom needed to model the structure. Real prismatic sections model one to one. This is not the case in finite element methods. Additionally, a number of the transient loads known to drive gun vibrations are functions of the mode shape derivatives. Since these functions are represented analytically, which is a characteristic of the Uniform Segment Method, the need to calculate derivatives by numerical algorithms is eliminated. Thus, exactness in derivative calculations is assured.

BIOGRAPHY:

PRESENT ASSIGNMENT: Mechanical Engineer, Tank Turret Section, Benet Weapons Laboratory (1985 - Present).

PAST EXPERIENCE: Mechanical Engineer, Special Projects Section, Benet Weapons Laboratory (1971 - 1985) and Mechanical Engineer, Automatic Weapons Section, Benet Weapons Laboratory (1968 - 1971).

DEGREES HELD: B.S.M.E., Rensselaer Polytechnic Institute, 1968 and M.S.M.E., Rensselaer Polytechnic Institute, 1978.

NORMAL MODES ANALYSIS OF GUN VIBRATIONS BY THE UNIFORM SEGMENT METHOD

Ronald G. Gast
US Army Armament Research, Development, and Engineering Center
Close Combat Armaments Center
Benet Laboratories
Watervliet, NY 12189-4050

BACKGROUND

At the Fourth U.S. Army Symposium on Gun Dynamics, which convened in May 1985, the author, in collaboration with H. J. Sneek, submitted a paper [1] in which a method for modelling the flexural vibrations of a tank gun using the normal modes technique was proposed and developed. In this paper, a number of shortcomings in both the model and analysis techniques are cited and will be reviewed briefly.

The first and most striking model shortcoming lies in the use of an axially prismatic beam as representative of the gun tube knowing full well that a gun possessing a prismatic barrel does not exist. The reason for the choice, however, lies in the fact that although guns are axially non-uniform, their deviation from the prismatic condition is small when compared to their overall length. For example, when viewed from a distance, any gun appears to be of uniform cross section. A less important reason for this choice was the ease in which this type of model could be developed. For the prismatic case, a single four-term mode shape equation results for each natural frequency considered.

The second involves the choice of support conditions. In this initial effort, the supports were modelled as linear, bi-directional springs rigidly attached to the breech end (origin of axial coordinate) of the beam. One spring resisted the transverse displacement, while the second restrained the rotational motion of the breech end. This type of support model is not exact, but rather an approximation of what actually exists on fielded weapons. In addition, supports possessing no clearance are not feasible from an assembly or operational standpoint and those possessing linear response properties regarding force/deflection are not likely.

The third involves the use of the Euler-Bernoulli beam equation without a strong claim regarding its applicability for gun/beam type structures. It was chosen based upon the results of an order of magnitude study on the equation's coefficients for the model of a gun system similar to the M60. A more viable approach comparing the results of a modelling effort using alternative equations would be a better means of justification.

A fourth condition involves the identified excitation sources (driving loads) developed into the model. There were five sources which included recoil inertia, pressure curvature, projectile trajectory, projectile rotational imbalance, and eccentricity. These, by far, are the most important loading sources, however, a more versatile model employing additional sources would be more realistic.

All of the above areas are addressed in the current analysis. This paper highlights the detailed improvements which have been developed into the current computer model dedicated to gun vibration analysis. The routines are available and running on Benet Weapons Laboratory's VM/SP Operating System.

FORMULATION OF THE CANNON BEAM DYNAMICS MODEL

General Modelling Equation and Solution Proposal

Beam dynamics as applied to gun tubes are represented in Figure 1 where the beam structure shown possesses axially varying geometric properties inferring that both bending and inertial resistance are functions of position. The transverse cross section is cylindrical and axisymmetric, and in its static state, the axis assumes in-plane curvature due to the beam's weight, environmental condition, and the results of manufacturing processes. The features drawn in phantom represent the additional mass of the breech, bore evacuator, and muzzle brake. Four types of forces and/or moments are represented and appropriately placed upon the structure.

CANNON/BEAM LOADING SCHEMATIC

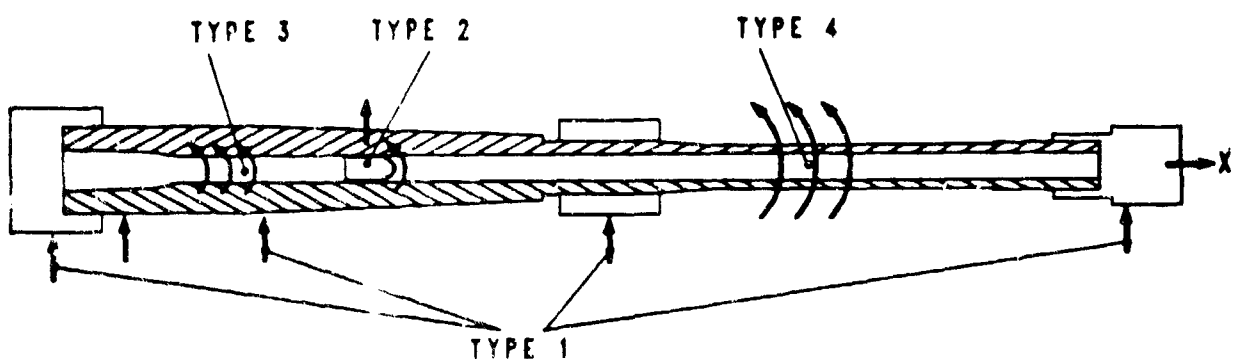


Figure 1. Cannon/beam loading schematic.

GAST

The equation which completely describes the transverse motion of this beam system according to Thomson [2] and others [3-6], is:

$$(EIy'')'' + \frac{w}{g} \ddot{y} - (J + \frac{EIw}{gkAg})\ddot{y}'' + (\frac{Jw}{gkAg})\ddot{y}''' = \sum_{i=1}^N [p_i(x,t,y,y',y'',\dot{y}') + \frac{J}{kAg} \ddot{p}_i(x,t,y,y',y'',\dot{y}') - \frac{EI}{kAg} p_i''(x,t,y,y',y'',\dot{y}')] - w \quad (1)$$

where

- E = Young's Modulus of material
- I = transverse moment of inertia
- J = pitch moment of inertia
- G = modulus of elasticity in shear
- A = area of beam's cross section
- k = shape factor of cross section
- w = weight per unit length of beam
- p_i = i-th forcing function (total of N)
- g = gravity acceleration
- x = axial coordinate (independent space variable)
- t = time (independent time variable)
- y = transverse displacement (dependent space variable)
- $\dot{}$ = time derivative
- ' = space derivative

This equation is commonly referred to as the Timoshenko equation. For a prismatic beam, the second differential operation on the first term could be placed within the brackets since the bending resistance becomes constant. The second term deals with the translational inertia of a beam segment, while the remaining two terms model rotatory inertia and shear deformation effects. All terms are on a per length basis. The right side of the equation contains the representative driving and reaction loads.

Reduced forms of this equation are used when the geometry causes some of the coefficients to be relatively insignificant. Other special cases arise for the analysis of prismatic beams for which all geometric properties are constant in space rendering all dependent variable coefficients constant. This allows for a closed-form solution to the homogeneous equation as will be addressed later. For 'thin' structures, terms involving rotatory inertia become small, thus modifying the coefficient of the third term and completely eliminating the fourth term. For 'long' structures, bending dominates shear, thus both terms three and four may be eliminated without loss of modelling accuracy. In this simpler form, the Timoshenko equation reduces to the Euler-Bernoulli equation, which upon the stipulation of constant cross-sectional properties, becomes

$$EIy'''' + \frac{W}{g} \ddot{y} = \sum_{i=1}^N [p_i(x, t, y, y', y'', \dot{y}')] - w \quad (2)$$

The solution technique for the proposed model in its full or any of the truncated forms is the same. The homogeneous equation will be solved by the separation of variables technique yielding the normal modes of vibration of a free-free beam structure. The model equation will be reassembled using the mode shape vectors, and upon invocation of the appropriate orthogonality principle, a system of ordinary differential equations (O.D.E.'s) containing time varying amplitude coefficients will result. There will be one equation for each mode shape considered. Due to the nature of the loadings, this system of O.D.E.'s is coupled, therefore, numerical matrix procedures will be needed to arrive at the total solution.

Assessing the Significance of Shear and Rotatory Inertia

The Timoshenko equation represents the most complete form of beam analysis available. For certain types of beam structures, the combined effect of shear deflection and rotatory inertia contributes little to the results while their inclusion is costly in terms of solution complexity. Since this modelling effort is to be applied to a certain class of structures, namely large caliber cannon tubes, these effects may be judiciously neglected in favor of the less complex Euler-Bernoulli model. The reason for this will be developed in the following comparative analysis of a uniform 'thin' beam.

Consider the free vibrations of an unrestrained prismatic beam. The Timoshenko equation (1) becomes

$$EIy'''' + \frac{W}{g} \ddot{y} - \left(J + \frac{EIw}{gkAG}\right)\ddot{y}'' + \left(\frac{Jw}{gkAG}\right)\ddot{y}' = 0 \quad (3)$$

Following the method used by Bozich [4] and identifying the parameters suggested by Kruzlewski [7], this equation may be reformulated in a dimensionless form.

$$\frac{1}{K_B^2} \left(\frac{d^4 y}{dz^4}\right) + (K_R^2 + K_S^2) \frac{d^2 y}{dz^2} - (1 - K_B^2 K_R^2 K_S^2) y = 0 \quad (4)$$

where

$$K_B^2 = \omega^2 L^4 \frac{W}{gEI} \quad (5a)$$

$$K_S^2 = \frac{1}{L^2} \frac{EI}{kAG} \quad (5b)$$

$$K_R^2 = \frac{1}{L^2} \frac{Jg}{w} \quad (5c)$$

with ω being a vibration frequency. These three coefficients represent the contributions of bending, shear, and rotatory inertia, respectively. Equation (4) represents the non-dimensional form of the Timoshenko model which reduces to the Euler-Bernoulli version by simply setting K_S and K_R to zero.

In terms of the non-dimensional coordinate z , the analytical solution to the equation is

$$y(x,t) = (C_1 \cos \alpha z + C_2 \sin \alpha z + C_3 \cosh \beta z + C_4 \sinh \beta z) \cos \omega t \quad (6)$$

where

$$\alpha = K_B \sqrt{\frac{+(K_R^2 + K_S^2) + \sqrt{(K_R^2 - K_S^2) + 4/K_B^2}}{2}} \quad (7a)$$

$$\beta = K_B \sqrt{\frac{-(K_R^2 + K_S^2) + \sqrt{(K_R^2 - K_S^2) + 4/K_B^2}}{2}} \quad (7b)$$

These equations are valid when the terms within the outer radical remain positive. By applying free-free boundary conditions and normalizing the mode shapes with respect to C_1 , the following characteristic equation for the natural frequencies may be derived:

$$2(1 - \cos \alpha \cosh \beta) + \left(\frac{\beta^2 - \alpha^2}{\alpha\beta}\right) \sin \alpha \sinh \beta = 0 \quad (8)$$

This equation, which is essentially a function of ω , has an infinite number of roots. It may be solved to any desired accuracy for a finite number of them by standard root finding techniques. A set of computer routines for solving this uniform beam frequency equation was written for the assessment analysis. The effect of shear deflection and rotatory inertia may be included or neglected in order that an evaluation of their effects may be made. The equation coefficients evaluated for each frequency are

$$C_1 = 1 \quad (9a)$$

$$C_2 = \left(\frac{\beta}{\alpha}\right) \left(\frac{\cos \alpha - \cosh \beta}{\sinh \beta - (\beta/\alpha) \sin \alpha}\right) \quad (9b)$$

$$C_3 = \left(\frac{\alpha}{\beta}\right)^2 \quad (9c)$$

$$C_4 = \left(\frac{\alpha}{\beta}\right)^3 C_2 \quad (9d)$$

These coefficients and their respective natural frequencies are used to evaluate and plot mode shapes as a function of the dimensionless coordinate z . The results, as calculated by the Timoshenko and Euler-Bernoulli models for a given structure, may then be compared to determine whether the shear deflection and rotatory inertia effects are significant for the class of beams to be analyzed.

In order to assess the effect of shear and rotatory inertia on cannon vibrations, three uniform cross section pipe structures resembling contemporary tank cannons were analyzed using this technique. The results of this analysis are contained in Figure 2 where the percent error (with respect to the full Timoshenko equation) is plotted against mode number for the three structures analyzed. The results indicate that both of the simpler models predict frequency values which are higher than those which the Timoshenko equation would yield. The 'thicker' structures are less accurate when the Euler-Bernoulli equation is used, however, the inclusion of rotatory inertia in the Timoshenko equation contributes very little for any of the structures. At an outer diameter of 8 inches, a 7.5 percent error in frequency would occur in the sixth mode using the simplest formulation, while only 1.5 percent error would result using the complex equation without rotatory inertia.

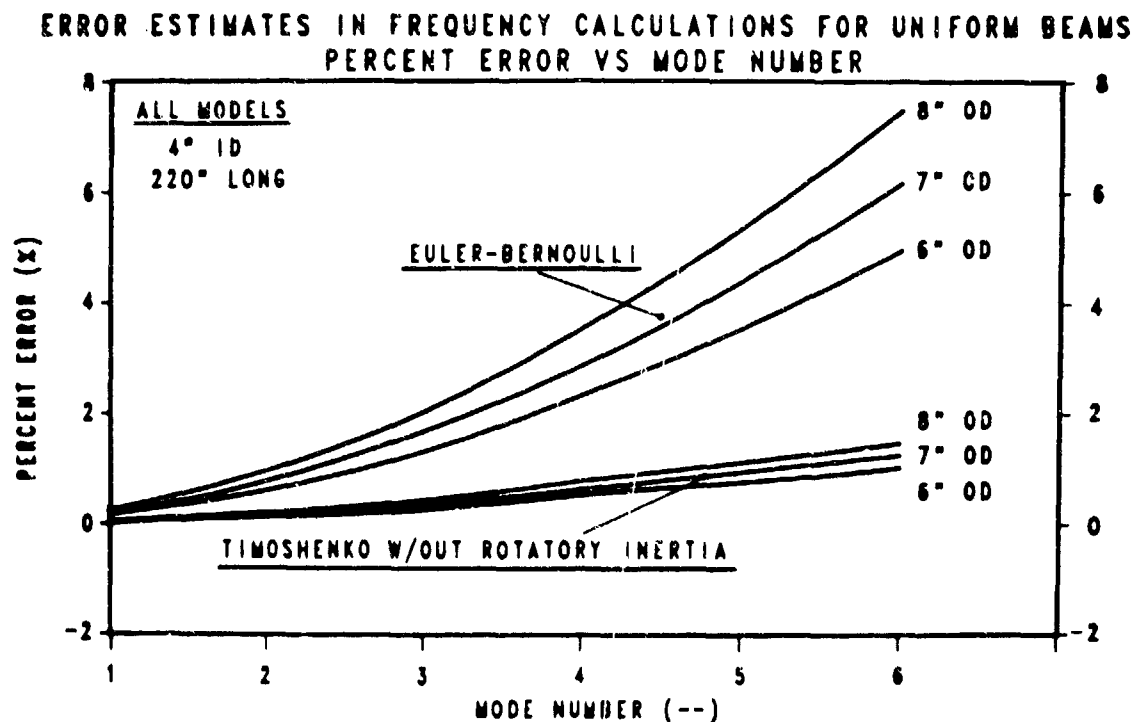


Figure 2. Error in frequency calculations for uniform beams.

A comparison of mode shapes for the sixth mode of the 8-inch beam is plotted in Figure 3. The upper curve represents the shape using the Timoshenko equation, while the lower is the same for the Euler-Bernoulli equation. As can be seen, they are quite similar except at the end points where a deflection error of -8.3 percent and a slope error of -0.75 percent results from the use of the simpler equation. Although this appears to be quite substantial, these error levels become less for the lower modes. Since mode shape contribution diminishes with increasing mode number, these error estimates become relatively unimportant to the overall transient response. In addition, a 220-inch long by 8-inch diameter 105-mm cannon is heftier than any fielded or developmental hardware, therefore, the reported errors become upper bounds when actual cannons are modelled. For these reasons, the Euler-Bernoulli formulation of the vibration equation was selected for the remainder of this analysis.

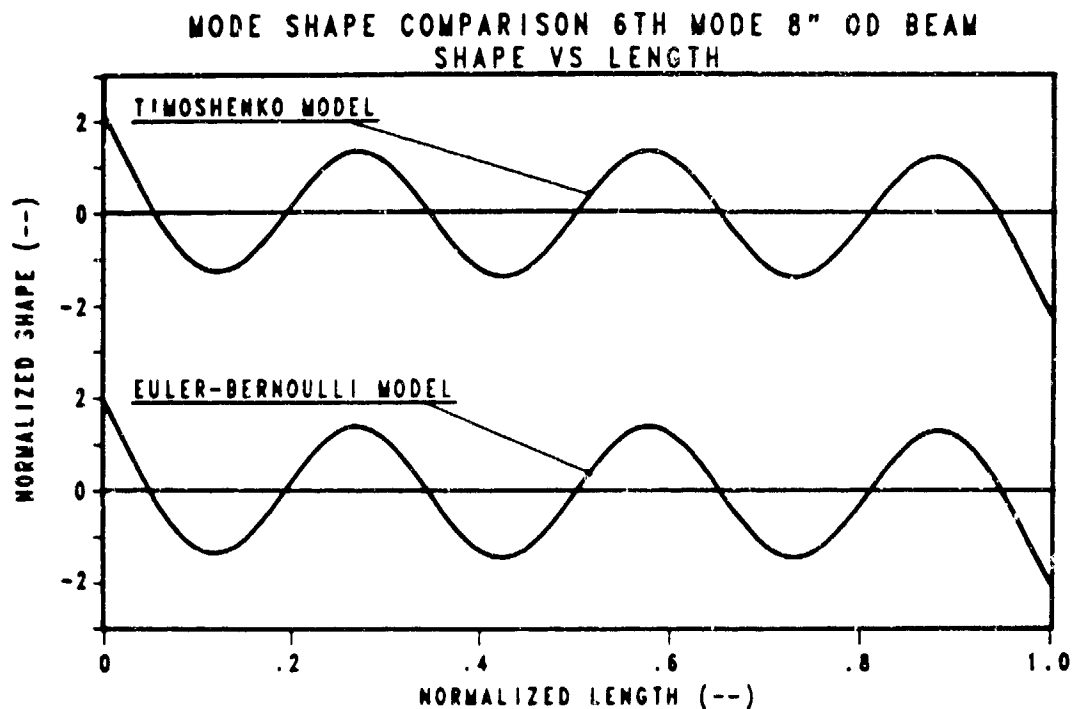


Figure 3. Mode shape comparison for uniform beam models.

Modelling the Non-Prismatic Effect

It goes without saying that the inclusion of non-prismatic geometries increases the complexity of this problem. The normal vibration functions for the uniform beam were shown to be analytic for any of the model equations chosen. This is a great advantage in solving transient problems where the modal functions need to be differentiated for certain types of driving loads. (This is especially true for gun tube loads as will be shown later.) If the modal

function is approximated by a set of tabular values (e.g., numeric tables from finite element analysis), accurate differentiation is difficult, even when the points are connected by approximating polynomials. Since the non-uniform nature of a gun tube is consistent in that it is composed of cylindrical sections, tapered sections, and step changes between sections, attempting to solve the free vibration equation with a single analytical function may be impossible.

A number of approaches were found during the research phase of the study [9-16]. Each of these authors attempted to resolve the problem of modelling the flexural dynamics of a non-prismatic beam. All, however, fell short of expectations in terms of fulfilling the need for analytically expressible mode shape functions differentiable through the second order. Canned finite element routines were ruled out early due to the lack of versatility in their ability to model loads which are functions of the dependent variable. In regard to their employment for determining the mode shapes, the only way a continuous analytical function could be achieved was through a least squares or spline fit using the normal modes displacement information. This was unattractive since it is well known that modal displacements approach sinusoidal shapes for beams with mild non-uniformities. Any method developed for structures of this type should attempt to exploit this property.

Upon conversing with and reviewing the work of Dr. Sneek [17], a method of dealing with the problem's non-prismatic nature was conceived. He suggested that the tube be divided into two uniform segments of differing cross sections, each of which is analyzed using the Euler-Bernoulli equation. By the separation of variables technique [2,3], the application of the appropriate boundary conditions, and the enforcement of interfacial continuity at segment boundaries, expressions involving trigonometric and hyperbolic terms for the mode shape functions will result. Each segment will have its own set of mode dependent coefficients. Continuity across segment boundaries will be accomplished by equating boundary values of displacement, slope, bending moment, and shear as calculated by each adjacent mode function. This method seemed ideal for the problem at hand, and it was chosen contingent upon its adaptability to cannon models where more than two segments would be needed. It was felt that any number of segments could be handled by this method, hence, the term "Uniform Segment Method" (USM) was coined.

The equation defining the mode shapes for a general case employing the USM is

$$\phi_{ij}(\bar{x}) = A_{ij} \cosh \alpha_{ij} \bar{x} + B_{ij} \sinh \alpha_{ij} \bar{x} + C_{ij} \cos \alpha_{ij} \bar{x} + D_{ij} \sin \alpha_{ij} \bar{x} \quad (10)$$

where:

i - segment number
j - mode shape number

\bar{x} - normalized length (x/L)
A, B, C, D - mode shape coefficients

α_{ij} - argument coefficient $[L\sqrt{\omega_j}(\frac{1}{g}(\frac{w}{EI})_i)]^{\frac{1}{4}}$

By employing this segmented mode shape function and the well-known separation of variables technique on the pure bending equation, the unknown coefficients and frequency for each mode may be tracked. For a model utilizing M sections, the imposition of the free-free boundary conditions will yield the following equations relating bending moment and shear at the extremities of the beam:

$$\phi_{1,j}''(0) = 0 \quad (11a)$$

$$\phi_{M,j}''(1) = 0 \quad (11b)$$

$$\phi_{1,j}'''(0) = 0 \quad (11c)$$

$$\phi_{M,j}'''(1) = 0 \quad (11d)$$

Continuity at the interfacial locations is preserved by equating the values of displacement, slope, bending moment, and shear as calculated by adjacent mode functions at the interfacial boundaries between segments. These conditions may be written as follows

$$\phi_{i-1,j}(\bar{x}_{i-1}) = \phi_{i,j}(\bar{x}_{i-1}) \quad (12a)$$

$$\phi_{i-1,j}'(\bar{x}_{i-1}) = \phi_{i,j}'(\bar{x}_{i-1}) \quad (12b)$$

$$(EI)_{i-1}\phi_{i-1,j}''(\bar{x}_{i-1}) = (EI)_i\phi_{i,j}''(\bar{x}_{i-1}) \quad (12c)$$

$$(EI)_{i-1}\phi_{i-1,j}'''(\bar{x}_{i-1}) = (EI)_i\phi_{i,j}'''(\bar{x}_{i-1}) \quad (12d)$$

where:

i - segment number

\bar{x}_k - normalized axial coordinate of segment k's right boundary

For a model containing M segments, there are 4M coefficients and one frequency to be evaluated for each mode shape. By setting $A_{1,j} = 1$ renders the system deterministic for which unique solutions exist at each natural frequency. A set of algebraic equations in the natural frequency (ω_j) and the 4M-1 unknown mode shape coefficients is presented in matrix form in Figure 4. The system matrix is shown to contain an orderly set of entries representing the boundary conditions (B.C.) and matching conditions (M.C.). A 2X4 sub array beginning at global location 1,1 contains the terms for evaluating the B.C. at $x = 0$, whereas a similar array ending at N,N ($N=4M$) represents the B.C. at $x = 1$. 'Walking' along the main diagonal are M-1 sub arrays 4X8 in size which represent the preservation of continuity across segment boundaries. The remaining terms in the matrix are zero. The non-zero entries are functions of the segment properties, boundary location, and the unknown natural vibration frequencies. Setting the determinant equal to zero and solving for the roots of the resulting characteristic equation produces values for these frequencies. At each frequency, a reduced system is developed by setting $A_{1,j} = 1$, eliminating the first row, and shifting the first column to the right side of the equation. The solution to this linear system yields the remaining normalized mode shape coefficients.

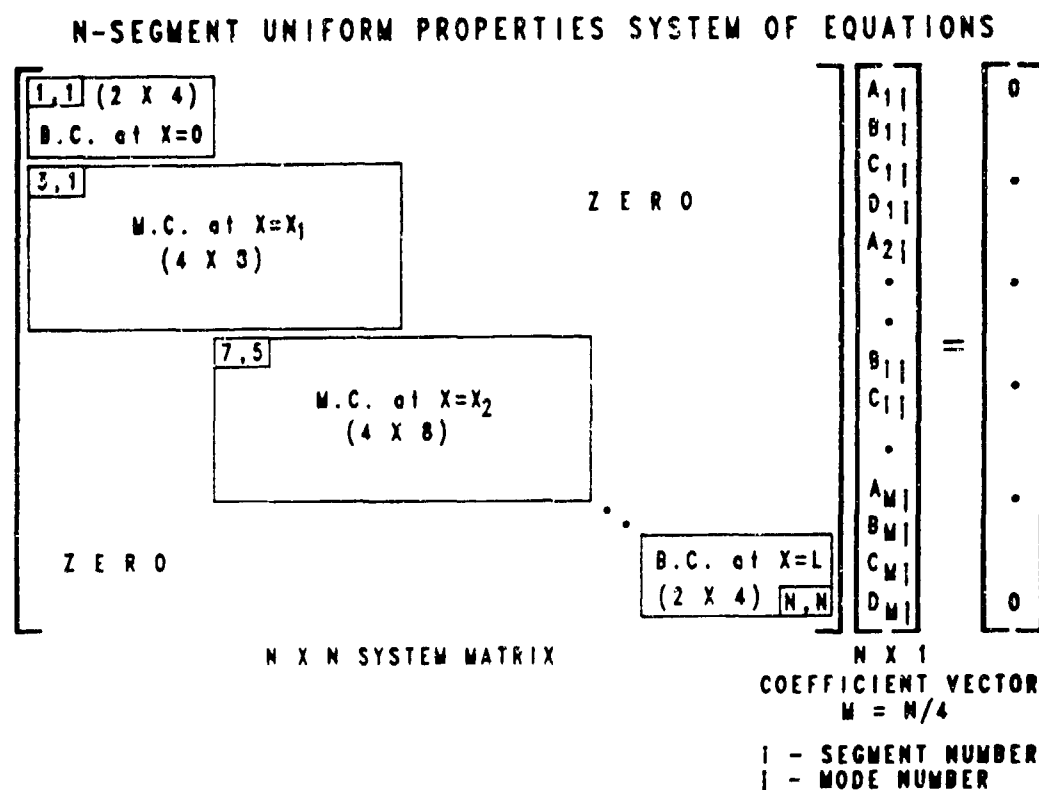


Figure 4. Uniform segment system of equations.

Unlike finite element techniques, this method does not require the segmenting of uniform sections. Rather, they transform on a one to one basis from the real to the model plane, thus only a few segments are needed to accurately represent gently varying non-uniformities. Additionally, the number of modes available for calculation is not a function of the number of segments. In finite elements, the mode shapes are defined by the displaced locations of the model's nodes. There are not enough points available for an accurate representation of the mode's shapes at higher natural frequencies. This is not the case for the USM, since nodeless elements using trigonometric and hyperbolic terms in the mode shape functions are employed.

To determine the accuracy of this method for free vibration modelling of gun structures, the predictions from an established finite element code (ABAQUS [18]) for a typical gun tube (105-mm M68) were compared to the results generated by the dedicated routines (MODE:) written by the author in support of this analysis. The gun and its modelling representations are shown in Figure 5.

105mm M68 GUN: COMPARISON OF ANALYTICAL MODELS

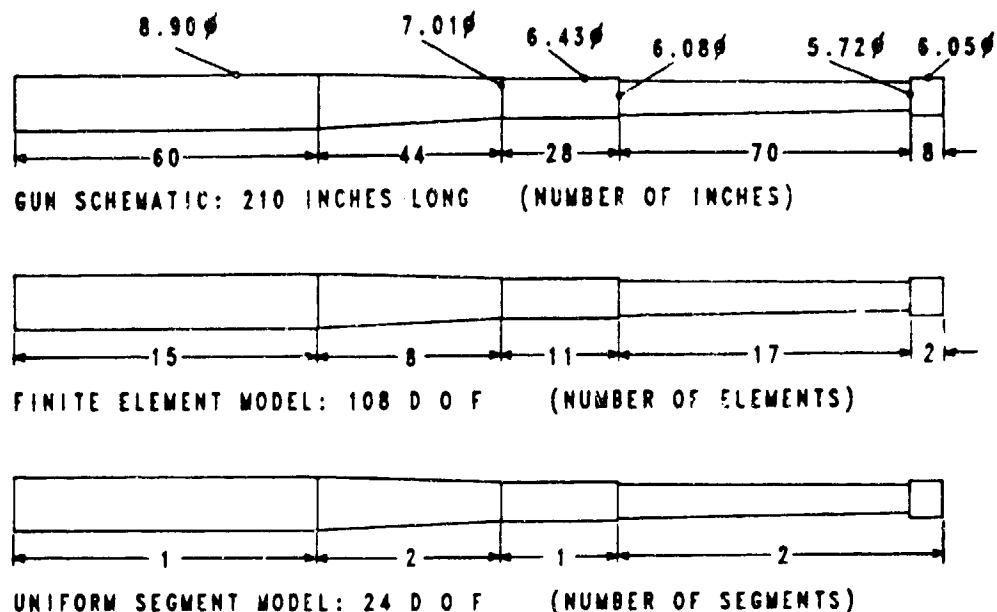


Figure 5. 105-mm M68 Gun: Comparison of analytical models.

The M68 gun tube is 210 inches long containing two tapered and three cylindrical sections. The physical schematic is shown in the top sketch in Figure 5. This finite element model (FEM) was comprised of 54 equally-spaced nodes with two degrees of freedom (dof) per node and 53 prismatic beam elements. The sketch in the middle of the figure indicates the element density in each physical section of the structure. On the lower sketch of the same figure, segmentation of the USM model is shown. Only six segments of four dof each were used for a total of 24 dof. The natural frequencies and mode shapes for the first six vibration modes were calculated using both the Timoshenko and Euler equations for the FEM. In the USM analysis, only the Euler equation is employed.

The results of the analysis are shown in Figures 6 and 7. In Figure 6 a comparison among the frequency calculations are presented in the form of a bar graph. The abscissa contains the first six mode numbers, while the ordinate is labelled with the \log_{10} value of the frequency. As is indicated, the FEM using the Timoshenko equation produces the lowest values for all six frequencies, while the USM produces the highest. The differences in the extremes is between six and ten percent with the greatest discrepancy occurring at the highest mode number.

105mm M68 GUN: NATURAL FREQUENCY ESTIMATES LOG₁₀ FREQUENCY VS MODE NUMBER

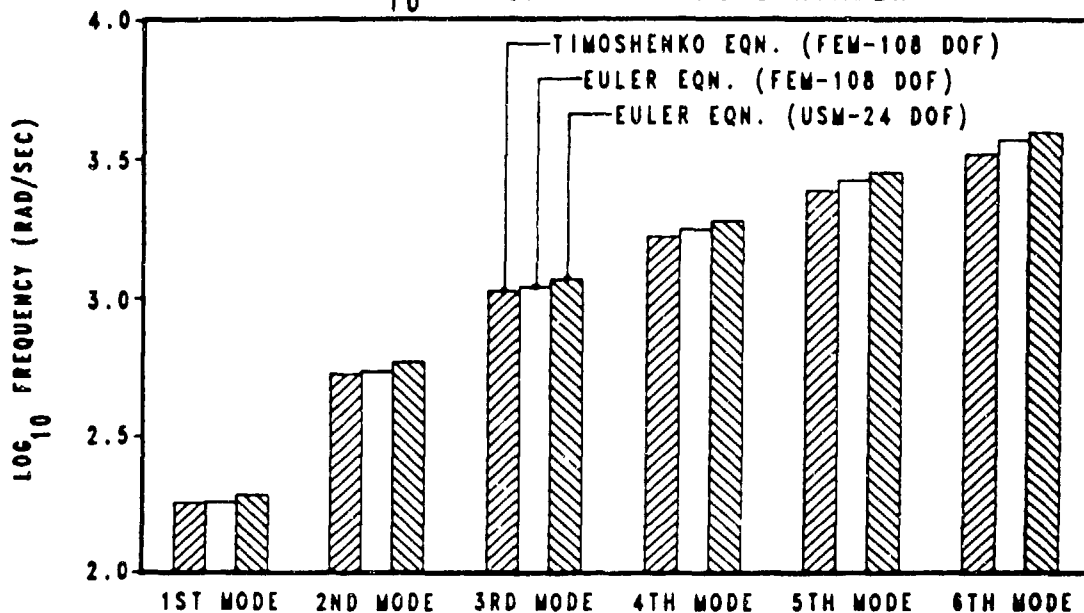


Figure 6. 105-mm M68 Gun: Natural frequency estimates.

105mm M68 GUN: MODE SHAPE COMPARISONS NORMALIZED SHAPE OF 6TH MODE

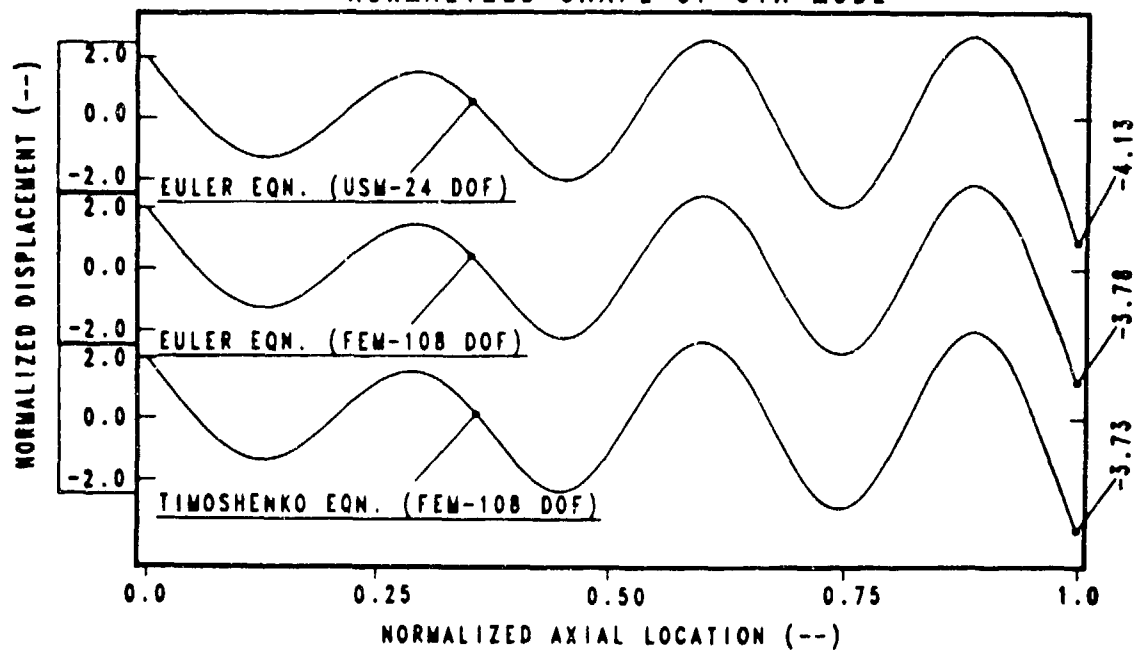


Figure 7. 105-mm M68 Gun: Mode shape comparison.

GAST

In Figure 7 the normalized mode shape plots for the sixth mode, as calculated by each of the models, is shown. The sinusoidal nature of the mode shape is evident on all three plots, while the subtle differences in displacement magnitude at the extreme end are perceptively indiscernible. Numerically, the magnitude of the displacement for the USM calculation is approximately ten percent higher than either of the other two FEM's. Overall, these results verify the worth of the USM in modelling mildly discontinuous beam structures. If greater accuracy is desired, more segments could be used for the tapered portions of the structure.

Modelling Initial Curvature

It is a generally accepted fact that the initial shape of the gun tube has a significant effect upon its dynamic response and shot accuracy. This dependence has been shown experimentally (Elder [19]) as well as analytically (Simkins [20], Warken [21]). Four prominent causes of static gun/beam curvature, which are part of the proposed model, are

1. Gravity droop
2. Thermal droop
3. Manufacturing tolerances
4. Non-structural weight (breech, etc.)

To implement these effects, an independent set of routines (INIT:) was developed to generate the initial conditions for the gun/beam. These routines accept the geometry from the normal modes analysis, adding two resilient supports, point loads simulating non-structural mass, and distributed loads representing each segment's weight. The deflection response of the supports may include clearance and non-linear elasticity. Initially, the rigid body solution for the gun/beam is solved. This yields support reactions, deflections, and the initial slope of the gun's axis. In the next portion, the static bending of the gun/beam due to weight and external mass is determined by numerical integration of the Euler-Bernoulli equation applied to the static case. The support reactions are redefined as external loads and their axial locations as points of zero bending deflection. This type of modelling is straightforward and well documented in structural mechanics literature [22]. Thermal response and manufacturing induced curvature is currently imported into this model via tabular files developed by empirical data or external analysis. The total vertical deflection is calculated by superimposing the individual responses and generating tabular files which will be used as data in the transient analysis.

Problem Closure: The Total Dynamic Response

Application of Orthogonality

Having a piecewise functional representation for the mode shapes and an approximating polynomial equation for initial deflection, closure to the problem involves solving particular forms of Eq. (2). Recalling:

$$EI y'''' + \frac{w}{g} \ddot{y} = \sum_{i=1}^N [p_i(x, t, y, y', y'', \dot{y}')] - w \quad (2)$$

is the equation for a uniform beam. The dependent variable (y) contains both static and dynamic terms. By separating the dependent variable thusly, this equation may be recast and rewritten on a per segment basis as follows:

$$(EI)_k \left[\sum_{i=1}^I \phi_{ki} \ddot{q}_i + y_s \right]'''' + \frac{w_k}{g} \frac{\partial^2}{\partial t^2} \left[\sum_{i=1}^I \phi_{ki} \ddot{q}_i + y_s \right] = \sum_{m=1}^M p_m(x, t, y, y', \dot{y}, y'', \dot{y}') - w_k(y) \quad (13)$$

where:

i :	i -th mode shape
I :	total number of modes
k :	k -th uniform segment
K :	total number of segments
m :	m -th applied load
M :	total applied loads
$(EI)_k$:	bending resistance of k -th segment
w_k :	weight/length of k -th segment
ϕ_{ki} :	i -th mode shape of k -th segment
q_i :	i -th modal amplitude
$p_m(x, t, \dots)$:	m -th applied load function
$w_k(y)$:	static mass load applied to k -th segment
y_s :	static deflection curve

Since the modal amplitudes are time-dependent only and the static deflection is space-dependent only, the above equation may be separated as follows:

$$(EI)_k \left(\sum_{i=1}^I \phi_{ki} \ddot{q}_i \right) + \frac{w_k}{g} \left(\sum_{i=1}^I \phi_{ki} \ddot{q}_i \right) = \sum_{m=1}^M p_m(x, t, \dots) \quad (14a)$$

$$(EI)_k y_s'''' = w_k(y) \quad (14b)$$

GAST

The solution to Eq. (14a) yields the dynamic response with respect to the initial shape of the beam. The solution to the second equation is the static deflection. Superposition of these leads to the total dynamic response with respect to a global inertial coordinate system. Since Eq. (14b) has already been solved (last section), the solution to Eq. (14a) will close the problem.

By the nature of the segment mode shape functions

$$\phi_{ki}'''' = \left(\frac{\alpha_{ki}}{L}\right)^4 \phi_{ki} \quad (15)$$

which leads to

$$\sum_{i=1}^I \phi_{ki} \left[\ddot{q}_i + g \left(\frac{EI}{w} \right)_k \left(\frac{\alpha_{ki}}{L} \right)^4 q_i \right] = \frac{g}{w_k} \left[\sum_{m=1}^M p_m(x, t, \dots) \right] \quad (16)$$

Recalling a parameter from Eq. (10) and employing current notation

$$\alpha_{ki} = L \sqrt{\omega_i} \left(\frac{1}{g} \left[\frac{w}{EI} \right]_k \right)^{\frac{1}{4}}$$

which upon substitution yields

$$\sum_{i=1}^I \phi_{ki} [\ddot{q}_i + \omega_i^2 q_i] = \frac{g}{w_k} \left[\sum_{m=1}^M p_m(x, t, \dots) \right] \quad (17)$$

For non-dissipative boundary conditions, the orthogonality of the mode shapes with respect to the weight function $w(x)/g$ leads to the following:

$$\int_0^L \frac{w(x)}{g} \phi_i \phi_j dx = \sum_{k=1}^K \int_{x_{k0}}^{x_{k1}} \frac{w_k}{g} \phi_{ki} \phi_{kj} dx =$$

$$0 \quad \text{for } i \neq j \quad (18a)$$

$$G_i \quad \text{for } i = j \quad (18b)$$

where

x_{k0} : axial location of lower boundary of segment k

x_{k1} : axial location of upper boundary of segment k

Note: $x_{k1} = x_{(k+1)0}$

$w(x)$: structural weight distribution

By multiplying Eq. (17) by $\frac{w(x)}{g} \phi_i$, integrating over the length and applying Eq. (18), the following ordinary differential for modal amplitudes results:

$$\ddot{q}_i + \omega_i^2 q_i = \frac{1}{G_i} \sum_{m=1}^M \sum_{k=1}^K \int_{x_{k0}}^{x_{k1}} p_m(x, t, \dots) \phi_{ki} dx \quad (19)$$

The solution to this equation yields a vector of modal amplitudes used to calculate the dynamic displacement, velocities, and slopes. These equations are as follows:

$$y_d(x) = \sum_{i=1}^I q_i(t) \phi_i(x) \quad (20a)$$

$$\dot{y}_d(x) = \sum_{i=1}^I \dot{q}_i(t) \phi_i(x) \quad (20b)$$

$$y'(x) = \sum_{i=1}^I q_i(t) \phi_i'(x) \quad (20c)$$

where

$$\phi_i(x) = \phi_{ki}(x_k) \text{ segment mode shape}$$

Representation of the Forcing Functions

Previous analyses and test results indicate that static droop dominates the overall curvature. Dynamic response is shown to be a displacement perturbation about the static shape. The maximum displacement levels are an order of magnitude less than the static muzzle deflection. Since the loading functions unique to gun dynamics are dependent upon a gun's overall shape, so is the dynamic response. Recalling the functional form for these load functions

$$p_m(x, t, y, y', \dot{y}, \ddot{y}, y'', \dot{y}')$$

from Eq. (14a), the following expression from Eq. (19)

$$\frac{1}{G_i} \sum_{m=1}^M \sum_{k=1}^K \int_{x_{k0}}^{x_{k1}} p_m(x, t, \dots) \phi_{ki} dx$$

GAST

must be evaluated for each load function considered. These load functions and evaluations will now be presented and discussed.

1. Recoil inertial load. An inertia couple develops within any segment k during recoil which is expressible as

$$p_1(t, x, y') = \frac{w_k}{g} a_r(t) [(l-x)y']' \quad (21)$$

where

$a_r(t)$: recoil acceleration

l : total length of gun

y : total transverse displacement (static and dynamic)

Details of the derivation may be found in Simkins [20]. Evaluation of the expression

$$\frac{1}{G_i} \int_0^l \frac{w_k}{g} a_r(t) [(l-x)y']' \phi_{ki} dx$$

upon the substitution of

$$y = \sum_{j=1}^I \phi_{kj} q_j + y_s \quad (22)$$

and normalizing with respect to tube length yields the following:

$$\begin{aligned} \frac{1}{G_i} \int_0^l p_1(x, t, y') \phi_{ki} dx &= K_1(t) \left\{ w_k \phi_{kj} [(1-\bar{x}) \left(\sum_{j=1}^I \phi'_{kj} q_j + y'_s \right)] \right\}_{\bar{x}=0}^{\bar{x}=1} \\ &= l \int_0^1 w_k \phi'_{ki} [(1-\bar{x}) \left(\sum_{j=1}^I \phi'_{kj} q_j + y'_s \right)] d\bar{x} \end{aligned} \quad (23)$$

where

$$K_1(t) = \frac{a_r(t)}{g G_i} l$$

$$\bar{x} = x/l$$

GAST

2. Pressure curvature load. Due to the nature of curvature within real bodies, diametrically opposite bore 'surfaces' possess differing 'areas'. A pressure load acting within this confined chamber will tend to straighten the chamber because the area of the concave 'surface' is greater than its convex counterpart. The expression for this load function [20] is

$$p_2(x, t, y'') = -A_B P_B(t) y'' \{H(x_p(t) - x)\} \quad (24)$$

where

A_B : bore area of tube
 $P_B(t)$: propellant gas pressure
 $x_p(t)$: projectile location
 $H(x_p - x)$: step function

Upon substitution from Eq. (22), the evaluation of the normalized integral yields

$$\frac{1}{G_i} \int_0^l p_2(x, t, y'') \phi_{ki} dx = K_2(t) \int_0^{\bar{x}_p} [\phi_{ki} \sum_{j=1}^I \phi_{kj}'' q_j + \phi_{ki} y_s''] d\bar{x} \quad (25)$$

where

$$K_2(t) = - \frac{A_B P_B(t)}{G_i} l$$

$$\bar{x}_p = x_p / l$$

3. Projectile trajectory load. The accelerating projectile, although of considerably less mass than the tube, can exert a significant transverse force when it is confined to travel along a curved path. Simkins [20] identified this loading and derived the following expression:

$$p_3(x, t, \dot{y}', y'', \dot{y}) = - \frac{w_p}{g} [\ddot{y} + 2\dot{x}_p(t)\dot{y}' + (\dot{x}_p(t))^2 y'' + g] \delta(x_p(t) - x) \quad (26)$$

where

w_p = projectile weight/unit length
 $\delta(x_p(t) - x)$ = Dirac delta function

Upon substitution of Eq. (22) and normalizing with respect to tube length, the integral expression becomes

$$\begin{aligned}
& \frac{1}{G_i} \int_0^1 p_3(x, t, \dot{y}', y'', \ddot{y}) \phi_{ki} \delta(\bar{x}_p(t) - \bar{x}) d\bar{x} = \\
& K_3 \phi_{ki}(\bar{x}_p) \left(\sum_{j=1}^I \phi_j(\bar{x}_p) \ddot{q}_j + 2\dot{\bar{x}}_p \sum_{j=1}^I \phi_j'(\bar{x}_p) \dot{q}_j + \right. \\
& \left. (\dot{\bar{x}}_p)^2 \left\{ \sum_{j=1}^I \phi_j''(\bar{x}_p) q_j + y_s''(\bar{x}_p) \right\} + g \right) \quad (27)
\end{aligned}$$

where

$$K_3 = \frac{W_p}{G_i g}$$

W_p = projectile weight

4. Projectile eccentricity. Wu [23] has postulated the existence of a couple exerted on the tube when the projectile propelling force does not pass through the projectile's mass center which is expressible as

$$p_4(x, t) = A_B P_B(t) \left(\frac{e_p}{l_p} \right) \delta'(x_p - x) \sin(\theta_0 + 2\pi \tau x_p) \quad (28)$$

where

e_p = radial eccentricity of projectile
 l_p = wheelbase of projectile
 τ = rifling twist (= 0 for smooth bore)

$$\int_{-\infty}^{\infty} \delta'(x_p - x) dx = 1$$

Upon substitution of Eq. (22) and normalizing, the integral expression becomes

$$\frac{1}{G_i} \int_0^1 p_4(x, t) \phi_{ki} dx = -K_4(t) \frac{l_p}{l} \phi_{ki}'(\bar{x}_p) \quad (29)$$

where

$$K_4(t) = \frac{A_B P_B(t)}{G_i} \left(\frac{e_p}{l_p} \right) \sin(\theta_0 + 2\pi \tau x_p) l$$

5. Projectile rotational load. As the projectile travels along a rifled tube, its mass center rotates causing a centrifugal load on the bore. The vertical component of this reaction is expressible as

GAST

$$p_5(x, t) = -\frac{w_p e_p}{g} (2\pi \dot{x}_p)^2 \delta(x_p - x) \sin(\theta_0 + 2\pi \tau x_p) - (2\pi \ddot{x}_p) \cos(\phi_0 + 2\pi \tau x_p) \delta(x_p - x) \quad (30)$$

where

\dot{x}_p = projectile axial velocity
 \ddot{x}_p = projectile axial acceleration
 τ = rifling twist in revolutions per inch

Upon substitution and normalization, as above, the integral evaluation becomes

$$\frac{1}{G_i} \int_0^1 p_5(x, t) \phi_{ki} d\bar{x} = K_5(t) \phi_{ki}(\bar{x}_p) \quad (31)$$

where

$$K_5(t) = -\frac{w_p e_p}{G_i g} [(2\pi \dot{x}_p)^2 \sin(\theta_0 + 2\pi \tau x_p) - (2\pi \ddot{x}_p) \cos(\phi_0 + 2\pi \tau x_p)]$$

6. Stationary mass reaction. The stationary non-structural masses (breech, bore evacuator, muzzle brake) cause transverse inertial loadings expressible as

$$p_6(x, t, \bar{y}) = -\frac{w_s}{g} \bar{y} \delta(x_s - x) \quad (32)$$

where

w_s : weight of stationary mass/length of mass
 \bar{y} : axial location of mass
 x_s : x_s/l

The integral evaluation is

$$\frac{1}{G_i} \int_0^1 p_6(x, t, \bar{y}) \phi_{ki} dx = K_6 \phi_{ki}(\bar{x}_s) \sum_{j=1}^I \phi_{kj}(\bar{x}_s) \ddot{q}_j \quad (33)$$

where

$$K_6 = -\frac{w_s}{G_i g}$$

w_s = weight of stationary mass

7. Stationary mass eccentricity. Should these masses possess vertical eccentricity with respect to the bore axis, a couple will develop causing a load expressible as

GAST

$$p_7(x, t) = - \frac{W_S}{W_R} A_B P_B(t) \left(\frac{e_S}{l_S} \right) \delta'(x_S - x) \quad (34)$$

where

W_R : total recoiling weight
 e_S : vertical eccentricity from bore axis (+ => above axis)
 l_S : wheelbase of eccentric mass

The integral evaluation of this load yields

$$\frac{1}{G_i} \int_0^l p_7(x, t) \phi_{ki} dx = K_7 \phi'_{ki}(x_S) \quad (35)$$

where

$$K_7 = - \frac{W_S}{G_i W_R} A_B P_B(t) (e_S)$$

8. Support reactions. The mounting supports may be characterized as non-linear spring elements which react actively with the total displacement of the tube. Initially, the support deflection balances the static loads. As the tube vibrates, the displacements of the tube's support locations change. For a general non-linear support spring, the reactive load may be expressed as

$$p_8(x, t, y) = F_{rn}(y) \delta(x_{rn} - x) \quad (36)$$

where

$F_{rn}(y)$: dynamic reaction force of n-th support (total reaction - static reaction)
 x_{rn} : axial location of n-th support

The integral equation is as follows:

$$\frac{1}{G_i} \int_0^l p_8(x, t, y) \phi_{ki} dx = K_8(y) \phi_{ki}(x_{rn}) \quad (37)$$

where

$$K_8(y) = \frac{F_{rn}(y)}{G_i}$$

9. Bore eccentricity load. Should the gun's bore and outer diameter be non-concentric, each differential segment of the beam contributes an inertia couple about the axis which may be distributed in varying degrees over the full length of the gun. The differential load per unit length may be expressed as follows:

GAST

$$p_g(x, t) = -w_k \bar{a}_R(t) e(x_e) \delta'(x_e - x) \quad (38)$$

where

$$\bar{a}_R(t) = \frac{F_B}{\bar{W}_R} : \text{normalized acceleration}$$

$$e(x_e) = \text{transverse eccentricity at } x_e$$

Since this is a differential load, its total contribution becomes

$$\frac{1}{G_i} \int_0^l p_g(x, t) \phi_{ki} dx = -K_g(t) e(\bar{x}_e) \phi_i'(\bar{x}_e) \Delta \bar{x} \quad (39)$$

where

$$K_g(t) = \frac{w_k \bar{a}_R(t) l}{G_i}$$

$$\Delta \bar{x} = \frac{\Delta x}{l} : \text{differential length over which the eccentricity is distributed}$$

The total load is the summation of the differential loads. When the formulation is cast in a continuous form, the final value for the load becomes

$$\frac{1}{G_i} \int_0^l p_g(x, t) \phi_{ki} dx = -K_g(t) \left\{ \frac{e(\bar{x}) \phi_i(\bar{x})}{l} \right\}_{\bar{x}_0}^{\bar{x}_1} - \int_{\bar{x}_0}^{\bar{x}_1} e'(\bar{x}) \phi_i(\bar{x}) d\bar{x} \quad (40)$$

Modal Amplitude O.D.E.'s and Numerical Solution Process

The algebraic rearrangement of the loading functions developed in the previous section results in a system of O.D.E.'s in the amplitude vector $q_i(t)$. The general equation is

$$[M] \ddot{q}_i(t) + [C] \dot{q}_i(t) + [K] q_i(t) = \sum_{m=1}^M f_{mi}(t) \quad (41)$$

where

- [M] = inertia matrix of order I
- [C] = Coriolis matrix of order I
- [K] = stiffness matrix of order I
- $f_{mi}(t)$ = i-th mode; m-th load driving force

The three matrices are fully populated unlike the case of a discrete spring, mass, and damper system in which the inertia matrix is diagonal. For the case concerning gun/beam dynamics, the projectile and stationary non-structural masses cause coupling between mode shapes showing up as off-diagonal

terms in the inertia matrix. The Coriolis matrix is appropriately named because its only contributing load is due to the moving projectile travelling along a moving path created by the vibrating tube. A Coriolis force component results from this interaction. Modal coupling is a characteristic of this load, therefore, matrix $[C]$ is fully populated. The stiffness matrix $[K]$ contains the natural vibration frequencies (ω_i) along the main diagonal as well as other contributions from recoil inertia, pressure curvature, and projectile trajectory forces. Inclusion of these terms causes the matrix to be fully populated.

The forcing functions on the right side of the equation are all time-dependent in that the ballistic force, recoil inertia, or projectile location and kinematic state is needed for their evaluation. The static slope is required for recoil inertia load evaluation, whereas curvature is needed in the pressure curvature and projectile trajectory loads. Point loads such as those due to projectile location travel along the structure, while those due to the stationary masses are fixed in the spatial coordinate. The support reactions require an evaluation of the total deflection of the tube at their fixed locations with the reaction force being a function of the total displacement.

From a solution standpoint, the problem is quite complex mainly due to the inertia coupling. In order to solve the system of equations using numerical procedures, the matrix $[M]$ must be triangularized by an elimination process (Gauss) with back substitution performed to arrive at a solution to the modal acceleration vector $\ddot{q}_i(t)$. Upon rearrangement of Eq. (41) and introducing a discrete time step yields

$$[M]\ddot{q}_i(t_n) = \sum_{m=1}^M f_{mi}(t_n) - [C]\dot{q}_i(t_n) - [K]q_i(t_n) \quad (42)$$

where t_n is any integration time. Initially,

$$t_0 = 0 \quad \text{and} \quad \dot{q}_i(t_0) = q_i(t_0) = 0 \quad (43)$$

These conditions allow for the startup of the solution process. Equation (42) is solved for $\ddot{q}_i(t_n)$ by back substitution into the triangularized inertia matrix. The resultant acceleration vector is integrated to yield the velocity, and finally the modal displacement vectors.

A predictor-corrector technique, based upon the Adams-Bashforth-Moulton multi-step formulation [24] adapted for systems of equations, was the algorithm chosen for the integration process. A fixed time-step with convergence control and limited iteration steps is provided by the user through computer input files. This multi-step method needs four starting values of the function being integrated. These values are generated by using a Taylor series approximation to the solution equation through the four initial time-steps. The predictor portion provides an initial solution for the modal velocity and displacement amplitudes by using an integrating algorithm based upon the Adams-Bashforth

GAST

Four-Step Method. This is an explicit method requiring function evaluations from four preceding time steps. The solution predicted is used in the corrector portion of the algorithm which is an implicit technique known as the Adams-Moulton Three-Step Method. Iterations on the approximate solution vector continue until convergence is assured based upon criterion supplied by the user. If the criterion cannot be met in the maximum number of iteration steps, the computer routines report this occurrence allowing for user intervention. Additionally, an error estimate including the number of iterations attempted is available as output for each integration step. This is useful for determining a suitable time step for a given analysis.

RESULTS AND DISCUSSION

At the time of this writing, these modelling routines were being debugged and tested against the predictions from standard solutions and other independent analyses. Subsequently, this modelling will be compared with experimental data (both field and laboratory generated) to identify any inherent shortcomings. Parametric studies addressing the projectile's exit vector (see Figure 7, Reference 1) and its sensitivity to perturbations in the design and operational parameters of fielded weapons will follow. Due to length constraints placed upon this paper, none of these will be reported, rather a verbal presentation will be given at the Symposium.

REFERENCES

1. Sneck, H. J. and Gast, R. G., "Normal Modes Analysis of Gun Tube Dynamics," Proceedings of the Fourth U. S. Army Symposium on Gun Dynamics, ARLCB-SP-85009, Vol. I, Benet Weapons Laboratory, Watervliet, NY, 7-9 May 1985, pp. I-22-I-50.
2. Thomson, W. T., Vibration Theory and Applications, Prentice Hall, Englewood Cliffs, NJ, 1965.
3. Timoshenko, S., Young, D. H., and Weaver, W. Jr., Vibration Problems in Engineering, 4th Edition, John Wiley and Sons, New York, 1974.
4. Bozich, W. F., "Transverse Vibration of Nonuniform Free-Free Beams," Masters Thesis, Air Force Institute of Technology, Wright-Patterson Air Force Base, Ohio, 1962.
5. Dolph, C. L., "On the Timoshenko Theory of Transverse Beam Vibrations," Transactions of the ASME, Vol. XII, No. 2, 1953, pp. 175-187.
6. Leibowitz, R. C., and Kennard, E. H., "Shear and Rotatory Inertia Effects on Beam Vibrations," Rep. 1822, David Taylor Model Basin, Washington D.C., July 1964.
7. Kruzlewski, T. T., "Effect of Transverse Shear and Rotatory Inertia on the Natural Frequencies of a Uniform Beam," NACA Tech Note 1909, Washington D.C., 1949.
8. Conte, S. C., Elementary Numerical Analysis, McGraw-Hill, New York, 1965.

GAST

9. Wang, H-C., "Generalized Hypergeometric Function Solutions on the Transverse Vibration of a Class of Nonuniform Beams," Journal of Applied Mechanics, September 1967, pp. 702-708.
10. Wang, J. T. S., "Dynamic Analysis of Cantilevered Beams," Pressure Vessels and Piping Division of the ASME, June 1979, 79-PVP-87.
11. Lau, J. H., "Vibration Frequencies for a Nonuniform Beam With End Mass," Journal of Sound and Vibration, Vol. 97, No. 3, 1984, pp. 513-521.
12. Goel, R. P., "Transverse Vibrations of Tapered Beams," Journal of Sound and Vibration, Vol. 47, No. 1, 1976, pp. 1-7.
13. Conway, H. D., Becker, E. C. H., and Dubil, J. F., "Vibration Frequencies of Tapered Bars and Circular Plates," Journal of Applied Mechanics, Vol. 31, No. 2, 1964, pp. 329-331.
14. Klein, L., "Transverse Vibrations of Nonuniform Beams," Journal of Sound and Vibration, Vol. 37, No. 4, 1974, pp. 491-505.
15. Mittendorf, S. C., and Greif, R., "Vibrations of Segmented Beams by a Fourier Series Component Mode Method," Journal of Sound and Vibration, Vol. 55, No. 3, 1977, pp. 431-441.
16. Resende, L., and Doyle, W. S., "A Variable Cross-Section 3-D Beam Finite Element for Static and Free Vibration Analysis," Technical Report 806S, Department of Civil Engineering, University of Capetown, South Africa, 1980.
17. Sneek, H. J., Professor, "Two Element Stepped Model," Unpublished notes, 10 pages, Mechanical Engineering Department, Rensselaer Polytechnic Institute, Troy, NY, May 1985.
18. Hibbitt, Karlsson & Sorenson, Inc., "ABAQUS Users Manual Version 4.5(a)," July 1985.
19. Elder, A. J., "Historical Review and Survey of Current Problems in Weapon Dynamics," Proceedings of Dynamics of Precision Weapons, 1977, pp. 1-26.
20. Simkins, T. E., "Transverse Response of Gun Tubes to Curvature Induced Load Functions," Proceedings of the Second U. S. Army Symposium on Gun Dynamics, ARLCB-SP-78013, Benet Weapons Laboratory, Watervliet, NY, 19-22 September 1978, Section I, pp. 66-77.
21. Warken, D., Wolf, K., Heiser, R., and Ballman, J. "The Effect of Barrel Curvature and Projectile Imbalance on Excitation of Gun Vibration," Proceedings of the Third US Army Symposium on Gun Dynamics, ARLCB-SP-82005, Benet Weapons Laboratory, Watervliet, NY, Vol. II, 11-14 May 1982, pp. III-43-III-63.
22. Hall, A. S., Holowenko, A. R., Loughlin, H. G., Theory and Problems of Machine Design, Schaum Publishing Co., New York, 1961, pp. 43-45.

GAST

23. Wu, J. J., "On the Dynamic Forces in Gun Tube Motions Analysis,"
Proceedings of the Third US Army Symposium on Gun Dynamics, ARLCB-SP-82005,
Benet Weapons Laboratory, Watervliet, NY, Vol. II, 11-14 May 1982, p.
III-85.
24. Burden, R. L., Faires, J. D., Reynolds, A. C., Numerical Analysis, Second
Edition, Prindle, Weber, and Schmidt, Boston, MA, 1981.

O'HARA

TITLE: USER EXPERIENCE WITH ABAQUS AT BENET LABORATORIES
G.P. O'HARA
US ARMY ARMAMENT RESEARCH, DEVELOPMENT, AND ENGINEERING CENTER
CLOSE COMBAT ARMAMENTS CENTER
BENET LABORATORIES
WATERVLIET, NY 12189-4050

ABSTRACT

After many years of experience with linear finite element programs, it became apparent that the demands of the design sections would soon require the regular use of non-linear analysis. As a point of fact, some non-linear work had been in progress for a number of years using slightly modified linear codes, research codes, and manual iteration. All of these are rather unsatisfactory in a production design environment. Therefore, a search was undertaken to find a suitable general purpose non-linear finite element code, which ended in the selection of ABAQUS. The code will perform static, dynamic, and thermal analysis on a broad range of structures using an excellent selection of materials. The analysis can include geometric non-linearities such as large deformations and contact surfaces. All this is controlled by a data structure that is simple and easy for the user to set up and read. As a further aid to the user, many of the functions of the analysis may be performed by a user supplied FORTRAN subroutine which is automatically linked to the code and supplements the standard ABAQUS libraries.

In the first three years of use at Benet Labs, ABAQUS has virtually replaced all other codes for routine design analysis of cannon structures. The applications have ranged from simple linear analysis of two-dimensional structures to complex three-dimensional structures. The work done in dynamic analysis of cannon tubes is of particular interest to this Symposium.

This paper was not available for printing in this publication. Every effort will be made to include this paper in a supplement at a later date.

COX AND POLCYN

TITLE: ADAPTING COSMIC NASTRAN TO GUN DYNAMICS PROBLEMS
P.A. COX AND M.A. POLCYN
SOUTHWEST RESEARCH INSTITUTE
SAN ANTONIO, TX 78284

ABSTRACT

Modifications have been made to COSMIC NASTRAN to make it more suitable for gun dynamics type problems. The approach taken was to provide for the computation, by NASTRAN, of the interior ballistics and tube-support interactions. The calculations are made based on input of the projectile parameters, breech pressure, projectile axial motions and the tube support parameters. Another goal of the program modifications was to provide, in a single NASTRAN module, all of the variables necessary for the calculation of the interior ballistics parameters. This will allow other users an opportunity to write and program their own gun dynamics forces with a minimum of DMAP alters.

The modifications were accomplished through the use of the DUMMOD provision in NASTRAN and DMAP alters. In all three DUMMODS were used. Two were used to collect and format all of the input and internal data which is necessary for calculating the gun dynamics forces. This data is then passed to a third DUMMOD which was written to replace the TRD (transient displacement) module. The "new" TRD module is very similar to the original module except that calculation of the nonlinear gun dynamics forces has been added. Features of the modified version of COSMIC NASTRAN include:

- structured input provisions for all input parameters which are unique to the gun dynamics calculations
- calculation of the tube-support interaction forces with provisions for clearances and friction
- calculation of the tube-projectile interaction forces (lateral forces, friction force and moments) for the assumption of point contact
- calculation of the Bourdon force
- calculation of the moments on the tube produced by axial accelerations coupled with lateral displacements

The NASTRAN changes and instructions for use of the modified code are documented in a final report.

This paper was not available for printing in this publication. Every effort will be made to include this paper in a supplement at a later date.

**TITLE: A SIMPLE THEORETICAL MODEL FOR PROJECTILE
 IN-BORE MOTION OF ELECTROMAGNETIC RAILGUNS
 SZU HSIUNG CHU**

**US Army Armament Research, Development and
Engineering Center
Picatinny Arsenal, Dover, New Jersey, 07801**

ABSTRACT:

The projectile in-bore motion of an electromagnetic railgun is different from that of a conventional gun. It is difficult to find a proper friction formulation. At present there are two popular models, namely the ideal and the friction correction models. The former ignores the friction and the latter uses an empirical correction factor to account for the friction effect. This report presents a simple theoretical approach to formulate the problem according to the principles of elasticity, solid mechanics, gasdynamics and hydromechanics. The resulted equations define the friction correction factor mathematically and they are used to predict the effects of many parameters such as the various material properties and the physical dimensions.

BIOGRAPHY:

PRESENT ASSIGNMENT: Mechanical Engineer, Electromagnetic Armament Technology Branch, Artillery Armaments Division, Fire Support Armament Center. U. S. Army Armament Research, Development and Engineering Center.

PAST EXPERIENCE: Research studies in applied mechanics related to the analysis of complex gun and ammunition dynamics since joining ARDEC in 1967.

DEGREES HELD: B. S. in Aeronautical Engineering, National Chiao-Tung University, Republic of China; M.S. in Applied Mechanics, Kansas State University; Ph.D. in Applied Mechanics, Polytechnic Institute of Brooklyn, New York.

A SIMPLE THEORETICAL MODEL FOR PROJECTILE IN-BORE MOTION OF ELECTROMAGNETIC RAILGUNS

SZU HSIUNG CHU

US Army Armament Research, Development and
Engineering Center

Picatinny Arsenal, Dover, New Jersey, 07801

INTRODUCTION

The projectile in the electromagnetic railgun has a completely different environment to that of a conventional gun. The projectile together with the armature is accelerated by the Lorentz force. It is under the influences of high current, high pressure, high temperature and high velocity. Consequently the friction forces are results of these effects, and a new approach must be used to compute the projectile in-bore motion.

Though the basic principle used to formulate the projectile motion is the same Newton's second law of motion, yet there are many different equations of motion formulated depending upon the model of defining the friction forces. This report first presents the popular state of art models of analysis, and then a simple model based on the accelerating conditions with the principles of elasticity, solid mechanics, gasdynamics and hydrodynamics. From the resulting equations effects of various parameters are discussed. A friction correction factor is derived from this formulation.

This report considers only the railguns with arc armatures. The cross-section of the projectile is either a square or rectangle. Other types of electromagnetic guns and projectiles will be investigated later.

BASIC EQUATION

The in-bore projectile motion equations are derived from Newton's second law of motion:

$$ma = F_p - f \quad (1)$$

where m = total mass of projectile and armature

a = projectile acceleration

F_p = accelerating force

f = friction force

The generally used formulation of the accelerating force for the arc armatures of electromagnetic guns is [1,2]

$$F_p = \frac{L' I^2}{2} \quad (2)$$

where L' = rail inductance per unit length
 I = rail current

The friction force is the problem area of the analysis. No suitable formulation has been found. The following two state-of-art models are the results of different methods of handling the friction.

STATE OF ART

At present, there are two models used to formulate the in-bore motion of the railgun projectile, which have been published [1,2]. These methods are as follows:

1. IDEAL MODEL

This model ignores the effect of friction. Consequently the equation of motion is

$$m a = \frac{L' I^2}{2} \quad (3)$$

The computed result using this model shows a large computation-test disagreement with the computed values larger than the measured data.

2. FRICTION CORRECTION MODEL

From the comparison of computations of the ideal model and the test data it is seen that the friction effect is equivalent to 20 to 40 percent of the accelerating force [1,2]. This may be expressed in the equation

$$f = C F_p \quad (4)$$

where C = friction correction factor
 = 20 to 40 percent

This model uses this friction expression, and the equation of motion becomes

$$ma = (1 - C) F_p \quad (5)$$

It has the advantage of reducing the computation-test disagreement as compared to the ideal model. However, the agreement will depend on which correction factor is selected, or in other words, the experience of the investigator.

NEW FORMULATION

A simple formulation is performed based on the considerations of elasticity, solid mechanics, gastrodynamics and hydromechanics. The forces acting on the projectile are the accelerating force on the rear surface, air resistance on the front surface, gravity at c. g. of element, normal pressure and friction force on the top, bottom and side surfaces, and the D'Alembert's force distributed on the projectile mass. The axial forces acting on the projectile are shown in Fig. 1. Consequently the equation of motion of the armature and the projectile is of the form:

$$m a = F_p - f_t - f_b - 2f_s - f_a \quad (6)a$$

where f_t = friction force on top surface of projectile
 f_b = friction force on bottom surface of projectile
 f_s = friction force on lateral surface of projectile
 f_a = air resistance in front of the projectile

The friction force of the arc armature is rather small and ignored in the formulation. For the projectile only, the equation of motion is

$$m_p a = F_{pj} - f_t - f_b - 2f_s - f_a \quad (6)b$$

where m_p = mass of the projectile
 F_{pj} = accelerating force at the rear side of the projectile

From Eqs. (6)a and (6)b, the projectile accelerating force is

$$F_{pj} = F_p - (m - m_p) a \quad (7)$$

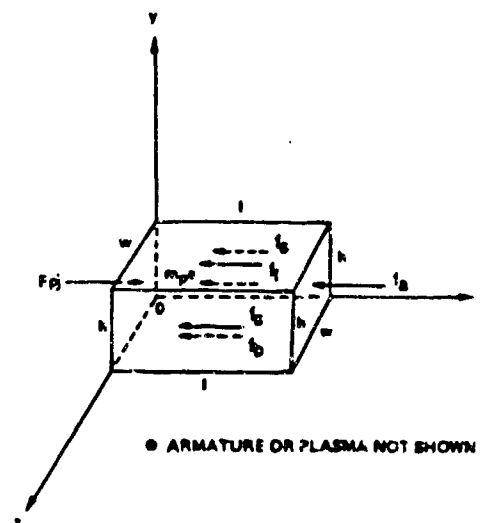


Figure 1 **Axial Forces on Projectile**

APPLIED FORCES

The various forces in Eq. (6)a are formulated as follows.

1 ACCELERATING FORCE, F_p

The generally accepted formulation of F_p is again used in the new formulation, namely

$$F_p = \frac{L' l^2}{2} \quad (2)$$

However, it may be modified when other methods of force formulations are available.

2 AIR RESISTANCE, f_a

The air resistance is exerted on the projectile when air is presented in the barrel. An equation similar to the aerodynamic drag is used to express this force. This equation is

$$f_a = \frac{1}{2} C_d \rho_a w h V^2 \quad (8)$$

where ρ_a = mass density of air
 h = height of cross-section of projectile
 w = width of cross-section of projectile
 V = projectile velocity
 C_d = drag coefficient.

3 FRICTION FORCES, f_t , f_b and f_s

The top and side surface friction forces are zero when there are clearances between the barrel and the projectile. This occurs at the time of starting launching and a short time after that. As the projectile accelerates rapidly the expansion of projectile will eliminate these clearances and the friction forces occur. Therefore

$$f_t = 0 \quad t < t_{ft} \quad (9a)$$

$$f_s = 0 \quad t < t_{fs} \quad (9b)$$

where t = time counted from start of launching
 t_{ft} = time when f_t friction force occurs
 t_{fs} = time when f_s friction force occurs

The values of t_{ft} and t_{fs} will be different for different clearances in vertical and horizontal directions. To simplify the analysis they are considered to be equal and denoted by t_f .

The friction force on the bottom surface is not zero when $t < t_f$, since the weight of the projectile always generates the friction force computed by the equation:

$$f_b = \mu_y m_p g \quad t < t_f \quad (10)$$

where μ_y = friction coefficient at y plane
 $m_p g$ = total weight of projectile

This friction force is the difference of the friction forces on the upper and the bottom surfaces. In other words, the friction force on the bottom surface is

$$f_b = f_t + \mu_y m_p g \quad (11)$$

When $t \geq t_f$ other friction forces occur. They are computed from the following formulations.

The computation is based on the assumption that the deformation and stress distribution across the projectile cross-section are uniform, and the plane surface remains plane.

First, the axial pressure per unit area at any cross-section location x of projectile is computed. Similar to the general hydrostatic formulation, the pressure gradient generated by the D'Alembert force due to the acceleration of projectile is computed with the equation,

$$dp_x = -\rho dx \quad (12)$$

where dp_x = x plane pressure gradient
 dx = x gradient
 ρ = mass density of projectile

Integrating from $x = 0$ to x , the pressure becomes

$$p_x = -\frac{F_{pj}}{hw} + \rho ax \quad (13)$$

where p_x = x plane pressure per unit area at location x .

The minus sign before F_{pj} is used to denote compression. The boundary condition

$$x = 0, \quad p_x = -\frac{F_{pj}}{hw} \quad (14)$$

has been used in Eq. (13).

According to the principle of elasticity, the strains and the stresses on a unit volume element are related by these equations :

$$\epsilon_x = \frac{1}{E} [p_x - \nu (p_y + p_z)] \quad (15a)$$

$$\epsilon_y = \frac{1}{E} [p_y - \nu (p_z + p_x)] \quad (15b)$$

$$\epsilon_z = \frac{1}{E} [p_z - \nu (p_x + p_y)] \quad (15)c$$

where $\epsilon_x, \epsilon_y, \epsilon_z$ = unit strain along x, y, z direction
 E = Young's modulus
 ν = Poisson's ratio
 p_y, p_z = unit area pressure on y, z plane

At the start of launching, there are clearances c_y and c_z between the projectile and the barrel in vertical and horizontal directions respectively. Therefore p_y and p_z are zero as mentioned before. The strains become

$$\epsilon_x = \frac{p_x}{E} \quad (16)a$$

$$\epsilon_y = -\frac{\nu p_x}{E} \quad (16)b$$

$$\epsilon_z = -\frac{\nu p_x}{E} \quad (16)c$$

The p_y and p_z are not zero when the ϵ_y or ϵ_z is larger than the clearance c_y or c_z per unit height or width of projectile. In other words, when the time t is larger than t_f . The axial pressure p_{xf} at time t_f is computed from either of the following equations:

$$\frac{c_y}{h} = -\frac{\nu p_{xf}}{E} \quad (17)a$$

$$\frac{c_z}{w} = -\frac{\nu p_{xf}}{E} \quad (17)b$$

where p_{xf} is the minimum axial pressure when friction force f_t or f_s occurs. Since the p_x is related to the time t , the t_f may be determined in turn.

When the p_y and p_z pressure occur, the rail or the barrel wall is also compressed by these pressures. Assuming the spring coefficients are known, then the deformations δ_y and δ_z in the y and z direction respectively may be computed as

$$\delta_y = - \frac{p_y}{k_y} \quad (18)a$$

$$\delta_z = - \frac{p_z}{k_z} \quad (18)b$$

where δ_y = y direction deformation of rail

δ_z = z direction deformation of barrel wall

k_y = y direction spring constant for per unit area of contact

k_z = z direction spring constant for per unit area of contact

The minus signs denote that the directions of the pressure and the deformation are opposite.

The strain of the projectile in the y and z direction will be the sum of the respective initial clearance and two times the deformation of the barrel (upper and bottom or two sides) per unit of projectile height or width. With this consideration, Eq. (15) becomes

$$E\epsilon_x = p_x - \nu (p_y + p_z) \quad (19)a$$

$$\frac{E(c_y + 2\delta_y)}{h} = p_y - \nu (p_z + p_x) \quad (19)b$$

$$\frac{E(c_z + 2\delta_z)}{w} = p_z - \nu (p_x + p_y) \quad (19)c$$

Substituting the deformation Eq. (18) into the second and third equations of Eq. (19), it is found that

$$\frac{E(c_y - \frac{2p_y}{k_y})}{h} = p_y - v (p_z + p_x) \quad (20)a$$

$$\frac{E(c_z - \frac{2p_z}{k_z})}{w} = p_z - v (p_x + p_y) \quad (20)b$$

Translating terms, the equations become

$$(1 + \frac{2E}{k_y h}) p_y - v p_z = \frac{Ec_y}{h} + v p_x \quad (21)a$$

$$(1 + \frac{2E}{k_z w}) p_z - v p_y = \frac{Ec_z}{w} + v p_x \quad (21)b$$

Solving these two equations for p_y and p_z , the results are

$$p_y = \frac{\frac{Ec_y}{h} (1 + \frac{2E}{k_z w}) + \frac{vEc_z}{w} + v (1 + v + \frac{2E}{k_z w}) p_x}{(1 + \frac{2E}{k_y h}) (1 + \frac{2E}{k_z w}) - v^2} \quad (22)a$$

$$p_z = \frac{\frac{Ec_z}{w} (1 + \frac{2E}{k_y h}) + \frac{vEc_y}{h} + v (1 + v + \frac{2E}{k_y h}) p_x}{(1 + \frac{2E}{k_y h}) (1 + \frac{2E}{k_z w}) - v^2} \quad (22)b$$

The friction force is the product of the normal pressure and the friction coefficient. For the whole surface on the top and side of the projectile respectively the total friction is computed by integrating the unit area friction force on the whole surface. This procedure results in the following equations:

$$\begin{aligned}
 f_t &= - \int_0^l \mu_y w p_y dx \\
 &= - \frac{\mu_y w l \left[\frac{E c_y}{h} \left(1 + \frac{2E}{k_z w} \right) + \frac{v E c_z}{w} - v \left(1 + v + \frac{2E}{k_z w} \right) \left(\frac{F_{pj}}{wh} - \frac{\rho a l}{2} \right) \right]}{\left(1 + \frac{2E}{k_y h} \right) \left(1 + \frac{2E}{k_z w} \right) - v^2} \quad (23)a
 \end{aligned}$$

$$\begin{aligned}
 f_s &= - \int_0^l \mu_z h p_z dx \\
 &= - \frac{\mu_z h l \left[-\frac{E c_z}{w} \left(1 + \frac{2E}{k_y h} \right) + \frac{v E c_y}{h} - v \left(1 + v + \frac{2E}{k_y h} \right) \left(\frac{F_{pj}}{wh} - \frac{\rho a l}{2} \right) \right]}{\left(1 + \frac{2E}{k_y h} \right) \left(1 + \frac{2E}{k_z w} \right) - v^2} \quad (23)b
 \end{aligned}$$

where the minus sign is used for compression pressure, μ_z is the friction coefficient for side surface and l is the length of projectile.

Having f_t determined, the friction force on the bottom surface, f_b , is computed with Eq. (11).

EQUATION OF MOTION

When $p_x < p_{xf}$ or $t < t_f$, all friction forces except that generated from gravity are zero. Substituting all forces into Eq. (6)a, the equation of motion is

$$ma = F_p - \mu_y m_p g - \frac{1}{2} C_d \rho_a w h V^2 \quad (24)$$

When $p_x \geq p_{xf}$ or $t \geq t_f$, all friction forces are present. Substituting all forces into Eq. (6)a and collecting terms, the equation of motion then becomes

$$\begin{aligned}
 & ma \left[\left(1 + \frac{2E}{k_y h}\right) \left(1 + \frac{2E}{k_z w}\right) - v^2 \right] \\
 &= \left[\left(1 + \frac{2E}{k_y h}\right) \left(1 + \frac{2E}{k_z w}\right) - v^2 \right] F_p - 2vl \left[\frac{\mu_y}{h} \left(1 + v + \frac{2E}{k_z w}\right) + \frac{\mu_z}{w} \left(1 + v + \frac{2E}{k_y h}\right) \right] F_{pj} \\
 &+ 2EI \left[\frac{\mu_y}{h} \left(w + \frac{2E}{k_z}\right) + \mu_z v \right] c_y + 2EI \left[\frac{\mu_z}{w} \left(h + \frac{2E}{k_y}\right) + \mu_y v \right] c_z \\
 &+ \rho v l^2 \left[\mu_y w \left(1 + v + \frac{2E}{k_z w}\right) + \mu_z h \left(1 + v + \frac{2E}{k_y h}\right) \right] a \\
 &- \left[\left(1 + \frac{2E}{k_y h}\right) \left(1 + \frac{2E}{k_z w}\right) - v^2 \right] \left(\mu_y m_p g + \frac{1}{2} C_d \rho_a w h V^2 \right) \quad (25)
 \end{aligned}$$

Defining the ratio of mass of the projectile to the total mass of the armature and the projectile to be

$$R_m = \frac{m_p}{m} \quad (26)$$

and computing the projectile mass from the equation,

$$m_p = \rho w h l \quad (27)$$

the product ρl may be expressed by the equation,

$$\rho l = \frac{R_m m}{w h} \quad (28)$$

Substituting Eqs. (7), (26), (27) and (28) into Eq. (25) and rearrange terms, the equation of motion then becomes

$$\begin{aligned}
& ma\left\{\left(1+\frac{2E}{k_y h}\right)\left(1+\frac{2E}{k_z w}\right)-v^2-vl(2-R_m)\left[\frac{\mu_y}{h}\left(1+v+\frac{2E}{k_z w}\right)+\frac{\mu_z}{w}\left(1+v+\frac{2E}{k_y h}\right)\right]\right\} \\
& = \left\{\left(1+\frac{2E}{k_y h}\right)\left(1+\frac{2E}{k_z w}\right)-v^2-2vl\left[\frac{\mu_y}{h}\left(1+v+\frac{2E}{k_z w}\right)+\frac{\mu_z}{w}\left(1+v+\frac{2E}{k_y h}\right)\right]\right\} F_p \\
& \quad + 2EI\left[\frac{\mu_y}{h}\left(w+\frac{2E}{k_z}\right)+\mu_z v\right] c_y + 2EI\left[\frac{\mu_z}{w}\left(h+\frac{2E}{k_y}\right)+\mu_y v\right] c_z \\
& \quad - \left[\left(1+\frac{2E}{k_y h}\right)\left(1+\frac{2E}{k_z w}\right)-v^2\right]\left(\mu_y m_p g + \frac{1}{2} C_d \rho_a w h V^2\right) \quad (29)
\end{aligned}$$

With the acceleration of the projectile computed from Eq. (29), the velocity and the travel of the projectile are calculated by integrating it successively with respect to time.

FRICTION CORRECTION FACTOR

In general the clearances are zero and the barrel is evacuated. Therefore, the forces due to clearances and air resistance may be ignored. The friction force due to the gravity is rather small in comparison to the accelerating force and therefore it may also be discarded when an approximate solution is desired. With these considerations the equation of motion is reduced to the following form,

$$\begin{aligned}
& ma\left\{\left(1+\frac{2E}{k_y h}\right)\left(1+\frac{2E}{k_z w}\right)-v^2-vl(2-R_m)\left[\frac{\mu_y}{h}\left(1+v+\frac{2E}{k_z w}\right)+\frac{\mu_z}{w}\left(1+v+\frac{2E}{k_y h}\right)\right]\right\} \\
& = \left\{\left(1+\frac{2E}{k_y h}\right)\left(1+\frac{2E}{k_z w}\right)-v^2-2vl\left[\frac{\mu_y}{h}\left(1+v+\frac{2E}{k_z w}\right)+\frac{\mu_z}{w}\left(1+v+\frac{2E}{k_y h}\right)\right]\right\} F_p \quad (30)
\end{aligned}$$

This equation may be reduced to the same form of Eq. (5) of the friction correction model. The resulting friction correction factor is

$$C = \frac{v l R_m \left[\frac{\mu_y}{h} \left(1 + v + \frac{2E}{k_z w} \right) + \frac{\mu_z}{w} \left(1 + v + \frac{2E}{k_y h} \right) \right]}{\left(1 + \frac{2E}{k_y h} \right) \left(1 + \frac{2E}{k_z w} \right) - v^2 - v l (2 - R_m) \left[\frac{\mu_y}{h} \left(1 + v + \frac{2E}{k_z w} \right) + \frac{\mu_z}{w} \left(1 + v + \frac{2E}{k_y h} \right) \right]} \quad (31)$$

Note that C is no more an empirical factor and it may be computed using data of material properties and physical dimensions. This equation is so important that it reveals many characteristics of the projectile. It is discussed later.

EXAMPLES OF COMPUTATION

It is rather easy to use the equations of motion for computation. The acceleration is computed by substituting the required data. Then the velocity and displacement may be obtained by integrating with respect to time. Hence, examples of computation of acceleration, velocity and displacement are not presented here. However, the friction correction factor for a cube projectile is computed with variations of mass ratio, Poisson's ratio and the average friction coefficient according to a simplified equation discussed in the next section. The maximum average friction coefficients for different Poisson's ratios are also computed. The results of computations are shown in figures mentioned in the following section.

DISCUSSIONS

The effects of many parameters may be seen clearly from the equations of motion and the friction correction factor. The accelerating forces and the total mass of the armature and the projectile are all the same in the following discussions to simplify the presentation.

In general the air resistance, the gravity force, the barrel-projectile clearance and the deformation of rails are rather small. Consequently they may be ignored and the equation of the friction correction factor is simplified to

$$C = \frac{v l R_m \left(\frac{\mu_y}{h} + \frac{\mu_z}{w} \right)}{1 - v - v l (2 - R_m) \left(\frac{\mu_y}{h} + \frac{\mu_z}{w} \right)} \quad (32)$$

From this equation it is seen that when the projectile length, the friction coefficient, the projectile mass ratio or the Poisson's ratio is increased, the numerator increases and the denominator decreases or increases much less. Therefore, C is increased. Figs. (2) to (7) indicate the effects of the mass ratio, Poisson's ratio and the friction coefficient on the friction correction factor.

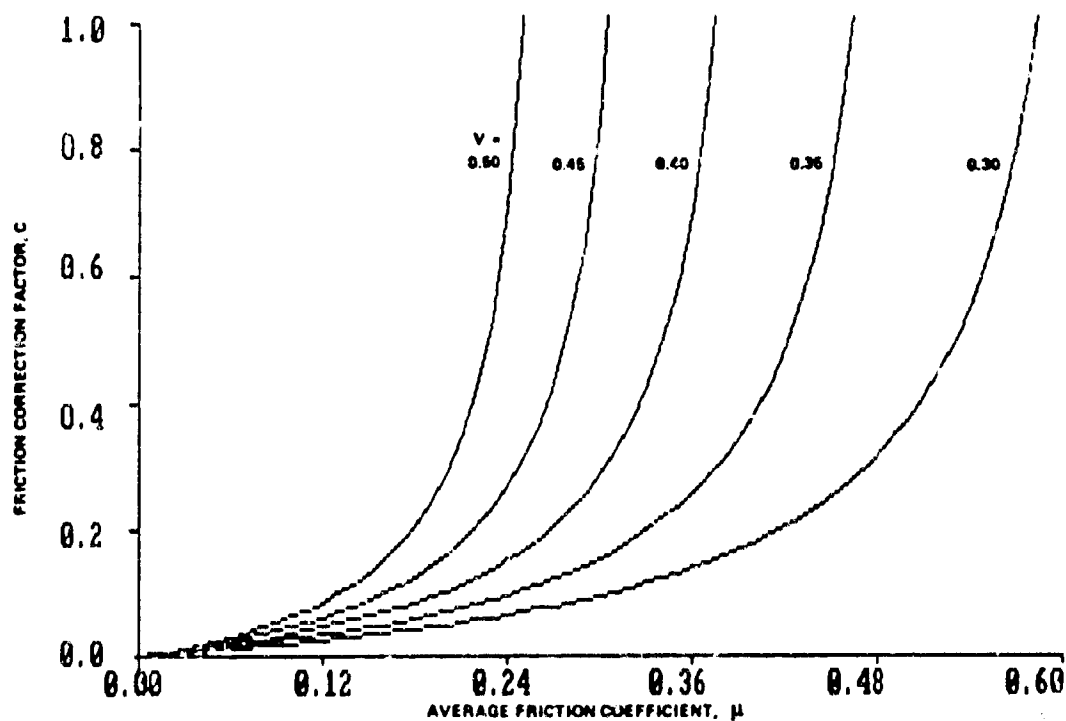


Figure 2 Friction Correction Factor vs Friction Coefficient for Cube Projectile
 $R_m = 0.20$

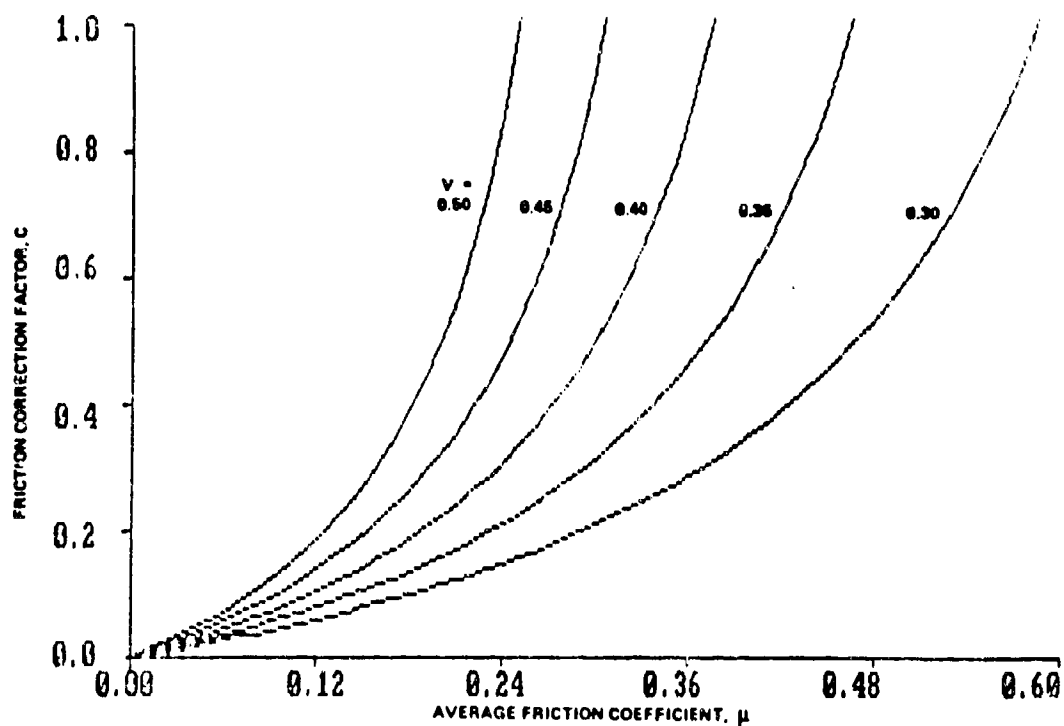


Figure 3 Friction Correction Factor vs Friction Coefficient for Cube Projectile
 $Re = 0.50$

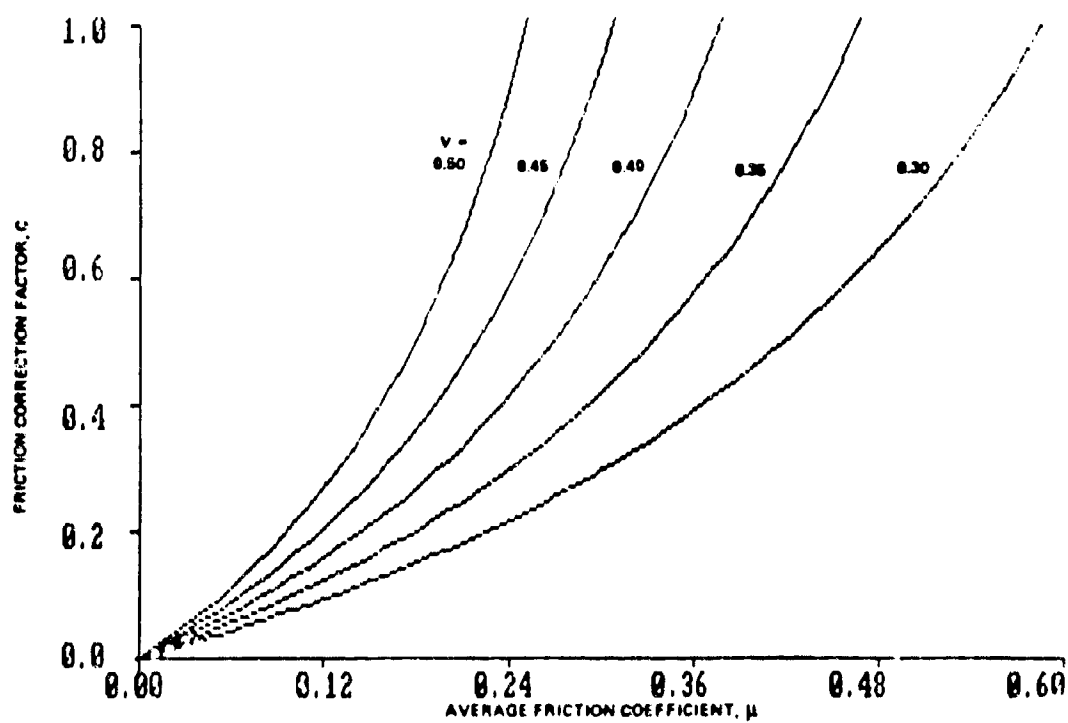


Figure 4 Friction Correction Factor vs Friction Coefficient for Cube Projectile
 $Re = 0.80$

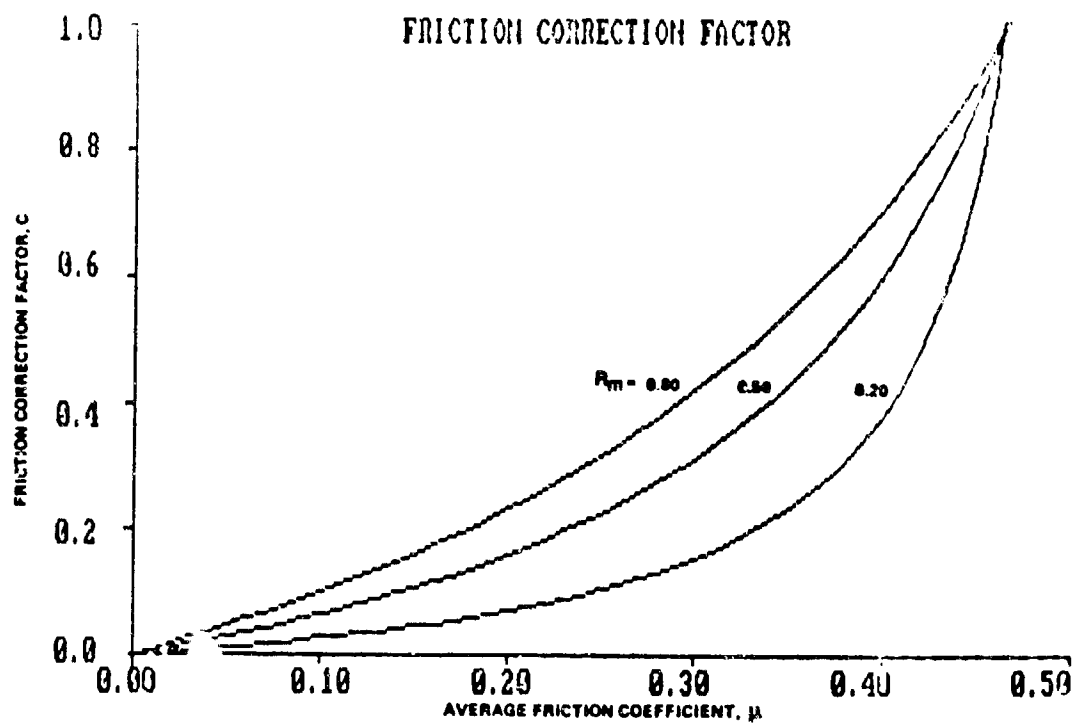


Figure 5 Friction Correction Factor vs Friction Coefficient for Cube Projectile
 $V = 0.35$

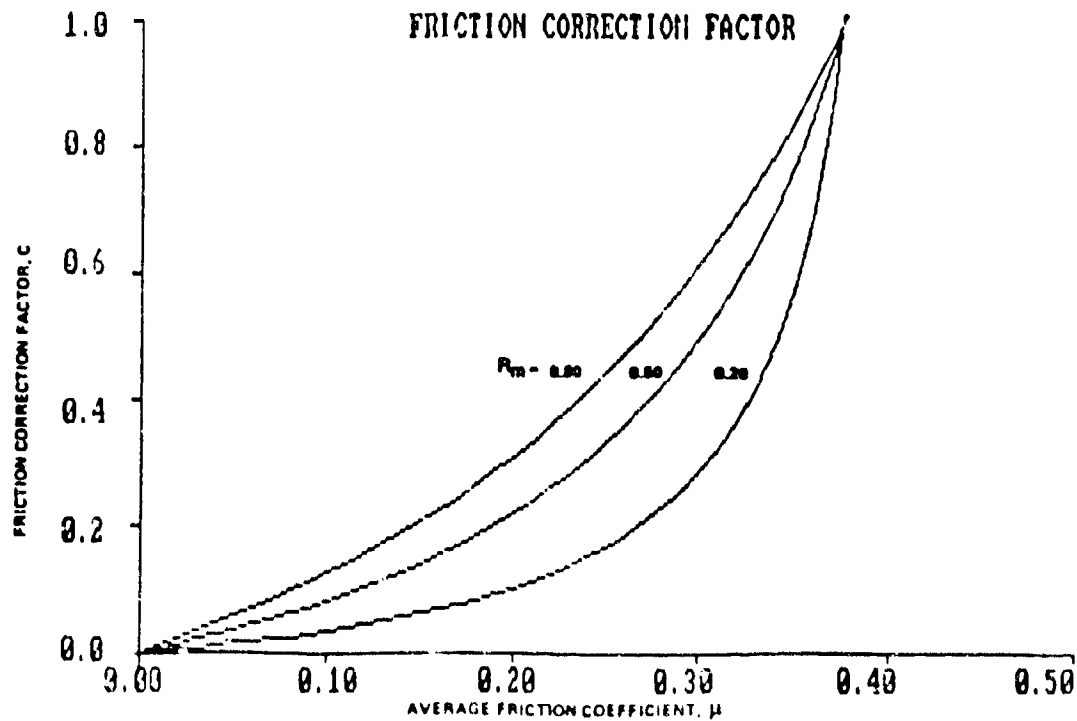


Figure 6 Friction Correction Factor vs Friction Coefficient for Cube Projectile
 $V = 0.40$

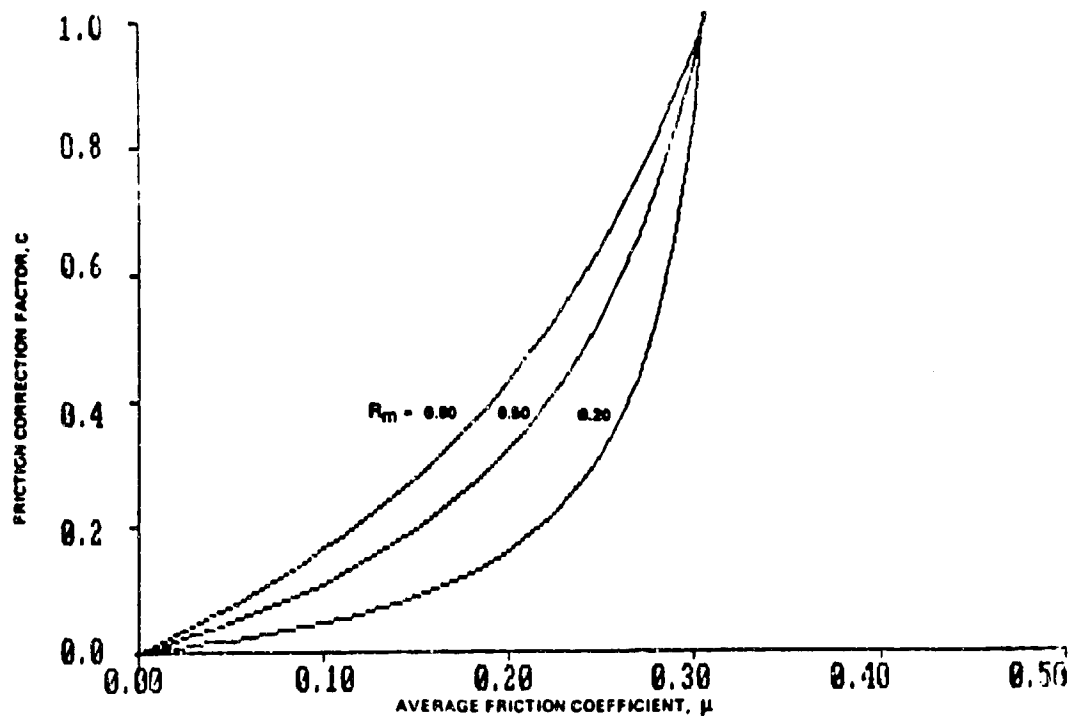


Figure 7 Friction Correction Factor vs Friction Coefficient for Cube Projectile

$$V = 0.45$$

The term $(\mu_y/h + \mu_z/w)$ has the similar effect as the length l , since it has the same effect in the equation. For a constant cross-sectional area of projectile, it is obtained from the calculus that for minimum C the height and the width ratio is

$$\frac{h}{w} = \frac{\mu_y}{\mu_z} \quad (33)$$

Since μ_y denotes the friction coefficient on the y surface with side w and μ_z on the z surface with side h , this means that h and w are inversely proportional to the friction coefficients of corresponding sides. It shows that a projectile with such h/w ratio will reduce the friction correction factor properly to generate larger acceleration. The square cross-section is good or more efficient only when the two friction coefficients are equal.

From Eq. (32) it is also seen that the ratios l/h and l/w instead of h or w plays an important effect, that is, the friction correction factor is the same for the same l/h and l/w ratios. This means that it depends on the shape and not on the size of the projectile.

To see the effects of material property more clearly a cube projectile is assumed to be examined. This means that the length, height and width are equal and the friction correction equation reduced to

$$C = \frac{v R_m (\mu_y + \mu_z)}{1 - v - v (2 - R_m) (\mu_y + \mu_z)} \quad (34)$$

If an average friction coefficient is used, this equation may be further simplified to

$$C = \frac{2\mu v R_m}{1 - v - 2\mu v (2 - R_m)} \quad (35)$$

where $\mu = \frac{\mu_y + \mu_z}{2}$
 = average friction coefficient

The friction correction factor C must be less than one. Otherwise, there will be no acceleration since the friction force is large enough to counteract the accelerating force. From Eq.(35) the condition for C to be less than one is that the denominator must be larger than the numerator. Consequently the relationship between the friction coefficient and Poisson's ratio is

$$\frac{1 - v}{4v} > \mu \quad (36)$$

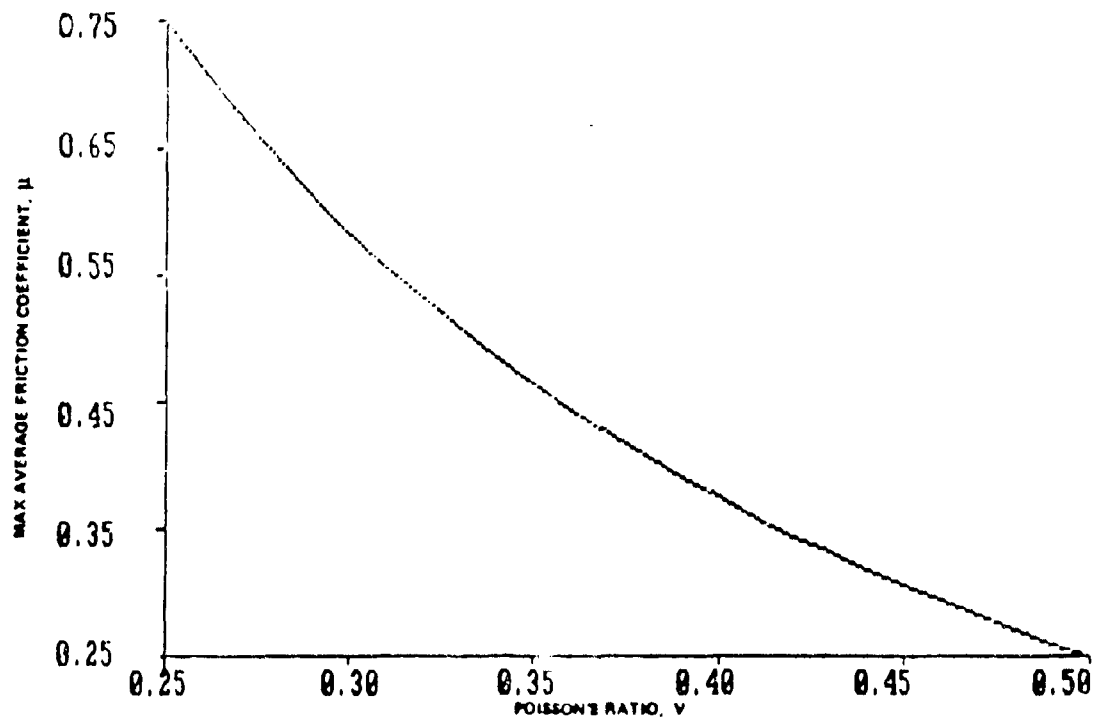


Figure 8 Max Average Friction Coefficient vs Poisson's Ratio for Cube Projectile

For example,

$$\begin{array}{ll} \text{and} & \nu = .25 \qquad \mu < .75 \\ & \nu = .5 \qquad \mu < .25 \end{array}$$

These conditions are met by ordinary materials generally used. Fig. 8 shows the μ - ν relationship for the maximum friction correction factor case.

CONCLUSION

A simple analytical tool to compute the in-bore motion of the railgun projectile has been developed. It may determine the friction correction factor according to the physical dimensions and material properties of the gun and the projectile.

From the equation of motion one learns that for a good projectile design, the length of the projectile should be as short as possible; the Poisson's ratio, friction coefficients and ratio of projectile mass to the total mass of projectile and arc armature as small as possible; and the square cross-section of the projectile is not the best section if the friction coefficients of the rail and the barrel wall are not the same. The friction correction factor depends on the shape of the projectile and is independent of the size. Materials with small Poisson's ratio and friction coefficient are desired to obtain larger acceleration of the projectile.

REFERENCES

1. Proceedings of First Symposium on Electromagnetic Launch Technology, November 4-6, 1980, San Diego, CA. pp. 3-216, IEEE Transactions on Magnetism, January 1982, Volume MAG-18, Number 1
2. Proceedings of Second Symposium on Electromagnetic Launch Technology, October 10-13, 1983, Boston MA. pp. 197-411, IEEE Transactions on Magnetism, March 1984, Volume MAG-20, Number 2

SESSION IV

EXPERIMENTS AND METROLOGY

HAUG, BORNSTEIN

TITLE: GUN DYNAMICS MEASUREMENTS FOR TANK GUN SYSTEMS
BAILEY.T. HAUG AND JONATHAN A. BORNSTEIN
U.S. ARMY BALLISTIC RESEARCH LABORATORY
ABERDEEN PROVING GROUND, MD 21005-5066

ABSTRACT:

As part of an investigation to examine the launch characteristics of tank gun systems, an extensive series of gun dynamics measurements were performed utilizing a number of overlapping experimental techniques. The methods included direct displacement measurements with optical trackers, proximity probes and coils, together with the determination of longitudinal bending strain employing standard strain gauges. The use of independent overlapping measurement techniques permitted both a comparison of experimental methods and a means for determining the accuracy of the measured displacement. As a result of initial comparisons, a technique combining measurements of tube displacement, obtained from proximity probes or coils, and longitudinal bending strain was employed for subsequent measurements.

The measurements indicated that the round to round variation of the gun tube dynamics (i.e. tube shape and muzzle crossing velocity at shot exit) for a given gun firing a particular type of projectile was small. This small variation was not necessarily mirrored by the initial yawing rates and trajectories of the projectiles indicating that the in-bore motion of projectiles may have a significant impact on the ultimate round to round dispersion.

BIOGRAPHY:

PRESENT ASSIGNMENT: Electronics Engineer, Interior Ballistics Division, Ballistic Research Laboratory, Aberdeen Proving Ground MD 21005

PAST EXPERIENCE: Thirteen years experience at the Interior Ballistics Division, BRL, in instrumentation, data acquisition and data analysis. Worked with optical measurement techniques, piezo-electric gauges for measuring pressure and acceleration, microwave interferometers and strain gauges, performing kinematic evaluations of gun system performance, tube vibration studies and numerous investigations into the performance of gun systems and projectiles

DEGREES HELD: B.S./M.S. in Electrical Engineering, Oklahoma State University, Stillwater OK (1972/1973)

GUN DYNAMICS MEASUREMENTS FOR TANK GUN SYSTEMS

BAILEY T. HAUG * AND JONATHAN A. BORNSTEIN
U.S. ARMY BALLISTIC RESEARCH LABORATORY
ABERDEEN PROVING GROUND, MD 21005-5066

INTRODUCTION:

Extensive mathematical models of the transverse motion of tank gun tubes during the launch cycle have been developed at the Ballistic Research Laboratory (BRL), other government agencies and under contract to the Army, but very little empirical data, if any, existed on the actual displacement of tank guns during firing, especially muzzle motion. The environment surrounding the muzzle of a tank gun as a kinetic energy round uncorks is extremely hostile to any instrumentation placed in the vicinity. In this environment, measuring displacements of tenths of millimeters during the seven to nine millisecond in-bore time with the accuracy required to determine muzzle pointing angles with a resolution of at least a tenth of a gunner's mil is challenging. To have the instrumentation survive to perform again and again was one challenge faced by the Launch and Flight and Interior Ballistics Divisions of the BRL during the recent Tank Gun Accuracy test program.

The objective of these measurements was to determine the position, pointing angle, and crossing velocity of the muzzle at shot exit, and the displacement profile of the gun tube during the launch cycle. From previous investigations, trends had been determined for the performance of specific gun tubes firing different classes of ammunition as reported at the last US Army Gun Dynamics Symposium.[1] In an effort to unravel the tube dependency of system performance, a detailed study of the dynamics of four gun tubes was conducted as part of a test program that included an investigation of sabot separation dynamics, free flight aerodynamics and impact data. It was presumed that gun tube dynamics played a major role in the tube to tube variation of impact locations for the same round types.

This paper will detail the overlapping instrumentation techniques used to measure gun tube dynamics, and to establish the shape of the tube during the in-bore time, with special attention paid to the orientation of the gun tube at shot exit. The agreement of the results obtained using the different approaches supports the validity of the measurements. The difficulties associated with each approach will be discussed. This comparison of the relative merits of each method ultimately led to the elimination of certain measurement approaches in the second phase of the program. Examples of the measurements, as well as a description of the analysis performed and the resulting displacements and tube shapes will be shown. The analysis of the tube shape followed slightly different paths within the two divisions working on the data, and a comparison

HAUG, BORNSTEIN

will be made of the results. The concluding remarks will address the application of the results to the validation of modeling efforts.

TUBE DISPLACEMENT MEASUREMENTS:

Test Objectives:

The objective of the efforts to measure the gun tube dynamics was to develop a time history of the tube displacement profile during the launch cycle, not just at the muzzle, but over the entire length of the exposed gun tube. The approach taken paralleled the efforts outlined by Biele[2]. By studying the drawings of the gun tube, recognizing the realistic limits of the volume of data that could be processed, and considering the frequency of the vibrations anticipated, a decision was made to use eight strain gauge stations to measure tube flexure. With the addition of the end condition at the muzzle, this allowed the determination of up to the fourth mode of vibration.

To implement the strain analysis of the tube shape, measurements of tube displacement were required for the constants of integration. To measure tube displacement during the in-bore cycle is readily done with smaller gun tubes using optical trackers and proximity gauges. To apply these approaches to tank guns required protection of instrumentation, and in the case of the optical trackers, the use of long focal length lenses to allow them to stand off at a safe distance. The displacements being measured are still on the same order of magnitude as those seen on smaller caliber tubes, and this further complicates the issue

Optical Trackers:

The original plans were to measure the vertical and horizontal muzzle motion using optical trackers. It was calculated that the trackers could stand off approximately ten meters, and with the use of 1200-mm focal length lenses, these devices could resolve tube displacements of less than .0254mm (.001in). To measure the muzzle pointing angle, two trackers were to be used for each axis. The trackers measuring the vertical motion were to look at the tube directly, and the two measuring the horizontal motion were to view the tube through a mirror placed below the muzzle.

The trackers were mounted on camera stands in such a way that each pair of vertical and horizontal displacement measurements were made at one cross section of the gun tube. The measurements were made at two planes, separated by .14m, and the rear plane was located .254m from the muzzle. Once in position, a blast shield with plexiglass windows was placed around the stands and trackers offering minimal protection.

During the initial firings, while working out the details of the instrumentation, some of the optical trackers were damaged due to the blast. It became apparent that the alignment of the trackers following the horizontal motion was tedious. It was very difficult to control the point on the tube which

was being tracked by the units, so the decision was made to drop the horizontal trackers and to concentrate on the vertical tube motion. With the extreme focal length lenses used and the distances involved between the trackers and the gun tube, the slightest motion at the tracker location caused alignment problems. The trackers are sensitive to light intensity variations, which complicated the setup as well as the data analysis. The vertical trackers were able to follow the motion of the muzzle from shot start to just prior to shot exit. At the point where the hot gases began to exit the tube ahead of the projectile, the trackers lost their ability to track the tube due to the change in the illumination level.

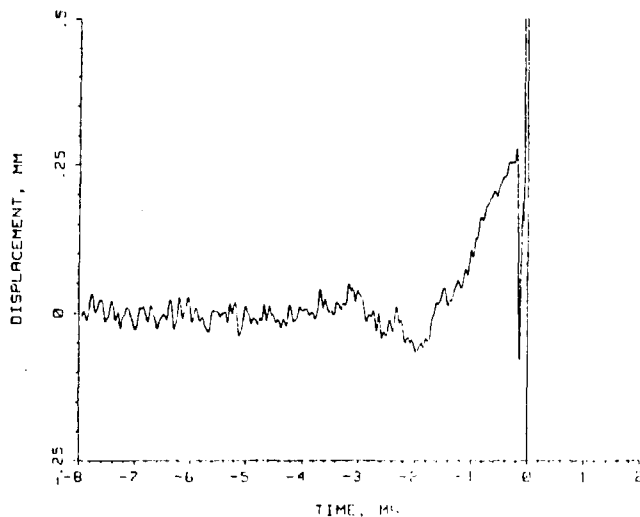


Figure 1. Forward optical tracker, vertical displacement.

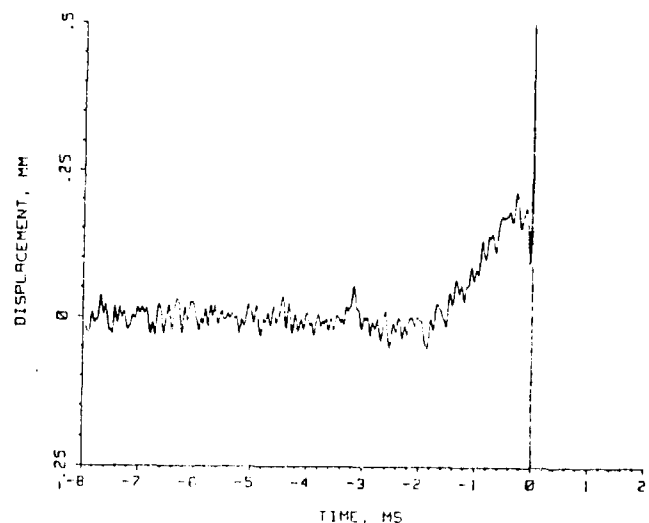


Figure 2. Rear optical tracker, vertical displacement

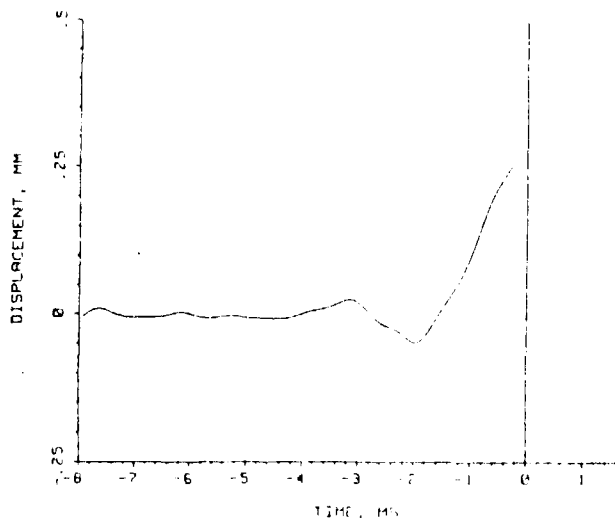


Figure 3. Forward optical tracker, processed data.

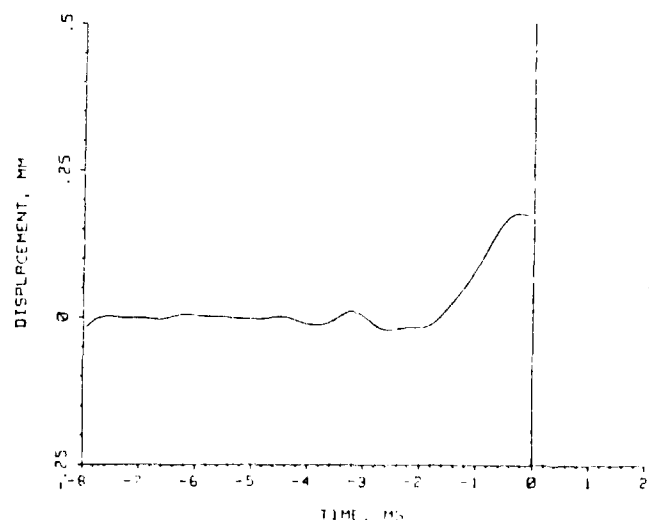


Figure 4. Rear optical tracker, processed data.

Figures 1 and 2 show the typical measurements of tube motion by the trackers during the launching of a kinetic energy round. The signal to noise

ratio was less than impressive due to the high gains necessary, but the underlying displacements are readily visible after some basic signal processing, figures 3 and 4. As with all the data displayed in this paper, the time is referenced to the exit of the projectile. The obvious reason for using a pair of trackers to measure muzzle motion was to allow the determination of pointing angle, and a typical plot of the muzzle pointing angle as measured by the optical trackers is presented in Figure 5.

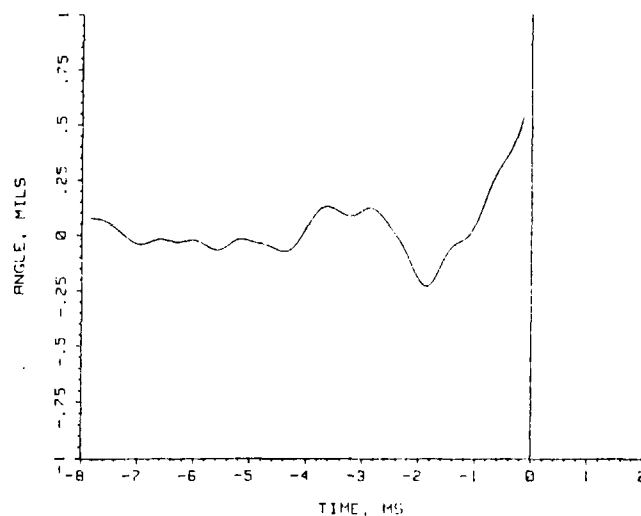


Figure 5. Pointing angle as measured by optical trackers.

Once the procedure for aligning the trackers was worked out, these instruments performed adequately for measuring displacements at the muzzle, up to the point where the hot gases interfered with the measurements. The displacements and angles measured were supported by the other instrumentation techniques, but because they could not track through shot exit, they fell short of our requirements on this test. During subsequent testing the trackers were dropped in favor of the eddy probe techniques.

Proximity Sensors:

One of the primary techniques utilized to determine gun tube translation employed commercially available inductive proximity sensors (Scientific-Atlanta model M-61 eddy probes coupled to model 606 eddy probe drivers). These small (diameter: 5mm, length: 35mm) transducers consist of an inductive element potted in an epoxy material. A high frequency electric current is passed through the device creating a magnetic field. When the transducer is in close proximity to a metallic surface, eddy currents are induced in the metal. The resulting loss of energy from the transducer is proportional to the gap between the unit and the surface. This is the same principle utilized in the design of the inductive loop or Muzzieschmidt.

The magnitude of the induced eddy current will be observed as a transducer output voltage that is proportional to the gap width. The nominal range for the device is 0 to 2.5mm with a sensitivity of 7.9 volts/mm. The transducers exhibit a high degree of linearity for gap widths between .25 and 2.0 mm and

good stability (variation of calibration over an extended period of time). The calibration does, however, appear to be a function of the ambient temperature (a temperature change of approximately 28 degrees Celsius resulted in a 6% change of the probe sensitivity) and a mild DC signal drift (perhaps 200 mv over the course of a day) has been observed.

For the analysis of the transducer output signals, it is assumed that the cannon may be represented as a tapered tube of circular cross-section. During the in-bore period, it can recoil along its central axis, translate in the vertical and horizontal directions and radially expand or contract. It is assumed that the gun will not twist in a plane perpendicular to its central axis and that its cross-section will remain circular. The change of the gap between transducer and tube surface then represented by equation 1.

$$G = G_i + [T_x \cos \alpha + T_y \sin \alpha] + \left[\frac{D^2}{4} - (-T_x \sin \alpha + T_y \cos \alpha)^2 \right]^{1/2} + [C/2] + \left[\frac{Z\theta}{2} \right] \quad (1)$$

As illustrated in figure 6, each of the four terms in square brackets is associated with a particular motion or deformation of the gun tube. The first term represents translation of the gun parallel to the probe axis, while the second is due to motion perpendicular to this axis. The third term results from the compression of the tube and the fourth is due to a combination of tube taper and recoil motion, which is measured by an optical scanner placed at the breech.

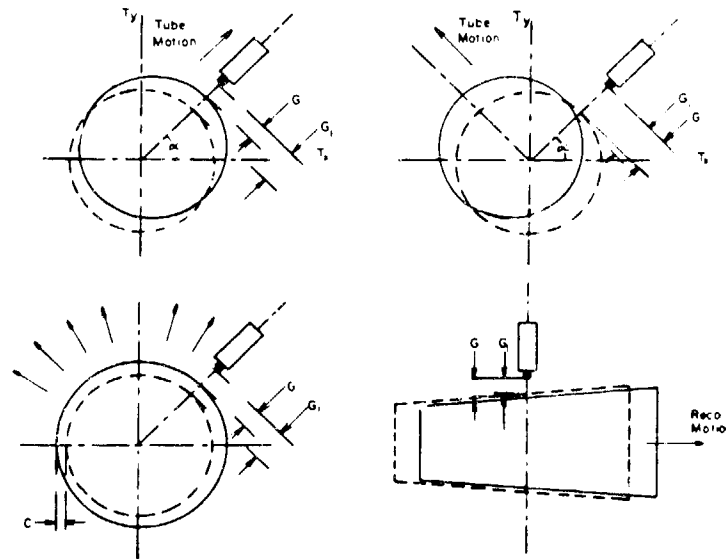


Figure 6. Change of gap between proximity probe and gun tube due to (a) tube motion parallel to the probe axis, (b) motion perpendicular to the tube axis, (c) expansion of the tube, (d) recoil motion

Three transducers are required to completely determine the translation and expansion of the gun at any position along its length. However, to simplify the data analysis, four transducers spaced 90 degrees apart around the circumference of the tube were utilized in the current experiment (figure 7). The difference of the gaps measured for two opposing probes will yield the translation of the

gun along the axis joining the probes

$$T_x = \frac{1}{2} [(G_c - G_{c_i}) - (G_a - G_{a_i})] \quad (2)$$

and the sum, when corrected for the effects of tube taper and motion perpendicular to this axis, gives the expansion or compression of the tube

$$C_x = [(G_c - G_{c_i}) + (G_a - G_{a_i})] - 2 \left[\frac{D^2}{4} - T_y^2 \right]^{1/2} - 2\epsilon \quad (3)$$

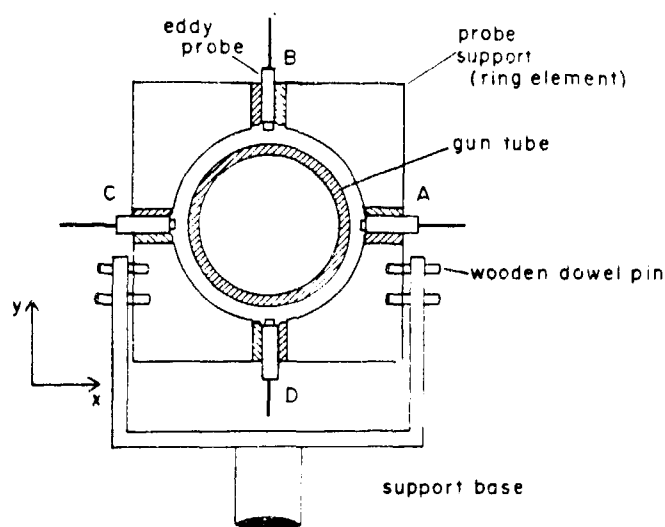


Figure 7. Arrangement of proximity probes in holder.

At each axial station, the probes were mounted in a support system consisting of two components: a support base which was attached to the ground and a ring element into which each of the four transducers was inserted (figure 7). The two parts were attached by four wooden dowel pins. This construction was necessitated by the relatively large transverse motion of the cannon which occurred during recoil, but after ejection of the projectile. The design provided the required rigidity during the inbore cycle, yet when the tube came into contact with the probe holder, the pins sheared permitting the section holding the transducers to ride the gun and survive the impact. Analysis has shown that the maximum error associated with the misalignment of the probe holder on the gun is approximately 4% [3].

Probes were placed at four locations along the tube: at two points in the vicinity of the muzzle (permitting the estimation of the muzzle pointing angle), near the center of the tube and towards the breech end of the gun. To accommodate the strain gauges which were mounted on the tube, the probes were mounted along perpendicular axes oriented at 45 degrees to the vertical and horizontal directions. Data were acquired using Nicolet digital oscilloscopes (effectively acting as transient recorders) which sampled the output signals from each of the probes at a rate of 200kHz at a resolution of 5mv. The digitized data were then processed on a VAX 8600 computer, using a standardized

analysis program. A complete description of the instrumentation and the analysis program are given in reference 3.

Figure 8 depicts the change of the gap ($G-G_i$) measured by each of the four probes situated near the gun muzzle during the firing of a sabot round. A number of features are apparent from this figure. First is the lack of any appreciable motion before 3ms prior to shot exit. This is followed by a general increase in all four of the gaps which is attributable to the taper of the tube and the recoil of the gun. Superimposed upon this is an oscillatory though not sinusoidal motion which continues until approximately 300 microseconds prior to shot exit when there is a sudden expansion causing an increase in all four gaps. This expansion is due to the passage of the projectile, subjecting the tube to the high pressure, high temperature combustion gases.

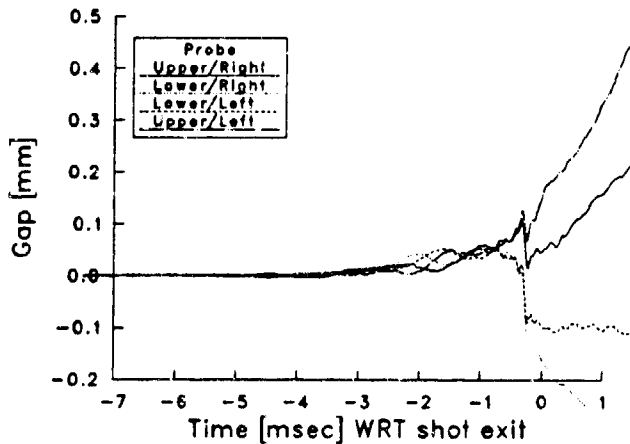


Figure 8. Change of gap width between probe and gun tube.

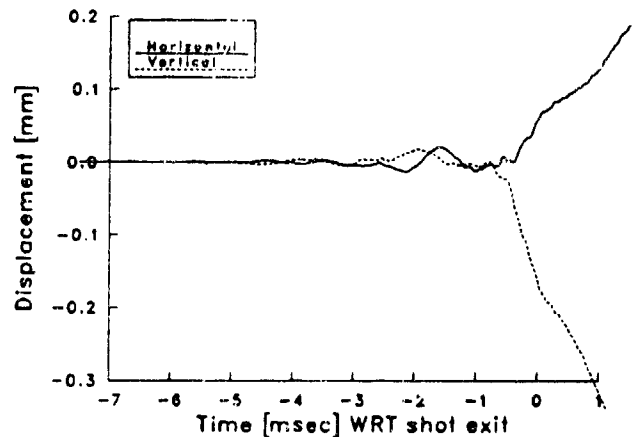


Figure 9. Transverse motion of the gun tube near the muzzle.

Application of equations (1) and (2) to the data permits the determination of the translation and expansion of the tube. The time histories of these quantities determined approximately 35cm behind the muzzle are depicted in figures 9 and 10 respectively. Figure 9 indicates that the small scale oscillatory motion observed prior to the passage of the projectile is better characterized as a spiral motion of the muzzle. This presumably is caused by the interaction of the projectile and gun tube due to the in-bore balloting motion of the bullet. Subsequent to bullet passage, the muzzle undergoes larger scale motions, both downward and towards the right. Despite the magnitude of the latter motion, the probes remain within their linear range until well after shot exit. As noted previously, passage of the projectile past the probe location is marked by a rapid expansion of the tube (fig. 10). A by-product of the muzzle proximity probe measurements is a coarse estimate of the projectile velocity obtained by comparing the bullet passage times at the two closely spaced muzzle probes.

A similar set of measurements was performed towards the breech end of the gun tube, somewhat forward of the trunnions. The results are shown in figure 11. The most interesting feature was the relatively large upward displacement found in the vertical plane, with a peak translation of 0.5mm measured approximately

1ms after shot exit. The motion in the horizontal plane is negligibly small. This relatively large vertical motion is mirrored by a downward translation of the breech seen in figure 12, indicating a sizable rotation of the gun tube about the trunnions which is not reflected in the muzzle measurement.

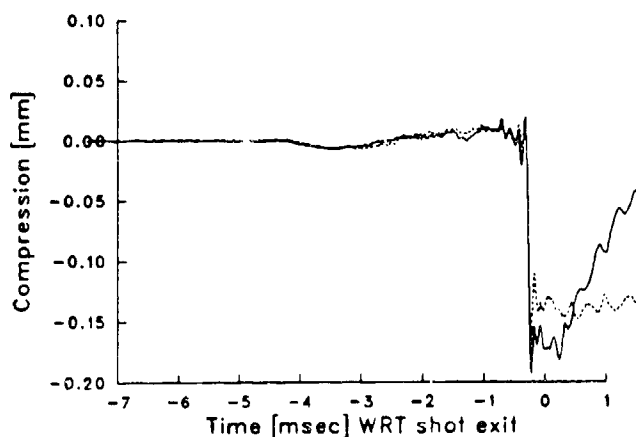


Figure 10. Compression of the gun tube near the muzzle.

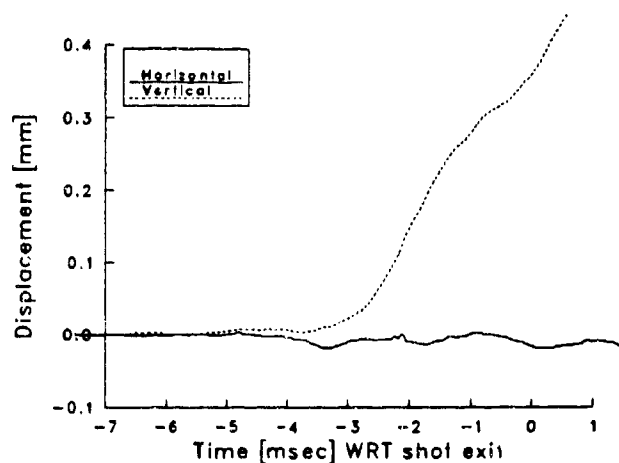


Figure 11. Transverse motion of the gun tube forward of the trunnion.

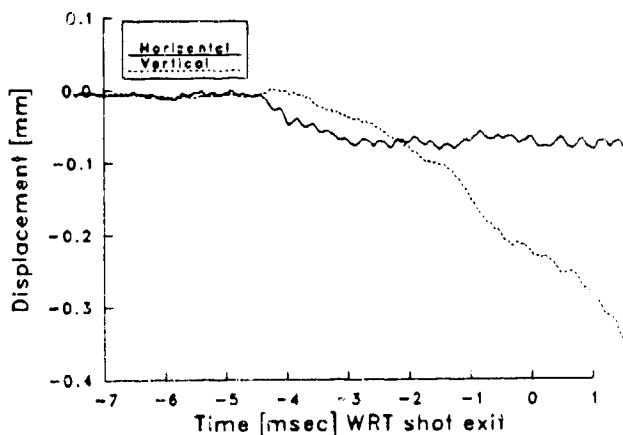


Figure 12. Transverse motion of the breech.

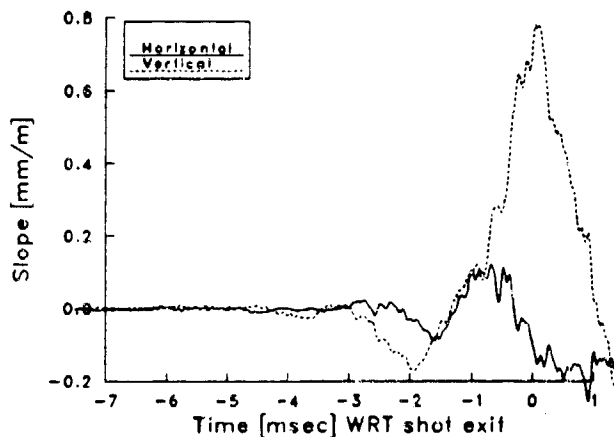


Figure 13. Muzzle pointing angle measured by proximity probes.

The relative motion at the two probe locations close to the muzzle permit an estimate of the muzzle pointing angle as a function of time (figure 13). Inherent in this estimate is the assumption that curvature of the tube (i.e. the longitudinal bending strain) between the measurement point and the muzzle is negligibly small; a criterion which cannot always be met. For these experiments, tube curvature in the vicinity of the muzzle and the proximity probes yield a good estimate of the pointing angle. Figure 13 indicates that for this type of projectile the pointing angle in the horizontal plane was nominally zero, while there was a substantial upward pointing angle. These results compare well with the other measurement techniques used to determine the tube shape.

Proximity Coils:

An alternate approach to measurement of the muzzle motion made use of the proximity coils designed by Jimmy Q. Schmidt of BRL (4). This technique had first been applied to a medium caliber weapon in an indoor range at RARDE, UK., and again, adapting it to a tank gun required designing a system that would survive the blast environment. Two two-dimensional systems were used to determine pointing angle. Each system consisted of two vertical and two horizontal coils, and these were connected so that the opposing coils were recorded in differential mode to eliminate common mode signals such as projectile passage, taper effects caused by recoil, etc. The systems were mounted so that after shot exit, as the tube recoiled, the printed circuits with the coils were pulled from the edge connectors where they were mounted and allowed to ride with the tube. This worked very well, and successfully avoided destroying the instrumentation.

It is readily apparent from the plots of displacement measured by the coils, figures 14 through 17, that the resolution and noise levels were at least an order of magnitude better with the coils than were obtainable with the optical trackers. The coils were able to track the motion from shot start right through shot exit and beyond. The front coil was located 304.8mm (12in) from the muzzle face, and the coils were separated by 228.6mm (9in). These data are from the firing of a kinetic energy round. The motion was similar for different kinetic energy rounds, and showed the expected differences for the heavier HE round. Unfortunately, the HE round caused enough displacement to drive the vertical signal off scale, which was not noticed in time to correct the problem.

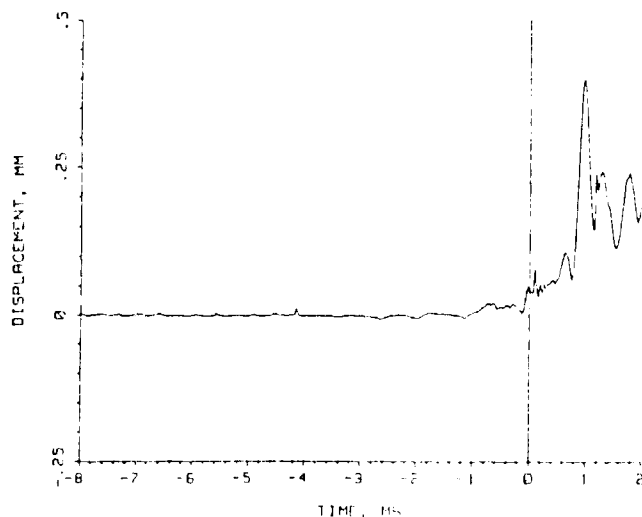


Figure 14. Front coil, vertical motion.

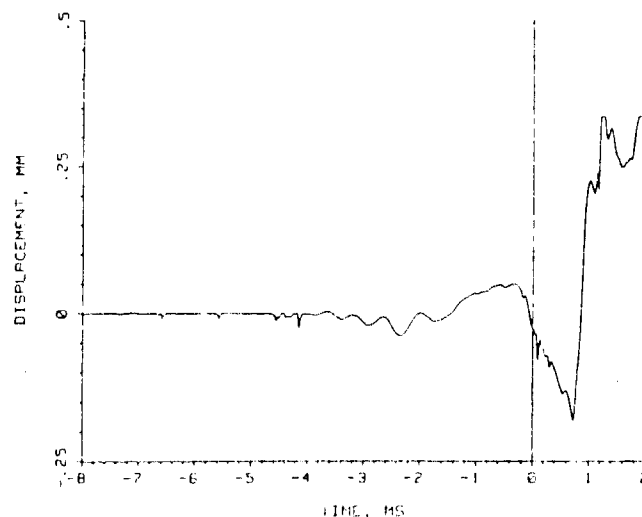


Figure 15. Front coil, horizontal motion.

Studying the data reveals the characteristic macromovement of tube motion at the coil positions for a KE bullet, muzzle rising approximately 0.0762mm (.003in) before shot exit, and falling as the projectile passes the coil position with the muzzle at or slightly below the static position at muzzle exit. A detailed examination of the test records reveals a discontinuity at the

time the bullet passes the coil positions, particularly in the horizontal plane. The nature of the coils are such that any common signals such as tube dilation due to projectile passage, recoil effects, etc., are removed by the differential amplifiers. A careful study of the instrumentation used left little doubt that this was a real measurement of displacement, and might be attributed to a misalignment of the centerlines of the projectile and gun tube. The optical trackers would never have detected this displacement because of the filtering used, and the trackers were not able to follow the motion through shot exit, and the trackers were locked on the larger diameter section of the tube at the muzzle. It appears to be a local effect and does not alter the global motion of the gun tube.

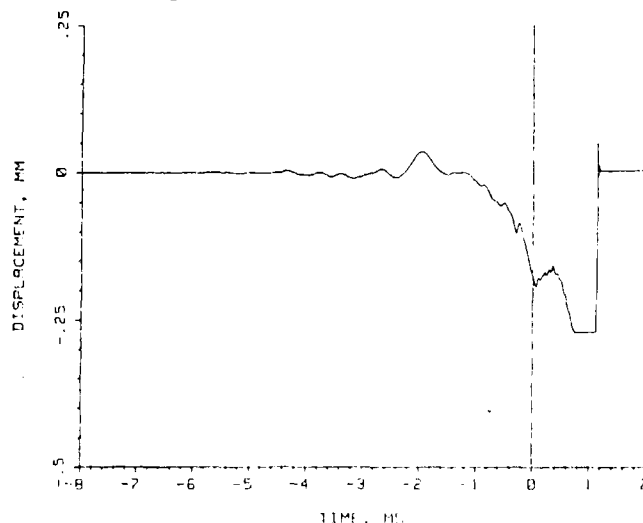


Figure 16. Rear coil, vertical motion.

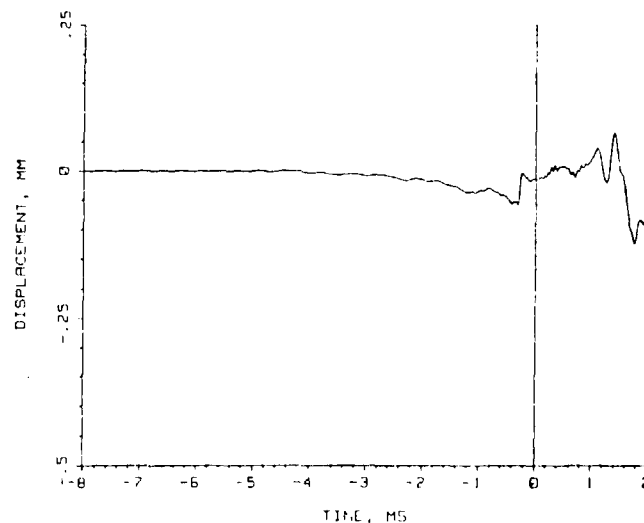


Figure 17. Rear coil, horizontal motion.

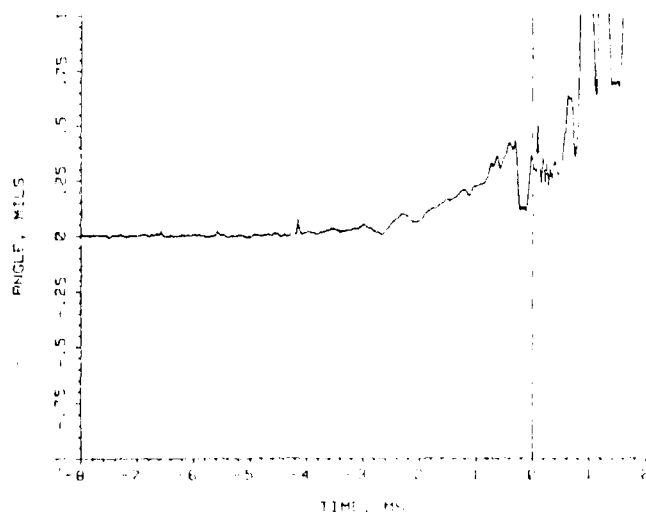


Figure 18a. Horizontal pointing angle as measured by the coils.

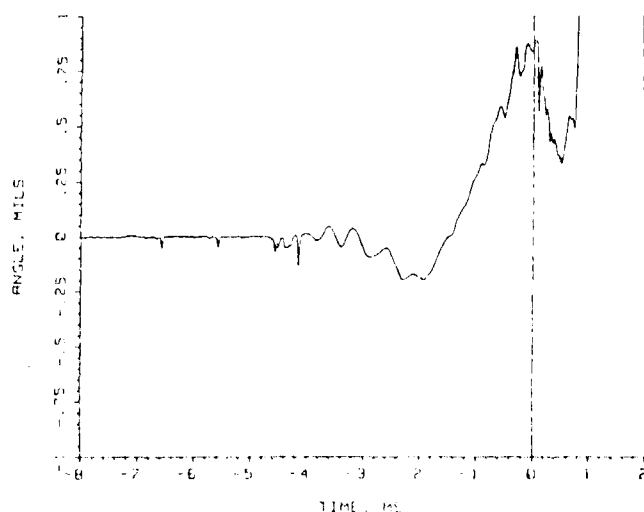


Figure 18b. Vertical pointing angle as measured by the coils.

A comparison of the pointing angle as measured by the coils is presented in

figure 18. When overlaid with the angular measurement made by the optical trackers, the two measurements support each other, as seen in figure 19. Without the coils, an attempt to extrapolate the muzzle position at shot exit from the optical tracker data could be misleading.

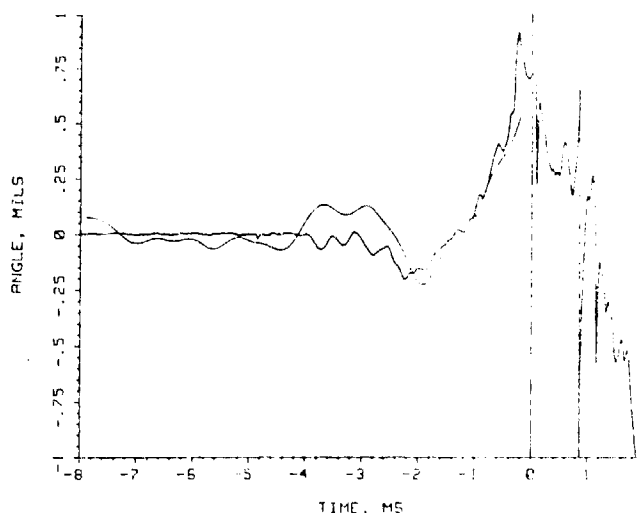


Figure 19. Comparison of angular measurements of coils and trackers.

The coils were only used for one gun tube, therefore there is no comparison of tube to tube variations in gun tube motion, but the round variations for the same tube appeared to be very small. As mentioned above, significant differences in tube motion can be observed between a KE round and an HE round. This tends to support the validity of the measurement as the HE round travels significantly slower and is heavier.

STRAIN GAUGES:

Following the procedure outlined by Biele[2], four strain gauges, mounted at 0, 90, 180 and 270 degree positions around the circumference of the gun, were placed at each of eight locations along the length of the tube. The gauges were oriented lengthwise along the tube and opposing transducers were wired together in the bridge circuit to minimize the effect of common mode signals (e.g. hoop or pure axial stresses) and maximize the sensitivity of the gauges to the longitudinal bending strain. Although the probes are most sensitive to longitudinal bending strains, they do possess a cross-axis sensitivity and the gauges can be slightly misaligned, hence the devices will respond other types of strain. During each test, data was obtained throughout the projectile in-bore cycle and stored on analog tape. Subsequent to the test, the record was played back, digitized, converted into engineering units and transferred for analysis to a VAX8600 computer.

The analysis developed by Heaps[5] treats the gun tube as a cylindric elastic beam which can deflect only due to longitudinal bending or rigid body motion. The longitudinal bending strain is related to the local curvature of

the tube, which for the case of small deflections simplifies to the form.

$$\epsilon = \frac{D}{2} \frac{D^2 v}{dz^2} \quad (4)$$

In this expression ϵ is the bending strain, D the diameter of the tube, v the deflection of the tube and z the axial coordinate of the tube. Performing a double spatial integration of this expression therefore yields the displacement due to bending or the instantaneous shape of the tube. The two constants of integration can be evaluated using information from the displacement probes (any combination of data from optical trackers, eddy probes or Muzzleschmidts).

To spatially integrate the strain data it is necessary to develop an analytic function which approximates the strain distribution over the entire length of the tube. A question arising in this context is the data density required to accurately describe the strain distribution. As shown in basic texts on data analysis[6], sampling theory requires that the interval between successive data points be no larger than half the shortest wavelength of the signal (i.e. mode shape) to be measured. If shorter wavelengths (or higher modes) are present, aliasing will occur. In the current experiments, strain has been determined at 9 points on the tube (8 measurements and a zero strain condition at the muzzle), implying that at best we can hope to faithfully represent the shape of the tube through the linear combination of the first four longitudinal vibration modes. If higher modes of vibration contribute substantially to the tube shape, the form generated by the integration of strain data will be inaccurate. Comparison of the tube shape determined from the strain data with local measurement of transverse displacement obtained from proximity probe data will provide an indication of the validity of our approximation.

Approximating the lowest vibration frequency of the tube to be 20Hz, this argument led us to use an anti-aliasing low pass filter with a cutoff frequency of 400Hz. Figure 20 shows a sample of both the filtered and unfiltered versions of strain data measured in the vicinity of the muzzle. The figure indicates that the relatively low cut-off frequency substantially smooths the strain signals.

Once the strain data were filtered, the data at any instant of time could be approximated by a polynomial expression to facilitate integration. As noted in the introductory remarks, two somewhat different procedures were adopted. In the first[3], the strain was approximated using a fourth order least squares fit for which the basis functions were Legendre Polynomials. In the second[6], a LaGrange interpolating polynomial was employed, using the argument that each data point represents an accurate measurement and utilizing an approximation simply introduces additional unnecessary errors. A comparison of the results obtained using each of these methods is shown in figure 21. Although both techniques yield results similar in appearance, some differences exist. Before further conclusions can be made about which approach is more valid, a study of the interaction of the projectile with the tube shape must be performed. An appropriate tool for making this comparison would be the S&D Dynamics modeling efforts currently being developed. For both procedures the resulting function was then integrated twice and proximity probe data used to evaluate the two

constants of integration. Figure 22 is a comparison of the resulting displacement as a function of position along the tube using both methods.

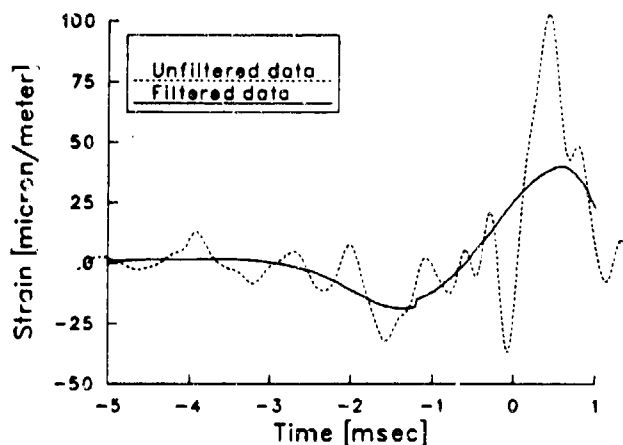


Figure 20. Sample strain data record.

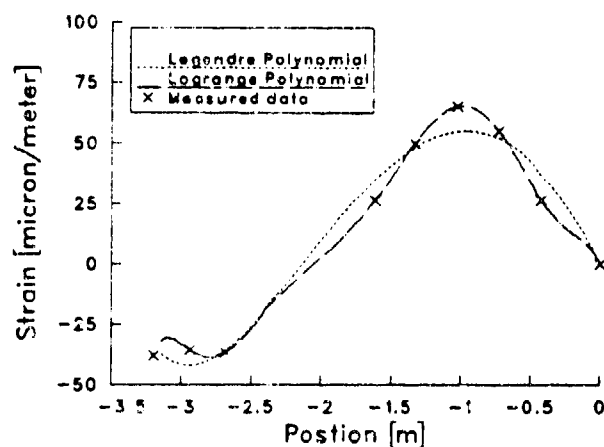


Figure 21. Sample of vertical bending strain data - at shot exit.

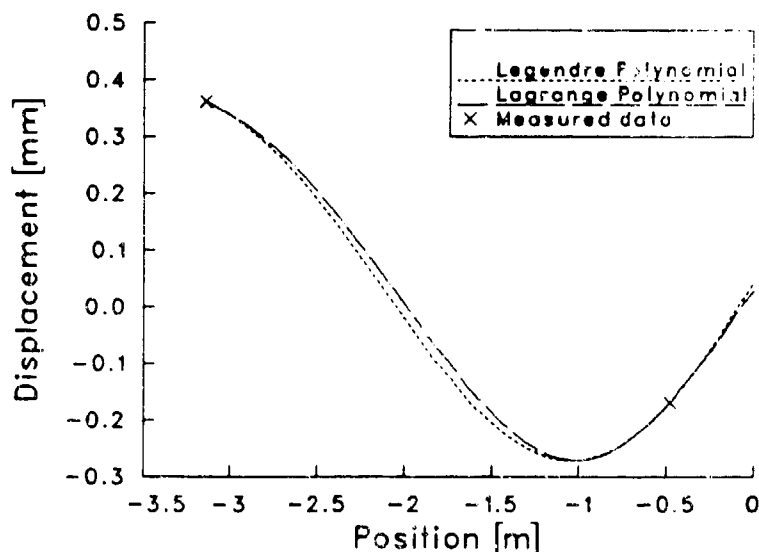


Figure 22. Vertical displacement (tube shape) determined from strain data at shot exit.

The same analysis has been carried out at a number of times during the in-bore cycle and the vertical deflection of the tube is shown in figure 23a and b. Each of the small drawings depicts the displacement of the section of the tube forward of the trunnion. The solid circles represent the instantaneous position of the projectile. One observes both the rotation of the tube about its support (the increasing elevation at the rear of the gun) and the flexural motion of the tube. In this instance both displacements appear to grow in magnitude as shot

exit is approached. Motion in the horizontal plane (figure 23b) appears to be much smaller in magnitude. This is in agreement with the commonly held opinion that the asymmetric breech represents a primary driving mechanism for the observed gun motion.

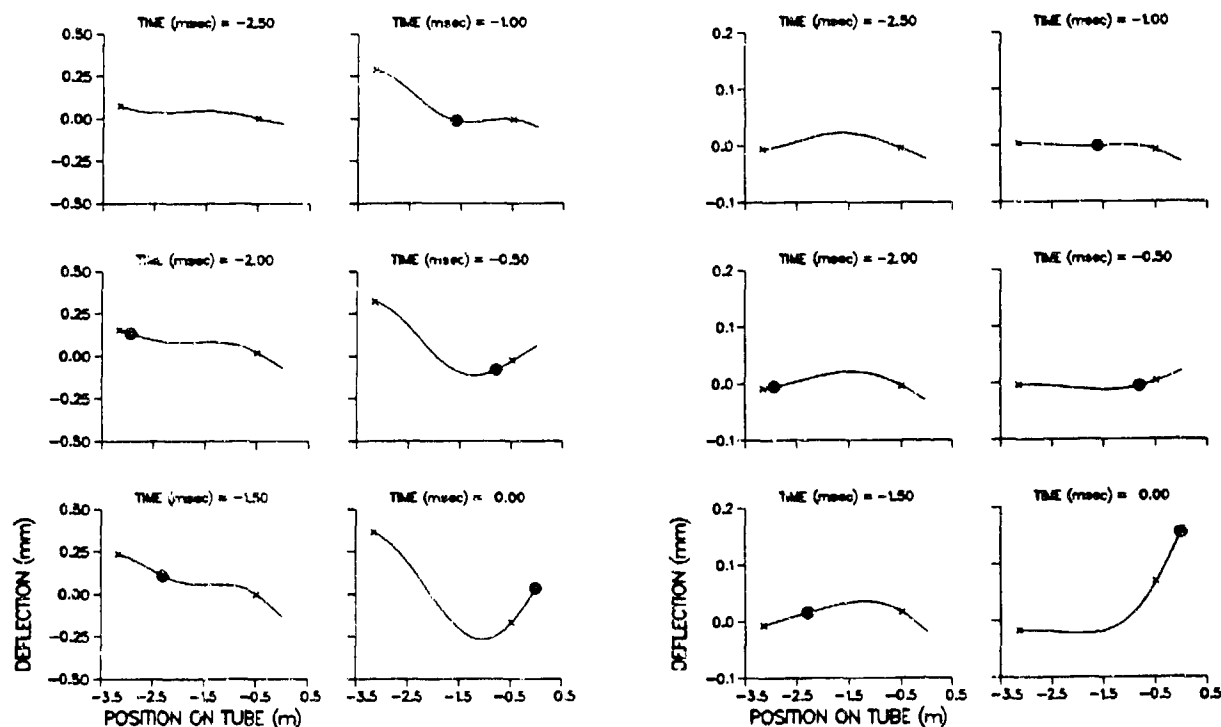


Figure 23a. Displacement of the tube in the vertical plane at $t = -2.0$ ms, -1.5 ms, -1.0 ms, -0.5 ms and shot exit.

Figure 23b. Displacement of the tube in the horizontal plane at $t = -2.0$ ms, -1.5 ms, -1.0 ms, -0.5 ms and shot exit.

Prior to these tests, it was assumed that gun dynamics could play a significant role in the observed round to round variation of impact point. Figure 24 depicts the instantaneous gun tube shape in the vertical plane for a single gun tube firing five rounds of the same type projectile. The tube shape and displacement (or rotation about the trunnions) is very similar for four of the five rounds. Examination of figure 23a suggests that shot exit occurred slightly later during the in-bore cycle for the fifth round. Results such as these imply that the round to round reproducibility of the gun tube motion is very good. However, the measurements can only indicate the motion of the tube and not in-bore trajectory of the projectile which will be affected by projectile/gun tube interaction or balloting. Thus, in-bore motion of the projectile may still be a significant source of dispersion.

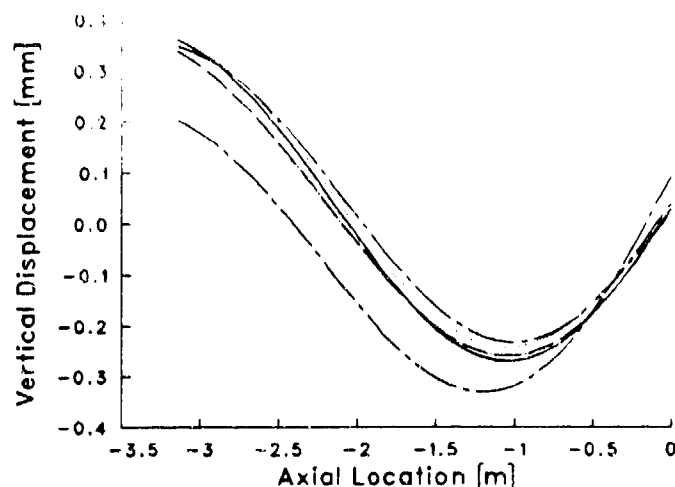


Figure 24. Shape of the gun tube in the vertical plane at shot exit for 5 rounds of the same type projectile.

CONCLUDING REMARKS

In this paper, four techniques for the determination of gun dynamics have been examined. It has been demonstrated that a combination of these methods can successfully measure tube motion to the desired accuracy. While optical methods (i.e. optical trackers) are intuitively attractive, since they represent a non-contact technique that due to their standoff distance may be less subject to blast effects, their sensitivity to illumination levels and obscuration make them unsuitable for application to large caliber guns. We have demonstrated that a technique which combines displacement measurements from either proximity probes or coils with the integration of the longitudinal bending strain measured by standard strain gauges can be used to determine the shape and transverse motion of the gun tube. Although in situations for which only the muzzle pointing angle and displacement are required, utilization of proximity sensors alone can provide a simpler solution.

In any application of the technique, one must consider the vibrational modes of the gun tube when establishing the number of measurement stations. If too few measurements are performed along the length of the gun, one runs the risk of having insufficient spatial resolution to accurately represent the dynamic shape of the gun tube.

The results of these measurements can provide an aid in the development of models for gun tube dynamics, particularly for new weapon systems. The measurements may be used as the driving function for models of projectile/gun tube interaction, although the primary application of the technique, to date

HAUG, BORNSTEIN

has been to establish the gun dynamics contribution to projectile launch conditions.

LIST OF SYMBOLS

SYMBOLS

C	Compression of the gun tube
D	Outer diameter of the gun tube
G	Width of the gap between proximity probes and the gun tube
T	Translation of the gun tube
Z	Recoil of the gun
v	Displacement of the tube in a plane orthogonal to the tube centerline
α	Angle between probe axis and horizontal axis
ϵ	strain
θ	Diametrical taper of the gun tube

SUBSCRIPTS

a,b,c,d	Proximity probe locations
i	value prior to the start of a test

References:

- (1) Walbert, James N., "The Relationship of Gun Dynamics to Accuracy in a 120-mm Tank Gun," Proceedings of the Fourth U.S. Army Symposium on Gun Dynamics, 7-9 May 1985
- (2) Biele, J.K., "Gun Dynamics Effects to Jump of Smooth Bore Tank Guns," 8th International Symposium on Ballistics, ADPA, Arlington VA, October 1984
- (3) Bornstein, J., "Application of Proximity Sensors for the Determination of Gun Tube Motion," Proceedings of the 33rd International Instrumentation Symposium, Instrument Society of America, May 3-8, 1987, Las Vegas NV.
- (4) Schmidt, Jimmy Q., Andrews, Thomas D., "Description of the Joint BRL-RARDE 40-mm Firing Experiment to Define Projectile Launch," Proceedings of the Fourth US Army Symposium on Gun Dynamics, 7-9 May 1985.
- (5) Heaps, C.W., "Determination of Gun Tube Motion from Strain Measurements," Memorandum Report BRL-MR-3562, US Army Ballistic Research Laboratory, Aberdeen Proving Ground MD, March 1987
- (6) Bendat, J.S. and Piersol, A.G., "Random Data: Analysis and Measurement Procedures," Wiley-Interscience, New York, 1971
- (7) Walbert, J., Private Communication

PENNY AND PERRY

TITLE: AN ACCOUNT OF SOME EXPERIMENTS UNDERTAKEN TO CORRELATE MEASURED GUN
BARREL FEATURES WITH THE MOVEMENT OF SERIAL MEAN POINTS OF IMPACT
P.H.G. PENNY and J.A. PERRY
ROYAL ARMAMENT RESEARCH AND DEVELOPMENT ESTABLISHMENT
CHERTSEY
SURREY KT16 0EE
ENGLAND

ABSTRACT

For many years now the results of gunnery trials have shown that movements of the Mean Point of Impact of ammunition serials can be correlated with changes to major mechanical items within the weapon system.

With the earlier types of kinetic energy projectile the ballistic dispersion was sufficiently large that movements of serial Mean Points of Impact, due to equipment changes, were often masked by the general movement of the MPI due to serial differences in the dispersion pattern.

With the introduction of the fin stabilised type of kinetic energy ammunition, the inherent ballistic dispersion has been significantly reduced, amongst other factors, and the variability of the Mean Point of Impact introduced due to physical changes to the gun system mechanics, now has a discernible effect on gun system accuracy. The manner in which parts of the gun system contribute toward a system bias is obviously of interest since improvements to gun accuracy could be obtained. Recent firing results indicate that changes to specific features of the gun barrel can have considerable effects. A limited firing programme was authorised in order to confirm these reported effects.

The paper describes the results of firing trials from a tank and a firing stand for four gun barrels selected from British Army use. The barrels were selected as covering the range of variability experienced by the Army whilst 'shooting-in' nearly five hundred tanks. The barrel parameters chosen for investigation were bore straightness and concentricity with the external diameter. The paper explains the methods used for barrel measurement and details the experimental procedures and measurements taken during the firing trials from both the tank and firing range stand.

A comparison between the features measured from the four selected barrels and the significance of the movements in serial Mean Points of Impact is made and the basis of further full scale firing experiments discussed.

A companion paper entitled "Theoretical Modelling of the Dynamics of Initially Non-Straight Barrels Using Finite Difference Techniques" by Powell and Penny, details a method of mathematically modelling the transient response of an initially non-straight gun barrel and discusses the predicted changes to the response.

This paper was not available for printing in this publication. Every effort will be made to include this paper in a supplement at a later date.

TITLE: INVERTED DYNAMIC CHARACTER OF SMOOTH-BORE CANNON
DONALD W. PETTY and JAMES N. WALBERT
US ARMY BALLISTIC RESEARCH LABORATORY
ABERDEEN PROVING GROUND, MD 21005-5066

ABSTRACT

Since the early 1950's investigations into the dynamics of a gun as it is fired and relating this action sequence to the resultant fall of shot have been partially physical examination but largely mathematical conjecture. Advance in understanding the structural strengths of tubular structures have brought about opportunities for unique experiments in gun dynamics. Metallurgical expertise in manufacture and structural integrity in design of recent tank cannon have allowed alteration of the physical constraints and still allow live firing.

The subject of investigation in this set of unique set of experiments is the 120-mm smooth bore cannon used as a weapon for many of the NATO alliance member's main battle tanks. This cannon's structural integrity has been proven during firing trials over many years and presents itself as a prime item for experimental use. Also, a background of firing performance and a history of dynamic measurements by the Ballistic Research Laboratory provides a clear picture of characteristic behavior for this gun system.

The actual set of experiments involved structural modification of a 120-mm smooth-bore cannon whose dynamic characteristics were documented so that it could be mounted in a main battle tank in an inverted position. Tube curvature profiles have been measured in inverted positions and calculation of gravitational force influence upon tube inversion have been expounded upon, but this is the first experiment which specifically altered a large caliber cannon for live firing when offset 180 degrees from the manufactured keyway mounting position. The alteration to the cannon also had to preserve the firing character of the gun in the original upright position so that any deviation from former characteristics due to structural modification could be observed. The experimental configuration that was finally realized was a large caliber cannon which could be fired as easily in an upside down position as in an upright (as manufactured) position.

This unique gun was used in a set of experiments using both kinetic energy and full-bore types of ammunition. The results were consistent with historical characteristics and showed that conjecture regarding tube curvature influence upon fall of shot to be correct only with certain types of ammunition. These experiments have filled a void in projectile/gun interaction studies and may lead to more informed manufacturing and curvature measurement processes. This may, in turn, evolve a dynamically balanced gun system.

This paper was not available for printing in this publication. Every effort will be made to include this paper in a supplement at a later date.

PFLEGL

**TITLE: EXPERIMENTAL MEASUREMENTS OF GUN TUBE MOTION DUE TO CURVATURE AND
SUPPORT INDUCED LOADS**

G.A. PFLEGL

US ARMY ARMAMENT RESEARCH, DEVELOPMENT, AND ENGINEERING CENTER

CLOSE COMBAT ARMAMENTS CENTER

BENET LABORATORIES

WATERVLIET, NY 12189-4050

ABSTRACT

Mankind has been concerned with the accuracy of aim and impact since he first learned to hurl a missile. Whether propelled by muscle, bowstring, or gunpowder, the reliability with which a target could be struck has always been of interest, especially in a defensive situation. Computer generated battle-field scenarios have demonstrated the necessity of a high first round hit probability in today's technologically based warfare. The advent of laser range finders, cryogenic night sights, and muzzle reference devices have given us significant improvements in pointing accuracy. However, they have also shown the need to understand the mechanisms which cause a gun to launch its projectile in a direction deviant from that in which it was pointed when the firing signal was initiated. Many mechanisms have been proposed to explain variations in the gun-projectile-mount system and there have been many efforts to try to measure the effects of these mechanisms. Failure to isolate individual variables and a lack of irrefutable instrumentation have produced spurious results which have often raised more questions than they have answered.

This paper reports on the efforts of an extensive test firing program in a highly controlled laboratory environment. The use of a specially prepared barrel has allowed the investigation of the effects of curvature and support induced loads on barrel motion through the period of shot ejection. Data has been collected using corroborative instrumentation methods of high accuracy and repeatability. A test firing plan has been used which sought to isolate individual parameters affecting behavior. Because of the unique barrel design, motion induced by several distinctive variations of support has been recorded. Various amounts of thermally induced curvature have also been induced and the resultant performance measured. The methods of measurement resolve translational motion directly and can be combined to assess rotational behavior at various points of the surface of the barrel. The latter characteristic will not be considered in this paper, but may be included in future analysis.

An evaluation of the recorded data will be discussed. This presentation will consider the claim of isolation of the specific parameters tested in order to ascertain the degree to which variations in the results can be attributed to the singular characteristics. The deviation of behavior within the recorded

PFLEGL

results of individual tests will be discussed in order to suggest the significance of variations between test groups. This comparison is then extended to evaluate the effects of the changes due to support and geometry variations. Some comparison is also made with analytical predictions for the same or similar cases. The presentation is illustrated with exemplary data for the cases considered.

This paper was not available for printing in this publication. Every effort will be made to include this paper in a supplement at a later date.

TITLE: State-of-the-Art of Techniques for the Measurement of the Initial Projectile Movement in Guns at the Ernst-Mach-Institute, FRG
GERD ZIMMERMANN*, HELMUT GRUMANN
Fraunhofer-Institut für Kurzzeitsdynamik, Ernst-Mach-Institut, Abteilung für Ballistik (EMI-AFB), Hauptstrasse 18, D - 7858 Weil am Rhein, West Germany

ABSTRACT:

In 1982, at the Third US Army Symposium on Gun Dynamics a review of the methods applied by the Ernst-Mach-Institut for the measurement of the initial projectile movement in guns was presented. Meanwhile, the significance of the forces, transmitted by the propellant grains to the projectile during the ignition phase becomes more and more evident. Without measuring these forces an analysis of the initial projectile movement for most ammunitions containing granular propellants seems to be impossible. Therefore, a new technique for the measurement of the total axial forces acting on the projectile base using piezoelectric foils has been developed, together with a low-cost method for gas pressure measurements directly on the projectile base. In parallel, a low-cost electronic circuitry has been developed, which allows the simultaneous transmission of two signals on a wire connecting the projectile nose through the muzzle to an outside receiver. The three techniques are described, together with measurement results at large and small calibers.

BIOGRAPHY:

Gerd Zimmermann

PRESENT ASSIGNMENT: Senior Scientist, Fraunhofer-Institut für Kurzzeitsdynamik (EMI-AFB)

PAST EXPERIENCE: EM gun; proximity fuze simulation and effectiveness calculation; electromagnetic compatibility of fuzing circuits; granular propellant ignition; projectile motion measurements; general ballistic measurement techniques

DEGREES HELD: Graduated in communication engineering, Technical University of Karlsruhe (FRG)

STATE-OF-THE-ART OF TECHNIQUES FOR THE MEASUREMENT
OF THE INITIAL PROJECTILE MOVEMENT IN GUNS AT THE
ERNST-MACH-INSTITUT, FRG

G. ZIMMERMANN, H. GRUMANN

FRAUNHOFER-INSTITUT FÜR KURZZEITDYNAMIK, ERNST-MACH-INSTITUT,
ABTEILUNG FÜR BALLISTIK (EMI-AFB)
HAUPTSTRASSE 18, D - 7858 WEIL AM RHEIN, WEST GERMANY

1. INTRODUCTION

Several years ago the Ernst-Mach-Institut has started investigations of the ignition process of granular propellants. At the same time, we developed methods for the measurement of the initial movement of the projectile as well as of the pressure on the projectile base. We soon recognized that a gas pressure measurement alone did not suffice to explain the early projectile acceleration. In most cases, the projectile started before the gas pressure reached the projectile base. The reason were gas pressure gradients travelling inside the porous bed, generating mechanical stress waves. These mechanical waves sum up on the projectile base, where the propellant grains transfer the forces to the projectile. We call the sum of the forces, divided by the projectile base cross-sectional area, the "grain pressure". From a physical point of view this word is not correct, but because of its descriptive brevity it soon became common use. After the arrival of the gas pressure wave, the sum of both pressures is exerted on the projectile base. It is called "total pressure".

The direct measurement of the grain pressure in presence of the gas pressure is rather difficult. It proved to be easier to measure the total pressure and by a separate gage the gas pressure. Then the grain pressure is determined by subtraction. For small calibers there is not enough space for an additional gas pressure gage at the projectile base, and the gas pressure must be determined by gages mounted at the sidewall of the gun chamber.

In addition to the pressure measurement, the projectile movement has to be determined. For our purposes, i.e., measurement of the initial movement and especially to determine the resistive forces on the projectile, accelerometers inside the projectile proved to be most suitable. From the acceleration the projectile velocity and its trajectory can be computed by integration. For longer trajectories position controlling stations along the barrel (e.g., pressure gages inside the barrel wall) are necessary for this technique, since offset errors during the acceleration measurement are integrated together with the correct signal and may lead to unacceptable errors. Offset errors are less significant in the case of optical or microwave measurements, but these signals must be differentiated at least once which introduces new problems.

The signals must be transmitted out of the gun barrel. For simplicity we use the hard-wire method (for small calibers a single wire, for larger calibers more than one). This means, the signals must be impedance-converted inside the projectile before they can be transmitted with the aid of an output circuitry.

In the present paper, the self-developed gages for the measurement of the total pressure and the gas pressure on the projectile base are described together with the circuit for signal transmission, and some remarks about the acceleration measurement are given. Typical measurement results are presented.

2. MEASUREMENT OF THE "TOTAL PRESSURE"

As mentioned before, the "total pressure" consists of the sum of the "grain pressure" and the gas pressure. Since the grains exert the force only pointwise on the projectile base and the points of contact can be too much dispersed compared to the dimensions of the active surface of common pressure transducers, such transducers were not suitable for this type of measurements. Gages with a large surface area had to be developed. The gages had to be insensitive both to acceleration and to the local distribution of grain-surface contact.

These conditions can be met by piezoelectric polyvinilydene fluoride foils (PVDF) as sensing element, covered by a low-mass pressure distribution plate made of light metal (Figure 1). These foils are commercially available with a thickness of 5 to 100 μm , completely polarized and metallized on both surfaces. They can be easily cut to the desired shape. Since the foils are heat-sensitive, they have to be protected against temperature changes during the shot. Therefore, the arrangement is enclosed in a thin metal cap, protected against the heat of the burning chamber by a small layer of epoxy

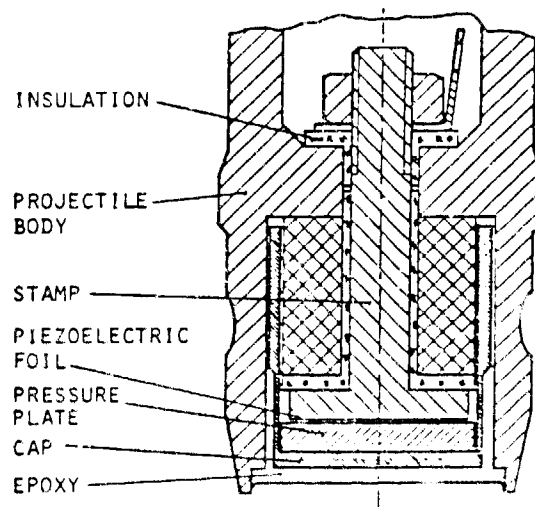


Figure 1 Projectile base pressure transducer with piezoelectric foil for small calibers

resine. Towards the interior of the projectile, the foil is supported by a stamp of high stiffness to prevent the bending of the foil which would lead to an additional lateral strain signal during the shot. At the same time the stamp provides one of the contacting electrodes of the sensor foil; the pressure distribution plate, in contact with the cap, forms the other one.

The extremely high impedance of the foil sensor is impracticable for signal transmission. It has to be adapted to a low value, e.g., $50\ \Omega$. Therefore, an impedance converter circuit has to be added to the sensor (Figure 2).

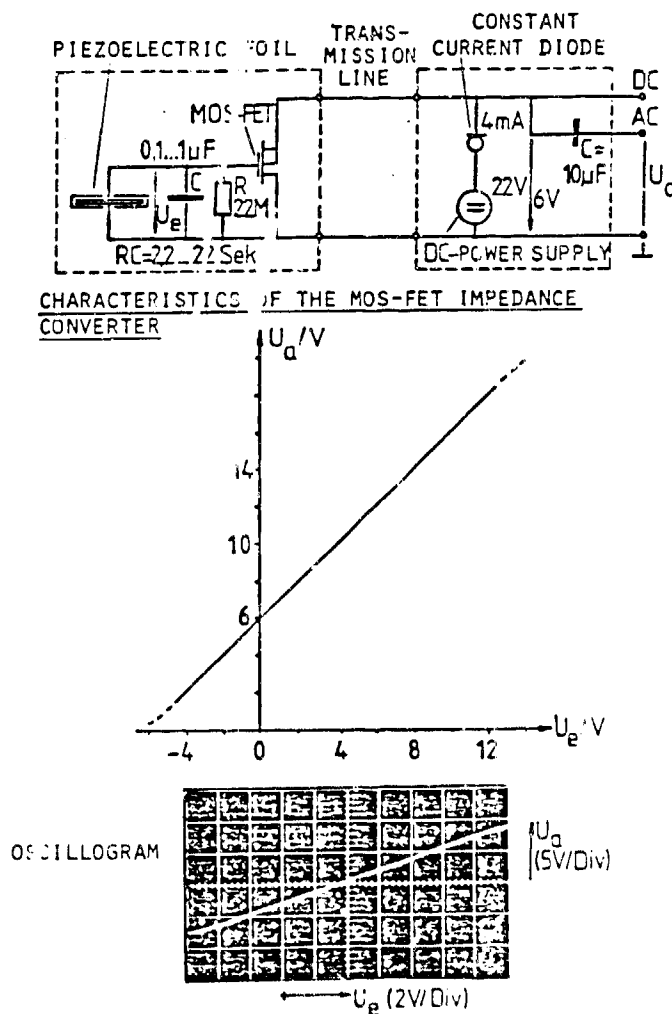


Figure 2 Impedance converter with p-channel MOS-FET

The principal element of the impedance converter consists of a MOS-FET, the input of which is paralleled by a resistor (e.g., $22\text{ M}\Omega$). This resistor gives a well-determined input resistance to the circuit. Since commercially available piezoelectric foils for the given application develop very high electrical charges, the input voltage to the MOS-FET has to be lowered by a paralleling capacitor, the capacity of which determines the sensitivity of the system.

The MOS-FET is powered by a constant current source so that its output voltage is linearly dependent on the input voltage and therefore on the pressure of the foil. The signal is coupled to the transmission line or to the telemetry circuit by a large capacitor. Consequently, the gage has a low-pass filter behaviour with a very low cut-off frequency; static pressures cannot be measured. The working point of the MOS-FET being about 6 V with the current source used, the output of the circuit ranges between -4 V and +12 V.

The foil gage together with the impedance converter is calibrated in a chamber shown in Figure 3. By combustion of a small amount of propellant a pressure rise is generated and recorded by both a commercial piezoelectric quartz gage and the foil gage. Calibration is achieved by comparing the gage signals. The depressurization afterwards is made by a special vent designed to meet the condition of uniform pressure distribution in the chamber during the calibration process.

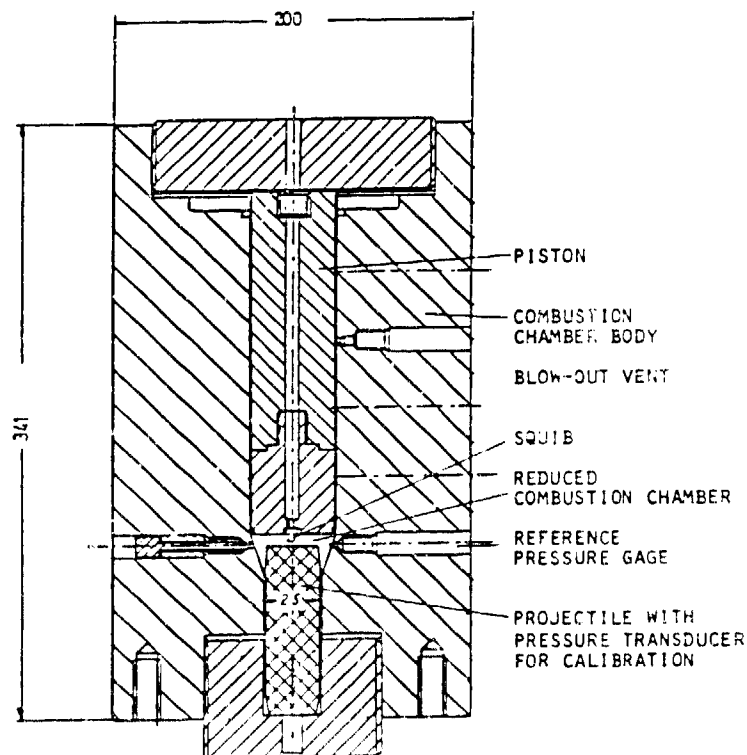


Figure 3 Modified 25-mm combustion chamber for dynamic calibration of projectile base pressure transducers

This calibration method has the advantage that it indicates bad heat insulation and simulates the dynamics of a real shot. The maximum calibration pressure used is normally below 100 MPa to prevent gage deformation during the calibration procedure caused by the long duration of the pressure pulse. In special tests, however, good linearity of the foil sensor calibration curve up to 300 MPa has been demonstrated. Three calibration cycles are carried out before the gage is released for interior ballistic measurements.

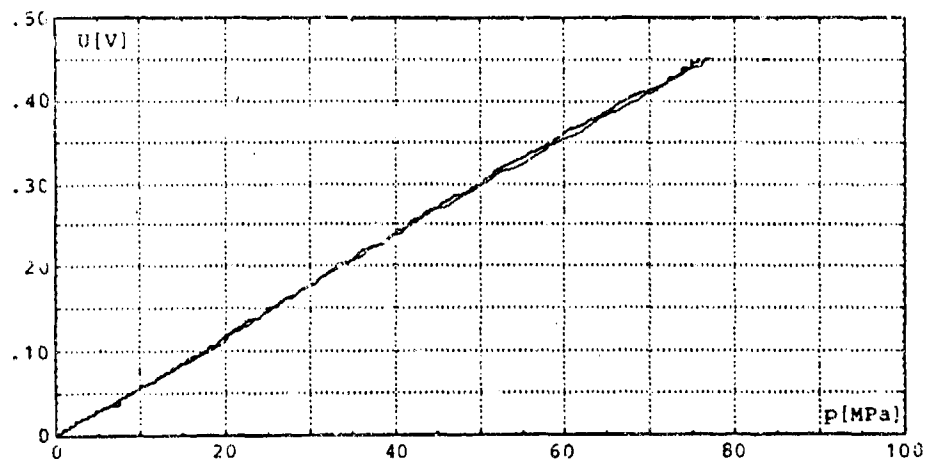


Figure 4 35-mm Simulator; foil-transducer calibration curve

For small calibers the gage construction always has to be adapted to the projectile shape. For large calibers it is possible to use a standardized gage type (Figure 5). The piezoelectric foil is placed between the anvil (6) and the cap (3). The insulation of the cap (3) to the anvil (6) is done by an insulating shell (4). Cap, anvil and insulating shell are glued together by epoxy resins and are screwed up to the receptacle (5), adding an insulating disk (7). The remaining gap between receptacle (5) and cap (3) is filled with epoxy. A 2-mm epoxy layer (1) on the cover of the cap serves as heat protection. The impedance converter is mounted into a borehole (10) at the bottom of the receptacle. The pressure signal is transmitted out of the projectile by means of two insulated copper wires.

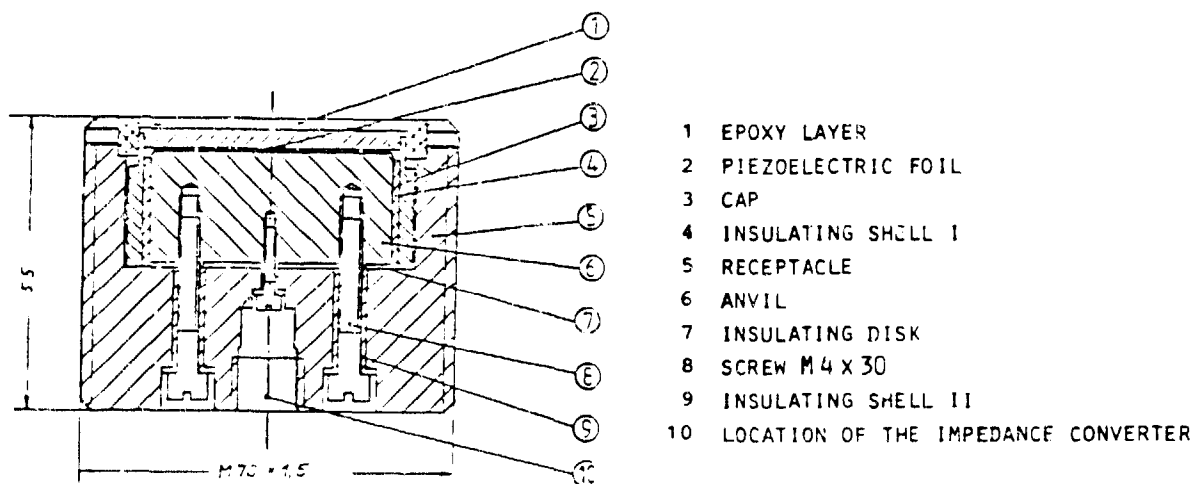


Figure 5 Standard base pressure transducer with piezoelectric foil for large calibers

Calibration of such a standardized transducer is accomplished by comparing the signal of the transducer under test with the signal of a reference transducer in a special calibration chamber. This chamber is shown in Figure 6.

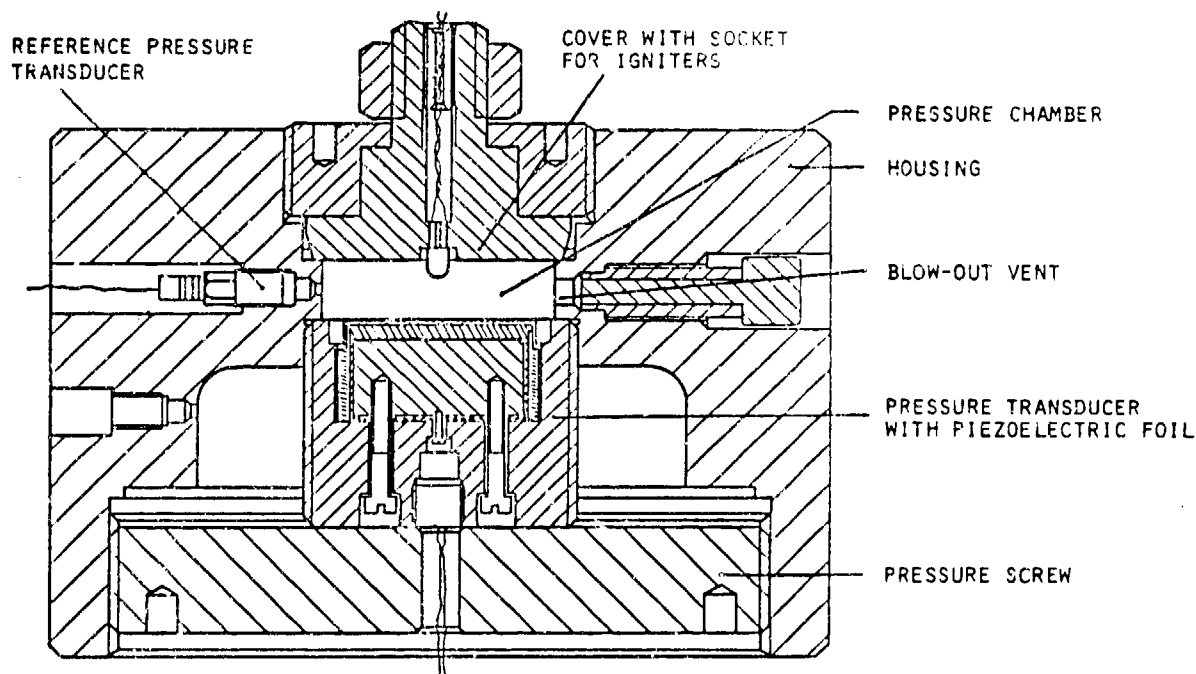


Figure 6 Calibration chamber for large caliber base pressure transducers

3. MEASUREMENT OF GAS PRESSURE AT THE PROJECTILE BASE FOR LARGE CALIBERS

For large calibers, it is possible to install small gages for the measurement of gas pressure alone at the foil gage surface. These gages consist of a carbofilm resistor as sensing element imbedded in silicon grease within a stiff titanium cylinder (see Figure 7). (Typically 470 Ω , 1/8 W resistors of Allen Bradley.) The top of the cylinder contains a small number of perforations to permit the gas pressure penetration into the interior of the cylinder. Since the metal housing keeps out the forces exerted by the grains on the gage and the grains cannot pass the holes on the top only the gas pressure acts via the silicon grease on the sensing element.

The resistance change as function of the applied gas pressure is determined with the aid of a Wheatstone bridge. The gas pressure gage is calibrated together with the foil gage during the same calibration tests. A calibration curve is shown in Figure 8. It has to be mentioned that similar gages have been successfully used by us since several years for gas pressure measurements inside large caliber granular propellant charges.

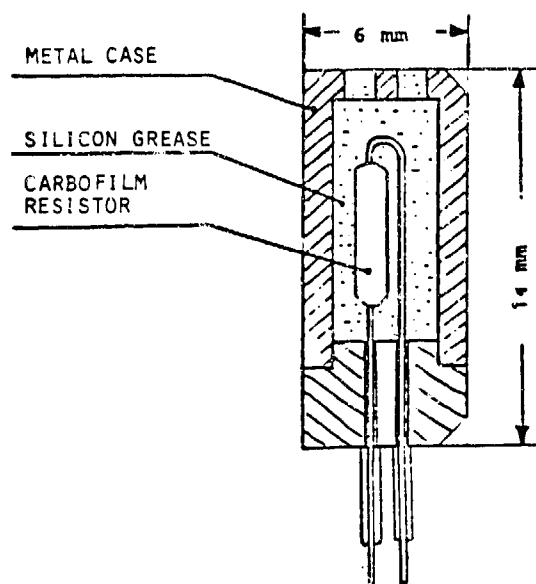


Figure 7 Gas pressure measurement gage with carbofilm resistor

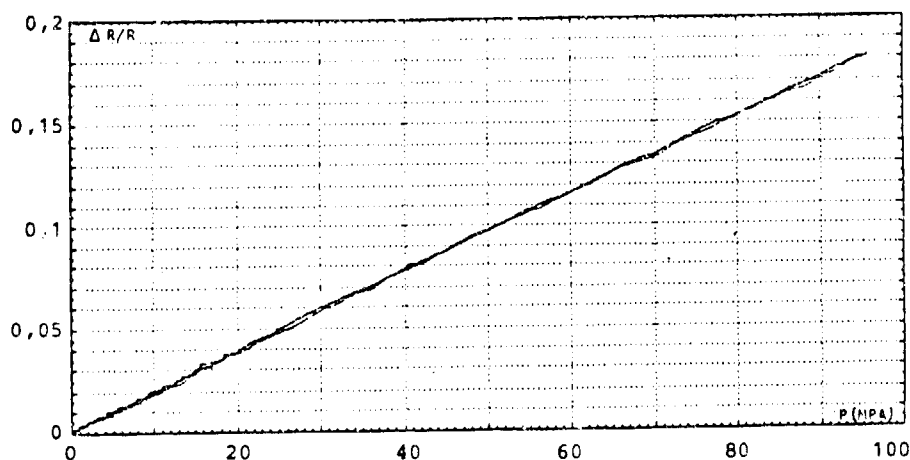


Figure 8 Dynamic calibration curve of a pressure gage on the base of a carbofilm resistor

4. ACCELERATION MEASUREMENTS

For projectile acceleration measurements, in our Institute only commercial piezoelectric transducers with built-in impedance converters were used up to now. In 20-mm guns we tested the following types: Dytran 32 000 A, Endevco 2255 A 01, Kistler 8642 A100, and PCB M 305 A. The gages differ

mainly from each other in the amplitude of their natural oscillations which often can be found on the negative ramp of the pressure-time signals at small caliber firings.

As for the installation of accelerometers inside projectiles, care must be taken to avoid the possibility of accelerometer case distortion during the shot [1]. An appropriate mounting of a gage inside a projectile is presented in Figure 9.

5. SIMULTANEOUS MEASUREMENT OF PROJECTILE BASE PRESSURE AND ACCELERATION IN SMALL AND MEDIUM CALIBER GUNS

Figure 9 shows an example of a 20-mm projectile instrumented with a base pressure transducer together with an accelerometer. In such a caliber, the base pressure transducer design has to take into account the limited volume available. The accelerometer is mounted in such a way that only its mounting screw has a direct link to the shell, the housing being kept free from outer stresses. The projectile top is designed as a receptacle for the signal transmitting wire. Indeed, it serves a second function too: it protects the projectile from impact damage during its soft recovery after the shot.

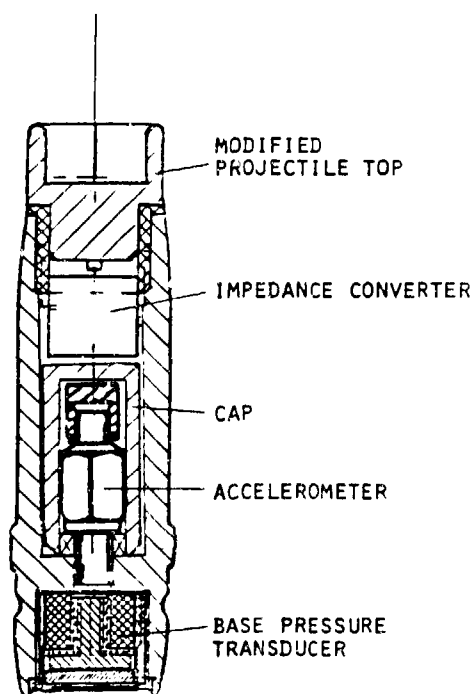


Figure 9 20-mm projectile instrumented with base pressure transducer and accelerometer

In order to transfer simultaneously the signal of both transducers via one wire a multiplex system was developed, the circuit of which is depicted in Figure 10.

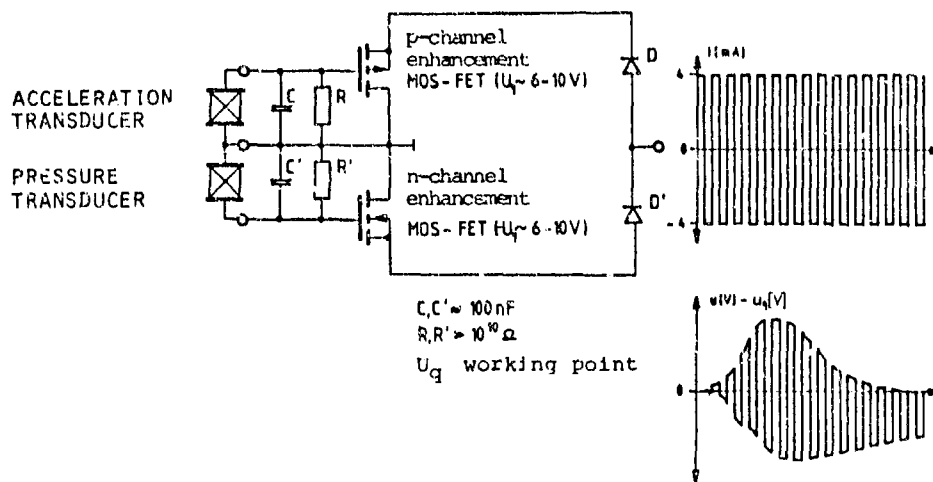


Figure 10 2-Channel multiplex circuit

The acceleration transducer contains an integrated impedance converter according to Figure 2. If this impedance converter is driven by +4 mA, a working point of about 10 V will result. The switching time is so short that a rectangular time-variable signal of 100 kHz can easily be used to switch it on and off. For the conversion of the impedance of the foil transducer a FET with inverse polarity is used, and the impedance converters of both transducers are decoupled by diodes. In that way, the supply current switched from positive to negative values will switch off the one FET and set the other to its working condition and vice versa. This results in an amplitude modulation of the positive part of the switching signal by the one transducer and of the negative part by the other. Outside the gun, both transducer signals can be separated again. Since this circuit built in lumped elements would take too big a volume for projectiles of e.g. 20 mm caliber, a hybrid circuit was developed in cooperation with industry (Figure 11). The circuit dimensions are $6.8 \times 7.5 \times 2.2 \text{ mm}^3$, and its mass is of the order of 0.2 g.

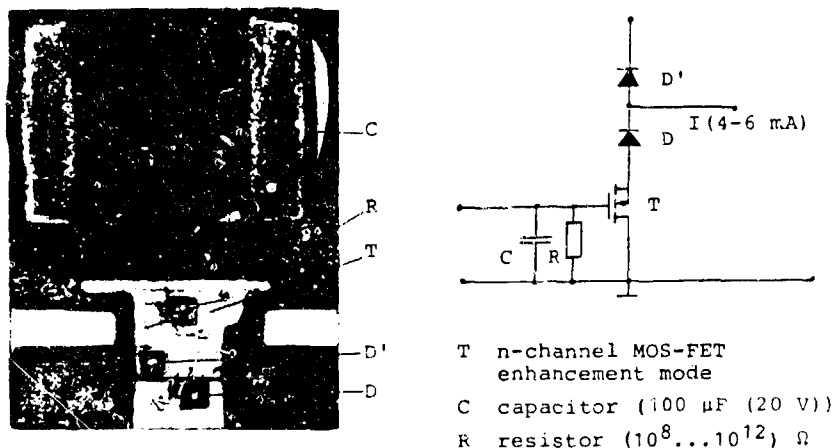


Figure 11 Hybrid circuit for 2-channel multiplex system

Outside the gun, the signals are separated, for example, by sample and hold-circuits or externally clocked transient recorders, the clocks being synchronized to the appropriate signal phases.

Figure 12 shows the projectile base pressure and the accelerometer signal together with the chamber pressure as function of time, recorded during the firing of an instrumented projectile as described above. For better comparison in Figure 12 the acceleration was multiplied by projectile mass and divided by its cross-sectional area. The result is the pressure required to impart the projectile the measured acceleration in case no resistive forces were acting on the projectile (sometimes called "effective pressure"). The difference between the total pressure on the projectile base and the effective pressure gives the resistive pressure, including case extraction and engraving.

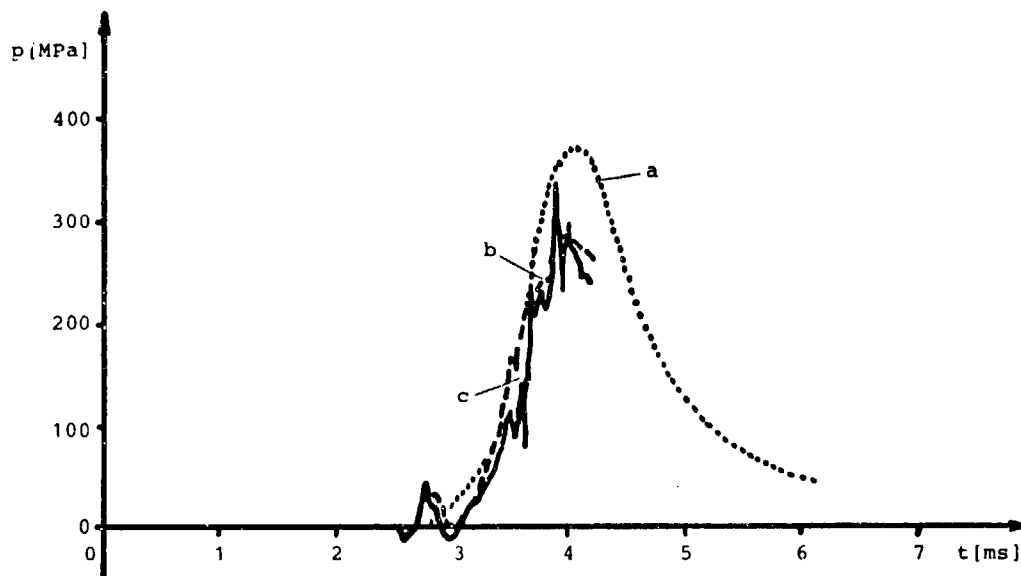


Figure 12 20-mm practice round
 a) Chamber pressure; b) projectile base pressure;
 c) acceleration multiplied by m/A (m = mass of the projectile,
 A = cross-sectional area of the gun tube)

6. SIMULTANEOUS MEASUREMENT OF PROJECTILE BASE PRESSURE AND ACCELERATION IN LARGE CALIBER GUNS DURING THE INITIAL PHASE OF PROJECTILE MOTION

In case of rifling a continuous signal transmission from the projectile to the outside of the barrel can only be accomplished for larger travel distances by means of a single wire (or wireless, but this is by far more expensive). For large caliber guns and especially if smooth bore guns are used, multiple wire transmission over a sufficiently long trajectory becomes possible. This allows to use more than two transducers inside the projectile. Accordingly, and because the projectile base is sufficiently large, the small gas pressure gage described in a previous chapter can be added to the instrumentation. In this case, the "grain pressure" can be determined in addition

to the total base pressure.

An example for a 105-mm test round equipped with all three types of transducers is shown in Figure 13. Since both the foil transducer and the accelerometer were equipped with impedance converters and the gas pressure sensor is of low impedance anyhow, a signal transmission with sufficiently high signal-to-noise ratio is possible. In this round, the impedance converters are supplied by separate constant current sources (about 4 mA each). The Wheatstone bridge necessary for the gas pressure measurement has to be installed near the gun in order to keep the wire length reasonably small. For reasons of safety, the bridge can be conditioned by a remote control system.

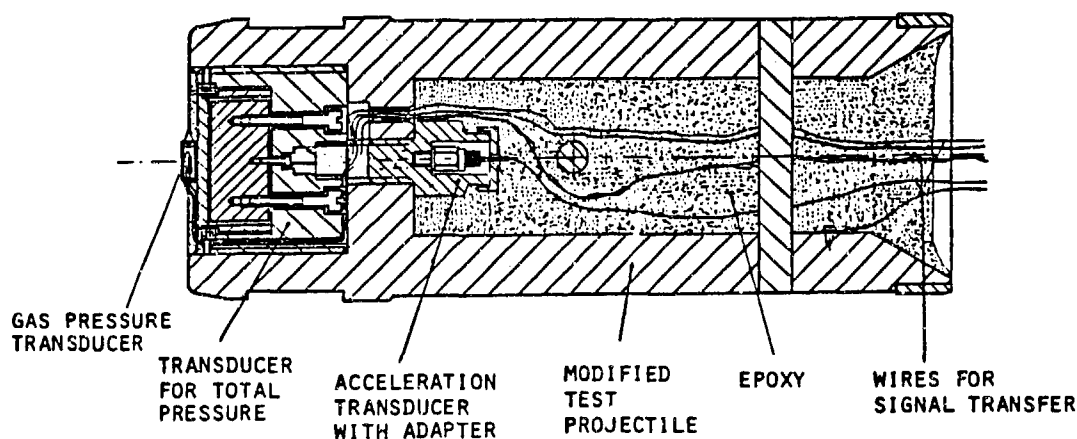


Figure 13 Instrumented 105-mm test projectile

Figure 14 depicts the data acquisition scheme used with such rounds. For these tests which were carried out at Meppen proving ground, FRG, a 105-mm tank gun with shortened barrel (called 105-mm simulator) was used.

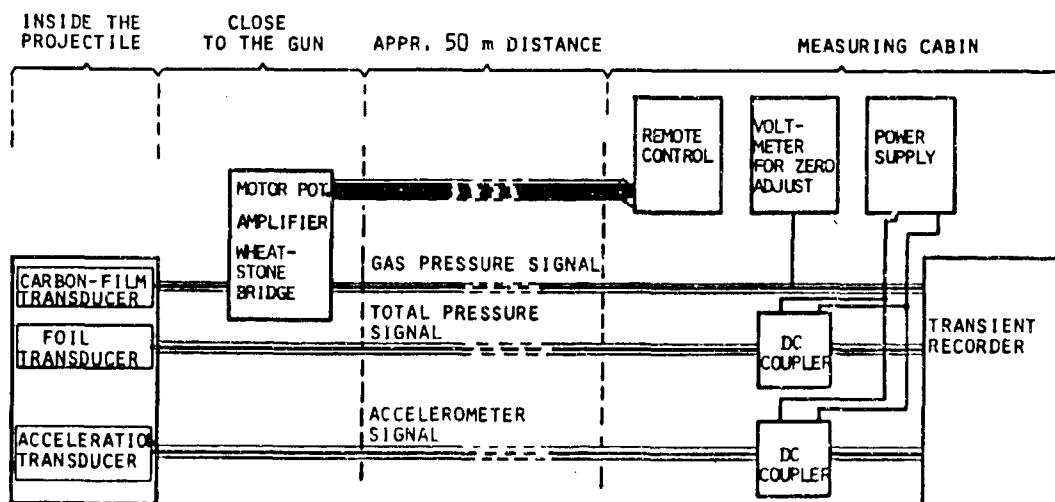


Figure 14 Three-channel data registration for an instrumented 105-mm test projectile

Data acquisition, supplementary gas pressure measurements at the breech and in the cartridge wall near the projectile base were performed by proving ground personnel. Figure 15 shows the results of such a test. In this case the ignition train was purposely altered by closing the outlet at the frontage of the primer tube by a cap in order to achieve an increased unilateral ignition near the breech. Such tests were carried out at a wide temperature range to determine the effect of unilateral ignition on gas pressure wave and grain pressure generation.

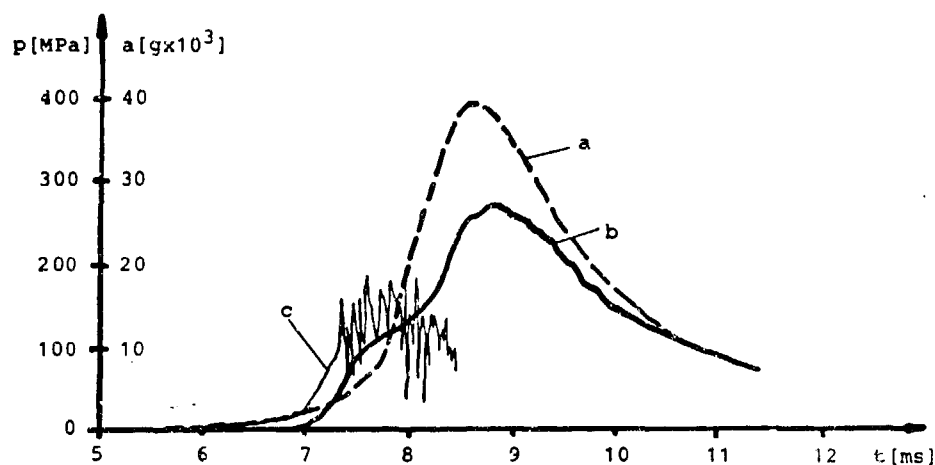


Figure 15a 105-mm simulator, manipulated primer
a) Breech pressure; b) gas pressure near the projectile base;
c) projectile acceleration

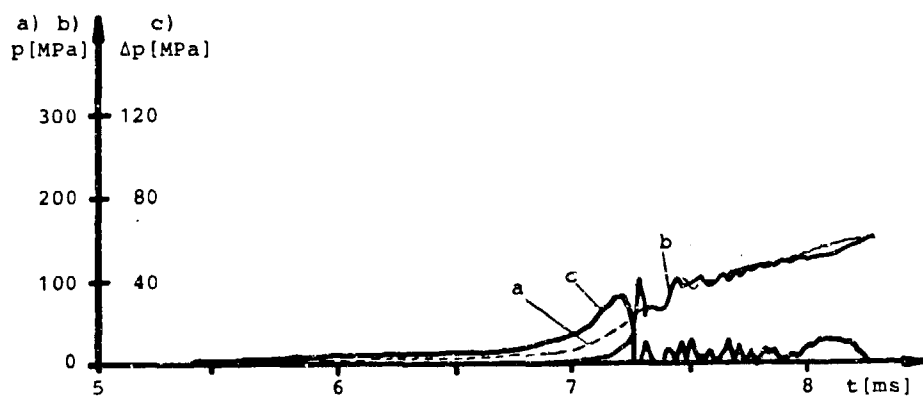


Figure 15b 105-mm simulator, manipulated primer
a) Total pressure; b) gas pressure; c) grain pressure
on the projectile base

In large caliber firings with nearly negligible resistive forces the "effective pressure", as defined above, the "total pressure", and the gas pressure should approach almost same values when the propellant burns along the total chamber length, since then the grain pressure quickly drops off. Thus, a check on the functioning of the transducers is possible.

7. CONCLUSIONS

About 50 rounds of caliber 105 mm at a wide temperature range (-35 °C to +50 °C) have been fired, and the results were excellent. Only in case of a very strong shock-like loading of the projectile base the measured signals were not completely satisfying. But, part of this difficulty seems to be due to an insufficient understanding of the phenomena occurring under such conditions.

For small calibers (~ 20 mm), the simultaneous measurement of the "total pressure" at the projectile base and of the projectile acceleration, aided by a simple multiplex system for data transmission, allows to acquire further information about the frictional forces inside a gun and thus leads to a better insight into the interior ballistics of guns using granular propellants.

8. REFERENCES

- [1] Zimmermann, G., "State-of-the-Art of Procedures Employed by EMI-AFB, FRG, for the Investigation of the Initial Phase of Projectile Movement", Proceedings of the Third US Army Symposium on Gun Dynamics, Vol. II of II, The Institute of Man and Science, Rensselaer Polytechnic Institute, N.Y., USA, 11-14 May 1982, pp. III-14-84

BARKER

TITLE: AN EXPERIMENTAL INVESTIGATION INTO IN-BORE YAW IN A RIFLED BARREL USING THE RMCS AIR POWERED GUN.

G BARKER

THE ROYAL MILITARY COLLEGE OF SCIENCE
SCHOOL OF MECHANICAL, MATERIALS AND CIVIL ENGINEERING
LAND SYSTEMS GROUP
SHRIVENHAM, SWINDON, ENGLAND.

ABSTRACT:

A compressed air powered gun which simulates many of the characteristics of a recoiling tank gun has been developed at RMCS. Many parameters can be easily varied, these include breech mass, breech inertia, breech volume, bearing spacing, shot mass, bearing clearance and breech pressure/time profile. The gun is instrumented to monitor breech acceleration, breech pressure, shot exit time, shot exit velocity, and the yaw and pitch of the shot as it travels up the barrel. The horizontal and vertical displacements of the barrel can also be measured at any point along its length.

This paper describes how a specially modified RARDEN 30 mm rifled barrel was fitted to the air powered gun to allow in-bore yaw in a rifled barrel to be investigated. A shot was developed specifically for the rifled barrel so that the shot parameters could be controlled very accurately for use in validating theoretical models. Firings were conducted with a variety of parameter changes and, in particular, a balanced and unbalanced shot.

The firing programme consisted of many firings which were conducted to ensure good round to round repeatability which the results confirmed.

This paper attempts to present as many of the results as possible in a concise format. It then demonstrates how they have been used to validate a mathematical simulation of the dynamics of in-bore yaw.

BIOGRAPHY:

PRESENT ASSIGNMENT : Research scientist, Cranfield Institute of Technology R.M.C.S. studying the dynamics of In-bore Yaw and the vibration of tank barrels.

PAST EXPERIENCE: The analysis of a semi-automatic breech opening mechanism.

DEGREES HELD : 2:1 Honours BSc.

BARKER

AN EXPERIMENTAL INVESTIGATION INTO IN-BORE YAW IN A RIFLED BARREL
USING THE RMCS AIR POWERED GUN.

G BARKER
THE ROYAL MILITARY COLLEGE OF SCIENCE
SCHOOL OF MECHANICAL, MATERIALS AND CIVIL ENGINEERING
LAND SYSTEM GROUP
SHRIVENHAM, SWINDON, ENGLAND.

1.0 INTRODUCTION

One of the factors contributing to round to round dispersion is the yawing motion of the shot. Previous work has suggested that the yawing motion of the shot was of major importance to gun accuracy, and that shot balloting (rattling in the bore) can cause severe shell engraving and uneven wear of the barrel.

To understand the cause of yaw for an aerodynamically stable shot, it is necessary to study barrel movements, shot in-bore motion, and the interaction of the barrel with the shot.

A considerable amount of experimental and theoretical work has taken place in the field of barrel motion an example of which being the work by Powell [1.0]. Mathematical modelling techniques are well developed, and can be divided into those using finite difference equations, a good example being RAMA [1.1],[1.2],[1.3] and those using the finite element method such as SIMBAD [1.4],[1.5]. The latter also incorporates the mathematical modelling of the shot and the shot-barrel interaction.

Validation of the models has been limited by the lack of experimental data, the reason for this being twofold. First, the use of full size guns for experimental studies is very expensive in both hardware and manpower, with small changes to the physical parameters of the gun system being difficult to achieve and quantify. Second, considerable difficulties in accurately and reliably measuring the performance of the gun system have been found. The harsh environment of the firing range easily damaging the delicate instruments necessary for accurate measurement of the gun system. Obscuration of the shot by gases from the charge leaking past the driving bands, has also made the optical study of in-bore yaw very difficult.

A compressed air powered gun was developed by the Royal Military College of Science (RMCS) [1.6] to allow in-bore yaw and the shot barrel interaction to be studied under laboratory conditions. The shot being driven by compressed air overcame the obscuration problems.

The gun of 30mm bore was designed to simulate many of the characteristics of a recoiling tank gun. Most parameters can be varied easily, these include breech mass, breech inertia, buffer stiffness, bearing spacing, shot mass, bearing clearance and breech pressure/time profile. Barrels can be interchanged within a few minutes and these include a smooth bore mild steel barrel with a wall thickness of 10 mm, a thin walled aluminium smooth bore barrel and a rifled barrel.

BARKER

A shot was developed to simulate the vibrations of a tank gun projectile [1.7], and was used in the validation of the theoretical models. It was symmetrical about the central axis but had provision for an off axis mass to be attached to create an out of balance round. The shot and its constituent components are shown in the photograph fig 1, and the section drawing of fig 2.

This paper gives the results from a firing programme conducted using the specially machined RARDEN 30 mm rifled barrel, which had a length of 1.61 meters and a constant outer diameter of 43.2mm. The gun was instrumented to monitor breech pressure, breech recoil acceleration, shot exit time, shot exit velocity, barrel displacement at the muzzle and half way along its length, and the yaw and pitch of the shot as it travelled up the barrel. The output from the various transducers was captured by four, two channel transient recorders in real time. The recordings were then down-loaded to an HP 9816 computer, so that they could be analysed and displayed graphically.

2.0 THE EXPERIMENTAL PROGRAMME

The firing programme was conducted with the barrel mounted on two bearings as shown in Fig 3. The clearance of the bearings was adjusted to minimum clearance so that the gun could repeatably recoil smoothly, this was checked before each firing.

A breech pressure of 50 psi (0.3485 MN/m^2) and an orifice diameter of 21 mm was used for all firings.

The position of the inner cup relative to the outer cup was recorded and maintained throughout the firing programme. The outer cup of the shot, and the barrel were marked to ensure that the shot was loaded into the barrel in the same position for each firing.

2.1 Shot development

The development of this shot has been discussed in previous publications [1.7]. The shot was improved from that used in [1.7], by fitting a PTFE disc to the rear of the shot. The PTFE disc, which replaced a steel disc, allowed the shot to travel more smoothly down the barrel.

The inner beam diameter was increased from that used in the smooth bore barrel from 2.8mm to 3.0mm to increase its stiffness. This allowed the shot to be fired at higher velocities and spun without permanent deformation of the inner beam occurring. This gave the new shot the following characteristics.

Total shot mass	85 g
Shot fundamental natural frequency	315 Hz
Equivalent front driving band stiffness	91560 N/m
Equivalent rear driving band stiffness	7284 N/m

The maximum angular displacement was determined by considering the couple that is produced by the off axis mass at maximum pressure. The breech pressure selected of 0.3485 MN/m^2 gave an acceleration of 1522 m/s^2 . The couple produced with an off axis mass of 2 grams which was 0.0105 meters from the shot axis was 0.03140 Nm.

In a simple finite element model of the shot, this couple was applied about the centre of gravity, this gave a deflection A and a slope θ_1 to the end of the inner beam of the shot. A gravitational load case was applied to the finite element model and this gave a deflection B and a slope θ_2 to the inner beam.

A shot supported on two sprung driving bands can be represented as shown in fig 4. For this shot the following assumptions were made;

1. The barrel had a constant bore diameter.
2. There was no friction between the barrel and the shot.
3. There is no play between the driving bands and the barrel
4. The yaw deflection were small such that $\sin \theta = \theta$.
5. The shot body, the driving bands and the barrel were inflexible.

Applying the deflections calculated from the finite element model the following equations were produced.

$$Mg = k_a(B - \theta_2 L_1) + k_b(B + \theta_2 L_2) \quad (2.1.1)$$

$$0 = -L_1 k_a(B - \theta_2 L_1) + L_2 k_b(B + \theta_2 L_2) \quad (2.1.2)$$

$$0 = k_a(A - \theta_1 L_1) + k_b(A + \theta_1 L_2) \quad (2.1.3)$$

$$T = -L_1 k_a(A - \theta_1 L_1) + L_2 k_b(A + \theta_1 L_2) \quad (2.1.4)$$

These equations were solved by putting $(L_1 + L_2)$, the distance between the driving bands, equal to that of the experimental shot. This gave values for the front and rear driving band stiffnesses (k_a and k_b) which could be used in the mathematical model SIMBAD.

The following data was required to run SIMBAD; breech mass, breech inertia, position of the bearings, bearing stiffness, bearing length, barrel profile, barrel inner diameter, shot start position, shot inertia, position of the shots' centre of gravity, shot mass and the shot driving band stiffnesses.

2.2 Firing programme

A firing programme of ten serials each of three firings was conducted. The shot was fired in five different conditions as shown in table 1, with a balanced breech, these are referred to as serials one to five. The gun was then fired in the same five conditions with an unbalanced breech, these are referred to as serials six to ten. All directions for the position of the off axis mass are when viewed from the muzzle to the breech.

For each serial three firings were conducted and if the in-bore yaw traces showed close agreement they were accepted as being representative for the given conditions. If however one of the traces showed significant differences from the other two, further firings were conducted until consistency was obtained. (This was only found to be necessary on two occasions when the diaphragm did not rupture cleanly). The three consistent firings A,B and C were then stored on disc.

2.3 Firing details Table one

Balanced breech

Serial Number	Shot Condition
1	Balanced round
2	Unbalanced round 2 grams added below horizontal axis
3	Unbalanced round 2 grams added left of vertical axis
4	Unbalanced round 1 gram added below horizontal axis
5	Unbalanced round 1 gram added left of vertical axis

Unbalanced breech (3Kg added 0.14 meters below horizontal axis)

6	Balanced round
7	Unbalanced round 2 grams added below horizontal axis
8	Unbalanced round 2 grams added left of vertical axis
9	Unbalanced round 1 gram added below horizontal axis
10	Unbalanced round 1 gram added left of vertical axis

3.0 RESULTS

Note, In-bore yaw about the transverse horizontal axis is referred to as Pitch and in-bore yaw about the vertical axis as Yaw for conciseness.



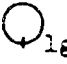



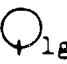

The graphical results of in-bore yaw, and in-bore pitch against time for the firing programme are given in figures 5 to 13. They are shown above the graphical output from the SIMBAD simulation. Table two gives the shot exit velocities and the shot conditions for the firing programme.

The initial runs of the program (figures 14 to 17) gave very encouraging results. The trends of the graphs being very similar to those measured. However the yaw amplitude given by SIMBAD was larger than that measured.

The angular damping coefficient for the shot was determined experimentally using the log. dec theory. The value found was then put into the shot data file and SIMBAD re-run. This gave the results given in figures 5 to 13.

The bearings of the gun were initially modelled as being pin jointed, they were then modified to have a stiffness of the order of $1E9$ N/m. This change made negligible difference to the graphs of in-bore yaw or barrel motion because the barrel that was used was comparatively very stiff. The maximum displacement of the barrel at the muzzle was measured to be less than 0.15 mm, this was confirmed by the output from SIMBAD.

Rifled Barrel Firing Programme Results Table two

Serial No	Shot Exit Velocity			Breech Condition	Shot Condition Viewed from Muzzle	Graphical Output
	Firing A	Firing B	Firing C			
1	60.09	62.07	61.54	Balanced	Balanced	A
2	60.65	59.56	58.69	Balanced		A
3	59.84	62.77	59.91	Balanced		A
4	62.65	62.46	60.17	Balanced		A
5	61.43	62.54	61.43	Balanced		A
6	63.33	62.23	62.74	3 Kg, 0.14m Below X axis	Balanced	A
7	62.74	59.56	58.96	3 Kg, 0.14m Below X axis		B
8	61.92	64.68	62.89	3 Kg, 0.14m Below X axis		A
9	60.31	61.23	61.01	3 Kg, 0.14m Below X axis		B
10	60.39	61.65	60.64	3 Kg, 0.14m Below X axis		B

4.0 DISCUSSION OF RESULTS

The important features of each firing is discussed and compared with the output from the simulation SIMBAD.

Firing one, a balanced round with a balanced breech.

As expected no output was obtained from SIMBAD for pitch and yaw as there was no input to set the shot vibrating. The experimental results showed no yaw or pitch motion, but a small low frequency waveform; which was believed to be due to the mirror on the front of the shot being out of alignment with the shot axes. Thus as the shot spun due to the rifling the instrumentation detected this as an angle of shot pitch or yaw.

Firing two, a 2g out of balance round with a balanced breech. Fig 5

The measured pitch angle shows how the added 2g mass below the horizontal axis caused the shot to pitch at shot start. However the shot does not start to yaw until it has progressed some way down the barrel. The same characteristics are shown by the SIMBAD graphs with one slight difference, the pitch angle is greater at shot start than that measured.

The measured pitch graphs show the first few cycles truncated, this phenomena was consistently produced by repeated firings. It is believed to be due to the voltage output from the instrumentation temporarily exceeding the capabilities of the digitizer, this problem is currently being investigated. This feature is present throughout all the pitch graphs but is especially noticable with the larger angles caused by the added 2g mass. The graphs all also show the shot yaw and pitch superimposed onto a low frequency waveform. As explained for the balanced shot, this was initially thought to be due to the misalignment of the shot mirror. However the SIMBAD graphs show the same characteristic. This motion could be caused by the centrifugal force on the added mass biasing the shot outwards as the shot spins up the barrel. This theory is reinforced when the graphs for an added mass of 1g are studied. These graphs show a smaller low frequency amplitude indicating that the amplitude is dependent upon the size of the added mass.

Firing three, a 2g out of balance round with a balanced breech. Fig 6

The graph of measured yaw angle shows how the added mass to the left of the vertical axis caused the shot to yaw immediately from shot start. Whereas, the shot does not start to pitch until the shot has travelled some way down the barrel. The graphs given by SIMBAD show the same characteristics. These two firings with the 2g added mass show how the yaw and pitch graphs can be significantly effected by the starting position of the centre of gravity.

Firing four, a 1g out of balance round with a balanced breech. Fig 7

This firings' graphs show that the 1g added mass does not cause the shot to yaw and pitch significantly. The pitch at shot start decays as the shot travels down the barrel such that at shot exit the pitch angle is small. The same trend is shown by the SIMBAD pitch graph, but with a smaller amplitude for the low frequency waveform. The low frequency waveform measured is almost certainly therefore due to the misalignment of the mirror on the shot rather than the effect of the added mass.

Firing five, a 1g out of balance round with a balanced breech. Fig 8

The graphs of this firing show that the added mass to the left of the vertical axis caused the shot to yaw initially and then for the yaw measured to decay until shot exit. The graphs show that the shot yawed more than it pitched, the opposite to the trends giving by the previous firing, once again highlighting the importance of the position of the out of balance mass at shot start.

Firings six to ten, with the unbalanced breech. Figs 9 to 13.

The graphs for the balanced shot, in an unbalanced breech show that a very small amount of yaw and pitch was predicted by SIMBAD, so despite the barrel being comparatively stiff it should have vibrated enough to excite the shot slightly. The measured graphs do show some yaw and pitch near shot start but this motion decays away by shot exit.

BARKER

The four other firing conditions show the same features as the firings with a balanced breech with perhaps a slight increase in the measured yaw motion with the lg out of balance round compared with the firings with a balanced breech. This again would tend to indicate that the unbalanced breech was causing the barrel to vibrate and so excite the shot.

The graphs shown in figs 14 to 17 show the initial output from SIMBAD compared with the actual firings before the damping coefficient was fed into the shot data file. The main difference between the graphs is the large yaw and pitch angle given by SIMBAD. This, as previously stated was reduced by adding in the shot damping coefficient and shows the importance for future simulations of accurately knowing the damping coefficient of the shot being modelled.

5.0 CONCLUSION

The firing programme described has shown that measurements using optical techniques can be made of the in-bore yaw and pitch of a shot travelling down a rifled barrel in the RMCS air powered gun. The effect of an off axis mass on the shot has also been shown to greatly increase the yaw and the pitch of the shot. The simulation SIMBAD accurately predicted the pitch and yaw traces for each firing condition. This gave confidence in the present results and showed one area where the instrumentation needed to be investigated.

Further work is now envisaged using a more flexible, rifled barrel with higher muzzle velocities.

6.0 ACKNOWLEDGEMENTS

This research is funded by the Royal Armament Research and Development Establishment (Fort Halstead).

7.0 REFERENCES

- 1.0 POWELL S.E.
A simple theoretical model of shot/barrel interaction within a smooth bore gun.
4th U.S. Army Symposium on Gun Dynamic, Riviera Beach, Florida, May 85.
- 1.1 RAMA (A computer program)
A computer package written and developed by RMCS under contract to RARDE (Fort Halstead) which models the motion of the barrel by the finite difference technique.
- 1.2 KING W.P.C., PAGAN G. and THOMAS M.D.
A model for tank gun movements during firing using an implicit difference numerical algorithm.
3rd U.S Army Symposium on Gun Dynamics, Rensselaerville, New York, May 82

BARKER

- .3 PENNY P.H.G. and KING W.P.C.
The predicted effect on 'gun jump' due to changes in gun cradle bearings and gun barrel stiffness.
4th U.S. Army Symposium on Gun Dynamics, Riviera Beach, Florida, May 85
- 1.4 SIMBAD (A computer program)
A computer package written by Dr D.N. Bulman of the Land Systems Group RMCS which models the motion of the barrel, the shot and the shot barrel interaction by the finite element method.
- 1.5 BULMAN D.N.
The effect of bearing clearance and barrel expansion on barrel response.
4th U.S. Army Symposium on Gun Dynamics, Riviera Beach, Florida, May 85
- 1.6 POWELL S.E.
The use of the RMCS Compressed Air Powered apparatus for the Measurement of In-bore Yaw.
TTCP WTP-2(KTA6), BRL Aberdeen, Maryland, October 83.
- 1.7 POWELL S.E.
An experimental round for in-bore measurement.
Shrivenham RMCS report LS/002/1405.
Presented at TTCP WTP-2 (KTA6), RARDE Fort Halstead September 1984

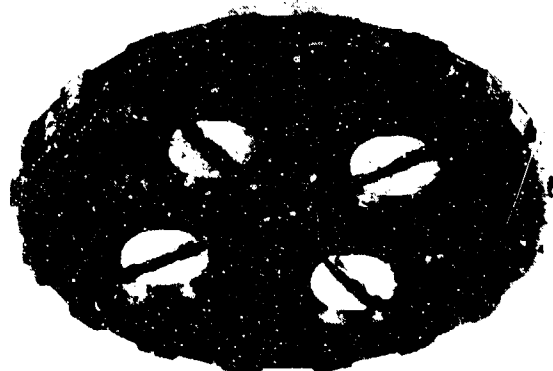


Fig 1. Rifled Barrel Round.

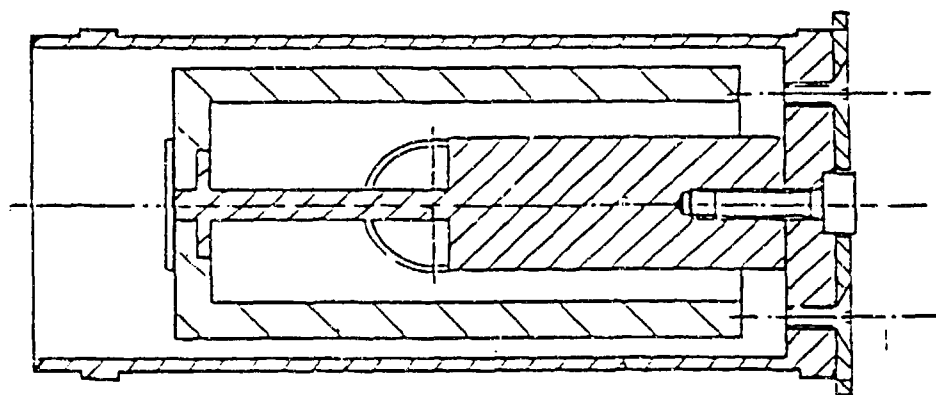


Fig 2. Cross section of experimental shot

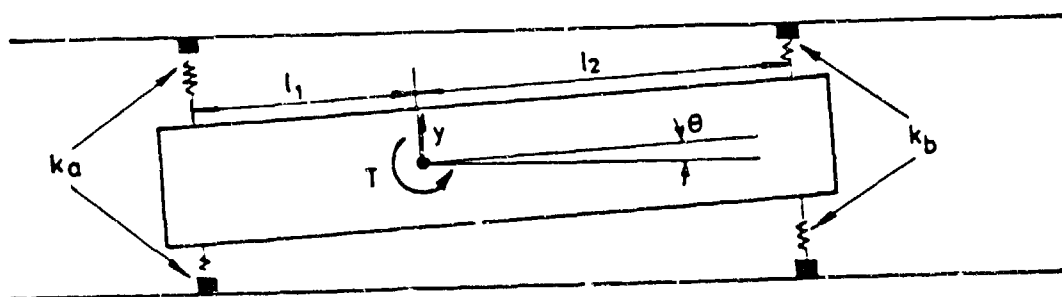


Fig 4. A shot supported on two sprung driving bands

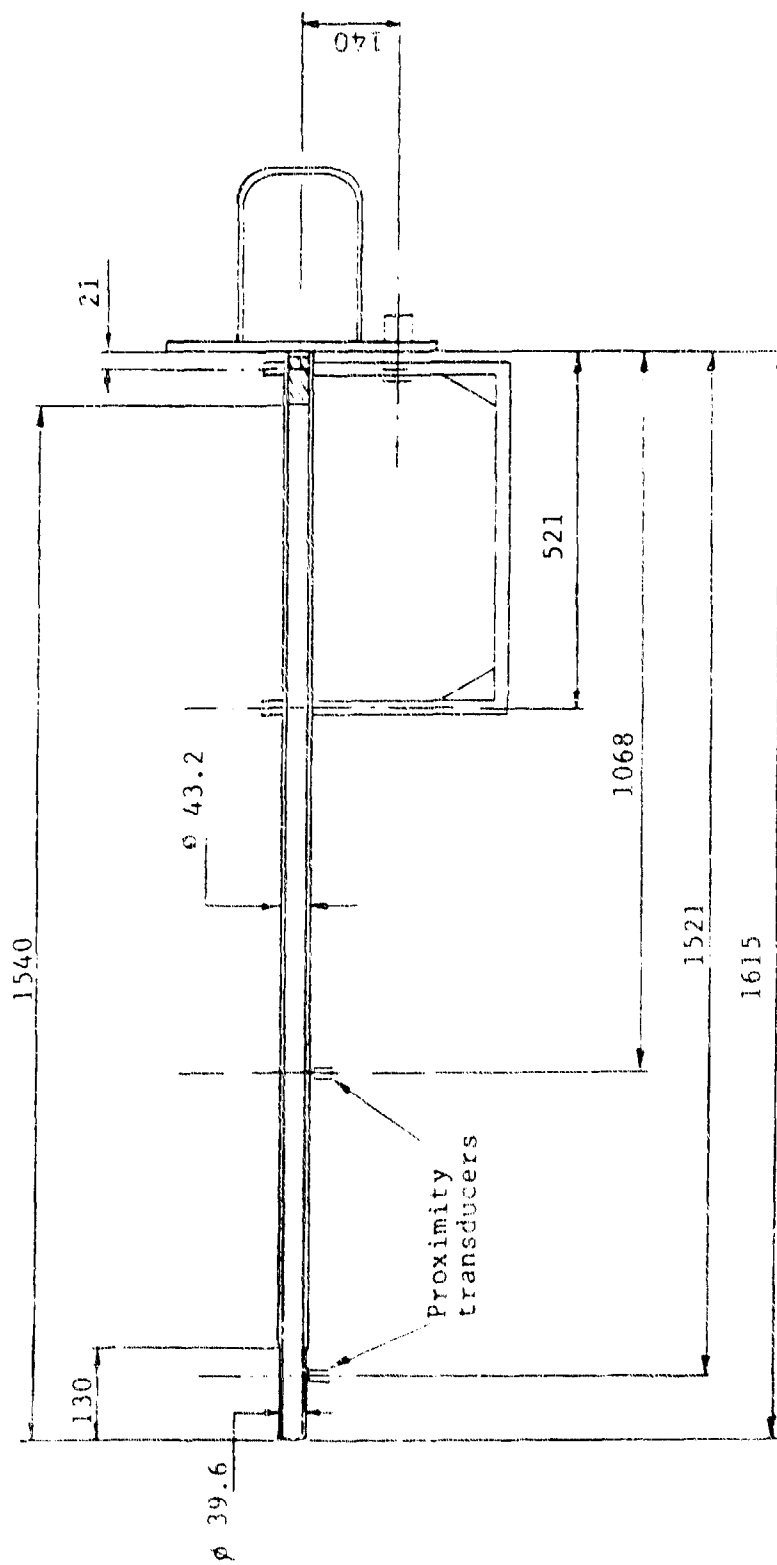


Fig 3. Principal dimensions in mm of the Air powered gun when fitted with the rifled barrel

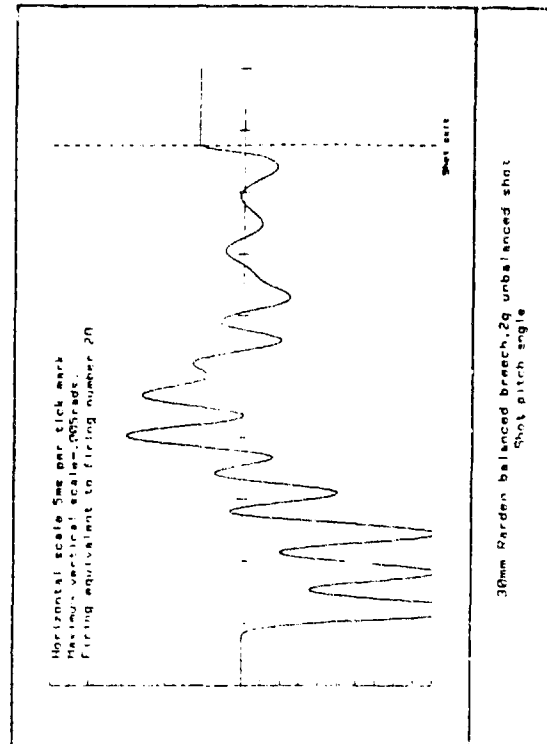
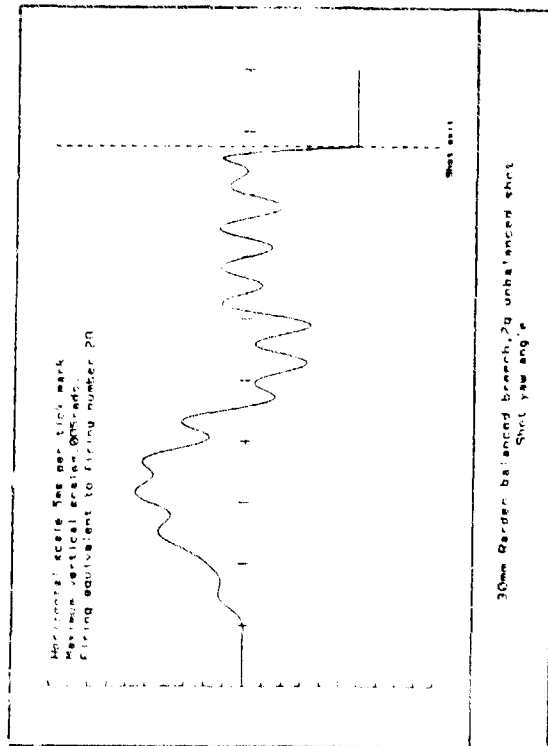
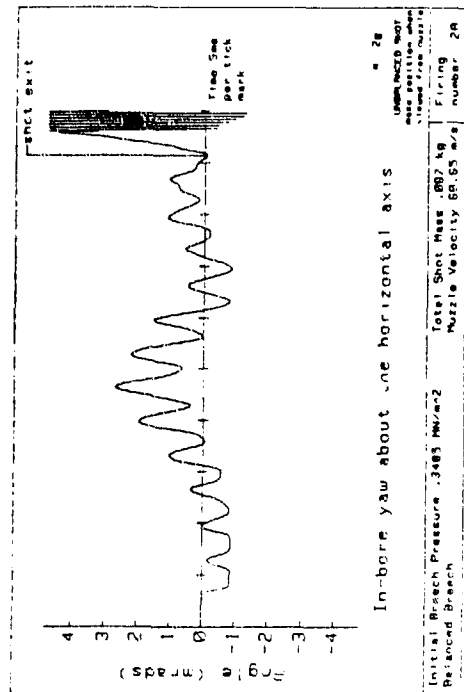
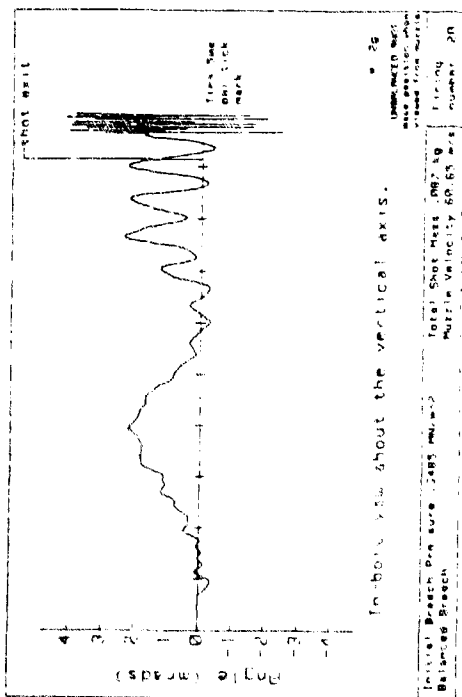


Fig 5.

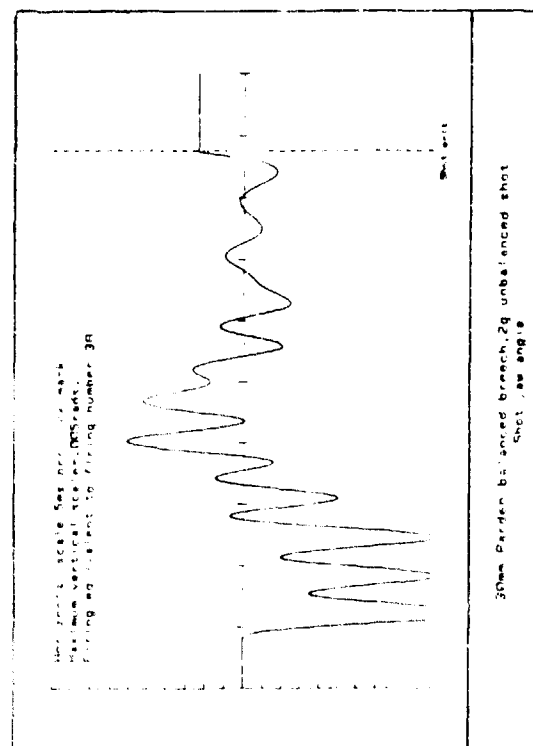
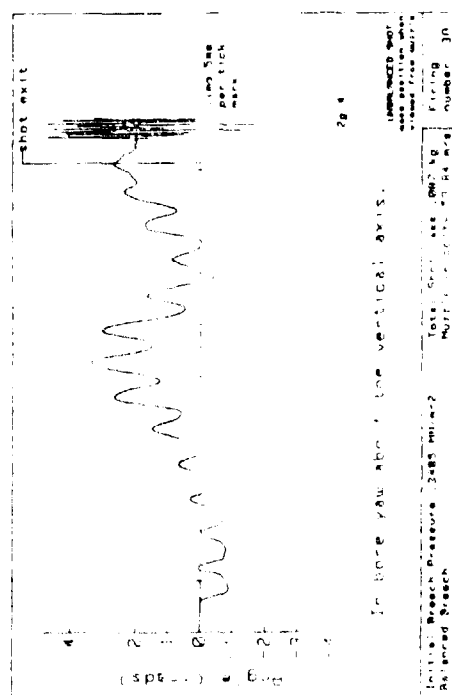
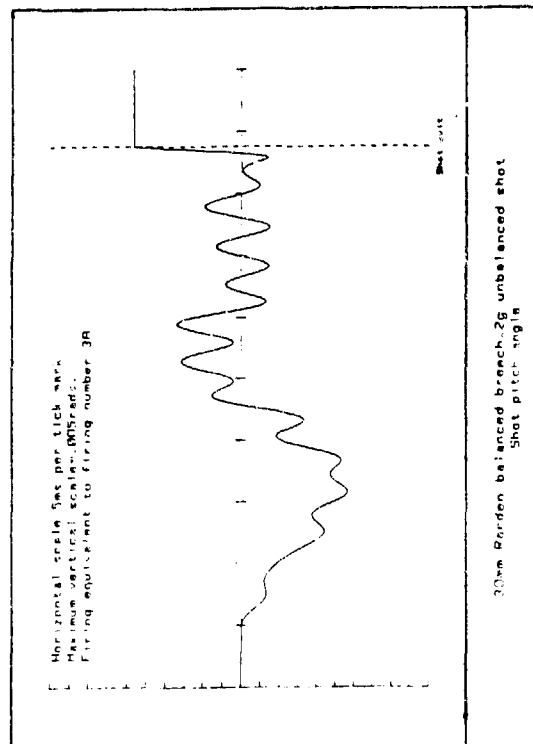
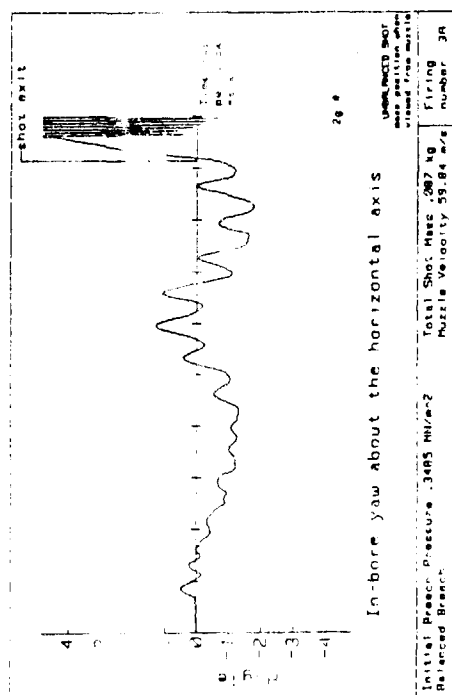


Fig 6.

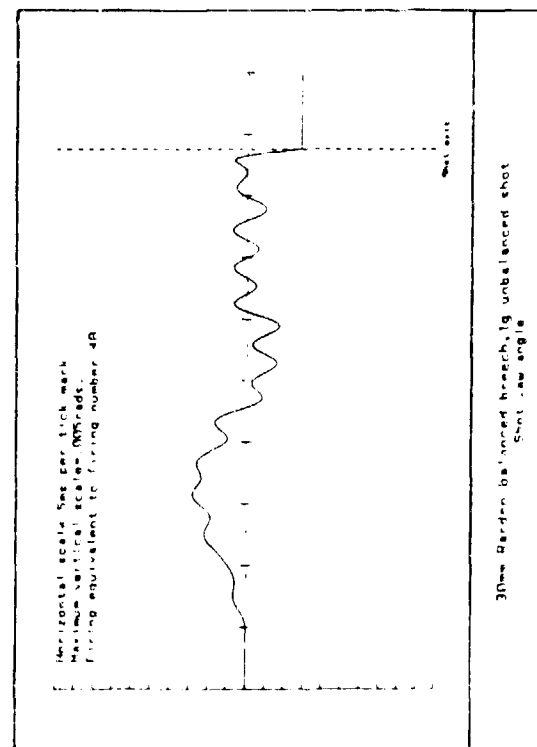
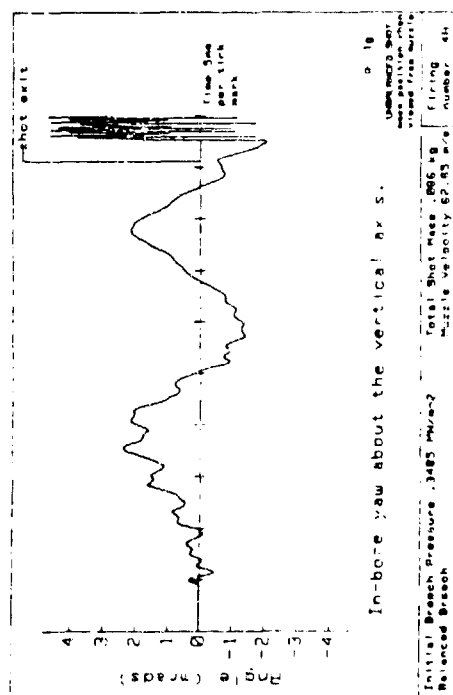
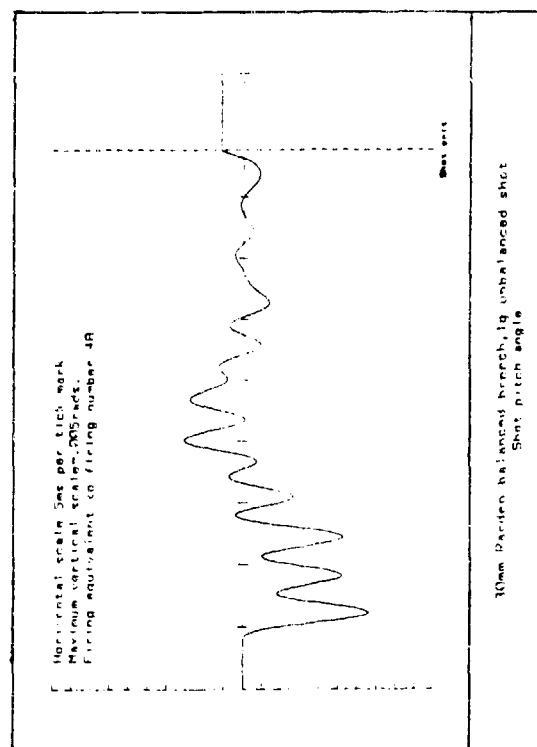
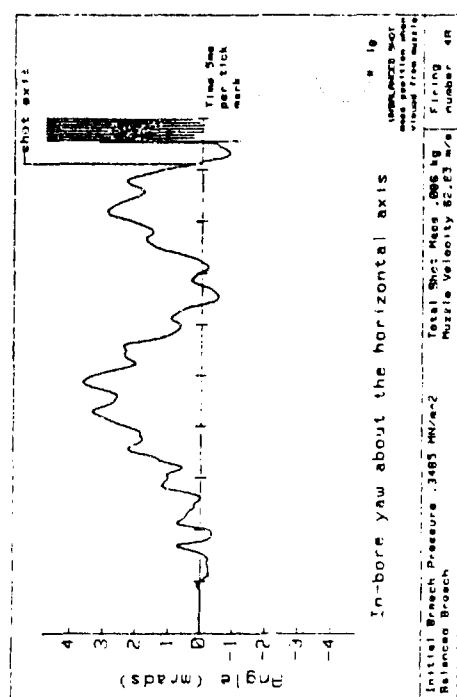


Fig 7.

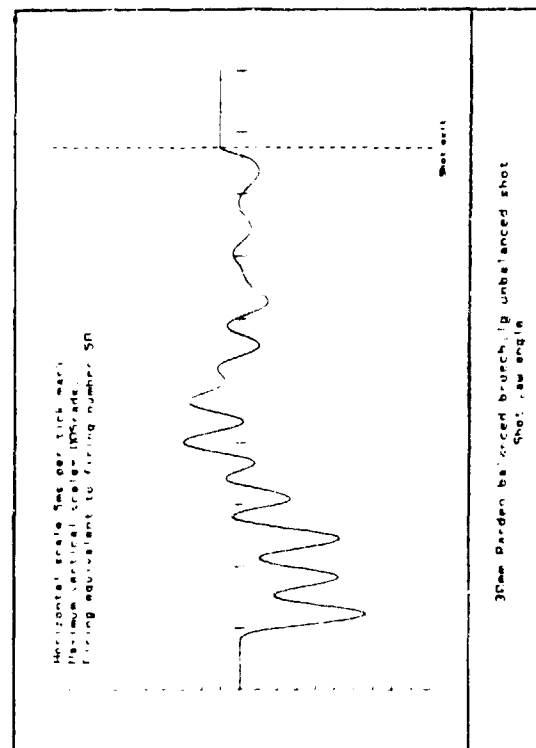
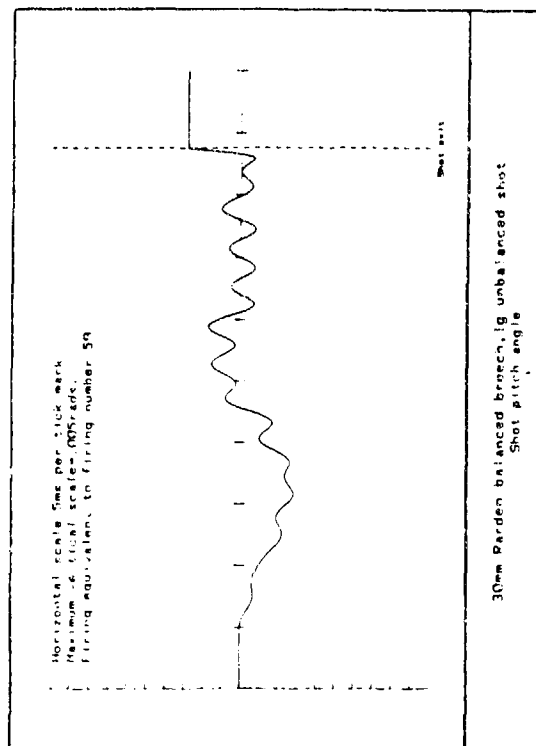
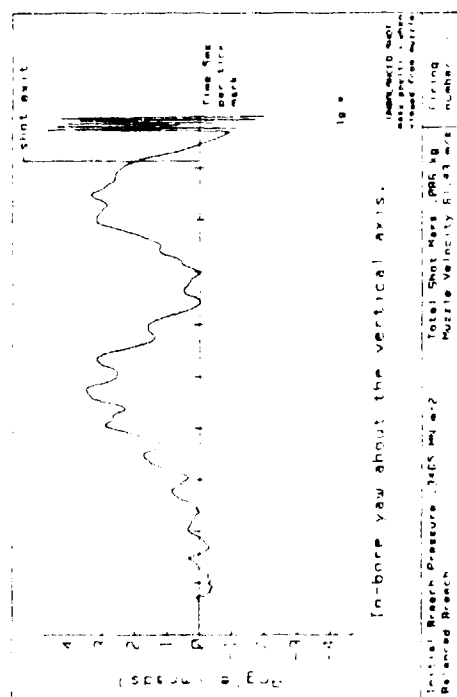
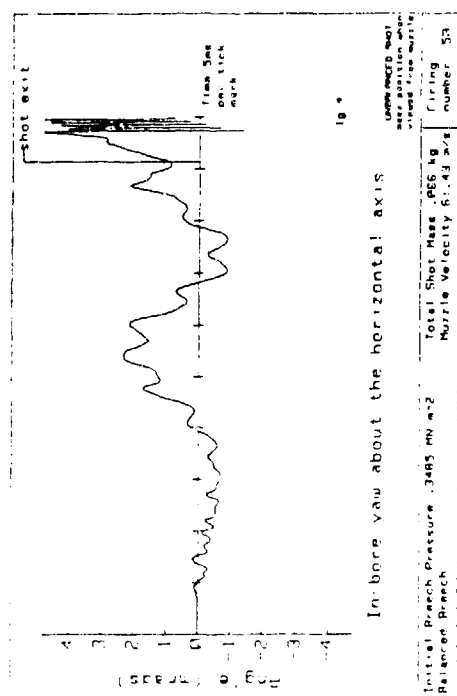


Fig 8:

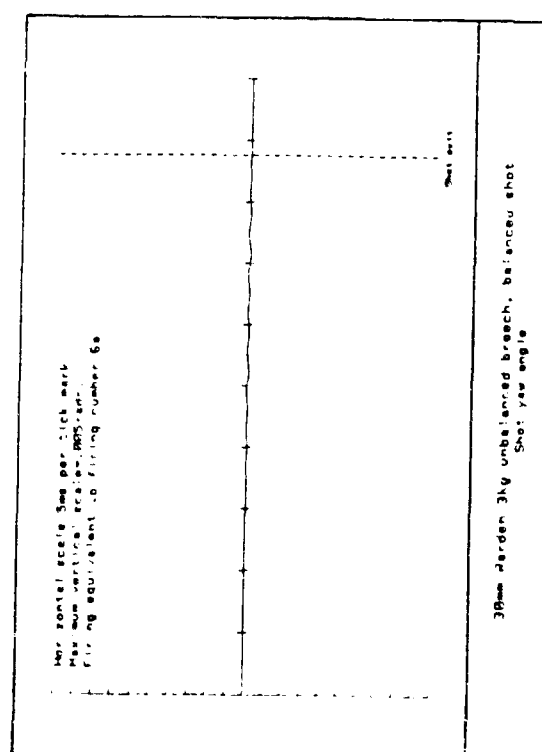
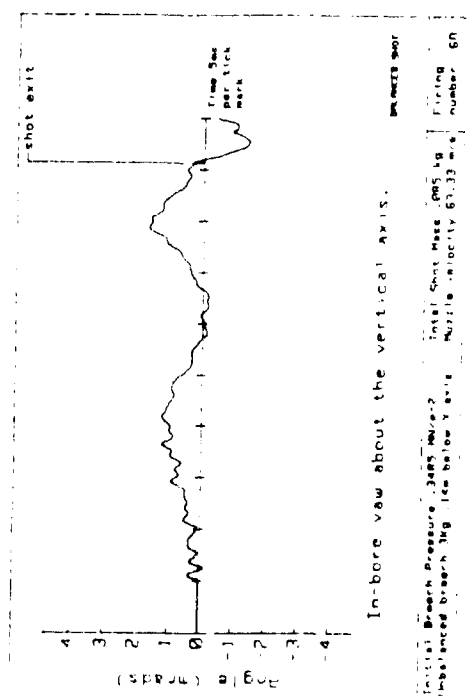
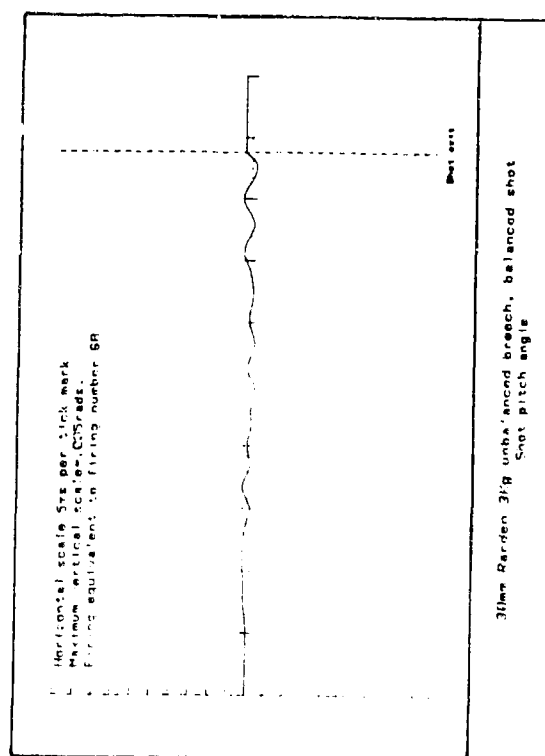
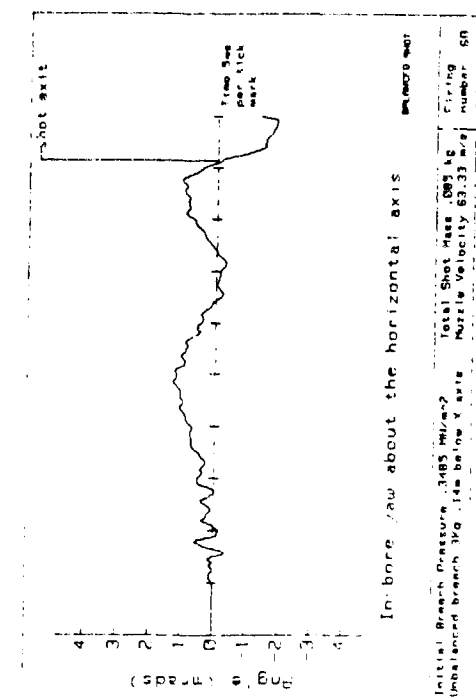


Fig 9.

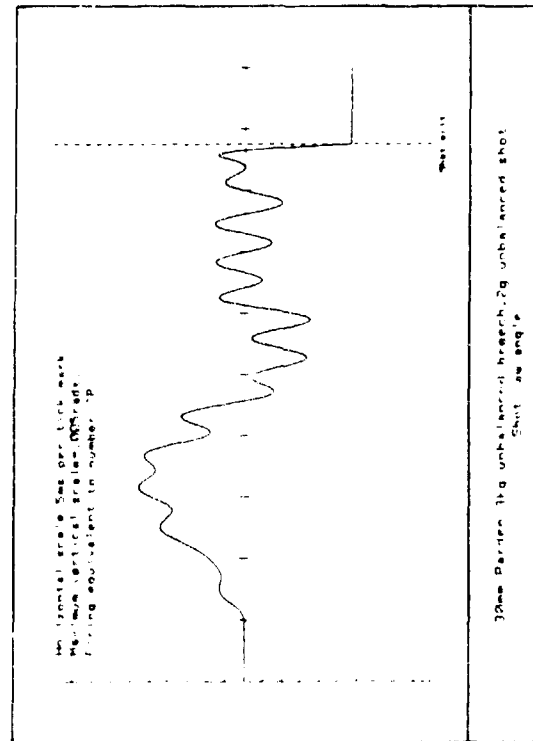
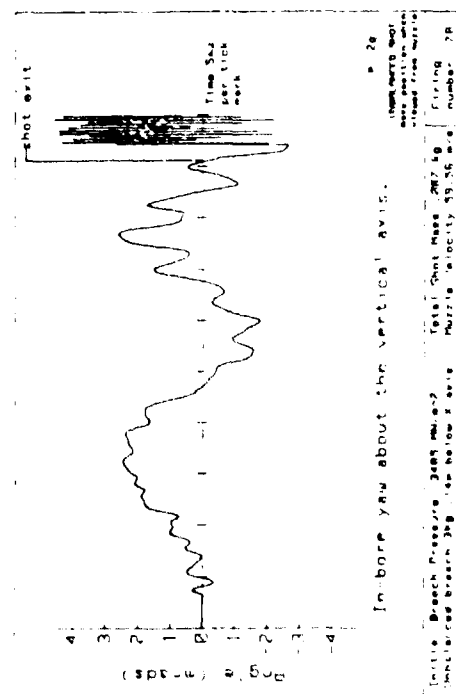
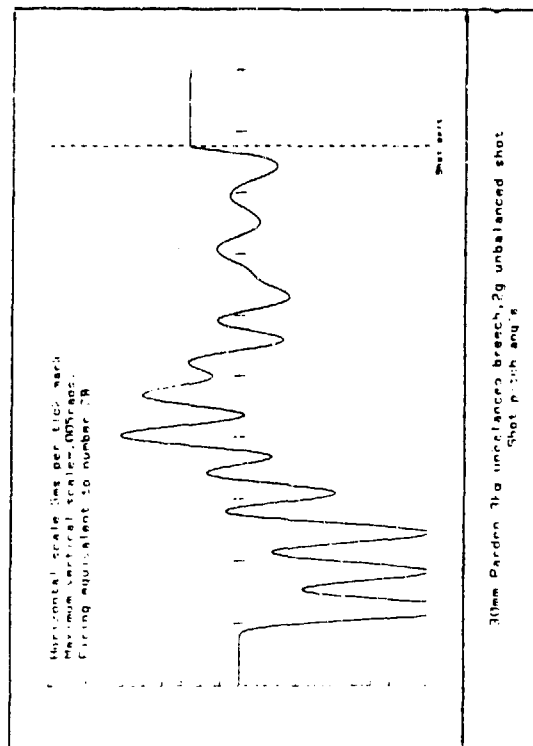
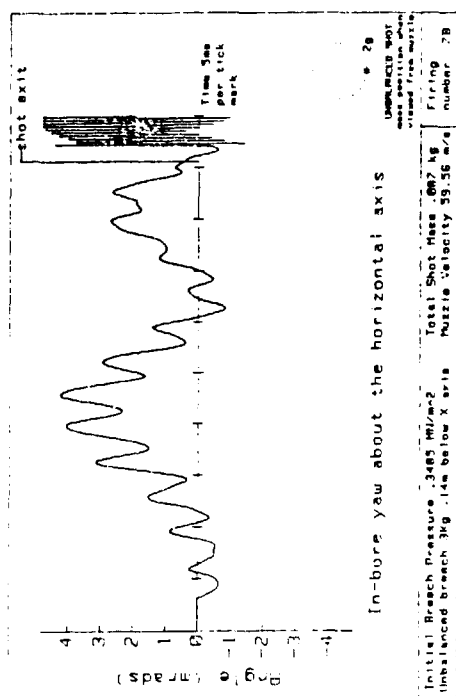


Fig 10.

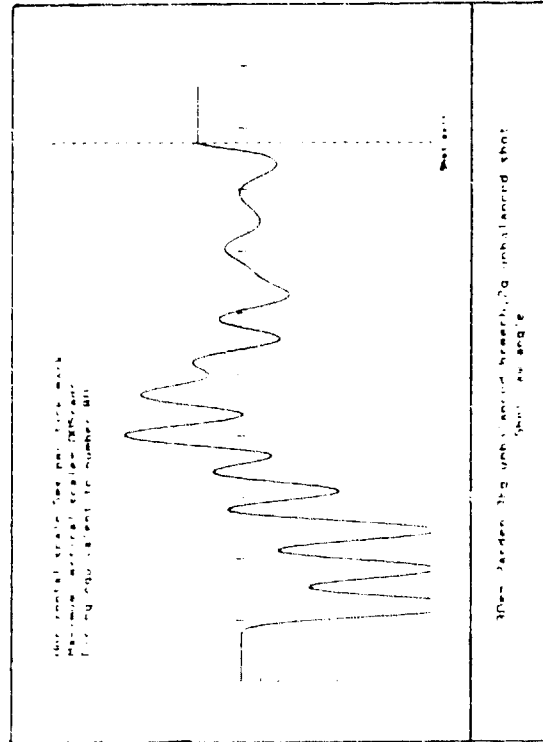
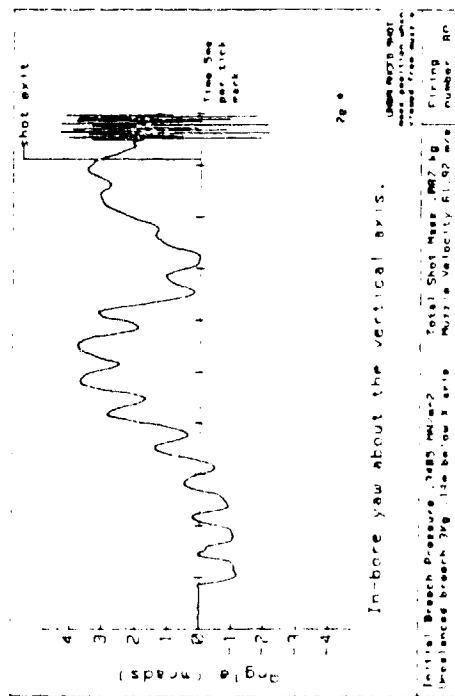
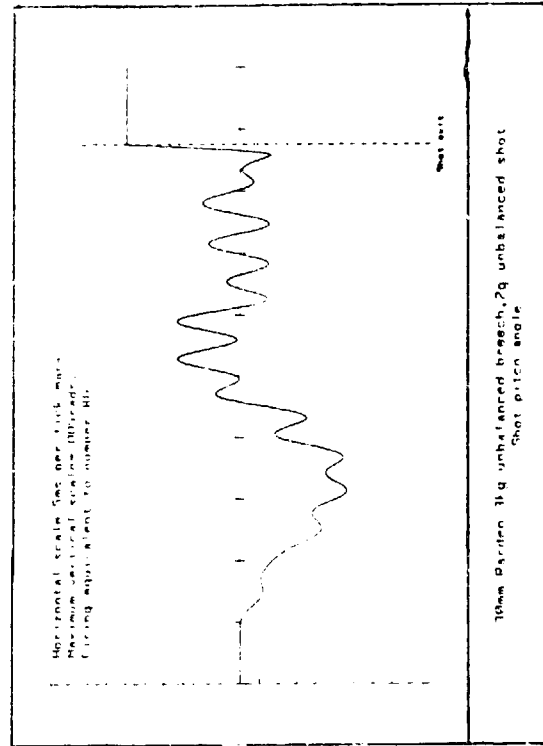
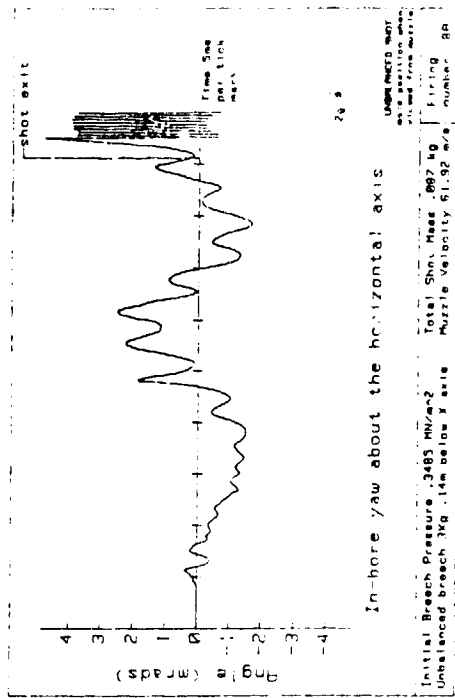


Fig 11.

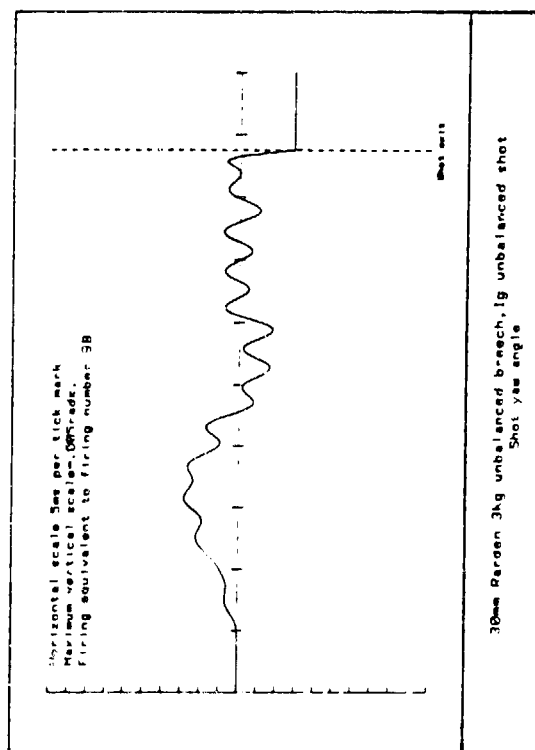
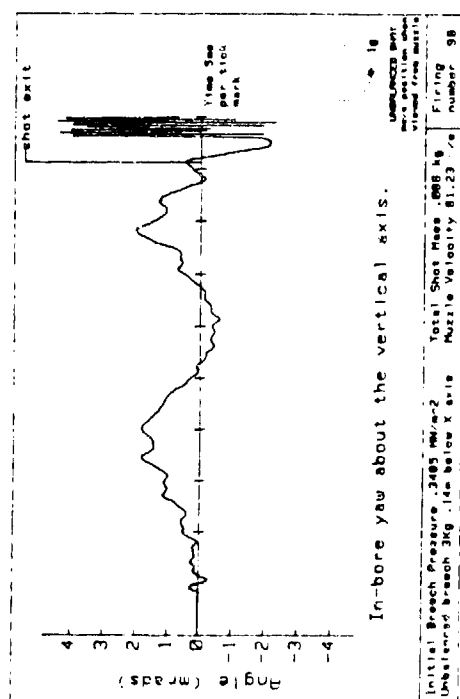
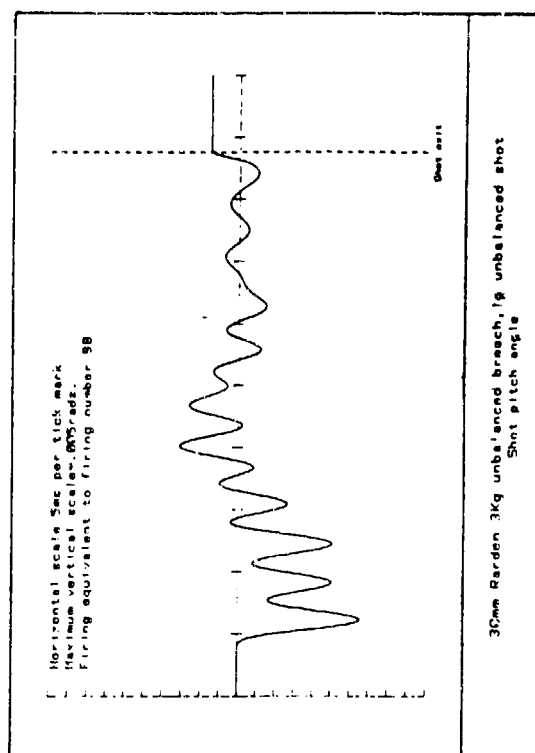
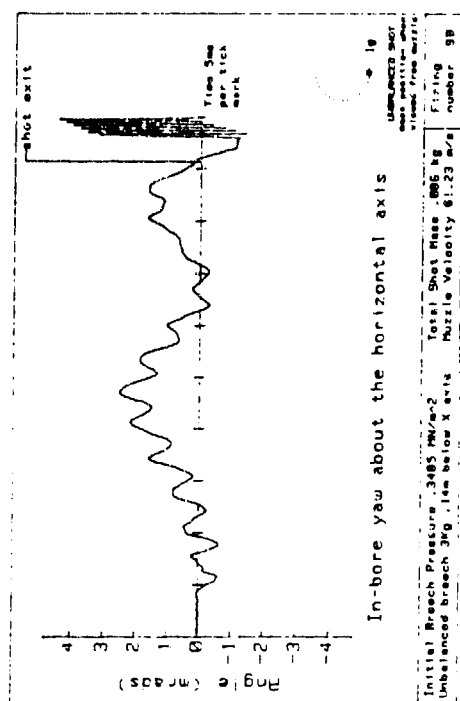


Fig 12.

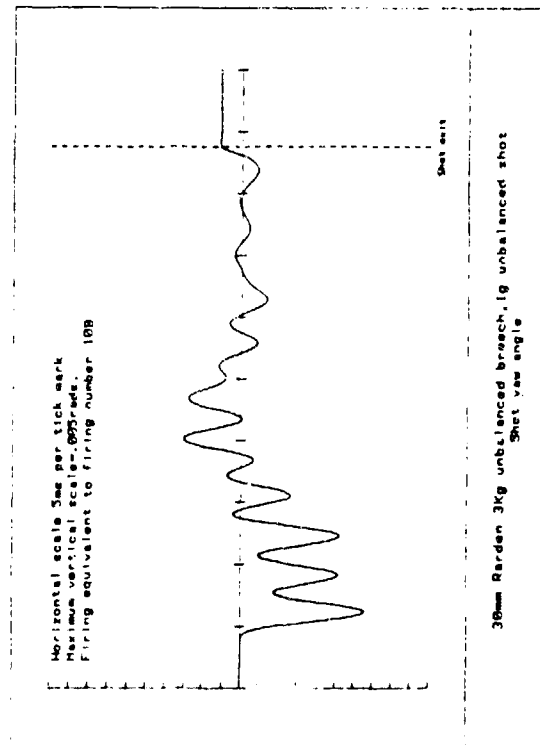
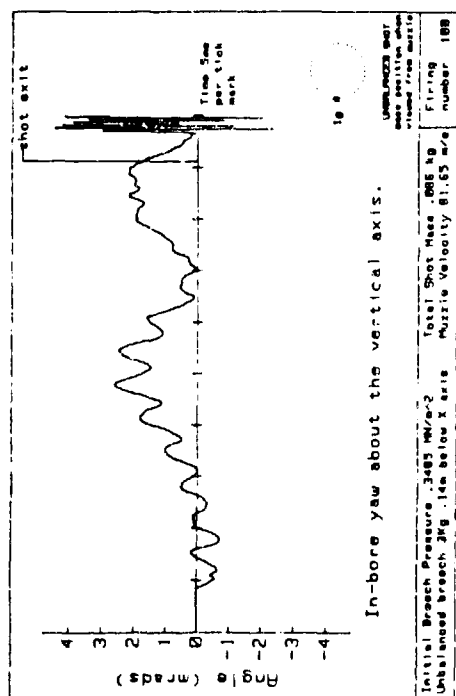
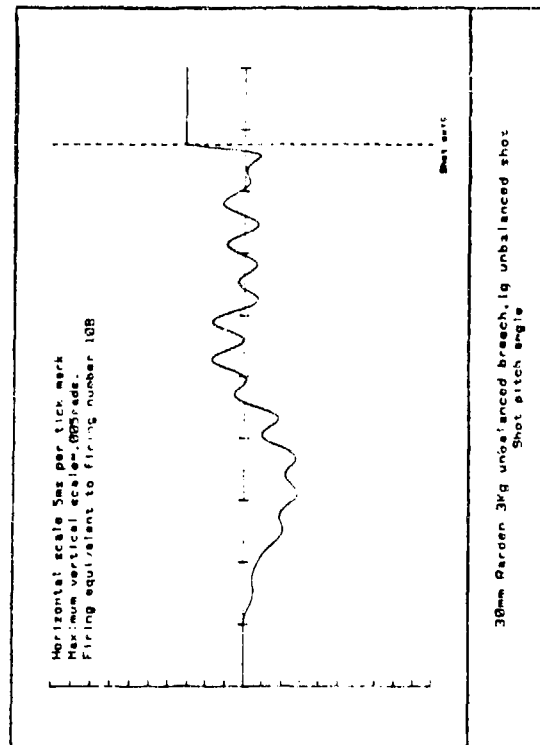
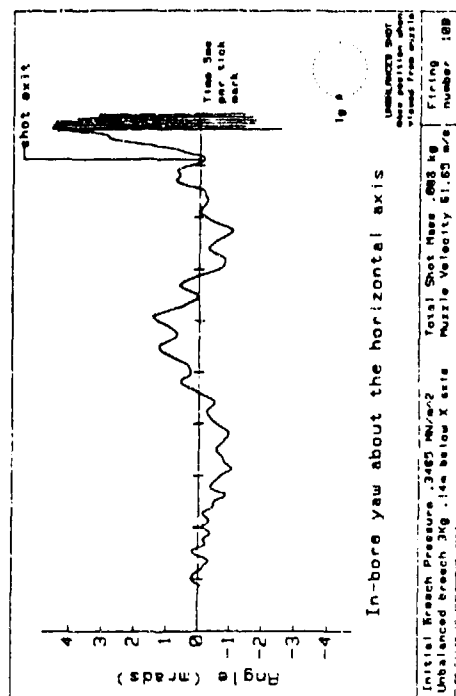
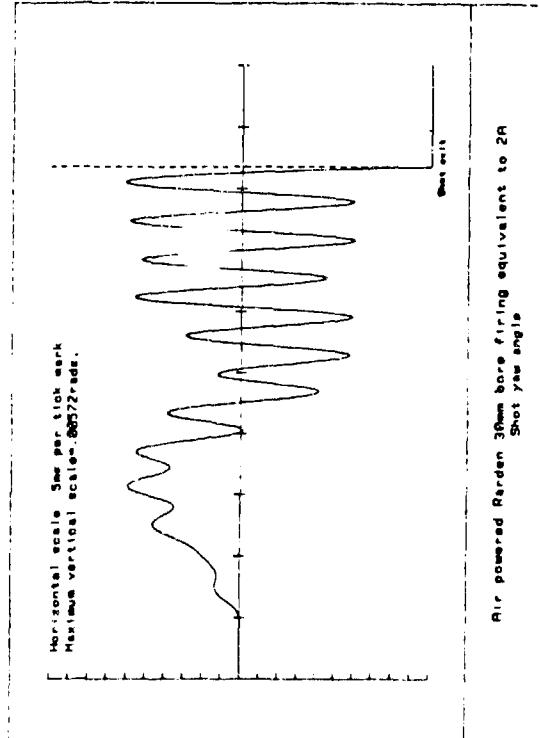
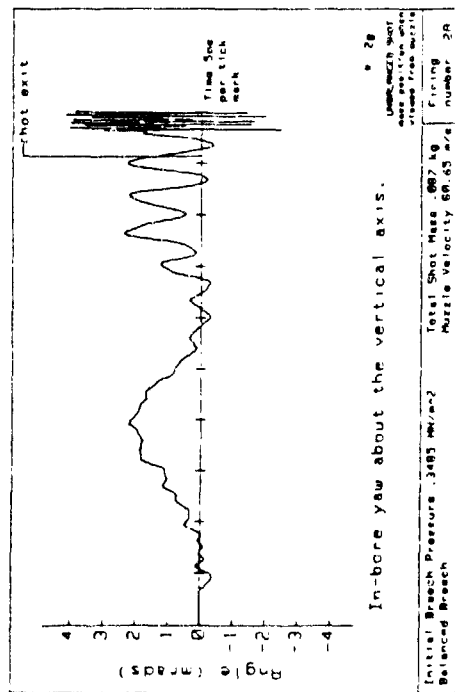


Fig 13.



280

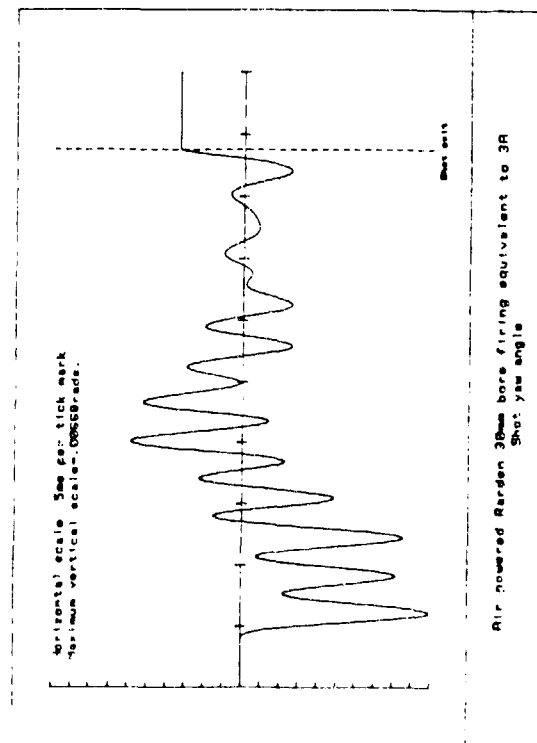
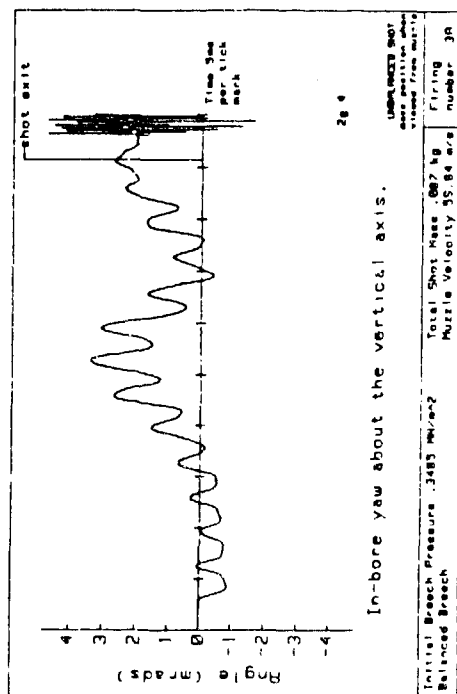
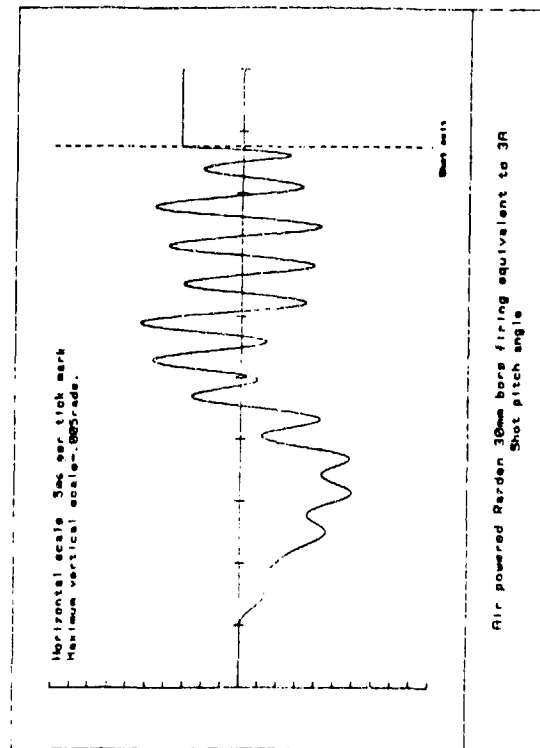
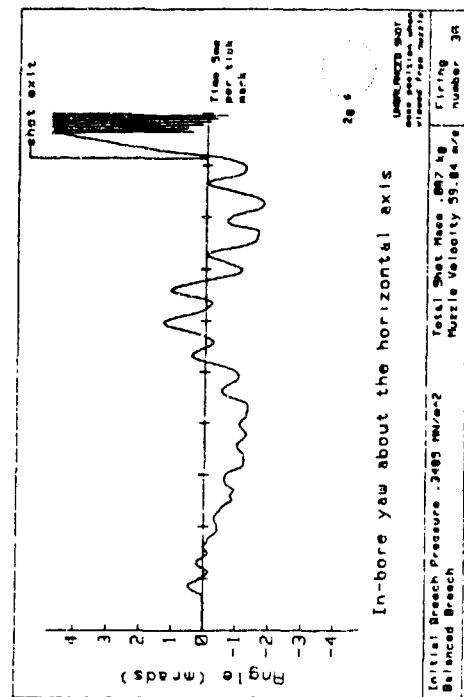


Fig 15.

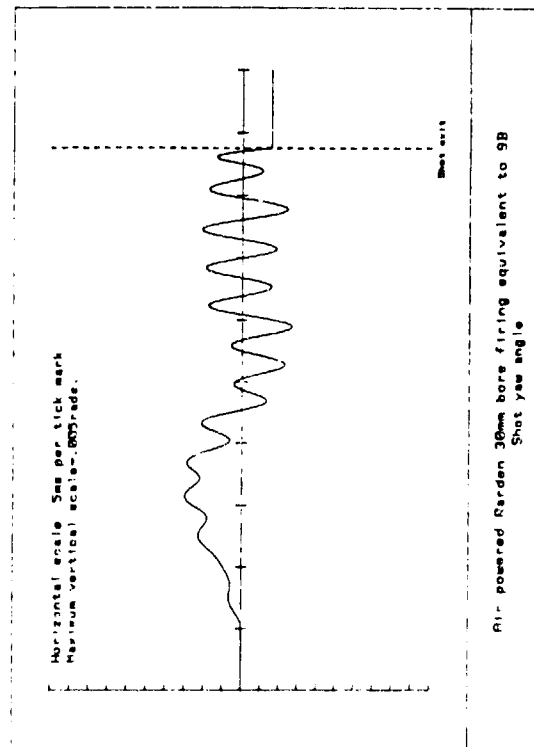
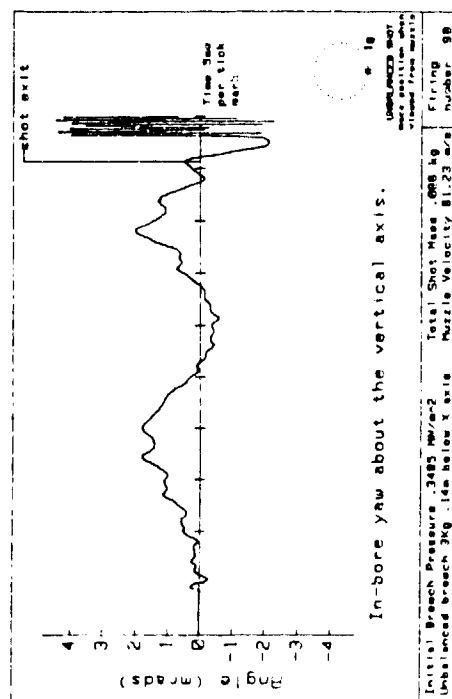
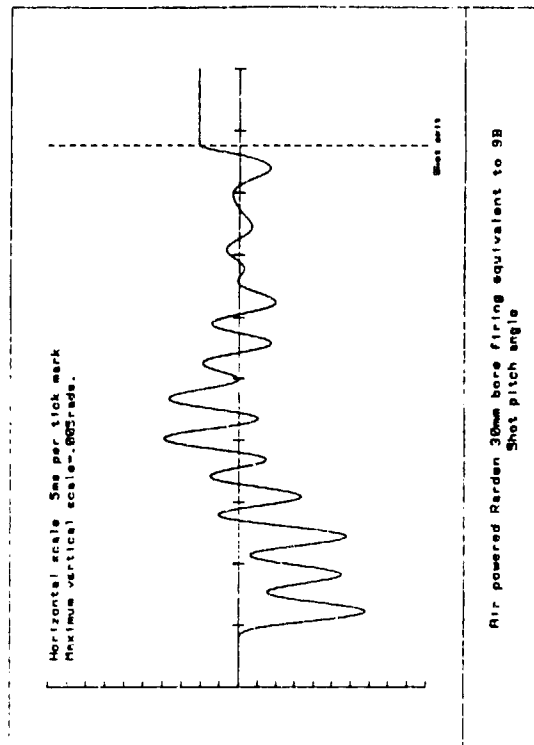
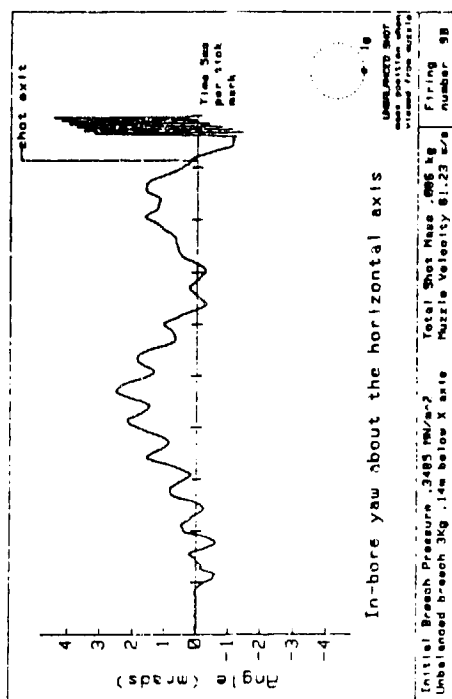


Fig 16.

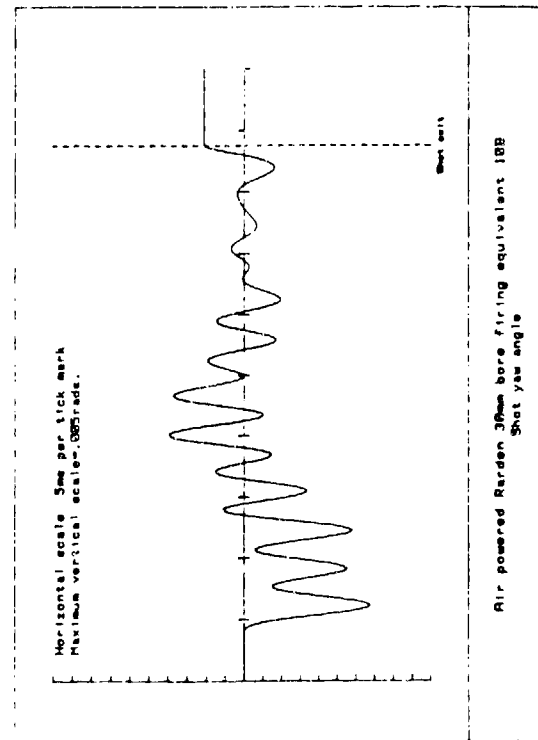
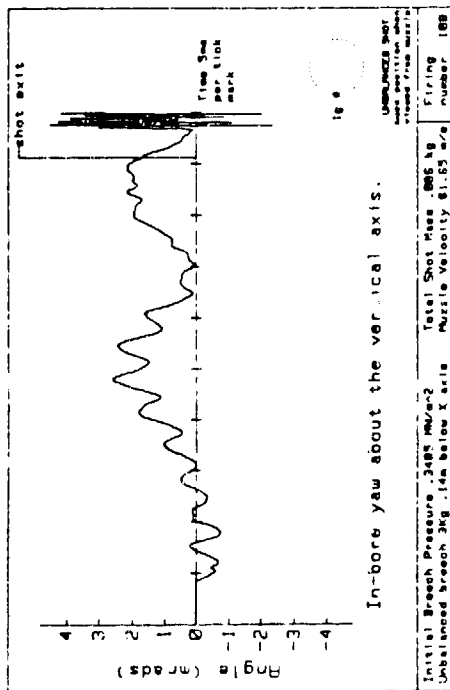
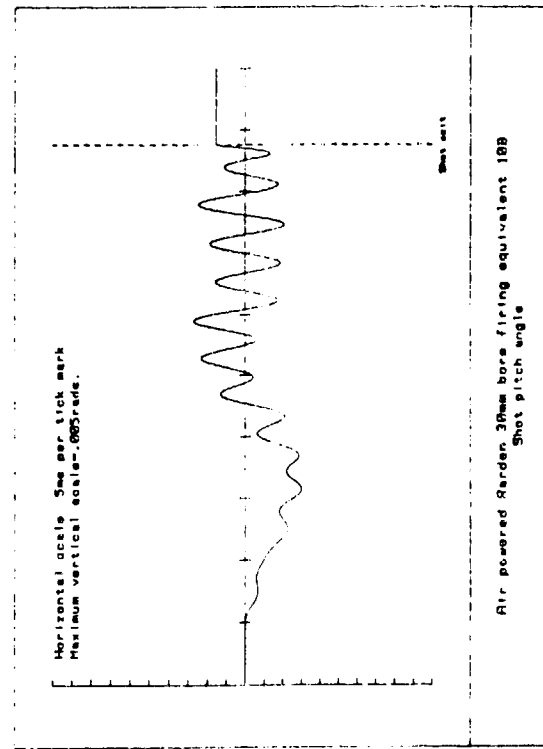
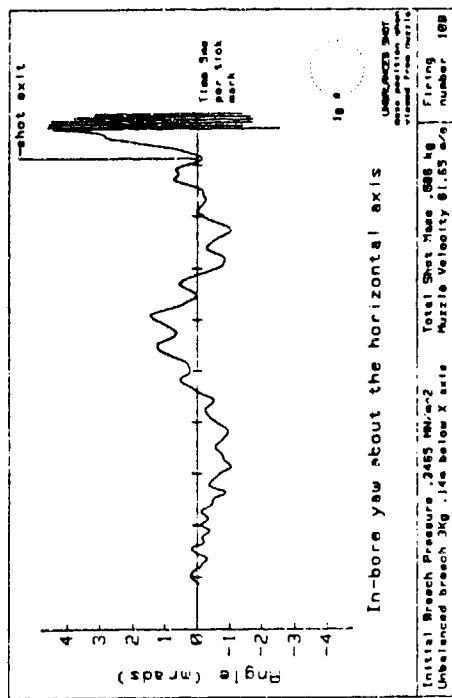


Fig 17.

SESSION V

ELECTROMAGNETIC PROPULSION/STOCHASTIC MODELING

TITLE: STOCHASTIC MODELING FOR IMPROVED WEAPON PERFORMANCE

Mr. Anthony Baran
Mr. John Groff
Ballistic Research Laboratory
Aberdeen, Maryland

Mr. James Cantor
Mr. Steve Carchedi
Mr. Bruce Gibbs
Business and Technological
Systems Inc.
Seabrook, Maryland

Mr. Herbert Cohen
Army Materiel Systems
Analysis Activity
Aberdeen, Maryland

ABSTRACT

This paper discusses the work jointly performed by the U.S. Army Materiel Systems Analysis Activity, the Business and Technological Systems Inc. Company and the Ballistic Research Laboratory in characterizing armored vehicle weapon tube flexure using stochastic modeling techniques. The motivation for performing this work stems from the fact that the contribution of gun bend related errors to projectile miss distance can be significant depending on such factors as:

- the physical composition and characterization of the weapon; and
- environmental conditions such as temperature and base motion disturbances, etc.

Hence the ability to predict the precise location of the weapon's muzzle as a function of time in terms of its past and current history as well as other sensor measurements could significantly enhance weapon system accuracy.

Previous efforts to develop muzzle flexure prediction algorithms has generally relied on purely deterministic techniques. That is, gun flexure was mathematically characterized by deterministic differential equations that were a function of such parameters as weapon angle position, rate and acceleration, linear acceleration, and bending of the gun tube. In the case of gun dynamics these techniques tended to be unsuitable for practical implementation because

- mathematically they may be extremely complicated,
- they do not account for modeling and measurement uncertainties, and
- they lack the robustness of being adaptive,

i.e., of being able to automatically change in order to reflect peculiar characteristics of an individual weapon tube and armored vehicle.

This study discusses the preliminary work that has been performed to develop practical algorithms that address the above problems. The overall technical approach was to

- apply time series analysis techniques to strain gauge and other test data obtained from the M1 Combat Tank mounting a 105mm weapon system and tested over a special Aberdeen Proving Ground Test Course,
- develop autoregressive-moving average (ARMA) models of the test data that characterize dynamic weapon flexure,
- convert the ARMA model to adaptive Kalman filter predictive algorithms,
- exercise the Kalman filter predictor models and compare predicted performance against measured muzzle flexure over various projectile in-bore times.

The paper concludes with a discussion of future modeling and field testing necessary to refine the existing Kalman filter/predictor algorithms.

BIOGRAPHY: John Groff

Present Assignment: Team Leader, Engineering and Analysis Section, Ballistic Research Laboratory, Aberdeen, Maryland.

Past Experience: General Engineer and Research Engineer with industry and government.

Degrees Held: B.S. Mathematics, University of Wisconsin; M.S.

Mathematics, Marquette University. Graduate work in electrical engineering at University of Wisconsin, Johns Hopkins University, and University of Delaware.

STOCHASTIC MODELING FOR IMPROVED WEAPON PERFORMANCE

Mr. Anthony Baran
Mr. John Groff
Ballistic Research Laboratory
Aberdeen, Maryland

Mr. Herbert Cohen
Army Materiel Systems
Analysis Activity
Aberdeen, Maryland

Mr. James Cantor
Mr. Steve Carchedi
Mr. Bruce Gibbs
Business and Technological
Systems Inc.
Seabrook, Maryland

1.0 INTRODUCTION

Since gun barrel bending contributes significantly to the total projectile error budget, efforts to predict the precise location of the gun muzzle as a function of time in terms of its past history could significantly improve the accuracy of the weapon system. Previous efforts by the U.S. Army Ballistic Research Lab (BRL) to develop precision aim techniques (PAT) have used a deterministic approach. Specifically, the gun motion was assumed to be described as a function of gun turret angles, angular rates and accelerations, tank vertical acceleration and bending (and bending rates) of the gun tube. The differential equation used to predict the position of the gun muzzle at projectile exit was derived using simple geometry and the equation for the fundamental bending mode. Although the deterministic approach is promising, it has not performed well in field tests at longer (e.g., 20 milliseconds) in-bore times.

An alternate approach is to use only strain gauge (gun tube deflection) and servo error data and model the gun deflection as a Markov process: a linear system driven by white noise. It is this stochastic approach which was investigated here.

In this paper we describe an adaptive model identification algorithm for predicting gun deflection as the projectile leaves the tube. The adaptability is necessary because of the potential great variability in the gun

motion due to tank velocity or variation in terrain (e.g., surfaced road to rough ground). Efficient operation is desirable as the algorithm could possibly serve as the basis of a real-time gun inhibit algorithm.

The paper is in five sections. In Section 2, a discussion of the data utilized for modeling is given. In Section 3, the technical approach is outlined and the method used for evaluating the algorithm is described in Section 4. The paper is concluded in Section 5 by a brief discussion and suggestions for future investigations.

2.0 TEST DATA

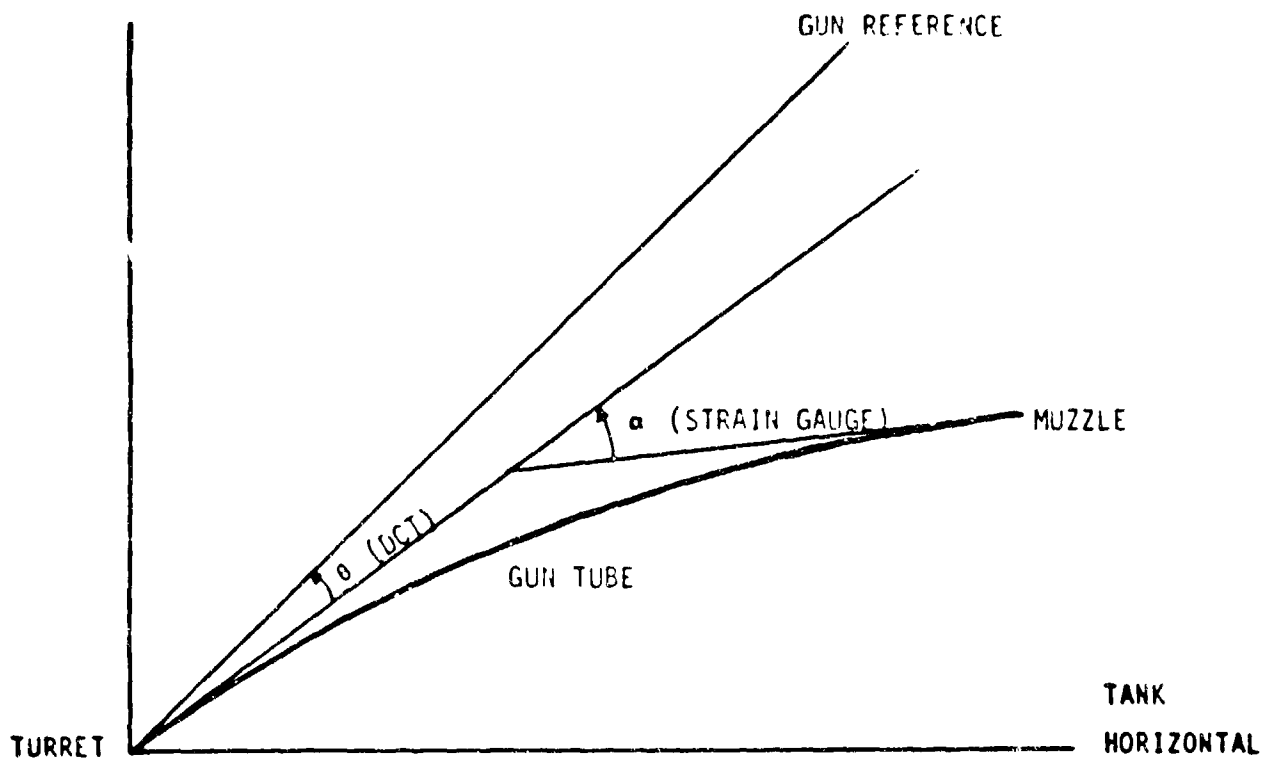
The available data was obtained from strain gauge and digital control transformer (DCT) sensors mounted on the gun tube of a heavy tank in wide use by the Army. The strain gauge measured the gun tube deflection while the DCT measured the angle of the gun tube with respect to the turret (see Figure 2-1). Both sensors were sampled at 250 Hz (4 milliseconds).

There were four tests available for analysis. Each test was conducted on the Profile IV bump course at Aberdeen Proving Ground at speeds of 5, 15, 22, and 30 miles per hour (one test at each speed). The course consists of approximately 460 feet of triangular and small wooden bumps up to 12 inches high with gravel lead in and exit areas. The Profile IV course is considered to be one of the most severe tests of a tank's ability to point the gun accurately while traversing rough terrain.

3.0 TECHNICAL APPROACH

We next describe the technical approach implemented for strain gauge, DCT, and resultant muzzle error identification and prediction. The basic approach was to model the data as a Gauss-Markov process. Specifically, based on the spectral analysis (discussed in 3.1), it was assumed that the data was best modeled as an autoregressive moving average (ARMA) model

Figure 2-1
Geometry of Gun Tube Deflection



(defined below) whose parameters are selected under the criterion of minimizing the prediction error. A good summary of ARMA modeling techniques can be found in [1].

3.1 Data Analysis

The data was first carefully examined to determine general characteristics and to identify statistically (locally) stationary segments. By comparing the data to a schematic of the bump course, segments representative of various physical situations or environments could be selected. These segments provided the means to investigate the spectral content as well as evaluate the eventual design (see Section 4).

Computation of data power spectra using the periodogram and the maximum entropy method (MEM) was performed to identify the dominant spectral bands and the bandwidth of these spectra. This analysis proved useful in relating the observed spectral content to the physical effects as well as in the determination of the appropriate model and approximate model order. Further, an important conclusion based on the spectral analysis is that tank speed had little effect on observed spectral frequencies. An estimate of the power spectrum of the muzzle error using MEM for a segment consisting primarily of small bumps is given Figure 3-1.

3.2 Identification

It is assumed that an ARMA (p,q) model

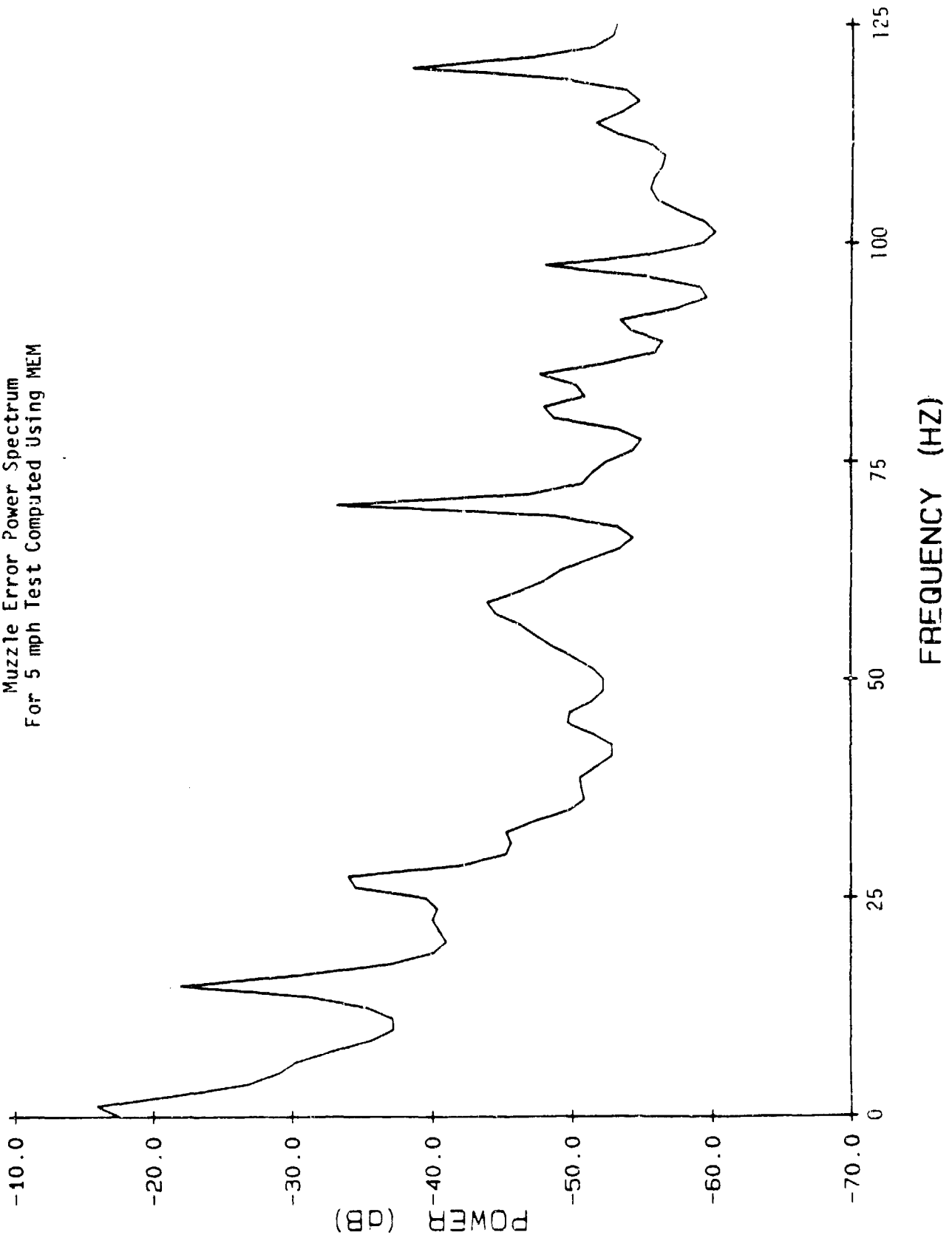
$$z(k) = - \sum_{i=1}^p a_i z(k-i) + \sum_{i=1}^q b_i w(k-i) + b_0 w(k) \quad (3-1)$$

is sufficiently general to model both the DCT and strain gauge data. In (3-1), a_i , $i=1,2,\dots,p$ and b_i , $i=1,2,\dots,q$ denote respectively the autoregressive (AR) and moving average (MA) coefficients, p and q are the AR and MA orders, and $w(k)$ is a zero mean, unit variance Gaussian white noise sequence. The use of the model for prediction therefore initially requires estimation of the orders and coefficients.

The autoregressive order (p) was estimated using a technique due to Cadzow [2] based on determining the effective rank of an associated overdetermined ARMA autocorrelation matrix. (The term overdetermined refers to AR and MA orders selected for estimation which are much larger than the true unknown orders.) As far as could be determined, no similar technique is available for estimating the MA order and for this reason, Cadzow's suggestion of simply setting the MA order equal to AR order was implemented.

As is well known [3]-[4], estimation of the AR coefficients under a least squares criterion results in a linear system of equations to be solved. However, the MA estimation is a nonlinear system. For this reason, the basic approach to coefficient estimation was to approximate the ARMA process by a

Figure 3-1
Muzzle Error Power Spectrum
For 5 mph Test Computed Using MEM



large order autoregression. (Note that any ARMA process can be represented by an AR process of possibly infinite order.) This viewpoint was adopted due to the severe computational constraints. The technique implemented essentially follows an approach described by Graupe et al. [5] which involves estimating the coefficients of a high-order AR model and transforming it to a lower order ARMA Model. The AR coefficients were computed from MEM utilizing Burg's algorithm [6].

3.3 Prediction

As discussed, accurate firing of the tank requires prediction of the muzzle error at some future time instant. The length of prediction step is dependent on, for example, the type of round, and the length of the gun, etc. This problem can be stated more formally as the optimal prediction of the ARMA process at step $k + n$ based on data up to step k .

Because of its many desirable features, the prediction method employed was the Kalman filter [7]. To utilize the Kalman filter, it was first necessary to convert the ARMA process to state space form. By defining the state equation

$$x(k+1) = A x(k) + B w(k) \quad (3-2)$$

where

$$A = \begin{bmatrix} -a_1 & 1 & 0 & \dots \\ -a_2 & 0 & 1 & \\ \vdots & & & \ddots \\ -a_{p-1} & & & & 1 \\ -a_p & 0 & \dots & & 0 \end{bmatrix}, \quad B = \begin{bmatrix} b_1 - a_1 b_0 \\ b_2 - a_2 b_0 \\ \vdots \\ \vdots \end{bmatrix}$$

then the observation equation

$$z(k) = [1, 0, \dots, 0] x(k) + b_0 w(k) \quad (3-3)$$

describes the ARMA process. In the above, the estimated orders and coefficients are utilized. Note that from (3-2)-(3-3), the process noise is correlated with the observation noise. In order to avoid the increased complexity incurred in the correlated noise case, an equivalent augmented system was implemented which removed the "measurement" noise. In any case, the Kalman filter recursively computes the conditional expectation:

$$\hat{x}(k|k) = E[x(k)|z(0), \dots, z(k)]$$

which is the minimum variance estimate (the estimate which produces the smallest variance of the difference of the state and the estimate based on the observations). The ARMA estimate is immediate from (3-3)

$$\hat{z}(k|k) = [1, 0, \dots, 0] \hat{x}(k|k)$$

and because the state matrix A does not depend on time, it can be shown that

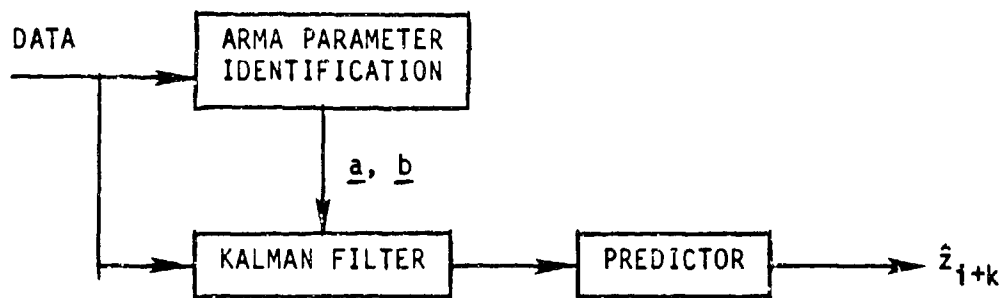
$$\hat{x}(k+n|k) = A^n \hat{x}(k|k) \quad (3-4)$$

The methodology was applied to the cases $n = 3$ (12 ms) and $n = 5$ (20 ms). It is important to emphasize that while (3-4) is optimal, the quality of the estimate deteriorates as n grows large.

3.4 Adaptive Estimation

Implementation of the prediction algorithm, shown in Figure 3-2, consists of estimating the ARMA order and coefficients using data during a "training" interval followed by prediction for a short interval following the training. By training continuously, the algorithm provides an adaptive algorithm for prediction. The approach was considered not only for its simplicity, but also for its (comparatively) small computational burden. An estimate of the computational burden was made for a simplified (reduced order) version of the algorithm and it appears that it can operate in real-time on a DEC MicroVax II. However, to realistically measure the true computational requirements, the algorithm was extensively evaluated.

Figure 3-2
Adaptive Filtering/Prediction Method



4.0 ALGORITHM EVALUATION

The implementation of the algorithm required selection of certain "variables" such as the number of autoregression coefficients (N) to use in the approximation or the length of the training interval. Due to the requirement of computational efficiency, it was of interest to set variables providing acceptable performance while yielding the shortest possible run-time. Initially, values which resulted in good identification and prediction were chosen, then the values were altered in a systematic manner until a "minimal" set was obtained.

4.1 Experimental Baseline

To evaluate the performance as well as the limitations of the ARMA approach, the methodology was applied to a variety of representative data segments from the four tests. The segments were selected to provide typical (modeling and prediction over similar data), as well as atypical (modeling and prediction over different data) conditions. To be more precise, by choosing a variety of training and prediction interval combinations, the approach was tested under different physical "scenarios" associated with the tank traversing different portions of the track. Since the track is composed of regions consisting of primarily small bumps or large bumps, six different combinations were identified. For example, one combination resulting in

a typical condition is training and prediction over data consisting primarily of large bumps. An atypical condition would result from training over large bumps and prediction over a segment consisting of small bumps. The ability of the algorithm to predict the data for a typical case is shown in figure 4-1.

To evaluate the quality of the muzzle pointing error, the sample standard deviation (RMS) of the error residual sequence $e(k)$,

$$e(k) = z(k) - z(k|k-n)$$

was computed. The error RMS was computed both over the entire segment and data and only over the zero crossings: the points at which the prediction is within 1/10 milliradian band of zero. This latter statistic is important, as only at the predicted zero crossing will the gunner will be allowed to fire. For comparison, the RMS of the data over the entire segment was also computed.

Results for the baseline set of experiments show that the algorithm provides an average error reduction of 32% for the typical and 23% for the atypical segments. The most dramatic reductions often occur at the higher speeds.

4.2 Reduction of Algorithm Run Time

Since the algorithm achieved suitable performance on the baseline segments, values of the algorithm were next individually varied to result in shorter run times. Specifically, the effect of reducing the training interval, the order of the autoregressive approximation (N), and the estimated AR and MA orders was measured. In order to quantify the effect of the various changes, the run time of each subroutine of the algorithm was calculated with a timing program. Execution time is most sensitive to ARMA order as it is directly related to the Kalman filter computation, often the most numerically expensive portion of the algorithm. Examples of results utilizing reduced values are given in Table 4-1. A typical run which used two seconds of data to establish the model followed by prediction over one second of data required approximately 4 to 5.5 seconds on a DEC MicroVax II.

Figure 4-1
Muzzle Pointing Error and Prediction

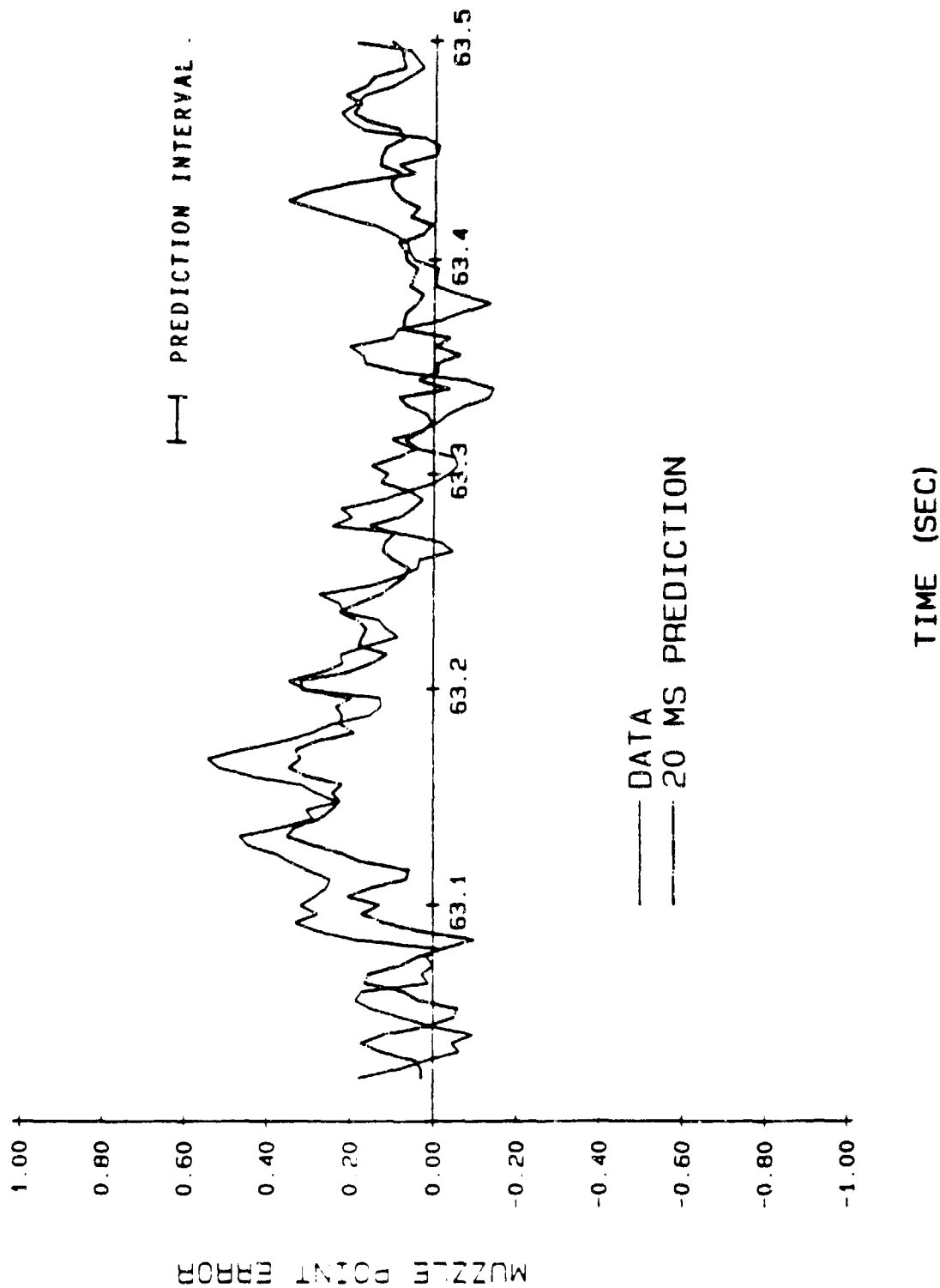


Table 4-1
Results of Variable Testing (2 sec training)

SPEED MPH	CASE*	RAW DATA RMS	BEST MODEL PREDICTION ERROR	REDUCED ORDER PREDICTION ERROR
5	A	0.3mr	0.2mr (15)	0.2mr (3)
	B	0.3	0.2 (1)	0.2 (1)
	C	0.2	0.2 (7)	0.2 (1)
15	A	0.3	0.3 (1)	0.3 (1)
	B	0.7	0.3 (4)	0.3 (1)
	C	0.5	0.4 (1)	0.4 (1)
30	A	0.6	0.4 (17)	0.4 (8)
	B	1.0	0.3 (9)	0.3 (4)
	C	0.9	0.4 (3)	0.4 (3)

* CASES

A: TRAIN ON SMALL BUMPS, PREDICT ON SMALL BUMPS
 B: TRAIN ON LARGE BUMPS, PREDICT ON LARGE BUMPS
 C: TRAIN ON SMALL BUMPS, PREDICT ON LARGE BUMPS

5.0

DISCUSSION AND EXTENSION TO FUTURE WORK

Considering the limited scope of this study (restriction of ARMA models and limited data types), the results are quite encouraging. For the baseline, the adaptive 20 millisecond ARMA predictor was able to reduce the total muzzle pointing error usually from 20% to 60% for the expected operational conditions (typical scenarios) and even for the atypical cases there was often a small to moderately large reduction. Usually, errors are between 0.1 and 0.4 milliradians. By reducing the training interval and forcibly decreasing the order of the model, a version of the algorithm with comparable performance was obtained which appears capable of real-time operation on commercially available microprocessors. It is almost certain that VHSIC technology will make real-time operation feasible.

Although the approach shows real promise, further work is required to refine the techniques and to investigate alternate forms of the adaptive filter. In particular, there is potential for great improvement if the ARMA modeling is augmented with physical modeling of the gun tube/turret and if additional data such as accelerometer/gyro or gunner servo error is used.

6.0

REFERENCES

- [1] H. Cohen, "Methodology for Stochastic Modeling," U.S. Army Materiel Systems Analysis Activity, Technical Report No. 410, January 1985.
- [2] J.A. Cadzow, "Spectral Estimation: an Overdetermined Rational Model Equation Approach," Proc. IEEE, Vol. 70, No. 9, Sept. 1982.
- [3] G.E. Box and G.M. Jenkins, Time Series Analysis Forecasting and Control, San Francisco, California, Holden-Day 1970.
- [4] J. Makhoul, "Linear Prediction: A Tutorial Review" Proceedings of the IEEE, Vol. 63, No. 4, pp.561-580, April 1975.

- [5] D. Graupe, D.J. Krause, and J.B. Moore, "Identification of Autoregressive Moving Average Parameters of Time Series," IEEE Trans. Automatic Control, AC-20, pp. 104-107, Feb. 1975.
- [6] T.J. Ulrych and T.N. Bishop, "Maximum Entropy Spectral Analysis and Autoregressive Decomposition," Rev. Geophysics and Space phys., Vol. 13, pp. 183-200, Feb. 1975.
- [7] B.D.O. Anderson and J.B. Moore, Optimal Filtering. Prentice Hall, New Jersey, 1979.

NUMERICAL PREDICTIONS OF EML SYSTEM PERFORMANCE

N. M. Schnurr, J. F. Kerrisk, and R. F. Davidson
Los Alamos National Laboratory
P.O. Box 1663
Los Alamos, New Mexico 87545

ABSTRACT

The performance of an electromagnetic launcher (EML) depends on a large number of parameters, including the characteristics of the power supply, rail geometry, rail and insulator material properties, injection velocity, and projectile mass. EML system performance is frequently limited by structural or thermal effects in the launcher (railgun). A series of computer codes has been developed at the Los Alamos National Laboratory to predict EML system performance and to determine the structural and thermal constraints on barrel design. These codes include FLD, a two-dimensional electrostatic code used to calculate the high-frequency inductance gradient and surface current density distribution for the rails; TOPAZRG, a two-dimensional finite-element code that simultaneously analyzes thermal and electromagnetic diffusion in the rails; and LARGE, a code that predicts the performance of the entire EML system. The NIKE2D code, developed at the Lawrence Livermore National Laboratory, is used to perform structural analyses of the rails.

These codes have been instrumental in the design of the Lethality Test System (LTS) at Los Alamos, which has an ultimate goal of accelerating a 30-g projectile to a velocity of 15 km/s. The capabilities of the individual codes and the coupling of these codes to perform a comprehensive analysis is discussed in relation to the LTS design. Numerical predictions are compared with experimental data and presented for the LTS prototype tests.

NUMERICAL PREDICTIONS OF EML SYSTEM PERFORMANCE

N. M. Schnurr, J. F. Kerrisk, and R. F. Davidson
 Los Alamos National Laboratory
 P.O. Box 1663
 Los Alamos, New Mexico 87545

INTRODUCTION

Electromagnetic launchers or railguns are devices that accelerate projectiles to high velocities by the interaction of an electric current and a magnetic field [1,2]. A schematic diagram of a railgun is shown in Fig. 1. The basic elements include two parallel stationary conductors (rails) that are bridged by a moving armature. When the main switch is thrown, the capacitor bank discharges, a voltage is applied across the rails, and an electric current flows down one rail, through the armature, and back through the other rail. The current in the rails gives rise to a magnetic field that interacts with the armature current to cause a Lorentz force on the

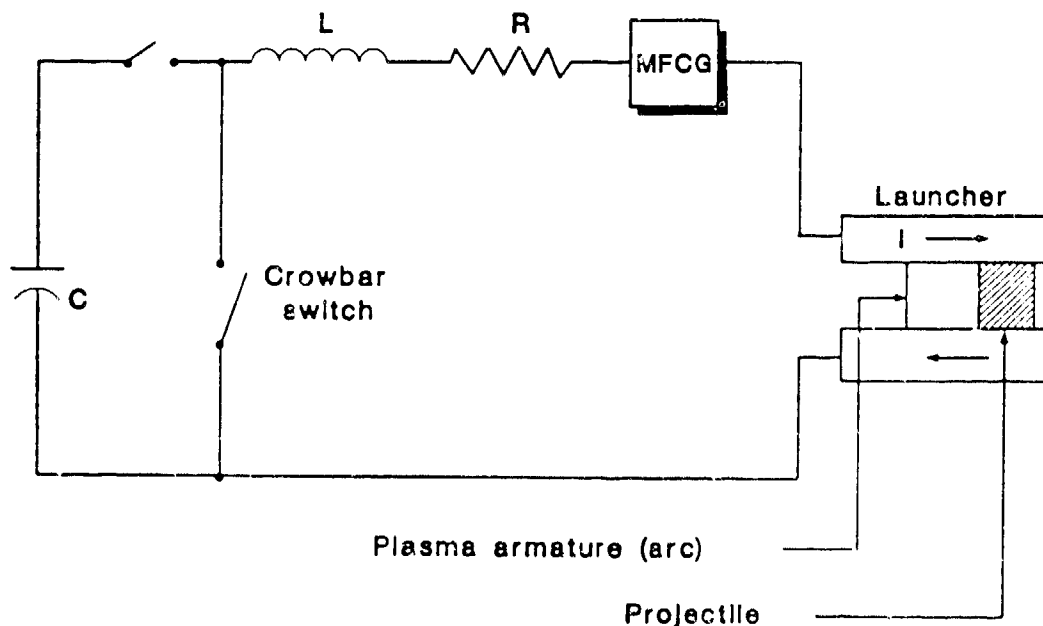


Fig. 1 Schematic diagram of a railgun

armature. The armature, in turn, exerts a force on the projectile causing a rapid acceleration.

A study of railguns has been in progress at Los Alamos since 1978. Although the work has been primarily experimental, a significant effort has also gone into developing extensive analytical capabilities. A series of codes has been developed to predict electrical, dynamic, structural, and thermal effects in a railgun system.

In the current railgun program, Los Alamos is designing and constructing the Lethality Test System (LTS), which has the goal of accelerating 20- to 30-g projectiles to velocities of 15 km/s. This paper describes the codes used to predict EML system performance and presents results specific to the LTS design. Numerical predictions are compared with experimental data and presented for the LTS low-pressure prototype.

ANALYTICAL CAPABILITIES

Figure 2 shows the interrelationships between the codes used for railgun analysis. In the initial step in a system analysis, the FLD code is used to

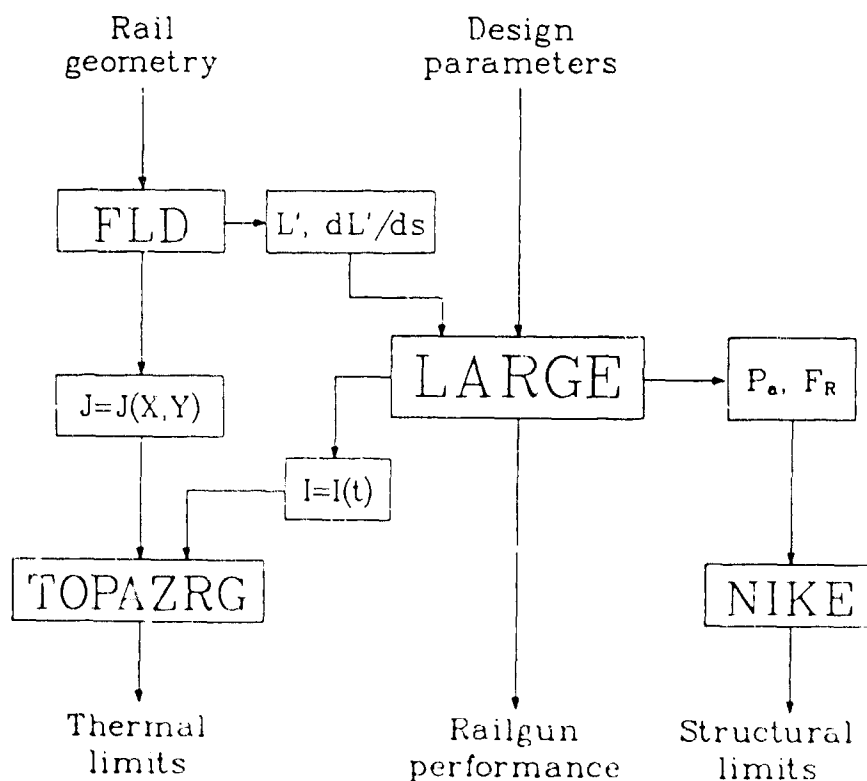


Fig. 2. Interrelationships among codes used for railgun analysis

determine the inductance gradient, L' , and the derivative of the inductance gradient with respect to rail spacing, dL'/ds , for the proposed launcher. The distribution of current density around the perimeter of the rail, $J(x,y)$, is also calculated. The inductance gradient and its derivative are used as input to the LARGE code, along with such design parameters as rail geometry, mass and injection velocity of the projectile, and power supply specifications. Parametric studies may be performed to determine projectile velocity for a range of design parameters. Additional results computed by LARGE include the rail current as a function of time, $I(t)$, and the pressure, P_a , and magnetic force, F_r , acting on the rails. These parameters are used as input to the thermal analysis code, TOPAZRG, and the structural analysis code, NIKE2D. These codes are used to ensure that the thermal and structural limits of the system are not exceeded. Each code is described in more detail in the remainder of this section.

FLD - Inductance Gradient Calculations

The FLD code [3] is used to calculate the current density distribution, magnetic field, and inductance of long, parallel conductors of arbitrary cross sections in the high-frequency limit. These results may be used for railguns as initial values, which are applicable until the current or magnetic field diffusion has significantly changed the current distribution. The method used here follows from the equivalence of the current distribution problem to the problem of charge distribution on equipotential (electrostatic) surfaces [4]. The axial component of the magnetic vector potential is equivalent to the electrostatic potential. The first step in the calculation is to find the current distribution that produces a constant value of the vector potential on each conductor surface. An existing computer program was used for these calculations [5]. The values of the magnetic vector potential on each conductor surface are determined by the total flow of current in the circuit and the geometric symmetry of the conductors. Once the current distribution is known, the magnetic field associated with the conductors can be calculated. In particular, the total flux that links the circuit can be determined from the field between the rails. The self-inductance of the circuit is easily calculated from the total flux linkage.

A series of calculations was performed to determine inductance gradients and current distributions for the LTS rails. The geometry of the LTS rail and support structure (anvil) is shown in Fig. 3. The bore radius is $R = 12.5$ mm. The effects of rail thickness, W , and anvil location, X_1 , on the inductance gradient and the derivative of inductance gradient with respect to rail spacing are shown in Figs. 4 and 5. These results indicate that both L' and dL'/ds increase with increasing X_1 and decreasing rail thickness. The Lorentz force accelerating the armature is proportional to L' , and thus L' should be as large as possible. Because the force tending to spread the rails apart is proportional to dL'/ds and must be kept small enough to prevent structural damage, a tradeoff is required in the selection of rail and anvil geometry. The geometric parameters selected, based largely on structural considerations, were $W = 14.53$ mm and $X_1 = 106.4$ mm.

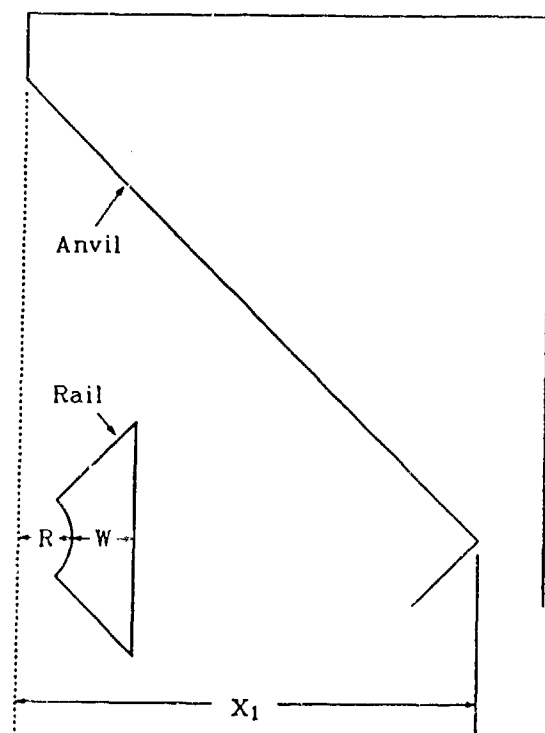


Fig. 3. Geometry of the LTS launcher.

The instantaneous relative current density distribution on the surface of the LTS rail is shown in Fig. 6. The zero value of arc length is at the center point of the bore (curved surface), and arc length is measured along the perimeter in the clockwise direction. Because of symmetry about the x-axis, results are shown for only the top half of the rail. The peaks represent the current densities at the corners of the rail. The current density would be unbounded for sharp corners. It is therefore necessary to specify a radius of curvature at the corners. The values selected here were 0.13 mm and 0.54 mm for the front and back corners respectively. The peaks in Fig. 6 can be reduced by using larger radii or curvature.

LARGE - EML Performance Predictions

The Los Alamos Rail Gun Estimator (LARGE) is a performance model that was written to calculate rail current and projectile velocity and position from a description of the power supply and railgun [6]. It can model a capacitor bank; large inductances in the power supply; explosively driven magnetic-flux compression generators (MFCGs); various railgun configurations such as square bore or round bore; staged systems; or distributed systems. All rail inductances and resistances are calculated from a physical description of the rails. The rail inductance gradient (high-frequency limit), calculated by FLD, is used to determine the force on the projectile. Estimates of how current diffusion changes rail inductance and resistance with time are also included [7].

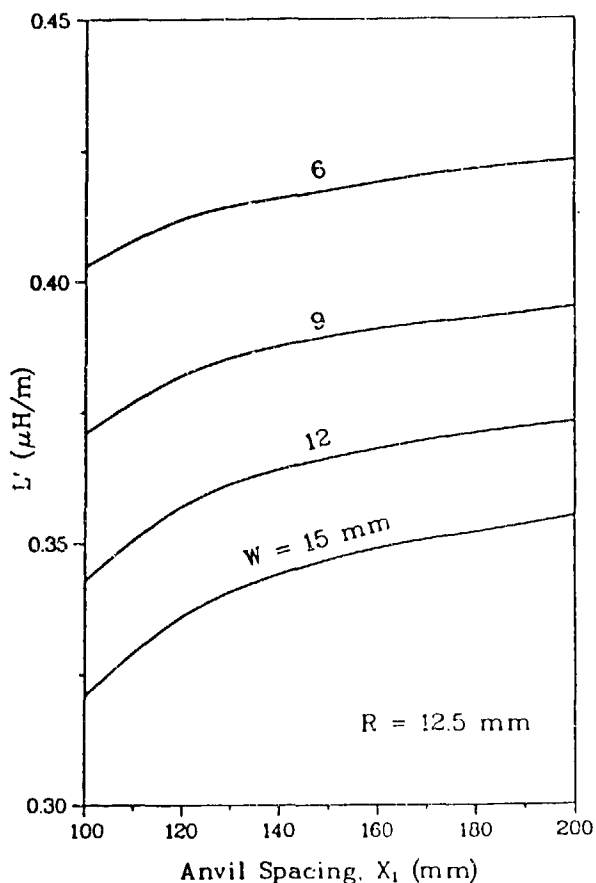


Fig. 4. Inductance gradients calculated by the FLD code for the LTS.

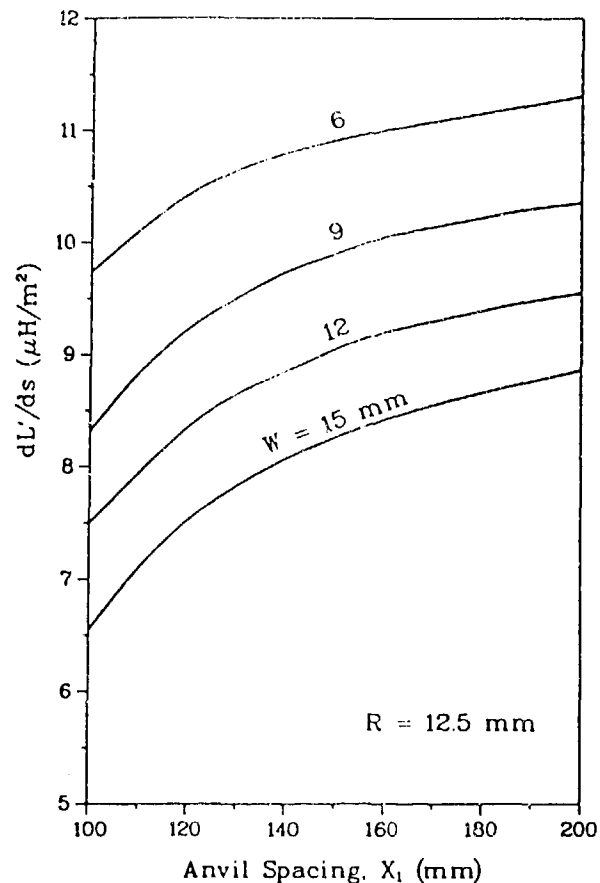


Fig. 5. Derivatives of inductance gradients calculated by the FLD code for the LTS.

One of the most important losses in plasma-armature railguns is caused by ablation of the rail and insulator material [8,9]. The radiant heat flux from the arc is so large that surface material can be vaporized and ionized within a few microseconds. The resulting material may be entrained in the arc. This causes an increase in the total mass that must be accelerated and a lower muzzle velocity. The increased size of the arc also causes an increase in arc drag [10]. An algorithm is included in LARGE which estimates the rate of ablation and computes the resulting arc mass and arc drag.

The LARGE code uses an explicit marching procedure so that parameters calculated at the end of a time step are based on conditions at the beginning of the time step. First, the rail current is computed by simultaneously solving the circuit equations for all stages. This is done numerically using Euler's method. The current is then used to compute Joule heating in the arc, and an energy balance is used to calculate ablation rates and changes in the mass and in the arc length. Finally, the

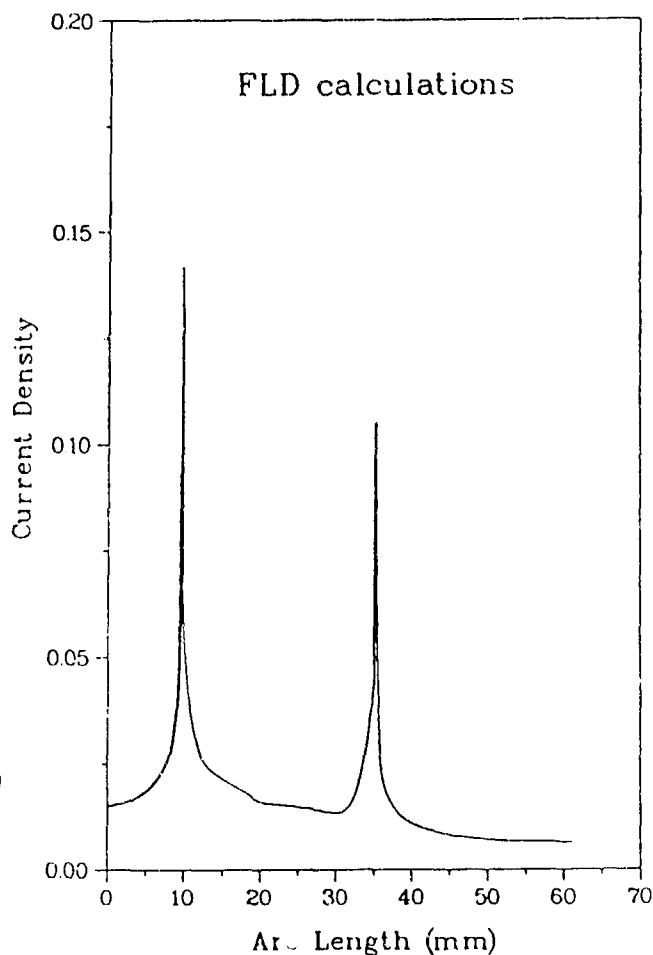


Fig. 6. Instantaneous relative current density distribution for the LTS rail calculated by the FLD code.

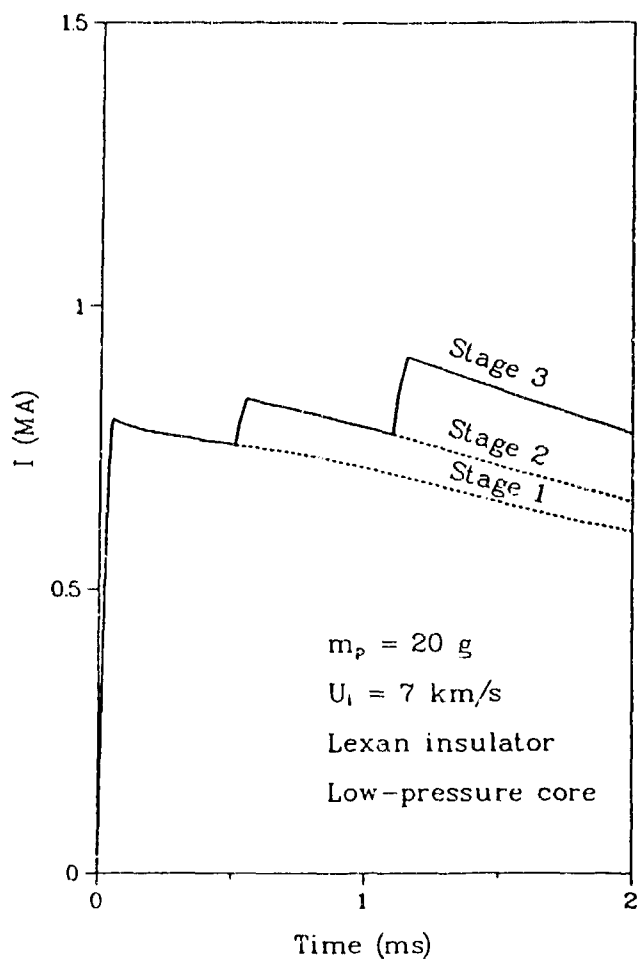


Fig. 7. Rail current profile for the LTS computed by the LARGE code.

conservation of energy principle applied to the arc and projectile is used to compute the acceleration, velocity, and displacement of the projectile.

The LARGE code was used to predict the performance of the LTS system. Results are shown in Figs. 7 and 8 for the case of the low-pressure core. The power supply parameters were adjusted so that the arc pressure would not exceed 30 ksi at any time during the launch. The projectile mass and initial velocity were specified as 20 g and 7 km/s. Electrical leads for the three stages were located at 0, 4, and 10 m from the breech.

The solid line in Fig. 7 represents the arc current. The dashed lines represent the current in the first and second stages. The rise time for each stage was 50 μ s. The velocity vs time plot (Fig. 8) indicates a muzzle

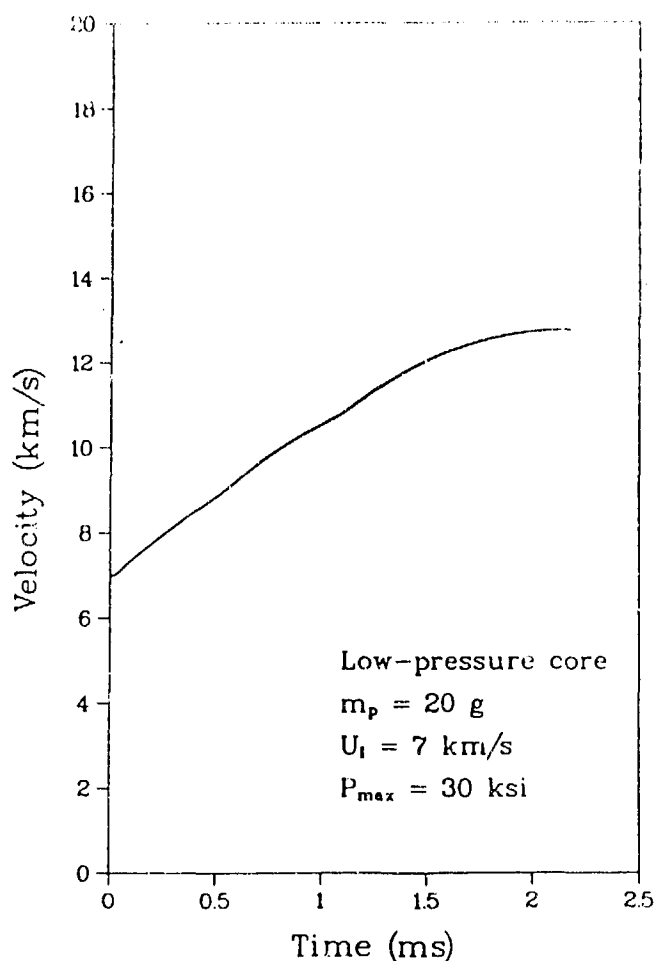


Fig. 8. Projectile velocities predicted by LARGE

velocity of 12.5 km/s. Velocities well above 15 km/s are predicted for the high-pressure core where higher rail currents cause higher accelerations of the projectile.

Some preliminary experiments have been completed using a prototype of the low-pressure LTS. The rails for the prototype are 3.66-m long, and a 1.88-MJ capacitor bank was used instead of the 50 MJ power supply that will be available for the full LTS. LARGE simulations were performed to check the accuracy of the code. A comparison of the numerical and experimental results is shown in Fig. 9. Current profiles were measured for each experiment, then the current vs time profiles were used as input to LARGE and the rail current calculations were bypassed. The differences between the numerical and experimental results are therefore primarily an indication of the accuracy of the ablation and arc drag algorithms. Note that in some cases two different current profiles were used. The breech current was measured just down-

stream of the electrical lead for this single-stage experiment. In some cases current measurements at a series of locations along the rail indicated that the plasma arc split into two segments after traveling some distance down the bore. The resulting data were used to infer a minimum effective current profile. That profile neglected any effect that the current in the trailing arc might have in producing a force that could be transmitted to the projectile. Simulations were also performed in which the effects of ablation and arc drag were omitted. These simulations are the ideal cases (solid points) shown in Fig. 9. Agreement between the numerical and experimental results is quite good. The numerical results for the ideal calculations significantly overpredict muzzle velocities. These results as well as other simulations discussed in Refs. 9 and 10 indicate that ablation and arc drag are important loss mechanisms and that the LARGE code is able to predict the performance of a wide variety of railgun systems.

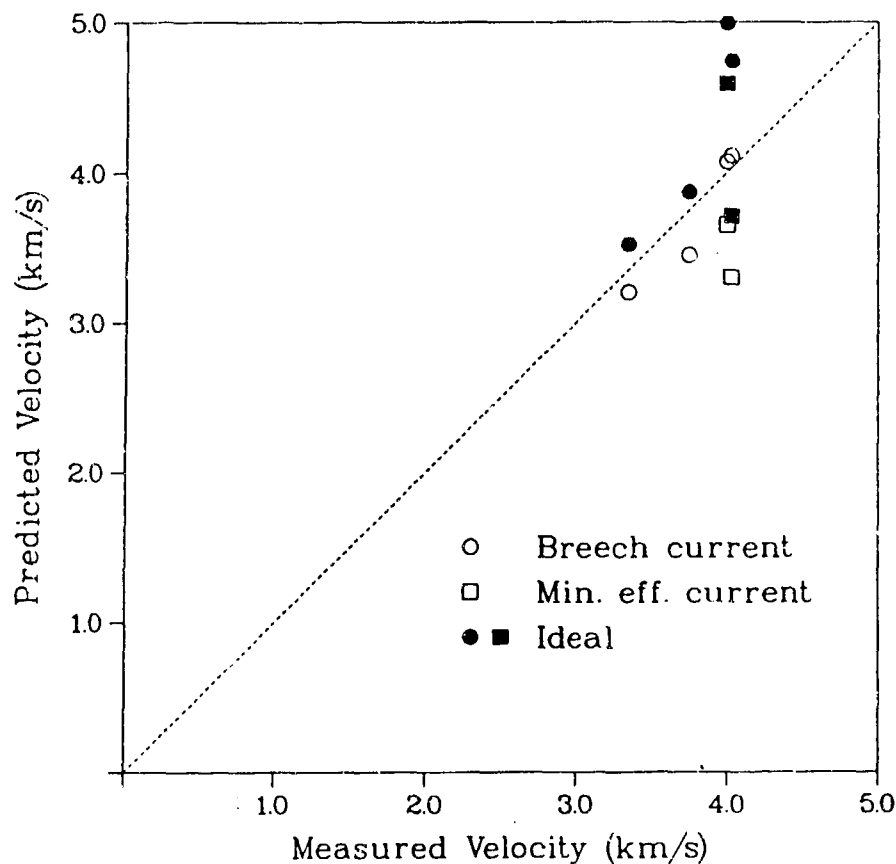


Fig. 9. A comparison of predicted and measured velocities for the LTS Low-Pressure Prototype.

TOPAZRG - Thermal Analysis

Thermal analysis of the rails was performed using the TOPAZRG [11] code, a two-dimensional, transient, finite-element code that solves the combined thermal/electrical field diffusion problem for the rails. The current profile (Fig. 7) and surface current density distribution (Fig. 6) were used as input along with specification of magnitude and duration of arc radiation impinging on the bore surface of the rails.

Thermal analyses were performed using TOPAZRG for segments of rail at the breech and at a small distance downstream from the third-stage electrical connections. Results for the TOPAZRG calculations at the breech are shown in Fig. 10. The arc radiation was assigned a magnitude of 1.0 MW/cm^2 (an effective average arc temperature of approximately $20,000 \text{ K}$) and a duration of $10 \text{ } \mu\text{s}$. This corresponds to a 7-cm-long arc moving at a velocity of 7000 m/s . Note that the temperature at the inside corner of the rail increases very rapidly to a temperature near the melting point. Temperatures along the bore surface have similar but slightly lower peaks because the Joule heating is less severe at points farther removed from the corner. The

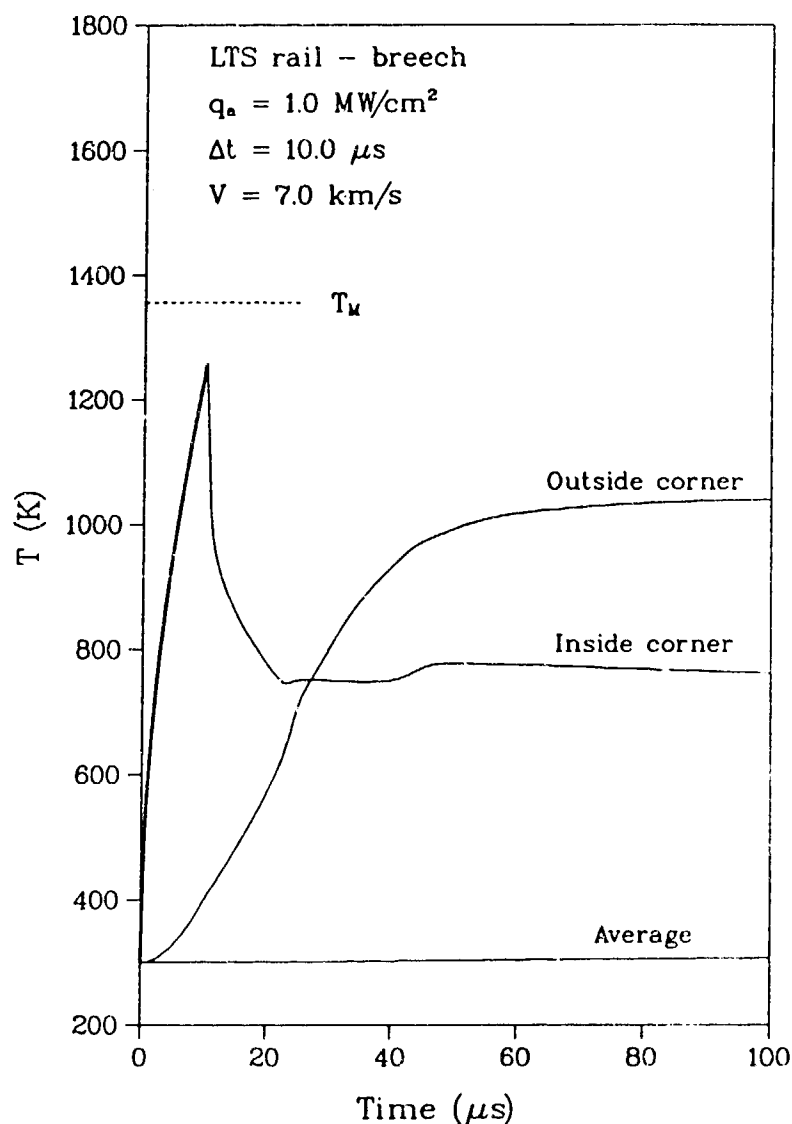


Fig. 10. Temperature profiles at the breech calculated by TOPAZRG.

temperature drops rapidly after the 10- μs radiant energy pulse because of thermal diffusion, then begins to rise again as the Joule heating increases. The first-stage current has a rise time of 50 μs , after which the rate of temperature increase drops somewhat as the rail current begins to decrease. Thermal diffusion finally causes the temperature at the inside corner to decrease after about 150 μs (not shown). Note that the temperature at the back corner is virtually unaffected by the radiant flux because the rail thickness is large compared with the thermal diffusion depth for the time scale of this simulation.

A simulation was also performed for a rail segment where the third-stage leads are connected because the maximum current occurs at that location. For that case, time was measured from the instant the projectile reached that location. The current was assumed to rise linearly from zero to the maximum value of Fig. 7 in the time it took the arc to pass. For this simulation, a value of $10\text{ }\mu\text{s}$ was used. This corresponds to a 12-cm-long arc moving at a velocity (calculated by LARGE) of 12 km/s. The larger and more rapid contribution of Joule heating for this case caused the predicted temperature at the inside corner to exceed the melting temperature of copper. Note that the temperature at the outside corner also exceeds the melting temperature.

The calculations described above assumed a single-phase material. They overpredict temperatures above the melting temperature because the absorption of energy that occurs with phase change is neglected. The TOPAZ2D code includes a phase-change algorithm so that the effects of melting can be assessed. Results of the calculations for the rail segment downstream of the third stage, including the phase-change algorithm, indicated temperatures with peaks approximately 150 K lower than those shown in Fig. 11. The corner temperatures also dropped below the melting temperature somewhat more rapidly. The inclusion of the phase-change algorithm has an extremely negative impact on computational speed. The number of iterations required at each time step increases dramatically because of the strong nonlinearities introduced by phase change. The time step required to maintain stability is limited to approximately $0.2\text{ }\mu\text{s}$. The computation for $20\text{ }\mu\text{s}$ using 400 elements required more than 15 min. of central processing unit (CPU) time on the Cray. The calculation that does not include melting is more than ten times faster.

It should be noted that corner temperatures somewhat above the melting point are not likely to cause severe problems. Temperatures at nodes adjacent to the corner nodes remained well below the melting temperature in most cases, so the high temperature region is extremely localized. The corner temperatures began to decrease because of thermal diffusion shortly after the arc had passed and the rail current had begun to decrease. They typically drop below the melting temperature within 1 to 2 ms. A small amount of melting at the outside corner of the rail is not expected to cause serious problems because the rail is surrounded by insulator material and has little room to deform. Only a small deformation is expected at the inside corner because the forces acting on the material there are primarily radially outward. They include the arc pressure (estimated to be in the range of 30 to 50 ksi) and the magnetic forces that tend to spread the rails apart.

NIKE2D - Structural Analysis

The structural analysis was performed using the NIKE2D [12] code. This is an implicit finite-element code for analyzing static and dynamic response of two-dimensional solids. Of the many material models available in NIKE2D, the elastic, elastic-plastic, orthotropic, and thermo-orthotropic were used for this analysis. The contact algorithm (slideline) in NIKE2D is useful

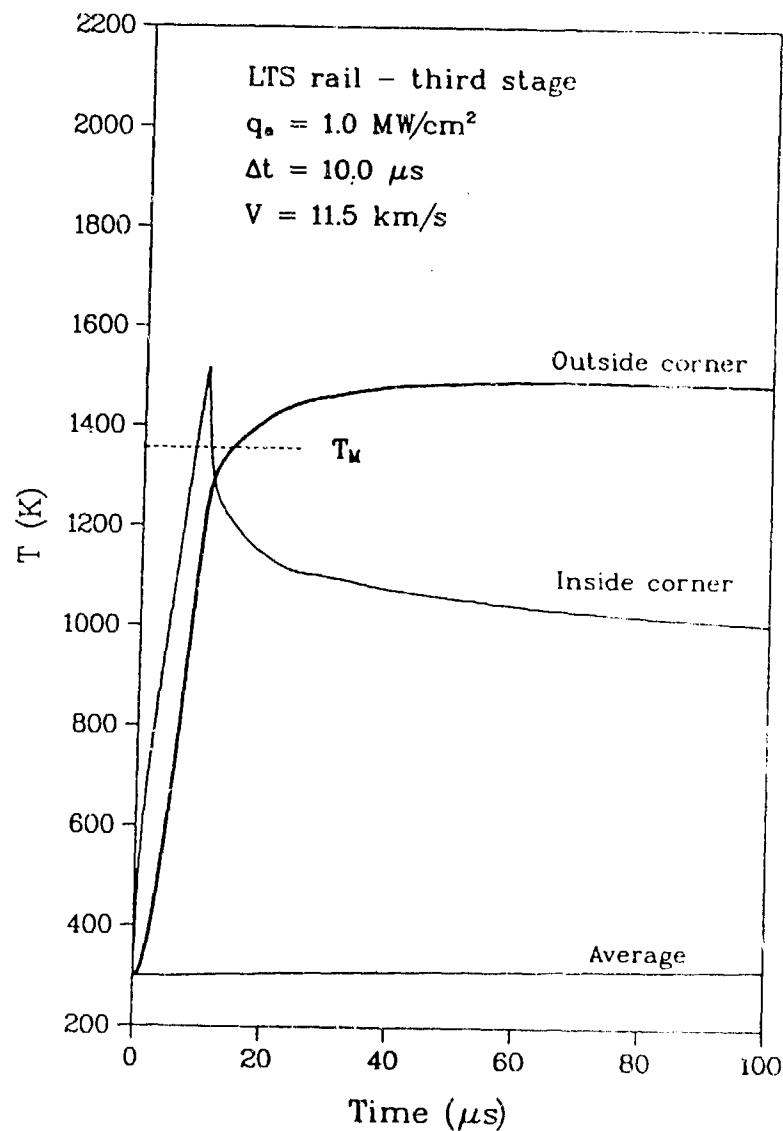


Fig. 11. Temperature profiles at the third stage calculated by TOPAZRG.

for railgun problems. The ability to calculate thermal stresses was used in an artificial manner for the preload analysis. The meshes for these calculations were generated using INGEN [13] and ESCHER [14]. The results were examined graphically with STRAPP [15] and TDAP [16].

For this analysis, the plane strain geometry assumption was made. Therefore, variations in the loading and structural response along the length of the launcher were not considered. The model is shown in Fig. 12.

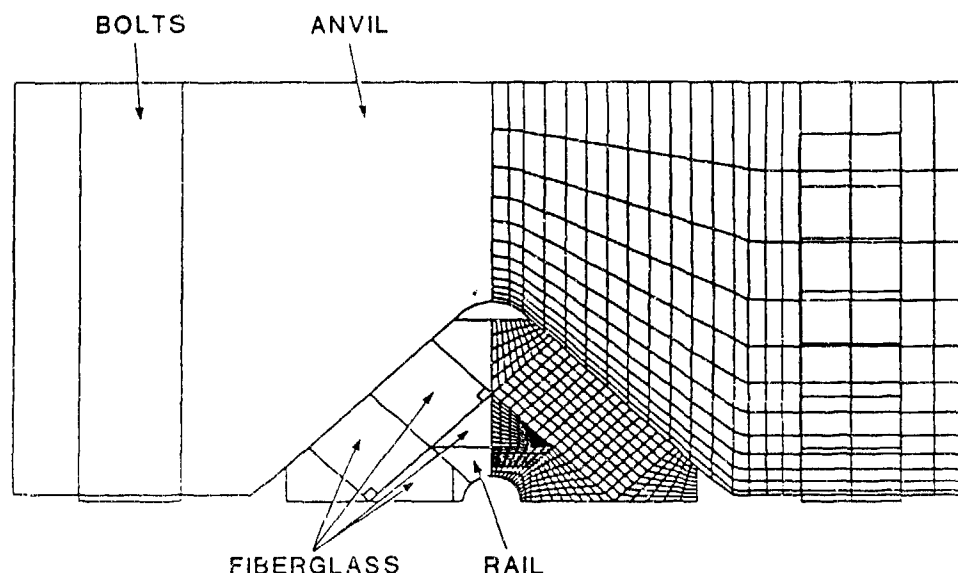


Fig. 12. LTS low-pressure core - FEM model.

Slidelines were used extensively to define the interactions between the various launcher components. The bolt preload was applied by artificially cooling the bolts until the correct (measured) preload was obtained. The dynamic loads on a launcher under firing conditions (the plasma pressure and rail force) were applied to the preload model. Thus, stresses and motions were determined resulting from the combined application of preload and firing loads. These analyses are described in more detail in Ref. 17.

The firing loads were determined at a critical longitudinal cross section by considering the arc current passing the point. The arc current and arc length were either determined by LARGE or taken from experimental data (Fig. 7). The inductance gradients necessary to determine plasma pressure and rail force were determined by FLD calculations (Figs. 4 and 5). Figure 13 shows the loading functions that occurred at the longitudinal cross section that contained the second current probe in Test 6 of the LTS low-pressure core prototype. This location corresponds to the longitudinal location of the arc when peak current was reached.

The rise time of the plasma pressure is assumed to be the time required for the projectile to pass the second current probe location. The plasma pressure decayed to zero when the tail of the arc passed. The rail force increased to a peak when the end of the arc passed. Note that the peak pressure and peak rail forces did not occur at the same time. The pressure load was applied to the inner surface of the bore, both to the rail and to the insulator (side wall). The rail force was distributed around the surface of the rail in a manner similar to the actual magnetic force distribution.

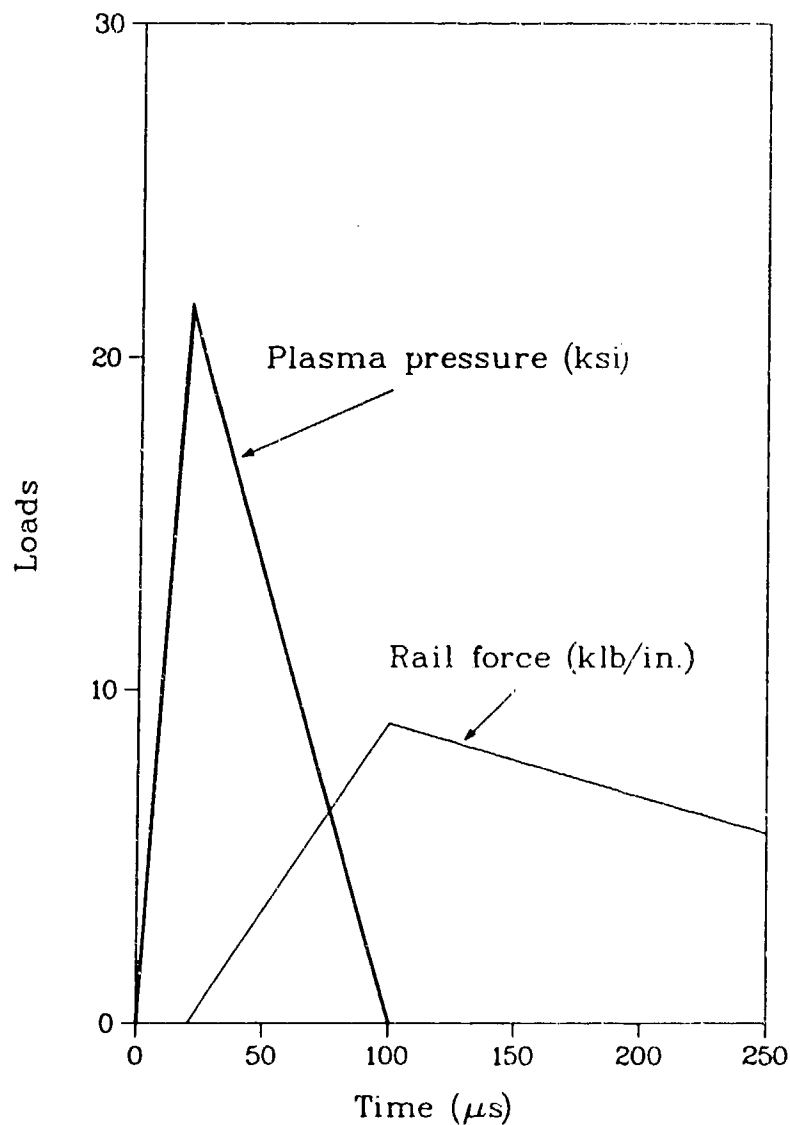


Fig. 13. Loads on LTS low-pressure prototype Test 6.

The structural analysis results yielded a wealth of information which we don't have space to discuss here. The results allowed prediction of the bolt preload, the stresses in internal components, and the interface gaps. Based on this information, the performance of the launcher was characterized and several design modifications were made. As an example of the analytical results, Fig. 14 shows the rail displacement as a function of time indicating a calculated peak deflection of 17 mils.

As an indicator of the accuracy of the structural analysis, Fig. 14 also shows the test data for the rail motion. The peak displacement was predicted with reasonable accuracy (17 mils predicted and 19 mils measured). The initial rail pinching (negative deflection at 340 μs) shown in the data does not show up in the analysis because rail pinching is caused by a

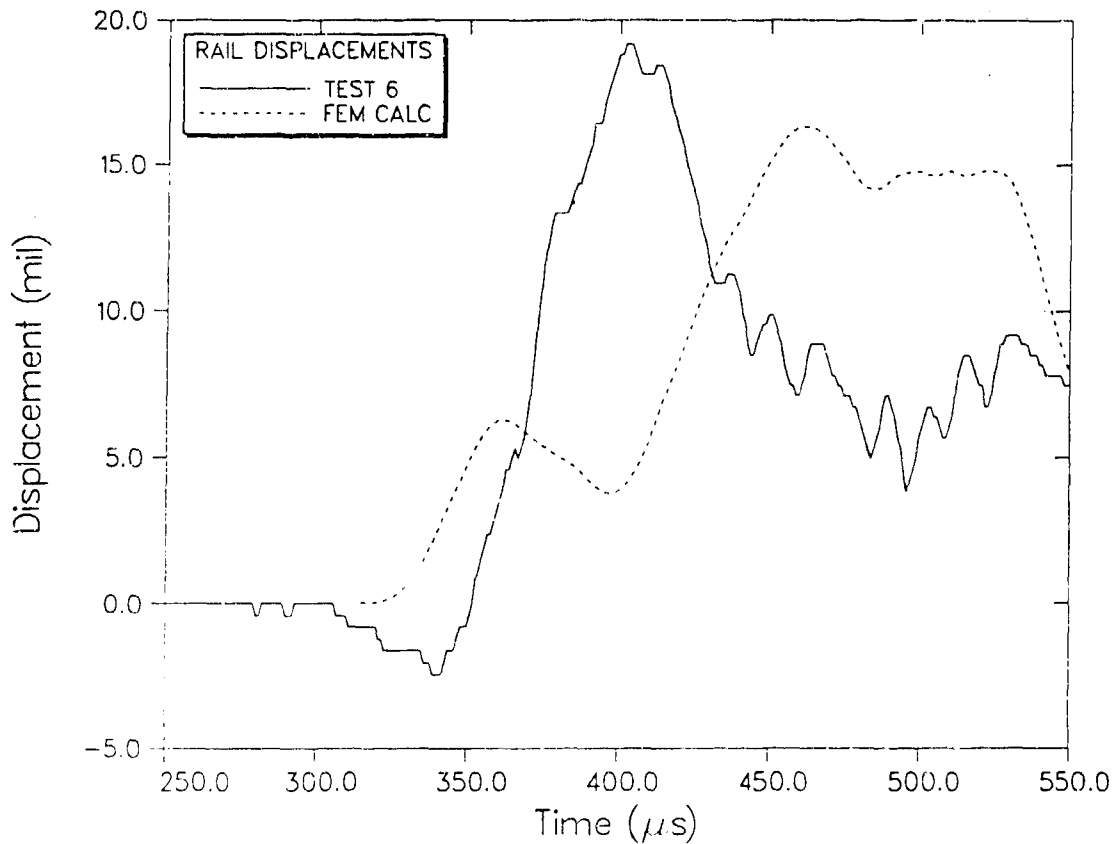


Fig. 14. Rail motion for LTS low-pressure core prototype Test 6.

longitudinal load variation that is not considered in this two-dimensional analysis. The difference in rise time and general response shape are probably due, at least partly, to uncertainties in the arc length used for the calculation. The accuracy of the calculated displacement history is certainly sufficient for design purposes.

SUMMARY

A series of computer codes has been developed to perform a complete analysis of EML systems. Analytical capabilities include detailed structural and thermal analysis of the launcher as well as performance simulations of the entire system. These codes have been instrumental in the design of the LTS at Los Alamos. Comparisons of analytical predictions with experimental results obtained for the LTS low-pressure prototype have shown generally good agreement.

ACKNOWLEDGMENTS

The authors wish to thank J. V. Parker and W. A. Cook for their technical support and M. M. Plehn and L. L. Shelley for their word processing and editorial assistance.

REFERENCES

1. R. A. Marshall, "The Australian National University Rail Gun Project," *Atomic Energy in Australia*, 18, 16-18 (1975).
2. S. C. Rashleigh and R. A. Marshall, "Electromagnetic Acceleration of Macroparticles to High Velocities," *J. Appl. Phys.* 49, 2540-2542.
3. J. F. Kerrisk, "Current Distribution and Inductance Calculations for Rail-Gun Conductors," Los Alamos National Laboratory report LA-9092-MS (October 1981).
4. H. R. Lewis, Jr., "Computation of Electrostatic and Rapidly Pulsed Magnetic Fields," *J. Appl. Phys.* 37, 2541-2550 (1966).
5. K. R. Crandall, "Computation of Charge Distribution on or Near Equipotential Surfaces," Los Alamos Scientific Laboratory report LA-3512 (December, 1966).
6. J. F. Kerrisk, "Electrical and Thermal Modeling of Railguns," IEEE Transactions on Magnetics, Vol. MAG-20, 399-402 (March 1984).
7. J. F. Kerrisk, "Current Diffusion in Railgun Conductors," Los Alamos National Laboratory report LA-9401-MS (June 1982).
8. J. V. Parker, "Performance Loss due to Wall Ablation in Plasma Armature Railguns," presented at AIAA 18th Fluid Dynamics and Plasmadynamics and Laser Conference, Cincinnati, Ohio, (July 16-18, 1985).
9. N. M. Schnurr and J. F. Kerrisk, "Numerical Studies of Ablation and Ionization of Railgun Materials," presented at the AIAA 18th Fluid Dynamics and Plasmadynamics and Laser Conference, Cincinnati, Ohio (July 16-18, 1985).
10. N. M. Schnurr, J. F. Kerrisk, and J. V. Parker, "Numerical Predictions of Railgun Performance Including the Effects of Ablation and Arc Drag," in Proceedings of the 3rd Symposium on Electromagnetic Launch Technology, April 21-24, 1986, Austin, Texas, pp. 271-278.
11. N. M. Schnurr, "Thermal Analysis of Electromagnetic Launcher Rails," Los Alamos National Laboratory report in progress.

12. J. O. Hallquist, "NIKE2D - A Vectorized, Implicit, Finite Deformation Finite Element Code for Analyzing the Static and Dynamic Response of 2-D Solids with Interactive Rezoning and Graphics," Lawrence Livermore National Laboratory report UCID-19677, Rev. 1, December, 1986.
13. W. A. Cook, "INGEN: A General Purpose Mesh Generator for Finite Element Codes," Los Alamos National Laboratory report LA-9402-MS (June 1982).
14. W. R. Oakes, Jr., "ESCHER User's Manual," Los Alamos National Laboratory report (in progress).
15. F. M. Guerra, "STRAPP User's Manual," Los Alamos National Laboratory report (in progress).
16. W. D. Birchler and B. M. Wheat, "TDAP User's Manual," Los Alamos National Laboratory internal report, 1985.
17. R. F. Davidson et al., "Predicting Bore Deformations and Launcher Stresses in Railguns," in Proceedings of the 3rd Symposium on Electro-magnetic Launch Technology, April 21-24, 1986, Austin, Texas. pp. 31-36.

BRASSARD AND HOMAN

TITLE: RAIL DAMAGE IN A SOLID ARMATURE RAIL GUN

HERESA BRASSARD

LONG BEACH NAVAL SHIPYARD

LONG BEACH, CA 90822

and

CLARKE G. HOMAN

US ARMY ARMAMENT RESEARCH, DEVELOPMENT, AND ENGINEERING CENTER

CLOSE COMBAT ARMAMENTS CENTER

BENET LABORATORIES

WATERVLIET, NY 12189-4050

ABSTRACT:

Two types of rail guns are currently under investigation to meet Army tactical missions. Plasma arc drive rail guns operate by forming a high temperature plasma behind the projectile using a thin metal fuze. These systems achieve the highest projectile velocities (~ 12 km/sec), since the driving force includes a substantial plasma pressure as well as the electromagnetic or Lorentz force. Unfortunately, severe rail damage occurs primarily from the intense temperatures generated by the plasma arc and the wiping motion of the armature itself. This severe rail damage is not compatible with Army tactical missions requiring multi-shot applications. The plasma armature gun will not be discussed in this paper.

The solid armature gun replaces the plasma armature with a conducting metal armature. Since the plasma arcing is reduced or eliminated, the projectiles are accelerated mainly by the Lorentz force. Thus, solid armature rail guns operate at lower projectile velocities. The important tradeoff is that there is a substantial reduction in rail damage for metal armature projectiles.

Several factors limit projectile velocities in the metal armature rail guns. The most obvious is the elimination of the plasma force. However, a more subtle limit is the speed at which the commutation process can take place. Although the latter limit is still not well understood, experimental evidence indicates a commutation limit may occur near 6 to 7 km/sec. This velocity limit is still attractive for Army tactical missions for rail guns.

The actual rail damage occurring with two types of metal armatures, wire brush contactors and monolithic metal contactors, and new developments in barrel technology, such as superconducting augmentation, will be presented in this paper.

BIOGRAPHY:

PRESENT ASSIGNMENT: Physicist, US Army ARDEC, Benet Laboratories, Materials Engineering Section, Watervliet, NY.

RAIL DAMAGE IN A SOLID ARMATURE RAIL GUN

Theresa Brassard
Long Beach Naval Shipyard
Long Beach, CA 90822

and

Clarke G. Homan
US Army Armament Research, Development, and Engineering Center
Close Combat Armaments Center
Benet Laboratories
Watervliet, NY 12189-4050

INTRODUCTION

Rail gun technology is rapidly being developed both for the Strategic Defense Program (SDI) and for tactical Army application. In general, rail gun technology will be required whenever projectile velocity or minimum projectile time of flight demands exceed the capabilities of normal chemical propellants. Under present chemical launch capabilities, muzzle velocities in excess of 2 km/sec will require some sort of an electromagnetic (EM) system.

The two types of armature drives, plasma and solid types, characterize present rail gun development. Both types have their advantages and disadvantages which will dictate the type used by system requirements.

The plasma armature rail gun adds a plasma push force to the normal Lorentz magnetic force to obtain extremely high projectile velocities (> 10 km/sec) in small mass systems. The main disadvantage of the plasma drives is the severe rail damage caused by the high temperature plasma arcs which limits barrel lifetimes to a few launches at most. However, single shot missions for very high velocity missions will probably use plasma armatures.

Since Army tactical missions require multi-shot capability, this paper will concentrate on the solid armature type propulsion in which rail damage is significantly reduced.

In the first section, a brief description of rail circuits will be presented to suggest some of the static and dynamic responses which may occur in these systems.

The second section will present actual launch results that illustrate some of the unusual loading conditions which can occur in these systems, either intentionally or accidentally, due to the electromagnetic origin of the propulsion force.

In the final section, we will present preliminary rail damage data obtained from two different metallic armatures to illustrate that the type and extent of rail damage is dependent not only on launch conditions, but on armature materials as well.

RAIL GUN CIRCUITS

Figure 1 is a schematic of the basic rail gun circuit. Electrical energy is supplied in a suitable pulse shape to the rail gun circuit. The resulting current waveform $I(t)$ will produce the propelling Lorentz force F_{SRG}

$$F_{SRG}(t) = \frac{1}{2} * L' I^2(t) \quad (1)$$

where L' is the magnetic self-inductance gradient of the rails. Although a constant high current has the highest launch velocity/energy input efficiency, actual rail guns are generally powered by a capacitive-like discharge from an energy source.

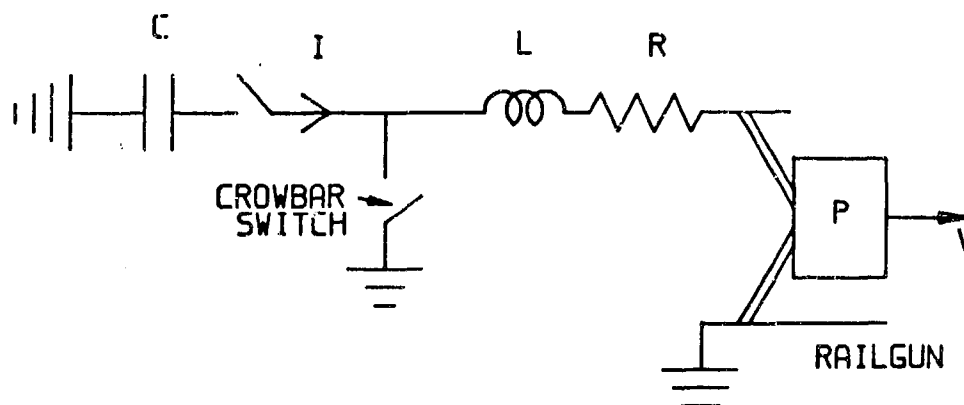


Figure 1. Rail Gun Circuit

After closing switch S , the electrical energy stored in the capacitor ($\frac{1}{2} QC^2$) is converted to current energy in the inductor ($\frac{1}{2} LI^2$). This is accomplished before the projectile P moves. At this point, the crowbar switch CS is normally closed, converting the electrical system from an oscillatory LCR circuit to a decaying LR rail gun circuit. (In the next section, we will discuss the rail gun behavior when the crowbar is not used.)

In an earlier publication [1] we showed that when the current decays to zero before the projectile reaches the end of the rails, the muzzle velocity v_f will be

$$v_F \approx \frac{L_0 E_0}{2mR} \quad (2)$$

where E_0 is the energy stored in the capacitor bank, m is the projectile mass, and R is the mean circuit resistance during launch. This formula was derived assuming frictional losses are negligible and has been shown to be in fairly good agreement with experimental data for low velocity launches [1]. Loss terms introduced at higher velocities such as the resonance losses described by Simkins at this conference [2] may lead to significant correction terms in these formulae, since in general, the rail gun system will be more compliant than a normal gun system.

The simple rail gun described above is not a very efficient system, since any magnetic field energy stored in the rail fields at the end of launch must be dissipated. It is possible to show, from general energy considerations, that an ideal rail gun, operating at constant current, equipartitions the energy extracted from the power source into magnetic energy and projectile work, and therefore the maximum efficiency of such a system is 50 percent. Real rail guns operating at nearly constant current dissipate some of the projectile work into Joule heating, friction, etc., so that actual launch efficiencies are about 10 percent.

In an effort to increase barrel efficiency, Benet Laboratories developed the concept of superconducting augmentation. Figure 2 shows schematically a superconducting augmentation coil operating in the persistent mode and magnetically coupled to the rail coil by the mutual inductance M

$$M = k \sqrt{LL_s} \quad (3)$$

where L and L_s are the self-inductance of the rail coil and supercoil, respectively, and k is the coupling constant whose positive value can approach unity. Both L and k are dependent on projectile position.

In the development of the equations that follow, it is important to note that these equations are peculiar to a rail gun with a superconducting augmentation coil, since the superconducting property of flux trapping was used in their derivation. A normally conducting augmentation coil, which cannot be placed in a persistent mode, will exhibit the same efficiencies as an unaugmented system. This latter fact can be shown quite generally for any system of linear normally conducting circuits.

We have shown that the armature force $F(x)$ for a SARG system is [3]

$$F(x) = \frac{1}{2} L' I^2 + I I_{s0} M' - x I^2 M'^2 / L_s \quad (4)$$

where the current I varies as

$$I = \frac{I_0 - x I_{s0} (M' / L_0)}{1 + x (L' / L_0) - x^2 (M'^2 / L_0 L_s)} \quad (5)$$

and I_{s0} is the initial supercurrent, L_0 is the pulse shaping inductance, and the distance x is measured along the rails.

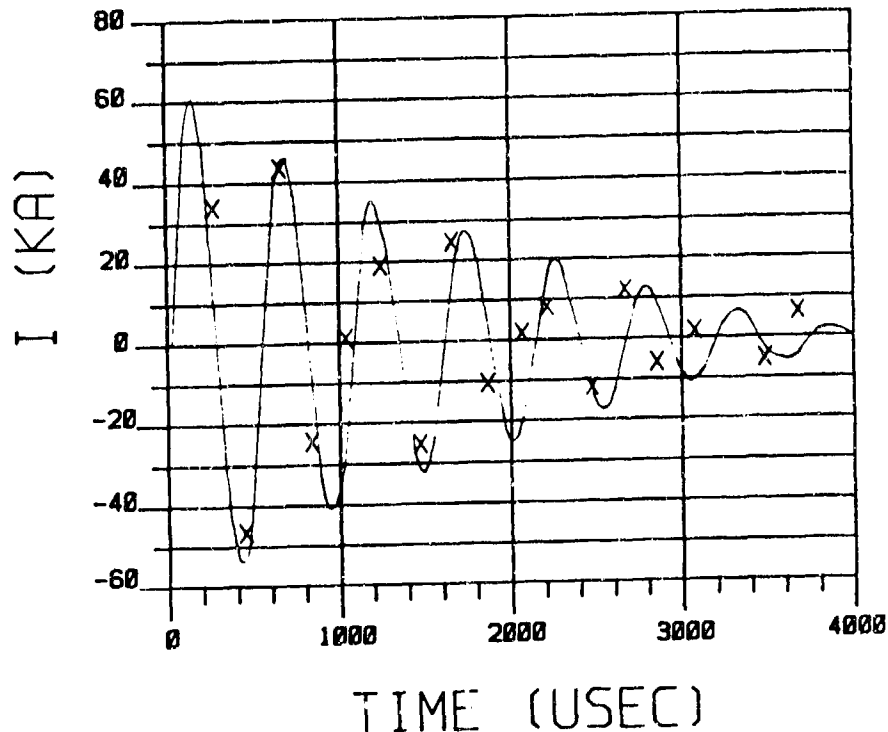


Figure 2. Current Oscillations in Non-Crowbarred Rail Gun.

Now the point in presenting all this theory is that although these equations give reasonably good results for projectile velocity, barrel launch efficiency, etc., they are totally inadequate for the evaluation of barrel deformation and dynamics. The reason for this is that implicit in these calculations is the assumption that the rail current has fully penetrated the rails and is uniform. In fact, at reasonable velocities, the current sheet may be limited to the surface by the skin effect and is nonuniform along the barrel as suggested in Figure 3. It is obvious that a systematic evaluation of barrel dynamics is not a trivial process, but requires the solution of the electro-dynamics of the system as well. At the present time, computer codes have been developed to try to evaluate barrel dynamics, however, no closed form solutions have been developed to date.



Figure 3a. Rail Damage at Origin of Launch for Niobium Brush Armature (20X).

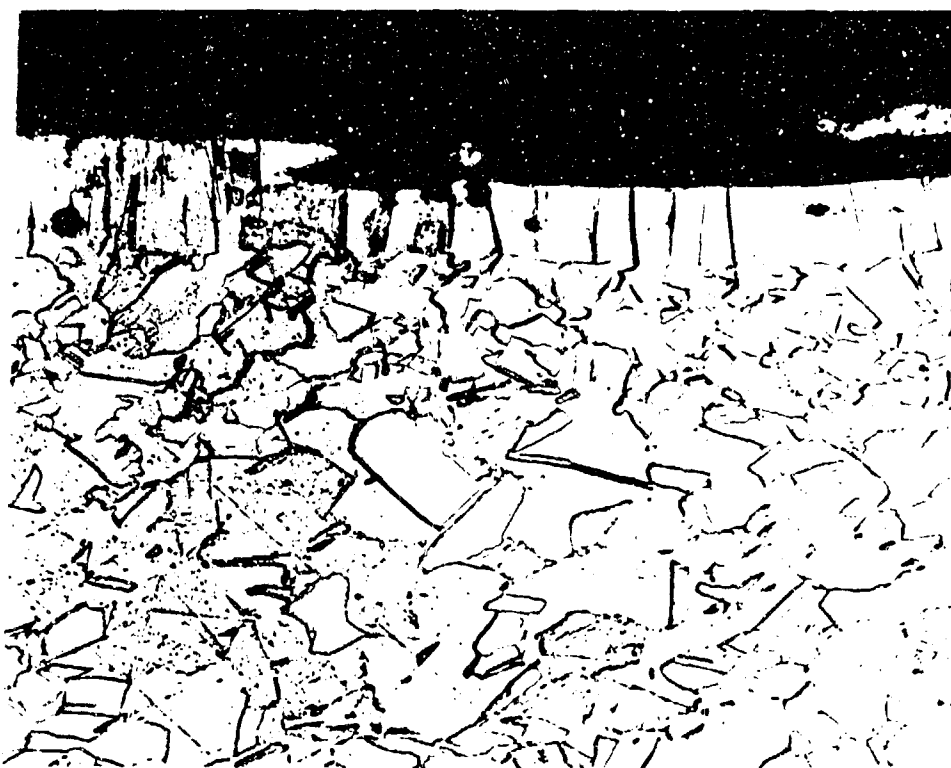


Figure 3b. Photomicrograph Showing Columnar Recrystallization Typical of Niobium Armature Launch (200X).

ACTUAL RAIL GUN PERFORMANCE AND ANALYSIS

In this section we will present the analysis used to evaluate the performance of a series of launches of a small rail gun at Los Alamos [1]. In particular, we chose special launch conditions to illustrate dynamic behavior which is peculiar to the electromechanical nature of rail gun systems.

Consider the circuit of Figure 1. If the crowbar switch is not closed for whatever reason, then the circuit remains a classical damped electromechanical oscillator. If all the circuit elements (rails, inductors, etc.) are rigid, then the system can be analyzed as an electrical oscillator obtaining the current

$$I(t) = -Q/LC_w * e^{-bt} * \sin wt \quad (6)$$

where $w = \sqrt{w_0^2 - b^2}$, $w_0^2 = 1/LC$, and $b = R/2L$. Interestingly, if the current decays to zero before the projectile exits the gun, we recover Eq. (2), i.e.,

$$v_F \approx \frac{LE_0}{2mR} \quad (7)$$

Thus, for low velocity systems, a suitable EM design could eliminate this complication of a crowbar switch, however, subjecting the mechanical system to an oscillatory driving force.

In Figure 4 we show the actual current response of an uncrowbarred rail gun, in which the mechanical behavior manifests itself through the temporal variation of w_0 and b . Also shown are the calculated currents from Eq. (6) using constant mean values of w_0 and b . In this system, these variations were found to be primarily due to the mechanical oscillation of the pulse shaping coil.

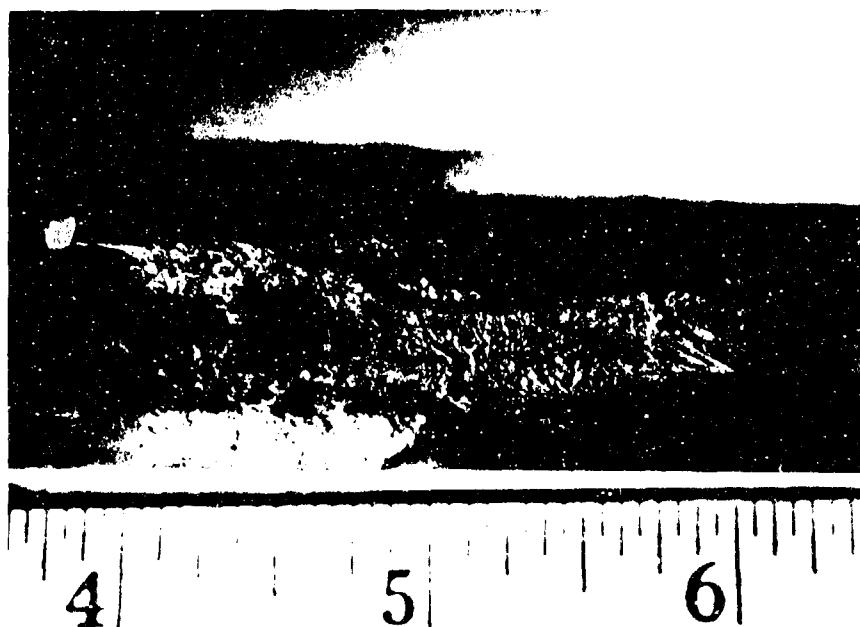


Figure 4a. Rail Surface Damage For Solid Aluminum Armature.



Figure 4b. Photomicrograph of Acicular Recrystallization Zone for Solid Aluminum Armatures. Several Different Aluminum-Copper Bronzes were Identified (1000X).

RAIL DAMAGE

In this final section, we will describe the typical damage solid armature rail guns experience during launch. The type of rail damage can be characterized principally by the materials present and, to a lesser degree, by launching conditions. On the other hand, the extent of damage is principally controlled by firing conditions. We will focus on the types of rail damage in this paper, relating when necessary to effects of firing conditions on the type of damage.

Before we proceed, we can make some general comments about the extent of rail damage due to launch conditions. Two major factors in the extent of damage are projectile velocity and armature condition. Since most rail damage is due to surface heating, it is obvious that a nonarcing solid armature will have less extensive rail damage than a plasma armature. Likewise, a fast moving armature is less damaging than a slow one. For these reasons, solid armature rail guns with projectile injection will probably be used for multi-shot tactical weapons.

Two different armature designs were tested in the Los Alamos launches. In this 3/8-inch square bore rail gun powered by a 15 kJoule capacitor bank through a 5 microhenry pulse shaping coil, projectiles were either Lexan rectangular parallelepipeds having an armature of niobium wires imbedded in a copper matrix or monolithic aluminum projectiles of the same shape.

The Lexan projectile armatures were made by etching the copper matrix material from the niobium wire of a superconducting cable, resulting in rather stiff, short bristle niobium brushes contacting the copper rails.

The aluminum projectiles had narrow contactor leaves machined into the rear of the projectile to concentrate the current and to be deformable by a Lexan plug to insure contact with the rails.

Both armatures suffered severe metallurgical damage characterized by melting, however, since armatures are expendable in a rail gun system, we will concentrate on the type of damage to the rails caused by the different armatures.

As mentioned earlier, the Lexan projectiles' niobium copper armatures experienced severe plasma arcing as witnessed by performance and rail damage. The as-received rail material was a high conductivity copper bar containing traces of zinc, aluminum, zirconium, titanium, cadmium, iron, magnesium, and cadmium with a hardness of Rockwell B53. Careful metallographic examination after each launch revealed three basic elements to the severe erosion which occurred at the initial projectile position. The primary modification was a metallurgically bonded columnar layered structure characteristic of melting and solidification. In addition, weld pools suggesting eddy current flow patterns and a spongy surface layer of copper oxide were observed. EDAX analysis of these areas detected elemental niobium and carbon in abundance, however, no compounds or second phases of niobium or copper were found with the exception of the surface oxides. This is not unexpected since the phase diagram indicates almost complete miscibility of the two elements. Figure 3 shows the typical damage obtained at the projectile initial position. Of course, farther down bore, much less damage occurs as the projectile accelerates. In the high velocity regions, the principal damage is a heavy surface coating of soot (CuO) caused by the plasma arc.

When the aluminum projectiles were used, hardly any arcing occurred and less severe rail damage was seen at the projectile origin position. However, the character of the damage was quite different. Careful metallography revealed an acicular type microstructure as shown in Figure 4. From preliminary EDAX analysis, at least two different compounds of aluminum copper were identified in this region. Examination of the aluminum copper phase diagram revealed several compounds (bronzes) for this system which explains the complex metallurgical behavior occurring in this zone.

CONCLUSIONS

The purpose of this paper was to present some of the new problems that can occur in rail guns and that may be of some interest to the gun dynamics community.

The uncrowbarred rail gun was presented in some detail to illustrate the rail gun as an electromechanical system, which is normally damped, but can be excited in a resonant condition.

Finally, a brief glimpse of rail damage as being related to the conditions of launch as well as the materials involved, was presented to introduce the gun dynamics community to these important factors which may play a strong role in any analysis of rail gun behavior.

REFERENCES

1. C. G. Homan, C. E. Cummings, C. M. Fowler, and M. L. Hodgson, "Superconducting Augmented Rail Gun (SARG) Development," to be published in the Proceedings of the Megagauss Conference by IEEE Magnetics, Sante Fe, New Mexico, 1986.
2. T. E. Simkins, "Resonance of Flexural Waves in Gun Tubes," Proceedings of the Fifth US Army Symposium on Gun Dynamics, Rensselaerville, NY, 23-25 September 1987.
3. C. G. Homan and W. Scholz, "Evaluation of Superconducting Augmentation on Rail Gun Systems," IEEE Transactions on Magnetics, Vol. MAG-20, 1984, p. 366.

O'HARA AND CASCIO

TITLE: STRUCTURAL INTEGRITY OF METALLIC ARMATURE RAIL GUNS
G. P. O'HARA AND M. CASCIO
US ARMY ARMAMENT RESEARCH, DEVELOPMENT, AND ENGINEERING CENTER
CLOSE COMBAT ARMAMENTS CENTER
BENET LABORATORIES
WATERVLIET, NY 12189-4050

ABSTRACT

The design of a rail system for an electromagnetic gun becomes more complicated when the transfer from a laboratory to a tactical system is considered. In the laboratory, weight and volume are not important and the system must be bolted together in order to be disassembled for study, modification, and repair. The tactical system must be of reasonable weight and volume, self-supporting, safe to use, have a long life, and be factory assembled. This set of design requirements must be reconciled with the function as a projectile guide and an electrical conductor. The first crude prototype 'barrel' must be manufactured from available materials which do not have the optimum properties. The design then becomes a series of compromises which are performed in the hope of a successful result.

BIOGRAPHY:

PRESENT ASSIGNMENT: Research Mechanical Engineer, US Army ARDEC, Benet Laboratories, Applied Mathematics and Mechanics Section, Watervliet, NY.

STRUCTURAL INTEGRITY OF METALLIC ARMATURE RAIL GUNS

G. P. O'Hara and M. Cascio
U.S. Army Armament Research, Development, and Engineering Center
Close Combat Armaments Center
Benet Laboratories
Watervliet, NY 12189-4050

INTRODUCTION

An electromagnetic rail gun is rather simple in concept. It consists of two parallel conductive rails with a projectile between them. At the rear of the projectile is an armature which is essentially a 'shorting bar' between the rails. When the rails are connected to an electrical power supply, a magnetic field is set up between the rails which interacts with the field set up by a current in the armature to propel the projectile up the rails and out of the gun. This is an attractive process because the electrical current can chase the projectile up the rails much more efficiently than the hot gasses of a chemically-based gun. In this way much higher projectile velocities can be achieved. However, there are many technical problems which must be overcome in order to create, control, and contain the large energy requirements of a reasonable size projectile. In this case, the high current density required to attain reasonable velocities produces magnetic fields which place substantial forces on the various rail gun structures.

Recent developments in power supplies for rail guns such as the homopolar generator have given promise to the development of a practical rail gun weapon. Therefore, interest was generated in the process of moving from the laboratory rail 'bolted up' system to a more portable rail system or a rail gun 'barrel'. This process seems to require a movement from the square bore of the usual laboratory gun to a round bore. At the same time it seems advantageous to shift from a plasma armature to a solid metallic armature. The solid armature is intended to eliminate the rail damage produced by the hot plasma. The first step in this process was taken earlier by this author in an investigation of square bore guns held together by a composite over-wrap [1].

The requirements for a rail system now become more complicated. It must still guide the projectile and provide a conductive path from the power source, but now the weight and volume become very important. Further, it must be self-supporting in bending so that it can be held in some reasonable turret and pointed in the desired direction. The ability to deliver the projectile in a particular direction will mean that the process of guiding becomes more critical because the projectile must be sent several kilometers to a target rather than a

few meters. The one factor which will help is that the plasma armature common in laboratory guns will be replaced with a solid metallic one and the plasma pressure is gone from the problem.

This paper deals with the design of an early prototype of a tactical rail system. The design is driven by the necessity of producing hardware from available materials using the available production machines, and this will be done with insufficient design information. The structural analysis was done largely with the ABAQUS [2] finite element code using nonlinear static analysis. This problem does have serious dynamic considerations; however, the static problem must come first because if the static problem is not solved there is no hope of any control of the dynamic cases.

In this paper, the definition of structural integrity will be expanded from the normal notion of relating integrity to some gross failure. Here the failure will also include failure to function, i.e., failure to complete all tasks correctly. The item of primary concern is rail expansion which must be minimized to insure good armature contact and precise alignment of the projectile in the desired direction. A major problem is that the armature design parameters are not available and the detailed design of tactical projectiles is still in the future. No guidelines have been quantified for permissible rail expansion values. The study must then look at ways to minimize these numbers and thus ease the burden of the projectile designer.

DESIGN LIMITATIONS

These early rail gun barrels were designed to take advantage of readily available materials and manufacturing facilities in order to produce hardware on a specific schedule. This, along with the lack of many specific items of design information, has resulted in a design which is far from the optimum. However, there has been time to look at alternate methods and materials in order to increase the design data base. In any case, the initial design parameters are the following:

1. A circular bore of 0.050 meter diameter and 5.0 meters long.
2. A maximum rail current of 1,500,000.0 amperes.
3. Rails made from OFHC tough pitch copper.
4. A composite-wrapped hoop for overall support.
5. Self-supporting in bending.
6. Metallic armature.
7. Insulating spacers between the rails machined from G-10 glass cloth-epoxy material.
8. Maximum possible contact surface for the armature.
9. The rail geometry may not include acute angles.
10. The rail system must look like a gun, however, an oval cross section is acceptable.
11. Any reasonable weight will do, however, the cost of available composite materials is very high.
12. Electrical insulation must be provided to isolate the two rails.

Of these design goals, the desire for a circular bore combined with goals 3, 8, and 9 provided the most serious limitations. Informal information from Los Alamos National Laboratory placed the maximum rail contact area at 120 degrees of arc in a round bore. Further, the use of soft copper rails and the desire to limit the use of acute angles required that the outer surface of the rail intersect the bore at a right angle. This is a very serious limitation, and if it can be eliminated, many improvements in structural performance are possible.

While not a design limitation, this work has also explored the full use of Standard International Units in the design and analysis. This has been very successful and can be recommended for all engineering work. Therefore, all units in this paper are metric using the standard meter, newton second system. Stresses and stiffnesses are given in pascals, or newtons per square meter.

RAIL GUN GEOMETRY

This paper is primarily concerned with the design of the basic cross section of the rail system or rail gun barrel. The basic concept is shown in Figure 1 which outlines the seven basic items. The primary components are the two electrically conductive rails (R). The rail spacing is controlled by two insulating spacers (S), which conform closely to the rails and fill in part of the inner bore surface. These four components are held together with a conforming hoop assembly of three more elements. The inner portion of the hoop is an insulating-wrapped composite (I) material to electrically isolate the rails from the structural hoop (H). The structural hoop is that portion which carries the major loads from the magnetic expansion force. The outer element (L) is a layer of composite material which is oriented in the longitudinal direction to provide bending stiffness for the overall structure.

Figure 2 shows the finite element grid (a one-quarter section) for one rail gun that was fabricated. The hoop has been flattened to an oval shape for two reasons. First, this reduces the weight and volume of the spacers which serve little structural purpose. Second, the oval shape reduces the length of the loaded hoop in an effort to reduce the expansion of the rails. The oval shape is generated by connecting circular arc segments of two different radii which meet in a smooth manner at the interface between the rail, the spacer, and the hoop assembly. This will insure a smooth transition during the composite wrapping process. In this paper the radius of the outside of the spacer (next to the insulating hoop) is twice that of the outside of the rail.

The rails were designed initially to provide for a round bore rail gun which has presented several problems. The primary problem is that electrical conduction problems prevent the use of acute angles in the rail so the rail sides must meet the bore at a right angle and then curve back to the hoop. At this point it is tempting to interlock the rail and spacer; however, insulating materials with good strength are not easy to come by and this work is limited to available materials. The poor strength of available insulating materials for the spacer also seemed to preclude an acute angle in the spacer at the bore. This idea also reinforced the notion that the rail spacer interface meet the bore at a right angle.

BASIC
GEOMETRY

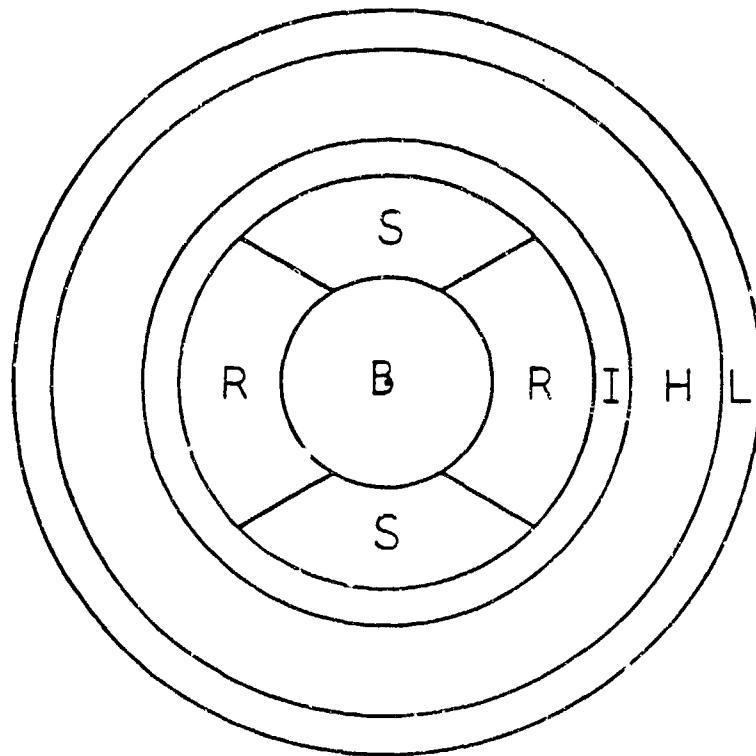


FIG. 1

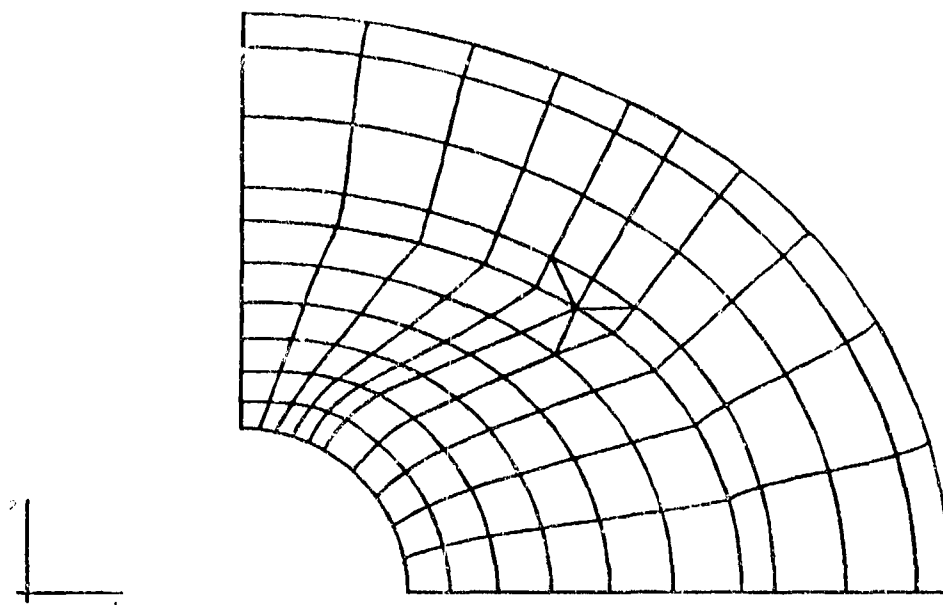


Figure 2. Finite element mesh for a round bore gun.

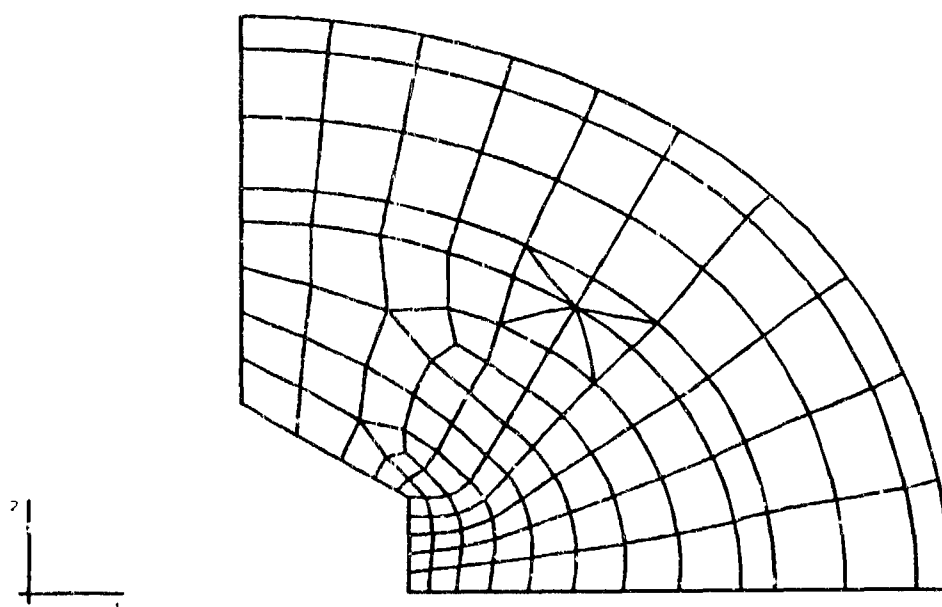


Figure 3. Finite element mesh for a hexagonal bore gun.

The spacer fills in the volume bounded by the rails, the bore, and the long radius portion of the hoop. In the round bore gun it will be pushed into the bore under the assumed magnetic loads. This appears to be a problem, however, the effect will primarily be in back of the projectile. It still seems that it should be controlled, and the hexagonal bore configuration shown in Figure 3 will be used to illustrate this point.

Most laboratory rail guns have a square bore because the rails are rectangular copper bars. Several round bore guns have been produced at Los Alamos National Laboratory [3], however they presented many difficulties. Here a hexagonal bore gun is suggested because of its ability to control spacer motion into the bore region. There is precedent for hexagonal bore guns as the Whitworth gun was used successfully by the Confederate Army during the Civil War. In this case, the hexagonal bore provides for a right angle corner in the rail at the bore and a short contact surface to control spacer movement into the bore. This control of spacer movement will be shown to be important in the control of rail expansion, however, the bearing stresses between the rail and the spacer become very large.

RAIL GUN MATERIALS

The materials for this work were, for the most part, defined by availability and past experience of other rail gun builders. It was assumed that high electrical conductivity was a mandatory requirement for the rails, which made copper the material of choice. A high purity copper was selected in the half-hard condition.

Copper:

Tensile Modulus - $E = 110.33 \text{ E } 9$
 Poisson's Ratio - $M = 0.330$
 Yield Strength - $Y = 170.6 \text{ E } 06$

The spacer material was selected because of its use in other rail guns and because it is readily available in large blocks. It is a standard insulating material called G-10. It is manufactured as a stack of fiberglass cloth layers bonded together with an epoxy matrix. In this gun the wrap direction [3] runs parallel to the rails, the filler runs between the rails [1], and the stacking runs out from the bore [2]. The following three-dimensional orthotropic properties were used.

G-10:

Tensile Moduli - $E1 = 26.36 \text{ E } 09$, $E2 = 15.35 \text{ E } 09$, $E3 = 30.77 \text{ E } 09$
 Poisson's Ratio - $M12 = 0.4455$, $M13 = 0.1050$, $M23 = 0.1448$
 $M21 = 0.2594$, $M31 = 0.1226$, $M32 = 0.2903$
 Shear Moduli - $G12 = 8.66 \text{ E } 09$, $G13 = 6.62 \text{ E } 09$, $G23 = 6.17 \text{ E } 09$

O'HARA AND CASCIO

The insulating layer of the hoop is assumed to be a fiberglass epoxy composite material wrapped in the hoop direction. The analysis used properties which assume a standard fiber volume fraction of 60 percent which resulted in the following properties.

S-Glass:

Tensile Moduli - $E1 = 12.85 \text{ E}09$, $E2 = 12.85 \text{ E}09$, $E3 = 52.85 \text{ E}09$
Poisson's Ratio - $M12 = 0.3584$, $M13 = 0.0628$, $M23 = 0.0628$
 $M21 = 0.3584$, $M31 = 0.2582$, $M32 = 0.2582$
Shear Moduli - $G12 = 4.73 \text{ E}09$, $G13 = 6.00 \text{ E}09$, $G23 = 6.00 \text{ E}09$

The outer bending layer of the hoop is assumed to be an IM-6 graphite epoxy composite with a fiber volume fraction of 0.60 which produces the following material properties.

IM-6:

Tensile Moduli - $E1 = 8.870 \text{ E}09$, $E2 = 8.870 \text{ E}09$, $E3 = 175.1 \text{ E}09$
Poisson's Ratio - $M12 = 0.3618$, $M13 = 0.0131$, $M23 = 0.0131$
 $M21 = 0.3618$, $M31 = 0.2588$, $M32 = 0.2588$
Shear Moduli - $G12 = 3.26 \text{ E}09$, $G13 = 5.51 \text{ E}09$, $G23 = 5.51 \text{ E}09$

The material for the structural portion of the hoop is a major concern of this paper and will be covered in detail in the remainder of the paper. However, the structural hoop will always be one of three classes of material. First, is a continuous fiber composite such as graphite-epoxy. The actual rail guns which have been fabricated or scheduled are glass or graphite composites. When these materials began to show large deformations, the analysis was changed to standard metals such as aluminum. Finally, as a projection into the future, some runs are reported using laminates of metal sheets (aluminum or titanium) separated by glass cloth-epoxy insulating layers. As will be seen, these choices can produce strong variations in the maximum rail expansion. In the initial part of this work, a plane hoop wrap was assumed, however, this evolved into a plus and minus 7.5 degree winding pattern. This will show up as a slight variation in the hoop stiffness of wrapped composite cases.

DETAILS OF THE ANALYSIS

The analysis was performed using the ABAQUS finite element code. Eight-node generalized plane-strain elements were used in conjunction with three-node per surface interface elements. There are three interface surfaces in this geometry: the rail-hoop interface, the spacer-hoop interface, and the rail-spacer interface. These three surfaces must be separated so that they may act independently. This has been done by using collapsed quadrilateral elements at the intersection point. In these elements, one side has been given zero length, while all three nodes are allowed to deform independently. This will keep the contact surfaces independent while allowing a 1/R singularity at the intersection point. This singularity is necessary to model the discontinuity of the sharp corner of the rail contacting the insulating layer of the hoop. In an actual system the soft copper rail will deform and eliminate this problem, however, for this analysis it is not necessary.

The magnetic load was applied as a uniform pressure on the bore surface of the rail with a total expansion force of $4.38 \text{ E}+06$ newtons per meter of rail. This figure was the initial estimate of the total expansion force for a $1.0 \text{ E}+06$ ampere current and an inductance gradient of $0.40 \text{ E}-06$ Henry. During the duration of this study, several different methods of calculating the rail expansion force from current distribution models were tested. However, none were better than the original crude estimates. This is also true of the distribution of load on the rail, where the application of load as a general body force did not result in significant changes in rail expansion.

The final analysis details relate to the required constraints. The finite element grid is a one-quarter section model which used symmetry constraints on the coordinate axes. Further, it uses generalized plane-strain elements which were constrained to keep the normal strain constant for all elements. However, this strain was allowed to be any value which produced a net axial force of zero.

A secondary analysis was performed to determine the droop of the gun when supported as an overhanging beam. In this case, a 5 meter-long barrel was assumed which was supported at one end and at a point 2 meters from that end. The tip deflection was calculated at the free end using simple beam theory. In order to calculate the section modulus (EI) of this complex section, a simple program was generated. This program used the ABAQUS finite element mesh to calculate the area and inertial properties of the section. These were then multiplied by the appropriate material modulus and summed to produce the overall composite section modulus. The same basic method was used to calculate the appropriate mass-per-unit length of the gun to use as a distributed load.

RESULTS

Figure 4 shows a typical deformed grid plot for the round bore gun with the deformation magnified by a factor of 10.0. This figure demonstrates the two primary problems. First is the rail expansion under load, and second is the spacer contraction due to sliding along the rail-spacer interface. The sliding has been allowed because of the small (0.02) value for the coefficient of friction. This is the general condition for the first two rail guns to be built. In contrast, the hexagonal bore model shown in Figure 5 still has a large rail expansion, but now the spacer contraction has been controlled and the gap in the rail-spacer interface has been replaced by a small region of high contact stress. This contact at the bore will have the effect of producing a bore seal against contaminants and any casual plasma which may exist. However, the price is a high contact force which must be carried by the soft rail material and the weak insulating spacer.

Figure 6 is a stress contour plot of the minimum principal stresses where the structural hoop is S-glass composite. The single most prominent feature is the contour loops near the rail-spacer-hoop intersection. These compressive stresses are the result of the sharp corner of the rail pressing on the hoop.

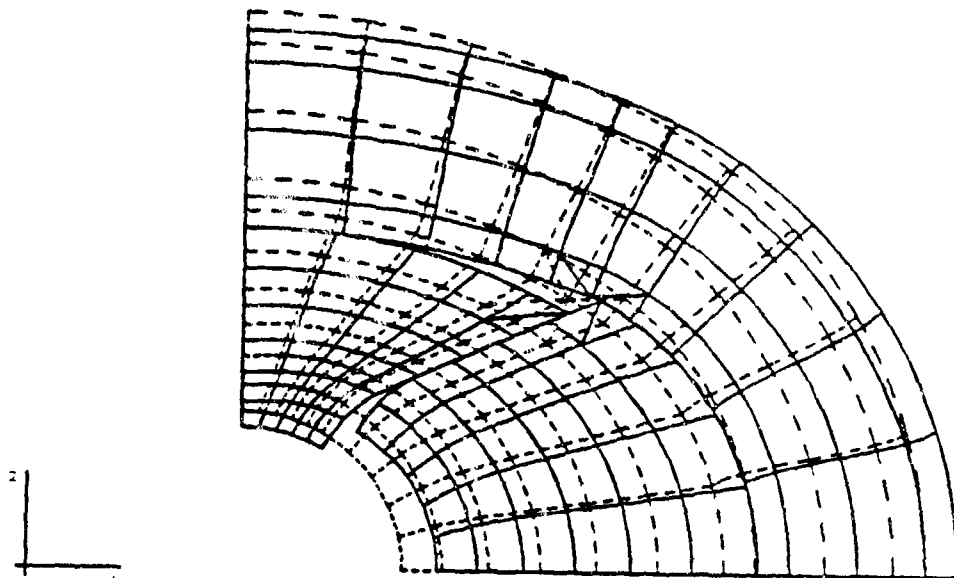


Figure 4. Deformed mesh for a round bore gun.

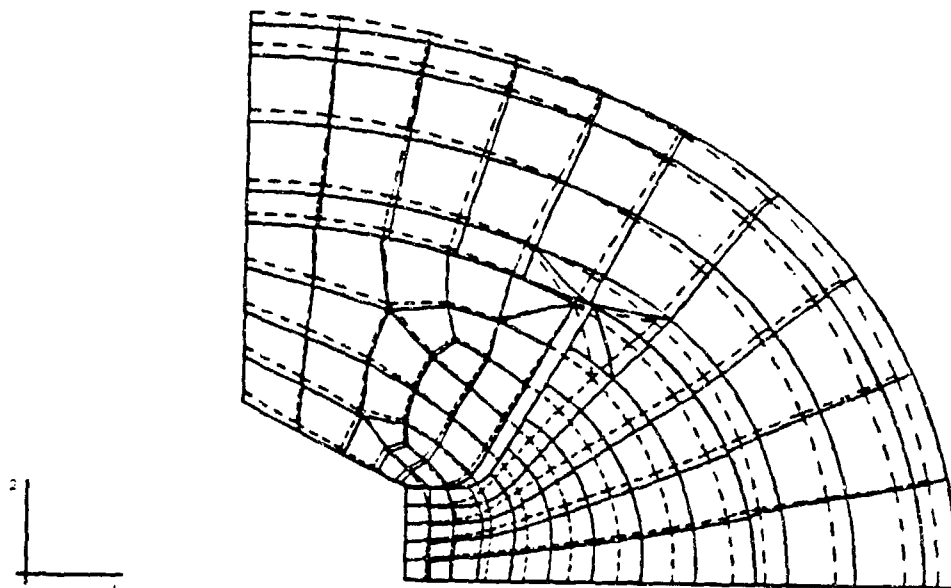


Figure 5. Deformed mesh for a hexagonal bore gun.

This is due in part to the mathematically sharp corner modeled by the singular elements. Three factors will reduce this effect: real corners have a radius, the rail deforms locally, and better hoop materials reduce overall system deformation.

Figure 7 is a stress contour plot for the case of an IM-6 graphite composite hoop. Here the contours are lines of constant maximum principal stress. The thing to note here is that the maximum tensile stress is in the hoop above the spacer. This stress is the highest near the insulation layer and decreases rapidly through the thickness of the hoop. This is a result of poor stress transfer in this class of materials because of low transverse and shear stiffnesses. Similar effects have been noted by Mansfield for pin-loaded composites [4] and this author for thick-wall cylinders [5].

The general level of stresses in all of the cases reported here is low. All of the data was plotted using 11 contours over a range of $-250.0 \text{ E}+06$ to $250.0 \text{ E}+06$ pascals. These stresses are acceptable to all of the structural materials involved (not the G-10). These generally low stresses had two notable exceptions. First is the high compressive stress at the mathematical singular point, and second is the high contact stress in the hexagonal bore configuration.

The primary result of this paper is the analysis of the rail expansion for different materials in the structural portion of the hoop. The materials may be isotropic metals such as steel or aluminum, organic composite materials such as S-glass or graphite, or a metallic and composite laminate of glass cloth epoxy layered with aluminum or titanium. Further, the round or hex bore configuration may be used with little difference in result. All of these are plotted as the radial displacement of the bore surface of the rail against the hoop stiffness of the particular materials. These are shown in Figure 8 for the following materials:

Isotropic

1. Steel
2. Titanium
3. Aluminum

Wrapped fiber composite

4. S-glass - epoxy
5. IM-6 graphite - epoxy
6. Steel wire - epoxy

Metal and composite laminate

7. Titanium - G-10
8. Aluminum - G-10

Note that there are two different families of data on this plot: the fiber-wrapped composites and everything else. The numeric data is shown in Table I.

MIN. PRINCIPAL STRESS
 I.D. VALUE
 1 -2.50E+02
 2 -2.00E+02
 3 -1.50E+02
 4 -1.00E+02
 5 -5.00E+01
 6 +0.00E+00
 7 +5.00E+01
 8 +1.00E+02
 9 +1.50E+02
 10 +2.00E+02
 11 +2.50E+02

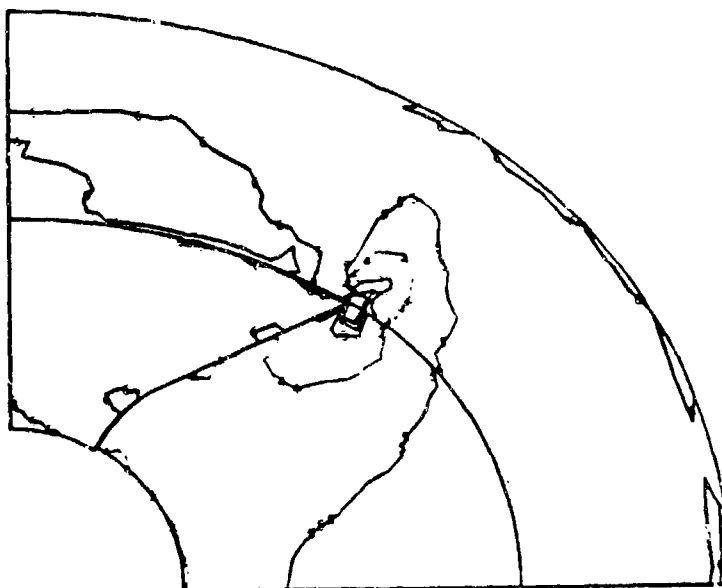
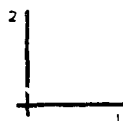


Figure 6. Minimum principal stress contour plot.

MAX. PRINCIPAL STRESS
 I.D. VALUE
 1 -2.50E+02
 2 -2.00E+02
 3 -1.50E+02
 4 -1.00E+02
 5 -5.00E+01
 6 +0.00E+00
 7 +5.00E+01
 8 +1.00E+02
 9 +1.50E+02
 10 +2.00E+02
 11 +2.50E+02

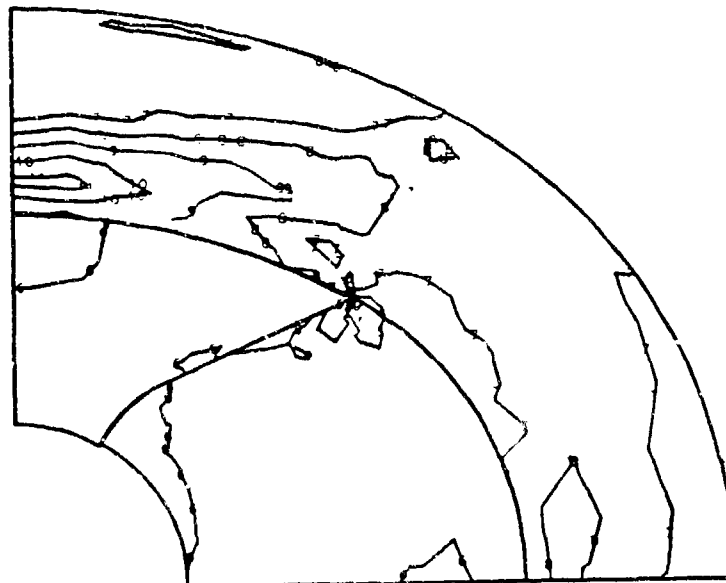
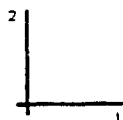


Figure 7. Maximum principal stress contour plot.

RAIL DISPLACEMENT vs. HOOP STIFFNESS

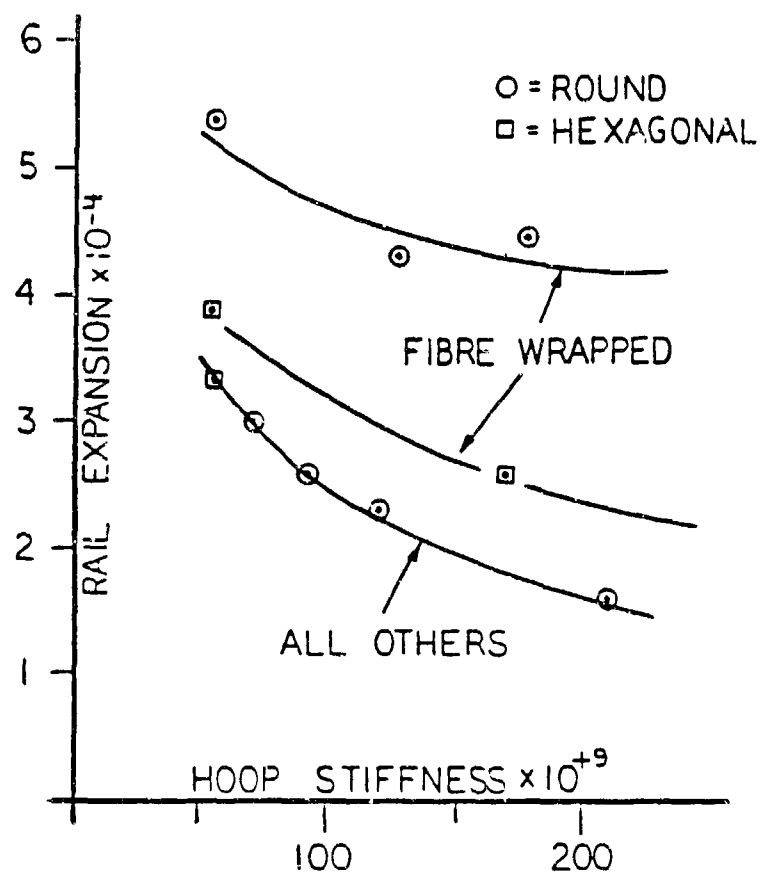


FIG. 8

TABLE I. RADIAL DISPLACEMENT DATA

Configuration of the Bore	Material Number	Hoop Stiffness	Displacement Meters
Round	1	206.8 E9	0.000154
Round	2	119.9 E9	0.000213
Round	4	52.85 E9	0.000518
Round	5	175.1 E9	0.000443
Round	6	125.4 E9	0.000414
Round	7	90.52 E9	0.000256
Hexagonal	3	68.95 E9	0.000294
Hexagonal	4	51.22 E9	0.000383
Hexagonal	5	167.5 E9	0.000257
Hexagonal	7	89.09 E9	0.000261
Hexagonal	8	55.18 E9	0.000329

The beam bending analysis was only performed for the S-glass and IM-6 structural hoop materials. They produced a mass of 101.3 and 95.3 kilograms per meter because the graphite fiber is lighter than the glass. However, because the transverse stiffness is nearly the same for both materials, the section moduli were close in value. These gun sections have two principal inertial axes and deflections were calculated for both. The results shown in Table II are barrel droop due to gravity when supported at two points 2.0 meters apart. In all cases the deflections seem to be rather small which verified the bending stiffness of this design. Further analysis demonstrated that the axial graphite in the outer layer of the hoop is about 5 percent of the total mass of the round bore barrels and accounts for about 50 percent of the bending stiffness of the overall section.

TABLE II. RAIL GUN BEAM BENDING DATA

	Unit Mass (kilograms)	Section Modulus	Deflection (meters)
S-Glass	101.3	5.182 E+06	0.00347
	101.3	2.978 E+06	0.00604
IM-6	95.3	5.020 E+06	0.00337
	95.3	2.861 E+06	0.00592

DISCUSSION

The first thing to note in this paper is that the first gun to be manufactured will be a round bore gun with an S-glass epoxy containment hoop. This is far from the best design, however, it does have the advantage of fitting into the limitations of time, cost, materials, and available equipment. The second gun will use an IM-6 graphite structural hoop which is stronger; however, it will do little to improve the rail expansion problem.

There are several things which would help reduce rail expansion. First would be the use of an isotropic structural hoop which would present many fabrication problems. The laminated hoop could be fabricated from thin plates, die cut into oval rings, and stacked with matching glass cloth-epoxy rings. The stack could then be cured into solid sections and assembled over the rails. This would be a time consuming and expensive process, however, it may also have some magnetic advantages.

Another way of reducing the expansion would be to find an insulating material which would be able to tolerate higher stresses. This, in conjunction with a higher strength rail material, would allow the rail and spacer to be interlocked and some loads transferred over a shorter path near the bore. This leads to the conjecture of using the new high temperature superconductors for the conductive path. In this case the definition of an insulator may change.

Lastly, is that if the bore contact circumference necessary for conduction to the armature could be reduced, some compromise between the round and hexagonal bore configurations would be possible. This type of improvement would also lead to an improved magnetic field in the bore. This is because the current round bore configuration tends to interfere with the development of the magnetic field between the rails.

CONCLUSION

If the definition of structural integrity is extended to include the concept of 'failure to function' as well as catastrophic failure, then these early rail guns may have a problem because the bore expansion could compromise the projectile guiding function or make the armature contact problem more difficult. However, reasonable solutions are possible using currently available materials. The nature of future guns will depend on developments in armature design, high strength insulators, high strength conductors, and structural composite materials. In currently available fiber composite materials, the low transverse and shear stiffnesses do present problems in this three-dimensional loading.

The state-of-the-art in the calculation of the correct loads for use in the structural analysis is a weak point in the analysis. This is a time dependent two- or three-dimensional problem with the interaction of current flow and the magnetic field. The problem will have to be resolved somewhat before more detailed structural analysis is performed.

REFERENCES

1. G. P. O'Hara and C. G. Homan, "Design Considerations on Composite Railguns," American Defense Preparedness Association Symposium on Composite Materials in Armament Applications, Dover, NJ, August 20-22, 1985.
2. "ABAQUS User's Manual," Version 4.5 (a), Supplied by Hibbitt, Karlsson, and Sorensen Inc., Providence, RI.
3. R. F. Davidson, W. A. Cook, D. A. Rabern, and N. M. Schnurr, "Predicting Bore Deformations and Launcher Stresses in Railguns," IEEE, Vol. MAG-22, 1986, p. 1435.
4. E. H. Mansfield, "Load Transfer from a Pin to a Wound Fiber Composite Strip," Journal of Composite Materials, Vol. 17, September 1983.
5. G. P. O'Hara, "Some Results on Orthotropic High Pressure Cylinders," ARDEC Technical Report ARCCB-TF-87015, Benet Weapons Laboratory, Watervliet, NY, June 1987.

TITLE: Transverse Vibrations of Electromagnetic Railguns
SZU HSIUNG CHU
US Army Armament Research, Development and
Engineering Center
Picatinny Arsenal, Dover, New Jersey, 07801

ABSTRACT:

This report documents the formulation of the transverse vibrations of the rails of an EM railgun using the theory of vibrations of beams on an elastic foundation. The modeling is based on a railgun with a square bore. The modulus of the elastic foundation is discussed. Forces on the projectile and the rails are included. The governing equations of motion of the projectile and the rail are formulated. Modal analysis and numerical methods are used to solve the derived equations. An example is presented with figures showing the normal modes and the resulting configurations of rail vibrations. Effects of numbers of normal modes on the solution is discussed.

BIOGRAPHY:

PRESENT ASSIGNMENT: Mechanical Engineer, Electromagnetic Armament Technology Branch, Artillery Armaments Division, Fire Support Armament Center, U. S. Army Armament Research, Development and Engineering Center.

PAST EXPERIENCE: Research studies in applied mechanics related to the analysis of complex gun and ammunition dynamics since joining ARDEC in 1967.

DEGREES HELD: B. S. in Aeronautical Engineering, National Chiao-Tung University, Republic of China; M.S. in Applied Mechanics, Kansas State University; Ph.D. in Applied Mechanics, Polytechnic Institute of Brooklyn, New York.

TRANSVERSE VIBRATIONS OF ELECTROMAGNETIC RAILGUNS

Szu Hsiung Chu
U.S. Army Armament Research,
Development and Engineering Center
Picatinny Arsenal, Dover NJ, 07801

INTRODUCTION

The force distribution inside a railgun is very different from that of a conventional gun. The firing pressure is axi-symmetrical in a conventional gun because of the circular construction of the gun tube. While in an EM railgun, the launching forces are symmetrical to the center plane located between the two rails due to the plane symmetrical construction of the barrel. Consequently, a different approach of analysis is needed to model the vibration problem of EM railguns. In most of the present designs, the EM gun tube and the projectile are rather light. Therefore, to simplify the formulation, it is advisable to ignore the effect of their weights and study only the transverse rail vibration by considering the rail as an elastic beam on an elastic foundation consisting of the insulation, barrel and support.

This report documents the formulation of the transverse vibrations of the rails of an EM railgun using the theory of vibrations of beams on an elastic foundation. The model considered is an EM rail gun with a square barrel. The armature force, rail force and the projectile force are included. The governing equations of motion of the projectile and the rails are formulated. Modal analysis and numerical methods are used to solve the derived equations. An example is presented with figures showing the normal modes and the resulting configurations of rail vibration.

GENERAL CONSIDERATIONS

The EM gun vibration problem is complicated by the unique construction of the gun and the distribution of forces applied on the rails, the armature and the projectile. To facilitate the formulation some simplifications are necessary.

The rail heating and wear are the critical problems of the EM railguns. However, their effects on the transverse vibrations of the rails may not be as severe as the bursting forces on the rails and therefore are not included in this formulation.

In the present investigation only the case having the breech end fixed during firing is considered. The gravitational forces of the gun tube and the projectile are rather small in comparison to the electromagnetic forces which are symmetrical to the center plane between the two rails. The principal forces acting on the rails are in the normal direction. Therefore, it is advisable to ignore the vibrations of the gun tube, and the transverse vibrations of the rails are only considered.

The plane symmetry of the construction of the rails and the distribution of the bursting forces lead to the consideration of the center plane between the rails as stationary. With the center plane stationary the possible motion of the rail is the vibration about this plane. The insulation and the gun tube function as an elastic foundation of the rail. The projectile is moving between the two rails, causing the bursting forces to change accordingly. Therefore the vibration of the rail may be considered as that of a transversely vibrating beam supported on an elastic foundation and the vibration is excited by the varying loads moving with the projectile. To analyze the problem it is necessary to determine the foundation modulus, the forces acting on the rail, the armature, and the projectile, and then to formulate the governing equations of motion of the projectile and the rails. These are discussed in the following sections.

A right-handed Cartesian coordinate system is used in the analysis. The rails are so arranged that they are in the top and bottom portion of the barrel. The origin of the coordinate system is located at the center of the barrel at the breech end. The x-axis is located along the centerline of the barrel and pointing to the muzzle. The y-axis is perpendicular to the rails and pointing upward. The z-axis is determined by the right-handed convention of the coordinate system.

FOUNDATION MODULUS

The modulus of the elastic foundation plays an important role in this formulation. It is not easy to obtain the exact expression. Three methods have been considered to acquire this modulus. The first method is an experimental determination of the deflection caused by forces applied to the rails for computing the constant. The second method is to compute the deformation of the rail from a finite element computer solution. The third method is to calculate the modulus using strength of material equations. The first and the second methods will not be discussed further and the third method is presented as follows.

Fig. 1 shows the cross-section of a square barrel element [1] of unit length. The deflection of the upper rail is considered to be the sum of the compression of the insulation between the rail and the upper barrel wall, the bending of the top barrel wall, and the vertical expansion of barrel side wall

in the direction of the rail deflection. These deflections are normal and referred to the center plane between the rails. Therefore, it may be expressed by the equation

$$\delta_r = \delta_t + \delta_s + \delta_i \quad (1)$$

where δ_r , δ_t , δ_s and δ_i are the vertical deflections of the rail, barrel top plate, side wall, and insulation element respectively.

The various deflections may be computed with appropriate strength of materials equations as

$$\delta_r = \frac{F_r}{k} \quad (2)a$$

$$\delta_s = \frac{F_r L_s}{2 A_s E_s} \quad (2)b$$

$$\delta_i = \frac{F_r T_i}{A_i E_i} \quad (2)c$$

$$\delta_t = \frac{F_r L_t^3}{48 E_t I_t} \quad (2)d$$

where

F_r = electromagnetic bursting force applied on the rail element

k = foundation modulus

L_s, L_t = effective width of barrel side wall, top plate element

T_i = thickness of insulation layer

E_s, E_i, E_t = Young's modulus of barrel side wall, insulation, barrel top plate

A_s, A_i = effective cross-sectional area of barrel side wall element, insulation element

I_t = section area moment inertia of barrel top plate element

Substituting Eqs. (2)a-(2)d into Eq. (1) and simplifying, the foundation modulus is

$$k = \frac{1}{\frac{L_s}{2A_s E_s} + \frac{T_i}{A_i E_i} + \frac{L_t^3}{48 E_t I_t}} \quad (3)$$

APPLIED FORCES ON THE RAIL

The forces acting inside the barrel depend on the rail, armature and projectile configuration (Fig. 2). The forces acting on the rail are the gravitational forces due to the weights of its various components, the bursting force from the current in the rail, the contact forces and the friction forces due to the contact of rail with the armature, the projectile, and the air inside the barrel. The forces acting on the armature and the projectile are their weights, the propulsive force from the armature, the air resistance, and the contact and friction forces which are the same as that acting on the rail but with opposite direction. To simplify the formulation of the rail vibration, the gravity force, the air resistance and the friction forces are ignored. The armature propulsive force on the projectile is expressed by the generally used equation,

$$F_a = \frac{L' I^2}{2} \quad (4)$$

where

F_a = armature propulsive force

L' = rail inductance gradient

I = rail current

This force is acting on the armature at the rear side of the projectile. By assuming a uniform current distribution in the rail and the armature circuit, the bursting force on the rail per unit length, F_r , is computed by dividing the armature force by the rail separation or the width of the bore. That is

$$F_r = \frac{L' I^2}{2h} \quad (5)$$

where

h = spacing between the two rails

This force is acting on all rail elements located between the breech and the projectile, and its action range is therefore changing with the projectile travel.

The rail-armature contact force is determined by the contact condition which depends upon the type and the design characteristics of the armature. To simplify the formulation, it is advisable to assume the force distribution to be uniform, a triangular shape, or a combination of these two types. For the case of a uniform force distribution (Fig. 3), the expression for the magnitude of the force element is

$$f_U(x) = f_U \quad x_p - L_a \leq x \leq x_p \quad (6)$$

where

$f_U(x)$ = magnitude of uniform rail-armature contact force element at location x

f_U = magnitude of uniform rail-armature contact force

x = location of uniform force element on the rail

x_p = travel of the projectile

L_a = length of the armature.

If the contact force is not uniformly distributed, it may be assumed that the force distribution is of triangular shape as shown in Fig. 4. The magnitude of the force element at the x position is

$$f_t(x) = \frac{f_h}{L_a} (x - x_p + L_a) \quad x_p - L_a \leq x \leq x_p \quad (7)$$

where

$f_t(x)$ = magnitude of force element at location x of triangular force distribution

f_h = height of force triangular distribution

The normal contact force between the projectile and the rail has also a triangular distribution if the air resistance is not presented. It is a combination of a triangular and a rectangular distribution if the air resistance is included. The rectangular portion is a uniform force and it is similar to that of Eq. (6). The triangular force distribution may have the minimum force at the front side and the maximum force at the rear side of the projectile as shown in Fig. 5. The magnitude of the force element $f_p(x)$ is

$$f_p(x) = \frac{f_{hp}}{L_p} (x_p + L_p - x) \quad x_p \leq x \leq x_p + L_p \quad (8)$$

where

$f_p(x)$ = magnitude of force element at location x of force triangular distribution for rail-projectile contact force

f_{hp} = height of triangular rail-projectile contact force distribution

Note that values of f_u , f_h and f_{hp} may be functions of time, depending on the design of the armature. This time effect should be included when more accurate computations are required.

When the projectile is leaving the muzzle the tip portion of the force triangle is truncated (Fig. 6) as the rail-projectile contact region decreases. The Eq. (8) still applies, but the range of x is changed to $x_p \leq x \leq L$. That is,

$$f_p(x) = \frac{f_{hp}}{L_p} (x_p + L_p - x) \quad x_p \leq x \leq L \quad (9)$$

where L is the effective length of the rail.

The component due to air resistance in front of the projectile should be included if air is presented and a more accurate result is required.

APPLIED FORCES ON THE ARMATURE AND PROJECTILE

The travel of the projectile is determined by its axial motion along the bore of the barrel. This is computed from Newton's second law of motion. The significant forces considered are the axial armature propulsive force, the friction forces between the projectile or the armature and the barrel insulation wall or the rail. The frictional forces are the product of the above-mentioned contact forces and the corresponding friction coefficients. The armature propulsive force has been expressed in Eq. (4). The difference of the friction and the propulsive force is the effective force of the projectile motion. A generally used expression of this force is taken as the product of the armature propulsive force and a friction correction factor [2]. This expression is

$$F_p = F_a (1 - C) \quad (10)$$

where

F_p = effective propulsive force on the projectile

C = friction correction factor

The constant C is determined by user's experience. A simple approximate mathematical equation to compute this constant for a projectile of rectangular cross-section has been derived as [2]

$$C = \frac{v L_p R_m \left[\frac{\mu_y}{h} \left(1 + v + \frac{2E_p}{k_z w} \right) + \frac{\mu_z}{w} \left(1 + v + \frac{2E_p}{k_y h} \right) \right]}{\left(1 + \frac{2E_p}{k_y h} \right) \left(1 + \frac{2E_p}{k_z w} \right) - v^2 - v L_p (2 - R_m) \left[\frac{\mu_y}{h} \left(1 + v + \frac{2E_p}{k_z w} \right) + \frac{\mu_z}{w} \left(1 + v + \frac{2E_p}{k_y h} \right) \right]} \quad (11)$$

where

v = Poisson's ratio of the projectile

R_m = ratio of the projectile mass to the total mass of armature and projectile

μ_y, μ_z = friction coefficient for projectile-rail contact in the y- (vertical and normal to rail), z-axis direction (horizontal and parallel to the rail)

w = width of barrel bore in the z-axis direction. For a square barrel, w is equal to h .

E_p = Young's modulus of the projectile

k_y, k_z = spring constant of the rail or insulation for per unit area of barrel-projectile contact, in the direction of y-axis, z-axis

GOVERNING EQUATIONS

The equation of transverse vibration of a beam on an elastic foundation is derived from the dynamic equilibrium condition of an Euler beam element [3,4]. The detailed derivations are not mentioned here. Considering the rail of an EM gun as a beam on an elastic foundation, under the influence of the above-mentioned forces, the equation of vibration of the rail is of the form

$$EI \frac{d^4 y}{dx^4} + m \frac{d^2 y}{dt^2} + k_y = F(x, t) \quad (12)$$

where

E = Young's modulus of rail material

I = section area moment of inertia of the rail

y = deflection of the rail

x = location of the rail element

m = mass of rail per unit length

t = time

$F(x, t)$ = total force applied on the rail element at location x . It is the sum of forces applied on the rail per unit length as mentioned before.

The solution of this equation is the sum of the homogeneous and the particular solution. Considering the rail fixed at the breech and freed at the muzzle and using the modal analysis it is obtained as

$$y = \sum_{n=1}^N \phi_n(x) \eta_n(t) \quad (13)$$

where $\phi_n(x)$ is the n th normal mode shape and $\eta_n(t)$ is the n th normal coordinate. They are expressed by the following equations

$$\phi_n(x) = \alpha_n (\sinh a_n x - \sin a_n x) + \cosh a_n x - \cos a_n x \quad (14)a$$

$$\alpha_n = - \frac{\cos a_n L + \cosh a_n L}{\sinh a_n L + \sin a_n L} \quad (14)b$$

$$a_1 = \frac{.597\pi}{L} \quad (14)c$$

$$a_n = \frac{(n-.5)\pi}{L} \quad n = 2, 3, 4, \dots \quad (14)d$$

where

α_n = constant in the n th normal mode equation

a_1, a_n = first, nth wave number

The $\eta_n(t)$ is solved from the equation

$$\frac{d^2 \eta_n(t)}{dt^2} + \omega_n^2 \eta_n(t) = F_n M_n \quad (15)a$$

$$\omega_n = \sqrt{\frac{EI a_n^4 + k}{m}} \quad (15)b$$

$$F_n = \int_0^L F(x,t) \phi_n(x) dx \quad (15)c$$

$$M_n = \int_0^L m \phi_n^2(x) dx \quad (15)d$$

where

ω_n = nth natural frequency of the beam vibration

F_n = nth generalized force and it is detailed in the next section

M_n = nth generalized mass

The projectile travels down the barrel during launch. This in-bore motion changes the location x_p and the applied forces in the above-mentioned equations. The simplified equation of motion of the projectile is [2]

$$m_p a = F_a (1 - C) \quad (16)$$

where a is the acceleration of the projectile and m_p is the total mass of projectile and armature. This equation is solved for the acceleration of the projectile. The velocity and the travel are obtained by subsequent integration.

GENERALIZED MASS AND FORCE

The solution of Eq.(15)a depends on computation of the generalized mass and force. The nth generalized mass is the integral of the product and the square of the nth normal mode shape, Eq. (15)d. The resulting integration is [3,4]

$$M_n = mL \quad (17)$$

The generalized force is the integral of the product of the applied force and the normal mode shape, Eq. (15)c. The resulting integrations for the various applied forces mentioned before have been computed as follows. The results depend on the position of the projectile, x_p . For time varying forces the time function may be included explicitly.

The nth mode generalized rail bursting force is computed by integrating from the breech end to the muzzle, and the forces are determined by the position of the projectile at time of computing. Substituting the normal mode $\phi_n(x)$ into Eq. (15)c and integrating, the resulting generalized bursting force, F_{rn} , is

$$F_{rn} = \frac{F_r}{a_n} [\alpha_n (\cosh a_n x_p + \cos a_n x_p - 2) + \sinh a_n x_p - \sin a_n x_p] \quad (18)$$

where F_{rn} = nth generalized rail bursting force

For the uniform rail-armature contact force, Eq. (6), the force acts from the start to the end of contact or the position of the projectile. The resulting expression for the nth generalized force is

$$F_{aun} = \frac{f_u}{a_n} \{ \alpha_n [\cosh a_n x_p - \cosh a_n (x_p - L_a) + \cos a_n x_p - \cos a_n (x_p - L_a)] \\ + \sinh a_n x_p - \sinh a_n (x_p - L_a) - \sin a_n x_p + \sin a_n (x_p - L_a) \} \quad (19)$$

where F_{aun} = nth generalized rail-armature uniform contact force

The generalized force for the nth mode of rail-armature contact force of triangular distribution, F_{atn} , is computed from the integration of the

product of Eq. (7) and the nth normal mode shape. The resulting equation is

$$\begin{aligned}
 F_{atn} = & \frac{f_h}{2a_n L_a} \{ \alpha_n [a_n x_p \cosh a_n x_p - \sinh a_n x_p - \sin a_n x_p + a_n x_p \cos a_n x_p \\
 & - a_n (x_p - L_a) \cosh a_n (x_p - L_a) + \sinh a_n (x_p - L_a) + \sin a_n (x_p - L_a) \\
 & - a_n (x_p - L_a) \cos a_n (x_p - L_a)] + a_n x_p \sinh a_n x_p - \cosh a_n x_p - \cos a_n x_p \\
 & - a_n x_p \sin a_n x_p - a_n (x_p - L_a) \sinh a_n (x_p - L_a) + \cosh a_n (x_p - L_a) \\
 & + \cos a_n (x_p - L_a) + a_n (x_p - L_a) \sin a_n (x_p - L_a) \} \\
 & - \frac{f_h}{2a_n L_a} (x_p - L_a) \{ \alpha_n [\cosh a_n x_p + \cos a_n x_p - \cosh a_n (x_p - L_a) - \cos a_n (x_p - L_a)] \\
 & + \sinh a_n x_p - \sin a_n x_p - \sinh a_n (x_p - L_a) + \sin a_n (x_p - L_a) \} \quad (20)
 \end{aligned}$$

The nth generalized force of the normal contact force between the projectile and the rail, F_{pn} , is computed by integrating the product of the nth normal mode shape and Eq. (8). The result is

$$\begin{aligned}
 F_{pn} = & \frac{f_{hp}}{2a_n L_p} \{ \alpha_n a_n (x_p + L_p) [\cosh a_n (x_p + L_p) + \cos a_n (x_p + L_p) - \cosh a_n x_p \\
 & - \cos a_n x_p] + a_n (x_p + L_p) [\sinh a_n (x_p + L_p) - \sin a_n (x_p + L_p) \\
 & - \sinh a_n x_p + \sin a_n x_p] - \alpha_n [a_n (x_p + L_p) \cosh a_n (x_p + L_p) \\
 & - \sinh a_n (x_p + L_p) - \sin a_n (x_p + L_p) + a_n (x_p + L_p) \cos a_n (x_p + L_p) \\
 & - a_n x_p \cosh a_n x_p + \sinh a_n x_p + \sin a_n x_p - a_n x_p \cos a_n x_p] \\
 & + a_n (x_p + L_p) \sinh a_n (x_p + L_p) - \cosh a_n (x_p + L_p) \\
 & - \cos a_n (x_p + L_p) - a_n (x_p + L_p) \sin a_n (x_p + L_p) \\
 & - a_n x_p \sinh a_n x_p + \cosh a_n x_p + \cos a_n x_p + a_n x_p \sin a_n x_p \} \quad (21)
 \end{aligned}$$

When the projectile reaches the muzzle the force triangle is truncated as

shown in Fig. 6. The n th generalized force, F_{pn} , is then computed to be

$$F_{pn} = \frac{f_{hp}}{2a_n L_p} \{ a_n(x_p + L_p) [\alpha_n (\cosh a_n L + \cos a_n L - \cosh a_n x_p - \cos a_n x_p) + \sinh a_n L - \sin a_n L - \sinh a_n x_p + \sin a_n x_p] - \alpha_n (a_n L \cosh a_n L - \sinh a_n L - \sin a_n L + a_n L \cos a_n L - a_n x_p \cosh a_n x_p + \sinh a_n x_p + \sin a_n x_p - a_n x_p \cos a_n x_p) + a_n L \sinh a_n L - \cosh a_n L - \cos a_n L - a_n L \sin a_n L - a_n x_p \sinh a_n x_p + \cosh a_n x_p + \cos a_n x_p + a_n x_p \sin a_n x_p \} \quad (22)$$

The total generalized force is the appropriate sum of Eq. (18)-(22), namely

$$F_n = F_{rn} + F_{aun} + F_{atn} + F_{pn} \quad (23)$$

EXAMPLE OF SOLUTION

An example of the solution has been obtained for an EM railgun of 2.5 meter length and a square bore as shown in Fig. 1. The values of the material properties used in the computations are tabulated in the following Table 1 and the rail current is shown in Fig. 7.

The normal frequencies and mode shapes are computed from Eqs. (14). The first twelve modes are shown in Fig. 8. The resulting vibrations of the railgun are shown in Fig. 9. The deflections are shown in exaggerated scale to indicate the vibration effect. The square dot denotes the projectile.

Computations are also done with 9, 6 and 3 normal modes respectively to show the effects of number of modes used in the solution. The results of the maximum deflections are presented in Table 2 and the resulting vibration shapes are shown in Figs. 10 to 12.

Table 1. Values Used for Computations

Item	Material	Density g/cm ³	Total Mass kg	Young's modulus 10 ³ MPa	Inductance Gradient 10 ⁻⁶ H/m
Rail	Copper	8.94		103.42	.45
Projectile	Kevlar, Steel		.457		
Armature	Copper		.176		
Barrel Plate	Steel	7.83		206.84	
Barrel Bolt	Steel	7.83		206.84	
Insulation	NEMA G11	1.80		5.65	

Table 2. Effect of Number of Modes on Rail Deflection Computations

Time,ms	1.5	2.0	2.5	3.0	3.5	4.0	4.53
Travel,m	.025	.114	.340	.713	1.218	1.805	2.473
Maximum Deflection, mm							
3 Modes	.005	.049	.111	.167	.140	.086	.170
6	.009	.083	.157	.195	.140	.086	.197
9	.013	.110	.183	.209	.140	.086	.197
12	.017	.131	.198	.216	.140	.086	.197

DISCUSSIONS

As shown in Fig. 8, the changes for successive frequencies and normal modes are rather small or slow in increasing. Consequently a large number of modes are necessary to obtain more accurate computations. This is evident from Table 2 and Figs. 9 to 12. It is seen that six modes are appropriate to compute the maximum deflection of the rail. With more modes included, the accuracy of the maximum computation is increased accordingly but rather small. However, the shape of the vibration curve did improved greatly.

The vibration shape of the rail shows clearly the effect of the change of the projectile travel on the vibration of the rail. The deflection is principally outward from the bore and it is large at the projectile location.

Therefore, it is seen that unless the projectile is extremely long, there will be no pinch effect of the rail on the front of the projectile.

At present, only simple computations have been done since many data are not available for analysis. Experimental measurements are to be devised to get data for more accurate force expressions and calculations to verify and improve the mathematical modeling.

CONCLUSION

A formulation of the transverse rail vibration based on the beam on elastic foundation theory has been achieved. The analysis gives a clear dynamic presentation of the rail vibration. The computations show a large number of normal modes are needed to obtain the accurate vibration configurations, but a few number of modes to compute the maximum value of the rail deflection. An interesting observation is that the pinch effect of the rail on the projectile may be not as severe as ordinarily conceived since the vibration figures show that the rail deflection is always positive at the location of the projectile. Experimental measurements are needed to further verify and improve the analysis model.

ACKNOWLEDGEMENT

The author wishes to thank Mr. Bruce Knutelsky for his help in preparing this paper.

REFERENCES

1. McNab, I. R., Barber, J. P., Bless, S. J., et al., DC Electromagnetic Launcher Development: Phase I, Contractor Report ARLCD-CR-80009, US Army ARRADCOM, Dover, New Jersey, May 1980
2. Chu, Szu Hsiung, A Simple Theoretical Model for Projectile In-Bore Motion of Electromagnetic Railguns, Proceedings of Fifth U.S. Army Symposium on Gun Dynamics, Institute on Man and Science, Rensselaerville, New York, September 23-25, 1987
3. Biggs, John M., Introduction to Structural Dynamics, McGraw-Hill, Inc. 1964
4. Timoshenko, S., Young, D. H., and Weaver, W. Jr., Vibration Problems in Engineering, Fourth Edition, John Wiley & Sons, New York, 1974

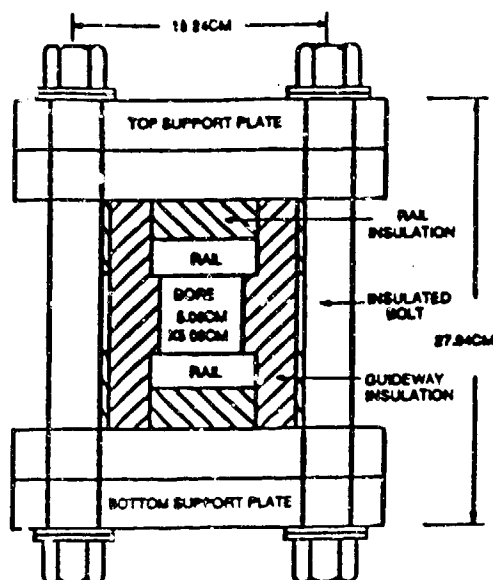


FIGURE 1 BARREL CROSS-SECTION

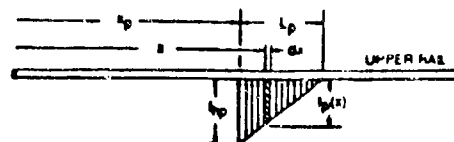


FIGURE 5 TRIANGULAR DISTRIBUTION OF RAIL-PROJECTILE CONTACT FORCE

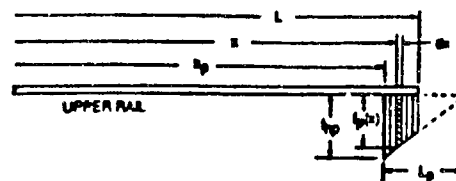


FIGURE 6 TRUNCATED TRIANGULAR DISTRIBUTION OF RAIL-PROJECTILE CONTACT FORCE

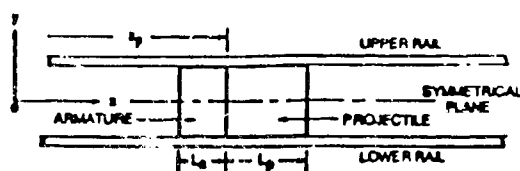


FIGURE 2 RAIL, ARMATURE AND PROJECTILE CONFIGURATION



FIGURE 3 UNIFORM RAIL-ARMATURE CONTACT FORCE

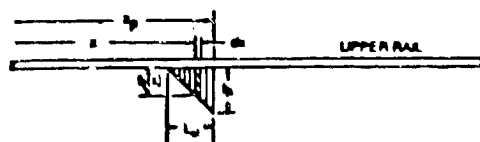


FIGURE 4 TRIANGULAR DISTRIBUTION OF RAIL-ARMATURE CONTACT FORCE

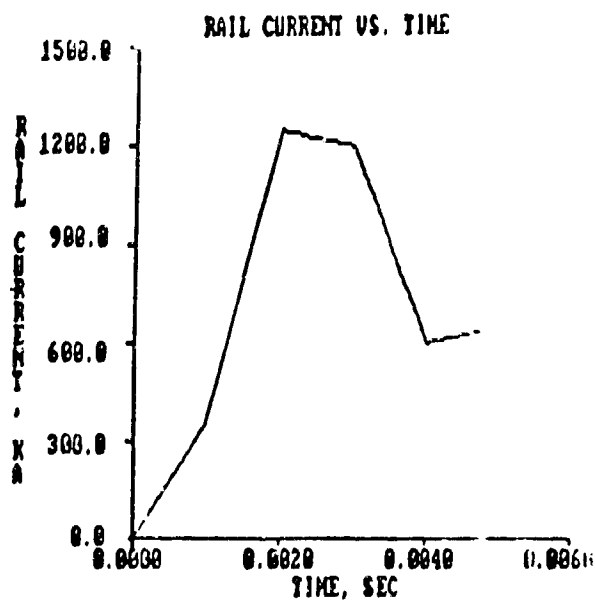


FIGURE 7 RAIL CURRENT

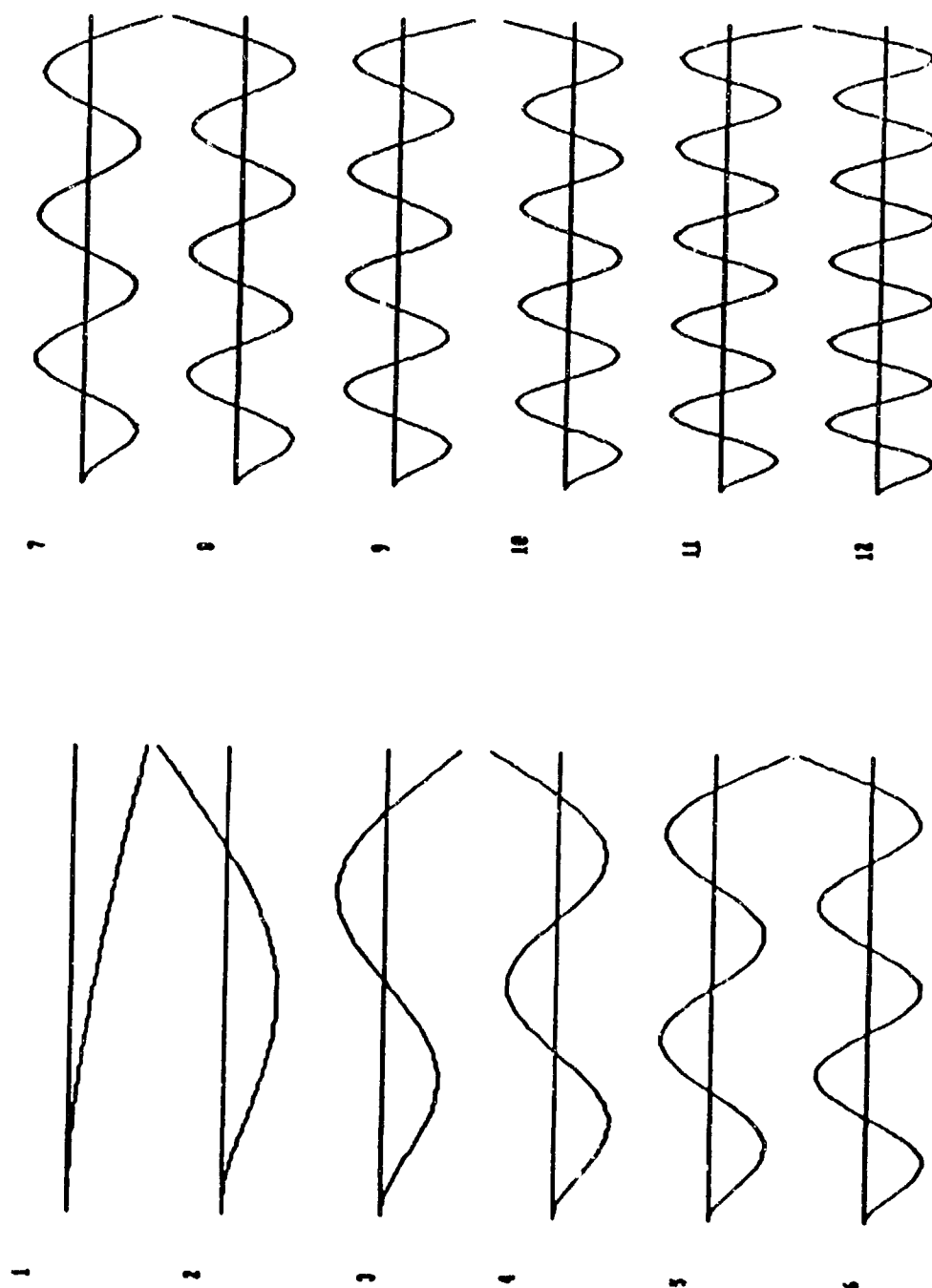


FIGURE 8 NORMAL MODES OF TRANSVERSE RAIL VIBRATION

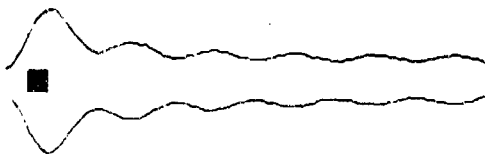
A. TIME = 0 SEC
RAIL CURRENT = 0 MA
CRANK MAX DEF = 0.491705E-03 IN
MUZZLE VEL = .807786 MPS
MAX DEFLECTION = 0 IN
TRAVEL = 0 IN
MAX RAIL = 1249.997 MA
MAX ACC = 15816.36 GEESS
(EXAGGERATED DEFORMATION FIGURE)



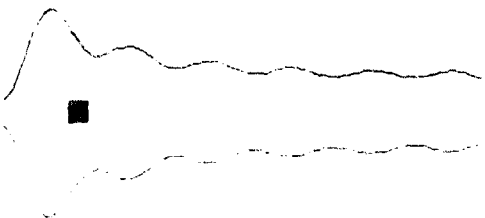
B. TIME = 1.499999E-03 SEC
RAIL CURRENT = 759.997 MA
CRANK MAX DEF = 0.491705E-03 IN
MUZZLE VEL = .807786 MPS
MAX DEFLECTION = 6.606268E-04 IN
TRAVEL = 1.001727 IN
MAX RAIL = 1249.997 MA
MAX ACC = 15816.36 GEESS
(EXAGGERATED DEFORMATION FIGURE)



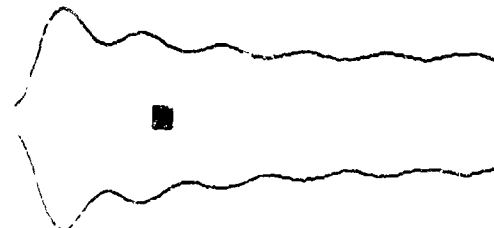
C. TIME = 1.999997E-03 SEC
RAIL CURRENT = 1249.997 MA
CRANK MAX DEF = 0.491705E-03 IN
MUZZLE VEL = .807786 MPS
MAX DEFLECTION = .0051469 IN
TRAVEL = 0.488291 IN
MAX RAIL = 1249.997 MA
MAX ACC = 15816.36 GEESS
(EXAGGERATED DEFORMATION FIGURE)



D. TIME = 2.500001E-03 SEC
RAIL CURRENT = 1225 MA
CRANK MAX DEF = 0.491705E-03 IN
MUZZLE VEL = .807786 MPS
MAX DEFLECTION = 7.804411E-03 IN
TRAVEL = 17.36548 IN
MAX RAIL = 1249.997 MA
MAX ACC = 15816.36 GEESS
(EXAGGERATED DEFORMATION FIGURE)



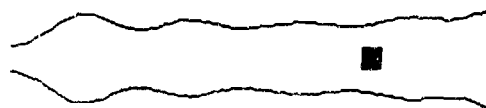
E. TIME = 3.000005E-03 SEC
RAIL CURRENT = 1199.997 MA
CRANK MAX DEF = 0.491705E-03 IN
MUZZLE VEL = .807786 MPS
MAX DEFLECTION = 0.491705E-03 IN
TRAVEL = 34.876 IN
MAX RAIL = 1249.997 MA
MAX ACC = 15816.36 GEESS
(EXAGGERATED DEFORMATION FIGURE)



F. TIME = 3.500009E-03 SEC
RAIL CURRENT = 879.997 MA
CRANK MAX DEF = 0.491705E-03 IN
MUZZLE VEL = .807786 MPS
MAX DEFLECTION = 9.931002E-03 IN
TRAVEL = 47.9716 IN
MAX RAIL = 1249.997 MA
MAX ACC = 15816.36 GEESS
(EXAGGERATED DEFORMATION FIGURE)



G. TIME = 4.000012E-03 SEC
RAIL CURRENT = 400.000 MA
CRANK MAX DEF = 0.491705E-03 IN
MUZZLE VEL = .807786 MPS
MAX DEFLECTION = 0.994198E-03 IN
TRAVEL = 77.05129 IN
MAX RAIL = 1249.997 MA
MAX ACC = 15816.36 GEESS
(EXAGGERATED DEFORMATION FIGURE)



H. TIME = 4.530017E-03 SEC
RAIL CURRENT = 626.9008 MA
CRANK MAX DEF = 0.491705E-03 IN
MUZZLE VEL = .807786 MPS
MAX DEFLECTION = 7.772196E-03 IN
TRAVEL = 97.35017 IN
MAX RAIL = 1249.997 MA
MAX ACC = 15816.36 GEESS
(EXAGGERATED DEFORMATION FIGURE)

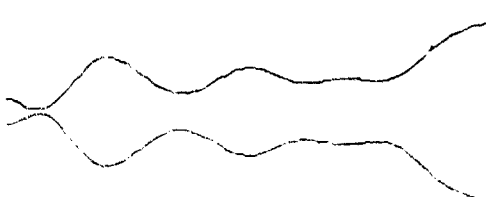
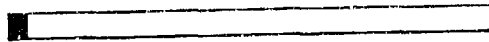
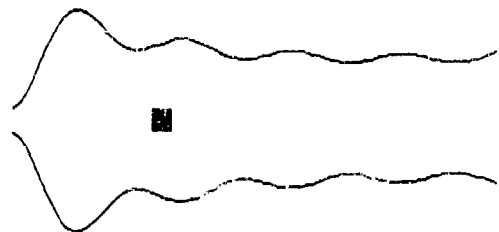


FIGURE 9 TRANSVERSE RAILGUN VIBRATION ANALYSIS, 12 MODES

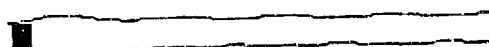
A. TIME = 0.000000E-03 SEC
 RAIL CURRENT = 0.000000E+00 KA
 GRANT MAX. DEFL. = 0.220112E-03 IN
 MUZZLE VEL = .007786 MPS
 MAX DEFLECTION = 0 IN
 TRAVEL = 0 IN
 MAX. RAIL I = 1249.997 KA
 MAX ACC = 15816.36 GEES
 (EXAGGERATED DEFORMATION FIGURE)



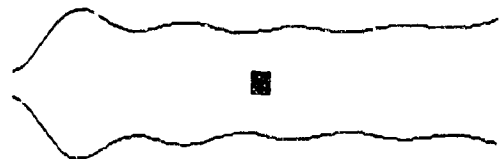
E. TIME = 3.000000E-03 SEC
 RAIL CURRENT = 1199.997 KA
 GRANT MAX. DEFL. = 0.220112E-03 IN
 MUZZLE VEL = .007786 MPS
 MAX DEFLECTION = 0.220112E-03 IN
 TRAVEL = 20.076 IN
 MAX. RAIL I = 1249.997 KA
 MAX ACC = 15816.36 GEES
 (EXAGGERATED DEFORMATION FIGURE)



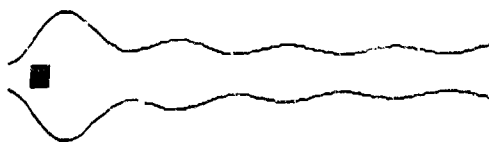
B. TIME = 1.499999E-03 SEC
 RAIL CURRENT = 799.997 KA
 GRANT MAX. DEFL. = 0.220112E-03 IN
 MUZZLE VEL = .007786 MPS
 MAX DEFLECTION = 5.184271E-04 IN
 TRAVEL = 1.001125 IN
 MAX. RAIL I = 1249.997 KA
 MAX ACC = 15816.36 GEES
 (EXAGGERATED DEFORMATION FIGURE)



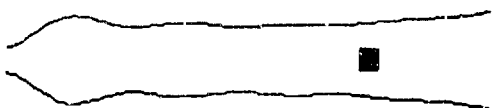
F. TIME = 5.500000E-03 SEC
 RAIL CURRENT = 899.997 KA
 GRANT MAX. DEFL. = 0.220112E-03 IN
 MUZZLE VEL = .007786 MPS
 MAX DEFLECTION = 5.531002E-03 IN
 TRAVEL = 47.9736 IN
 MAX. RAIL I = 1249.997 KA
 MAX ACC = 15816.36 GEES
 (EXAGGERATED DEFORMATION FIGURE)



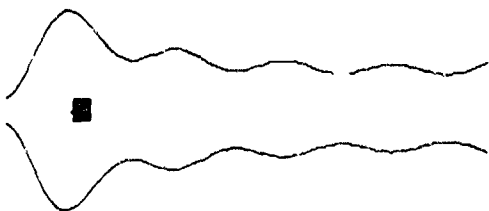
C. TIME = 1.999997E-03 SEC
 RAIL CURRENT = 1249.997 KA
 GRANT MAX. DEFL. = 0.220112E-03 IN
 MUZZLE VEL = .007786 MPS
 MAX DEFLECTION = 4.319272E-03 IN
 TRAVEL = 4.408281 IN
 MAX. RAIL I = 1249.997 KA
 MAX ACC = 15816.36 GEES
 (EXAGGERATED DEFORMATION FIGURE)



G. TIME = 4.000000E-03 SEC
 RAIL CURRENT = 600.0000 KA
 GRANT MAX. DEFL. = 0.220112E-03 IN
 MUZZLE VEL = .007786 MPS
 MAX DEFLECTION = 0.394190E-03 IN
 TRAVEL = 71.85825 IN
 MAX. RAIL I = 1249.997 KA
 MAX ACC = 15816.36 GEES
 (EXAGGERATED DEFORMATION FIGURE)



D. TIME = 2.500001E-03 SEC
 RAIL CURRENT = 1225 KA
 GRANT MAX. DEFL. = 0.220112E-03 IN
 MUZZLE VEL = .007786 MPS
 MAX DEFLECTION = 7.211991E-03 IN
 TRAVEL = 19.36548 IN
 MAX. RAIL I = 1249.997 KA
 MAX ACC = 15816.36 GEES
 (EXAGGERATED DEFORMATION FIGURE)



H. TIME = 4.530017E-03 SEC
 RAIL CURRENT = 826.5086 KA
 GRANT MAX. DEFL. = 0.220112E-03 IN
 MUZZLE VEL = .007786 MPS
 MAX DEFLECTION = 7.772196E-03 IN
 TRAVEL = 97.35017 IN
 MAX. RAIL I = 1249.997 KA
 MAX ACC = 15816.36 GEES
 (EXAGGERATED DEFORMATION FIGURE)

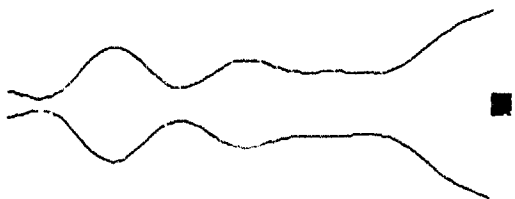
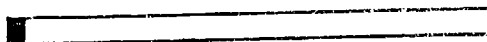
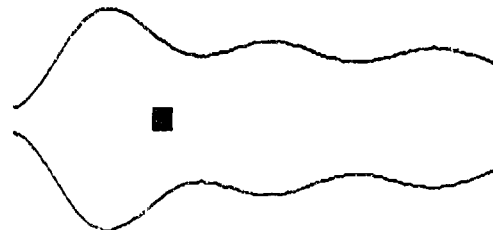


FIGURE 10 TRANSVERSE RAILGUN VIBRATION ANALYSIS, 9 MODES

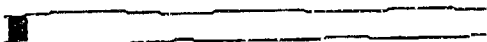
A. TIME = 0.000000E+00 SEC
RAIL CURRENT = 0.000000E+00 KA
GRAND MAX. DEF. = 7.772196E-03 IN
MUZZLE VEL = .007786 KPS
MAX. DEFLECTION = 0 IN
TRAVEL = 0 IN
MAX. RAIL = 1249.997 KA
MAX ACC = 15816.36 GEES
(EXAGGERATED DEFORMATION FIGURE)



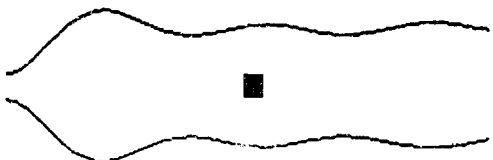
E. TIME = 3.060000E-03 SEC
RAIL CURRENT = 1199.997 KA
GRAND MAX. DEF. = 7.772196E-03 IN
MUZZLE VEL = .007786 KPS
MAX. DEFLECTION = 7.677438E-03 IN
TRAVEL = 28.074 IN
MAX. RAIL = 1249.997 KA
MAX ACC = 15816.36 GEES
(EXAGGERATED DEFORMATION FIGURE)



B. TIME = 1.000000E-03 SEC
RAIL CURRENT = 799.997 KA
GRAND MAX. DEF. = 7.772196E-03 IN
MUZZLE VEL = .007786 KPS
MAX. DEFLECTION = 0.580062E-04 IN
TRAVEL = 1.000123 IN
MAX. RAIL = 1249.997 KA
MAX ACC = 15816.36 GEES
(EXAGGERATED DEFORMATION FIGURE)



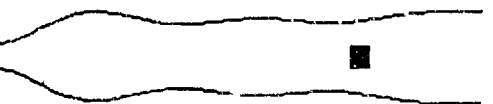
F. TIME = 3.580000E-03 SEC
RAIL CURRENT = 899.997 KA
GRAND MAX. DEF. = 7.772196E-03 IN
MUZZLE VEL = .007786 KPS
MAX. DEFLECTION = 5.591082E-03 IN
TRAVEL = 47.9736 IN
MAX. RAIL = 1249.997 KA
MAX ACC = 15816.36 GEES
(EXAGGERATED DEFORMATION FIGURE)



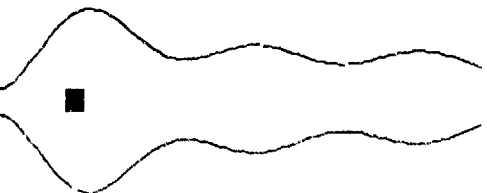
C. TIME = 1.999997E-03 SEC
RAIL CURRENT = 1249.997 KA
GRAND MAX. DEF. = 7.772196E-03 IN
MUZZLE VEL = .007786 KPS
MAX. DEFLECTION = 0.245514E-03 IN
TRAVEL = 4.486781 IN
MAX. RAIL = 1249.997 KA
MAX ACC = 15816.36 GEES
(EXAGGERATED DEFORMATION FIGURE)



G. TIME = 4.000012E-03 SEC
RAIL CURRENT = 600.000 KA
GRAND MAX. DEF. = 7.772196E-03 IN
MUZZLE VEL = .007786 KPS
MAX. DEFLECTION = 0.394198E-03 IN
TRAVEL = 71.05029 IN
MAX. RAIL = 1249.997 KA
MAX ACC = 15816.36 GEES
(EXAGGERATED DEFORMATION FIGURE)



D. TIME = 3.999917E-03 SEC
RAIL CURRENT = 1225 KA
GRAND MAX. DEF. = 7.772196E-03 IN
MUZZLE VEL = .007786 KPS
MAX. DEFLECTION = 6.165858E-03 IN
TRAVEL = 13.96548 IN
MAX. RAIL = 1249.997 KA
MAX ACC = 15816.36 GEES
(EXAGGERATED DEFORMATION FIGURE)



H. TIME = 4.999917E-03 SEC
RAIL CURRENT = 626.500 KA
GRAND MAX. DEF. = 7.772196E-03 IN
MUZZLE VEL = .007786 KPS
MAX. DEFLECTION = 7.772196E-03 IN
TRAVEL = 97.95017 IN
MAX. RAIL = 1249.997 KA
MAX ACC = 15816.36 GEES
(EXAGGERATED DEFORMATION FIGURE)

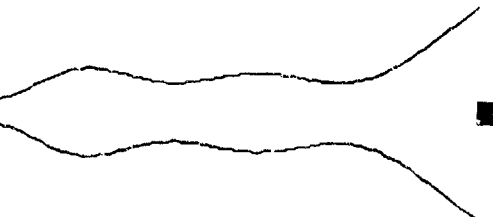
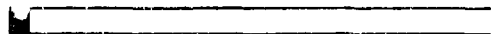
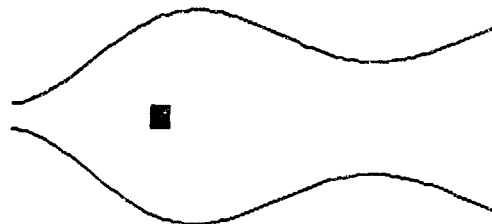


FIGURE 11 TRANSVERSE RAILGUN VIBRATION ANALYSIS, 6 MODES

A. TIME = 0.000000E-03 SEC MAX DEFLECTION = 0 IN
 RAIL CURRENT = 0 KA TRAVEL = 0 IN
 GRAND MAX DEFL = 6.67849E-03 IN MAX RAIL = 1249.997 KA
 MUZZLE VEL = .007786 MPS MAX ACC = 15816.36 GEES
 (EXAGGERATED DEFORMATION FIGURE)



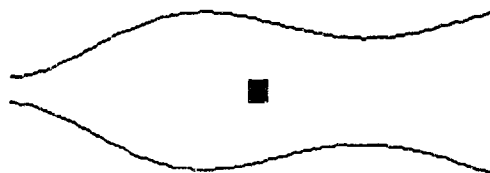
E. TIME = 2.000000E-03 SEC MAX DEFLECTION = 6.563060E-03 IN
 RAIL CURRENT = 1199.997 KA TRAVEL = 2.00E-07 IN
 GRAND MAX DEFL = 6.67849E-03 IN MAX RAIL = 1249.997 KA
 MUZZLE VEL = .007786 MPS MAX ACC = 15816.36 GEES
 (EXAGGERATED DEFORMATION FIGURE)



B. TIME = 1.000000E-03 SEC MAX DEFLECTION = 1.017961E-04 IN
 RAIL CURRENT = 999.997 KA TRAVEL = 1.00E-12 IN
 GRAND MAX DEFL = 6.67849E-03 IN MAX RAIL = 1249.997 KA
 MUZZLE VEL = .007786 MPS MAX ACC = 15816.36 GEES
 (EXAGGERATED DEFORMATION FIGURE)



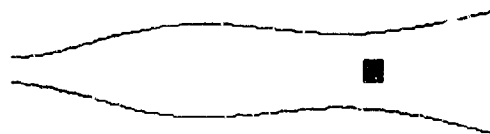
F. TIME = 3.000000E-03 SEC MAX DEFLECTION = 5.531002E-03 IN
 RAIL CURRENT = 899.997 KA TRAVEL = 3.00E-07 IN
 GRAND MAX DEFL = 6.67849E-03 IN MAX RAIL = 1249.997 KA
 MUZZLE VEL = .007786 MPS MAX ACC = 15816.36 GEES
 (EXAGGERATED DEFORMATION FIGURE)



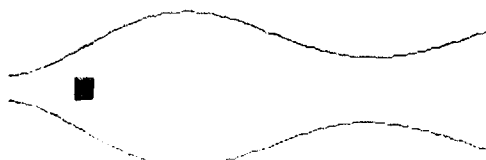
C. TIME = 1.999997E-03 SEC MAX DEFLECTION = 1.911646E-03 IN
 RAIL CURRENT = 1249.997 KA TRAVEL = 4.488281E-07 IN
 GRAND MAX DEFL = 6.67849E-03 IN MAX RAIL = 1249.997 KA
 MUZZLE VEL = .007786 MPS MAX ACC = 15816.36 GEES
 (EXAGGERATED DEFORMATION FIGURE)



G. TIME = 4.000012E-03 SEC MAX DEFLECTION = 3.394190E-03 IN
 RAIL CURRENT = 600.000 KA TRAVEL = 4.00E-07 IN
 GRAND MAX DEFL = 6.67849E-03 IN MAX RAIL = 1249.997 KA
 MUZZLE VEL = .007786 MPS MAX ACC = 15816.36 GEES
 (EXAGGERATED DEFORMATION FIGURE)



D. TIME = 2.500001E-03 SEC MAX DEFLECTION = 4.359903E-03 IN
 RAIL CURRENT = 1225 KA TRAVEL = 1.736548E-07 IN
 GRAND MAX DEFL = 6.67849E-03 IN MAX RAIL = 1249.997 KA
 MUZZLE VEL = .007786 MPS MAX ACC = 15816.36 GEES
 (EXAGGERATED DEFORMATION FIGURE)



H. TIME = 4.500017E-03 SEC MAX DEFLECTION = 6.57849E-03 IN
 RAIL CURRENT = 626.500 KA TRAVEL = 9.735017E-07 IN
 GRAND MAX DEFL = 6.67849E-03 IN MAX RAIL = 1249.997 KA
 MUZZLE VEL = .007786 MPS MAX ACC = 15816.36 GEES
 (EXAGGERATED DEFORMATION FIGURE)

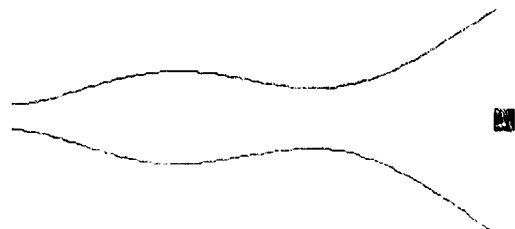


FIGURE 12 TRANSVERSE RAILGUN VIBRATION ANALYSIS, 3 MODES

AUTHOR INDEX

	<u>Page</u>
Baran, A.	284
Barker, G.	259
Becker, R.S.	129
Benzkofer, P.	44
Bornstein, J.A.	224
Brassard, T.V.	317
Bulman, D.N.	153
Bundy, M.L.	80
Cantor, J.	284
Carchedi, S.	284
Carofano, G.C.	10
Cascio, M.	328
Chang, C.W.	44
Chu, S.H.	204;
	344
Coates, S.A.	95
Cohen, H.	284
Cox, P.A.	203
Davidson, R.F.	300
Erline, T.F.	150
Gast, R.G.	175
Gibbs, B.	284
Groff, J.	284
Grumann, H.	245
Haug, B.T.	224
Homan, C.G.	317
Kerrisk, J.F.	300
Kregel, M.D.	150
O'Hara, G.P.	202;
	328
Penny, P.H.G.	151;
	241
Perry, J.A.	241
Petty, D.W.	242
Pflegl, G.A.	243
Polcyn, M.A.	203
Powell, S.E.	151
Schnurr, N.M.	300
Shabana, A.A.	44
Simkins, T.E.	64
Sneck, H.J.	30
Soifer, M.T.	129
Tadzbakhsh, I.G.	1
Walbert, J.N.	79;
	242
Yagla, J.J.	106
Zimmermann, G.	245

TECHNICAL REPORT INTERNAL DISTRIBUTION LIST

	NO. OF COPIES
CHIEF, DEVELOPMENT ENGINEERING BRANCH	
ATTN: SMCAR-CCB-D	1
-DA	1
-DC	1
-DM	1
-DP	1
-DR	1
-DS (SYSTEMS)	1
CHIEF, ENGINEERING SUPPORT BRANCH	
ATTN: SMCAR-CCB-S	1
-SE	1
CHIEF, RESEARCH BRANCH	
ATTN: SMCAR-CCB-R	2
-R (ELLEN FOGARTY)	1
-RA	1
-RM	1
-RP	1
-RT	1
TECHNICAL LIBRARY	5
ATTN: SMCAR-CCB-TL	
TECHNICAL PUBLICATIONS & EDITING UNIT	2
ATTN: SMCAR-CCB-TL	
DIRECTOR, OPERATIONS DIRECTORATE	1
ATTN: SMCWV-OD	
DIRECTOR, PROCUREMENT DIRECTORATE	1
ATTN: SMCWV-PP	
DIRECTOR, PRODUCT ASSURANCE DIRECTORATE	1
ATTN: SMCWV-QA	

NOTE: PLEASE NOTIFY DIRECTOR, BENET WEAPONS LABORATORY, ATTN: SMCAR-CCB-TL, OF ANY ADDRESS CHANGES.

TECHNICAL REPORT EXTERNAL DISTRIBUTION LIST

	NO. OF COPIES		NO. OF COPIES
ASST SEC OF THE ARMY RESEARCH AND DEVELOPMENT ATTN: DEPT FOR SCI AND TECH THE PENTAGON WASHINGTON, D.C. 20310-0103	1	COMMANDER ROCK ISLAND ARSENAL ATTN: SMCRI-ENM ROCK ISLAND, IL 61299-5000	1
ADMINISTRATOR DEFENSE TECHNICAL INFO CENTER ATTN: DTIC-FDAC CAMERON STATION ALEXANDRIA, VA 22304-6145	12	DIRECTOR US ARMY INDUSTRIAL BASE ENGR ACTV ATTN: AMXIB-P ROCK ISLAND, IL 61299-7260	1
COMMANDER US ARMY ARDEC ATTN: SMCAR-AEE	1	COMMANDER US ARMY TANK-AUTMV R&D COMMAND ATTN: AMSTA-DDL (TECH LIB) WARREN, MI 48397-5000	1
SMCAR-AES, BLDG 321	1	COMMANDER	
SMCAR-AET-O, BLDG 351N	1	US MILITARY ACADEMY	1
SMCAR-CC	1	ATTN: DEPARTMENT OF MECHANICS	
SMCAR-CCP	1	WEST POINT, NY 10996-1792	
SMCAR-FSA	1		
SMCAR-FSM-E	1	US ARMY MISSILE COMMAND	
SMCAR-FSS-D, BLDG 94	1	REDSTONE SCIENTIFIC INFO CTR	2
SMCAR-MSI (STINF)	2	ATTN: DOCUMENTS SECT, BLDG. 44B4	
PICATINNY ARSENAL, NJ 07806-5000		REDSTONE ARSENAL, AL 35898-5241	
DIRECTOR US ARMY BALLISTIC RESEARCH LABORATORY ATTN: SLCBR-DD-T, BLDG. 305	1	COMMANDER US ARMY FGN SCIENCE AND TECH CTR ATTN: DRXST-SD	1
ABERDEEN PROVING GROUND, MD 21005-5060		220 7TH STREET, N.E. CHARLOTTESVILLE, VA 22901	
DIRECTOR US ARMY MATERIEL SYSTEMS ANALYSIS ACTV ATTN: AMXSY-MP	1	COMMANDER US ARMY LABCOM	
ABERDEEN PROVING GROUND, MD 21005-5071		MATERIALS TECHNOLOGY LAB	
		ATTN: SLCMT-IML (TECH LIB)	2
COMMANDER HQ, AMCCOM		WATERTOWN, MA 02172-0001	
ATTN: AMCMC-IMP-L	1		
ROCK ISLAND, IL 61299-5000			

NOTE: PLEASE NOTIFY COMMANDER, ARMAMENT RESEARCH, DEVELOPMENT, AND ENGINEERING CENTER, US ARMY AMCCOM, ATTN: BENET WEAPONS LABORATORY, AMCAR CEB-11, WATERVLIET, NY 12189-4050, OF ANY ADDRESS CHANGES.

TECHNICAL REPORT EXTERNAL DISTRIBUTION LIST (CONT'D)

	NO. OF COPIES		NO. OF COPIES
COMMANDER US ARMY LABCOM, ISA ATTN: SLCIS-IM-TL 2800 POWDER MILL ROAD ADELPHI, MD 20783-1145	1	COMMANDER AIR FORCE ARMAMENT LABORATORY ATTN: AFATL/MN EGLIN AFB, FL 32543-5434	1
COMMANDER US ARMY RESEARCH OFFICE ATTN: CHIEF, IPO P.O. BOX 12211 RESEARCH TRIANGLE PARK, NC 27709-2211	1	COMMANDER AIR FORCE ARMAMENT LABORATORY ATTN: AFATL/MNG EGLIN AFB, FL 32542-5000	1
DIRECTOR US NAVAL RESEARCH LAB ATTN: MATERIALS SCI & TECH DIVISION CODE 26-27 (DOC LIB) WASHINGTON, D.C. 20375	1 1	METALS AND CERAMICS INFO CTR BATTELLE COLUMBUS DIVISION 505 KING AVENUE COLUMBUS, OH 43201-2693	1

NOTE: PLEASE NOTIFY COMMANDER, ARMAMENT RESEARCH, DEVELOPMENT AND ENGINEERING CENTER, US ARMY AMCOM, ATTN: BENT WEAPON LABORATORY, 1000 CAMP WATERS LIFT, NY 12189-4050, OF ANY ADDRESS CHANGES.